ISBN: 978-3-95450-223-3 ISSN: 2673-7000 doi:10.18429/JACoW-NAPAC2019-MOOHC2

THE US ELECTRON-ION COLLIDER ACCELERATOR DESIGNS

A. Seryi*, Jefferson Lab, Newport News, VA; F. Willeke, BNL, Upton, NY
Z. Conway, M. Kelly, B. Mustapha, U. Wienands, A. Zholents, ANL, Lemont, IL
E. Aschenauer, G. Bassi, J. Beebe-Wang, J.S. Berg, M. Blaskiewicz, A. Blednykh, J.M. Brennan,
S. Brooks, K.A. Brown, K.A. Drees, A.V. Fedotov, W. Fischer, D. Gassner, W. Guo, Y. Hao,
A. Hershcovitch, H. Huang, W.A. Jackson, J. Kewisch, A. Kiselev, C. Liu, V. Litvinenko,
H. Lovelace III, Y. Luo, F. Meot, M. Minty, C. Montag, R.B. Palmer, B. Parker, S. Peggs, V. Ptitsyn,
V.H. Ranjbar, G. Robert-Demolaize, T. Roser, S. Seletskiy, V. Smaluk, K.S. Smith, S. Tepikian,
P. Thieberger, D. Trbojevic, N. Tsoupas, E. Wang, W.-T. Weng, H. Witte, Q. Wu, W. Xu,
A. Zaltsman, W. Zhang, BNL, Upton, NY; D. Barber, DESY, Hamburg, Germany
T. Mastoridis, California Polytechnic State University, San Luis Obispo, CA
I. Bazarov, K. Deitrick, G. Hoffstaetter, Cornell University, Ithaca, NY
D. Teytelman, Dimtel Inc., Redwood City, CA; Z. Zhao, Duke University, Durham, NC
S. Benson, A. Bogacz, P. Brindza, M. Bruker, A. Camsonne, E. Daly, P. Degtyarenko, Ya. Derbenev,
M. Diefenthaler, J. Dolbeck, D. Douglas, R. Ent, R. Fair, D. Fazenbaker, Y. Furletova, R. Gamage,
D. Gaskell, R. Geng, P. Ghoshal, J. Grames, J. Guo, F. Hannon, L. Harwood, S. Henderson,
H. Huang, A. Hutton, K. Jordan, D. Kashy, A. Kimber, G. Krafft, R. Lassiter, R. Li, F. Lin,
M. Mamun, F. Marhauser, R. McKeown, T. Michalski, V. Morozov, E. Nissen, G. Park, H. Park,
M. Poelker, T. Powers, R. Rajput-Ghoshal, R. Rimmer, Y. Roblin, D. Romanov, P. Rossi, T. Satogata,
M. Spata, R. Suleiman, A. Sy, C. Tennant, H. Wang, S. Wang, C. Weiss, M. Wiseman, W. Wittmer,
R. Yoshida, H. Zhang, S. Zhang, Y. Zhang, Jefferson Lab, Newport News VA
E. Gianfelice-Wendt, S. Nagaitsev, Fermilab, Batavia, IL
J. Qiang, G. Sabbi, Lawrence Berkeley National Laboratory, Berkeley, CA
J. Maxwell, R. Milner, M. Musgrave, Massachussetts Institute of Technology, Cambridge, MA
Y. Hao, P. Ostroumov, A. Plastun, R. York, Michigan State University, East Lansing MI
V. Dudnikov, R. Johnson, Muons, Inc., IL
B. Erdelyi, P. Piot, Northern Illinois University, DeKalb, IL
S. De Silva, J. Delayen, C. Hyde, S. Sosa, B. Terzic, Old Dominion University, Norfolk, VA
D. Abell, D. Bruhwiler, I. Pogorelov, Radiasoft LLC, Boulder, CO
Y. Cai, Y. Nosochkov, A. Novokhatski, G. Stupakov, M. Sullivan, C. Tsai, SLAC, Menlo Park, CA
J. Fox, Stanford University, Menlo Park, CA; G. Bell, J. Cary, Tech-X Corp., Boulder, CO
P. Nadel-Turonski, Stony Brook University, Stony Brook, NY
J. Gerity, T. Mann, P. McIntyre, N. Pogue, A. Sattarov, Texas A&M University, College Station, TX

Abstract

With the completion of the National Academies of Sciences Assessment of a US Electron-Ion Collider, the prospects for construction of such a facility have taken a step forward. This paper provides an overview of the two site-specific EIC designs: JLEIC (Jefferson Lab) and eRHIC (BNL) as well as brief overview of ongoing EIC R&D.

EIC DESIGNS OVERVIEW

The Electron-Ion Collider – the instrument that will enable deeper understanding of quark-gluon structure of matter – was selected in the joint DOE-NSF U.S. Nuclear Physics Long Range plans of 2007 [1] and 2015 [2] as the top priority for R&D (2007) and new construction (2015). These recommendations were reinforced in 2018 by the National Academies of Science assessment of US-based EIC science [3]. The requirements of an EIC as described in the White Paper [4] include: "highly polarized (~70%) electron and nucleon beams; ion beams from deuteron to the heaviest nuclei (uranium or lead); variable center of mass energies from ~20 to ~100 GeV, upgradable to ~140 GeV; high collision luminosity of ~10^{33}-10^{34} cm^{-2}s^{-1}; possibilities of having more than one interaction region". A multi-laboratory collaboration is presently working on two site-specific EIC designs – eRHIC [5] and JLEIC [6]. Both designs are based on ring-ring approach and both benefit from existing Nuclear Physics infrastructure.

eRHIC design takes full advantage of the existing accelerator infrastructure of the RHIC complex at BNL, using the Yellow Ring of the RHIC heavy ion collider together with the entire hadron beam injector chain (Fig. 1). A new electron storage ring in the RHIC tunnel will provide polarized

---

* seryi@jlab.org

LHC STATUS AND PLANS

X. Buffat, CERN, Geneva, Switzerland

Abstract

Performance and accelerator physics challenges from LHC Run 2 are reviewed, along with the ongoing preparation and plans for LHC Run 3 and beyond.

INTRODUCTION

The Large Hadron Collider (LHC) [1] features two high energy hadron beams steered by superconducting magnets on circular trajectories of about 27 km. Those beams circulate with opposite directions in separate beam pipes and collide with a high rate at the centre of four detectors at distinct locations around the ring. As illustrated in Fig. 1, the first run of the LHC featured a maximum energy 4 TeV per beam. Following the consolidation of the splices of the main dipoles' superconducting busbars during the first Long Shut down (LS1) [2], the machine could be restarted for a second run at an energy of 6.5 TeV, just below the design energy of 7 TeV. The first section is dedicated to the performance of the LHC during its second run while the second section describes its High Luminosity upgrade, the HL-LHC [3], including the tests of some technologies performed during run 2. Eventually, some considerations about the challenges for the third run of the LHC will be discussed in the last section.

RUN 2

Figure 2 shows the peak luminosity achieved during run 2 of the LHC. The first year was dedicated to the recovery from the LS1 down with emphasis on high energy operation with a large number of bunches, i.e. with a 25 ns spacing between the bunches, enhancing electron cloud effects [4]. β^* and crossing angle were reduced in 2017 thus approaching the limit imposed by the physical aperture of the triplet and long-range beam-beam interactions as illustrated by Fig. 3. In this configuration the design luminosity could be exceeded. The β^* was further reduced in 2017 profiting from the experience acquired with the limits imposed by the non-linearities of the forces that the two beams exert on each other in the common chamber around each experiment, the so-called long-range beam-beam interactions [5]. Additionally, dynamic changes of the crossing angle during data acquisition phases were introduced to follow the relaxation of the limits as the beam intensity decays [6]. This strategy was further pushed in 2018 by reducing the β^* while the beams are colliding [7]. Not only these complex operational procedures improved the integrated luminosity by some percent, they also constitute valuable experience for the HL-LHC whose operational scenario is based on β^* levelling [3].

To achieve the low operational β^* of 30 to 25 cm, the Achromatic Telescopic Squeeze (ATS) [8] was used with a telescopic index of 1.3 to 1.6. An optics featuring a telescopic index of 3.1, corresponding to the HL-LHC baseline [3], was tested in dedicated experiments with high intensity beams. The correctability of this optics could be demonstrated as well as additional benefits including the enhancement of the effective strength of the arc octupole for Landau damping as well as for global compensation of long-range beam-beam effects [9].

The correction of the non-linear aberrations of the final focusing magnets became unavoidable for operation with β^* lower than 40 cm as their impact on the amplitude detuning, and consequently Landau damping, became significant. Additionally, the accuracy of the β^* was affected to a level that an imbalance could be detected in the luminosity delivered to the two main experiments [10]. A combination of K-modulation and AC-dipole measurements are used to obtain the required accuracy in the linear and non-linear optics correction [10, 11].

The energy stored in each beam reached 320 MJ during run 2. The sensitive equipment are protected from particle losses by a hierarchy of collimators. For both safe and efficient usage of the physical aperture, the collimators are placed as close to the beam as possible, yet respecting the hierarchy which is critical to maintain the efficiency of this multistage cleaning scheme. This imposes tight constraints on the orbit and optics correction, as well as its stability [12]. Efficient alignment and validation procedures were implemented to ensure the robustness of the operation with minimum commissioning time, e.g. the time dedicated to alignment was reduced from 20 hours to 30 minutes thanks to the implementation of BPM embedded in the collimator jaws and the usage of fully automated procedure [13]. The tightening of the collimation hierarchy improved the fraction of proton lost outside of the designated areas, i.e. the cleaning inefficiency, down to 10^{-4} which is a factor 6 lower than design [14]. The corresponding increase of the transverse impedance along with the reduction of the Landau damping generated by the octupoles at a higher energy makes the beam stability significantly more critical with respect to the first run of the LHC at 4 TeV. Nevertheless the brightness limit arising from transverse instabilities observed in run 1 [15, 16] was lifted mostly by the significant improvements in the control of linear coupling [17, 18] and by the improved controls of non-linearities above mentioned.

A significant fraction of the achievements in term of luminosity at the LHC can be attributed to the performance of its injectors, providing bunch trains with a 25 ns longitudinal spacing with transverse emittances more than twice as low as estimated at the design stage for the same intensity [19]. The brightest beam based on the Batch Compression Merging and Splitting (BCMS) [20] in the PS features slightly less bunches per train, 48 instead of 72. Consequently the total

ISBN: 978-3-95450-223-3	ISSN: 2673-7000	doi:10.18429/JACoW-NAPAC2019-MOYBA2

COMMISSIONING OF THE PHASE 2 AND PHASE 3 SuperKEKB / B-Factory

S. Nakamura†, KEK, 1-1 Oho, Tsukuba, Ibaraki 305-0801, Japan

Abstract

SuperKEKB is an asymmetric-energy electron-positron collider for Belle 2 experiment to search new phenomena in B-meson decays. Designed luminosity of the SuperKEKB is 40 times higher than that of KEKB. In order to accomplish the high luminosity, beam currents of the both beams are twice as large as that of the KEKB and vertical beta function at interaction point (IP) is squeezed down to bunch length by using the novel "nano-beam" collision scheme. After phase 1 commissioning without collision, final focus superconducting magnet system (QCS) and Belle 2 detector without a vertex detector were installed in interaction region (IR). Then phase 2 commissioning with beam collision to confirm the "nano-beam" scheme had been successfully completed in 2018. The vertex detector was installed in the Belle 2 detector before phase 3 commissioning. The phase 3 commissioning for the full-scale collider experiment had been started at 11 March 2019. We report the recent progress and accomplishments of the commissioning in phase 2 and 2019 spring operation of phase 3.

INTRODUCTION

The SuperKEKB is an asymmetric-energy electron-positron collider [1] constructed by 7 GeV electron high energy ring (HER) and 4 GeV positron low energy ring (LER). Its design luminosity is 8×10^{35} cm^{-2}s^{-1}, which is 40 times the performance of the previous KEKB B-factory, which had been operated for 11 years until 2010 [2]. To achieve such high intensity, the SuperKEKB is designed using a "nano-beam" scheme based on large-angle collision scheme, which was first proposed by P. Raimondi [3]. When sufficiently narrow beams are collided with a large crossing angle, longitudinal overlap of the colliding beams is shortened. As a result, the luminosity is expected to be increased by squeezing vertical beta-function at the IP (β_y^*). The "nano-beam" scheme does not require extremely short bunch length to increase the luminosity, so the bunch length comparable to that of the KEKB is allowed. The SuperKEKB is designed to achieve such high luminosity, which is 40 times higher than that of the KEKB, by doubling stored beam current and squeezing β_y^* down to 1/20 of the KEKB.

The SuperKEKB commissioning is divided by 3 stages; phase 1, phase 2 and phase 3. The phase 1 was started after the LER and the HER had been modified. The phase 1 commissioning [4] without the QCS and the Belle 2 detector was performed from February 1, 2016 to June 28, 2016. The subjects were low emittance tuning for new arc lattice, vacuum scrubbing for new vacuum vessels replace with ante-chambers, and beam background study for preparing to installation of the Belle 2 detector. The QCS and the Belle 2 detector except for the vertex detector were installed during a long shutdown between the phase 1 and the phase 2.

The phase 2 commissioning [5] was performed from March 19, 2018 to July 17, 2018 in order to confirm the "nano-beam" scheme. Prior to the main ring commissioning, beam commissioning of a positron damping ring had started on February 8, 2018. Specific luminosity as a function of bunch current product multiplied by number of bunches was improved by squeezing β_y^* down to 3 mm, which is almost half of the bunch length, in the phase 2 commissioning. After the phase 2 commissioning, the IR had been reconstructed in order to install the Belle 2 detector with the vertex detector into the IP.

First part of the following the phase 3 commissioning was performed from March 11, 2019 to July 1, 2019 with full-scale Belle 2 experiments. The major subjects of the 2019 spring operation were reestablishment of the luminosity performed in the phase 2 commissioning for further β_y^* squeezing, background study for improving the collision experiment data taking, and establishment of continuous beam injection with detector data taking to improve integral luminosity performance.

HARDWARE UPDATES

Between each commissioning states, the following hardware updates were carried out.

Between Phase 1 and Phase 2

System design of the QCS started in 2009 and construction was completed in March 2017. Figure 1 shows the layout of the superconducting magnets in two cryostats. The QCS consists of 55 superconducting magnets. The 25 magnets are assembled in QCS-L cryostats in the left side and the 30 magnets are assembles in QCS-R cryostats in the right side [6].

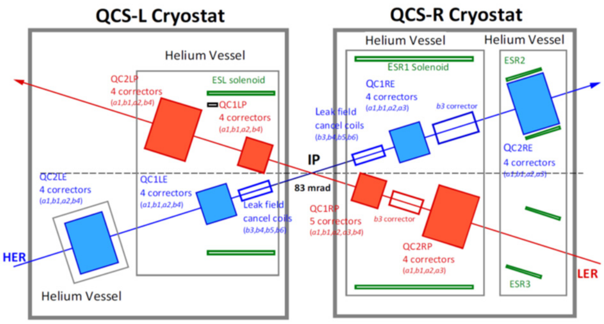

Figure 1: Layout of superconducting magnets in the QCS.

The QCS was commissioned from May to August 2017 after assembling cryostats into the Belle 2 detector without

---

† shu.nakamura@kek.jp

eRHIC DESIGN UPDATE*

C. Montag†, G. Bassi, J. Beebe-Wang, J.S. Berg, M. Blaskiewicz, A. Blednykh, J.M. Brennan,
S.J. Brooks, K.A. Brown, K.A. Drees, A.V. Fedotov, W. Fischer, D.M. Gassner, Y. Hao,
A. Hershcovitch, C. Hetzel, D. Holmes, H. Huang, W.A. Jackson, J. Kewisch, Y. Li, C. Liu,
H. Lovelace III, Y. Luo, F. Meot (F. Méot), M.G. Minty, R.B. Palmer, B. Parker, S. Peggs, V. Ptitsyn,
V.H. Ranjbar, G. Robert-Demolaize, S. Seletskiy, V.V. Smaluk, K.S. Smith, S. Tepikian,
P. Thieberger, D. Trbojevic, N. Tsoupas, W.-T. Weng, F.J. Willeke, H. Witte, Q. Wu, W. Xu,
A. Zaltsman, W. Zhang, Brookhaven National Laboratory, Upton, NY, U.S.A.,
E. Gianfelice-Wendt, Fermi National Accelerator Laboratory, Batavia, IL, U.S.A.,
Y. Cai, Y. Nosochkov, SLAC National Accelerator Laboratory, Menlo Park, CA, U.S.A.

Abstract

The future electron-ion collider (EIC) aims at an electron-proton luminosity of 10^{33} to 10^{34} cm^{-2}sec^{-1} and a center-of-mass energy range from 20 to 140 GeV. The eRHIC design has been continuously evolving over a couple of years and has reached a considerable level of maturity. The concept is generally conservative with very few risk items which are mitigated in various ways.

INTRODUCTION

The proposed electron-ion collider eRHIC will collide polarized electron and polarized light (proton, deuteron, or ^{3}He) or unpolarized heavy ion beams up to uranium at center-of-mass energies ranging from 20 to 140 GeV (electron-proton equivalent). The projected e-p luminosity of the facility reaches 10^{34} cm^{-2}sec^{-1}, thus meeting all the requirements laid out in the U.S. Nuclear Physics community's White Paper [1]. The machine design is based on the existing RHIC facility with its 3.8 km circumference tunnel and its hadron injector complex. The eRHIC hadron beam will be stored in the superconducting "Yellow" RHIC ring, while a new electron storage ring and a rapid cycling synchrotron [2] will be added in the same tunnel. Table 1 lists the main electron-proton parameters of eRHIC at a center-of-mass energy of 105 GeV, where the highest luminosity is reached.

INTERACTION REGION DESIGN

The eRHIC interaction region [3] is based on superconducting magnets to focus the beams at the interaction point, with vertical β-functions as low as a few centimeters. The peak magnetic fields of these quadrupoles, defined here as $B_{\rm peak} = R \times g$, where R and g denote the aperture radius and the gradient, respectively, do not exceed 6 T. Therefore, all magnets can be built using NbTi superconductors. Furthermore, only a few magnets need to be built as collared magnets, while the majority can be manufactured using direct-wind technology.

Table 1: eRHIC Electron-Proton Parameters at 105 GeV Center-of-Mass Energy

	proton	electron
no. of bunches	1160	
energy [GeV]	275	10
bunch intensity [10^{10}]	6.9	17.2
beam current [A]	1.0	2.5
$\epsilon_{\rm RMS}$ hor./vert. [nm]	9.6/1.5	20.0/1.2
$\beta^*_{x,y}$ [cm]	90/4	43/5
b.-b. param. hor./vert.	0.014/0.007	0.073/0.100
σ_s [cm]	6	2
$\sigma_{{\rm d}p/p}$ [10^{-4}]	6.8	5.8
$\tau_{\rm IBS}$ long./transv. [h]	3.4/2.0	N/A
L [10^{33} cm^{-2}sec^{-1}]	10.05	

Separation of the two beams is accomplished by a 25 mrad crossing angle. A spectrometer dipole on the forward side of the ±4.5 m long central detector is equipped with detector components to increase the forward acceptance of the detector. The large aperture of this magnet is shared by both the eletron and the hadron beam. A bucking coil shields the electron beam from the magnetic field of the spectrometer. A dipole magnet on the forward side of the detector separates the hadron beam from the ±4 mrad forward neutron cone which is then detected in the zero degree calorimeter. The aperture of the electron quadrupoles on the rear side is large enough to accommodate the synchrotron radiation fan generated from a 12.5σ electron beam in the quadrupoles on the forward (incoming) side of the detector. Luminosity monitoring is based on detection of Bethe-Heitler photons generated in the interaction. Figure 1 shows a schematic view of the eRHIC interaction region.

ELECTRON STORAGE RING

The electron storage ring is based on FODO cells using conventional room-temperature magnets. The bending sections are realized as so-called super-bends, where each dipole is actually comprised of three individual magnets - two long dipoles with a short magnet in-between. The purpose of this arrangement is to generate additional synchrotron radiation damping and enhance the equilibrium emittance at energies

---

* Work supported by Brookhaven Science Associates, LLC under Contract No. DE-AC02-98CH10886 with the U.S. Department of Energy.

† montag@bnl.gov

ISBN: 978-3-95450-223-3 ISSN: 2673-7000 doi:10.18429/JACoW-NAPAC2019-MOYBA5

WEAK-STRONG SIMULATION OF BEAM-BEAM EFFECTS IN SUPER PROTON-PROTON COLLIDER

L.J. Wang†, [1], J.Y. Tang, Institute of High Energy Physics, Beijing, China
T. Sen, Fermi National Accelerator Laboratory*, Batavia, USA
[1]visiting student at Northern Illinois University, DeKalb, USA

Abstract

A Super Proton-Proton Collider (SPPC) that aims to explore new physics beyond the standard model is planned in China. Here we focus on the impact of beam-beam interactions in the SPPC. Simulations show that with the current optics and nominal tunes, the dynamic aperture (DA) with all the beam-beam interactions is less than 6 σ, the dominant cause being the long-range interactions. First, we show the results of a tune scan done to maximize the DA. Next, we discuss the compensation of the long-range interactions by increasing the crossing angle and also by using current carrying wires.

INTRODUCTION

The super proton proton collider (SPPC) is a 100 km circular accelerator that aims to reach a luminosity of 1.01^{35} $cm^{-2}s^{-1}$ [1].Two proton beams with a design energy of 37.5 Tev travel in opposite directions in separate beam pipes, then collide in 2 interaction regions (IR), one where the beams collide in the horizontal plane, and at the other in the vertical plane. A major limit to the luminosity arises from the beam beam effects, the nominal beam beam parameter for each IP is 0.0075. In addition to the head-on interaction at each IP, there are 82 long-range interactions in each IR [2]. Table 1 lists the main SPPC nominal parameters.

Table 1: SPPC Nominal Parameters

parameter	Value
Beam energy at collisions [TeV]	37.5
Number of bunches	10080
$\beta *$ [m]	0.75
Crossing angle[μrad]	110
Intensity [10^{11} p/bunch]	1.5
Norm. trans. emittance [μm]	2.4
Peak luminosity [10^{35} $cm^{-2} \cdot s^{-1}$]	1.01

TUNE FOOTPRINTS AND DYNAMIC APERTURE

In the nominal lattice design, the tune is (120.31, 117.32), the fractional parts being the same as in the LHC. At present, the only nonlinearities in the machine lattice are from the chromaticity correcting sextupoles. Figure 1 shows the beta functions in one IR. Figure 2 shows the plot of the LR separations at all the beam-beam interactions in each IR. The minimum separation is 9~10 σ, which occurs at 20 parasitic interactions in each IR. The weak-strong simulations reported here are done using the code BBSIM [3]. Figure 3 shows the tune footprint from the head-on and long-range interactions.

Dynamic aperture (DA) calculations are done in six dimensional phase space with particles tracked for a million turns. Tracking with only the sextupoles and the head-on interactions show that the DA is the same as the physical aperture of 23.6 σ. Adding the long-range interactions reduces the DA to 5.5 σ, which is unacceptably low. Since this model does not yet include all the magnetic nonlinearities or errors, we have to find ways to increase the DA.

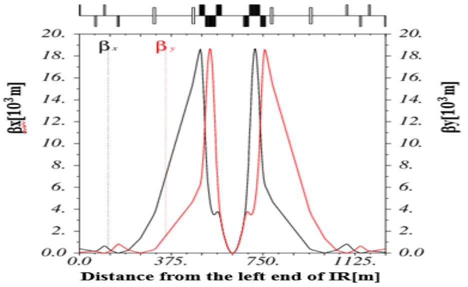

Figure 1: The beta functions in an IR.

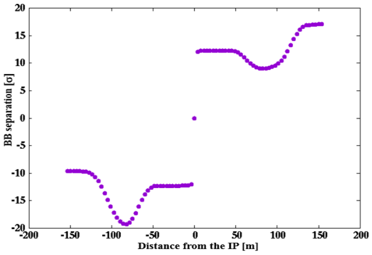

Figure 2: The BB separation of all LR interactions are normalised by its horizontal beam size in IR.

---

† wanglj@ihep.ac.cn

* Operated by Fermi Research Alliance, LLC under Contract No. DeAC02-07CH11359 with the United States Department of Energy.

ACCELERATOR PERFORMANCE DURING THE BEAM ENERGY SCAN II AT RHIC IN 2019

C. Liu*, I. Blacker, M. Blaskiewicz, K.A. Brown, D. Bruno, K.A. Drees, A.V. Fedotov, W. Fischer,
C.J. Gardner, C. Giorgio, X. Gu, T. Hayes, H. Huang, R. Hulsart, D. Kayran, N. Kling, Y. Luo,
D. Maffei, B. Martin, G. Marr, A. Marusic, K. Mernick, R. Michnoff, M. Minty, C. Montag,
J. Morris, C. Naylor, S. Nemesure, I. Pinayev, S. Polizzo, V. Ranjbar, D. Raparia,
G. Robert-Demolaize, T. Roser, J. Sandberg, V. Schoefer, F. Severino, T. Shrey, K. Smith,
S. Tepikian, P. Thieberger, A. Zaltsman, K. Zeno, I. Zhang, W. Zhang,
Brookhaven National Lab, Upton, NY, USA

Abstract

RHIC provided Au-Au collisions at beam energies of 9.8, 7.3, 4.59 and 3.85 GeV/nucleon during the first year of the Beam Energy Scan II in 2019. The physics goals at the first two higher beam energies were achieved. At the two lower beam energies, bunched electron beam cooling has been demonstrated successfully. The accelerator performance was improved compared to when RHIC was operated at these energies in earlier years. This article will introduce the challenges to operate RHIC at low energies and the corresponding countermeasures, and review the improvement of accelerator performance during the operation in 2019.

INTRODUCTION

The Beam Energy Scan was proposed [1, 2] to explore the nature of the transformation from Quark-Gluon plasma (QGP) to the state of hadronic gas [3]. In particular, the Beam Energy Scan at relatively low energies at RHIC is designed to investigate the first-order phase transition and determine the location of a possible critical point. The beam energy scan I (BES-I) [4] was completed in 2014 and resulted in improved understanding of many physics phenomena [5]. However, the transition between QGP and hadronic gas has not been understood yet due to limited statistics at lower energies. Therefore, the beam energy Scan II (BES-II) was conceived with a planned luminosity improvement of factor of ~ 4 at the same beam energies as BES-I (3.85, 4.59, 5.75, 7.3 and 9.8 GeV/nucleon).

In the first year of BES-II, RHIC operated in colliding mode at 9.8 and 7.3 GeV/nucleon for physics data taking, also at 4.59 and 3.85 GeV/nucleon for electron cooling commissioning. In addition, RHIC also operated in fixed target mode as part of the Beam Energy Scan II operation, of which the operational experience is reported separately [6].

MACHINE CONFIGURATION

At BES-II energies, the beam lifetime is limited by some physical effects [7–9], of which the most significant are intrabeam scattering (IBS), space charge, beam-beam, and persistent current effects. To combat IBS, Low Energy RHIC electron Cooling (LEReC) has been commissioned at beam energies 3.85 and 4.59 GeV/nucleon. The physics program with operation of LEReC is planned for 4.59 GeV/nucleon in 2020 and 3.85 GeV/nucleon in 2021. The progress of LEReC cooling is briefly introduced in the "LEReC cooling" section in this report and more details are available in [10].

To reduce the space charge effect, three 9 MHz cavities were used instead of the 28 MHz cavities at 3.85 and 4.59 GeV/nucleon to lengthen the bunches to 50 ns full width. As a consequence, the spacing between consecutive bunches is reduced to 60 ns. Therefore, the injection kicker termination was reconfigured [11, 12] to shorten the rise time and also to flatten the top part of the kicker pulse. The 28 MHz cavities were used for operation at 9.8 and 7.3 GeV/nucleon to concentrate the collision events in a short vertex region [13].

The working points at 9.8 and 7.3 GeV/nucleon were chosen to be (0.093, 0.085) for a large tune space for the space charge dominated beams with beam-beam effects [9]. The lifetime of the first injected beam is better with this working point instead of (0.235, 0.229), which is the nominal heavy working point, when injecting the second beam. The working point at 3.85 and 4.59 GeV/nucleon was set at (0.235, 0.229) because the lifetime was better when the ion beams were interacting with the electron beam for cooling in addition to their collision at the experiment [10].

To reduce the persistent current effects, demagnetization cycles were implemented for all above-mentioned beam energies in 2019. The persistent current induced magnetic field errors and their variations in time were significantly reduced [14]. The switching between physics mode (at 9.8 and 7.3 GeV/nucleon) and LEReC commissioning mode (at 4.59 and 3.85 GeV/nucleon) were as frequent as twice a day. Therefore, quickly establishing stable machine condition was essential. This was achieved by a combination of mode-switch, automatic restoration of system settings for different energies, and demagnetization cycles (Fig. 1).

ACCELERATOR PERFORMANCE

To reach the design bunch intensity, 6 bunches were merged into 1 in AGS for operation at 9.8 and 7.3 GeV so that 2 bunches were injected into RHIC during each AGS cycle. As a comparison, nominally only 2 bunches are merged into 1 in AGS at 4.59 and 3.85 GeV/nucleon, however, 6 bunches can be extracted from AGS during each cycle therefore the

---

* cliu1@bnl.gov

RECENT ADVANCE IN ECR ION SOURCES*

G. Machicoane†, N. Bultman, P. Morrisson, M. Omelayenko, X. Rao
Facility for Rare Isotope Beams, Michigan State University, East Lansing, MI, USA
D. Arbaelez, A. R. Hafalia, H. Pan, S. Prestemon
Lawrence Berkeley National Laboratory, Berkeley, CA, USA

Abstract

Since their inception in the 1970s, Electron Cyclotron Resonance (ECR) ion sources have been and continue to be used extensively as injector for ion accelerators due in part to the high continuous wave (CW) current of high charge state ions that can be extracted but also because of many operational advantages including current stability, long lifetime and the availability of a wide range of primary beams from many gas and solid elements. Many of the next generation ion accelerators now require very intense beams of highly charged ion and as a result need to develop state of the art ECR ion sources. This paper discuss beam requirements for production of high intensity heavy ions and then focus on the 28 GHz ECR ion source in development for the facility for Rare Isotope beams (FRIB) at Michigan State University and discuss new concept and challenges for developing and operating ECR ion source at frequencies beyond 28 GHz.

INTRODUCTION

The Facility for Rare Isotope Beam (FRIB) built on the campus of Michigan State University (MSU) is based on a superconducting-RF linear accelerator designed to reach a beam power of 400 kW on the production target. Installation and commissioning of the accelerator is making significant progress and a beam energy over 20 MeV/u has already been reached after acceleration through the first linac segment as reported in [1, 2]. Based on the number of secondary beams and reaction products that can be generated, heavy ion beams such as Uranium represent one of the most interesting and important primary beams to develop and it is also the most challenging beam to develop at high intensity from the ion source. The choice of the charge state selected depends on the intensity that can be extracted from the ion source, the final beam energy and the overall acceleration scheme. For FRIB, the Superconducting linac is made of three accelerating sections. A charge stripper is located after the first accelerating section where the beam energy reaches about 20 MeV/u. Because the charge state distribution after the stripper is weakly dependent on the beam energy, the choice of the selected charge state from the ion source is not critical as long as the Q/A meet the injection criteria for the RFQ (Q/A> 1/7). More important is the beam intensity requirement on the ion source of 13 pμA for FRIB in order to reach the final beam power of 400 kW. However, the FRIB accelerator is also designed to accelerate two charge states which lesser the intensity requirement on the ion source. These considerations are important to ensure reliable and long operation from the ion source. Other project like the Heavy Ion Accelerator Facility (HIAF) in China or the Radioactive Isotope Beam Factory (RIBF) in Japan have even higher beam intensity requirement from the ion source which has to deliver 30 pμA of CW ^{238}U^{35+} and 50 pμA of ^{238}U^{35+} in pulsed operation [3] for HIAF and about 15 pμA of ^{238}U^{35+} for RIBF. These intensity requirements combined with the intrinsic advantage of starting with a higher charge state to gain more energy or help lower the cost of the accelerator continues to drive the development of ECR ion source and will be essential for the next generation of heavy ion accelerators.

FEATURES OF AN EFFICIENT ECRIS

Ion Sources for highly charged ions such as ECR or Electron Beam Ion Sources (EBIS) rely on electron impact ionization. Because the cross section for single ionization are much greater than double ionization, high charge states are created in a stepwise process requiring confinement times for the ions, τi of a few ms to tens of ms for very high charge states. Also ionization cross section decrease quickly with charge state while charge exchange cross section are large and mostly depends on the neutral gas pressure. Therefore unlike high current singly charged ions sources which operate at high pressure, ECR have to operate a very low gas pressure. A higher operating pressure has to be compensated by a higher ionization rate to translate into higher current, requiring to increase the electronic density n_e. The product of $n_e \tau_i$ (cm^{3}s^{-1}) represent a fundamental requirement for an ion source to produce highly charged ions [4].

Long ion confinement times in an ECR relies on a magnetic trap achieved by creating a minimum-B configuration using a combination of solenoids along the longitudinal axis and magnetic multipole, usually a sextupole, in the radial direction. Loss cones using the axial magnetic maxima and minima can be defined using the mirror ratio R=Bmax/Bmin. The electrons are heated by interacting with the injected microwave when crossing the closed ECR surface usually referred to as B_{ECR}, where the electron Larmor frequency (ω_L) is equal to the wave frequency (ω_{RF}) according to

$$\omega_L = \frac{eB}{m_e} = \omega_{RF} \qquad (1)$$

Increasing the electronic density n_e is usually achieved by increasing the microwave power injected. However there are some limitations as to what density can be achieved for a given magnetic trap and operating excitation frequency

---

[*] Work supported by the U.S. Department of Energy (DOE) Office of Science under Cooperative Agreement DE-SC0000661

[†] machicoane@frib.msu.edu

PROGRESS IN Nb_3Sn SRF CAVITIES AT CORNELL UNIVERSITY*

R. D. Porter[†], H. Hu, M. Liepe, J. Tao, N. Stilin, Z. Sun
Cornell Laboratory for Accelerator-Based Sciences and Education (CLASSE),
Ithaca, NY, USA

Abstract

Niobium-3 Tin (Nb_3Sn) is the most promising alternative material for next-generation SRF cavities. The material can obtain high quality factors ($> 10^{10}$) at 4.2 K and could theoretically support ≈ 96 MV/m operation of a TESLA elliptical style cavity. Current Nb_3Sn cavities made at Cornell University achieve high quality factors but are limited to about 17 MV/m in CW operation due to the presence of a surface defect. Here we examine recent results on studying the quench mechanism and propose that surface roughness is a major limiter for accelerating gradients. Furthermore, we discuss recent work on reducing the surface roughness including chemical polishing, modification of material growth, and tin electroplating.

INTRODUCTION

Niobium-3 tin (Nb_3Sn) is the most promising alternative material to niobium (Nb) for superconducting radio frequency (SRF) accelerator cavities. This material has nearly twice the critical temperature (T_c = 18 K *vs.* 9.2 K [1]) compared to Nb and nearly twice the superheating magnetic field (≈ 425 mT *vs.* ≈ 220 mT [2]). The high T_c allows for higher quality factors (Q) and for 4.2 K operation where complex cryogenic equipment can be removed from the accelerator or cryocoolers can be used for small scale accelerators. The increased superheating field allows for larger accelerating gradients (E_{acc}), with the potential to reach ≈ 96 MV/m in a TESLA style elliptical cavity.

Cornell University has a strong program to create Nb_3Sn accelerator cavities [3–7]. Due to the material being brittle it cannot be shaped after it is created. Instead, a niobium cavity is formed and then coated in Nb_3Sn. This is done by vaporizing Sn in a higher temperature vacuum furnace and allowing it to absorb into the Nb.

Figure 1 shows a temperature profile of the coating process [8]. The first stage is a nucleation step where Sn_2Cl is vaporized at 500 C for 5 hrs. This material has a much higher vapor pressure at 500 C then Sn and decomposes on the surface of the cavity to leave Sn nucleation sites. After the nucleation phase the temperature of the cavity is raised to ≈ 1120 C for a coating step. Simultaneously a crucible of Sn is raised to 1400 C to increase the flux of Sn vapor reaching the cavity. Coating occurs for 1.5 hrs and then the Sn crucible heater in turned off and the temperature drops to 1120 C where the Sn vapor pressure is much lower. The cavity is held at this temperature for 1 hr as an annealing step to allow excess Sn to absorb into the cavity. After the process is complete the cavity is covered in 2–3 µm of Nb_3Sn.

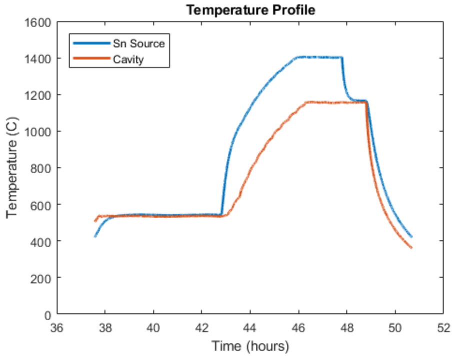

Figure 1: Temperature profile from the coating of a Nb_3Sn cavity. Both the temperature of the cavity and the Sn source are shown.

Current state-of-the art Nb_3Sn cavities at Cornell university achieve a 4.2 K quality factor of $2 \cdot 10^{10}$ and a maximum accelerating gradient of 15–18 MV/m at 1.3 GHz. Figure 2 shows an example Q *vs.* E_{acc} plot. The accelerating gradient achieves a usable field level but is much below the theoretical limit. Increasing the quench field is active area of research [9].

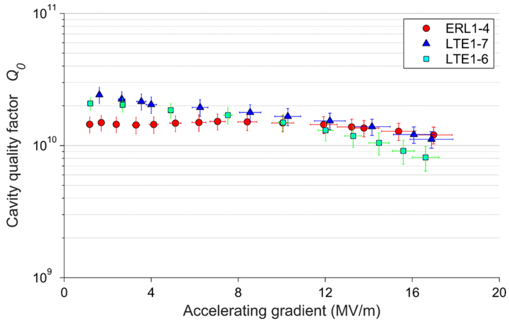

Figure 2: Q *vs.* E at 4.2 K of several 1.3 GHz TESLA elliptical cavities made at Cornell University.

Recent progress at Cornell University has focused on increasing the frequency [10, 11] and accelerating gradients of these cavities. In this paper we discuss recent progress in understanding the quench field. We propose that reducing the surface roughness of Nb_3Sn cavities should increase the achievable accelerating gradient. Finally, we discuss recent results in creating smoother Nb_3Sn.

---

[*] This workwas supported by U.S. DOE award DE-SC0008431 (cavity tests and development). This work was supported by the U.S. National Science Foundation under Award PHY-1549132, the Center for Bright Beams (sample coating and analysis). This work made use of the Cornell Center for Materials Research Shared Facilities which are supported through the NSF MRSEC program (DMR-1719875).

[†] rdp98@cornell.edu

LARGE-SCALE DEWAR TESTING OF FRIB PRODUCTION CAVITIES: STATISTICAL ANALYSIS*

C. Zhang[#], W. Chang, W. Hartung, S. Kim, D. Norton, J. Popielarski, K. Saito, J. Schwartz, T. Xu
Facility for Rare Isotope Beams, Michigan State University, East Lansing, MI, USA

Abstract

The Facility for Rare Isotope Beams (FRIB) requires a driver linac with 324 superconducting cavities to deliver ion beams at 200 MeV per nucleon. About 1/3 of the cavities are quarter-wave resonators (QWRs, 80.5 MHz); the rest are half-wave resonators (HWRs, 322 MHz). FRIB cavity production is nearly complete, with more than 90% of the required cavities certified for installation into cryomodules. We have accumulated a large data set on performance of production QWRs and HWRs during Dewar certificating testing of jacketed cavities. In this paper, we will report on the data analysis, including statistics on the BCS resistance, residual resistance, and *Q*-slope. Additionally, we will discuss performance limitations and conditioning (multipacting, field emission).

INTRODUCTION

The Facility for Rare Isotope Beams' (FRIB) driver linac requires 4 types of superconducting radio-frequency (SRF) cavities: quarter wave resonators (QWRs) with β = 0.043 and 0.086 and half wave resonators (HWRs) with β = 0.29 and 0.54 [1, 2]. Drawings of the cavities are shown in Fig. 1; cavity parameters and operating goals are given in Table 1. The resonators are made of high-purity niobium sheet (RRR>250) by deep drawing and electron beam welding. Cavities with helium jackets are delivered to FRIB by industrial suppliers, and the final preparation steps are done at Michigan State University (MSU) [3, 4].

Cryogenic RF testing of the FRIB cavities is done in the SRF vertical test area (VTA) at MSU. Figure 2 shows a β = 0.086 QWR in the magnetically-shielded test cryostat. About one hour is needed for the cavity to cool down from the room temperature to 4.3 K. At 4.3 K, continuous wave (CW) and modulated RF measurements are done and multipacting is conditioned, if needed. During the cool-down from 4.3 K to 2 K, Q_0 is measured at approximately constant field. At 2 K, CW and modulated measurements are repeated and field emission is conditioned, if needed [3]. Statistical data on production resonator performance has been gathered for a large number of cavity tests. Data analysis results and performance limitations will be discussed in this paper.

Figure 1: Isometric sectional views of jacketed cavities.

Table 1: FRIB Production Resonators: RF Parameters, Operating Goals, and Cavity Counts (f_0 = resonant frequency; Q_0 = intrinsic quality factor; E_a = accelerating gradient; E_p = peak surface electric field; B_p = peak surface magnetic field)

Cavity Parameters				
Type	QWR	QWR	HWR	HWR
β	0.043	0.086	0.29	0.54
f_0 (MHz)	80.5	80.5	322	322
E_p/E_a	6.1	6.0	4.3	3.6
B_p/E_a [mT/(MV/m)]	10.8	12.4	7.7	8.6
Goals for linac operation (2 K)				
E_a (MV/m)	5.1	5.6	7.7	7.4
E_p (MV/m)	30.8	33.4	33.3	26.5
B_p (mT)	54.6	68.9	59.6	63.2
Q_0	1.2E9	1.8E9	5.5E9	7.6E9
Cavity Certification Requirements (2 K)				
E_a (MV/m)	6.1	6.7	9.2	8.9
Q_0	1.4E9	2.0E9	6.7E9	9.2E9
Number of Cavities				
Needed	12	92	72	148
Tested	16	106	75	145
Certified	16	106	72	138
Completion	100%	100%	100%	93%

---

*Work supported by the U.S. Department of Energy Office of Science under Cooperative Agreement DE-SC0000661.
[#] zhangco@frib.msu.edu

CHARACTERIZATION AND PERFORMANCE OF PLASMA WINDOW FOR GAS FLOW RESTRICTION IN DIFFERENT GEOMETRIES *

A. LaJoie†
National Superconducting Cyclotron Laboratory, Michigan State University, East Lansing, MI, USA
J. Gao, F. Marti
Facility for Rare Isotope Beams, Michigan State University, East Lansing, MI, USA

Abstract

The plasma window (PW) is a DC cascaded arc whose function is to restrict gas flow from a high pressure (order of 100 torr) region to a low pressure region (order of 100 millitorr) without the use of any solid separation. As a result, the PW allows a greater pressure to be maintained than otherwise would be possible, a beneficial characteristic for gas targets such as charge strippers for heavy ion accelerators, since the higher pressures enable the gas stripper to be shorter while allowing the same amount of interactions in the stripping region. The reduction in flow rate is directly related to the increase in gas temperature resulting from the power deposition into the plasma (order of 10 kW) via the cathodes, resulting in a dramatically increased viscosity. The flow rate reduction, depends upon the properties of the plasma, including the electron density and temperature, pressure, and electrical conductivity. As a result, understanding these plasma properties in multiple cascaded arc geometries – in this work having either 6 mm or 10 mm channel diameter – provides a means of understanding how the PW can be optimized for a given design choice. Determinations of these plasma properties for different conditions are shown, and results are compared with a simulation created in PLASIMO, which has been shown to yield comparable properties to measurements in an argon arc.

INTRODUCTION

One challenge facing high intensity heavy ion charge strippers is the need for charge stripping media that are able to sustain continuous high energy depositions over durations in excess of a week. Due to the energy deposition being so high in facilities that are pushing the beam intensity frontier, such as the upcoming Facility for Rare Isotope Beams, traditional solid strippers do not meet this survival time criterion and liquid or gas stripping alternatives must be sought [1]. Gas charge strippers require some design constraints which make their implementation challenging. Studies performed by RIKEN's charge stripper group indicate that generally lower mass gases yield the highest equilibrium beam charge state distributions, as summarized in Table 1 [2, 3].

Table 1: Equilibrium Charge States (Q_e) for ^{238}U

Material	**Q_e at 11 MeV/nucleon**
He	66+
Ar	56.6+
N_2	56+
CO_2	55.7+
C (solid)	72+

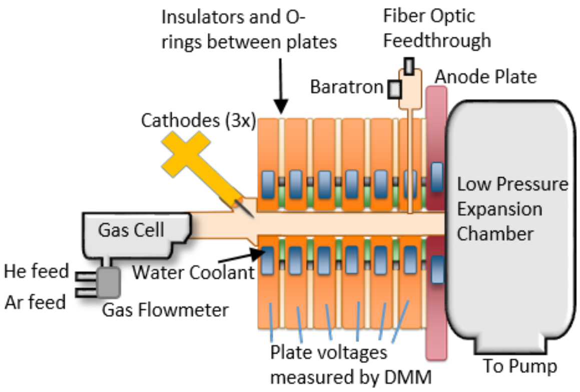

Figure 1: Key components of the plasma window. The gas cell represents the gas charge stripper chamber. Plasma and ion beam travel coaxially through the channel. The final plate before the anode illustrates the diagnostic plate setup with pressure and optical emission measurement ports.

The chamber must be at a high pressure to give a target thickness great enough to achieve charge state equilibration [1, 3], and the chamber entrance large enough to accept the beam without scraping. However, the combination of these features results in a high gas flow rate which must be recycled by pumps so as to transition to beamline pressures of 10^{-8} torr. This challenge is greatest for the low mass gases like helium due to their high diffusion rate. The PW is a device that can in part mitigate this by heating the gas, increasing viscosity [4]. This work focuses on argon and helium and investigates the nature of the effectiveness of the flow rate reduction phenomena. Flow rate in this work is measured in standard liters per minute (SLM).

EXPERIMENT

The plasma window is a DC cascaded arc whose channel is coaxial with the beam, in which a plasma significantly heats and plugs the flow of gas out of the charge stripping chamber. It is comprised of three needle cathodes, several stacked metal plates, and finally an anode plate for a total length of about 7 cm. More details on the components and structure is described in [5]. This work will also briefly

---

* Work supported by NSF Award PHY-1565546.

† lajoie@nscl.msu.edu

X-RAY DETECTOR ARRAY FOR SPATIAL AND TEMPORAL DIAGNOSTIC AT THE LANSCE LINAC*

M. Sanchez Barrueta†, G.O. Bolme, J.T.M. Lyles, J.E. Zane, AOT-Division,
Los Alamos National Laboratory, Los Alamos, NM, USA
R.Z. Pinsky, University of Michigan, Ann Arbor, MI, USA

Abstract

A recent industrial development has made possible the use of chip-scale radiation detectors by combining a Cerium-doped Lutetium based scintillator crystal optically coupled with a Silicon Photomultiplier (SiPM) as a detector. At the Los Alamos Neutron Science Center (LANSCE), there has been an ongoing effort to determine the location of high voltage breakdowns of the accelerating radio-frequency field inside of an evacuated resonant cavity. Tests were conducted with an array of 8 X-ray detectors with each detector observing a cell of the Drift Tube Linac (DTL) cavity. The array can be moved along the DTL cavity and record X-ray emissions from a section of the cavity and their timing with respect to the RF field quench using a fast 8 channel mixed-signal oscilloscope. This new diagnostic allowed us to map the most energetic emissions along the cavity and reduce the area to investigate. A thorough visual inspection revealed that one of the ion pump grating welds in the suspected area was exposing a small gap and melting copper on both sides. Sparking across this discontinuity is believed to be a source of electrons that drive the high voltage breakdowns in the drift tube cells.

DETECTOR AND TESTS

A photon absorbed in silicon will create an electron-hole pair. Reverse-biasing a photodiode will set up an electric field across the depletion region that will accelerate the electron towards the cathode and the hole towards the anode. When a sufficiently high electric field is applied to the depletion region, a single photon can trigger a self-perpetuating ionization cascade through which the silicon becomes conductive. A series resistor will reduce the electric field on the photodiode when it breaks down and limits the current caused by the photon absorption. Once the current has been stopped, the photodiode can recharge to the nominal voltage, ready to detect another photon. The time it takes to recharge to nominal voltage is the recovery time. An SiPM uses a multitude of these photodiode/resistor pairs (microcells) in parallel. The sum of currents from the microcells determines the magnitude of the photon flux [1]. Low voltage operation, inexpensive development, fast response time, lack of hygroscopic deterioration and a square millimeter size make these detectors a reasonable alternative to a traditional Thallium-doped Sodium Iodide scintillator coupled with a photomultiplier tube. Industries such as positron emission tomography, security scanners, and high energy physics calorimeters are already benefiting from the use of these devices.

Detector Construction

The chosen detector was a Ketek PM1125-WB, contain-ing 1600 microcells and with a recovery time of 30 ns. The detector alone can be used to detect high energy X-rays, but for the purposes of our application, it was used as a readout for a Cerium doped Lutetium-based crystal ($Lu_{1.8}Y_{.2}SiO_5$:Ce) LYSO scintillator that has a decay time of 40 ns. The detector output is a current, the amplitude of which relates to the number of photons received in the cell, which in turn relates to the energy of the incident X-rays. This current output was converted into a voltage and am-plified via an Advatech AMP-0611 preamplifier (Fig. 1) into a signal that could be displayed and compared with an oscilloscope. The whole ensemble was placed into a small light-sealed box (Fig. 2) with connectors that can supply the 28 VDC for the SiPM reverse biasing and the 9 VDC necessary for the preamplifier power supply.

Figure 1: Scintillator mounted on SiPM detector (left), LYSO scintillator, SiPM detector and preamplifier.

Figure 2: Packaging of the full detector. The hole on the front was aligned with the collimator in the shielding and covered with opaque tape so that light would not trigger the detector.

High Voltage Breakdown Location

One of the evacuated cavities of the LANSCE 100 MeV DTL has seen an increase on the number of RF cavity field faults (fast discharge of energy stored in the cavity) for the last few years. RF field breakdowns occur between points with the greatest field gradient, which in the case of the cavity, happens to be between the drift tubes. When a breakdown occurs, the resulting spark produces light inside

---

* Work supported by the United States Department of Energy, National Nuclear Security Agency, under contract No. 89233218CNA000001
† maria.sanchez.barrueta@lanl.gov

LCLS-II SC LINAC: CHALLENGES AND STATUS[*]

M. C. Ross[†], SLAC National Accelerator Laboratory, Menlo Park, CA, USA

Abstract

The Linac Coherent Light Source II (LCLS-II) project requires the assembly, test, and installation of 37 cryomodules (CM) in order to deliver a 4 GeV CW electron beam to the FEL undulators for production of both hard and soft X-ray pulses at a repetition rate of up to 1 MHz. All of the cryomodules will operation in continuous wave mode, with 35 operating at 1.3 GHz for acceleration and 2 operating at 3.9 GHz to linearize the longitudinal beam profile. The assembly and testing of the 1.3 GHz cryomodules is nearing completion and the 3.9 GHz cryomodules work is entering to assembly and testing phase. Roughly 60% of the cryomodules have been shipped to SLAC for installation in the accelerator enclosure. The status and challenges of these efforts will be reported in this paper.

INTRODUCTION

The LCLS-II Free Electron Laser (FEL) project [1] takes advantage of the excellent performance of the LCLS FEL [2] and the successful development of superconducting RF technology, done in part in preparation for a future linear collider [3,4]. Following the completion of the International Linear Collider (ILC) Technical Design Report [5] in 2013, a partnership of US accelerator labs initiated the US Department of Energy (DOE) Critical Decision (CD) process and quickly obtained permission to baseline and start procurements for the roughly 1.04 billion USD project. Completion (CD-4) is planned for 30 June 2022. LCLS-II machine parameters are shown in Table 1.

LCLS-II is the first application of low cryogenic-loss nitrogen doping SRF technology [6]. Nitrogen doping reduces the high purity niobium 'BCS' resistance (R_BCS) by a factor of three to four enabling large CW accelerator facilities to operate with 15-20 MV/m acceleration gradients (*E_acc*). The doping is applied to the now-standard 1300 MHz nine-cell niobium sheet elliptical cavity.

Figure 1 shows the layout of the LCLS-II SRF linac (from the end of the injector), housed in the first kilometer of the SLAC infrastructure formerly used for the normal-conducting linac. Each cavity is powered by its own 4.8 kW solid-state amplifier (SSA) with nominal loaded Q (Q_ext) of 4e7, considered a practical match of low beam current and anticipated microphonics. Q_ext can be manually adjusted within a +/- factor 3 range.

Cryogens for the facility are provided by two independent 4kW (at 2.0K) helium refrigerators, based closely on the five-stage full cold compression Jefferson Lab CHL-2 design, commissioned in 2012 [7]. The complex is expected to be loaded to capacity following the completion of LCLS-II-HE; only one of the two is required for LCLS-II. A ~300 m long two-arm cryo distribution system (CDS) feeds cold helium to the cryomodule strings [8]. Two distribution boxes (labeled DB in Fig. 1), each containing a 2-4 K heat exchanger, are located in the surface building directly above the cryomodule connection points.

European XFEL

The SRF technology deployed for LCLS-II follows very closely that developed and constructed for the European XFEL. Niobium, cavity, coupler, cryomodule, and auxiliary components are mechanically almost identical to that used for the recently completed European XFEL (XFEL) [9]. Changes to the cavity higher-order-mode extractor, fundamental power coupler (FPC), cavity tuner, and magnetic shielding were required to manage the 1) higher dynamic heat load, 2) higher Q_ext, 3) higher average beam current, and 4) higher sensitivity to magnetic field. (*B_amb*). The CM hardware was fabricated by many of the same companies and was tested by institutes that have close collaborative relationships with XFEL institutes. The most-important collaborators from outside the DOE system are DESY, CEA/Saclay, INFN (Milano), and KEK.

DOE Office of Science Lab Partnership

Fermilab and Thomas Jefferson Lab (JLab) each constructed and tested roughly half of the 37 cryomodules (35 each 1.3 GHz CM and two each 3.9 GHz linearizer CM). In addition, the JLab cryogenics group designed and managed the production of the 2.0 K cryoplant and Fermilab provided the cryogenic distribution system. SLAC was responsible for integration of the linac, cryoplant, and cryogenic distribution system.

Table 1: LCLS-II Machine Parameters

Parameter	Value	Units
Energy	4	GeV
Beam I	100	μ Amp
Duty Factor	CW	
RF	1300	MHz
Cavity	8	per CM
Cryomodules	35	each
Linearizer CM	2	each
Cryoplant cap.	8	kW@2.0K
SSA	4.8	kW

LCLS-II-HE

In 2018, the same partnership initiated the CD process for LCLS-II-HE to make X-rays up to 12.8 keV [10]. The new project received CD-1 (approval of the conceptual design and cost-range) in September 2018. Twenty CM with an improved doping scheme and higher *E_acc* of 20.8 MV/m will be built from 2021 to 2023 using the same partnership scheme as for LCLS-II. A prototype will be built

---

[*] Work supported by US DOE Contract DE-AC02-766SF00515

[†] mcrec@slac.stanford.edu

ISBN: 978-3-95450-223-3 ISSN: 2673-7000 doi:10.18429/JACoW-NAPAC2019-MOZBA2

OPERATIONAL EXPERIENCE WITH SUPERCONDUCTING UNDULATORS AT APS*

K. C. Harkay†, L. Boon, M. Borland, J. C. Dooling, L. Emery, V. Sajaev, Y. P. Sun
Argonne National Laboratory, Lemont, IL, USA

Abstract

APS has been developing superconducting undulators for over a decade. Presently, two planar and one helical device are in operation in the Advanced Photon Source (APS) storage ring, and a number of devices will be installed in the APS Upgrade ring (APS-U). All superconducting devices perform with very high reliability and have very minor effect on the storage ring operation. To achieve this, a number of storage ring modifications had to be done, such as introduction of the beam abort system to eliminate device quenches during beam dumps, and lattice and orbit modifications to allow for installation of the small horizontal aperture helical device with magnet coils in the plane of synchrotron radiation.

INTRODUCTION

The APS has been developing superconducting undulators (SCUs) for over a decade [1]. SCUs provide a higher peak field on axis for a given undulator gap and period length [2, 3]. Two planar and one helical SCU are in operation in the APS [4, 5]. All of the SCUs are highly reliable and minimally impact APS operations, including the quality and stability of the storage ring electron beam.

It is noted that in the worldwide landscape, SCUs are in operation only at APS and at Karlsruhe Research Accelerator, Karlsruhe Institute of Technology (KIT)/Noell [6, 7]. All of these devices use niobium titanium (NbTi) conductors, and all devices are cooled to ~4 K using cryocoolers. The APS devices include a closed-loop liquid helium (LHe) circuit.

Technical details of the APS SCU designs have been published elsewhere [1, 4, 5, 8, 9]. In this paper, we describe the operational experience with, and integration of, the SCUs into the APS storage ring.

OPERATIONAL HISTORY

After the first 0.33-m-long, 16-mm period superconducting undulator (SCU) was successfully developed, installed, and commissioned in APS in 2013 [1,10], two 1.1-m-long, 18-mm period planar SCUs [4] and a 1.2-m-long, 31.5-mm period helical SCU (HSCU) [5] have been installed and are presently in operation. An extensive beam commissioning plan was executed for SCU0: the equivalent of 5 days [10]. Lessons learned allowed for more compressed commissioning plans for the next devices: the equivalent of 1-2 days. All SCUs were turned over to the beamline for operations immediately after its commissioning period, and all have been very reliable.

The basic operational history for each device (through August 2019) is shown in Table 1. The device operational names are listed; the formal names are in the footnote. SCU operation (power and excitation current) is controlled by the individual beamline. The availability is expressed as the ratio of SCU operating hours relative to the sum of the SCU operating hours and device downtime. The operation percent is given by the ratio of the total hours of SCU operation relative to the total hours of APS user beam delivered (APS delivers just under 5000 hours per year). It is noted that the beamline operating SCU6 was down in calendar year 2019, and user demand for HSCU has been relatively low so far; this explains the lower operation ratios for these two devices. Detailed operational statistics can be found in [11].

Table 1: Basic Operational History of SCUs at APS

Device name	Operation period	Availability	Operation	# Quenches beam/self
SCU0	Jan. 2013- Sep. 2016	98.9%	92.3%	98/6
SCU1[1]	May 2015[3]	99.992%	96.6%	40/5
SCU6[2]	Sep. 2016[3]	99.89%	84.9%	32/3
HSCU	Jan. 2018[3]	100%	14%	0/0

[1] Also known as SCU18-1
[2] Also known as SCU18-2
[3] Presently in operation

The last column in the table shows the total number of times each device quenched during APS operation. A quench refers to the sudden loss of superconductivity when the temperature of any part of the SCU magnet coil windings is raised above the superconductivity threshold temperature. As a result, the windings suddenly develop a finite resistance. A quench detection interlock shuts off the power supply, and the coil heating causes a sudden boil-off of the liquid helium (LHe), which temporarily raises the LHe tank pressure [8]. Quenches are transparent to APS operation.

There are two types of quenches. The majority of quenches are caused when the Machine Protection System (MPS) dumps the stored beam due to a machine fault unrelated to the SCU; the number of instances is given by the first number in the last column in the table. The devices typically recover rapidly [4]; i.e., the magnet temperatures return to ~4 K and the LHe tank pressure reduces to operational levels, such that the devices can be re-energized after the stored beam is recovered. The controls system monitors the status and automatically restores the excitation current if the device is ready. This rapid recovery, 30-45 min. overall, and automation minimizes the device downtime. The second type of quench is when the device quenches while the beam is stored; this is referred to as a

---

* Work supported by U. S. Department of Energy, Office of Science, under Contract No. DE-AC02-06CH11357. † harkay@anl.gov.

ISBN: 978-3-95450-223-3 ISSN: 2673-7000 doi:10.18429/JACoW-NAPAC2019-MOZBA3

STRONGLY TAPERED HELICAL UNDULATOR SYSTEM FOR TESSA-266

T. J. Campese[†], R. B. Agustsson, I. I. Gadjev, A. Y. Murokh, RadiaBeam, Santa Monica, CA, USA
P. E. Denham, P. Musumeci, Y. Park, UCLA, Los Angeles, CA, USA
W. Berg, A. Zholents, Argonne National Lab, Lemont, IL, USA

Abstract

RadiaBeam, in collaboration with University of California Los Angeles (UCLA) and Argonne National Laboratory (ANL)*, is developing a strongly tapered helical undulator system for the Tapering Enhanced Stimulated Superradiant Amplification experiment at 266 nm (TESSA-266). The experiment will be carried out at the Advanced Photon Source (APS) Linac Extension Area (LEA) facility at ANL and aims at the demonstration of very high energy conversion efficiency in the Ultraviolet (UV). The undulator system was designed by UCLA, engineered by RadiaBeam, and is presently in fabrication at RadiaBeam. The design is based on a permanent magnet Halbach scheme [1] and includes a short 30 cm long buncher section and four 1 m long undulator sections. The undulator period is fixed at 32 mm and the magnetic field amplitude can be tapered by tuning the gap along the interaction. Each magnet can be individually adjusted by 1.03 mm, offering up to 25% magnetic field tunability with a minimum gap of 5.58 mm. A custom designed 316L stainless steel beampipe runs through the center with a clear aperture of 4.5 mm. This paper discusses the design and engineering of the undulator system, fabrication status, and plans for magnetic measurements, and tuning.

INTRODUCTION

Recently, a novel regime of operation has been proposed to greatly increase Free-Electron-Laser (FEL) efficiency using prebunched electron beams, intense seed laser, and strongly tapered undulators (so called TESSA scheme) [1]. An experimental demonstration of the TESSA concept in the mid-infrared was carried out at Brookhaven National Lab (BNL) [2] where energy extraction efficiency as high as 30% was demonstrated. The current TESSA-266 project, planned for construction at the APS linac at ANL, aims at pushing the performances of the proof-of-principle BNL experiment, by exploring for the first time this interaction in the high gain regime and extending the scheme to shorter wavelengths where high efficiency radiation sources would be extremely attractive (EUVL) [3].

A critical component in the project is the out of vacuum, strongly tapered helical undulator which will be used to couple the electromagnetic waves and relativistic electron beams. Helical undulators have an important advantage over planar designs since the transverse component of the electron velocity is never zero enabling continuous energy transfer and much more efficient interaction [4].

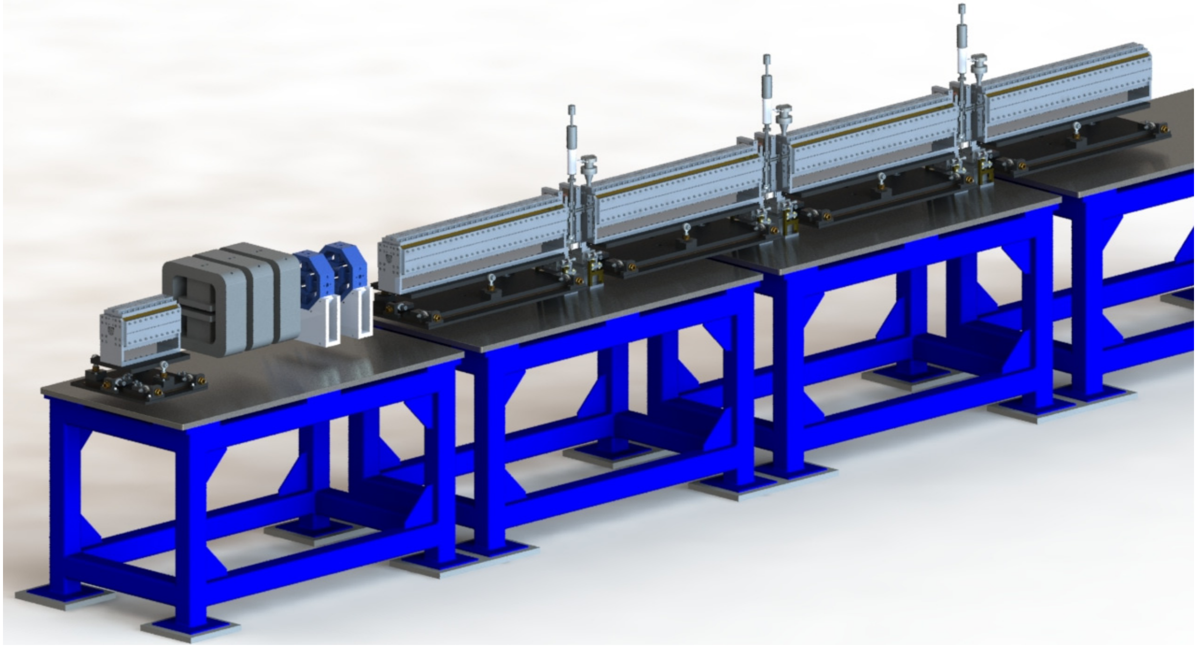

Figure 1: TESSA-266 overview showing, from left to right, the prebuncher, chicane (3 dipoles), quadrupole doublet, THESEUS 1, break section assembly 1 (quadrupole, phase shifter dipole, diagnostic, quadrupole), THESEUS 2, break section assembly 2, THESEUS 3, break section assembly 3, and THESEUS 4.

This paper discusses, in detail, the design of the THESEUS (Tapered HElical Segmented Undulator System), being developed for this experiment (Fig. 1).

---

* Work supported by DOE SBIR Award No. DE-SC0017102
[†] campese@radiabeam.com

ISBN: 978-3-95450-223-3 ISSN: 2673-7000 doi:10.18429/JACoW-NAPAC2019-MOZBA4

RECENT DEVELOPMENTS IN HIGH POWER HIGH BRIGHTNESS DOUBLE BUNCH SELF-SEEDING AT LCLS-II

A. Halavanau, F.-J. Decker, Y. Ding, C. Emma, Z. Huang, A.A. Lutman, G. Marcus, C. Pellegrini
SLAC National Accelerator Laboratory, Menlo Park, CA, USA

Abstract

We discuss the power and spectral characteristics of an X-ray FEL, LCLS-II, operating in a double bunch self-seeding scheme (DBFEL). We show that it can reach very high power levels in the photon energy range of 4-8 keV. We discuss the system implementation on LCLS-II, including the design of a four-bounce crystal monochromator, and linac wakefields effects. Finally, we offer multiple applications of the DBFEL for high-field QED, AMO physics and single particle imaging.

INTRODUCTION

Two- and multi-bunch copper RF (CuRF) linac operation capability expands the capabilities of the existing X-ray free electron lasers (XFELs) [1–5]. For example, we have previously shown that it greatly helps in producing very high power and nearly transform limited XFEL pulses [6].

The idea of double bunch FEL (DBFEL) is similar to fresh slice self-seeding scheme, except in the former case the entire first bunch is used for SASE radiation generation, and the entire second bunch is seeded and used for lasing. DBFEL requires a number of critical components to be added to a nominal XFEL beamline. First, two electron bunches must be produced in a photoinjector. In practice this is done by splitting the existing UV laser pulse into two pulses with a variable delay, or by using two individual lasers.

Second critical component is the four crystal Bragg monochromator, which provides narrow bandwidth radiation for seeding, and also delays the radiation by the amount of bunch separation. For practical implementation of the monochromator, it must be compact to fit in the existing HXRSS chicane space, therefore imposing a constraint on the double bunch delay time. We have discussed the geometry of the monochromator in [7].

Both bunches must be properly controlled in the linac and undulators, to alleviate wakefield effects, and to put the second bunch initially off-axis in the SASE section, and return it back on-axis in the amplifier section. This will be done by using an ultra-fast transmission line kicker with the rise time of 0.5 ns. The kicker parameters and conceptual design was presented in [7].

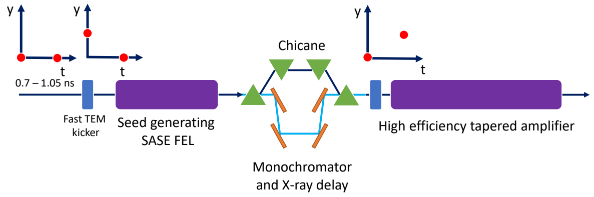

Figure 1: DBFEL schematics: two bunches with 0.7 - 1.05 ns separation are used to generate a high power seed on the second cold bunch at the entrance of the tapered amplifier.

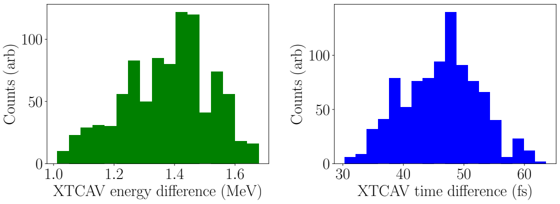

Figure 2: Energy and time-separation jitter for 50 ns double bunch separation. The RMS values are 0.3 MeV and 6.2 fs for energy and time jitter accordingly.

Currently, we are considering a DBFEL setup at LCLS-II hard X-ray (HXR) undulator shown in Fig. 1. The length of the SASE section is 7 undulators and the amplifier section consists of 25 undulators. To minimize detrimental effects of the long range wakefields in the CuRF linac, we consider 0.7 ns or two-bucket double bunch separation.

DOUBLE BUNCH JITTER MEASUREMENTS

LCLS CuRF linac has repeatedly demonstrated multi-bunch capability for various bunch separations [8–11]. An important parameter for a successful DBFEL operation is the double bunch separation jitter. For the first round of measurements, we generated two bunches at about 50 ns or 143 RF-buckets separation, and collected about 1000 XTCAV images. We then deconvolved first and second bunch from the image, to determine their individual center of mass position, and the RMS jitter in time and energy separation.

We found RMS energy jitter to be 0.3 MeV and RMS time jitter to be 6.2 fs respectively; see Fig. 2. The values are updated with more data from previously reported cases. We expect the jitter to be significantly smaller for shorter separations. A detailed study is planned shortly after LCLS-II commissioning. Double- and multi-bunch jitter are also critically important parameters for the successful operation of cavity based XFEL, such as the proposed regenerative amplifier FEL (RAFEL) at LCLS-II [5].

SIMULATIONS OF DBFEL PERFORMANCE

We note, that in our initial studies we used a quasi flat-top current distribution, previously considered and experimen-

North American Particle Acc. Conf. NAPAC2019, Lansing, MI, USA JACoW Publishing
ISBN: 978-3-95450-223-3 ISSN: 2673-7000 doi:10.18429/JACoW-NAPAC2019-MOZBA5

OPTIMIZED LINEAR AND SECOND ORDER CHROMATICITY SETPOINTS FOR THE ADVANCED PHOTON SOURCE UPGRADE*

Y.P. Sun†, Argonne National Laboratory, Lemont, IL, USA

Abstract

The nominal single particle dynamics optimizations of the Advanced Photon Source upgrade (APS-U) lattice are performed with dense numerical simulations of local momentum acceptance and dynamic acceptance. These simulations are quite time consuming, which may take weeks for optimizing one setpoint of linear chromaticity. In this paper, an alternative optimization method is adopted to generate optimized linear and second order chromaticity setpoints for the Advanced Photon Source upgrade lattice. This method is efficient in computing time needed, which is capable to generate a grid of optimized linear chromaticity setpoints in a relatively short time. The performance of these lattice solutions are verified by simulations with reasonable errors. These lattice solutions with different linear (or second order) chromaticity may be useful for the future APS-U commissioning and operations.

INTRODUCTION

For next generation storage rings light source, the combination of small physical apertures (for both insertion device and the arc sections) and strong chromaticity correction sextupoles introduces small dynamic acceptance and short lifetime. To optimize the nonlinear beam dynamics performance and achieve better injection efficiency and lifetime, the effectiveness of several different optimization methods and objectives [1] were benchmarked for the nonlinear beam dynamics optimization of Advanced Photon Source upgrade (APS-U) lattice [2].

In addition to these different optimization methods [1], recently it was found that optimizing the overall tune spread from transverse and energy offsets (this method is named as DET) seems to be a better approach, which is reliable and computationally efficient. The nominal single particle dynamics optimizations of the APS-U lattice are performed with direct simulations of local momentum acceptance (LMA) and dynamic acceptance (DA). This nominal approach is very reliable, as it employs same optimization and evaluation objectives. However, the LMA/DA simulations are quite time consuming, which may take weeks for optimizing one setpoint of linear chromaticity.

In this paper, DET optimization method is adopted to generate optimized linear and second order chromaticity setpoints for the APS-U lattice. This method is computationally efficient and capable to generate a set of optimized chromaticity setpoints in a relatively short time. Although using tune spread as the optimization objective, it is shown that the derived solutions have good performance, when evaluated with different objectives of LMA and DA.

OPTIMIZED LINEAR CHROMATICITY SETPOINTS

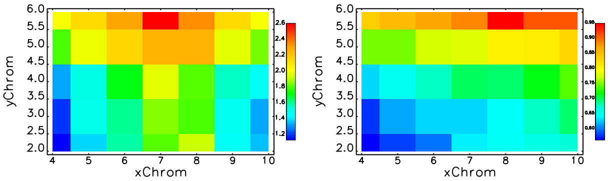

Figure 1: Initial (left) and final tune spread penalty on a grid of linear chromaticity setpoints. Max penalty reduced from 2.6 to 0.9.

Linear chromaticity knobs are widely used in storage ring operations. For APS DBA ring, the combination of two sextupole families (one focusing and one defocusing) out of a total of four families is employed for linear chromaticity knobs. As the optics are different at different families of sextupoles, it is not possible to group all sextupoles into the knob. Naturally for APS-U lattice (hybrid MBA lattice [3]), there are 'similar' optics parameters at all the focusing sextupoles SF, or at all the defocusing sextupoles SD. If using all the APS-U sextupoles for linear chromaticity knob, sextupoles strength will be continuous and smooth. However, the solution may not be optimized, even starting from a well optimized lattice.

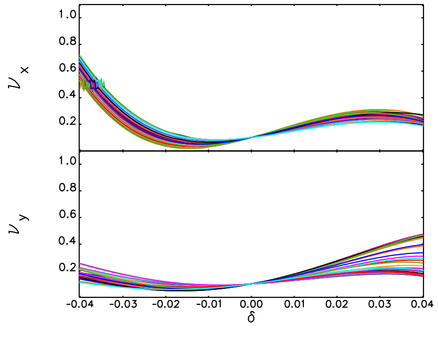

Figure 2: Chromatic detuning of optimized linear chromaticity setpoints.

On the other hand, it is possible to employ the DET method for efficiently generating a grid of linear chromaticity setpoints, as it takes much less computing time. For this approach, independent optimization is performed at each

---

* Work supported by the U.S. Department of Energy, Office of Science, Office of Basic Energy Sciences, under Contract No. DE-AC02-06CH11357.

† yisun@aps.anl.gov

ISBN: 978-3-95450-223-3 ISSN: 2673-7000 doi:10.18429/JACoW-NAPAC2019-MOZBA6

THE BROAD-BAND IMPEDANCE BUDGET IN THE ACCUMULATOR RING OF ALS-U PROJECT*

D. Wang†, K. Bane, D. Li, T. Luo, S. De Santis, M. Venturini
Lawrence Berkeley National Laboratory, Berkeley, USA

Abstract

Design work is underway for the upgrade of the Advanced Light Source (ALS-U) to a diffraction-limited soft x-rays radiation source. It consists of an accumulator and a storage ring. In both rings, coupling-impedance driven instabilities need careful evaluation to ensure meeting the machine high-performance goals. This paper presents the broad-band impedance budget of the accumulator ring both longitudinally and transversely. The budget includes the resistive wall impedance as well as the geometric impedance from the main vacuum components. Our calculations primarily rely on electromagnetic simulations with the CST code; when possible validation has been sought against analytical modeling, typically in the low-frequency limit, and good agreement generally found. Collective-instability current thresholds are also discussed.

INTRODUCTION

ALS-U is under design to upgrade the existing Advanced Light Source (ALS) at LBNL to a diffraction-limited soft x-rays radiation source, with brightness about tow orders of magnitude higher than that of ALS. The upgrade program includes the replacement in the storage ring (SR) of the existing triple-bend achromat with a multi-bend achromat lattice and the installation of a new low emittance accumulator ring (AR) in the existing tunnel, with the purpose of enabling swap-out injection into the SR small aperture [1].

One of the significant factors potentially limiting performance in a ring is the beam's interaction with electromagnetic fields induced in a vacuum chamber by the beam itself, which is described with short-range wakefield (time domain) or, equivalently, broad-band (BB) impedance (frequency domain) [2]. BB impedance in the ring is caused by resistive wall as well as the localized elements such as BPM, RF cavity, pump screens, etc. BB impedance can affect the machine performance/operation in several ways including overheating of vacuum chamber components and giving rise to instability of beam motion, leading to deterioration of the beam quality and limitation of the beam intensity [3].

In this paper, the BB impedance budget of the AR in the ALS-U has been extensively surveyed using a combination of analytical models and numerical simulations. The total impedance budget has been computed for the beam with nominal bunch length of 5 mm rms. We also calculated the short range wakefield of a 1mm rms drive beam to serve as the pseudo-Green function for beam dynamics study. The collective-instability study to determine the single bunch current thresholds for both longitudinal and transverse instability is performed by *elegant* [4].

IMPEDANCE MODELING

The BB impedance comes from the resistive wall and the geometric components. We calculate the resistive wall impedance with analytical formulas [5] and determine the geometry impedance with the numerical solver CST Particle Studio [6].

Resistive Wall Impedance

The resistive wall impedance is an important part in the impedance model. The lattice design of the accumulator ring is TBA periodic structure, with three bending magnets in each sector. There are 12 sectors and the total the circumference C≈182 m. Figure 1 shows the layout of a normal arc section and Table 1 shows the characteristics of the three different types of vacuum chamber sectors for the sector shown in Fig. 1.

We adopt the common infinite-thickness wall, DC conductivity resistive-wall model. In an elliptical chamber the impedance in longitudinal and transverse plane are [4]:

$$Z_{||}(\omega) = \frac{Z_0 \delta \omega}{4\pi\, bc}(sign(\omega) - i) \times \mathrm{F}_{YOKOYA} \quad (1)$$

$$Z_{\perp}(\omega) = \frac{Z_0 \delta \omega}{2\pi\, b^3}(sign(\omega) - i) \times \mathrm{F}_{YOKOYA}\,, \quad (2)$$

with b is the smaller chamber half-axis, $\delta = \sqrt{2/\mu_0 \sigma_c |\omega|}$ the skin depth depending on the material conductivity, F_{YOKOYA} the Yokoya geometry factors [7]. For AR dipole chamber with 2a = 40mm major and 2b = 14mm minor axis, the Yokoya's foctors are Fz = 0.98 (longitudinal), Fd,x = 0.43 (dipole, horizontal), Fd,y = 0.83 (dipole, vertical), and Fq = 0.4 (quadruple).

Table 1: Types and Features of the Normal Arc Section in the Accumulator Ring as Shown in Fig. 1

Type	ID (mm)	Profile	Length (m)	Material
Dipole	14(y) 40(x)	ellipse	3.0	Aluminum
Arc	28	round	7.8	Stainless steel
Straight	47	round	4.2	Stainless steel

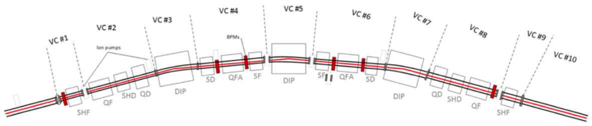

Figure 1: Layout of a normal arc section.

---

[1] Work supported by the Director Office of Science of the U. S. Department of Energy under Contract No. DE-AC02-05CH11231.

† dwang2@lbl.gov

EXPERIMENTS WITH METAMATERIAL-BASED METALLIC ACCELERATING STRUCTURES

X. Lu[1]*, I. Mastovsky, J. F. Picard, M. A. Shapiro, R. J. Temkin
Massachusetts Institute of Technology, Cambridge, MA, USA
[1]currently at SLAC National Accelerator Laboratory, Menlo Park, CA, USA
M. Conde, S. Doran, G. Ha, C. Jing[2], M. Peng, J. G. Power, J. Seok,
J. Shao, E. E. Wisniewski
Argonne National Laboratory, Lemont, IL, USA
[2]also at Euclid Techlabs LLC, Solon, Ohio, USA

Abstract

We present experimental studies of metamaterial (MTM) structures for wakefield acceleration. The MTM structure is an all-metal periodic structure with its period much smaller than the wavelength at X-band. The fundamental TM mode has a negative group velocity, so an electron beam traveling through the structure radiates by reversed Cherenkov radiation.

Two experiments have been completed at the Argonne Wakefield Accelerator (AWA), namely the Stage-I and Stage-II experiments. Differences between the two experiments include: (1) Structure length (Stage-I 8 cm, Stage-II 20 cm); (2) Bunch number used to excite the structure (Stage-I up to 2 bunches, Stage-II up to 8 bunches). In the Stage-I experiment, two bunches with a total charge of 85 nC generated 80 MW of RF power in a 2 ns long pulse. In the Stage-II experiment, the highest peak power reached 380 MW in a 10 ns long pulse from a train of 8 bunches with a total charge of 224 nC. Acceleration of a witness bunch has not been demonstrated yet, but the extracted power can be transferred to a separate accelerator for two-beam acceleration or directly applied to a trailing witness bunch in the same structure for collinear acceleration.

INTRODUCTION

Metamaterials (MTMs) refer to a category of periodic structures with the period much smaller than the operating wavelength, so they can be treated as artificial media with the effective permittivity ϵ and permeability μ determined by the unit cell design. MTMs are built out of natural materials, while by arranging the subwavelength periodic elements in carefully designed shapes and patterns, novel electromagnetic properties not found in nature can be realized in MTMs, such as a negative refractive index from double negative ϵ and μ. Many interesting applications have been demonstrated on double negative MTMs, including perfect lens, cloaking and advanced antennas [1].

For active MTMs where a relativistic beam is present, the novel physics phenomenon is the reversed Cherenkov radiation [2, 3]. In normal materials with a positive refractive index $n > c/v$, where c is the speed of light and v is the speed of the beam, Cherenkov radiation travels forward with respect to the beam. In this case, the energy flow and the wave vector are parallel. By contrast, in the reversed Cherenkov radiation, energy flow is antiparallel with the wave vector, so the energy flows backward with respect to the beam. This paper investigates the application of the reversed Cherenkov radiation in MTMs to wakefield acceleration excited by short electron bunches.

Structure-based wakefield acceleration (SWFA) [4–7] is an advanced acceleration concept, where a high charge drive beam traverses a wakefield structure in vacuum and transfers its energy by wakefield radiation to a high power radiofrequency (RF) pulse. The RF pulse can then be used to accelerate a witness beam in the same structure behind it (collinear wakefield acceleration) or in a different structure for the witness beam (two-beam acceleration). SWFA is promising to achieve high gradient acceleration, since the RF breakdown rate increases with gradient and decreases with pulse length [8]. As a result, SWFA operating at short RF pulses (a few nanoseconds) has a better chance to eliminate RF breakdowns at high gradient.

To make the structure withstand high power and high gradient wakefield, we designed it as an all-metal MTM structure. The advantages of such a design include resistance to beam damage, possibilities to optimize in the huge parameter space of the MTM unit cell and high shunt impedance and high group velocity at the same time to maximize the extracted RF power.

The following sections will first introduce the experimental facilities at the Argonne Wakefield Accelerator (AWA) [9], and then introduce two experiments carried out there on X-band MTM structures, Stage-I experiment with a 8 cm long MTM structure driven by up to two bunches, and Stage-II experiment with a 20 cm long MTM structure driven by up to eight bunches.

EXPERIMENTAL FACILITIES

The MTM structures built by MIT have been tested at the AWA Facility [9]. Figure 1 shows the drive beam line at AWA. The electron beam with a high charge can be generated by a laser photocathode and then accelerated to 65 MeV in

---

* xylu@slac.stanford.edu

MAGNETIZED ELECTRON SOURCE FOR JLEIC COOLER*

R. Suleiman†, P.A. Adderley, J. F. Benesch, D.B. Bullard, J. M. Grames, J. Guo, F. E. Hannon,
J. Hansknecht, C. Hernandez-Garcia, R. Kazimi, G. A. Krafft[1], M. A. Mamun, M. Poelker,
M.G. Tiefenback, Y.W. Wang, S. Zhang,
Thomas Jefferson National Accelerator Facility, Newport News, VA, USA
J. R. Delayen, S. A. K. Wijethunga, J. T. Yoskowitz, Old Dominion University, Norfolk, VA, USA
[1]also at Old Dominion University, Norfolk, VA, USA

Abstract

Magnetized bunched-beam electron cooling is a critical part of the Jefferson Lab Electron Ion Collider (JLEIC). Strong cooling of ion beams will be accomplished inside a cooling solenoid where the ions co-propagate with an electron beam generated from a source immersed in a magnetic field. This contribution describes the production and characterization of magnetized electron beam using a compact 300 kV DC high voltage photogun and bi-alkali antimonide photocathodes. Beam magnetization was studied using a diagnostic beamline that includes viewer screens for measuring the shearing angle of the electron beamlet passing through a narrow upstream slit. Correlated beam emittance with magnetic field (0-1.5 kG) at the photocathode was measured for various laser spot sizes. Measurements of photocathode lifetime were carried out at different magnetized electron beam currents up to 28 mA and high bunch charge up to 0.7 nano-Coulomb was demonstrated.

INTRODUCTION

To achieve the required luminosity, ion beams at JLEIC must be cooled. In general, this is accomplished when an electron beam co-propagates with the ion beam. The cooling rate can be improved by about two orders of magnitude if the process occurs inside a solenoidal field that forces the electrons to follow small helical trajectories thereby increasing the interaction time with ions and improving the cooling efficiency [1]. This cyclotron motion also suppresses electron-ion recombination, a serious problem, especially for heavy ions. Cooling rates of a magnetized electron beam are ultimately determined by electron longitudinal energy spread rather than the transverse emittance as the transverse motion of the electrons is quenched by the strong magnetic field.

The envisioned JLEIC magnetized cooler is part of the ion collider ring and aims to counteract emittance degradation induced by intra-beam scattering, to maintain emittance during electron-ion collisions and extend the luminosity lifetime. To implement cooling at relatively high energy, the electron beam must be bunched and accelerated in an SRF Linac. The required electron beam parameters from the magnetized electron source are difficult to achieve due to both the very high charge (3.2 nC) and high average current (140 mA) [2].

To implement cooling inside a solenoid, the electron beam must be generated inside a magnetic field. Otherwise, the electron beam will have mechanical angular momentum inside the cooling solenoid per Busch's theorem [3] induced by the radial fringe field as the electron beam enters the solenoid. This paper reports on generation and characterization of magnetized electron beams from a 300 kV DC high voltage magnetized electron source.

MAGNETIZED ELECTRON SOURCE

This prototype magnetized electron source consists of drive laser system, bi-alkali antimonide photocathode preparation chamber, photogun HV chamber, cathode solenoid, and diagnostic beamline (see Fig. 1), as described in details in the following subsections.

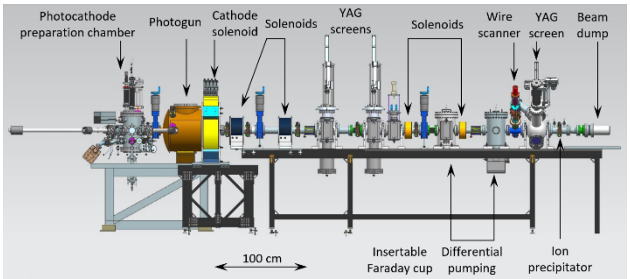

Figure 1: Schematics of main components of the magnetized electron source.

Drive Lasers

There were two different drive lasers used to generate magnetized beam. For high beam currents, a master-oscillator-power-amplifier system, composed of a 1066 nm gain-switched diode laser and multi-stage Yb-fiber amplifier chain followed by a harmonic converter, was constructed to provide Watts of power with picosecond light pulses at 533 nm. Good harmonic conversion efficiency up to 30% was achieved using a PPLN crystal. For high bunch charge, a commercial ultrafast laser with pulse duration less than 0.5 ps, 20 µJ pulse energy, operating at 50 kHz pulse repetition and 1030 nm wavelength was used. The IR beam was converted to 515 nm using a BBO crystal.

Photocathode Preparation Chamber

Bi-alkali antimonide photocathodes were grown inside a preparation chamber using co-evaporation of Cs and K from an effusion source onto a thin Sb layer deposited on

---

* Authored by Jefferson Science Associates, LLC under U.S. DOE Contract No. DE-AC05-06OR23177. Additional support comes from Laboratory Directed Research and Development program. The U.S. Government retains a non-exclusive, paid-up, irrevocable, world-wide license to publish or reproduce this manuscript for U.S. Government purposes.
† suleiman@jlab.org

ISBN: 978-3-95450-223-3 ISSN: 2673-7000 doi:10.18429/JACoW-NAPAC2019-MOZBB6

MEASURING THE MEAN TRANSVERSE ENERGY OF PUMP-PROBE PHOTOEMITTED ELECTRONS

C. M. Pierce*, I. V. Bazarov, L. Cultrera, J. Maxson, Cornell University, Ithaca, New York

Abstract

Low effective mass semiconductor photocathodes have historically failed to exhibit the sub-thermal mean transverse energies (MTEs) expected of them based on their band structure. However, conservation of transverse momentum across the vacuum interface, and therefore a low MTE in these materials, has been observed in time resolved ARPES. To help bridge this gap, we measured the MTE of the pump probe photoemitted electrons seen in the ARPES experiment using methods typical of accelerator physics. We compare the results of these measurements with those of both communities and discuss them in the context of photoemission physics.

INTRODUCTION

The discovery of new low MTE photocathodes is a requirement for those seeking to improve the brightness of photoinjectors operating at the charge extraction limit. In photoinjectors with a fixed electric field there is a minimum initial spot size $\sigma_{x,\mathrm{min}}$ for every bunch charge due to the virtual cathode instability. This is called the charge extraction limit. Since the charge extraction limit sets a maximum charge density in the spatial coordinate and cathode MTE sets the density in the momentum coordinate, the maximum brightness can be written as $B_{\mathrm{4D,max}} \propto (\sigma_{x,\mathrm{min}}^2 \mathrm{MTE})^{-1}$. The only way to improve the brightness of photoinjectors operating at or near $\sigma_{x,\mathrm{min}}$ is to drive down the MTE of photocathodes.

Low Effective Mass Semiconductor Photocathodes

Low effective mass semiconductors offer a promising path towards new low MTE photocathodes. Conservation of transverse momentum across the photocathode's surface means that the transverse energy of electrons is scaled by the mass ratio m_e^*/m_e upon emission. For near threshold photoemission from a negative electron affinity (NEA) photocathode, the transverse energy of electrons comes from the Fermi tail and is $k_B T$. The MTE is then $(m_e^*/m_e)k_B T$ and makes us interested in candidate photocathodes with small m_e^*. Some semiconductors, such as GaAs, have an effective mass ratio as small as $m_e^*/m_e = 0.07$ and should have MTEs as low as 1.7 meV for near threshold photoemission at room temperature [1]. Compare this with the MTE of polycrystalline copper, a commonly used metallic photocathode, which has been measured at 85 meV near threshold [2].

The MTE of NEA GaAs near threshold has been consistently measured at more than 25 meV which is $k_B T$ at room temperature [3–8]. There is only one reported measurement of the expected 1.7 meV MTE and it has not been reproduced since [9]. There is currently no consensus on why the MTE is so much larger than what the material's low effective mass would lead us to believe. Some proposed explanations include physical/chemical roughness of the surface, scattering of electrons in the Cs overlayer, and the effects of electron-phonon scattering [1, 10, 11].

The narrow dispersion of the GaAs conduction band is observed in time resolved ARPES (trARPES). In a trARPES measurement, electrons are excited into empty conduction band states by pump photons and emitted into the vacuum some time later with probe photons. These photoelectrons are filtered by angle of emission and longitudinal energy in a hemispherical analyzer. Kanasaki et al. measured a photoelectron distribution from GaAs which can be naively converted to a transverse energy distribution with 1.7 meV MTE [12]. Photoinjectors, however, do not have the energy filtering capabilities of an ARPES style detector. An accurate measurement of MTE for these applications must include the full photoelectron distribution, not a narrow subset of it.

MEASUREMENTS OF THE OUT OF EQUILIBRIUM PHOTOCATHODE

The photocathode was prepared by solvent cleaning and etching a p-type GaAs (110) wafer obtained from a commercial source. The wafer was Zn doped to a p-type carrier concentration of 1×10^{19} cm^{-3} and came polished to a surface roughness of better than 0.4 nm RMS. Before introduction to a vacuum chamber at better than 1×10^{-10} Torr pressure, the wafer was cleaned in acetone and etched in a 1% HF solution for 30 s. Inside the preparation chamber, the sample was annealed at 550 °C for 8 hours to remove surface oxides. The band gap was measured at 1.40 eV using photoluminescence spectroscopy with illumination at 633 nm. We estimate the workfunction of the sample to be 4.6 eV based off of measurements of quantum efficiency (QE) as photon energy was changed. The data, in Fig. 1, was fit to a model with quadratic dependence of QE on excess photon energy.

An optical parametric amplifier was used to generate the 750nm pump and some of the 1030 nm output of an Yb fiber laser driving it was diverted and frequency tripled for use as the probe. Both were overlapped at the sample and aligned in time of arrival. The intensity of the pulses was increased to the point that each caused multiphoton photoemission from the sample and those multiphoton beams were used to center the laser spots on the cathode and align them with each other. The cross correlation of the pulses was measured as less than 400 fs full width at half maximum by watching

---

[*] CMP285@cornell.edu

ISBN: 978-3-95450-223-3 ISSN: 2673-7000 doi:10.18429/JACoW-NAPAC2019-MOPLM01

ALTERNATIVE INJECTION SCHEMES TO THE NSLS-II USING NONLINEAR INJECTION MAGNETS*

R.P. Fliller III[†], G. Bassi, A. Blednykh, C. Hetzel, V.V. Smaluk, C.J. Spataro, P. Zuhoski[‡],
Brookhaven National Laboratory, Upton, NY, USA

Abstract

The NSLS-II storage ring uses the standard four bump injection scheme to inject beam off axis. BESSY and MAX-IV are now using a pulsed multipole magnet as an injection kicker. The injected beam sees a field off axis for injection while the stored beam experiences no field on the magnet axis. The principle advantage of using a pulsed multipole for injection is that the stored beam motion is greatly reduced since the field on axis is negligible. The number of pulsed magnets is reduced from five in the nominal scheme (septum and four bumps) to two or three thereby reducing the possible failure modes. This also eliminates the need to precisely match the pulse shapes of four dipole magnets to achieve minimal stored beam motion outside of the bump. In this paper we discuss two schemes of injecting into the NSLS-II using a pulsed multipole magnet. The first scheme uses a single pulsed multipole located in one cell downstream of the injection septum as the injection kicker. The second scheme uses two pulsed multipoles in the injection straight to perform the injection. We discuss both methods of injection and compare each method.

INTRODUCTION

The NSLS-II storage ring injection system uses a standard four bump injection scheme to inject beam off axis. Though this is a proven and well-established design for injection into a light source ring, it suffers from several drawbacks. Space is required for the four kickers. Closing of the bump is generally only possible for the maximum amplitude of the bump. Mismatches on the pulses and the chamber coats make matching the fields at all amplitudes difficult. Another reason may be that the bump passes through sextupoles which provide an amplitude dependant kick. This stored beam motion is not desirable to users, particularly imaging beamlines or those with samples sensitive to damage.

Reliability of the pulsers is an issue since there are multiple pulsers that may fail. This would stop the injection process, and likely kick the stored beam from the machine. Depending upon the design of the pulser, this may require access into the storage ring tunnel for repair. Therefore a method of injection that can solve these issues would be beneficial to light source operation.

Several light sources are pioneering a pulsed multiple for injection to resolve these issues [1, 2]. The idea is that the injected beam would experience the necessary field while the stored beam would see no field. BESSY II and MAX-IV have pioneered the use of a nonlinear kicker for injection [3]. This kicker is not a pure multipole and allows for the possibility of zero or reduced gradient at the injected beam location as well as for zero field and gradient at the center of the magnet for the stored beam.

In this paper we discuss two schemes for using nonlinear kicker magnets for injection into the NSLS-II storage ring. The first scheme uses a single kicker magnet for injection, and the second scheme uses two such magnets. We compare and contrast the two methods. We also discuss heating concerns for the ceramic chambers.

SINGLE KICKER INJECTION

The nonlinear kicker used is based on the BESSY II and MAX-IV design. In this design, eight wires are placed in an X pattern about the center with two wires on each leg of the X are radii R_1 and R_2. All of the wires carry the same current with the outer wires having opposite sign. This give zero field and gradient in the center and a field maximum on the horizontal and vertical axis at $R_1<R<R_2$, as shown in Fig. 1 [3].

It is possible that the inner and outer wires do not necessarily form a single X while maintaining the necessary field parameters. This allows some additional freedom for increasing the vertical aperture as well as other optimizations.

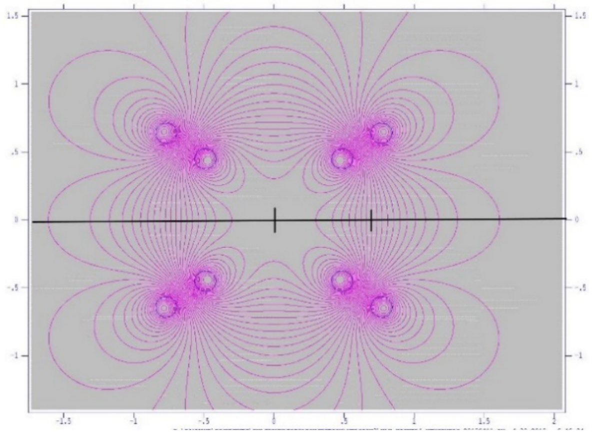

Figure 1: Field Map of the Nonlinear Kicker. The vertical lines show the zero field and maximum field locations on the horizontal axis.

Table 1 lists the relevant parameters of the injection kicker magnet. The field maximum location was chosen to that this same magnet could be used in both scenarios and

---

* This manuscript has been authored by Brookhaven Science Associates, LLC under Contract No. DE-SC0012704 with the U.S. Department of Energy.

[†] rfliller@bnl.gov

[‡]Deceased

North American Particle Acc. Conf. NAPAC2019, Lansing, MI, USA JACoW Publishing
ISBN: 978-3-95450-223-3 ISSN: 2673-7000 doi:10.18429/JACoW-NAPAC2019-MOPLM03

CORRELATIONS BETWEEN BETA BEATING AND APS-U SINGLE PARTICLE DYNAMICS PERFORMANCE*

Y. P. Sun†, ANL, Lemont, IL, USA

Abstract

In the optimizations and evaluations process of the Advanced Photon Source upgrade (APS-U) lattice, it was observed that there are negative correlations between beta beating and APS-U single particle dynamics performance (such as dynamic acceptance and local momentum acceptance). These correlations are not always present due to different reasons. To understand these and possibly to assist in directing the future optimizations, in this paper a systematic simulation study is performed to understand the correlations between beta beating and APS-U single particle dynamics performance. Relatively high beta beatings are generated to reveal these possible correlations. In general a negative correlation is found between APS-U single particle dynamics performance and beta beating. Such correlations may vanish with relatively small beta beating, where the performance may be determined by physical apertures, resonances strength, and other factors.

INTRODUCTION

The Advanced Photon Source (APS) is undergoing an upgrade [1], where the double bend achromat lattice (DBA) is replaced by a hybrid multi bend achromat (HMBA) lattice [2], reducing the emittance from 3nm to 42pm. To achieve this, dispersion D_x is greatly reduced with more and weaker dipole magnets. Also quadrupole focusing is much stronger which in turn requires strong sextupole magnets for the chromaticity correction. Although the HMBA lattice provides optimum phase advance between sextupole pairs which eliminates many geometric abberations, the APS-U nonlinear optics optimization is still very challenging.

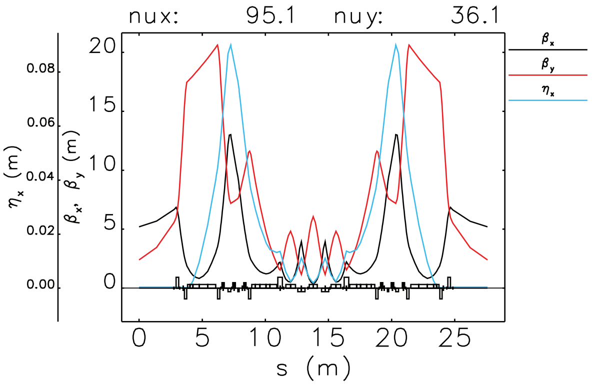

Figure 1: Linear optics of the final APS-U lattice.

Often when the optimized lattice solution is evaluated with errors, one observes a correlation between beta beating and single particle dynamics performance (such as dynamic acceptance and local momentum acceptance). However, these correlations are not always present, due to the complication with closed orbit and physical apertures. With improved APS-U commissioning simulation procedures, the range of resulting beta beating after commissioning simulation is also smaller, which makes it harder to establish any correlations. Here, a systematic simulation study is performed to understand the correlations between beta beating and APS-U single particle dynamics performance, with relatively high beta beatings intentionally generated.

The optics functions in one of fourty sectors for APS-U final lattice [1] are shown in Figure 1. There are six sextupole magnets in the dispersive region of each sector, which are grouped into three pairs.

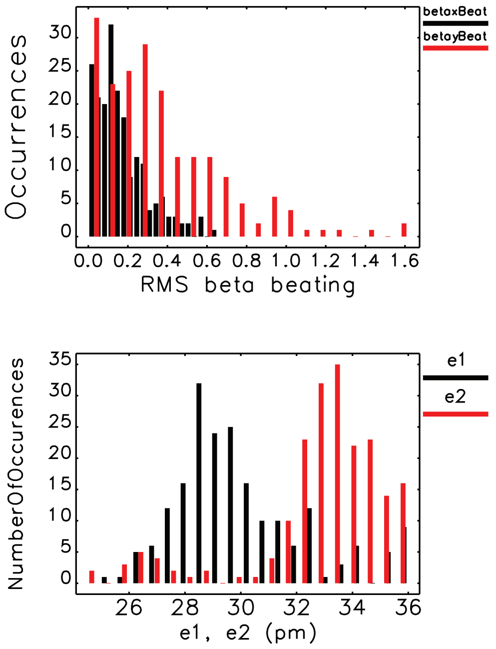

Figure 2: Histogram of beta beating (top) and beam moments of 200 filtered random seeds.

GENERATING BETA BEATING IN A LARGE RANGE

As discussed above, beta beating are intentionally generated in a large range to reveal the correlations between beta beating and APS-U single particle dynamics performance. Nominal quadrupole focusing errors (K1) and skew

---

* Work supported by the U.S. Department of Energy, Office of Science, Office of Basic Energy Sciences, under Contract No. DE-AC02-06CH11357.

† yisun@aps.anl.gov

ISBN: 978-3-95450-223-3 ISSN: 2673-7000 doi:10.18429/JACoW-NAPAC2019-MOPLM04

FIRST ATTEMPTS AT APPLYING MACHINE LEARNING TO ALS STORAGE RING STABILIZATION*

S.C. Leemann†, P. Amstutz, W. Byrne, M.P. Ehrlichman, T. Hellert, A. Hexemer, S. Liu,
M.A. Marcus, C.N. Melton, H. Nishimura, G. Penn, F. Sannibale, D.A. Shapiro, C. Sun,
D. Ushizima, M. Venturini, Lawrence Berkeley National Laboratory, Berkeley, CA 94720, USA

Abstract

The Advanced Light Source (ALS) storage ring operates multiple feedbacks and feed-forwards during user operations to ensure that various source properties such as beam position, beam angle, and beam size are maintained constant. Without these active corrections, strong perturbations of the electron beam would result from constantly varying insertion device (ID) gaps and phases. An important part of the ID gap/phase compensation requires recording feed-forward tables. While recording such tables takes a lot of time during dedicated machine shifts, the resulting compensation data is imperfect due to machine drift both during and after recording of the table. Since it is impractical to repeat recording feed-forward tables on a more frequent basis, we have decided to employ Machine Learning techniques to improve ID compensation in order to stabilize electron beam properties at the source points.

INTRODUCTION

To large extent the success of 3rd-generation light sources (3GLSs) such as the ALS lies in their stability, resulting in constant position, angle, and intensity of radiation delivered at a tunable wavelength with narrow width. In order to maintain constant intensity, a combination of top-off injection (maintaining constant beam current on a sub-percent level) [1,2] and precise control over source position and size is required. In 3GLSs source position and angle have been successfully stabilized through combined application of insertion device (ID) feed-forwards (FFs) and orbit feedback (FB) [3–5] resulting in sub-micron rms orbit stability over the course of many hours.

Source size stability, however, requires additional effort. Usually this calls for a local optics correction to compensate for perturbations caused by changes of ID settings (primarily focusing and skew quadrupole errors, but in some instances also higher-order corrections to maintain injection efficiency and lifetime) in combination with global optics corrections to ensure overall machine performance is maintained (tunes, betatron coupling) [4,6–14]. Local optics corrections are commonly realized through a FF (local quadrupole and skew quadrupole FFs), while global corrections are often a combination of FF (e.g. systematic tune correction against ID motion) and FB (global tune correction).

Limitations of Feed-Forward Corrections

The FFs employed to correct systematic focusing and skew quadrupole errors resulting from ID motion are usually based on a physics model describing how e.g. the local vertical focusing is perturbed by a change of vertical gap along with measurements to determine which local quadrupole excitation is required to compensate for this effect. The result is commonly referred to as a *lookup table*. Such a lookup table is then employed by the local FF to compensate for ID motion. Two aspects about this approach are problematic: First, the physics model the approach is based on relies on several approximations (ideal IDs, linear expansion, linear superposition) which do not always hold well as experimental data shows. Secondly, the storage ring and the instrumentation involved in recording these lookup tables are susceptible to drift. This is a serious issue since recording lookup tables require large amounts of dedicated machine time so they can not be re-recorded on a frequent basis (1–2 recordings per EPU a year is the maximum that can realistically be expected at ALS). So as the machine drifts (e.g. temperature, ground settlement, tidal motion, etc.) during the period a table is being used, the fidelity of the FF compensation based on this table will reduce with time. However, even if tables were re-recorded more frequently, drift remains a fundamental problem since the machine instrumentation already drifts during the lengthy process to record the table[1].

SOURCE SIZE STABILITY

Standard practice in 3GLSs is to maintain transverse beam size stability to within 10% of the rms electron beam size [16, 17]. This performance is indeed routinely achieved at ALS and other 3GLSs despite machine drift and imperfections in the compensation for ID gap/phase changes. Now however, the latest experiments at these sources are starting to show limitations arising from such levels of source size control. While top-off injection and orbit FBs are routinely reaching sub-percent level stability, source sizes still vary on the level of several percent even in the most advanced 3GLSs after much optimization (cf. below for an example from a STXM end station at ALS) and thereby become the limitation for overall source stability.

It is also evident that with the advent of *4th-generation storage rings* (4GSRs)—sometimes referred to as *diffraction-limited storage rings*—delivering high-brightness x-ray beams with high coherent flux, electron beam sizes will become smaller by many more factors than perturbations

---

[*] This research is funded by the US Department of Energy (BES & ASCR Programs), and supported by the Director of the Office of Science of the US Department of Energy under Contract No. DEAC02-05CH11231.

[†] SCLeemann@lbl.gov

[1] At ALS an EPU [15] requires on the order of one 8-hour machine shift to record a full lookup table.

ISBN: 978-3-95450-223-3 ISSN: 2673-7000 doi:10.18429/JACoW-NAPAC2019-MOPLM06

HIGH VOLTAGE DESIGN OF A 350 kV DC PHOTOGUN AT BNL

W. Liu, O. H. Rahman and E. Wang
Brookhaven National Laboratory, Upton, NY 11973, USA

Abstract

Brookhaven National Laboratory is constructing a 350 kV DC high voltage photogun to provide spin-polarized electron beam for the proposed eRHIC facility. The photogun employs a compact inverted-tapered-geometry ceramic insulator that extends into the vacuum chamber and mechanically holds the cathode electrode. By operating at high voltage, the photogun will provide lower beam emittance, thereby improving the beam transmission through the injector apertures, and prolong the operating lifetime of the photogun. However, high voltage increases the field emission, which can result in high voltage breakdown and even lead to irreparable damage of the ceramic insulator. This work describes the methods to minimize the electric field around the metal-vacuum-insulator interface, and to avoid high voltage breakdown and ceramic insulator damage. The triple point junction shields are designed. The simulated electric field, field emission and beam transportation will be presented.

INTRODUCTION

The Electron Ion Collider (EIC) will open a new frontier in nuclear physics, which help to quantitative study the properties of matter from the deeply fundamental Quantum Chromo-Dynamics (QCD) constituents [1]. Brookhaven National Laboratory (BNL) is proposing eRHIC, an electron ion collider based on the existing Relativistic Heavy Ion Collider (RHIC) facility with an additional electron storage ring [2]. The eRHIC requires a direct current (DC) high voltage photoemission electron gun (photogun) to generate spin-polarized electron beam by illuminating a strained superlattice GaAs photocathode with circularly polarized light. The polarized electron beams is injected into the electron storage ring for collision with the polarized protons or heavy ions of RHIC. In the eRHIC design, the polarized electron injector need to provide high current and high bunch charge. A photogun, aimed to provide electron beam with 10 mA average current and 5.3 nC bunch charge, is under development at BNL [3].

In this paper, we report on the high voltage design of the 350 kV DC photogun with the compact "inverted" insulator structure, which can provide smaller volume and less surface area to contribute a gas load, resulting in better achievable vacuum. The photogun also has less metal that was biased at high voltage and contributed to field emission, due to the insulator serves as the cathode electrode support structure, compared to the "standard" photogun that applied the metal stalk to hold the cathode electrode. A triple-point-junction shield (TPJS) was attached together with the cathode electrode to reduce the electric field around the metal-vacuum-insulator interface (triple point junction) to eliminate the field emission from this junction, and to avoid the damage of insulator. Design and optimization of the TPJS structure will be described. The affects to the electron beam by introducing the TPJS will also be present.

HIGH VOLTAGE STRUCTURE DESIGN

Figure 1 shows the 3D model of the DC high voltage photogun with its major components. This photogun applied the inverted-tapered-geometry ceramic insulator structure that extends into the spherical vacuum chamber (91.44 cm diameter) and mechanically holds the spherical cathode electrode (20 cm diameter). The cathode electrode was manufactured by welding two hydroformed hemisphere stainless steel shells and was polished by mechanical polishing to obtain a exceptionally smooth surface. An internal fixture was installed in the spherical electrode, which serves to fix the electrode to the insulator and also to hold the photocathode puck. The high voltage cable (0.5 cm diameter) was covered with vulcanized rubber plug and was placed inside the hollow ceramic insulator. One end of the cable was connected to the endpoint of the ceramic insulator, where a stainless steel bulk was tightly mechanically jointed to the insulator by Kovar (nickel-cobalt ferrous alloy) that is a good insulator-to-metal seal material. Another end of the cable was connected to a high voltage power supply that can provide a voltage up to 400 kV.

The "inverted" photogun has been successfully operated at 100-200 kV, and recently test the photogun at 350 kV at JLab [4–6]. However, breakdown and puncher often hap-

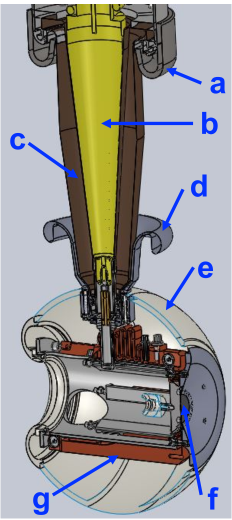

Figure 1: The 3D model of the high voltage structure, a) ground TPJS, b) ceramic insulator, c) rubber cable plug, d) HV TPJS, e) cathode electrode, f) photocathode sample, g) internal fixture.

ISBN: 978-3-95450-223-3 ISSN: 2673-7000 doi:10.18429/JACoW-NAPAC2019-MOPLM07

SIMULATION OF BEAM ABORTS FOR THE ADVANCED PHOTON SOURCE TO PROBE MATERIAL-DAMAGE LIMITS FOR FUTURE STORAGE RINGS *

M. Borland, J. Dooling, L. Emery, R. R. Lindberg, V. Sajaev, Y.-P. Sun,
ANL, Lemont, IL, USA

Abstract

Damage to tungsten and copper beam dumps has been observed in the Advanced Photon Source (APS), a 7-GeV, third-generation storage ring light source. This issue is expected to be much more severe in the APS Upgrade, owing to doubling of the stored charge and much lower emittance. An experiment was conducted at 6 GeV in the existing APS ring to test several possible dump materials and also assess the accuracy of predictions of beam-induced damage. Prior to the experiments, extensive beam abort simulations were performed with `elegant` to predict thresholds for material damage, dependence on vertical beam size, and even the size of the trenches expected to be created by the beam. This paper presents the simulation methods, simple models for estimating damage, and results. A companion paper in this conference presents experimental results.

INTRODUCTION

Beam dumps are required in storage rings to localize losses and protect sensitive equipment when the beam is aborted due to, e.g., an rf trip. Given that damage to tungsten and copper beam dumps has been observed in the APS [1], there is significant concern about the beam dumps for the APS upgrade (APS-U), since it will have twice the stored current and 100-fold lower horizontal emittance. The decoherence kicker proposed [2] to protect the APS-U swap-out dump is not helpful here, because the entire beam will be lost when the rf trips, for example; this, coupled with the rapid loss of beam following an rf trip, the possibility for kicker failure, and the limited effectiveness of decoherence in inflating the emittance, makes it unavoidable that the whole-beam dumps will be damaged. Doses on the APS-U whole-beam dumps are predicted to be as high as 35 MGy (35×10^6 J kg^{-1}), though they are typically expected to be lower because the losses are usually spread over five dumps.

We realized that it is possible to approach APS-U conditions in APS by adjusting the optics at the dump location to provide reduced horizontal beam size (RHB), reducing the vertical emittance, and running at 6 GeV, since that allows raising the beam current as high as 300 mA. In addition, by moving the beam dump surface close to the closed orbit, we reduce diffusion of the beam from resonances as it spirals inboard during the beam aborts. We selected two alloys, Al6061 and Ti6Al4V as target materials for tests, as reported in [3]. The aluminum alloy was chosen because we have never observed damage to this material in APS, while the titanium alloy was chosen because of its high melting temperature, relatively low Z, and high strength. The target materials were installed on a horizontal-movable scraper in Sector 37 of the APS.

SIMULATION METHODS

Simulations used the parallel version of `elegant` [4–6]. Because we must predict when and where the beam is lost, we used element-by-element tracking with a calibrated lattice model based on the response matrix fit method [7, 8]. We further included a model of the short-range wakefields [9–12], which has been validated in various experiments [12–14]. The rf systems (16 cavities driven by two klystrons) were included as an `RFMODE` element, which models beam loading, rf feedback [15], and muting of the generator output; these features allow bringing a multi-bunch beam to equilibrium, then tripping the rf systems.

The experiments are described in more detail elsewhere [3]. They involved making a series of fills from a few milliamps to just under 70 mA, limited by unrelated operations issues. For each fill level, the bunch pattern was different, based on operational considerations. The fill pattern details for each case are included in the simulations. Once each fill is created, the scraper is moved to within 2 mm of the closed orbit and a vertical beam bump is created with an amplitude that is unique to each case; this allows unambiguously relating any material damage to the conditions (beam current) prior to the abort. The details of the vertical bumps, including their effect on the vertical emittance through non-zero orbit in vertical sextupoles as well as the attempted nulling of this effect through adjustment of skew quadrupoles, are included in the simulations. However, for reasons still to be understood, the simulations predict significantly larger vertical emittances than measured, by up to a factor of two.

Figure 1 shows information on the timing of the simulated particle losses. The elapsed time relative to the rf trip event for loss of half the beam decreases as the stored current increases, due to beam loading in the rf cavities. The slope is about 50% larger in experiments [3], which suggests that improvements are needed to the rf cavity parameters used in the simulations. The time interval for loss of the central 80 or 90% of the beam also decreases as the stored current increases, for the same reason; the slope is in rough agreement with experiments. This shorter loss interval accentuates the impact of the dose on the dump, since there is less time for thermal diffusion.

---

* Work supported by the U.S. Department of Energy, Office of Science, Office of Basic Energy Sciences, under Contract No. DE-AC02-06CH11357.

ISBN: 978-3-95450-223-3 ISSN: 2673-7000 doi:10.18429/JACoW-NAPAC2019-MOPLM08

CONTROLLING TRANSIENT COLLECTIVE INSTABILITIES DURING SWAP-OUT INJECTION*

R. R. Lindberg†, Argonne National Laboratory, Lemont, IL USA

Abstract

Previous work has shown that collective instabilities at injection may reduce injection efficiency even for on-axis injection as planned for the APS-Upgrade [1]. Stability at injection is governed by a number of factors, including phase-space mismatch between injected and stored bunch, strength of the impedance, degree of nonlinearities, and feedback. We find that the large tune-shift with amplitude of the most recent APS-U lattice largely tames the transient instability via Landau damping, and show that using octupoles to increase the nonlinear tune shift can stabilize the transient instability at injection that plagued a previously unstable lattice.

INTRODUCTION

Predicting and controlling collective instabilities is an important part of storage ring design. In addition to ensuring stability at equilibrium, it has also been found that non-equilibrium conditions during injection may lead to conditions that are uniquely susceptible to collective effects. Reference [2] showed several such effects, including one in which transient beam loading in passive rf cavities drove longitudinal instabilities while filling the ring from zero current, so that controlling such rf transients in a passive bunch-lengthening cavity such as is planned for the APS-U requires filling the ring in a balanced way and in multiple stages. Recently, we identified a transient transverse instability at injection that can lead to particle loss even for on-axis injection [1]; such phenomena must be considered when designing stabilizing feedback systems. In this paper we review this last transient transverse instability at the APS-U, and describe one way that it can be stabilized using the nonlinear betatron tune-shift provided by octupole magents.

THE TRANSIENT TRANSVERSE INSTABILITY

The APS-U storage ring is a seven-bend achromat based upon ESRF's hybrid design [3]. The APS-U lattice has been steadily improved over the last several years, including the addition of reverse bends to bring the equilibrium emittance down to 42 pm [4], and many iterations of MOGA optimization to improve lifetime and dynamic aperture. A few years ago we reported on a transient instability at injection that we observed in the lattice used for the preliminary design report (PDR). While the impedance model predicted that a bunch was stable to transverse instabilities up to a single-bunch current of 10 mA, simulations also showed a rather strong transverse instability during the injection of a 4.2 mA bunch. At that time we concluded that single-bunch, turn-by-turn feedback was necessary to avoid significant particle loss during injection into the planned 48-bunch mode.

Our studies of the transient instability at injection found that it depended upon several factors, including:

1. The strength of the transverse impedance.
2. The size of the initial transverse offset.
3. The longitudinal phase space mismatch between injected and stored beam.
4. Nonlinear resonances experienced by particles in the (relatively) large emittance injected beam.

The first two factors are relatively easy to understand, in that the collective transverse force is directly proportional to both the impedance and the transverse offset. The third point was further explained in Ref. [1] and can be summarized as follows: the longitudinal mismatch leads to "tumbling" in the rf bucket, which in turn gives rise to transient current spikes and anomalously high wakefields. In fact, we have found that the transverse feedback requirements can be relaxed somewhat by more closely matching the injected beam length and, importantly, energy spread, to that of the stored beam. Finally, simulations indicate that nonlinear resonances can exacerbate all these issues.

As progress on lattice modeling was refined and further optimization of the sextupole strengths continued, we discovered that not all variants of the 42-pm lattice were equally plagued by the transient instability at injection. In particular, we found that the lattice proposed in the final design report (FDR) eliminated the instability entirely. We discovered this using element-by-element tracking for a subset of 13 commissioned lattices, including the three errors sets with the worst dynamic aperture (DA), and one case randomly selected from each 10th percentile of DA. We found that the losses in every case was $< 0.1\%$ once the orbit was moved to within 200 microns of the injected beam (which simulates the expected transverse offset resulting from the accumulated injection system errors). Furthermore, we found that the instability was tamed and injection losses were low even if the assumed transverse impedance was doubled; the instability appeared when the impedance was increased by a factor of 2.25, while feedback improved this margin to about a factor of 3.

Because there appeared to be many contributing factors to the transient instability at injection, it was initially not clear why the final lattice was stable. After some work, we noticed that the stable, final lattice had a significantly larger tune-shift with amplitude, which we conjectured might

---

* Work supported by U.S. Dept. of Energy Office of Sciences under Contract No. DE-AC02-06CH11357.

† lindberg@anl.gov

HIGH-POWER DESIGN OF A CAVITY COMBINER FOR A 352-MHz SOLID STATE AMPLIFIER SYSTEM AT THE ADVANCED PHOTON SOURCE*

G.J. Waldschmidt†, D.J. Bromberek, A. Goel, D. Horan, A. Nassiri
Argonne National Laboratory, Lemont, IL, USA

Abstract

A cavity combiner has been designed as part of a solid state amplifier system at the Advanced Photon Source with a power requirement of up to 200 kW for the full system. Peak field levels and thermal loading have been optimized to enhance the rf and mechanical performance of the cavity and to augment its reliability. The combiner consists of 16 rotatable input couplers, a reduced-field output coupler, and static tuning. The power handling capability of the cavity will be evaluated during a back-feed test where an external klystron source will be used to transmit power through the cavity into loads on each of the input couplers.

INTRODUCTION

The Advanced Photon Source is upgrading its facility to a 4th generation multi-bend achromatic light source. Given a reduction of the total beam energy to 6 GeV, the total number of cavities required in the APS storage ring will be reduced from 16 to 12 cavities. However, due to the cost and availability of klystron amplifiers, a solid state amplifier system is being developed and tested.

The 352 MHz solid state amplifier modules will produce up to 2 kW. As a result, combining networks are necessary to produce a total of up to 200 kW. The topology of such a system using cavity combiners is being evaluated at the APS. ESRF and others have previously explored their adoption [1]. An advantage of cavity combiners is the relatively small space consumption and the reduction in the number of external combining networks from large-scale coaxial combiner networks such as at Soleil and elsewhere [2]. Additionally, the number of inputs supported by a single cavity combiner is relatively easily adjusted based on the needs of the overall system.

A single solid state amplifier system producing up to 200 kW will be used for each storage ring cavity in the APS, requiring a total of 12 systems for the full storage ring after final integration. The initial prototype system will be designed with the capability of dynamically adjusting the DC voltage input of each of the amplifiers to optimize the efficiency of the amplifiers, ad hoc, based on changes in the beam loading thereby altering the thermal loading of the cavity combiner. The APS plans to install a prototype solid state amplifier system for a single storage ring cavity before construction of the APS-U begins in 2022.

DESIGN

The geometry of the cavity combiner shown in Fig. 1, focuses on creating a design with reliable, maximal power-handling capability. Particular emphasis was made on reducing the peak electric fields, preventing rf breakdown phenomenon, and minimizing thermal effects. For that reason, the geometry of the output coupler was selected, as well the elliptical shape of the input couplers, the tuner dimensions, surface finish requirements, as well as the integrity of all critical interface joints between components.

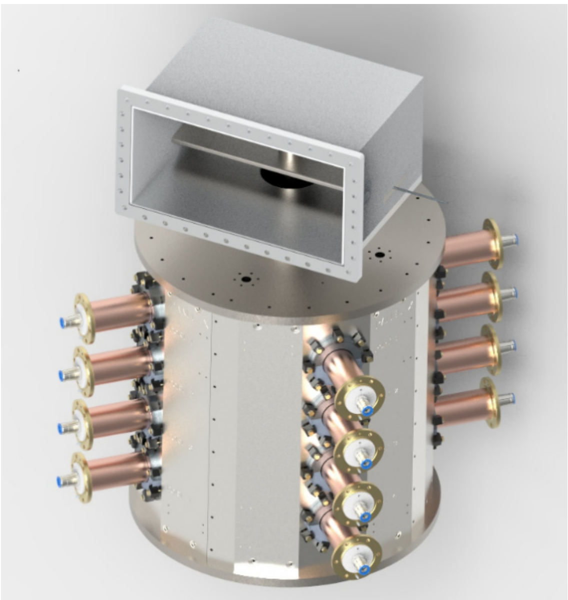

Figure 1: Cavity combiner geometry.

The cavity is monitored for breakdown effects with fast interlocks for arc detectors and on forward and reflected power levels. To ensure breakdown limits are not compromised due to its operation in air, the environmental conditions surrounding the cavity are monitored and interlocked on humidity levels, in addition to the constant circulation of air through the cavity.

The cavity combiner prototype was designed as a flexible platform for evaluating features and performing optimizations for the final combiner. The input couplers are fully rotatable to perform optimal tuning during assembly and account for the longitudinal variability of the cavity field strength. While tuning, the input coupling is adjusted on a single coupler, while all others are terminated with a short circuit, such that the reflection coefficient is fixed at $\Gamma = \frac{-(m-2)-N}{m+N}$, where m=1 is the number of unshorted input ports and N is the total number of inputs. The cavity will

---

* Work supported by US DOE under contract DE-AC02-06CH11357
† waldschm@anl.gov

North American Particle Acc. Conf. NAPAC2019, Lansing, MI, USA JACoW Publishing
ISBN: 978-3-95450-223-3 ISSN: 2673-7000 doi:10.18429/JACoW-NAPAC2019-MOPLM10

SIMULATION STUDY WITH SEPTUM FIELD MAP FOR THE APS UPGRADE*

A. Xiao[†], M. Abliz, M. Borland, ANL, Argonne, IL 60439, USA

Abstract

One of the biggest challenges faced by the Advanced Photon Source Upgrade injection system design is the septum magnet. Not only does the required leakage field inside the stored beam chamber need to be smaller than for the present ring, the magnet has to be slightly rotated about the z-axis to provide a gentle vertical bend that brings the injected beam trajectory close to $y = 0$ when it passes through the storage ring quadrupole magnets upstream of the straight section. For the convenience of magnet design, the magnet has also yaw and pitch angle about the stored beam coordinate system. This paper describes the coordinate system transformation necessary to properly model the magnet from field maps. The main field is checked by tracking the injected beam backwards, while leakage fields are included in dynamic aperture simulation and beam lifetime calculation. Simulation results show that the magnet design satisfies the physics requirements.

INTRODUCTION

On-axis swap-out vertical injection was chosen for the Advanced Photon Source Upgrade [1] (APS-U) to allow pushing the beam emittance to an extremely low value [2]. Detailed descriptions of the beam transport line design and the extraction/injection section optimization can be found elsewhere [3, 4].A schematic of injection section is shown in Fig. 1. The septum magnet needs to be slightly rotated about the stored beam z-axis (roll angle) to provide a gentle vertical bend that brings the injected beam trajectory close to $y = 0$ when it passes through the upstream storage ring quadrupole magnets Q1 and Q2 as shown in Fig. 1. To best utilize the uniform field region of the magnet, the magnet is also installed with a yaw angle respect to the stored beam z-axis. Finally, to reduce the leakage field inside the stored beam chamber, the septum sheet that separates the injected beam and the stored beam chamber has a gradually reduced thickness from ~4.4 mm at the upstream end to 2 mm at the downstream end, i.e. a pitch angle. Details on the magnet design can be found in [5, 6].

To verify the magnet design, both the injected beam trajectory and the impact of leakage field to the stored beam dynamics are simulated using the field map calculated from the magnet design model. Due to the complexity of magnet geometry (three rotation angles), a careful coordinate system transformation is required. This paper describes the way to obtain the transformation matrix, then gives simulation results for both the injected and stored beam. Simulation results show that the magnet design satisfies the physics requirements.

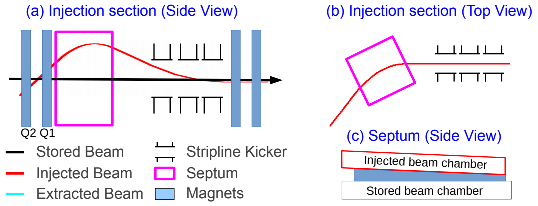

Figure 1: Schematic drawing of injection region and septum placement. (a) The septum has a roll angle to provide a gentle vertical bend; (b) The septum has a yaw angle; (c) The septum has a pitch angle to reduce the leakage field.

COORDINATE SYSTEM TRANSFORMATION

The septum magnet is designed using Opera-3D [7]. The coordinate system used in the design is fixed to the magnet and is referred as local coordinate system (X,Y,Z) in this paper. To simulate the leakage field, the field map needs to be transformed to the stored beam coordinate system, which is referred to as the global coordinate system (x,y,z) in this paper. To calculate the transformation matrix (also to check the magnet design), we use points on the upstream and downstream edge of stored beam chamber as fiducial points. Their global coordinates (x,y,z) are known from the design requirement, while their local coordinates (X,Y,Z) are given from Opera-3D. The fiducial marks are selected so that the x, y, and z-axis can be easily determined, as shown in Fig. 2. One can see that to determine the transformation matrix, a minimum of four fiducial markers is required. We used eight points to obtain some redundancy. As one can see from the same figure, one erroneous data point was found. The

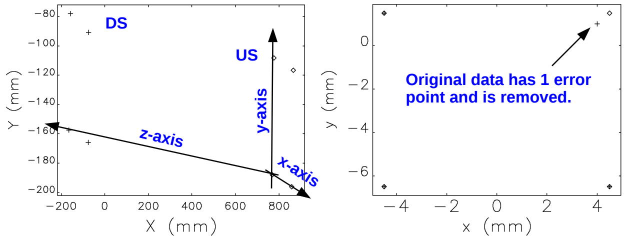

Figure 2: Coordinates of fiducial markers on the stored beam chamber edge: left - local coordinate system; right: global coordinate system (an error in one data point was found).

---

[*] Work supported by the U.S. Department of Energy, Office of Science, Office of Basic Energy Sciences, under Contract No. DE-AC02-06CH11357.

[†] xiaoam@anl.gov

PROGRESS ON THE INJECTION TRANSPORT LINE DESIGN FOR THE APS UPGRADE*

A. Xiao†, M. Borland, ANL, Lemont, IL USA

Abstract

An on-axis vertical injection scheme was adopted for the Advanced Photon Source Upgrade (APS-U) multi-bend achromat lattice. As the design of the injection scheme has become more detailed, the booster to storage ring transport line (BTS) has advanced, including effects such as the septum field map and stray fields of storage ring magnets. Various error effects are simulated for setting specifications and predicting expected performance. The beam diagnostic scheme, including emittance measurement, is incorporated into the beamline design.

INTRODUCTION

The BTS line design for APS-U has advanced as detailed information became available, such as the septum magnet design [1, 2]; stray fields from the storage-ring magnets, and beam-based measurement results using the current BTS line. Issues have been identified and addressed in studies.

The injected beam will inevitably pass through some storage ring magnets (Q1 and Q2) as its trajectory merges with the stored beam trajectory, and similarly the stored beam will pass through the septum magnet and stripline kickers. These beams will see different magnetic fields and alignment, as well as different path length. These effects are included in the current BTS line design and results presented here, leading to revised geometry and optical solutions. In addition, a coupling issue was identified and a simple solution was found to minimize the effect.

For beam diagnostics, an emittance measurement station is included in the optical design; the required screen resolution was obtained from simulation results. Simulations of optics measurements and correction were just started. Some beam-based measurements and simulation results for BPM noise, booster extracted beam jitter, quad alignment errors, and dispersion measurement are also presented here.

INJECTION SECTION DESIGN

In the injection section, both stored and injected beam pass through the same elements on different trajectories, i.e. from the upstream end of Q2 magnet to the downstream end of stripline kickers, as shown in Fig. 1. Since we are doing on-axis injection, this section is designed using backward tracking of the the injected beam. From Fig. 1, one can see that the injected beam and stored beam have different path lengths in same elements; even for elements that are the same (for example the three stripline kickers), the path length of injected beam, i.e. the effective length, are slightly different due to different entrance/exit angles. The path length of each element can be calculated analytically, or using a simulation code such as `elegant` [3] to fit the floor coordinates. We use the latter method since it's simple and reduces human errors.

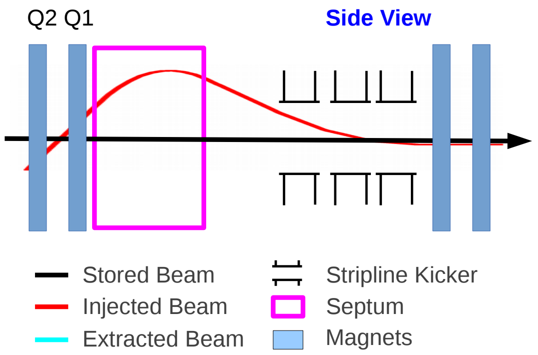

Figure 1: Schematic drawing of injection region.

The septum field map [4] from 3D OPERA simulations is included in the updated BTS line design instead of a hard edge dipole magnet; the details of simulation with the septum field map are described in [5]. The difference in the injected beam trajectory between a hard edge magnet model and the field map is shown in Fig. 2. This difference requires rematching the BTS line geometry.

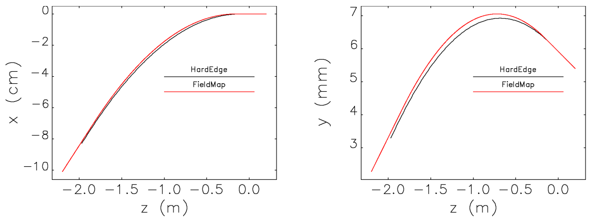

Figure 2: Calculated injected beam orbit from hard edge model (black), and septum magnetic field map (red).

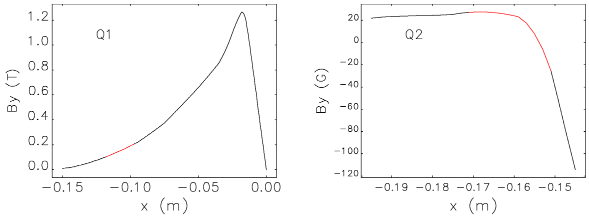

Figure 3: Stray field profile (B_y vs x at $y = 0$ and $z = 0$), red-line shows injected beam centroid range when it goes through the storage ring Q1 and Q2 magnets.

---

* Work supported by the U.S. Department of Energy, Office of Science, Office of Basic Energy Sciences, under Contract No. DE-AC02-06CH11357.

† xiaoam@anl.gov

ISBN: 978-3-95450-223-3 ISSN: 2673-7000 doi:10.18429/JACoW-NAPAC2019-MOPLM13

INVESTIGATIONS OF THE ELECTRON BEAM ENERGY JITTER GENERATED IN THE PHOTOCATHODE RF GUN AT THE ADVANCED PHOTON SOURCE LINAC*

J. Dooling†, Y. Sun, D. Hui‡, A. Lumpkin, K. P. Wootton, A. Zholents, T. Smith
Argonne National Laboratory, Lemont, IL USA

Abstract

Characterizations continue of the electron beam properties of a recently installed S-band photocathode (PC) rf gun at the Advanced Photon Source Linac facility. In this case, we have utilized a low-energy spectrometer beam line located 1.3 m downstream of the gun cavity to measure the electron beam energy, energy spread, and energy jitter. The nominal energy was 5.4 MeV using a gun gradient of 110 MV/m, and the energy spread was 17 keV when driven by a 2.5-ps rms duration UV laser pulse at the selected rf gun phase. An energy jitter of 25 keV was initially observed in the spectrometer focal plane images. This jitter was partly attributed to the presence of both the 2nd and 3rd harmonics of the 119 MHz synchronization signal provided to the phase locked loop of the drive laser oscillator. (The nominal rms jitter from the timing stabilizer is 1.6 ps.) The addition of a 150-MHz low-pass filter in the 119-MHz line strongly attenuated the two harmonics and resulted in a reduced energy jitter of 15 keV. Comparisons of the gun performance to ASTRA simulations will also be presented.

INTRODUCTION

Installation of an LCLS-I-style, dual-waveguide-feed photocathode (PC) gun at the upstream end of the Advanced Photon Source (APS) linac was completed in 2015. A spectrometer line is included with the PC Gun to allow measurement of gun energy and energy spread. A YAG screen and current monitor upstream of the spectrometer dipole magnet enables solenoid-scan emittance and quantum efficiency measurements as well. The spectrometer dipole magnet current is interlocked to permit parallel operation of the PC Gun with user beam. A schematic of the PC Gun beam line is presented in Figure 1. For upcoming experiments overlapping photon and electron beams, e.g. tapering enhanced stimulated superradiant amplification (TESSA) [1,2], requirements are rms jitter <300 fs and peak current >1 kA.

ANALYSIS

While measuring beam energy using the YAG screen at the end of the spectrometer line (YAGBend), fluctuations in horizontal position were observed. Motion of the laser spot on the cathode, as measured on the virtual cathode (VC), is small. An image from the VC covering 2 mm x 2 mm is shown in Figure 2. Over a 5-minute interval, the spot centroid was observed to vary by 8 μm. Dispersion in the spectrometer line suggests the fluctuations are due to energy variations which are in turn caused by differences between the arrival time of the laser pulse and phase of the rf on the gun photocathode surface. The energy fluctuations or jitter can be determined once the dispersion at the YAGBend screen is known; the dispersion will be modified by the quadrupole magnet just upstream of the screen.

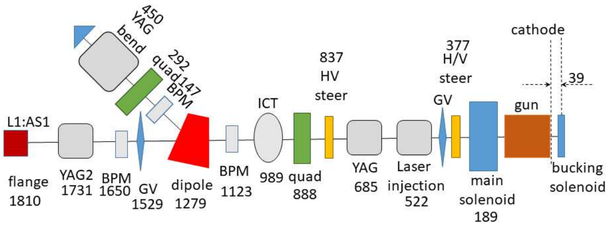

Figure 1: APS PC Gun beam line schematic.

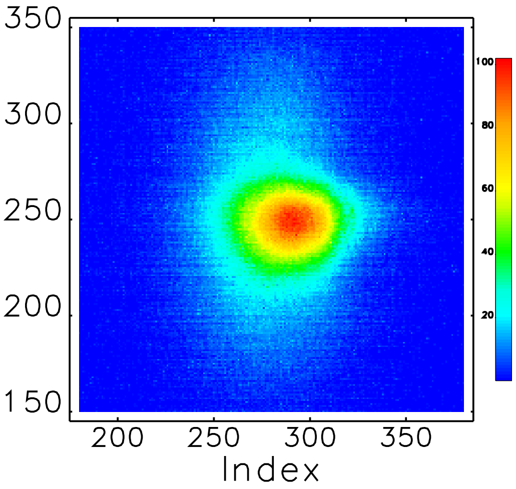

Figure 2: Laser spot on the VC camera; rms x- and y-spot sizes are 0.24 mm and 0.22 mm. FOV: 2 mm x 2 mm.

Dispersion

Examining the x-z components of the transfer matrix from the entrance of the dipole to YAGBend,

$$\vec{x}_1 = \boldsymbol{R}_s \vec{x}_0, \tag{1}$$

---

* Work supported by the U.S. Department of Energy, Office of Science, Office of Basic Energy Sciences, under Contract No. DE-AC02-06CH11357.

† jcdooling@anl.gov

‡ present address: Physics Department 1118 E 4th St., PAS 353, Tucson, AZ 85721-0081

North American Particle Acc. Conf. NAPAC2019, Lansing, MI, USA JACoW Publishing
ISBN: 978-3-95450-223-3 ISSN: 2673-7000 doi:10.18429/JACoW-NAPAC2019-MOPLM14

STUDIES OF BEAM DUMPS IN CANDIDATE HORIZONTAL COLLIMATOR MATERIALS FOR THE ADVANCED PHOTON SOURCE UPGRADE STORAGE RING*

J. Dooling†, W. Berg, M. Borland, G. Decker, L. Emery, K. Harkay, R. Lindberg, A. Lumpkin,
G. Navrotski, V. Sajaev, Y-P. Sun, K. P. Wootton, A. Xiao
Argonne National Laboratory, Lemont, IL, USA

Abstract

We present the results of experiments on the effects of beam dumps on candidate collimator materials for the Advanced Photon Source Upgrade (APS-U) storage ring (SR). Due to small transverse electron beam sizes, whole beam loss events are expected to yield dose levels in excess of 10 MGy in beam-facing components, resulting in localized melting. Whole beam aborts have characteristic time scales ranging from 100s of ps to 10s of microseconds which are either much shorter than or roughly equal to thermal diffusion times. Aluminum and titanium alloy test pieces are each exposed to a series of beam aborts of varying fill pattern and charge. Simulations suggest the high energy/power densities are likely to lead to damage in any material initially encountered by the beam. We describe measurements used to characterize the beam aborts as well as results of post-experiment inspection. The goal of this work is to guide the design of APS-U SR collimators. Simulations are discussed in a companion paper at this conference.

INTRODUCTION

The Advanced Photon Source (APS) is building a fourth-generation storage ring to replace the present double-bend achromat lattice with a multibend achromat [1], allowing generation of ultra-bright x-ray beams. The APS upgrade (APS-U) [2] will be able to produce these ultra-bright beams because of a 100-fold reduction in horizontal emittance and a two-fold increase in current. The APS-U electron beam has such high energy and power densities that virtually any material the beam strikes will be damaged [3].

We have previously seen damage from beam strikes in high-Z, high-density materials such as copper and tungsten use to fabricate vertical and horizontal scrapers at various locations at APS [4]. Two promising materials for the APS-U horizontal, whole-beam-dumps are aluminum alloy 6061-T6 (Al) and titanium alloy Ti-6Al-4V (Ti6Al4V or TiA); the former for its high thermal diffusivity and low Z, the latter for its strength and high melting temperature. Two collimator test pieces, one from each alloy, were fabricated and used during this study. Photographs of the copper scraper body with the Al and TiA test pieces are presented in Fig. 1 prior to testing with beam. The scraper is shown fully extended into the vacuum chamber, with the Al collimator on top. A 1-mm vertical gap exists between the test pieces.

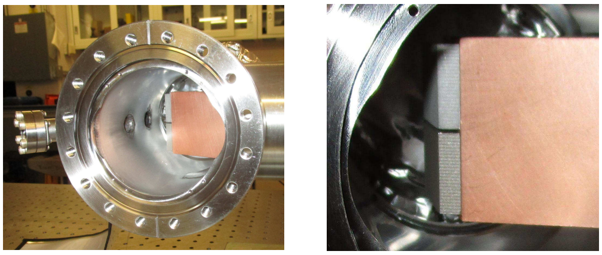
(a) Inboard view. (b) Outboard view, zoomed.

Figure 1: Upstream views of the Cu scraper and mounted Al- and Ti-alloy collimator test pieces.

A significant simulation effort was undertaken to support the collimator irradiation studies using `elegant` [5] and its parallellized version `Pelegant` [6–8]. Simulation details are provided in a companion paper [9] at this conference.

EXPERIMENT

Studies were conducted May 18-19, 2019 at a beam energy of 6 GeV. The scraper/collimator assembly was installed in the Sector 37 (S37) straight section. One of the goals called for increasing beam current up to 150 mA to more closely match the on-target dose expected in APS-U.

Study Setup

The aluminum and titanium alloy collimators were mounted on a calibrated, LVDT-actuated scraper for horizontal insertion into the beam chamber. Temperature and pressure readings were closely monitored during the study. Along with the regular suite of diagnostics including BPMs, current monitors, and pinhole emittance monitor, a camera system was installed to look directly at the beam-facing collimator surface before, during, and after beam irradiation. Fast beam loss monitors (BLMs) were also employed to observe the temporal evolution of the dump process.

Prior to the planned beam dumps, an experiment was conducted to accurately measure the location of the 1-mm gap between the collimator pieces (see Fig. 1b). This was done at low-current (~2 mA) by first moving the scraper such that the collimator surface was within a few millimeters of the beam, horizontally. The beam was then scanned vertically. Due to variations in horizontal acceptance, the beam lifetime (LT) is reduced as the beam approaches the vacuum chamber

---

* Work supported by the U.S. Department of Energy, Office of Science, Office of Basic Energy Sciences, under Contract No. DE-AC02-06CH11357.

† jcdooling@anl.gov

ISBN: 978-3-95450-223-3 ISSN: 2673-7000 doi:10.18429/JACoW-NAPAC2019-MOPLM15

DESIGN OF THE ASU PHOTOCATHODE LAB

C.J. Knill*, S.S. Karkare, Arizona State University, Tempe, USA
J.V. Conway, B.M. Dunham, K.W. Smolenski, Xelera Research LLC, Ithaca, USA
H.A. Padmore, Lawrence Berkeley National Laboratory, Berkeley, USA

Abstract

Recent investigations have shown that it is possible to obtain an order of magnitude smaller intrinsic emittance from photocathodes by precise atomic scale control of the surface, using an appropriate electronic band structure of single crystal cathodes and cryogenically cooling the cathode. Investigating the performance of such cathodes requires atomic scale surface diagnostic techniques connected in ultra-high vacuum (UHV) to the epitaxial thin film growth and surface preparation systems and photo-emission and photocathode diagnostic techniques. Here we report the capabilities and design of the laboratory being built at the Arizona State University for this purpose. The lab houses a 200 kV DC gun with a cryogenically cooled cathode along with a beam diagnostics and ultra fast electron diffraction beamline. The cathode of the gun can be transported in UHV to a suite of UHV growth chambers and surface and photoemission diagnostic techniques.

INTRODUCTION

Increasing electron beam brightness is central to many accelerator applications like Free Electron Lasers (FEL) [1], Ultrafast Electron Diffraction (UED) setups [2], and Energy Recovery Linacs (ERL) [3]. Beam brightness is inversely proportional to the square of the intrinsic emittance of the photocathode producing the electron beam. The intrinsic emittance is described by the equation $\epsilon_n = \sigma_x\sqrt{\frac{\mathrm{MTE}}{mc^2}}$, where MTE is the mean transverse energy of the photoemitted electrons, σ_x is the rms laser spot size on the cathode, m is the rest mass of an electron, and c is the speed of light in vacuum [4]. Thus, the development of low MTE (or low intrinsic emittance) cathodes is crucial to increasing beam brightness.

Various theoretical and experimental investigations performed over the last decade show that the MTE of electrons obtained from the cathode depends on the excess energy (i.e the difference between the photon energy and the work function) [5], the lattice temperature [4, 6], the surface non-uniformities of physical roughness and work function variations [7, 8], the band structure [9] and non-linear photoemission effects of electron heating and multiphoton emission [10]. Recently, by minimizing contributions from all of the above an MTE as low as 5 meV was demonstrated from the atomically ordered Cu(100) surface cooled to 30 K when photon energies close to the photoemission threshold were used. However, due to the low quantum efficiency (QE), it is not possible to extract large charge densities at 5 meV MTE from this surface and higher QE materials that can minimize the MTE are essential [11].

In general reducing the excess energy and the lattice temperature reduces the MTE [4, 6]. Hence it is essential to investigate the cathode performance at cryogenic temperature with a photon energy that can be tuned very close to the photoemission threshold. Minimizing the effects of surface non-uniformities requires the use of atomically flat, ordered, single crystalline surfaces as cathodes [7, 8]. This necessitates the cathode surfaces to be grown/prepared and characterized in UHV and requires atomic scale surface diagnostics connected to photoemission diagnostics in UHV. Achieving the smallest MTE also requires that the emission does not occur from electronic states with a large transverse momentum, and hence choosing single crystal cathodes with the right band structure is essential [10]. Finally, demonstration of low MTE performance at large charge extraction densities is essential. This requires testing at cryogenic temperatures in a relatively high field electron gun.

Identifying cathode surfaces that satisfy all criteria to achieve low MTE will require testing a wide variety of cathode materials requiring a relatively quick transfer of the cathode between the various growth and characterization chambers.

To enable such complete characterization and to identify low MTE cathode materials, we are developing an advanced photocathode lab at the Arizona State University. The lab will house 200 kV DC gun with a cryogenically cooled cathode along with a beam diagnostics and ultra fast electron diffraction beamline. The cathode of the gun can be transported in UHV to a suite of UHV growth chambers and surface and photoemission diagnostic techniques. In this paper we highlight the design and the various capabilities of this lab.

LAB DESIGN

Figure 1 shows the 3-D model of the ASU photocathode laboratory. The laboratory will house two growth chambers, an atomic scale surface diagnostics chamber, an electron energy analyzer, and a DC electron gun all connected in UHV using a trolley based sample transfer mechanism. The details of the various experimental capabilities in the lab are outlined below:

Sample Transfer

The various UHV chambers will be connected in UHV by a single long transfer line that is designed to have vacuum pressures of 10^{-10} torr or lower. This will prevent the possibility of contamination of the cathode that could arise when transporting it between the different UHV chambers.

---

* cknill2@asu.edu

DESIGN OF A 200 kV DC CRYOCOOLED PHOTOEMISSION GUN FOR PHOTOCATHODE INVESTIGATIONS

G. S. Gevorkyan[*], S. S. Karkare, Arizona State University, Tempe, AZ, USA
I. V. Bazarov, L. Cultrera, A. Galdi, W. H. Li, J. M. Maxson, Cornell University, Ithaca, NY, USA

Abstract

Intrinsic emittance of photocathodes limits the brightness of electrons beams produced from photoemission guns. Recent advancements have shown that an order of magnitude improvement in intrinsic emittance over the commonly used polycrystalline metal and semiconductor cathodes is possible via use of single crystalline ordered surfaces of metals, semiconductors and other exotic materials at cryogenic temperatures as cathodes. However, due to practical design considerations, it is not trivial to test such cathodes in existing electron guns. Here we present the design of a 200kV DC electron gun being developed at the Arizona State University for this purpose. The design is based off the Cornell DC cryogun but can use the omicron paddle-shaped sample holder and is connected in UHV to a suite of surface preparation and characterization chambers designed to test single crystalline ordered surfaces as cathodes. The omicron paddle-shaped holder allows for easy cathode characterization in standard surface science instruments and allows for a large flexibility in terms of the cathode shape and size enabling the study of numerous commercially available and epitaxially grown single crystal materials. Here we present the mechanical, electrostatic and the thermal design of this gun.

INTRODUCTION

Linear accelerator applications like X-ray Free Electron Lasers and Ultrafast Electron Diffraction setups are critically dependent on the intrinsic emittance of the photocathode [1]. Existing photoemission electron guns used for such applications have so far employed polycrystalline cathodes with disordered surfaces and generally operate with the cathode at near room temperatures. Recent studies suggest that an order of magnitude improvement in the intrinsic emittance of cathodes is possible by using single crystalline cathodes with atomically ordered surfaces that have the appropriate electronic band-structure and are cooled to LHe temperatures in ultra-high-vacuum (UHV) [2]. However, existing electron guns do not allow for use of such cathodes without significant modifications to the cathode transfer mechanism. Moreover, existing electron guns are often designed to use a specific size and shape of the cathode restricting the exploration of a wide range of potential single crystal materials that are more easily available in different sizes and shapes as cathodes. To overcome this issue, we are developing a 200 kV DC photoemission gun with a cryocooled cathode (cryogun) at Arizona State University for photocathode research. The design of this gun is based off the design of the 200 kV DC cryogun already in operation at Cornell University [3]. However, the ASU cryogun has a better thermal cooling design allowing for temperatures lower than 20 K at the cathode and has been designed to use a variable size cathode wafer mounted on to an omicron flag style sample holder compatible with several surface science instruments. The cathode transfer system is designed to allow easy UHV transport of the cathode from the gun into a wide range of surface science instruments, photoemission diagnostics and single crystal growth capabilities available at the ASU Photoemission and Bright Beams laboratory [4]. This gun will allow easy investigation of a wide range of both single and polycrystalline cathode materials as ultra-low emittance electron sources. Here we present the mechanical, thermal cooling and the electrostatic design of the ASU cryogun.

MECHANICAL DESIGN

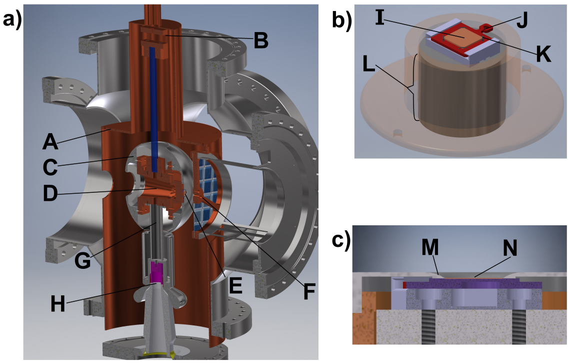

Figure 1: (a) Cross-section of the overall mechanical design of the gun. The cryoshield (A) connects to the cryostat at the copper strap (B). The spherical electrode (C) encloses the copper core (D). The photocathode (E) is inserted into the core and faces the anode (F). The thin wall tube (G) connects the core to the DC plug. A stainless steel collar shields the ceramic covering the HVPS plug from high fields at the triple point junction (H). The design is based on the Cornell DC cryogun [3]. (b) The photocathode (I) strapped onto the omicron paddle (J) using tantalum foil (K) and inserted into the cathode plug (L). (c) A closer view of the electrode and photocathode cross-section, more clearly showing the pierce electrode (M) with the photocathode (N) inserted.

The mechanical design of the ASU cryogun is based off the Cornell DC cryogun with a few modifications to allow for better radiation shielding, a flexible cathode size and a continuous flow cryostat based cooling system.

---

[*] Ggevorky@asu

ISBN: 978-3-95450-223-3 ISSN: 2673-7000 doi:10.18429/JACoW-NAPAC2019-MOPLM17

LONGITUDINAL IMPEDANCE MODELING OF APS PARTICLE ACCUMULATOR RING WITH CST*

C. Yao†, J. Carvelli, K.C. Harkay, L.H. Morrison, Argonne National Laboratory, Lemont, IL, USA
J.S. Wang, Dassault Systems, Waltham, MA, USA
D. Hui, University of Arizona, Tucson, AZ, USA

Abstract

The APS-U (APS upgrade) ring plans implement a "swap out" injection scheme, which requires an injected beam of 15.6 nC single-bunch beam. The Particle Accumulator Ring (PAR), originally designed for up to 6 nC charge, must be upgraded to provide 20 nC single bunch beam. Our studies have shown that bunch length of the PAR beam, typically 300 ps at lower charge, increases to 800 ps at high charge due to longitudinal instabilities, which causes low injection efficiency of the downstream Booster ring. We completed beam impedance simulation of all the PAR vacuum components recently with CST wakefield solver [1].

3D CAD models are directly imported into CST and various techniques were explored to improve and verify the results. The results are also cross-checked with that from Gdfidl and Echo [2,3] simulation.

We identified 23 bellow- and 24 non-bellow flanges that contribute to as much as 40% of the total loss factor. We are considering upgrade options to reduce overall beam energy loss and longitudinal impedance.

Beam tracking simulation is in progress that includes the longitudinal impedance results from the CST simulations. This is not reported here.

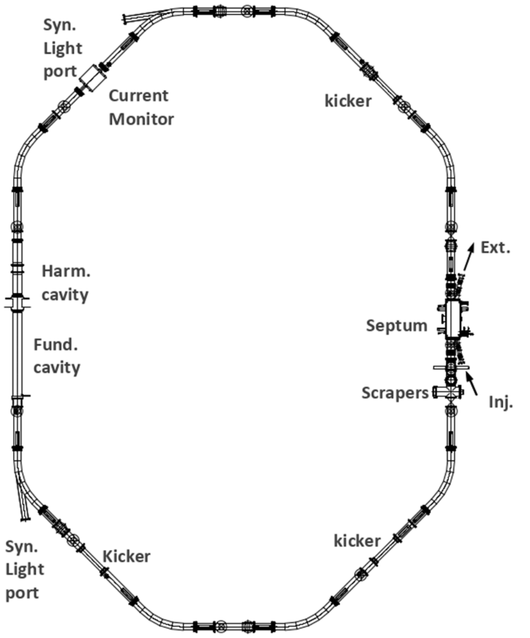

Figure 1: Layout of the PAR vacuum chamber.

INTRODUCTION

A layout of the PAR vacuum chamber is shown in Fig. 1. It consists of an injection section, an rf cavity section that houses a fundamental cavity and a 12th harmonic cavity, eight 45° bending chambers, and six straight chambers for BPMs, kickers, etc.

CST Studio Suite was selected because its ability of importing models directly from CAD models and it is available both on Windows PC and Linux workstation. Most of the simulations were performed with a bunch length of 50 ps and a total wake length of ~50 ns. The PAR beam has a bunch length of from about 300 ps to 1 ns, depending on rf settings and beam current. This selection of parameters is a compromise between desired bandwidth and frequency resolution, and computer resources and simulation time.

Table 1 is a list of all the components that are included in the simulation

LOSS FACTOR RESULTS

A 20 nC beam in the PAR loses significant amount of energy due to cavity and chamber impedance. In table 1 we listed the loss factor result from wakefield simulations. Most significant contributors are: kicker chambers, bending chambers, florescent screens and scraper chambers.

The kicker ceramic chamber has a resistive coating of 75 Ω per square, which contributed to the high loss factor. We plan to do a surface resistance measurement to confirm the specifications.

Figure 2 shows a plot of beam loss factor vs bunch length, which is computed based on the impedance results and Gaussian beam distribution. Based on this results a 20 nC PAR beam with 600ps bunch length will lose 1.32 kW of power. This must be considered in the overall power requirement of the rf system.

Loss factor measurement of the PAR are performed [4], which showed a loss factor of 160 V/nC for a 10nC with a bunch length of 1nS. Comparing with simulation there is a 16% difference. We plan to further investigate the causes of the discrepancy and revisit some components that contribute large portion of losses, such as kicker, florescent screens, and bellowed chambers.

IMPEDANCE RESULTS

Figure 3 shows the total real and imaginary longitudinal impedance of the PAR. Longitudinal beam tracking is under way with the results from these impedance results.

---

* Work supported by the U.S. Department of Energy, Office of Science, under Contract No. DE-AC02-06CH11357
† cyao@anl.gov

DESIGN OF THE 2-STAGE LASER TRANSPORT FOR THE LOW ENERGY RHIC ELECTRON COOLING (LEReC) DC PHOTOGUN*

P. Inacker-Mix†, L. Nguyen, S. Bellavia, A. Curcio, A.V. Fedotov, W. Fischer, D. Gassner,
J. Jamilkowski, P. Kankiya, D. Kayran, R. Lehn, R. Meier, T. Miller, M. Minty, S. Nayak, L. Smart,
C. Spataro, B. Streckenbach, A. Sukhanov, J. Tuozzolo, Z. Zhao
Brookhaven National Laboratory, Upton, NY, USA

Abstract

The electron beam for the recently constructed Low Energy RHIC electron Cooler (LEReC) at Brookhaven National Laboratory is generated by a high-power fiber laser [1] illuminating a photocathode. The pointing stability of the low-energy electron beam, which is crucial to maintain within acceptable limits given the long beam transport, is highly dependent on the center-of-mass (CoM) stability of the laser spot on the photocathode. For reasons of accessibility during operations, the laser itself is located outside the accelerator tunnel, leading to the need to propagate the laser beam 34m via three laser tables to the photocathode. The challenges to achieving the required CoM stability of 10 microns on the photocathode thus requires mitigation of vibrations along the transport and of weather- and season-related environmental effects, while preserving accessibility and diagnostic capabilities with proactive design. After successful commissioning of the full transport in 2018/19, we report on our solutions to these design challenges.

INTRODUCTION

The Low Energy RHIC electron Cooling (LEReC) project is the first to demonstrate electron cooling using RF-accelerated bunched electron beams. It successfully completed commissioning in 2018 [2] and subsequently demonstrated cooling of gold ions for collisions in the Relativistic Heavy Ion Collider (RHIC) at the Brookhaven National Laboratory (BNL) in 2019 [3].

LEReC is located inside the RHIC radiation enclosure. The radiation levels, environmental conditions, and limited access during the accelerator run make it necessary to locate the drive laser outside the enclosure, about 30 m in optical distance from the LEReC electron gun. This circumstance makes a laser transport system necessary.

At the same time, the Center-of-Mass (CoM) stability of the laser spot on the aperture located next to the electron gun, which gets imaged to the photocathode to generate a desired truncated Gaussian profile, needs to be <50 µm rms, driven by the required CoM stability of the image (<10 µm rms) to allow the 100 m long electron beam transport required for cooling of both ion beams in RHIC with the same electron beam.

The laser transport constructed for LEReC successfully finished commissioning in 2018 with the addition of a camera-based feedback system [4] to correct for slow drifts due to weather-driven ground motion.

LEReC LASER TRANSPORT OVERVIEW

The laser transport system consists of a launch system located on the drive laser table in the laser trailer; a relay table located just inside the RHIC enclosure to lift the laser beam above the RHIC beam pipes; and a receiving gun table which holds the aperture that gets imaged onto the photocathode.

Laser tables along the transport host a light-tight enclosure and are interconnected via straight vacuum tubes that are not supported by the tables themselves. The laser beam is elevated or lowered by A-frames specifically designed to provide rigid support for mirrors.

Solid concrete blocks bind the relay and gun tables to the foundation of the accelerator. The drive laser table is not rigidly attached to the laser trailer, but rather held by five thermally insulated steel legs welded to two 21-metric-ton steel blocks located 34 in below ground.

Figure 1 shows a schematic of the transport system.

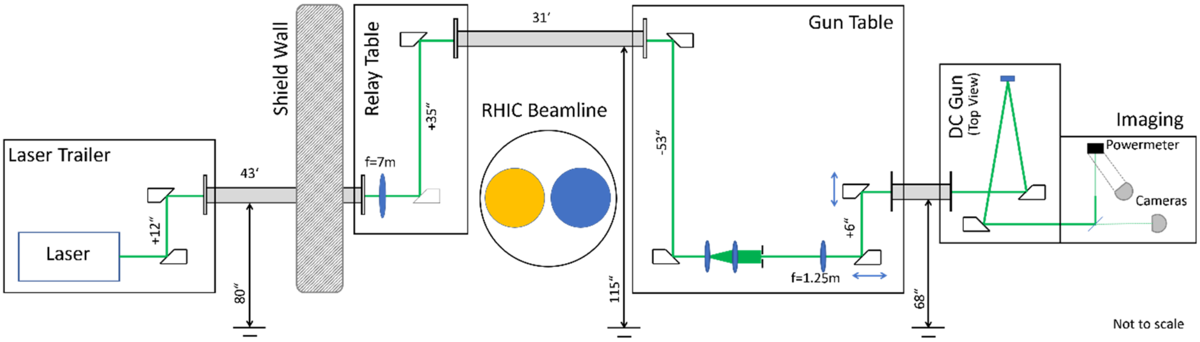

Figure 1: Schematic of the LEReC Laser Transport System.

---

* Work supported by U.S Department of Energy
† E-Mail: pinacker@bnl.gov

IMPEDANCE CONSIDERATIONS FOR THE APS UPGRADE*

R. R. Lindberg†, Argonne National Laboratory, Lemont, IL USA
A. Blednykh, Brookhaven National Laboratory, Upton, NY USA

Abstract

The APS-Upgrade is targeting a 42 pm lattice that requires strong magnets and small vacuum chambers. Hence, impedance is of significant concern. We overview recent progress on identifying and modeling vacuum components that are important sources of impedance in the ring, including photon absorbers, BPMs, and flange joints. We also show how these impact collective dynamics in the APS-U lattice.

IMPEDANCE MODELING

BPM-bellows Assembly

We need to ensure that the impedance associated with the BPM-bellows assembly is minimal, both to ensure a manageable impact to collective instabilities, and to minimize the levels of RF heating. Figure 1(a) shows a CAD-generated model of the BPM-bellows assembly. The GlidCop RF fingers are shown in light gray; each finger is tapered from 0.5 mm at the root to 0.3 mm at the tip and will be coated with 13 microns of silver. The central BPM housing is 12 mm from the beam and will be plated in Rhodium. A magnified GdfidL representation of a single BPM button is in Fig. 1(b). The BPM button is 8 mm in diameter and 2 mm thick, while the BPM pin dimensions have been tailored to best match the characteristic impedance to 50 Ohm (the minimum pin diameter is 0.65 mm).

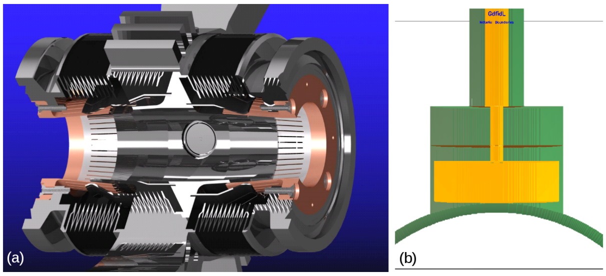

Figure 1: a) CAD model of the BPM-bellows assembly. b) GdfidL model of a single BPM button.

We used `GdfidL` [1] to compute the impedance of assembly; we plot the real and imaginary parts of the longitudinal $Z_{\parallel}$ in Fig. 2(a). The lowest resonance mode due to the button geometry is expected to have a frequency $f_{H11} \sim 11$ GHz, which we clearly see. This is well-beyond the bunch spectrum of the beam, so that we do not expect the beam to interact strongly with the bunch. Adding the real part $Z_{\parallel}$ to the contribution of the resisitive wall, we then computed the loss factor over a range of bunch lengths σ_z, from which we computed the expected RF heating shown in Fig. 2(b). In the case that the bunch-lengthening higher-harmonic cavity (HHC) is not functioning, we predict that $\sigma_z \approx 12$ mm and the power lost by the beam is sbout 2.8 W. If the HHC is tuned to flatten the potential we have $\sigma_z \approx 25$ mm and a power of 0.15 W, while if the HHC is set to maximize the lifetime by overstretching the bunch the loss is 0.05 W.

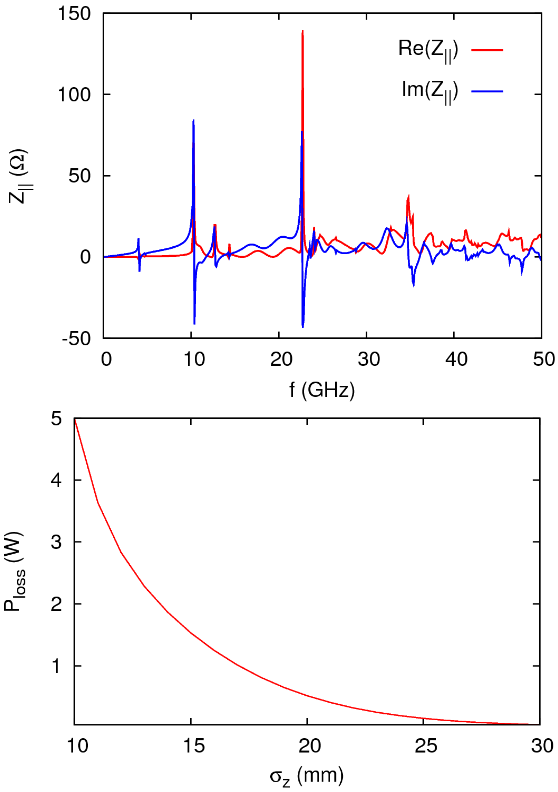

Figure 2: The real and imaginary parts of the BPM-bellows assembly impedance. Predicted RF heating level as a function of bunch length.

These levels of RF heating all appear to be manageable, but further simulations of precisely where the heat is deposited and how efficiently it can be transferred are planned. Finally, the assembly was just installed and removed for testing in the NSLS-II ring, and will be installed in the present APS for tests under beam.

In-line Photon Absorbers

What we call "in-line photon absorbers" are tapered restrictions whose purpose is to mask sensitive components from small to moderate levels of synchron radiation. Ray tracing simulations indicate that the absorbers must protrude into the chamber by typically 2–4 mm to provide the required

---

* Work supported by U.S. Dept. of Energy Office of Science under Contract No. DE-AC02-06CH11357.

† lindberg@anl.gov

CIRCUIT MODEL ANALYSIS FOR HIGH CHARGE IN THE APS PARTICLE ACCUMULATOR RING*

K.C. Harkay†, J.R. Calvey, J.C. Dooling, L. Emery, R.R. Lindberg, K.P. Wootton, C. Yao
Argonne National Laboratory, Lemont, IL 60439, USA

Abstract

The Advanced Photon Source (APS) particle accumulator ring (PAR) was designed to accumulate linac pulses into a single bunch with a fundamental rf system, and longitudinally compress the beam with a harmonic rf system prior to injection into the booster. For APS Upgrade, the injectors will need to supply full-current bunch replacement with high single-bunch charge for swap-out in the new storage ring. Significant bunch lengthening, energy spread, and synchrotron sidebands are observed in PAR at high charge. Lower-charge dynamics are dominated by potential well distortion, while higher-charge dynamics appear to be dominated by microwave instability. Before a numerical impedance model was available, a simple circuit model was developed by fitting the measured bunch distributions to the Haissinski equation. Energy scaling was then used to predict the beam energy sufficient to raise the instability threshold to 18-20 nC. With the beam in a linear or nearly linear regime, higher harmonic radio frequency (rf) gap voltage can be used to reduce the bunch length at high charge and better match the booster acceptance.

INTRODUCTION

The APS Upgrade (APS-U) currently under production is based on reverse-bend multibend achromat optics [1,2]. One of the consequences of the 1-2 orders of magnitude reduction in the horizontal emittance is a much-reduced transverse acceptance, which will require on-axis injection. The most straightforward on-axis injection scheme is swap-out, where the injectors produce enough single-bunch charge to perform complete bunch replacement. This presents a challenge for the injector [3].

The plan is to meet the APS-U injection requirements through upgrades of the injector complex, while keeping the basic structure. The linac provides 1-nC pulses at a 30-Hz rate. Up to 20 pulses are accumulated and damped in the particle accumulator ring (PAR) [4] at the fundamental rf frequency of 9.776 MHz. In the final 230 ms of the 1-s cycle, the single bunch is captured in a 12th harmonic rf bucket and the bunch length is further compressed. The bunch is injected into the booster where it is ramped to full energy and extracted into a transport line that was redesigned for matching into the MBA storage ring (SR) [5].

The PAR was designed for a maximum charge of 6 nC, and needs to provide up to 20 nC in a single bunch for APS-U. Lower-charge dynamics are dominated by potential-well distortion (PWD), while higher-charge dynamics are dominated by microwave instability. Significant bunch lengthening and synchrotron sidebands are observed at high charge. PAR bunch lengths above ~650 ps rms result in unacceptably low injection efficiency into the booster (high beam loading is also a concern in booster [3,6]). Figure 1 shows various measurements in PAR of charge accumulation and charge-dependent bunch distributions [7], bunch length, and longitudinal bunch spectra at high charge after compression (~900 ms in cycle). Spectra at 375, 425, and 450 MeV indicate a more stable beam at higher energy. An impedance model based on numerical computation was recently completed [8], and will be used to simulate the instability. In the meantime, a simple circuit model was used to predict the beam energy needed to raise the instability threshold such that the bunch length can be compressed to ~650 ps at 20 nC full charge.

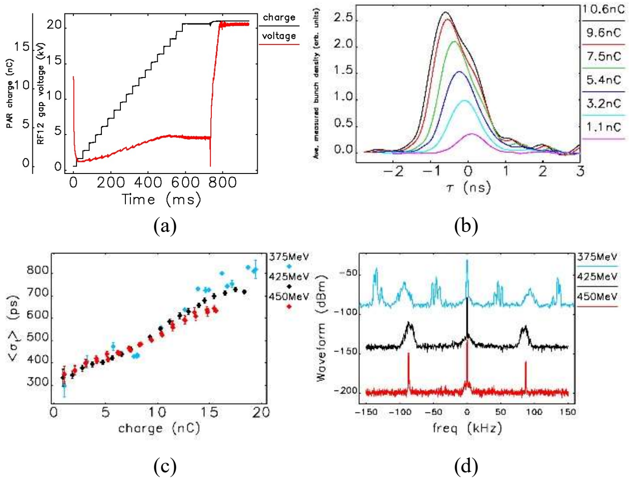

Figure 1: PAR measurements: (a) charge and harmonic rf waveform over cycle, (b) bunch distributions, (c) rms bunch length, and (d) synchrotron tune spectra for 16nC.

CIRCUIT MODEL ANALYSIS

Assuming that the low-charge dynamics is predominantly in the PWD regime, equilibrium bunch density distributions were computed using the Haissinski equation [9] in a dual rf system and a circuit model for the impedance. The code uses expressions in Bane *et al* [10,11]. The code was generalized to model both a main and higher-harmonic rf potential; the harmonic can be phased for either bunch shortening, as in PAR, or for bunch lengthening.

Fit results using bunch duration monitor (BDM) [7] measurements at 425 MeV are shown in Fig. 2. The initial analysis assumed no energy spread growth in a pure PWD regime. Circuit model reactance Z/n = 25 Ω and resistance R = 1300 Ω gave the best fit for both the bunch length and bunch shape "leaning" towards the head of the bunch (to-

---

* Work supported by U. S. Department of Energy, Office of Science, under Contract No. DE-AC02-06CH11357.
† harkay@anl.gov.

ISBN: 978-3-95450-223-3 ISSN: 2673-7000 doi:10.18429/JACoW-NAPAC2019-MOPLM23

SENIS HALL PROBE SPEED DEPENDENCE ISSUES*

I. Vasserman†, Argonne National Laboratory, Argonne, IL, USA

Abstract

An extensive test of a Senis 2-axis Hall probe was done at the Advanced Photon Source (APS) using the Undulator A device. Strong dependence of the measurement data on the speed of the sensor is observed. Discussion of the possible reason of such dependence is provided.

TEST RESULTS

We recently found that the LCLS-2 prototype wiggler measurement results collected at the APS and at SLAC are different, and an investigation of this issue was performed. It was found that peak field results are speed dependent. First test of these Hall probes performed at APS did not test this type of errors [1]. To identify the reason for this difference, additional test measurements of the undulator A device using a Senis 131-15 two-axis Hall probe were performed. The first test was done using different scanning speeds (150 mm/s; 50 mm/s) and different step sizes (0.2 mm; 0.1 mm). Results of this test (see Fig. 1) showed strong dependence on the speed and no dependence on the step size.

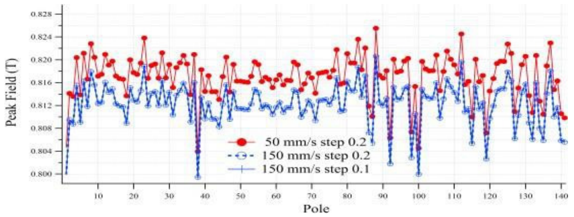

Figure 1: Senis 131-15 Hall probe scan; Una33#2, gap 11.5 mm; scan speed 150 mm/s vs. 50 mm/s.

The scan with the step size of the undulator period (33 mm) was done also to measure only the peak field of one sign (close to -8000 G). The difference is the same as for the measured, real alternating field of the device with a step of 0.1 mm. (see Fig. 2).

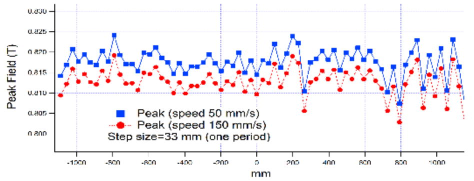

Figure 2: Scan speed 150 mm/sec vs. 50 mm/sec. Step size 33 mm.

Only speed itself is important, not the shape of the field at the measurement point or the frequency of measurements (step size). It seems as if something inside the probe produces a speed dependent signal. It could be wires or some conductive pieces. This is not a critical issue for the APS devices since the results are consistent and reproducible, but awareness of this issue is useful, as it can be important for some applications.

The next step in the test was to cover the entire range of the scanning speed to find where the results are the same as with the conditions during calibration when the Hall probe measures only the stable field (see Fig. 3).

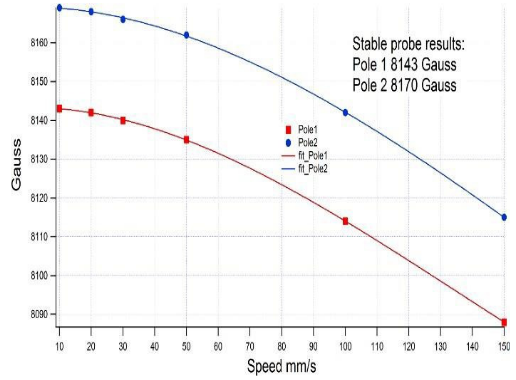

Figure 3: 33-mm-period device; Senis 131-15 Hall probe peak field speed dependence.

As a reference, peak field was measured with the Hall probe in rest over two poles in the middle of the device. One of the possible sources of the error we described earlier is Faraday's law, which states that the electromagnetic force (EMF) through the wire loop is given by the rate of change of the magnetic flux:

$$E = -d\emptyset/dt\,. \tag{1}$$

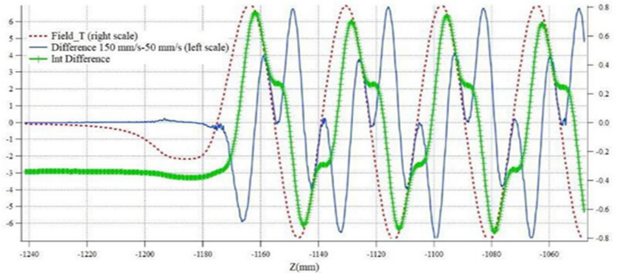

Figure 4: Magnetic field vs Z for 33-mm-period Una#2 device (right scale) and difference of the field measured at scans with speed of 150 mm/s and 50 mm/s (left scale); integrated difference (left scale).

We can see from Fig. 4 that the difference between results is close to 0 in the regions with no longitudinal gradient, and it becomes strong in the regions with such a gradient. From Eq. (1) we can write the expression for the flux going through the wire loop as:

$$\emptyset = -\int E * dt + C \tag{2}$$

Therefore, if the difference in the scan results is due to the wire loop, the integral of this difference is proportional

---

*Work supported by the U.S. Department of Energy, Office of Science, under Contract No. DE- AC02- 06CH11357

† vasserman@aps.anl.gov

LCLS-II INJECTOR COMMISSIONING BEAM BASED MEASUREMENTS*

C. Zimmer†, T. Maxwell, F. Zhou, SLAC, Menlo Park, CA, U.S.A.

Abstract

Injector commissioning is underway for the LCLS-II MHz repetition rate FEL, currently under construction at SLAC. Methodology of injector beam-based measurements and early results with low beam charge will be presented, along with the software tools written to automate these various measurements.

INTRODUCTION

LCLS-II is an upgrade to the existing LCLS Free Electron Laser, and is currently being installed at SLAC National Accelerator Laboratory. LCLS-II is a MHz repetition rate 1.3 GHz superconducting linear accelerator currently being installed in the first third of the existing 3 km accelerator tunnel. It will complement the existing normal-conducting 2856 MHz copper linear accelerator currently occupying the last third of the tunnel. Two new undulator lines are being installed, each utilizing variable gap undulators. Fed with electron beam from either the copper or superconducting accelerators, these undulators will enable the generation of hard and soft X-rays at energies ranging from 0.2 to 25 keV. Figure 1 gives an overview of the LCLS-II upgrade.

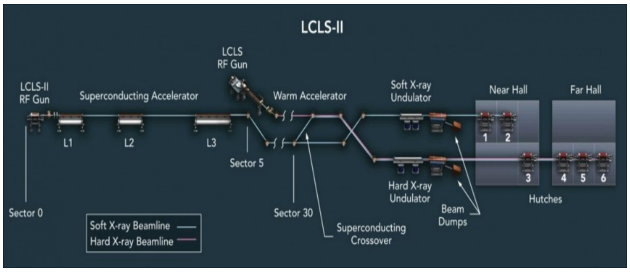

Figure 1: Schematic of LCLS-II upgrade.

INJECTOR SOURCE

The injector source for LCLS-II is currently installed and comprises approximately 2 meters of beamline. There are several important components of the injector source:

- 186 MHz CW normal conducting electron gun.
- 1.3 GHz CW normal-conducting buncher.
- Two moveable solenoids.
- Five horizontal and five vertical corrector dipoles.
- YAG screen for transverse profile measurements.
- Two stripline beam position monitors.
- One toroid.
- A faraday cup (measures charge and average current).

A Cesium-Telluride coated cathode inside of the electron gun produces electron beam when struck by a UV laser with a wavelength of 257.5 nm. The gun accelerates this beam to 750 keV, where it is then longitudinally compressed inside of the buncher. The injector beamline, for the early injector commissioning phase of operation, terminates at a faraday cup located before the endcap for the first cryomodule. Figure 2 shows a detailed injector layout schematic.

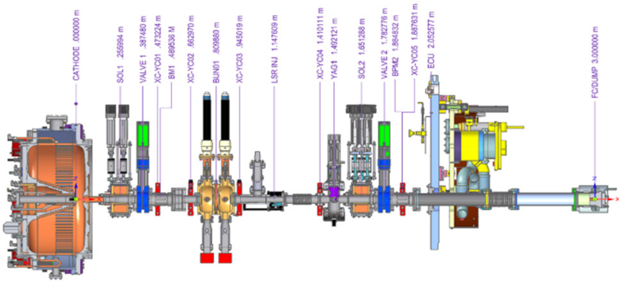

Figure 2: LCLS-II injector layout.

Nominal bunch charge is 100 pC, and the nominal peak current is 12 A. Emittance is expected to be on the order of 0.4 um-rad. Table 1 summarizes important injector source beam parameters [1].

Table 1: LCLS-II Injector Parameters

Parameter	**Nominal**
Gun energy (keV)	750
Bunch repetition rate (MHz)	0.93
Bunch charge (pC)	100
Peak current (A)	12
Slice emittance (µm*rad)	0.4

BEAM-BASED MEASUREMENTS

The LCLS-II injector source is currently in the early injector commissioning phase. In order to characterize this new source and precisely control the electron beam characteristics, a variety of beam-based measurements need to be repeatedly and reliably made. These measurements include:

- Electron gun electric field amplitude.
- Buncher electric field amplitude.
- Laser launch phase.
- Buncher phase.
- Laser alignment on cathode.
- Solenoid alignment.

As the LCLS-II injector source does not have a diagnostic line or dispersive region during this commissioning phase, a corrector dipole-based method has been employed as a means of making accurate energy and phase measurements.

Energy Measurement Method

A corrector is used to scan the electron beam position with several different field settings, and for each setting the

---

* Work supported by US DOE under grant No. DE-AC02-76SF00515
† zimmerc@slac.stanford.edu

ISBN: 978-3-95450-223-3 ISSN: 2673-7000 doi:10.18429/JACoW-NAPAC2019-MOPLS01

SPECTROSCOPIC CORRELATIONS TO RESISTIVE SWITCHING OF ION BEAM IRRADIATED FILMS*

K. N. Rathod†, N. A. Shah, P. S. Solanki
Department of Physics, Saurashtra University, Rajkot, India
J. P. Singh, K. H. Chae
Advanced Analysis Center, Korea Institute of Science and Technology, Seoul, Republic of Korea
K. Asokan
Inter University Accelerator Centre, Aruna Asaf Ali Marg, New Delhi, India

Abstract

Researchers concentrated on resistive random-access memories (RRAMs) due to excellent scalability, high integration density, quick switching, etc. Intrinsic physical phenomenon of RRAMs is resistive switching. In this work, ion beam irradiation was used as a tool to modify resistive switching of pulsed laser deposited (PLD) $Y_{0.95}Ca_{0.05}MnO_3$/Si films. Ion irradiation induced optimal resistive switching with spectroscopic correlations has been attributed to oxygen vacancy gradient. Resistive switching ratio is estimated to be increased for the film irradiated with fluence 1×10^{11} ions/cm^2 due to irradiation induced strain and oxygen vacancies verified by X–ray diffraction (XRD), Raman, atomic force microscopy (AFM), Rutherford backscattering spectrometry (RBS) and near–edge X–ray absorption fine structure (NEXAFS) measurements. Strain relaxation and oxygen vacancy annihilation have been realized for higher fluence (1×10^{12} and 1×10^{13} ions/cm^2) owing to local annealing effect. Present study suggests that the films understudy can be considered as emerging RRAMs.

INTRODUCTION

Hysteretic resistive switching (RS) based resistive random access memories (RRAMs) in the transition metal oxides have attracted considerable attention because of exceptional scalability, high integration density, fast switching, etc [1, 2]. Many metal oxide materials present a noteworthy part of promising memristive materials due to the presence of RS characteristics [3]. In recent times, it is reported that nanostructures containing manganites can also exhibit RS behavior [4, 5]. Trivial change in oxygen stoichiometry causes strong deviation in electrical conductivity and magnetic state [6]. Therefore, materials with non inherent RS may accomplish this feature with new findings.

RS is the phenomenon in which various resistance magnitudes can be executed such as write, read and erase by applying the suitable voltages. In general, two different resistance states such as high resistance state (HRS) and low resistance state (LRS) are observed per device. The device can be toggled between HRS and LRS by SET and RESET processes, respectively. For unbiased device, particular voltage is required to start the forming process which triggers the RS for the successive cycles. There are two switching modes broadly classified, namely, unipolar switching and bipolar switching. SET and RESET processes are obtained at the same polarity in unipolar switching. In the case of bipolar switching, reverse polarity of bias is required for SET and RESET processes.

Ion irradiation is the tool which can create controlled structural disorder as well as localized strain [7, 8]. Sensitive nature of manganites towards strain and structural disorder lead to significant modifications in transport and magnetic properties of ion irradiated hole doped manganites [8, 9]. In present study, we report the results on the effects of ion irradiation on resistive switching of $Y_{0.95}Ca_{0.05}MnO_3$ thin films.

EXPERIMENTAL

Thin film of $Y_{0.95}Ca_{0.05}MnO_3$ (YCMO) was grown on *a*-axis-oriented n-type single crystalline Si substrate by pulsed laser deposition (PLD) technique under effective conditions using pure target of YCMO (prepared by solid–state reaction method). After deposition process, the thin film of YCMO was cut into four identical pieces to maintain the uniform growth. One piece of PLD grown film was kept virgin, while other three pieces of films were irradiated with 100 MeV O^{7+} ion beam at 15 UD Tandem Pelletron Accelerator, IUAC, New Delhi, India. The pristine YCMO film is referred as PRI, while irradiated films with different ion fluences such as 1×10^{11}, 1×10^{12}, 1×10^{13} ions/cm^2 are denoted as 1E11, 1E12, 1E13, respectively. The irradiation was carried out under an elevated vacuum condition (~10^{-6} Torr). The thickness of all the films (~100 nm) was obtained by thickness profilometer. X–ray diffraction (XRD), Raman measurement, atomic force microscopy (AFM), Rutherford backscattering spectrometry (RBS) and near–edge X–ray absorption fine structure (NEXAFS) measurements (not shown here) and their outcomes have been discussed. Schematic diagram of the irradiated as well as the pristine films is displayed in Fig. 1. Silver paste was used to provide Ohmic contact with YCMO and Schottky contact with Si (as Ag ions diffuse through narrow SiO_x).

RESULTS & DISCUSSION

X–ray diffraction (XRD), Raman spectroscopy, Atomic force microscopy (AFM), Rutherford backscattering spec-

---

* Work supported by SERB, India
† rkunalsinh@gmail.com

ISBN: 978-3-95450-223-3 ISSN: 2673-7000 doi:10.18429/JACoW-NAPAC2019-MOPLS06

Mu*STAR: AN ACCELERATOR-DRIVEN SUBCRITICAL MODULAR REACTOR

R.P. Johnson†, R.J. Abrams, M.A. Cummings, T.J. Roberts, Muons, Inc., Batavia, IL, USA

Abstract

We present a conceptual design for a new modular, accelerator-driven subcritical reactor based on a molten salt. Mu*STAR is a reactor, that without re-design, can burn a variety of nuclear fuels, with the beam tuned to that fuel. We will discuss the elements of this system: the accelerator, the reactor, the spallation target, and the fractional distillation to separate volatile fission products. Our GAIN project with ORNL is successfully completed, with a design of the Fuel Processing Plant that will convert spent nuclear fuel into the molten-salt fuel for Mu*STAR.

INTRODUCTION

The Mu*STAR Accelerator-Driven System includes a 500 MWt subcritical, graphite-moderated, thermal-spectrum, molten-salt fueled, reactor design that was described in the Handbook of Nuclear Engineering in 2010 [1]. The reactor parameters are larger by a factor of 4 in linear dimension than the ORNL 8 MWt Molten Salt Reactor Experiment (MSRE) done in the late 1960s [2]. The reactor operates subcritically, with additional neutrons generated by an internal spallation target that is driven by a superconducting RF (SRF) linear proton accelerator, similar to that in the ORNL Spallation Neutron Source (SNS). Unlike the SNS, the target is not subjected to shock from the beam, which in Mu*STAR is rastered over the face of a solid uranium target that is cooled by molten salt fuel. Muons, Inc. and its collaborators have simulated engineering solutions to combine the accelerator and reactor with an internal uranium spallation target that is cooled by the MS fuel.

Simulations described in the Handbook article indicated that spent nuclear fuel (SNF) from light water reactors (LWR) could be burned such that in five passes of 40 years each, about 7 times as much energy could be produced from the fuel as was generated by the LWR [1]. Once the oxide-based fuel rods are converted to molten fluoride fuel, no further processing of the fuel is needed since the neutron absorption by the accumulated products can be overcome by increasing the beam power for each successive 40 year pass.

In 2017, Muons, Inc. was awarded a GAIN voucher award with ORNL, INL, and SRNL to design and cost a facility to convert LWR SNF into molten salt (MS) fluoride fuel suitable for use in Mu*STAR [3]. Our expectations are that such a facility will be relatively small and inexpensive enough to consider building one at each of the existing reactor sites in the US and abroad wherever SNF is stored.

CONCEPTS AND INNOVATIONS

Our concept is to install Mu*STAR accelerator-driven subcritical systems at existing light-water reactor (LWR) sites, transform the LWR spent nuclear fuel (SNF) using on-site technology developed under our GAIN award into molten salt fuel, and to burn it to produce electricity for at least 200 years. The concept is shown in Fig. 1. The additional neutron flux provided by the accelerator permits a much deeper burn such that several times more energy can be produced from the SNF than was generated by the LWR. The limit is reached when the accelerator cannot economically overcome the neutron absorption by fission products. This innovative and disruptive concept eliminates the need for uranium mining, fuel enrichment, fuel rod manufacture, SNF off-site storage and transport, and encourages local communities to consider consent-based storage of SNF combined with continued operation of their power utility using Mu*STAR when their LWR is retired.

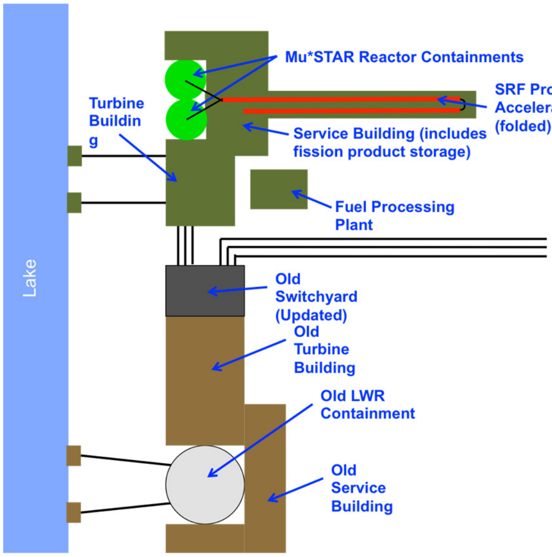

Figure 1: Mu*STAR installed at an old LWR site.

Leaving the SNF on the site where it was produced solves many problems that have long confounded the US government that is legally required to eventually take title to the SNF.

Two important consequences of the Mu*STAR are: 1) the conversion of the SNF to MS does not require fission products to be removed by chemical reprocessing and 2) the accelerator neutrons allow a deeper burn to extract as much as seven times as much energy from the SNF than was extracted by the LWR. Normalized to the energy produced, the amount and toxicity of the SNF will be reduced by more than a factor of 7 over the course of a few centuries of operation.

---

†rol@muonsinc.com

ISBN: 978-3-95450-223-3 ISSN: 2673-7000 doi:10.18429/JACoW-NAPAC2019-MOPLS08

ERROR TOLERANCE CHARACTERIZATION FOR THE HUST MeV ULTRAFAST ELECTRON DIFFRACTION SYSTEM*

Y. Song†, K. Fan, C.-Y. Tsai, Huazhong University of Science and Technology, Wuhan, China

Abstract

Ultrafast electron diffraction (UED) is a powerful tool for probing atomic dynamics with a femtosecond resolution. Such a spatiotemporal resolution requires error tolerance for the UED system which includes the RF system, the laser system, the beamline elements, etc. To characterize the error tolerance of the required spatiotemporal resolution for the 1.4-cell MeV UED we are developing, we use ASTRA to simulate the UED model with errors including initial transverse beam centroid offset, RF amplitude jitter and injection phase jitter, etc. By performing simulations with different errors omitted, we can characterize the contribution of each error and thus set the tolerance for each error to obtain the required performance of UED experiment. In the end, we present the error tolerance for 10% emittance growth and 100 fs time of flight variation to maintain the required spatiotemporal resolution.

INTRODUCTION

Ultrafast electron diffraction (UED) is a powerful pump-probe system which has shown promising potential in the last decades in investigating nano-structure dynamics with a femtosecond-level resolution [1-5]. Such a high spatiotemporal resolution requires setting of error tolerances which can be challenging in aspects of hardware and software. To perform a UED experiment, the normalized transverse emittance of electron beam (referred as transverse emittance hereby) needs to be small enough (<0.1 π mm·mrad) to obtain a sharp diffraction pattern which corresponds to the spatial resolution directly. The temporal resolution of UED is mainly limited by the time of flight (TOF) variation (between beam pulses) and bunch length of electron beam [6]. Since bunch length can be compressed by RF compressing cavity or other method [7, 8], we will focus on the TOF variation in the following discussion.

In this paper. we use ASTRA to simulate some possible error sources including initial transverse beam centroid offset, injection phase jitter, RF amplitude jitter, and beam charge jitter. By omitting certain error source, we can evaluate its contribution on concerned beam parameters which are the transverse emittance and TOF variation in the case. By this method, we pinpointed the error sources that have the most contributions to emittance growth and TOF variation. First, the emittance growth is mostly the contribution of initial transverse beam centroid offset, which may be caused by laser misalignment or pointing jitter. Second, the TOF variation is mainly caused by RF amplitude jitter instead of injection phase jitter for 1.4-cell RF gun. Next, we determine the relationship between emittance growth and initial transverse beam centroid offset (referred as beam centroid offset hereby) by ASTRA simulation and thus conclude the error tolerance for emittance growth less than 10%. For TOF variation, we analyse it by taking its first order derivative with respect to RF amplitude, injection phase and beam centroid offset to approximately evaluate their contribution and thus characterize the error tolerance for a 100fs or less TOF variation.

ERROR SOURCES FOR 1.4-CELL UED

The simplified layout of the 1.4-cell HUST (Huazhong University of Science and Technology) MeV UED is presented in Fig. 1.

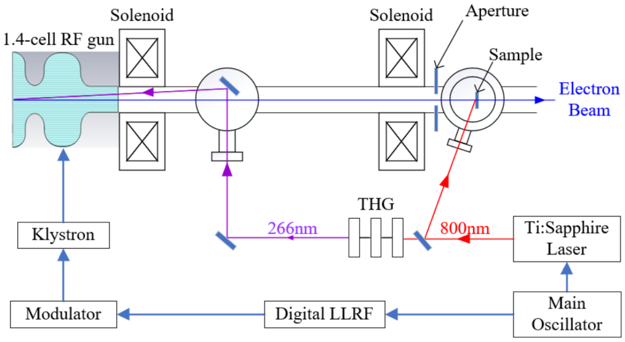

Figure 1: Layout of 1.4-cell HUST MeV UED.

The laser set up in Fig. 1 may have misalignment and pointing jitter on photocathode at the same time, which cause initial transverse beam centroid offset. The modulator produces pulsed high voltage on klystron with a 0.5% (RMS) pulse-to-pulse amplitude jitter, which also causes phase jitter of klystron once applied. Thus, the RF field in the 1.4-cell RF gun suffers from injection phase jitter and RF amplitude jitter. We assume that the RF amplitude jitter in RF gun is also 0.5% and the injection phase jitter 100fs according to other UED systems [9, 10]. The laser pulse-to-pulse energy jitter is below 0.5% (RMS) for the Ti: Sapphire laser we purchased [11]. We consider electron beam charge jitter equal to this pulse-to-pulse laser energy jitter. Besides, we presume that all the errors are random and Gaussian distributed and their rms values are summarized in Table 1.

Table 1: Error Sources

Error	RMS value
Beam centroid offset	0.5 mm
RF amplitude jitter	0.5%
Injection phase jitter	100 fs (0.103°)
Beam charge jitter	0.5%

---

* Work supported by the National Natural Science Foundation of China (NSFC) 11728508

† d201780370@hust.edu.cn

ENGINEERING DESIGN OF GALLIUM-NICKEL TARGET IN NIOBIUM CAPSULE, WITH A MAJOR FOCUS ON DETERMINING THE THERMAL PROPERTIES OF GALLIUM-NICKEL THROUGH THERMAL TESTING AND FEA, FOR IRRADIATION AT BLIP*

S.K. Nayak[†], S. Bellavia, H. Chelminski, C. S. Cutler, D. Kim, D. Medvedev,
Brookhaven National Laboratory, Upton, NY, USA

Abstract

The Brookhaven Linac Isotope Producer (BLIP) produces several radioisotopes using a variable energy and current proton beam. The targets irradiated at BLIP are cooled by water and required to be isolated in a target capsule. During the design stage, thermal analysis of the target and cladding is carried out to determine the maximum beam power a target can handle during irradiation without destruction.

In this work we designed a capsule for Gallium-Nickel (*Ga* 80%, *Ni* 20%) alloy target material and irradiated the target at the BLIP to produce the radioisotope *Ge-68*. Since no literature data is available on Ga_4Ni's thermal conductivity (K) and specific heat (C), measurements were carried out using thermal testing in conjunction with Finite Element Analysis (FEA). Steady-state one dimensional heat conduction method was used to determine the thermal conductivity. Transient method was used to calculate the specific heat. The test setup with same methodologies can be used to assess other targets in the future. Here, we will detail these studies and discuss the improved design and fabrication of this target.

INTRODUCTION

The BLIP produces a variety of radioactive isotopes by striking proton beams on different target materials. The target material, sealed in a container further referred as capsule, when subjected to proton beam absorb proton energy most of it in a form of heat. To limit the temperature rise of the capsule, target irradiation is carried out by keeping the capsule cool by continuously flowing water along its faces [1]. After a detailed thermal analysis of the capsule, suitable beam power is determined for irradiation so that structural integrity of the capsule is maintained, and irradiated target material is not exposed to water. Any structural failure of capsule will lead to the release of radioactivity to the water tank, loss of radioisotope and may affect operation time.

BLIP traditionally irradiated pure *Ga* metal targets to produce *Ge-68* radioisotope, but targets' survivability in the beam was poor [2] and *Ge-68* yields were inconsistent. We designed a capsule for Ga_4Ni alloy target material (ACI Alloys, Inc., CA, USA) and irradiated at BLIP to produce the radioisotope *Ge-68*. Precise knowledge of thermal conductivity of the target material is key in the steady-state thermal analysis which yields optimum irradiation parameters. Since no literature data is available on Ga_4Ni's thermal conductivity value, thermal testing was carried out to calculate the same. Using the same test and FEA, its specific heat was also estimated. Specific heat will be required if there is a need in the future to run transient thermal analysis.

DESIGN

Gallium attacks most common metals such as Aluminium and Stainless Steel (*SS*) by diffusing into the metal lattice and making them brittle [3]. Niobium which is more resistant is one of the best choices of metal for this application and was used to make the capsule [2, 3]. It has good resistance to *Ga* attack up to 400 ^{0}C. In the initial design, the Ga_4Ni target was enclosed by a ring and two thin (0.012") windows (Fig. 1, upper drawing). The overall dimension of the capsule is 2.750" diameter and 0.220" thick. The windows were laser welded to the ring in an environment of helium gas. This design is typical to most isotope production at BLIP due to simplicity of capsule manufacturing and welding.

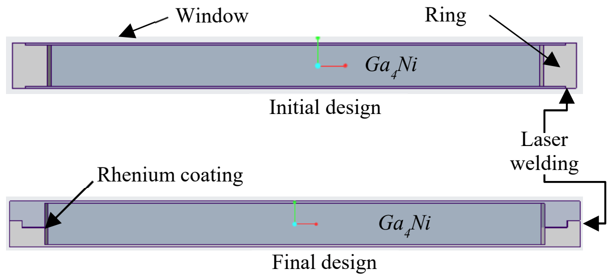

Figure 1: Ga_4Ni target in Niobium capsule.

During test irradiation (about 33 MeV proton energy at 160 µA, i.e 5294 W of beam power), the welding joint between the window and the ring failed at a very small section. Due to this failure, the irradiated Ga_4Ni got exposed to flowing cooling water along the capsule face meant for cooling and washed away. The reason for the failure could be one or more of the following; at high temperature *Ga* reacted with Niobium, welding joint failed at high temperature.

In the next generation design, the capsule was made of two halves (Fig. 1, lower drawing) where the thin window was a part of the ring rather than welded to the ring. This design has been used for most of the targets irradiated at Isotope Production Facility at Los Alamos National Laboratory (Los Alamos, NM, USA) [4]. The welding joint at the rim produces a high penetration stronger welding joint than in the initial design. The mating area of two halves provide

---

*This paper is authored by BSA operated under contract number DE-SC0012704. This research is supported by the U.S. DOE Isotope Program, managed by the Office of Science for Nuclear Physics.

[†] snayak@bnl.gov

ISBN: 978-3-95450-223-3 ISSN: 2673-7000 doi:10.18429/JACoW-NAPAC2019-MOPLH02

STUDY OF PHOTOCATHODE SURFACE DAMAGE DUE TO ION BACK-BOMBARDMENT IN HIGH CURRENT DC GUN*

J.P. Biswas, Stony Brook University, Stony Brook, NY-11794, USA
O.H. Rahman, E. Wang†, Brookhaven National Laboratory, Upton, NY-11973, USA

Abstract

In high current DC gun, GaAs photocathode lifetime is limited by the ion back-bombardment. While gun operation ions are generated due to the impact of electrons with residual gas molecules. These ions accelerate back towards the cathode and remove the activation layer's material from the photocathode surface, thus causing the photoemission performance degradation. We have developed an object-oriented code to simulate the ion generation due to dynamic gas pressure and ion trace in the electromagnetic field. The pressure profile varies from cathode position towards the transfer line behind the anode, which signifies the importance of dynamic simulation for ion back-bombardment study. In our surface damage study, we traced the energy and position of the ions on the photocathode surface and performed the Stopping and Range of Ions in Matter(SRIM) simulation to count the number of Cesium atoms removed from the surface due to single impact. Cesium atom removal is directly related to the photocathode Quantum Efficiency(QE) decay. Our new dynamic simulation code can be used in any DC gun to study ion back-bombardment. We have used this new code to better understand the ion generation in prototype BNL HVDC gun, and we also estimated the normalized QE decay due to ion back-bombardment.

INTRODUCTION

The Quantum Efficiency(QE) of GaAs photocathode in DC gun degrades mainly due to ion back-bombardment. While extracting electron beam from the photocathode, the emitted electron collide with the residual gas molecule and ionize the gas species. The dominant gas species in DC gun is hydrogen, as a result the ions generated are hydrogen ions. Ions generated in between DC gap could have wide range of energy when hit back on the cathode surface, and it depends at which position ions are created along the beam trajectory. While ions generated beyond the anode position could still trap in the beam and drift towards the dc gap, and hit photocathode with full potential of the maximum gun voltage [1]. GaAs is usually activated by depositing a thin layer of Cesium and Oxygen on photocathode surface which produce Negative Electron Affinity(NEA) state. Ions of sufficient energy could sputter away the activation layer material such as Cesium and Oxygen from the photocathode surface. Implantation also occurs, which creates vacancies and interstitials that negatively affect the photoemission [2]. Once photocathode is activated, the QE depends on surface Cs loss, chemical poisoning and lattice damage. In our study we have assumed that, the amount of Cs loss is directly proportional to the photocathode QE decay.

BEAMLINE AND PRESSURE PROFILE

To study ion back bombardment all the existing models consider constant pressure from cathode position to the beamline. However, while DC gun is in operation, dynamic pressure can vary substantially from main gun chamber to the beamline. Therefore, to understand the cathode damage mechanism due to ion-back bombardment we need to consider the variable pressure profile from cathode position to the beamline. In our analysis we have considered Brookhaven National Laboratory(BNL) 350 kV DC gun geometry [3], and simulated the pressure profile from anode position to the beamline. Pressure profile is totally dependent on specific gun geometry, pumping arrangement and pumping rate. Simple modification of gun geometry, or pumping parameters can change the outcome of the pressure profile. In our simulation we have used molflow+ [4] to simulate the variable pressure profile from cathode position to the beamline. In figure 1 molflow+ model and pressure profile is presented.

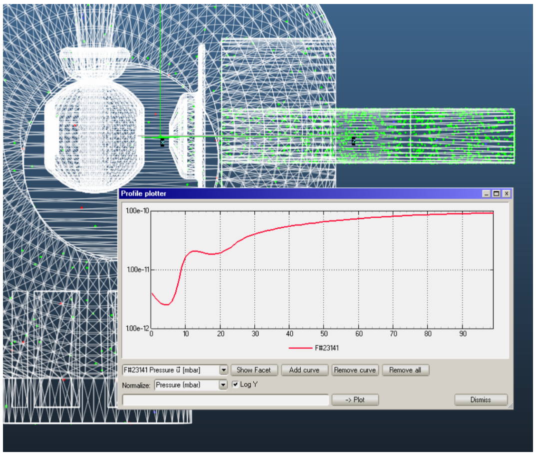

F#23141 Pressure $\vec{u}$ [mbar]

Normalize: Pressure (mbar)

☑ Log Y

Figure 1: Vacuum model of the BNL 350 kV DC gun and corresponding pressure profile from cathode position towards the beamline. In molflow+ pressure is presented in mbar unit.

DYNAMIC PRESSURE CODE DEVELOPMENT

We used General Particle Tracer(GPT) [5] code to simulate the ion back-bombardment on cathode surface in DC gun. The ionization rate as a function of kinetic energy can be written as, $R(E) = I\sigma(E)\rho\Delta z$. Where σ is the ionization

---

* This work was supported by Brookhaven Science Associates, LLC under Contract No. DE-SC0012704, with the U.S. DOE.

† wange@bnl.gov

ISBN: 978-3-95450-223-3 ISSN: 2673-7000 doi:10.18429/JACoW-NAPAC2019-MOPLH04

DESIGN FOR HyRES CATHODE NANOTIP ELECTRON SOURCE

R. M. Hessami, A. Amhaz, P. Musumeci
Department of Physics and Astronomy, University of California Los Angeles, California, USA

Abstract

A new ultrafast electron diffraction (UED) instrument is being developed by UCLA-Colorado University collaboration for the STROBE NSF Center with the goal of using electron and EUV photon beams to reveal the structural dynamics of materials in non-equilibrium states at fundamental atomic and temporal scales. This paper describes the design of the electron beamline of this instrument. In order to minimize the initial emittance, a nanotip photocathode, 25 nm in radius, will be used. This requires a redesign of the cathode and anode components of the electron gun to allow for the tip to be properly aligned. Solenoidal lenses are used to focus the beam transversely to a sub-micron spot at the sample and a radiofrequency (RF) cavity, driven by a continuous wave S-band RF source, longitudinally compresses the beam to below 100 fs, required for atomic resolution.

INTRODUCTION

By combining X-ray-based and tip-enhanced electron beams for simultaneous measurements of a sample properties, the influence of nanoscale structure and behavior on extended mesoscale structure can be determined. Nanoscale heterogeneity is common in a wide variety of materials. Therefore, being able to study material properties at the nanoscale, map them, and relate them to their effects on the macroscopic behavior is a major challenge to be addressed by modern physics instrumentation developers. In order to address this challenge, plans exist to build a Hybrid Photon-Electron Functional Microscope System (HyRES) at the University of Colorado Boulder that will allow for real-time imaging of nanostructured materials.

The electron-based section of the instrument includes an ultrafast electron diffraction beamline, which will aim to record diffraction patterns from microscale spot sizes with better than 100 fs temporal resolution. Even though relativistic electron diffraction [1, 2] has recently shown, capitalizing on the relativistic suppression of space charge effects, capable of excellent spatial and temporal resolution [3, 4], the electron beam energy for this system is chosen to be below 100 keV as we target systems that can be repeatedly pumped (reversible dynamics), and in order to simplify the compatibility with the X-ray beamline and reduce size and costs.

Due to the brightness limitations of conventional photocathodes [5], it was decided that such resolution could only be produced in a photoemissive source using a nanotip, to minimize the emittance and produce a smaller, more focused beam [6]. This choice causes a variety of challenges in the design of the gun, as the nanotip design requires a high degree of movement precision to ensure its proper position relative to the anode so that the emitted electrons experience the correct on-axis field. This paper addresses the design of the gun source. Dealing with this alignment issue is a critical aspect of the design. Additionally, acceleration and manipulation of the beam is necessary to optimally bring it to the target. The design of the beamline, fine tuned using particle tracking simulations in GPT [7], is addressed to ensure the system can deliver a beam with less than 100 fs duration and less than 1 µm transverse spotsize.

Simultaneously focusing the beam transversely and longitudinally is challenging due to the effects of space-charge repulsion. At the proposed beam energy of 50 keV there is no significant space charge suppression. Accomplishing sufficient simultaneous compression requires optimization of the position and phase of the RF cavity and positions and currents of the solenoids.

BEAMLINE DESCRIPTION

The beamline was designed with the goal of generating a beam shorter than 100 fs and with a transverse spotsize less than 1 µm. Transverse spotsize was mainly controlled through the use of solenoids while bunching was done primarily through the radiofrequency (RF) cavity.

An initial solenoid of lower field strength was placed near the exit of the gun to prevent emittance growth. A stronger solenoid was placed after the compressor such that its focus coincided with that of the RF cavity. The solenoid parameters are given in Table 1.

Table 1: Parameters Used for the Beamline Simulation

Element	Field strength (T)	Centroid position (m)
Solenoid 1	0.0099	0.15
Solenoid 2	0.0118	0.70

The phase of the RF cavity was calibrated so that the front of the bunch is decelerated, while the back is accelerated, effectively compressing the bunch longitudinally. The cavity, placed 60 cm from the photocathode, requires 250 W of power, delivered by a waveguide coupler driven by a CW S-band RF source.

GUN DESIGN

To achieve very low emittance in the electron beam, a copper nanotip is planned to be used as the electron source, as opposed to a flat or curved copper source. The pointlike nature of the nanotip, which has a radius of 25 nm, means that the spatial distribution of the beam at the source is extremely small, greatly reducing emittance. However, using such a tip requires a redesign of the gun holder, as the laser used to generate photoemission must come in from the side of

ISBN: 978-3-95450-223-3 ISSN: 2673-7000 doi:10.18429/JACoW-NAPAC2019-MOPLH06

STUDY OF THE MEAN TRANSVERSE ENERGY AND THE EMISSION MECHANISM OF (N)UNCD PHOTOCATHODES

G. Chen*, L. Spentzouris, Illinois Institute of Technology, Chicago, IL,USA
S.P. Antipov, E. Gomez, Euclid Techlabs LLC, Bolingbrook, IL, USA
S.V. Baryshev†, T. Nikhar, Michigan State University, East Lansing, MI,USA
G. Adhikari, W.A. Schroeder‡, University of Illinois at Chicago, Chicago, IL,USA

Abstract

Nitrogen incorporated ultrananocrystalline diamond ((N)UNCD) is promising for photocathode applications due to its high quantum efficiency (QE). The mean transverse energy (MTE) which, along with QE, defines the brightness of the emitted electron beam which must be thoroughly characterized and understood for (N)UNCD. Our previous work [APL 114, 093103 (2019)] further corroborated the important role of graphitic grain boundaries (GB's). UNCD consists of diamond (sp^3-hybrized) grains and graphitic (sp^2-hybrized) GB's: GB's are behind the high emissivity of (N)UNCD and therefore play a crucial role in defining and controlling the MTE. In this work, the MTE of two different (N)UNCD samples having different ratios of sp^3/sp^2 were measured versus the primary photon energies. As a reference, MTE of highly oriented pyrolytic graphite (HOPG, canonical sp^2-hybrized graphite) was also measured.

INTRODUCTION

Challenges in photocathode studies include achieving *i*) high quantum efficiency (QE) *ii*) low thermal emittance/mean transverse energy (MTE) and *iii*) rapid response time. The ratio of the emitted electrons to the beam emittance determines the photocathode brightness. The emitted charge depends directly on the QE of the photcathode material, and the beam emittance is directly related to the MTE of the photoelectrons. The MTE is primarily dependent on cathode material band structures.

(N)UNCD is an *n*-type photocathode that has high electron conductivity through the bulk; it consits sp^3 diamond grains and sp^2 graphitic grain boundaries. Higher QE (10^{-3}) [1, 2, 3] may potentially be achieved simply via hydrogen surface termination. The roughness of synthesized (N)UNCD is low (<10 nm) due to its nanoscale crystalline size. Its low physical roughness implies less surface scattering during the process of transporting photoelectrons over the surface barrier. Experimental measurements of the MTE of (N)UNCD as a photocathode was reported by our group [4]. A relatively low average value of 266 meV was demonstrated, while the MTE dependence on the primary photon energy demonstrates a nonconventional behavior. To elaborate on the emission mechanism of (N)UNCD, MTE of two samples with different sp^3/sp^2 ratios were measured. Additionally, MTE of a HOPG sample was also measured for comparison.

(N)UNCD SYNTHESIS

The (N)UNCD films were deposited on two highly doped *n*-type silicon substrate by using the microwave assisted plasma chemical vapor deposition (MPCVD) in a $N_2/CH_4/H_2$ precursor gas mixture. To tune the sp^3-to-sp^2 ratio, the deposition temperature was varied. Raman spectra confirming the physico-chemical UNCD bonding structures of both samples are shown in Fig. 1. The (N)UNCD#1 (red) was grown at $945\ °C$: it is more graphitized, resistivity measured on intrinsic Si coupon is $9.5\times10^{-5}\ \Omega\times cm$. The (N)UNCD#2 (blue) was grown at $860\ °C$: the film is less conductive with resistivity estimated to be $2.07\ \Omega\times cm$. The film thicknesses for both samples were found to be ~430 nm.

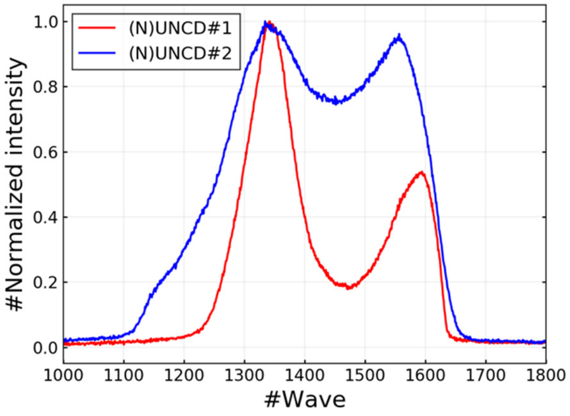

Figure 1: Raman spectra of the two (N)UNCD samples #1 (red) and #2 (blue) showing the characteristic diamond grain (~1350 cm^{-1}) and graphite GB (~1550 cm^{-1}) peaks. Laser wavelength was 532 nm.

EXPERIMENTAL SETUP

The method of the double-solenoid scanning [5] has been used to measure the MTE. The schematic diagram of the experimental setup is shown in Fig. 2.

---

* also a [2]Euclid Techlabs LLC
† serbar@msu.edu
‡ andreas@uic.edu

TESTS OF Cs-FREE OPERATION OF THE SNS RF H^- ION SOURCES*

B.X. Han†, S.M. Cousineau, S.N. Murray Jr., T.R. Pennisi, M.P. Stockli, C.M. Stinson, R.F. Welton,
Spallation Neutron Source, Oak Ridge National Laboratory, Oak Ridge, TN, USA
T. Sarmento, O. Tarvainen, ISIS Pulsed Spallation Neutron and Muon Facility,
Rutherford Appleton Laboratory, Harwell OX11 0QX, UK

Abstract

Tests were performed at SNS in collaboration with visiting colleagues from ISIS, UK to evaluate the uncesiated beam performance of the SNS RF H^- ion sources. Two spare experimental sources, one with internal antenna and one with external antenna were used for the tests. The beam currents achieved with Cs-free operations accounted for about 1/3 to 1/2 of the beam currents produced with cesiated operations. ~17 mA uncesiated H^- current was demonstrated within the tested RF power range up to 65 kW with the internal antenna source and ~15 mA with up to 40 kW RF with the external antenna source. In Cs-free operations, the power supply for the electron dumping electrode was loaded down below its set voltage but was not too drastic to tamper the operation.

INTRODUCTION

The Spallation Neutron Source (SNS) at Oak Ridge National Laboratory (ORNL) employs an RF-driven, multicusp H^- ion source. This type of source was conceptualized and developed at Lawrence Berkeley National Laboratory (LBNL) initially for the Superconducting Super Collider project and then for the Spallation Neutron Source project in 1990s to early 2000s. There were reports of ~30 mA H^- current when operated as a volume source without Cs in the early years. However, to produce higher beam current, Cs was introduced to enhance the H^- production through surface mechanism [1-3]. Since the source was delivered to ORNL in 2002, it has been operated and further developed to highly reliable, long lifetime (several months), persistent high current (>50 mA) H^- source operating at 6% duty-factor (1 ms, 60 Hz) [4, 5]. Figure 1(a) shows a cut view of the SNS H^- ion source in its present form. A porcelain coated copper tube antenna placed inside the stainless-steel source chamber drives the plasma. A SNS inhouse developmental source with AlN ceramic chamber and an external RF antenna is shown in Figure 1(b) [6]. Both sources operate in the same way in terms of Cs system, beam extraction and suppression of co-extracted electrons. A solid reaction Cs dispenser system, the Cs collar in the figures, with cartridges containing a mixture of Cs chromate (Cs_2CrO_4) and getter materials (Zr, Al) is used to release elemental Cs for ion source cesiation by heating it up to ~550 °C. Since the mission of the ion source efforts at SNS is to produce high current H^- beam for the operation and future upgrade of the SNS facility, the focus has always been with Cs enhanced operation of the ion sources. However, the ISIS Facility in the UK expressed interest in testing the performance of the SNS H^- ion sources in Cs-free operation to aid their efforts in developing a moderate current (~35 mA) RF-driven H^- ion source preferably without using Cs [7]. This work presents the tests performed at SNS for this purpose in collaboration with ion source colleagues from ISIS.

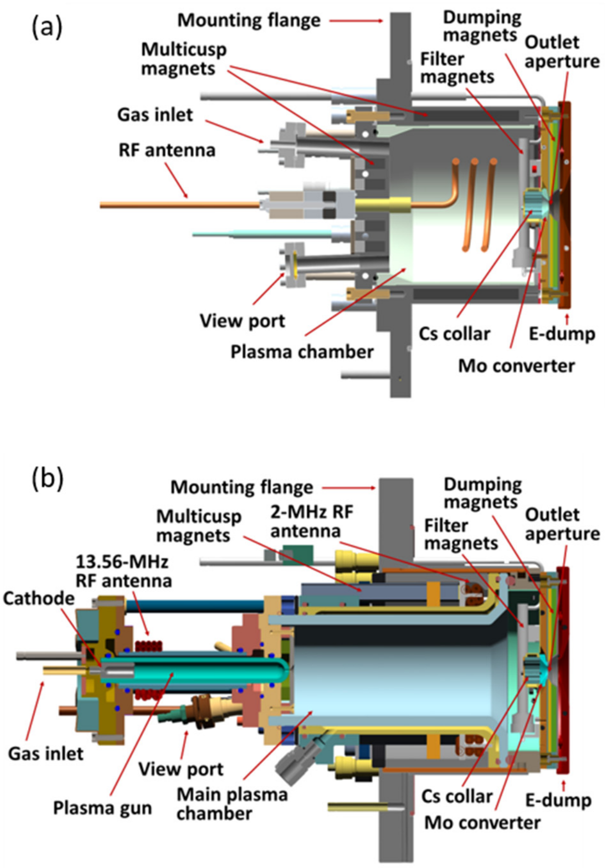

Figure 1: SNS RF-driven H^- ion sources, (a) with internal antenna and (b) with external antenna.

EXPERIMENTAL SETUP

The production tier ion sources for the SNS accelerator operation (internal antenna sources Int#2, 3, 4, 6) and the external antenna sources used on the SNS 2.5 MeV Beam Test Facility (Ext#3, 4) were not available for testing. An experimental ion source (Int#5) from the internal antenna

---

* This work was performed at Oak Ridge National Laboratory, which is managed by UT-Battelle, LLC, under contract number DE-AC05-00OR22725 for the United States Department of Energy.

† hanb@ornl.gov

ISBN: 978-3-95450-223-3 ISSN: 2673-7000 doi:10.18429/JACoW-NAPAC2019-MOPLH09

PHOTOLUMINESCENCE STUDIES OF ALKALI-ANTIMONIDE PHOTOCATHODES

P. Saha*, O. Chubenko, and S.S. Karkare, Arizona State University, Tempe, AZ, USA
H.A. Padmore, Lawrence Berkeley National Laboratory, Berkeley, CA, USA

Abstract

Alkali-antimonide photocathodes have a very high quantum efficiency and a low intrinsic emittance, making them excellent electron sources for Energy Recovery Linacs, X-ray Free Electron Lasers, Electron Cooling, and Ultrafast Electron Diffraction applications. Despite numerous studies of their photoemission spectra, there has been nearly no conclusive experimental investigation of their basic electronic and optical properties (e.g. band gap, electron affinity, optical constants, etc.), which determine the nature of photoemission. Therefore, the systematic study and deep understanding of fundamental characteristics of alkali-antimonide photocathodes are required in order to develop next-generation electron sources with improved crystal and electronic structures to fit specific application. Here we report on the development of an experimental setup to measure photoluminescence (PL) spectra from alkali-antimonide photocathodes, enabling estimation of a material band gap and defect state energies, and provide preliminary results for Cs_3Sb films.

INTRODUCTION

Increasing the electron beam brightness is critical to advance the performance of such linear accelerator applications like Energy Recovery Linacs, X-ray Free Electron Lasers, Electron Cooling, and Ultrafast Electron Diffraction. The intrinsic beam brightness is defined by emission mechanisms and fundamental material properties of electron sources. For example, it has been shown that the maximum possible brightness from low quantum efficiency (QE) metallic photocathodes is limited by such nonlinear photoemission processes as electron heating and multi-photon emission [1, 2].

Alkali-antimonide compounds like Cs_3Sb, K_2CsSb, and Na_2KSb have long been known for their high QE in the visible spectrum, sub-picosecond response time, and low intrinsic emittance. Furthermore, due to their low electron affinity and high QE at the photoemission threshold, it is expected that contribution of the nonlinear photoemission processes will be reduced and near-threshold operation from such compounds will enable an order of magnitude increased brightness [3]. However, a precise quantitative estimation of nonlinear effects [4] and development of methods enabling further increase in brightness require detailed experimental study of the photoemissive, structural, electronic, and optical properties of these materials.

Despite numerous measurements of QE and intrinsic emittance [3], and some investigations of the structural properties using X-ray diffraction and reflectivity [5], very little work has been performed to experimentally obtain the electronic and optical properties of alkali-antimonide thin films. A few optical absorption and photoconductivity measurements on alkali-antimonides have been performed several decades ago [6–11]. These experiments have given us some experimental insights into the optical and electronic properties of alkali-antimonide thin films. However, there are still many undetermined parameters that are crucial for detailed modeling of photoemission from alkali-antimonide semiconductors [12]. Furthermore, the measurements made previously were primarily performed on alkali-antimonides grown in photo-multiplier tubes on insulating quartz or pyrex surfaces. The properties of such films could potentially be very different from the thin films grown in Ultra High Vacuum (UHV) chambers on metallic or semiconducting substrates typically used in electron accelerators.

The biggest challenge in measuring the optical and electronic properties of alkali-antimonides is their extreme sensitivity to vacuum conditions. Since these films oxidize rapidly in any non-UHV environment, all measurements must be performed in the UHV growth chamber or in a separate chamber connected via UHV to the growth chamber. In this paper, we report on the development of an experimental setup for PL measurements connected to an UHV alkali-antimonide growth chamber and present preliminary measurement attempts for Cs_3Sb.

EXPERIMENTAL SETUP

Growth Chamber

Figure 1shows the UHV chamber used for the growth of alkali-antimonides along with the setup used for PL measurements. This chamber has been used in the past for a co-deposition growth of alkali-antimonide films and is connected via UHV to an AFM/KPFM instrument for studying the surface morphology of these films [13]. The chamber uses an effusion cell to evaporate Sb metal on to a substrate (typically Si) and SAES getters to evaporate alkali-metals to form alkali-antimonide thin films. The chamber has a base pressure in the low 10^{-10} Torr range.

PL Measurement Setup

A 520 nm 1 W CW diode laser is focused onto a 100 μm rms spot on the sample to induce the PL. The laser light is incident at an angle of 30° to the normal to the sample surface. During and after the growth, the sample faces a 4-1/2 inch viewport, which is used for collecting the PL spectra.

A double convex lens system is used for collecting the light emitted by the sample into the spectrometer [14]. A schematic of this system is shown in Figure 2. Collecting the

---

* psaha6@asu.edu

ISBN: 978-3-95450-223-3 ISSN: 2673-7000 doi:10.18429/JACoW-NAPAC2019-MOPLH10

FIELD-EMISSION ELECTRON SOURCE EMBEDDED IN A FIELD-ENHANCED CONDUCTION-COOLED SUPERCONDUCTING RF CAVITY*

D. Mihalcea, O. Mohsen, P. Piot†, Department of Physics and Northern Illinois Center
for Accelerator & Detector Development, Northern Illinois University, DeKalb, IL, USA
V. Korampally, A. McKeown, I. Salehinia,
Department of Engineering Northern Illinois University, DeKalb, IL, USA
R. C. Dhuley, M. I. Geelhoed, and J. C. T. Thangaraj,
Fermi National Accelerator Laboratory, Batavia, IL, USA

Abstract

We present simulations and experimental progress toward the development of a high-current electron source with the potential to deliver high charge electron bunches at GHz-level repetition rates. To achieve these goals electrons are generated through field-emission and the cathode is immersed in a conduction-cooled superconducting 650-MHz RF cavity. The field-emitters consist of microscopic silicon pyramids and have a typical enhancement factor of about 500. To trigger field-emission, the peak field inside the RF cavity of about 6 MV/m is further enhanced by placing the field-emitters on the top of a superconducting Nb rod inserted in the RF cavity. So far, we cannot control the duration of the electron bunches which is of the order of RF period. Also, the present cryocooler power of about 2 W limits the beam current to microamp level.

INTRODUCTION

There is an increasing demand for high power electron injectors for a large variety of applications that range from building new radiation sources to medical applications and treatment of wastewater in large metropolitan areas [1]. To achieve multi-megawatt power the injectors should generate a beam average current in ampere range assuming a typical energy gain of a few MeV's. Such a large beam current requires that the injector operates at a repetition rate comparable with the RF frequency and the electron pulses charge is at nanocoulomb level.

The repetition rate of the high power normal conducting electron guns is constrained by the efficiency of heat dissipation through the walls of the RF cavity. Superconducting technology is increasingly a more appealing solution to avoid this limitation despite the relatively higher cost of the cryogenic systems [2]. Typically, the superconduction of RF cavities is achieved by immersion into a liquid helium reservoir. A different approach, that we follow in the research presented here, is to lower the temperature of the RF cavity to superconduction domain through heat conduction to a cryocooler [3, 4]. This technique eliminates the need for cooling fluids, greatly simplifies the cryogenic system and it could beneficiate from the fast growing technological developments in cryo cooling.

Photoemission is the most used process to extract electron bunches from the cathode with thermal emittance in the sub-micron range. The laser systems used to generate photoemission are expensive and repetition rate is relatively low (several kilohertz) in high power regime. Therefore, our option is to use a cathode consisting of an array of field-emitters [5]. In this case the repetition rate is the RF frequency and the total electron beam power is very close to the input RF power when the heat loses are substantially reduced by operating the RF gun in superconducting regime.

In this contribution we present a 650 MHz RF cavity operated in superconducting regime. The cavity temperature is lowered by a cryocooler through direct heat conduction. We present electromagnetic (EM) analysis of the RF cavity and the status of the experiment.

SETUP OVERVIEW

The electron source we use for this project is based on a 650 MHz SRF cavity designed and tested at Fermilab [6]. The elliptically shaped resonator, depicted in Fig. 1, is made of superconducting niobium with critical temperature $T_c = 9.2$ K and optimized to accelerate particles with $\beta = 0.9$. The RF power is supplied into the cavity through a 32 mm long copper antenna attached to the input flange. A bi-directional coupler connected to power supply and to input antenna allows the determination of input and reflected powers P_{in} and P_r. The input flange is also thermally connected to the cryocooler (Cryomech PT420) through conduction aluminum links. A similar probe antenna is attached to the pickup flange on the opposite side of the resonator to determine the transmitted power P_t. The pickup flange also incorporates an 40 mm-radius copper disc to measure the electron beam current. Both flanges are made of stainless steel. The overall length of the cavity, including the two 50 mm-radius pipes that flank the resonator is 560 mm.

In this design the amplitudes of the fields reach their maxima at the center of the resonator and they rapidly decay toward the two flanges. Therefore, a 2 mm-radius circular

---

[*] This work was supported by the U. S. Department of Energy (DOE) under contract DE-SC0018367 with Northern Illinois University. Fermilab is managed by the Fermi Research Alliance, LLC for the U. S. Department of Energy Office of Science contract number DE-AC02-07CH11359.

[†] also at Fermi National Laboratory, Batavia, IL 60115, USA

NANOSTRUCTURED PHOTOCATHODES FOR SPIN-POLARIZED ELECTRON BEAMS*

E.J. Montgomery[†], C. Jing, S. Poddar, Euclid BeamLabs LLC, Gaithersburg, MD, USA
A. Afanasev, George Washington University, Washington, DC, USA
S. Zhang, Jefferson Laboratory, Newport News, VA, USA
R. Kumar, G. Salamo, University of Arkansas, Fayetteville, AR, USA

Abstract

We present progress on incorporation of nanopillar arrays into spin-polarized gallium arsenide photocathodes in pursuit of record high tolerance to ion back-bombardment. Our goal is to exceed the 400 Coulomb record for a high polarization milliampere-class electron source set at Jefferson Laboratory in 2017, while maintaining high quantum efficiency (QE) and spin polarization with a superlattice.

Because the Mie effect is resonant, uniformity and careful control over nanostructure geometry is key. We report excellent uniformity and straight sidewall geometry with improved optical absorption using a painstakingly optimized inductively coupled plasma reactive ion etch. We also report the application of Kerker theory to spin-polarized photocathode nanopillar arrays, setting new requirements on nanostructure dimensions to avoid spoiling spin polarization. Finally, we also report initial steps toward re-establishing U.S. production of strained superlattice photocathodes towards integration with nanopillar arrays.

INTRODUCTION

Nanopillar arrays (NPAs) in gallium arsenide (GaAs) photocathodes have been reported to enhance quantum efficiency (QE) [1-2]. Spin polarization (P) and charge lifetime in the presence of ion back-bombardment was not quantified. These prior works also used p-type (zinc-doped) bulk GaAs, rather than state-of-the-art superlattices.

We have extended prior work in the present study to optimize the NPA nanofabrication process, to be discussed in the Fabrication section. We are preparing to measure cathode lifetime and anticipate it may increase significantly: non-normal nanopillar surfaces receive low ion bombardment but may contribute most of the QE with appropriate tuning of the dipole Mie resonance via NPA dimensions. Optical Mie resonance in nanopillar arrays preferentially traps light near nanopillar sidewalls. In a direct current gun, nearly zero back-bombardment ion flux will reach vertical sidewalls. The portion of QE attributable to sidewall emission is anticipated to tolerate back-bombardment.

KERKER THEORY

Light in Mie resonance can be depolarized resulting in deterioration of circular polarization. GaAs requires pure circular polarization to achieve high spin polarization of photoelectrons. Special conditions of conserving polarization are known as Kerker's conditions [3]. The polarization is preserved if the magnetic and electric polarizabilities of the scatterer are equal, resulting in suppression of backward scattering. We have performed simulations of Mie scattering with the miepython package (Fig. 1), where we plot the absorption efficiency of a GaAs sphere (orange curve) and the backscattering efficiency (blue curve) versus the size parameter, defined as $x = \pi d/\lambda$ where d is the sphere diameter and λ the optical wavelength.

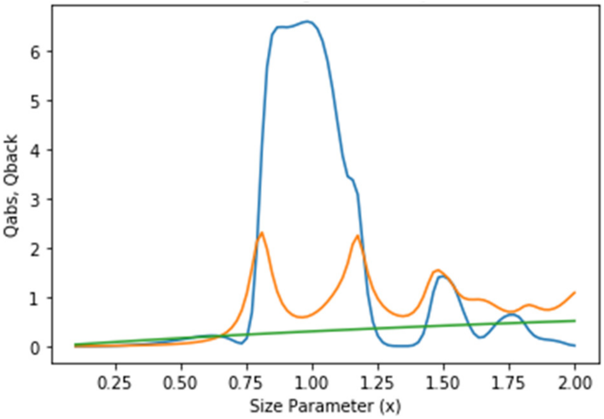

Figure 1: GaAs sphere Mie efficiency for backscatter (blue, Qback) and absorption (orange, Qabs)., vs. absorption of infinite slab, thickness equal to sphere diameter (green).

Based on the simulation, we can optimize a choice of nanostructure dimensions to simultaneously enhance QE and preserve photon polarization, hence preserve spin polarization of the photoemitted electron beam. We note this has been done successfully in non-photoemissive studies: the zero backscattering condition has been experimentally demonstrated in single GaAs nanoparticles [4].

Kerker's conditions lead to a non-intuitive design paradigm for Mie-resonant structures in spin-polarized photocathodes. Instead of optimizing on resonant absorption for QE, minima should be found in the back-scattering curve (in Fig. 1, at x=0.75 and x=1.3 to 1.4) which restricts the nanopillar size parameter, and then the best absorption for QE found in this subset (in Fig. 1, at x=0.75). Work is progressing to do this for cylindrical structures on planar substrates and for nanopillars capped by superlattices.

---

* Work supported by the U.S. Department of Energy, Office of Science, Office of Nuclear Physics, SBIR grant no. DE-SC0019599. Use of the Center for Nanoscale Materials, an Office of Science user facility, was supported by the U.S. Department of Energy, Office of Science, Office of Basic Energy Sciences, under Contract No. DE-AC02-06CH11357.

[†] e.montgomery@euclidtechlabs.com

ISBN: 978-3-95450-223-3 ISSN: 2673-7000 doi:10.18429/JACoW-NAPAC2019-MOPLH13

STARRE LAB: THE SUB-THZ ACCELERATOR RESEARCH LABORATORY[*]

J.F. Picard, S.C. Schaub, R.J. Temkin
Plasma Science and Fusion Center, Massachusetts Institute of Technology, Cambridge, MI, USA

Abstract

This work presents the development of the STARRE Lab, a facility at MIT for testing breakdown in high gradient accelerator structures at 110 GHz. The system utilizes a Laser-Driven Semiconductor Switch (LDSS) to modulate the output of a megawatt gyrotron, which generates 3 μs pulses at up to 6 Hz. The LDSS employs silicon (Si) and gallium arsenide (GaAs) wafers to produce nanosecond-scale pulses at the megawatt level from the gyrotron output. Photoconductivity is induced in the wafers using a 532 nm Nd:YAG laser, which produces 6 ns, 230 mJ pulses. A single Si wafer produces 110 GHz pulses with 9 ns width, while under the same conditions, a single GaAs wafer produces 24 ns 110 GHz pulses. In dual-wafer operation, which uses two active wafers, pulses of variable length down to 3 ns duration can be created at power levels greater than 300 kW. The switch has been successfully tested at incident 110 GHz RF power levels up to 720 kW. The facility has been used to successfully test an advanced 110 GHz accelerator structure built by SLAC to gradients in excess of 220 MV/m.

INTRODUCTION

With the potential for high efficiency in a small form factor, there has been growing interest in linear accelerator concepts driven at sub-THz and THz frequencies. Testing of these high-frequency structures requires RF pulses on the nanosecond timescale to avoid excessive pulsed heating. However, few sources exist that can achieve such short pulse widths at the required power levels. This paper presents a new test facility, the **S**ub-**T**erahertz **A**ccelerato**R** **RE**search Laboratory, or STARRE Lab, which utilizes a laser-driven semiconductor switch (LDSS) to produce megawatt-level, nanosecond-duration, sub-THz pulses to test advanced accelerator concepts. Previous experiments have documented LDSS behavior from microwave to the far-IR range but have been limited to the kilowatt power level [1]–[13]. The implementation of an LDSS with a megawatt-class gyrotron at 110 GHz, as in the STARRE Lab, represents a three order of magnitude increase in switched power over previous experiments and an exciting development in high-frequency accelerator testing capability. A full description of the behavior and testing of the LDSS has been published in [14].

FACILITY CAPABILITIES

Fig. 1 shows the setup of the STARRE Lab. A megawatt gyrotron produces 3 μs pulses of 110 GHz at up to 6 Hz. Each pulse has a flat-top power up to 1.5 MW [15]. The linearly-polarized output couples to the HE_{11} mode of a 31.75 mm diameter corrugated waveguide [16]. Power from the gyrotron can be continuously varied using a quasioptical microwave attenuator consisting of a half-waveplate and five quartz plates at the Brewster angle. Microwaves then enter a laser enclosure containing the LDSS.

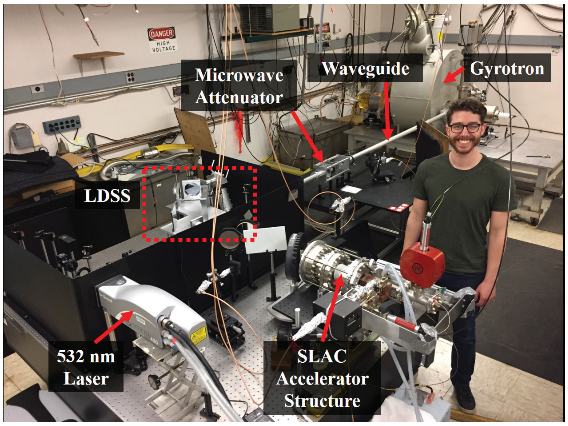

Figure 1: The STARRE Lab. A 1.5 MW, 110 GHz, gyrotron provides the input pulse to the LDSS, which is contained within a laser enclosure at center. The LDSS produces a shortened pulse, which exits the enclosure into the accelerator test stand (see Fig. 3).

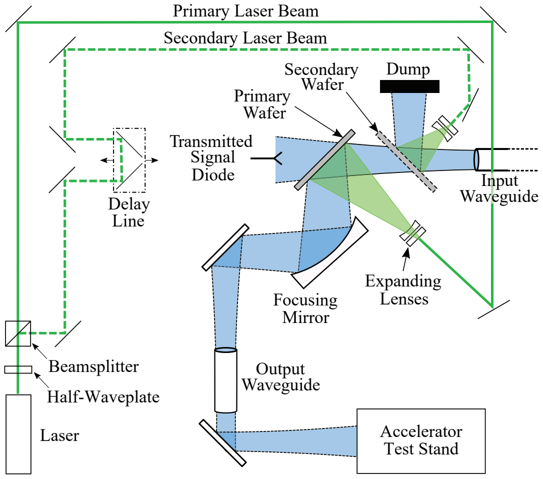

Figure 2: Experimental setup of the LDSS which feeds the accelerator test stand. 110 GHz microwaves generated by the MIT megawatt gyrotron are in blue and enter the setup from the input waveguide. Laser beams are shown in green.

A functional schematic of the LDSS system in the STARRE Lab can be seen in Fig. 2. 110 GHz radiation

---

[*] jpicard@mit.edu

ISBN: 978-3-95450-223-3 ISSN: 2673-7000 doi:10.18429/JACoW-NAPAC2019-MOPLH14

ULTRAFAST NONLINEAR PHOTOEMISSION FROM ALKALI ANTIMONIDE PHOTOCATHODES*

W. H. Li†, M. B. Andorf, I.V. Bazarov, L. Cultrera,
C. J. R. Duncan, A. Galdi, J. M. Maxson, C. A. Pennington,
CLASSE, Cornell University, Ithaca, NY, USA

Abstract

Alkali antimonides photocathodes are a popular choice of electron source for high average brightness beams, due to their high quantum efficiency (QE) and low mean transverse energy (MTE). This paper describes the first measurements of their nonlinear photoemission properties under sub-ps laser illumination. These measurements include wavelength-resolved power dependence, pulse length dependence, and temporal response. The transition between linear and nonlinear photoemission is observed through the wavelength-resolved scan, and implications of nonlinear photoemission are discussed.

INTRODUCTION

High brightness photoinjectors are an integral part of ultrafast electron diffraction (UED) and free electron laser (FEL) beamlines. For both UED and FELs, lower emittance and shorter bunches contribute to better performance. The lowest emittance achievable in a beamline is constrained by Liouville's theorem to be the emittance of the beam immediately on birth, while bunch length is determined primarily by the pulse length of the laser used to photoemit the electrons as well as any downstream compression optics. The maximum brightness of a photoinjector, defined as current divided by emittance, is determined solely by the mean transverse energy (MTE) of the photocathode and the accelerating gradient. Due to space charge effects near the cathode, there is a fundamental tradeoff between having low emittance beams and having ultrashort beams.

Thus, one clear path for improving the quality of electron beams in photoinjectors is decreasing the MTE of the photocathodes. Alkali antimonides are a class of photocathodes that have not only relatively low MTEs, but also have high quantum efficiency (QE), requiring fewer photons to produce the same number of electrons. For ultrafast, high power applications, this can be critical for lowering the laser power requirements to practical levels.

However, in 1964, Spicer [1] discovered nonlinear photoemission, where multiple photons transfer energy to an electron and emit it, in exactly this class of materials. Nonlinear photoemission causes the effective MTE to increase drastically, as the MTE is linear with photon energy [2], and the photon energy is effectively multiplied by the number of photons that participated in the photoemission. At short wavelengths, the single photon energy is large enough that linear photoemission is the dominant phenomenon. However, in order to reduce MTE, generally, it is preferred to use photon energies near threshold, which has the consequence of reducing QE. As the linear photoemission becomes weaker, nonlinear photoemission is responsible for a larger proportion of the emitted electrons. This can cause the MTE to actually begin to increase as the photon energy is reduced, as has been calculated for copper [3].

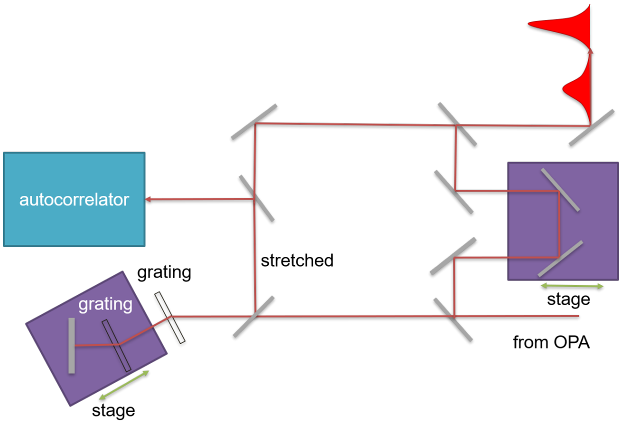

Figure 1: Schematic of the optics setup used for this experiment. The laser from the OPA is split into two different branches. One is sent through a delay stage, while the other is sent into a pulse stretcher/compressor to vary the pulse length. This is measured with a downstream autocorrelator before the pulses are recombined and sent into the gun.

In this paper, we describe the first measurements of ultrafast nonlinear photoemission phenomena from alkali antimonides. These were focused on measuring the photoemission yield to determine the photon energies at which nonlinear photoemission begins to become measurable and the proportion of electrons that are emitted in this fashion.

EXPERIMENTAL SETUP

The experimental apparatus consisted of two main components, the laser and the beamline. The laser was a commercially available Yb fiber laser coupled to an optical parametric amplifier (OPA), manufactured by Amplitude/APE. An OPA was used to generate wavelength-tunable sub-ps pulses. Typical pulse lengths are around 300 fs, and the laser can be tuned from UV to IR wavelengths with very little difficulty.

The light from the OPA is split into two legs, as shown in Fig. 1. One leg is sent through a delay stage, while the other is stretched by a double-grating pulse stretcher before

---

* This work was supported by the U.S. National Science Foundation under Award No. PHY-1549132, the Center for Bright Beams.

† Email: whl64@cornell.edu

ISBN: 978-3-95450-223-3 ISSN: 2673-7000 doi:10.18429/JACoW-NAPAC2019-MOPLH16

FEMTOSECOND LASER MICROFABRICATION FOR ADVANCED ACCELERATOR APPLICATIONS

S.P. Antipov, E. Dosov, E. Gomez, S.V. Kuzikov, Euclid Techlabs LLC, Bolingbrook, IL, USA
A.A. Vikharev, Institute of Applied Physics, Nizhny Novgorod, Russia

Abstract

Femtosecond laser microfabrication allows for precise dimension control and reduced thermal stress of the machined materials. It can be applied to a wide range of materials from copper to diamond. Combined with secondary operations like polishing, laser microfabrication can be utilized in various state of the art components required for the AAC community. In this paper, we will review several applications of laser microfabrication for Advanced Accelerator research and development. These will include wakefield structures (corrugated metal and dielectric loaded), plasma capillaries, x-ray refractive optics, high power laser optical components: mirrors, phase plates.

INTRODUCTION

In recent years, laser micromachining has made impressive advancements in terms of accuracy, scalability, and surface finish. Furthermore, the availability of extremely short pulse, femtosecond lasers now makes possible the process of ablation without melting. Surfaces processed in this manner exhibit less structural damage, and are expected to have a very high optical damage threshold. We developed an in-house femtosecond laser ablation system for the production of diamond lenses and phase plates [1]. We propose to use this approach (fs laser ablation) for the production of various accelerator – related components, from field emission cathodes to high frequency RF components to CO2 laser diffraction optical elements. A combination of galvanometer-controlled ("galvo") mirror scanning and high precision translation stages allows for large-scale grating production, limited only by the translation range of the stage.

In this paper we will review the laser ablation microfabrication process and present several accelerator applications of this fabrication technique.

LASER ABLATION

Laser ablation is a complex multiparameter process. In our laser cutter layout, we have a 50–100 kHz repetition rate, ~ 200 fs pulse length laser, operating in the second harmonic (515 nm). This laser passes through two key optical elements. One is a motorized lens, which allows focus adjustment in the range of 4 mm. The second unit consists of computer-controlled "galvo" mirrors with a so-called theta lens, which rasters the laser beam on the worktable (Fig 1). It is the interplay of the galvo mirror motion along with computer-controlled signal for the laser to fire or delay firing, and the specifics of the mirror motion control, that consists not only of steady movement, but also acceleration, deceleration and settling effects, that make the process incredibly complex and flexible.

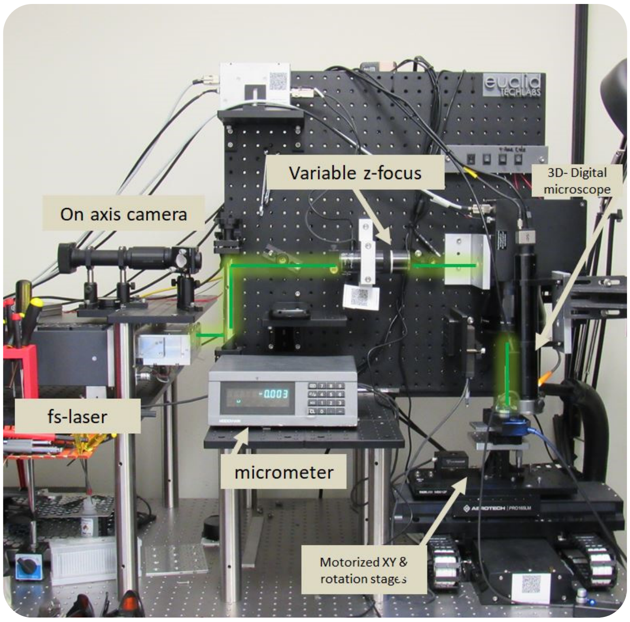

Figure 1: Femtosecond laser ablation system.

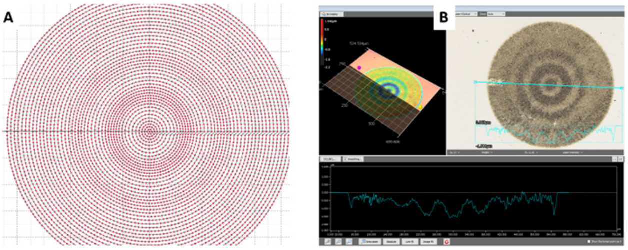

Figure 2: A. Laser ablation pattern. B. Metrology of ablated profile in diamond.

Typical ablation script is a path of the laser rastering created to produce specific ablation features at desired locations. Most geometries are produced by layering basic shapes (circles, squares, etc.) that are field with laser path lines. A more sophisticated strategy can involve variable density path lines for micron-level feature control (Fig 2). The single point ablation regime allows the ability to reproduce a specific set of ablation craters on the surface of different materials. An example of copper ablation with a random point pattern for high-power mirror reflectivity control is shown on Fig. 3. The typical size of the crater is a 10-micron aperture with quarter micron depth. There are number of considerations that are accounted for in the ablation scripting: layer decomposition, symmetrization of ablation with respect to the inherently elliptical laser spot, structure edge effects, kerf, laser delay and corresponding under or over exposure of the work piece to the laser beam, incorporation and synchronization of external motorization and focal plane adjustment during laser cutting procedure.

---

s.antipov@euclidtechlabs.com

ENHANCED ROBUSTNESS OF GaAs-BASED PHOTOCATHODES ACTIVATED BY Cs, Sb, AND O_2

J. Bae*, I. Bazarov, L. Cultrera, A. Galdi, F. Ikponmwen, J. Maxson, Cornell University, Ithaca, USA

Abstract

GaAs-based photocathodes are widely used to produce highly spin polarized electron beams at high currents. Spin polarized photoemission requires activation to achieve Negative Electron Affinity (NEA). The NEA surface is extremely vacuum sensitive, and this results in rapid QE degradation. In this work, we activated GaAs samples with unconventional methods using Cs and Sb. We confirmed NEA activation on GaAs surfaces and more than a order of magnitude enhancement in charge extraction lifetime compared to the standard Cs-O_2 activation without significant loss in spin polarization.

INTRODUCTION

GaAs-based photocathodes are the most popular electron sources for producing highly spin polarized electron beams at high currents in accelerator physics and condensed matter physics. To achieve a high Quantum Efficiency (QE) and high spin polarization, Negative Electron Affinity (NEA) is required, where the vacuum level is below the minimum of the conduction band [1]. Activation of NEA can be achieved by exposing GaAs samples to cesium vapor. Then, the Cs monolayer forms a dipole layer on the surface that lowers the potential barrier of electron extraction [2]. Additionally, oxidants, such as O_2 and NF_3, are commonly used to make the dipole layer stronger for a higher QE.

Activation layers for NEA are notorious for extreme vacuum sensitivity, and this results in rapid degradation of QE during beam operations. Conventional activation layers, such as Cs-O_2 and Cs-NF_3, are monolayers weakly bound to the GaAs surface with high chemical reactivity. Therefore, GaAs photocathodes are typically operated under extreme high vacuum (XHV) conditions, but still suffers from the rapid degradation. Various approaches were suggested to improve this sensitivity. Deflecting the electron beam near the laser spot was proposed to minimize one of the main surface degradation mechanisms, ion-back bombardment, and demonstrated enhanced lifetime in GaAs and alkali antimonide photocathodes [3–6]. In another study, chemical immunity enhancement was achieved by using two alkali materials, Cs and Li, for activation along with NF_3 oxidant [7,8]. Recently, activation with alternative semiconductor layers was proposed to improve the lifetime. In particular, successful NEA activation was demonstrated with Cs_2Te layer without any significant loss in spin polarization and QE while improving the charge extraction lifetime by a factor of 5. [5,9]

A heterojunction model suggests an alternative semiconductor activation layer on GaAs needs to satisfy two conditions to achieve NEA on the surface (Fig. 1): (i) the energy difference between the Fermi level and vacuum level should be smaller than the band gap of GaAs (1.43 eV), and (ii) the band gap of activation layer should be greater than that of GaAs for transparency of photons used for spin polarized photoemission. Cs_3Sb has a small electron affinity of 0.4 eV and the band gap of 1.6 eV that satisfy the two conditions as illustrated in Fig. 1. In this work, we demonstrate NEA activation on GaAs surface using Cs and Sb vapors. Additionally, we exposed the sample to oxygen during the growth for one of the samples and observed improved performance in QE and lifetime.

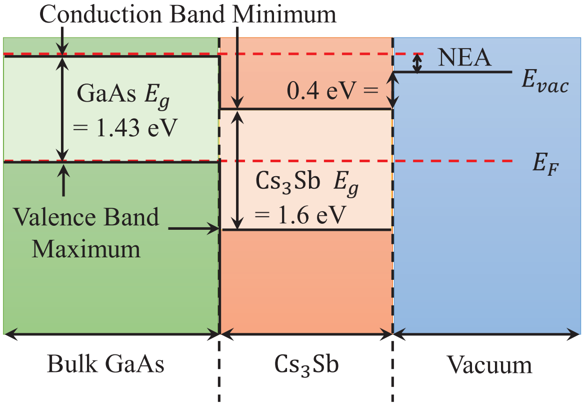

Figure 1: Energy band diagram of GaAs activated with Cs_3Sb based on heterojunction model. An alternative semiconductor activation layer needs to satisfy two conditions mentioned in the text to achieve NEA.

EXPERIMENT

Growth

Highly *p*-doped (Zn $5 \times 10^{18} cm^{-3}$) GaAs (100) wafers were cleaved in air with a diamond scribe. Each sample was solvent cleaned with isopropanol, and rinsed in de-ionized water. Samples are wet-etched with 1% HF solvent for 30 s and rinsed again with de-ionized water before loading under vacuum. The growth chamber has a base pressure of 10^{-9} Torr, and Cs and Sb effusion cells are installed with shutters that control the flux on the sample. Each sample was heat cleaned at ~ 500° for ~ 12 hours and cooled down to 130° for activation with Cs, Sb, and O_2. Samples were grown with three different methods:

1. Cs and O_2 are codeposited at room temperature for a reference sample.

---

* jb2483@cornell.edu

North American Particle Acc. Conf. NAPAC2019, Lansing, MI, USA JACoW Publishing
ISBN: 978-3-95450-223-3 ISSN: 2673-7000 doi:10.18429/JACoW-NAPAC2019-MOPLH19

BEAM DYNAMICS SIMULATIONS FOR A CONDUCTION-COOLED SUPERCONDUCTING RF ELECTRON SOURCE [*]

O. Mohsen[†], V. Korampally, A. McKeown, D. Mihalcea, P. Piot[‡], I. Salehinia
Northern Illinois University, DeKalb, IL, USA
R. Dhuley, M.G. Geelhoed, J.C.T. Thangaraj
Fermi National Accelerator Laboratory, Batavia, IL, USA

Abstract

The development of robust and portable high-average power electron sources is key to many societal applications. An approach toward such sources is the use of cryogen-free superconducting radiofrequency cavities. This paper presents beam-dynamics simulations for a proof-of-principle experiment on a cryogen-free SRF electron source being prototyped at Fermilab [1]. The proposed design implement a geometry that enhances the electric field at the cathode surface to simultaneously extract and accelerate electrons. In this paper, we explore the beam dynamics considering both the case of field and photoemission mechanism.

INTRODUCTION

Electron accelerators are finding a great interest in many scientific [2,3], industrial and societal applications [4]. Their advancement relies heavily on the development of electron sources and the coupled accelerating structures. Some of the contemplated applications call for low-cost, rugged, and portable electron accelerators capable of producing high-average-power beams. Recent advances in photo-injectors, specifically, the coupling between photoemission sources and Superconducting radio-frequency (SRF) technologies enabled the generation of very high peak current and low emittance beams [2,5]. So far, this required the operation of an auxiliary laser system which usually increases the cost and the complexity of the accelerator. Moreover, current laser systems can generate high power pulses on a moderate repetition rate [$\mathcal{O}$(kHz)], which ultimately limits the average current. On the contrary, field emission (FE) enables the emission of electrons from the bulk of a material subjected to intense electric fields [6]. Thus, an FE source does not require the additional triggering by a laser system. Likewise, when integrated into an RF structure, the emission from the FE cathode is self gated by and synchronized with, the RF electric field. Such a feature enables the extraction of electrons in every RF cycle, which pave the way to the production of high-average-power beams [7,8].

In this paper, we perform numerical simulations of a proposed superconducting RF (SRF) FE electron source experiment in preparation at Fermilab [1]. This concept experiment will investigate FE cathodes operation in SRF cavities. However, the source can in principle also operate with photoemission cathodes and the corresponding beam dynamics is also explored.

CONCEPTUAL DESIGN: OVERVIEW

The initial design of the proposed electron source is based on a niobium 650 MHz single-cell elliptical resonator with the geometry shown in Fig. 1(a) [1]. The resonator is flanked with 50 mm beam pipes with flanges on each side. In order to support experiment on electron emission, the resonator was modified by inserting a stud of length $L = 0.22$ m and radius $r = 5$ mm; see Fig. 1(b). The addition of the stud modifies the resonant modes inside the resonator, thus changing the electromagnetic field distribution inside the resonator. The altered configuration enables the field at the stud extremity where the cathode is located to be maximum. To avoid significant field enhancement at the edge of the rod, its tip is rounded with a fillet with 1-mm radius of curvature. The dimensions of the rod and the radius of curvature of the fillet were determined in a previous study based on the electromagnetic and thermal simulations available experimental equipment [1]. Thermal consideration prevented us to maximize the field by locating the rod extremity exactly at the center of the cell (instead it had to be slightly retracted). Both end flanges at $z = 0.0$ m and $z \sim 0.56$ m (input and

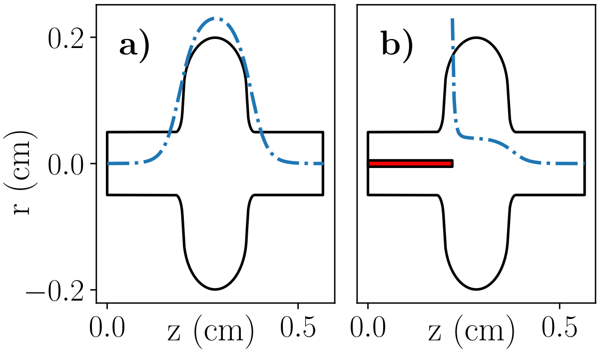

Figure 1: Geometry of the nominal (a) and modified cavity (b). The blue dashed lines corresponds to the on-axis electric field $Ez(z, r = 0)$.

---

[*] This work was supported by the US Department of Energy (US DOE) under award No. DE-SC0018367 with Northern Illinois University. Fermilab is managed by the Fermi Research Alliance, LLC under US DOE contract No. DE-AC02-07CH11359. This research used resources of the National Energy Research Scientific Computing Center which is supported by the US DOE contract No. DE-AC02-05CH11231.

[†] omohsen@niu.edu

[‡] also at Fermi National Accelerator Laboratory, Batavia, IL, USA

ISBN: 978-3-95450-223-3 ISSN: 2673-7000 doi:10.18429/JACoW-NAPAC2019-MOPLH22

FOCUSING STUDIES OF AN ELECTRON BEAM IN DIAMOND FIELD EMITTER ARRAY CATHODES*

R.L. Fleming†, H.L. Andrews, D. Gorelov, C. Huang, D. Kim, J.W. Lewellen, K.E. Nichols,
V.N. Pavlenko and E. I. Simakov, Los Alamos National Laboratory, Los Alamos, NM, USA

Abstract

We report the results of tests and simulations for focusing studies performed on diamond field emitter array cathodes. This experiment utilized a simple variable-focus solenoidal lens to focus the beam produced by a diamond field emitter array cathode. The spot size was measured by scanning a thin copper wire across the beam in 1 µm increments, with voltage being measured and averaged at each location in order to map the location and intensity of the beam. Scans were taken at different distances away from the magnetic center of the lens. However, there were some unforeseen challenges associated with measuring the exact spot size of the beam, and we will explain them here.

INTRODUCTION

At Los Alamos National Laboratory (LANL), we have the ability to fabricate diamond array cathodes for use as electron beam sources [1, 2]. These cathodes feature nanometer scale emitting areas (10-20 nm radius per tip) and high current per tip (up to 15 µA per-tip), diamond field emitter arrays (DFEAs) are promising candidates for use in a dielectric laser accelerator (DLA). However a DLA structure requires a very tightly focused beam (1 µm scale) [1, 3]. In order to achieve this requirement we have been conducting focusing studies on diamond pyramids to learn if we can sufficiently focus the beam.

FOCUSING STUDIES

Experimental Setup

Figure 1 (a) is a schematic of the experimental setup for our focusing studies. Figure 1 (b) is a photograph of the experimental setup, and another photograph Fig. 1 (c) shows the copper wire in place attached to the wire holder. Table 1 shows the setup parameters for the experiment.

The experimental setup included a cathode in a cathode holder, a mesh anode, a focusing lens with a collimator, a copper wire, and a conductive luminescent screen. The cathode being used was a 3 by 3 array of diamond pyramids, each with a 25 µm base and 1000 µm spacing. A 100 lines per inch, mesh anode was mounted on a single axis controllable stage in order to vary the intensity of the electric field from cathode to anode. The anode to cathode distance (AK gap) was set at 5.5 mm. The variable focus magnetic lens [4] was mounted in a fixed position, 48.1 mm behind the mesh anode, and had a peak magnetic field of 1200 Gauss. The copper wire, and ZnO:Al_2O_3 (AZO) screen are mounted on a two axis stage, grounded and are isolated from each other electrically in order to allow us to measure the current collected by the wire across a 20 kΩ resistor separately from the current that is deposited on the AZO screen. The wire is positioned between 13.5 mm and 16 mm from the magnetic center of the lens depending on where we wanted to measure the size of the beam. The screen was used to align the wire with the beam path, as well as to understand the beam's behavior and for troubleshooting purposes.

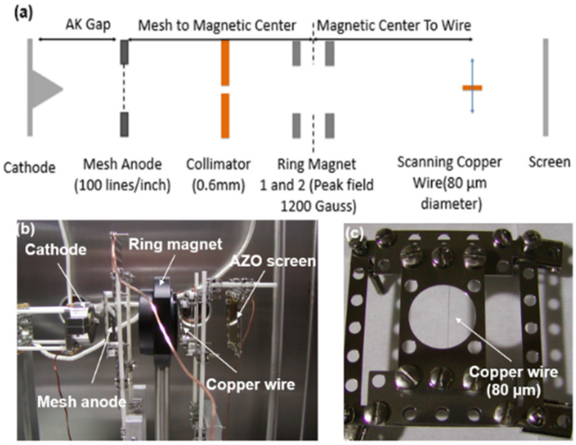

Figure 1: (a) Schematic of the scanning wire focusing studies. (b) Photograph of the focusing study setup. (c) Photograph of the wire holder. The wire in the photo is a copper wire, 80 µm in diameter. A 5 µm tungsten wire was also used in the experiment in place of the copper wire.

Table 1: Setup Parameters

Experimental Parameter	Value
AK Gap	5.5 mm
AK Voltage	-40 kV
Lens to Wire Distance	13.98 mm, 14.50 mm, 15.48 mm
Lens to Mesh Distance	48.1 mm
Pyramid Base	25 µm and 20 µm
Pyramid Spacing	1000 µm and 900 µm
Peak Magnetic Field	1200 Gauss
Wire Diameter	80 µm and 5 µm
Wire Material	Copper or Tungsten
Computed focal length	15.1 mm
Computed focal diameter	10 µm

Methodology and Initial Results

We performed beam spot size measurements utilizing a wire scan method. We began by moving the 80 µm copper wire in one direction in increments of 1 µm. We measured the current collected on the wire and observed the images on the screen. During the first scan the wire was located

---

* The authors gratefully acknowledge the support of Los Alamos National Laboratory (LANL) Laboratory Directed Research and Development (LDRD) program.
†rfleming@lanl.gov

ISBN: 978-3-95450-223-3 ISSN: 2673-7000 doi:10.18429/JACoW-NAPAC2019-MOPLH23

AN ANALYSIS OF A POTENTIAL COMPACT POSITRON BEAM SOURCE

R. M. Hessami*, Department of Physics and Astronomy, UCLA, Los Angeles, USA
S. J. Gessner†, CERN, Geneva, Switzerland

Abstract

For positron studies in plasma wakefield accelerators such as AWAKE, the development of new, cheaper, and compact positron beam sources is necessary. Using an electrostatic trap with parameters similar to other experiments, this paper explores converting that trapped positron plasma into a usable beam. Bunching is initially accomplished by an electrostatic buncher and the beam is accelerated to 148 keV by pulsed electrostatic accelerators. This is necessary for injection into the β-matched rf cavities operating at 600 MHz, which bring the positron beam to a transverse emittance of 1.3 π mrad mm, a longitudinal emittance of 93.3 π keV mm, σ_z of 1.85 mm and an energy of 22 MeV. The beamline used here is far simpler and less expensive than those at many facilities, such as SLAC, allowing for a cheap source of positron beams, potentially opening up positron beam studies to many facilities that could not previously afford such a source.

INTRODUCTION

Plasma wakefield acceleration (PWFA) is a promising way of accelerating charged particles that is far more efficient and compact than traditional radiofrequency (RF) accelerators. However, the acceleration of positron beams in plasma is an unsolved challenge [1–6]. In RF cavities, the phase can simply be changed to account for the different sign of the beam charge, while no such symmetry is easily exploitable in the case of PWFA. One of the greatest barriers to furthering research on this topic is the lack of experimental facilities that can generate the positron beams necessary for these studies. SLAC is the only laboratory that has provided positron beams for PWFA experiments. FACET-II at SLAC is the next facility planning to deliver positron beams and it is over 1 km long [7]. On the other hand, a method of generating a trapped, low-energy positron plasmas with at least 10^8 particles has been developed [8]. The potential exists for this beam to reach 10^{10} particles within a few years [9]. In this paper, the possibility of using this trap as a source for a positron beam is addressed, as well as the small and inexpensive linac needed to compress and accelerate this plasma into a usable beam that can be fed into the AWAKE plasma cell, just as electron beams are currently fed in. While PWFA applications are the primary interest of this paper, such a compact positron source would be of great interest to any facility interested in studying positron physics.

POSITRON BEAM SOURCE

Positron beams may be generated either by using a positron emitter like ^{22}Na or impacting an electron beam on a target, utilizing pair production [9]. The beams generated this way have a wide energy spread, so a moderator is then used to make the beam that will enter into the trap. The potential walls used to trap the beam longitudinally need to be of greater magnitude than the space charge potential, which in this case was about 10 V.

Many of the properties of the beam inside the electrostatic trap can be defined in terms of the trap's parameters. The trap used in the simulations here had the properties defined in Table 1. Note that in this case, the plasma dimensions were defined and trap properties to match it were found from there, but the opposite can also be done using the equations

$$\Omega_C = \frac{qB}{m}, \tag{1}$$

$$\omega_r = \frac{qn}{2\epsilon_0 B}. \tag{2}$$

The cyclotron frequency needed to produce such a beam is given by Eq. (1), where B is the magnetic field strength inside the trap, while the rotational frequency of the trap is given by Eq. (2), where n is the density of the plasma. ω_r is a parameter externally implemented by the rotating wall effect.

Table 1: Parameters Used to Define the Initial Plasma Distribution Inside the Trap

Parameter	Value
Trap radius	0.004 m
Trap length	0.1 m
Magnetic field	1 T
Plasma radius	0.001 m
Plasma length	0.09 m
Temperature	273 K
Number of positrons	10^8 particles
Emittance	0.11 µm

The Debye length for this plasma was found to be 60.6 µm. When the Debye length is much smaller than the plasma radius, the plasma can be considered to be of uniform density up until one Debye length from the edge of the plasma, so this approximation was utilized to generate the initial distribution for the beamline simulation [10].

ANALYTIC EQUATION FOR TRANSVERSE EMITTANCE

From the standard equation for transverse emittance, an analytic equation for the transverse emittance of a plasma

---

[*] rafimah@ucla.edu
[†] spencer.j.gessner@cern.ch

ISBN: 978-3-95450-223-3 ISSN: 2673-7000 doi:10.18429/JACoW-NAPAC2019-MOPLH24

TOWARDS THE OPTIMIZATION OF PHOTOCATHODE PROPERTIES VIA SURFACE SCIENCE TECHNIQUES: A STUDY ON Cs$_3$Sb THIN FILM GROWTH[*]

A. Galdi[†], J. Balajka, J. B. Baretz, I. V. Bazarov, L. Cultrera, W. J. I. DeBenedetti,
M. A. Hines, F. Ikponwmen, J. M. Maxson, S. A. McBride
Cornell University, Ithaca NY, USA

Abstract

Surface science measurement techniques such as x-ray photoemission spectroscopy (XPS) and scanning tunnel microscopy (STM) can provide quantitative information about the composition and the morphology of thin film samples. We successfully transferred Cs-Sb samples from the growth chamber to a surface science XPS/STM system by use of an UHV suitcase and measured their properties. This will allow to study the properties of photocathode films and ultimately how to control the growth process to achieve the best performances, including high efficiency, ruggedness and low emittance.

INTRODUCTION

Photocathodes are the electron sources of choice for cutting edge linear accelerator applications, such as free electron lasers (FEL) [1] and ultrafast electron diffraction (UED). [2] The transverse momentum spread of the photoemitted electrons is critical for these applications, since it determines the shortest achievable wavelength in FEL and the coherence lenght for electron diffraction. When high efficiency is required, alkali antimonide based photocathodes have demonstrated to have excellent performance with visible light. [3] At the same time, when operated at cryogenic temperatures (90 K) and near the photoemission threshold (690 nm), they provide electron beams characterized by very low intrinsic emittance, down to 0.17 μm/mm (i.e. the normalized emittance per unit area, proportional to the rms transverse momentum). [4] A limiting factor to achieving the lowest possible intrinsic emittance has been identified in the surface inhomogeinities of photocathodes, such as the surface roughness and workfunction variations. [5, 6] The study of the surface properties of this class of materials is limited by their reactivity, that require the samples to be in ultra-high vacuum (UHV) to avoid degradation and decomposition. X-ray photoemission spectroscopy (XPS) has been a powerful tool to characterize the composition and reactivity of alkali antimonides, thanks to its particular sensitivity to the surface composition. [7–11] Scanning probe techniques, such as atomic force microscopy in UHV, have been employed to characterize the morphology and roughness. [12] Another very powerful technique is scanning tunnel microscopy (STM), that is typically performed in UHV and it is capable to achieve atomic-scale resolution. UHV suitcases are typically used to transport air-sensitive cathodes from the growth system to the photoinjector. [11, 13] Here we use a vacuum suitcase to interface the alkali antimonide growth system to a standard XPS-STM surface science apparatus, using commercially available sample holders and manipulation tools. The first results on coupled STM and XPS measurements on Cs-Sb thin film samples grown on different substrates are presented.

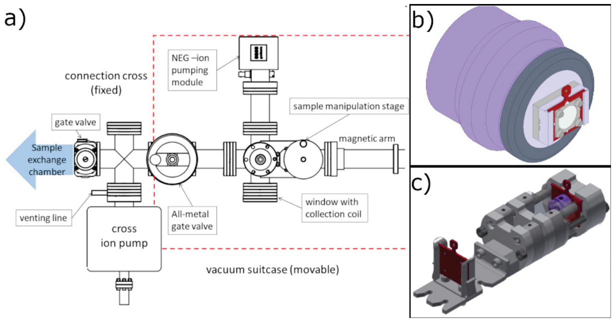

Figure 1: (a) schematics of the vacuum suitcase; (b) standard growth puck (purple) with the adapter (light purple) holding the Omicron sample holder (red). The sample (light yellow) is held by a metal retaining plate and screws (light gray); (c) multi sample carrier installed in the vacuum suitcase.

EXPERIMENTAL

Film Growth and Transfer

Cs-Sb samples were deposited on (001) rutile TiO$_2$ and (10-10) Al$_2$O$_3$ insulating substrates. Lattice-matched substrates are of interest to promote anisotropic growth of Cs$_3$Sb and possibly yielding single oriented, lower roughness surfaces.

The Cs-Sb samples were grown in the growth system described in ref. [14] at a temperature of 70°C , using pure Cs and Sb metals. Substrates were mounted on an standard sample holder shown in Fig.1(b), using a metal retaining plate in order to provide electrical contact to the sample surface (relevant both to measure the photocurrent during growth and for successive STM-XPS measurements); the sample plate was then installed on the standard growth puck. [14] The photocurrent emitted by the sample was monitored during growth by exciting the cathode with a 504 nm diode laser and by measuring the drain current from the cathode biased at -18 V with a lock-in amplifier locked to the fre-

---

[*] This work was supported by the U.S. National Science Foundation under Awards OIA-1549132, the Center for Bright Beams, and PHYS-1535279.

[†] ag733@cornell.edu

ISBN: 978-3-95450-223-3 ISSN: 2673-7000 doi:10.18429/JACoW-NAPAC2019-MOPLH25

CHARACTERIZATION OF FEMTOSECOND-LASER-INDUCED ELECTRON EMISSION FROM DIAMOND NANO-TIPS*

V. Pavlenko†, H. L. Andrews, R. L. Fleming, D. Gorelov, D. Kim, E. I. Simakov,
Los Alamos National Laboratory, Los Alamos, NM, USA
D.S. Black, K.J. Leedle, Stanford University, Stanford,CA, USA

Abstract

Nanocrystalline diamond is a promising material for electron emission applications, as it combines robustness of diamond and ability to easily conform to a pre-defined shape, even at nano-scale. However, its electron emission properties are yet to be fully understood. Recently, we started to investigate femtosecond-laser-induced strong-field photoemission from nanocrystalline diamond field emitters with very sharp (~10 nm apex) tips. Initial results show that the mechanism of electron emission at ~10^{10} W/cm^2 light intensities in the near UV to near IR range is more complex than in metals. We present our latest experimental results obtained at Stanford University, while LANL's strong-field photoemission test stand is being commissioned. We show that strong-field photoemission occurs not only at the nano-tip's apex, but also on flat diamond surfaces (e.g., pyramid sides), that is why extra care needs to be taken to differentiate between emission spots on the chip. Qualitatively, we discuss the models that explain the observed dependences of electron emission on the optical power, polarization of the light, etc.

INTRODUCTION

This work supports development of a dielectric laser accelerator (DLA) [1], which will benefit from a very compact laser-triggered electron source. Diamond nano-tips are attractive candidates for that role [2], and a manufacturing technique for such samples has been fully adopted and refined by LANL. Experimental characterization of the strong-field photoemission from diamond nano-tips was conducted jointly with Stanford University DLA laboratory, within the framework of the Accelerator on a Chip International Collaboration (ACHIP) [3].

DIAMOND SAMPLES

Diamond nano-tip samples were fabricated as diamond field emitter arrays (DFEA) [4, 5]. Currently, manufacturing technology cannot produce equally sharp tips, even within one chip. Prior to testing, sharpest tips with the apex curvature radius of ~10 nm are identified by SEM, because those supposedly produce high emission currents as both DC and optical field enhancement factor is expected to be larger for sharper tips. Different array configurations were manufactured, including linear arrays on a narrow (about 300 µm wide) substrate (Fig. 1).

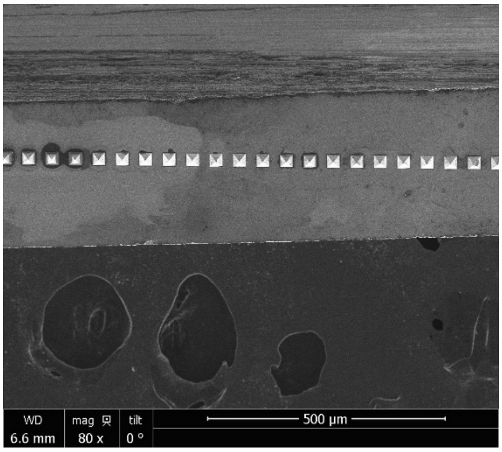

Figure 1: SEM image of a linear nano-tip array (Cu-03), top view. Pyramids have 25 µm base side length.

EXPERIMENTAL SETUP

The layout and photo of LANL's strong-field photoemission test stand is shown in Fig. 2. The layout is based on Stanford University's test stand with some modifications intended to make the system more flexible and modular. Experimental procedure outlined below is universal with respect to different test stands, the actual measurements' results reported here were obtained at Stanford University.

Laser parameters need to be carefully considered in the design of the beam line so that the intensity of the light at the focal spot can achieve ~10^{10} W/cm^2, where strong-field photoemission is typically observed [6].

Characteristics of individual diamond nano-tips are obtained by focusing the laser light onto one tip at a time, which is established by observing the scattered laser light with a sample microscope camera and fine-tuning the laser focal spot position to achieve maximum electron emission current. Typically, for a setup that employs a small vacuum chamber and a focusing lens just outside of a vacuum viewport, one can focus a 5 mm diameter laser beam down to several tens of microns, which is commensurate with a DFEA pyramid's size (Fig. 1). Larger DFEA chip sizes (e.g., 5x5 mm^2), necessitate the use of oblique angle of incidence of 5-10 degrees with respect to the substrate plane in order to avoid incident laser beam being partially occluded by the substrate, while narrow substrates (Fig. 1) allow laser beam alignment parallel to the substrate.

DC field emission without laser illumination is used to align a nano-tip with the anode axis, subsequent strong-

---

* The authors gratefully acknowledge the support of Los Alamos National Laboratory (LANL) Laboratory Directed Research and Development (LDRD) program. This work was performed, in part, at the Center for Integrated Nanotechnologies, an Office of Science User Facility operated for the U.S. Department of Energy (DOE) Office of Science by Los Alamos National Laboratory (Contract DE-AC52-06NA25396) and Sandia National Laboratories (Contract DE-NA-0003525).

†pavlenko@lanl.gov

DESIGN OF A COMPACT WAKEFIELD ACCELERATOR BASED ON A CORRUGATED WAVEGUIDE

A.E. Siy[1], University of Wisconsin, Madison, WI, USA
G.J. Waldschmidt, A. Zholents, Argonne National Laboratory, Lemont, IL, USA
[1]also at Argonne National Laboratory, Lemont, IL, USA

Abstract

A compact wakefield accelerator is being developed at the Argonne National Laboratory for a future multiuser x-ray free electron laser facility. A cylindrical structure with a 2 mm internal diameter and fine corrugations on the wall will be used to create Čerenkov radiation. A "drive" bunch producing radiation at 180 GHz will create accelerating gradients on the order of 100 MV/m for the "witness" bunch. The corrugated structure will be approximately half meter long with the entire accelerator spanning a few tens of meters. An ultra-compact transition region between each corrugated structure has been designed to accommodate an output coupler, a notch filter, an integrated offset monitor, bellows, pumping and water cooling ports. The output coupler will extract on the order of a kilowatt of power from the Čerenkov radiation unused by the witness bunch. The integrated offset monitor is a novel diagnostic which will measure the cumulative offset of the electron beam in the corrugated structure upstream of the monitor. The specific details of the rf design will be presented here.

INTRODUCTION

The generation of wakefields in dielectric and corrugated structures is a well-known phenomenon that results in the generation of high gradient electromagnetic fields [1]. Harnessing these fields for particle acceleration requires the design of a corrugated waveguide along with couplers to extract unused RF power and beam position monitors to ensure the accelerated beam is centered in the structure. The design of these components will be the focus of this paper.

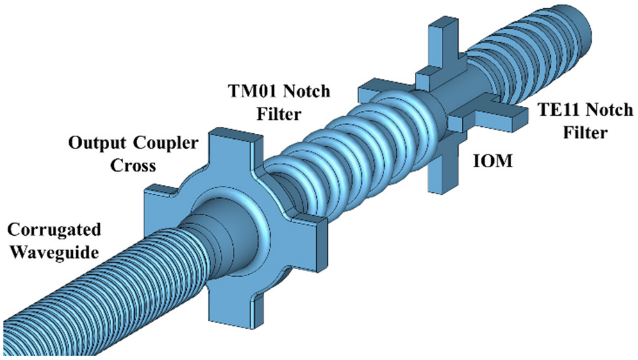

Figure 1: Corrugated waveguide and supporting RF components, showing vacuum region from CST model.

A section of the proposed accelerator is depicted in Fig. 1. Each of the components in the figure will be described and a brief explanation of design methodology will be provided. The final structure will consist of many identical sections, connected end to end by mechanical bellows. This paper will focus on the design of a single accelerating section which can then be generalized to a much longer structure.

CORRUGATION DESIGN

The corrugated waveguide is designed to support a propagating TM01 mode which is synchronous with the drive and witness bunches at the operating frequency of 180 GHz. Analytic approximations exist for estimating the corrugation dimensions [2], which are valid for small corrugation depth compared to the waveguide diameter. Simulation in CST Microwave Studio Eigenmode Solver [3] allows a more precise calculation of the corrugation dimensions for a given frequency by specifying the cell to cell phase shift in terms of the corrugation period and relating this to the phase velocity of the propagating wave. The dimensions are then found through an optimization process subject to the constrained corrugation period as shown in Fig. 2.

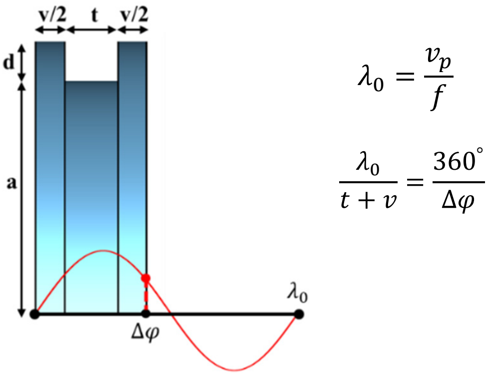

Figure 2: Corrugation unit cell with constraint equations for synchronous TM01 propagation at frequency *f*.

The resulting combinations of dimensions lie on surfaces of constant frequency in parameter space, as shown in Fig. 3. Plotting design metrics on these surfaces shows how the overall performance of the corrugated waveguide can be optimized. It is desirable to maximize both the group velocity and acceleration gradient of the corrugated structure which is accomplished by choosing a geometry in which the corrugation tooth width *t* is less than the vacuum width *v*. Also of critical importance is the transformer ratio [4, 5], which is a function of the drive bunch shape and found by simulation to be constant across all considered geometries.

ISBN: 978-3-95450-223-3 ISSN: 2673-7000 doi:10.18429/JACoW-NAPAC2019-MOPLO01

A BEAM SPREADER SYSTEM FOR LCLS-II*

T.G. Beukers†, J.W. Amann, Y.M. Nosochkov
SLAC National Accelerator Laboratory, Menlo Park, CA, USA

Abstract

For the LCLS-II project, the SLAC National Accelerator Laboratory is installing a new superconducting RF linac capable of continuously delivering 4 GeV electron bunches spaced 1.1 microseconds apart. A spreader system is required to distribute the beam between a soft X-ray or hard X-ray undulator, and a beam dump. An additional beam diverter is required in the front end of the linac to divert 100 MeV electrons to a diagnostic line. Both the spreader and diagnostic diversion systems are designed to operate on a bunch by bunch basis via the combination of fast kickers and a Lambertson septum. This paper presents a summary of the beam transport, kicker, and septum design. Of specific interest is the unique challenge associated with building a high repetition, high stability spreader capable of diverting a single bunch without disturbing neighbouring bunches. Additional discussion includes the application of the spreader technology to the proposed S30XL beamline. This beamline will accept micro bunches evenly spaced between the undulator bound bunches, thus requiring a kicker with the same repetition rate as LCLS-II but a pulse width extended to approximately 600 ns.

INTRODUCTION

The LCLS-II [1] free electron laser (FEL) project at the SLAC National Accelerator Laboratory will produce 4 GeV electron bunches from a superconducting linac (SRF) at a repetition rate of 929 kHz. These bunches will be steered via a spreader to a hard X-ray (HXR) undulator, a soft X-ray (SXR) undulator, or an electron beam dump in the Beam Switch Yard (BSY). Each undulator requires a dedicated beam diverter consisting of three kickers and a septum. The kickers are pulsed simultaneously to produce an integrated kick sufficient to direct each bunch into the high field region of a septum magnet where the bunch is steered towards the corresponding undulator. When neither set of kickers is pulsed, the beam traverses the zero-field region of both septa and is transported to the BSY dump. This spreader design has the capability to produce semi-arbitrary bunch-by-bunch beam patterns between the two undulators and the BSY dump. Primary components of the spreader have been designed, built, and tested, including the kickers and septa. Discussion will include beam transport through the spreader, kicker design and testing results, modification of the kicker design for high strength or long pulse applications, and septum design.

BEAM TRANSPORT

After the SRF linac, the 4 GeV beam is transported via a dogleg and existing 2-km bypass line to the beam spreader system located at the end of the existing LCLS [2] CuRF linac and in the BSY. The spreader fast vertical kickers and horizontal septa divert the SRF bunches either to HXR or SXR undulator beamlines or allow them to pass to the 250 kW dump in the BSY muon wall. The 3 – 17 GeV bunches from the CuRF linac are also diverted in this region to the HXR or SXR or to the existing End Station-A beamline (ESA) using low repetition kickers. Consequently, several beamlines occupy less than 1 m^2 cross-section in this area.

The spreader layout is shown in Fig. 1, where the fast kickers and septa (in dash boxes) divert the SRF beam to HXR and SXR beamlines (green and light blue), to BSY dump (black box), or to ESA through S30XL (red). The CuRF beam is diverted to the HXR, SXR or ESA. The different beamlines are at different elevation level.

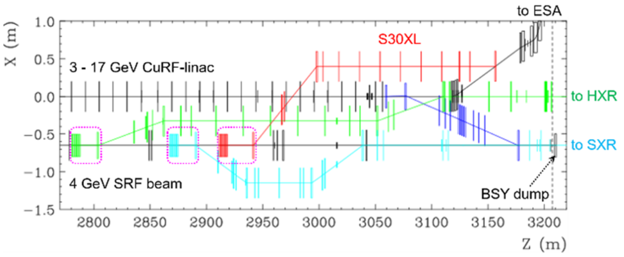

Figure 1: Top view of the spreader.

The SRF beam pattern consists of the primary FEL bunches spaced 1.1 µs apart, intended for the undulators, and the dark current buckets between them which are populated at the LCLS-II RF gun (with 5.4 ns spacing) or may be seeded by a 46-MHz laser oscillator (21.5 ns spacing). The first fast kickers on the SRF beam path are for the HXR (see Fig. 1). When these kickers' pulse is on, the FEL bunches are deflected through the HXR septum high-field hole into the HXR beamline; otherwise they proceed straight ahead through a field-free hole towards the SXR kickers and septum. Similarly, if the SXR kickers' pulse is on, the FEL bunches are deflected into the SXR beamline; otherwise they pass towards the BSY dump. The 4 GeV LCLS-II uses three fast kickers for each undulator, while for the future LCLS-II high energy upgrade (8 GeV) the number of kickers will be increased to six.

Due to the short kicker pulse, the dark current between the FEL bunches is not affected by the HXR and SXR kickers and nominally goes to the BSY dump. Lately a new beamline, named sector 30 transfer line (S30XL – red line in Fig. 1), formerly DASEL [3], has been proposed which

---

*Work supported by Department of Energy contract DE-AC02-76SF00515.

† beukers@slac.stanford.edu

ISBN: 978-3-95450-223-3 ISSN: 2673-7000 doi:10.18429/JACoW-NAPAC2019-MOPLO03

FINAL CONVERSION OF THE SPALLATION NEUTRON SOURCE EXTRACTION KICKER PULSE FORMING NETWORK TO A HIGH VOLTAGE SOLID-STATE SWITCH*

B. Morris[†], R.B. Saethre, Oak Ridge National Laboratory, Oak Ridge, TN, USA

Abstract

The Spallation Neutron Source (SNS) extraction kicker 60 Hz pulsed system uses 14 Blumlein pulse-forming network (PFN) modulators that require timing synchronization with stable rise times. A replacement design has been investigated and the kickers have been converted to use a solid-state switch design, eliminating the lifetime and stability issues associated with thyratrons and subsequent maintenance costs. All kickers have been converted, preventing thyratron jitter from impacting the beam performance and allowing higher-precision target impact. This paper discusses the completion of the conversion of the high-voltage switch from a thyratron to a solid-state switch with improved stability of the extraction system and associated accelerator beam stability.

INTRODUCTION

The Spallation Neutron Source (SNS) extraction kicker system performs magnetic deflection of the proton beam during a gap in beam current to transfer beam to the target. Variations in the extraction kicker pulsed current timing, amplitude, and width can cause beam loss during extraction and transport to the mercury target [1]. The magnet field transitions from zero to full amplitude during the 250 ns gap. Turning on too early or too late will cause the head or tail of the beam to intercept the septum, likely resulting in beam loss and activation of the structures downstream [2].

Each extraction kicker is a pulsed modulator charged to 33 kV and fired 60 times a second. Each kicker can be controlled independently for trigger timing and high-voltage charge set point. The high-voltage switch in the extraction kicker system is a model C1925X thyratron from E2V Technologies. These thyratrons are stable upon initial installation but require daily monitoring to maintain low jitter and drift.

The original thyratron-based system required constant maintenance of the thyratrons after an initial period of stability. This involved adjusting a filament resistor shunt and verifying that the filament and reservoir heater supplies were in the correct ranges and were stable without movement [3]. Improvements have been made to the heater power supplies on each of the extraction kickers, which eliminated line sync and daily excursions related to AC power and improved jitter [3]. But the end-of-life mechanism of excessive turn-on jitter and drift continued to be an issue, with thyratron replacement occurring after an average of 11,794 hours of high-voltage operation. A solid-state thyristor-based high-voltage switch model from Silicon Power, the S56-12, was installed and tested in a test stand PFN [2]. The average yearly cost of thyratron replacements is $150,000. The chosen thyristor stack has no defined end of life or yearly cost for replacement, making thyristors an attractive solution.

EXTRACTION KICKER CONVERSION

Turn-On Time Reduction

The initial testing of the thyristor on a PFN tank into a dummy resistor load was positive with pulse jitter reduced, but turn-on and rise times were slower, leading to excessive time from triggering to full current flow that was resolved by raising the capacitance of the first 2 stages [2]. The magnet current rise time decreased to 150 ns, which is above the 91 ns seen on a thyratron. The gap in the beam for extraction is derived from the configuration of the proton beam pulse width to obtain 1.3 GeV. This results in a gap time of 251 ns. With a thyratron, there is allowed margin for jitter in the width of the gap as the tube ages. With a thyristor, the aging jitter factor does not occur and a 150 ns rise time that is extremely stable is sufficient to extract the beam without losses (Fig. 1). A saturable inductor was considered to shorten the risetime, but due to the previous discussion was deemed unnecessary.

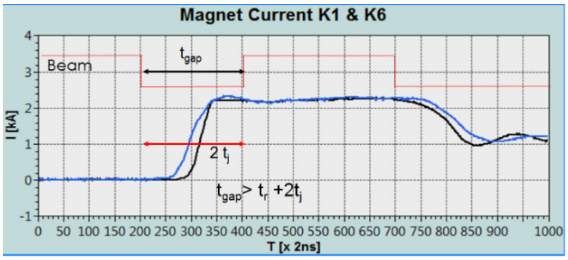

Figure 1: Gap time vs. rise time of thyratron (kicker 1) and thyristor (kicker 6).

Cooling Testing

An initial installation on an operational kicker in 2015 showed promise as well, but it failed at 108 days by destroying one of the stages. A detailed analysis was performed and thermal data were taken, looking at the rise

---

* This manuscript has been authored by UT-Battelle, LLC, under contract DE-AC05-00OR22725 with the US Department of Energy (DOE). The US government retains and the publisher, by accepting the article for publication, acknowledges that the US government retains a nonexclusive, paid-up, irrevocable, worldwide license to publish or reproduce the published form of this manuscript, or allow others to do so, for US government purposes. DOE will provide public access to these results of federally sponsored research in accordance with the DOE Public Access Plan (http://energy.gov/downloads/doe-public-access-plan).

[†] email: morrisb@ornl.gov

ISBN: 978-3-95450-223-3 ISSN: 2673-7000 doi:10.18429/JACoW-NAPAC2019-MOPLO04

PROGRESS IN TIME-RESOLVED MeV TRANSMISSION ELECTRON MICROSCOPY AT UCLA*

P. Denham†, N. Burger D. Cesar, D. Dang, P. Musumeci,
University of California Los Angeles, Los Angeles, CA, USA

Abstract

We present current progress on the implementation of two new enhancements developed for the time-resolved relativistic electron microscope at the UCLA PEGASUS Lab based on the use of a radiofrequency photoinjector as an ultrafast electron source and permanent magnet quadrupoles as electron lenses. The first enhancement is a flexible optical column design which would add the capability to switch between imaging the sample and its diffraction pattern, and a collimator to improve imaging contrast. The second enhancement is a high-frequency (X-band) cavity downstream from the (S-band) photoinjector to reduce the beam energy spread. These additions are crucial for improving contrast and image quality. Furthermore, a pulse-wire alignment method is used to fiducialize the quadrupole positions to (better than 20-um precision) to reduce the aberrations induced by misalignment and achieve spatial resolution at the 20 nm-level.

INTRODUCTION

Time-resolved electron microscopes capable of delivering single-shot real-space images with a spatial/temporal resolutions of 10 nm/10 ps are highly desired scientific tools in the material science community [1]. For example, in the study of defect/dislocation motion. In order to reach these levels of spatio-temporal resolutions, relativistic electron energies are required to suppress the space charge effects which would otherwise limit the performance of the instrument. A recently discussed concept for MeV electron microscopy [2] relies on high gradient quadrupole triplet lenses compatible with the higher energies and compact space, and radiofrequency technology to quickly accelerate, ballistically bunch, reduce the energy spread of, or streak the electron beam [3]. By utilizing RF-technology and advancements in pulsed laser systems, a variety of imaging modalities can be exploited as for example a double exposure electron column [4] intended for studying irreversible processes just before and right after they happen.

The Pegasus single-shot picosecond TEM (SPTEM) design [2] starts with a high-gradient RF gun operating in the cigar regime in order to optimize transverse beam brightness [3, 5]. A two solenoid condenser then transports and focuses the beam down onto the sample, after which permanent magnet quadrupole (PMQ) triplets [6] form the objective and projector/magnification lenses. In previous work [7, 8], we have demonstrated 40x magnification with the PMQ system [6] and demonstrated that they are a viable choice for an MeV microscope.

In this work we consider few improvements to the microscope design: firstly we discuss adding an intermediary lens to the optical column which can be used to image the back focal plane of the objective lens; secondly we consider using an RF cavity to reduce the bunch energy spread; lastly we discuss the pulse wire technique as a method to align each quadruple within the triplet.

FLEXIBLE OPTICAL COLUMN

A crucial requirement of a microscope is the ability to switch between imaging the diffraction pattern and the projected shadow of a sample. In particular, flexible optics with the ability to instantly transition between diffraction and real space imaging must be paired with a collimator to provide a contrast mechanism to distinguish between the unscattered and scattered electrons [7]. Here we show that inserting an electromagnetic (EM) quadrupole triplet in-between the objective and magnification lenses can provide the necessary flexibility. When the EM triplet is off, the sample is imaged onto the detector. When the EM triplet is turned on, the back focal plane (BFP) is imaged. Then a collimator on a actuator will be placed at one of the BFPs of the first triplet (the other BFP is actually inside the triplet). The purpose of this will become clear shortly. The optical layout is shown in Fig. 1.

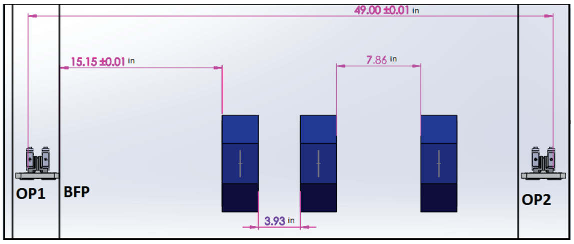

Figure 1: The two object planes of each PMQ triplet are labelled OP1 and OP2 respectively as solid lines. One of the BFPs of the objective lens is indicated as well. The positions are qualitatively placed for perspective. The blue quadrupole triplet is made from electromagnetic quadrupoles which are tuned to image the BFP at OP2.

The currents in the EM triplet are numerically optimized by using a thick lens matrix model of the entire optical setup. For our optimization, the dynamics for each transverse dimension is described by an algebraic system consisting of

---

* Work supported by the US National Science Foundation under grant DMR-1548924 and PHY-1734215

† Pdenham@physics.ucla.edu

ISBN: 978-3-95450-223-3 ISSN: 2673-7000 doi:10.18429/JACoW-NAPAC2019-MOPLO06

BLACK GUN TECHNOLOGIES FOR DC PHOTOINJECTORS*

E. Montgomery†, J. Butler, C. Jing, S. Poddar, Euclid BeamLabs LLC, Gaithersburg, MD, USA
S. Zhang, Jefferson Laboratory, Newport News, VA, USA

Abstract

Euclid Beamlabs is developing a new "Black Gun" concept in direct current (DC) photoinjectors. To reduce electron-stimulated desorption indirectly influenced by stray photoemission, we are testing advanced optical coatings and low-scattering optics compatible with the extreme high vacuum (XHV) environment of modern DC photoinjectors. Stray light in DC photoinjectors (in proportion to the photoemitted charge) causes off-nominal photoemission, initiating electron trajectories which intercept downstream surfaces. This causes electron-stimulated desorption of atoms, which ionize and may back-bombard the cathode, reducing its charge lifetime. Back-bombardment is key for high average current or high repetition rate. First, we report on progress developing optical skimmers based on Butler baffles to collimate both incoming and outgoing laser beams. Second, we describe candidate coatings for reduction of scattered light. Requirements for these coatings are that they be conducting, optically black at the drive laser wavelength, conformally applied to complex geometry, and XHV-compatible with negligible outgassing.

INTRODUCTION

The “Black Gun” DC photoinjector concept, first suggested by Matt Poelker at Jefferson Lab (JLab), is intended to reduce back-bombardment of sensitive photocathodes in DC electron guns. We follow a two-pronged attack to identify a feasible appproach: physical collimation of the laser beam, and blackening of internal surfaces.

Physical collimation is hampered by the need to place any collimators after the last scattering optical element (a Kodial glass viewport) - an extreme high vacuum (XHV) environment. Among all-metal XHV-compatible collimating apertures, the design which presents the minimal amount of forward scattering is the Butler baffle, a thin conical funnel with a knife-edge entrance [1]. These are not commercially available and we have re-developed the manufacturing expertise to produce and test them for Black Gun applications. A sharp knife edge minimizes forward scatter during skimming. In the forward direction, the beam is collimated and stray light eliminated. In the counter-propagating direction after cathode reflection, small angular spread in the beam glances through and exits.

Blackening of internal surfaces is a challenge in existing DC guns at JLab, in part because non-evaporable getter (NEG) coatings cover gun internal surface area [2]. These microns-thick coatings are optically gray. Therefore selective blackening is at the cost of some pumping speed, and must not increase total gas load significantly. In addition, charging is unacceptable, therefore the coating must be conducting. The coating must be applied conformally (chemical vapor deposition, or CVD, is one such technique). Finally, broad spectral absorption is not required but the reflectance at the drive laser wavelength (typically about 780 nm for spin-polarized GaAs) must be very low.

EXPERIMENTAL PROGRESS

Fabrication of Butler Baffles

Fabrication of a Butler baffle starts with a mandrel to be later electroformed. We have prepared stainless steel mandrels with two step lathe turning. First a conical point is cut into a 1” diameter rod. Next, using a radius cutter mounted to the lathe tool holder, the cone is turned concave, to achieve a tip diameter about 1 mm as the radius cutter is tangential to the turning axis.

Electroforming of copper and nickel has been completed on these mandrels, approximately 200 microns thick. The outer surface is polished, and then the electroformed layer is pressed off the mandrel. Once separated, the baffle can be more gently adhered to the mandrel and the tip abrasively removed from the baffle without damaging the mandrel using fine grit paper and then an ink eraser. Fabricated baffles are currently undergoing testing at Euclid. We intend report upon performance of these baffles as a function of metal (copper or nickel), aperture, and mechanical design in an upcoming publication. The prototypes are shown in Fig. 1.

Figure 1: Butler baffles on mandrels (L) and after polishing, blackening, and mounting for optical testing (R).

Black Coatings

Table 1 describes our comparison of commercially available black coating technologies for use in DC photoinjectors. One material met all criteria: Acktar^{TM} Vacuum Black® [3]. We have characterized Acktar^{TM} Spectral Black®, a related coating, using electron dispersive spectroscopy (EDS), confirming it is comprised of vacuum-safe materials, primarily aluminium and aluminium oxides.

---

* Work supported by the U.S. Department of Energy, Office of Science, Office of Nuclear Physics, SBIR grant no. DE-SC0019688. Use of the Center for Nanoscale Materials, an Office of Science user facility, was supported by the U.S. Department of Energy, Office of Science, Office of Basic Energy Sciences, under Contract No. DE-AC02-06CH11357.

† e.montgomery@euclidtechlabs.com

MEMS BASED MULTI-BEAM ION LINAC*

Q. Ji, M. Garske, G. Giesbercht, A. Persaud, P. Seidl, T. Schenkel†
Lawrence Berkeley National Laboratory, Berkeley, CA, USA
A. Lal, K. K. Afridi, D. Ni, S. Sinha, Cornell University, Itaca, NY, USA

Abstract

We report on the development of multi-beam RF linear ion accelerators that are formed from stacks of low cost wafers. Wafers are prepared using MEMS techniques. We have demonstrated acceleration of ions in a 3×3 beamlet array with ion currents in the 0.1 mA range and acceleration of 10 keV in a lattice of RF (13 MHz) acceleration units and electrostatic quadrupoles. We will describe the status and plans for scaling to 10×10 beams, ion currents >1 mA and ion energies >100 keV in a compact, low cost setup for applications in materials processing.

INTRODUCTION

Beams of energetic ions are widely used in manufacturing and for the development of nuclear materials where the energetic ions mimic damage induced by neutrons. Today, energetic ions are delivered to targets from accelerators in single beams with ion currents in the range of microampere to a few milliampere. The achievable ion current density is limited by space charge forces and the total ion current is limited by the size of the extraction aperture from which ions can be extracted to form a beam with low enough emittance for efficient transport in the beam line [1]. The concept of multi-beam ion accelerators was developed in the late 1970s by Maschke et al. with the concept of a Multiple Electrostatic Quadrupole Linear Accelerator (MEQALAC) [2]. MEQALACs are RF-driven linear accelerators where the total ion current can be scaled by adding more beams and the ion kinetic energy can be increased by adding accelerator modules. In the first implementations, MEQALACs used RF cavities to achieve ion acceleration with high voltages driven at frequencies in the 25 MHz range [3]. We have recently reported on the development of multi-beam RF accelerators that we assemble from stacks of low cost wafers [4, 5]. We form RF-acceleration structures and electrostatic quadrupole (ESQ) focusing elements on printed circuit board and silicon wafers with 10 cm diameter using standard microfabrication techniques [6]. In our prior work, we have extracted 0.1 mA Ar^+ ions through an array of 3×3 beamlets and demonstrated beam acceleration at an energy gain of 2.6 keV/gap [7]. In the article, we will describe the status and plans for scaling to 10×10 beams, ion currents >1 mA and ion energies >100 keV in a compact, low cost setup for applications in materials processing.

STATUS OF POWER SCALING

The approach we have taken to scale the ion current to 1 mA is to use more beamlets. With an aperture of 0.5 mm in diameter, we expect to extract 10 µA of Ar^+ from each aperture and reach a total current of 1 mA, a factor of ten increase compared to our prior experimental results. This uses our existing ion source, where we have not invested into pushing the current density. Ion sources with improved current densities can be adapted to our beamlet arrays in the future, further boosting the total ion current.

We have fabricated a new ion extraction column, that consists of total 120 beamlets, as shown in Fig. 1. The size of each extraction aperture is 0.5 mm in diameter, and the center-to-center distance is 3 mm. The region that covers all the 120 apertures is about 3.5 cm in diameter. This design is denser than the original 3×3 arrays (center to center distance was 5 mm). Further optimization of beamlet density might be possible and we will learn about this from the performance of our new arrays.

Figure 1: Extraction column with total of 120 beamlets (each of which is 0.5 mm in diameter, and 3 mm center-to-center spacing).

With the new extraction column, we were able to achieve a current of ~0.5 mA of Ar^+ ions, as shown in Fig. 2. We are still investigating the reason why the total current we measured is a factor of 2 lower than expected. One cause may be that the region of uniform plasma in our ion source is estimated to be about 2 cm in diameter, only covering about 33% of the total 120 beamlets. We are in the process of improving the ion source uniformity.

To realize higher current, we have started fabrication of RF (radio-frequency) and ESQ (electrostatic quadrupole) wafers with 120 beamlets. Compared with the 3×3 wafers developed previously, we decrease the center-to-center distance of adjacent unit cell from 5 mm to 3 mm.

---

[*] Work at LBNL was conducted under the auspices of the US DOE (DE-AC0205CH11231) and supported by ARPA-E. Device fab at the Cornell Nano Fab facility was supported by NSF (Grant 384 No.ECCS-1542081).

[†] corresponding author: t_schenkel@lbl.gov

ISBN: 978-3-95450-223-3 ISSN: 2673-7000 doi:10.18429/JACoW-NAPAC2019-MOPLO09

A PULSED, CURRENT REGULATED MAGNET POWER SUPPLY FOR SMALL MAGNETS*

G.D. Wyche[†], B.L. Beaudoin, L. Dovlatyan, D.F. Sutter,
Institute for Research in Electronics and Applied Physics
University of Maryland, College Park, MD, USA

Abstract

The University of Maryland Electron Ring (UMER) has two pulsed quadrupoles in the injection section that must be current regulated to the same precision as the other DC quadrupoles in the ring, as well as accurately synchronized to the ring operating cycle. To meet this need a practical pulsed current, regulated power supply has been designed and built using a commercial power operational amplifier for output, standard operational amplifiers for feedback control and monitoring, and matched resistor pairs to produce the desired transfer function of 10 Volts to 6 Amperes. For other applications the circuit can be modified to produce a range of transfer functions by varying the appropriate resistor pair ratios. Output pulse width and timing are generated by a standardized TTL pulse from the control system that gates the output of the amplifier. Installed safety circuitry detects the absence of a proper control pulse, an open circuit or shorted output, and measures and returns to the control system the operating amplitude of the current pulse. In this paper we present the design, implementation, and operational results of the prototyped pulsed current source.

INTRODUCTION

A detailed description of UMER can be found in reference [1]. It was built as an instrument to study the physics of charged particle beams with extreme space charge; that is, beams with incoherent tune shifts that are more than several integer values and coherent tune shifts of more than 0.5. The original motivation was research in support of the heavy ion fusion concept which would have operated in these space charge extremes. Because the UMER design goal was for a simple inexpensive machine with a beam kinetic energy of 10 keV, the magnets were designed using windings of precision, flexible mylar based printed circuits mounted in nonmagnetic aluminum alloy housings.

As the resulting magnetic fields are rather low, the lattice is densely packed with 72 quadrupoles and 36 dipoles in an 1152 cm circumference, or about 10.5 cm center-to-center spacing. Injection is a special problem as the beam pipe had to be enlarged from a 5 cm diameter to 8 cm over ~ 62 cm to facilitate the beam offsets at injection. This larger diameter meant the two injection quadrupoles are larger, requiring more current to match the gradients in the rest of the ring - ~4.5 A. The PC windings overheat at these currents and so are pulsed. Originally powered by discharging capacitor banks using IGBTs, the resulting current droop over the 10,000 turn storage, remedied with a recently installed RF cavity, is unacceptable. Thus, use of precision power operational amplifiers was indicated, and in the absence of affordable commercial units the design presented here was undertaken.

BASIC DESIGN REQUIREMENTS

Normally operated at 60 Hz, the most extreme case for quadrupole heating, the ring can operate as low as 10 Hz. At 10,000 turns and a 0.2 μsec revolution period, injection quadrupoles have to be driven for at least 2.0 msec. There is an additional need to let the eddy currents, induced in the stainless steel beam pipe during turn-on, to decay sufficiently before beam is injected into the machine adding an additional 250 μsec for a total of 2.25 msec on-time out of the 60 Hz period of 16.7 msec. While the injection quadrupoles normally operate from 4 to 5 A, an operating range of 3 to 6 A is assumed to allow for a range of settings that may be needed to match injection into ring optics. The requirement at the maximum heating case, set by the 13.5% duty cycle and pulsed current amplitude of 6 A, is that no runaway heating occurs in either the quadrupoles or the final stage power operational amplifier.

Two other major amplifier requirements are: (1) that the precision of the current signal be 2 mA out of 6000 mA and (2) the output of the amplifier be short circuit protected. The first is consistent with the required current regulation precision in the regular DC ring quadrupoles, which sets the resolution of the digital-to-analog conversion (DAC) at 12 bits or 1.5 mA per bit. This also includes read back confirmation of the desired operating current level by the control system, adding the necessity for a strobed analog-to-digital converter (ADC) of the same precision. The second requirement is standard in current regulated power supplies but has to be specifically accommodated in a custom design such as this one.

Control timing is via a single pulse generated by a computer controlled pulse generator in the ring central control system which signals the timing and duration in the operating cycle of the two quadrupoles. As noted above the maximum number of turns allowed is 10,000 but the ring can be set to operate at any number of turns less than this by shortening the control pulse.

In addition to the current foldback protection, there needs to be a number of internal monitoring and control functions including timing of the ADC sample pulse, missing control pulse detection, and detection of analog set current signal and analog output current mismatch.

---

* Work supported by U. S. Department of Energy grant number DESC00010301.
† glenndwyche@gmail.com

ISBN: 978-3-95450-223-3 ISSN: 2673-7000 doi:10.18429/JACoW-NAPAC2019-MOPLO12

THE RF BPM PICKUP ELECTRODES DEVELOPMENT FOR THE APS-MBA UPGRADE*

X. Sun†, R.M. Lill, Argonne National Laboratory, Argonne, IL, USA

Abstract

Beam stability is critical for the Advanced Photon Source (APS) multi-bend achromat (MBA) lattice upgrade and will employ 560 radio frequency (RF) beam position monitors (BPMs). The RF BPMs will provide the primary measurement of the electron beam. Design goals for the BPM assembly include high sensitivity, low wakefield impedance, and ultra-mechanically stability. The design, electromagnetic simulation, manufacturing tolerance and prototype testing will be presented in this paper.

INTRODUCTION

The APS Upgrade project (APS-U) has recently completed the final design milestone and now moves into the production phase. The upgrade will require 560 BPM assemblies to achieve the beam stability requirements outlined in Table 1. For the final design, both the horizontal and vertical AC rms beam stability requirements are based on 10% the rms beam size at the ID source points from 0.01 to 1000 Hz. In addition, long-term drift over a 7 day period may be no more than 1 µm.

Table 1: APS-U MBA Beam Stability Requirements

Plane	AC Motion, rms (0.01 – 1000 Hz)	Long-term Drift, rms (7 days)
Horizontal	1.25 µm 0.25 µrad	1.0 µm 0.6 µrad
Vertical	0.4 µm 0.17 µrad	1.0 µm 0.5 µrad

THE RF BPM PICKUP ELECTRODES DESIGN

There are 560 RF BPMs in APS-U storage ring with 14 BPMs per sector and 40 sectors. There are 3 types of BPM assemblies per sector – 10 standard-, 2 P0- and 2 keyhole BPM assemblies. The P0 BPMs are located upstream and downstream of the insertion device. The keyhole BPMs have anti-chamber slots to prevent beam interception.

The four pickup electrodes used in each standard and P0 BPM assembly are evenly distributed circumferentially around the 22 mm diameter circular MBA beam pipe, shown in Fig. 1, and provide the primary measurement of the electron beam trajectory in the storage ring. In keyhole shaped BPM assemblies, 4 buttons position with 60° spacing. Each RF BPM includes 4 orthogonal button electrodes that are integrated into a vacuum chamber and are terminated with SMA connectors.

The APS-U MBA pickup electrode design was developed using the existing APS BPMs as the baseline design. This design operated at the APS for over 20 years with an extremely low failure rate for the BPM buttons. The design uses an alumina vacuum seal and feature a removable female SMA mating pin [1].

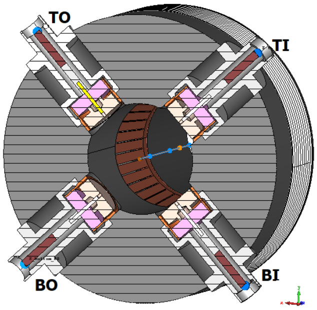

Figure 1: Standard APS-U MBA BPM assembly.

The design version 3 (v3) is shown in Fig. 2. The Alumina disk serves as dielectric, mechanical support, vacuum boundary and sets the mechanical concentric. The button material is Molybdenum which provides good thermal conductive. The Cu-Ni shell and Nickel center conductor rod are used to improve brazing procedure. The protruding fingers between the dielectric and the electrode can support/positioning the electrode as a hard stop [2] and improve the thermal conduction. The space between the dielectric and the electrode can supress the high frequency modes in the gap [3] and decrease the capacitance to increase the induced voltage on the button. The feedthrough with characteristic impedance of 50 Ω is designed to couple the beam signals out to the cable and electronics.

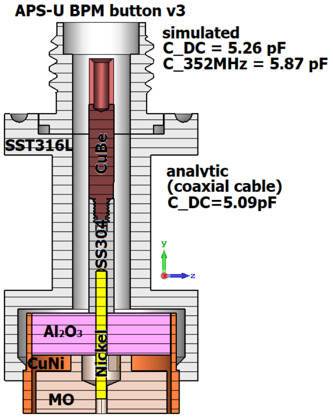

Figure 2: APS-U BPM button design v3.

The APS-U BPM button v3 was simulation studied using CST Microwave Studio (MWS) [4]. Its simulated capacitance is 5.26 pF at DC and 5.87 pF at 352 MHz. Its analytic capacitance according to the capacitance formula for coaxial cable is 5.09 pF.

---

* Work supported by the U. S. Department of Energy, Office of Science, Office of Basic Energy Sciences, under Contract No. DE-AC02-06CH11357.

† xiang@aps.anl.gov

ISBN: 978-3-95450-223-3 ISSN: 2673-7000 doi:10.18429/JACoW-NAPAC2019-MOPLO13

FIELD QUALITY ANALYSIS OF INTERACTION REGION QUADRUPOLES FOR JLEIC*

G. L. Sabbi†, Lawrence Berkeley National Laboratory, Berkeley, CA, USA
B.R. Gamage, T.J. Michalski, V.S. Morozov, R. Rajput-Ghoshal, M. Wiseman,
Jefferson Laboratory, Newport News, VA, USA
Y.M. Nosochkov, M.K. Sullivan, SLAC National Laboratory, Menlo Park, CA, USA

Abstract

The JLEIC physics goals of high luminosity and a full acceptance detector result in significant design challenges for the Interaction Region quadrupoles. Key requirements include large aperture, high field, compact transverse and longitudinal dimensions, and tight control of the field errors. In this paper, we present and discuss field quality estimates for the IR Quadrupoles of both electron and ion beamlines, obtained by integrating experience from previous projects with realistic designs consistent with the specific requirements of the JLEIC collider.

INTRODUCTION

The Jefferson Lab Electron-Ion Collider (JLEIC) is a proposed next-generation facility addressing the goals of the U.S. Nuclear Physics program: CM energy of 20 to 100 GeV (upgradable to 140 GeV); luminosity of 10^{33} to 10^{34} $cm^{-2}s^{-1}$ over the full energy range; beam polarization above 70%; and a full acceptance detector [1-4].

The JLEIC design [5-6] is based on two vertically-stacked collider rings with a circumference of 2.3 km and an innovative figure-8 layout which helps preserving spin polarization. Collision energies are in the range of 3 to 12 GeV for electrons and 30 to 200 GeV for protons. The electron beam energy is limited by synchrotron radiation, and the resulting asymmetry causes a significant fraction of the collision products to be nearly collinear with the ion beam direction. A 50 mrad crossing angle is used to separate these particles from the electron beam and provide transverse space for accelerator components [7].

Due to large beam size in the Interaction Region (IR) Quadrupoles, their field quality has dominant effect on the collider dynamic aperture (DA) and needs to be carefully evaluated [8-9]. The results of these studies will generate updated magnet requirements to be incorporated in future design iterations.

MAGNET REQUIREMENTS AND DESIGN

The JLEIC IR quadrupoles must incorporate a combination of challenging features to address both experimental and accelerator physics requirements:

- Large bore to accommodate the beam optics and provide the required acceptance;
- Compact size with excellent field quality in a broad operating range, and control of magnet fringe fields to minimize perturbations on the adjacent beam.

Table 1: Quadrupole Requirements: Magnetic Length; Bore, Good Field, Outer Radii; Gradient (Normal, Skew)

Magnet name	L_{mag} [m]	R_{bore} [cm]	R_{field} [cm]	R_{out} [cm]	G_{normal} [T/m]	G_{skew} [T/m]
eQDS1	0.6	4.5	1.7	8.0	-33.75	-4.89
eQDS2	0.6	4.5	2.8	8.5	36.22	5.25
eQDS3	0.6	4.5	2.4	10.0	-18.72	-2.71
eQUS1	0.6	4.5	2.0	10.0	-36.94	8.10
eQUS2	0.6	4.5	3.2	11.0	33.66	-7.38
eQUS3	0.6	4.5	1.5	11.0	-20.80	4.56
iQDS1a	2.25	9.2	4.0	23.1	-37.23	-1.23
iQDS1b	2.25	12.3	4.0	31.0	-37.23	-
iQDS2	4.50	17.7	4.0	44.4	25.96	-
iQUS1a	1.45	3.0	2.0	10.0	-97.88	-3.08
iQUS1b	1.45	3.0	2.0	10.0	-97-88	-
iQUS2	2.10	4.0	3.0	12.0	94.07	-

In addition, in order to reduce the magnet cost and development time, the coil peak fields are chosen to be within the operational limits of the well-established NbTi superconductor and associated magnet technologies.

The resulting parameters for the electron and ion final focusing quadrupoles are shown in Table 1. The naming convention starts with e/i for electron/ion, followed by Q for quadrupole, DS/US for downstream/upstream of the IP (based on the traveling direction of the corresponding beam), and a sequence number moving away from the IP.

The pole tip fields (product of G_{normal} and R_{bore}) are in the range of 0.7-1.7 T for the electron quadrupoles and 3.7-4.6 T for the ion quadrupoles. These values are compatible with NbTi technology, but the design is made challenging by large forces and stored energy, stringent field quality requirements, and space constraints limiting the optimization options.

With this in mind, we assume that all magnets will be based on keystone Rutherford cables and a cos2θ coil layout surrounded by a collar structure for mechanical support and pre-load. This well proven design approach provides excellent magnetic efficiency, stable operation to a high fraction of the conductor limit, tight geometric tolerances, control of large magnetic forces and reliable insulation against the internal voltages generated during a quench. Past experience with this approach in technical areas such as conductor design, field quality optimization, material properties and positioning tolerances was used as a basis for the field quality analysis.

---

* Work supported by the U.S. DoE under Contracts No. DE-AC05-06OR23177, DE-AC02-76SF00515, and DEAC03-76SF00098.

† GLSabbi@lbl.gov

ISBN: 978-3-95450-223-3 ISSN: 2673-7000 doi:10.18429/JACoW-NAPAC2019-MOPLO14

FROM START TO FINISH: USING 3D PRINTING TECHNIQUES TO BUILD CBETA*

G.J. Mahler[†], S.J. Brooks, S.M. Trabocchi,
Brookhaven National Laboratory, Upton, NY, 11973, USA

Abstract

Accelerator components and ancillary equipment can benefit from 3D printing technologies. Mechanical components that previously had been machined using conventional methods can now be 3D printed. This paper will discuss some of the successes using this technology and specifically will track from initial development of a particular set of Halbach magnets used on the Cornell Brookhaven Experimental Test Accelerator (CBETA) [1] project to the final design.

INTRODUCTION

Many industries are starting to embrace 3D printing technology mainly for economic reasons and this is also true within the accelerator community. One such facility, the Collider Accelerator Department at Brookhaven National Laboratory, is currently using five desktop variety 3D printing units. The unit makes and models are as follows:

- Makerbot Replicator 2X
- Ultimaker 2 Extended (2units)
- Ultimaker 3 Extended
- Ultimaker s5

We have printed parts from two types of plastic: ABS (Acrylonitrile Butadiene Styrene) and PLA (Polylactic Acid), converging to using PLA plastics exclusively. PLA is a bioplastic, meaning that it is derived from renewable plant products like corn and sugarcane. PLA is biodegradable, has less tendency to warp due to its low melting temperature, develops sharper corners / finer features, and is far less toxic when compared to ABS. One of the distinct advantages of ABS plastic is what can be perceived as overall strength, though it is the ductility of ABS that is responsible for this perception. PLA and ABS possess quite similar mechanical tensile strengths, but the ductility of each is quite different. ABS is more ductile than PLA so it tends to stretch more before breaking, which in turn gives the perception of PLA being a weaker plastic due to its brittle nature.

THE CBETA HALBACH MAGNET

Final CBETA Magnet Assembly

CBETA had a need for Halbach variety quadrupoles of the order in strength, depending on type, of 10 T/m and Halbach variety dipoles up to 0.3T [2]. One type of final Halbach dipole magnet assembly including the windowframe type iron corrector is shown in Fig. 1. Note that this is the final design that was installed in the CBETA lattice, but this paper also discusses the iterations that lead to this design and in specific the integration of 3D printed components.

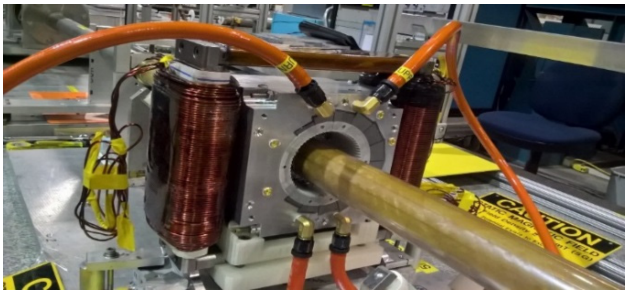

Figure 1: Final design CBETA Halbach magnet with iron core corrector.

Halbach Magnets

The Halbach magnet itself is essentially a series of permanent magnet volumes, each with a specifically defined magnetization direction, arranged in a circular array. A typical Halbach array is depicted in Fig. 2. The array has a spatially rotating pattern of magnetization direction, as shown by the red arrows, which cancels the field on one side but boosts field on the other. The major advantages of Halbach arrays are that they can produce strong magnetic fields on one side while generating very small stray field on the opposite side. In this case, the magnetic field inside the aperture is large and the magnetic field on the outer diameter is extremely small.

Figure 2: Typical Halbach array.

Early CBETA Halbach Magnet Designs

The permanent magnet material in the CBETA magnet array was specified to be Neodymium/Iron/Boron, which is one of the strongest rare earth magnet materials. The forces between two adjacent magnets in the array are large enough to require a supporting structure to both retain and position all magnets within the array. In early iterations of these Halbach magnet assemblies we used 3D plotted ABS frames as shown in Fig. 3. This allowed us to economically change both configuration and dimensional specifications due to tolerances associated with assembly, as the cost this

---

* Work supported by NYSERDA contract with BNL
[†] Mahler@bnl.gov

ISBN: 978-3-95450-223-3 ISSN: 2673-7000 doi:10.18429/JACoW-NAPAC2019-MOPLO15

ENGINEERING AND FABRICATION OF THE HIGH GRADIENT STRUCTURE FOR COMPACT ION THERAPY LINAC

O. Chimalpopoca, R.B. Agustsson, S.V. Kutsaev, A.Yu. Smirnov, A. Verma,
RadiaBeam Systems, Santa Monica, CA, USA
A. Barcikowski, R.L. Fischer, B. Mustapha, Argonne National Laboratory, Lemont, IL, USA

Abstract

RadiaBeam is fabricating a novel ultra-high gradient linear accelerator for the Advanced Compact Carbon Ion LINAC (ACCIL) project. The ACCIL is an Argonne National Laboratory (ANL) led project, in collaboration with RadiaBeam, designed to be capable of delivering sufficiently energized carbon ions and protons while maintaining a 50 m footprint. This is made possible by the development of S-Band 50 MV/m accelerating structures for particles with beta of 0.3 or higher. Such high gradient accelerating structures require particular care in their engineering details and fabrication process to limit the RF breakdown at the operating gradients. The details of fabrication and engineering design of the accelerating structure will be presented.

BACKGROUND

When it comes to cancer treatment, there are a wide variety of treatment options. Usable cancer treatment devices need to be able to successfully produce 200-250 MeV protons and/or 400-450 MeV/u carbon ions [1]. Currently, cyclotrons and synchrotrons are most commonly used to do this; however, their large footprint can make them very expensive to manufacture. Additionally, dose confinement of protons using these devices is less precise compared to carbon ion therapy [2]. ACCIL will be capable of producing 450 MeV/u $^{12}C^{6+}$ ions and 250 MeV protons while maintaining a small footprint. This is possible due to the development of an high gradient accelerating structure capable of providing 50 MV/m for particles with beta from 0.3 to 0.7 [3]. The novel structure will operate at the -1st harmonic and will produce 50 MV/m gradient at peak fields of <160 MV/m [4]. However, for the high gradient structure to successfully perform, particular care and attention to detail must be applied when producing and assembling the RF components of the structure.

ENGINEERING DESIGN

A 15 cell RF profile was designed, as shown in Fig. 1. A manufacturable accelerator structure was then designed around the vacuum profile with the intention of assembly through brazing. The final design consists of two coupler bodies, thirteen cells, and four cooling blocks as shown assembled in Fig. 2. Two cells are designed to bond to the couplers and one is a mirror cell used to ‘flip’ the mating features in the cell stack. The final mechanical design of the cells was driven by the RF and thermal designs, with acute consideration for the ease of assembly, handling, and tuning of the structure, along with generous vacuum pumping capabilities.

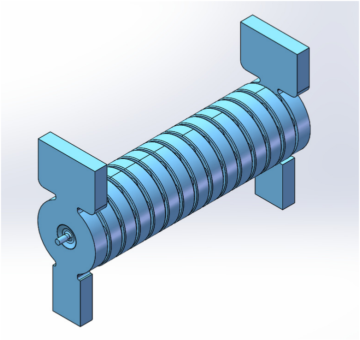

Figure 1: ACCIL high gradient structure RF profile.

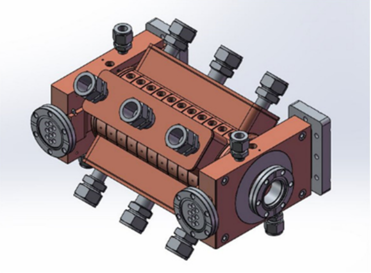

Figure 2: ACCIL high gradient structure assembly model.

The main cells have male and female mating features which are used to both align the cells with each other, and braze the cells together. The mirror cell has two male mating sides which are used in mating one of the main cells with the output coupling cell. Both of the coupling cells have female mating features used to either mate with the mirror cell or a main cell. Between cell and coupler mating features, a nominal gap of .0005” was preserved to both hold the RF profile to specification and allow braze alloy to flow. All but the mirror cells have tuning ports. These ports will house a custom tuning pin that will be used to manipulate the RF volume until the structure is tuned. Manipulation of RF volume is done through deformation of the thin wall that is at the base of the tuning pins. Finally, each main cell and coupler body was equipped with thermocouple holes. This feature is used to position a thermocouple during braze cycles to monitor the parts temperature without needing to contact the RF surfaces of the parts.

The couplers also had their profile designed after the RF profile that was developed, but a particular care was given to design the part such that certain tool ratios were followed. Namely, radii in the coupler bodies were selected such that the ratio between the diameter of the cutter used and the cut length did not exceed 1:3. This allows us to successful machine RF profiles that meet profile and finish

ISBN: 978-3-95450-223-3 ISSN: 2673-7000 doi:10.18429/JACoW-NAPAC2019-MOPLO17

LARGE-SCALE DEWAR TESTING OF FRIB PRODUCTION CAVITIES: RESULTS*

W. Hartung, W. Chang, S.H. Kim, D. Norton, J.T. Popielarski, K. Saito, J.F. Schwartz, T. Xu,
C. Zhang, Facility for Rare Isotope Beams, Michigan State University, East Lansing, MI, USA

Abstract

The superconducting driver linac for the Facility for Rare Isotope Beams requires 104 quarter-wave resonators (QWRs, 80.5 MHz) and 220 half-wave resonators (HWRs, 322 MHz). The resonators are Dewar tested before installation into cryomodules. All of the required QWRs have been fabricated and certified via Dewar tests; 95% of the HWRs have been certified (as of August 2019). The certification tests have provided valuable information on the performance of production QWRs and HWRs.

INTRODUCTION

The Facility for Rare Isotope Beams (FRIB) [1, 2], under construction at Michigan State University (MSU), requires a superconducting linac to accelerate ion beams to $\geq$ 200 MeV per nucleon. Quarter-wave resonators (QWRs) and half-wave resonators (HWRs) for the linac are produced by industrial suppliers; they are etched, rinsed, and tested at MSU before installation into cryomodules.

All of the required $\beta_m = 0.043$ QWRs, $\beta_m = 0.086$ QWRs, and $\beta_m = 0.29$ HWRs resonators have been certified (β_m = optimum normalized beam speed v/c); as of August 2019, 138 out of 148 of the $\beta_m = 0.54$ HWRs have been certified. After Dewar testing, certified cavities are assembled into a cryomodule [3]; the cryomodules are bunker tested [4] prior to tunnel installation. In-tunnel RF commissioning [5] and beam commissioning [6] of the QWR cryomodules is finished, and the cool-down of the first HWR cryomodules is in progress. QWR beam commissioning was done at 4.5 K, but 2 K operation is planned for both QWR and HWR cryomodules.

Methods and results of Dewar certification testing of FRIB production resonators have been presented previously [7, 8]. This paper will provide updated information about Dewar testing. Results for the $\beta_m = 0.54$ HWRs (the cavity type needed in largest quantity for the linac) will be presented as an example. Conditioning of multipacting and mitigation of field emission will be discussed. A statistical analysis of the FRIB Dewar test results can be found in a separate paper [9].

RESONATOR FABRICATION AND PREPARATION

Drawings of the FRIB resonators and RF parameters can be found in previous papers [7–9]. Resonators are made from high-purity sheet Nb via deep drawing and electron beam welding. Parts for a production $\beta_m = 0.54$ HWR are shown in Fig. 1. Jacketed resonators are delivered to FRIB. Dimensional checks, surface inspections, bulk etching (Buffered Chemical Polishing, BCP), hydrogen degassing, light etching (BCP), high-pressure water rinsing (HPWR), and cleanroom assembly are done at MSU [10].

CERTIFICATION TESTING

Resonators are tested in the FRIB SRF facility at MSU [11]. Testing is done with liquid helium in the jacket surrounded by insulating vacuum, which approximates the cryomodule environment. Continuous wave (CW) measurements are done at 4.3 K and about 2 K with a solid state RF amplifier (50 to 100 W). Conditioning of multipacting barriers is usually done in CW at 4.3 K. Results of 4.3 K measurements, 2 K measurements, and pump-down measurements for all 4 cavity types were presented previously [8]. Updated results for the $\beta_m = 0.54$ case (including 16 additional cavities) will be presented in this section.

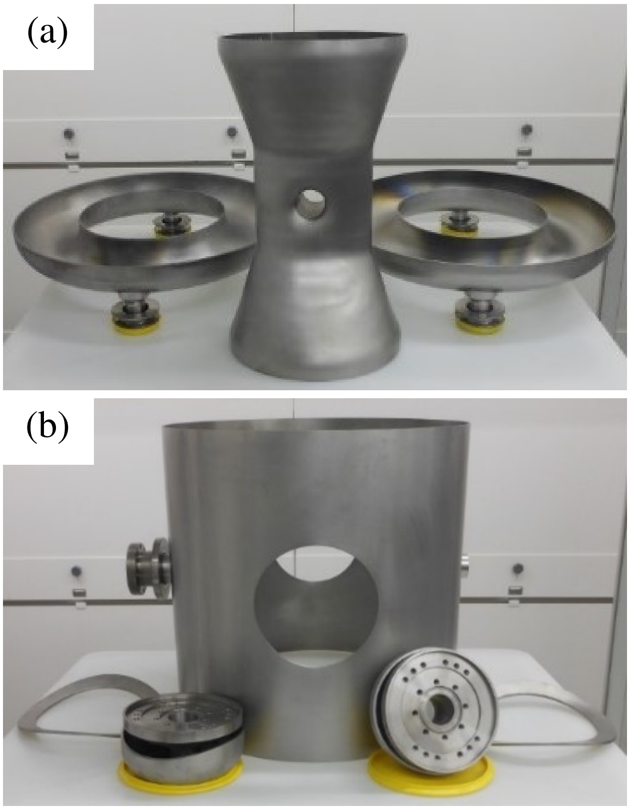

Figure 1: Partially-assembled $\beta_m = 0.54$ HWR: (a) inner conductor and short plates; (b) outer conductor and beam port cups.

---

* Work supported by the US Department of Energy Office of Science under Cooperative Agreement DE-SC0000661.

ISBN: 978-3-95450-223-3 ISSN: 2673-7000 doi:10.18429/JACoW-NAPAC2019-MOPLO18

THERMAL ANALYSIS OF THE LANSCE H+ RFQ TEST STAND FARADAY CUP*

E. N. Pulliam[#], I. N. Draganic, J. L. Medina, J. P. Montross, J. F. O'Hara, L. J. Rybarcyk
Los Alamos National Laboratory, Los Alamos, NM, USA

Abstract

The Los Alamos Neutron Science Center (LANSCE) operates one of the nation's most powerful linear accelerators (LINAC). Currently the facility utilizes two 750 keV Cockcroft-Walton (CW) based injectors for transporting H+ and H- beams into the 800 MeV accelerator. A Radio Frequency Quadrupole (RFQ) design is being proposed to replace the aged CW injectors. An important component of the RFQ Test Stand is the Faraday cup that is assembled at the end of the Low Energy Beam Transport (Phase 1 LEBT) and Medium Energy Beam Transport (Phase 3 MEBT). The Faraday cup functions simultaneously as both a beam diagnostic and as a beam stop for each of the three project phases. This paper describes various aspects of the design and analysis of the Faraday cup. The first analysis examined the press fit assembly of the graphite cone and the copper cup components. A finite element analysis (FEA) evaluated the thermal expansion properties of the copper component, and the resulting material stress from the assembly. Second, the beam deposition and heat transfer capability were analyzed for LEBT and MEBT beam power levels. Details of the calculations and analysis will be presented.

INTRODUCTION

LANSCE functions as a National User Facility with the LINAC supporting fundamental research and science for a wide variety of projects including isotope production, materials research, proton radiography, and more. The facility was originally opened in 1972 and used a state of the art Cockcroft-Walton based injector system to transfer H$^+$ and H$^-$ beams into the 800 MeV accelerator. These injector systems are difficult to maintain and operate, and currently an RFQ based design is being developed to replace them [1]. The RFQ design is intended to modernize the facility and reduce long term operational risks. An RFQ is a high current structure that simultaneously accelerates and focuses the charged particle beam. Integrating this system into the current LINAC has the potential to improve beam reliability and production. An RFQ Test Stand is being assembled at the LANSCE H$^+$ RFQ injector lab to test performance of the Kress-GmbH designed RFQ [2]. Figure 1 shows the current assembly of the Test Stand LEBT.

An important piece of the RFQ Test Stand is the Faraday cup that is located at the end of the Phase 1 LEBT and Phase 3 MEBT. The Faraday cup functions simultaneously as both a beam diagnostic and as a beam stop for each of the three phases [3]. Multiple analysis steps were required to validate that the design was appropriate for its intended use. This paper describes various aspects of the design, assembly, and analysis of the LANSCE RFQ Faraday cup.

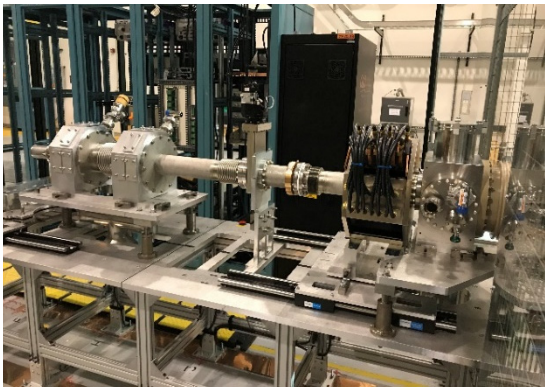
Figure 1: H$^+$ RFQ Test Stand LEBT assembly.

FARADAY CUP DESIGN

The unique Faraday cup design accomplishes multiple tasks for the RFQ Test Stand. The assembly acts as a beam stop for multiple phases of testing, a beam current measurement system, and serves as a mechanism for heat dissipation. Figure 2 shows the individual components, assembly, and internal section view of the Faraday cup.

Figure 2: H$^+$ RFQ Test Stand Faraday cup components.

The beam direction is perpendicular to the top face and is deposited into the graphite cone. The conical section of the graphite is designed so the beam has a large surface area to deposit into, and helps reduce secondary electrons. The graphite is captured inside the copper using a tight interference fit to improve heat transfer. Electrical connections are made to the copper flange allowing for beam current measurement. The copper cup is surrounded by the flanged stainless steel jacket which has an internal water channel that directly cools the outer copper surfaces. This stainless steel flange is then bolted to the end of the beamline. The assembly also uses a pair of MACOR® [4] ring insulators on either side of the copper cup flange in order to isolate

---

* Work supported by the United States Department of Energy, National Nuclear Security Agency, under contract DE-AC52-06NA25396
# eliasp@lanl.gov

ISBN: 978-3-95450-223-3 ISSN: 2673-7000 doi:10.18429/JACoW-NAPAC2019-MOPLO19

TEST RESULTS OF PIP2IT MEBT VACUUM PROTECTION SYSTEM

A.Z. Chen[†], R. Andrews, C.M. Baffes, D.D. Lambert, L.R. Prost, A.V. Shemyakin, T.J. Zuchnik,
Fermilab, Batavia, IL USA

Abstract

The central part of PIP-II program of upgrades proposed for Fermilab's injection complex is an 800 MeV, 2 mA, CW-compatible H$^-$ SRF Linear Accelerator. Acceleration in the superconducting cavities begins with an injected 2.1 MeV beam produced by a Warm Front End (WFE). The first cryomodule, a Half Wave Resonator (HWR), abuts this WFE. To minimize the amount of gas that may enter the SRF linac in a case of a vacuum failure occurring in the warm front end, a vacuum protection system is envisioned to be used in the PIP-II MEBT (which is a component of the WFE). It features a fast closing valve (FV) with two sensors and a differential pumping insert (DPI). A prototype of this system was installed in the PIP-II Injector Test (PIP2IT) accelerator and successfully tested in several modes modelling a variety of vacuum failures. The report presents the design of the vacuum protection system and results of its tests.

INTRODUCTION

The Injector Test of PIP2, (referred to as PIP2IT [1, 2]) is composed of an H- ion source, low energy beam transfer section, RFQ, medium energy beam transfer section (MEBT), a cryomodule of half wavelength resonator (HWR), a cryomodule of single spoke cavity resonator (SSR1), and high energy beam transfer section (HEBT) with beam dump. The HWR and SSR1 are cryomodules with superconducting RF cavities operating under 2K.

The performance quality of superconducting cavity critically relies upon the quality of a low particulate and ultra-high vacuum environment [3]. Since the beam line vacuum space is in common for all beam devices, a vacuum failure in a warm section poses a significant risk to the SRF cavities. In case of a serious vacuum failure, the large gas flux into a cryomodule not only destroys the superconducting status, but also moves any loose particles from an adjacent area into the superconducting cavity and ruins its performance. It is necessary to equip the warm section adjacent to cryomodules, such as MEBT, HEBT with measures to preclude the propagation of gas into the vacuum of the superconducting cavities at speeds of hundreds of meters per second.

THE DESIGN OF THE VACUUM PROTECTION SYSTEM

A typical way to achieve this isolation is to utilize a fast closing valve, such as the one by VAT. A VAT's 75 series fast closing valve is specified to close with 10 ms. At PIP2IT, in order to prevent large amount of gas (and particles will move with) flux into HWR (the 1st cryomodule of PIP2) during any possible vacuum failure in MEBT. The fast closing valve is placed about 1 m upstream of HWR. The 1st sensor will be placed at the beam absorber in Fig. 1 and the 2nd sensor at the bunch cavity near HWR. The absorber was chosen as the location of the first sensor because all chopped beam (rated for 20KW CW [4]) will be placed there and a large amount of gas is produced as well as the creation of particulate. The bunch cavity was chosen as the location for 2nd sensor because of some risk of leaking cooling water into vacuum.

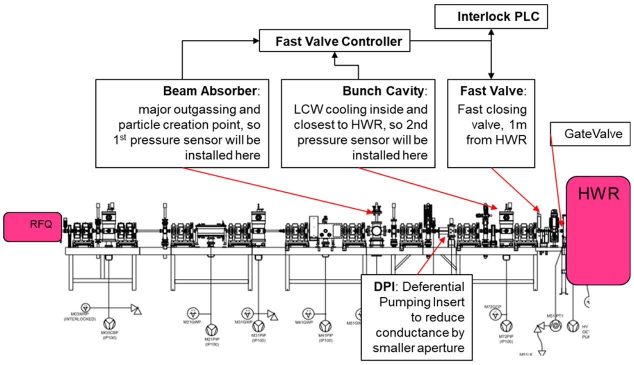

Figure 1: The configuration of vacuum protection system at MEBT.

A differential pumping insert (DPI) with a small aperture of 10mm in dia., 200mm long is placed downstream of the absorber to significantly reduce the gas flux from any possible vacuum failure in the upstream part of the Warm Front End. The DPI helps to achieve UHV in the region next to HWR.

The pressure rise detected from either sensor will trigger the fast closing valve and close it within 10ms. However, gas propagation in vacuum is very fast, closing the valve within 10ms will not be fast enough to completely prevent gas flux passing the valve before the valve is closed; especially if a failure occurs near the valve. The test for measuring this amount of gas passed by the valve before full closure was carried out to qualify the design. That is: can this design provide meaningful protection of the HWR? It should be noted that the closing time of the valve was not measured.

FIRST TEST SETUP AND RESULTS

Along with the progress of PIP2IT, the 1st measurement was carried out in less ideal configuration in Fig. 2. The 1st sensor was installed on the beam scraper near the prototype absorber, and the 2nd was on the beam scraper near a bunch cavity. The DPI was placed in between. In this setup, the vacuum space at upstream of the fast valve is 36.5 litres, and 95.1 liters at the downstream. The large volume at the

---

* This manuscript has been authored by Fermi Research Alliance, LLC under Contract No. DE-AC02-07CH11359 with the U.S. Department of Energy, Office of Science, Office of High Energy Physics.

†alexchen@fnal.gov

ISBN: 978-3-95450-223-3 ISSN: 2673-7000 doi:10.18429/JACoW-NAPAC2019-MOPLO20

QUENCH PERFORMANCE AND FIELD QUALITY OF THE 15 T Nb_3Sn DIPOLE DEMONSTRATOR MDPCT1 IN THE FIRST TEST RUN*

A.V. Zlobin†, E.Z. Barzi, J.R. Carmichael, G. Chlachidze, J. DiMarco, V.V. Kashikhin, S. Krave,
I. Novitski, C.R. Orozco, S. Stoynev, T. Strauss, M.A. Tartaglia, D. Turrioni,
Fermilab, Batavia, IL, USA

Abstract

Fermilab has developed and fabricated a 15 T Nb_3Sn dipole demonstrator for a post-LHC hadron collider. In June 2019, the magnet was tested and reached a world record field of 14.1 T at 4.5 K. The 15 T dipole demonstrator design and the first results of magnet cold tests including quench performance and field quality are presented and discussed.

INTRODUCTION

Fermilab in the framework of the U.S. Magnet Development Program (US-MDP) [1] has designed and fabricated a 15 T Nb_3Sn dipole demonstrator for a post-LHC hadron collider (HC). The main objectives of this work are demonstration of the field level, suitable for a future HC, and study of the high-field magnet performance, including quench performance, operation margins, field quality, and quench protection.

The 15 T dipole demonstrator, called also MDPCT1, is using optimized "cos-theta" coils and a cold iron yoke [2, 3]. An innovative mechanical structure based on strong aluminum I-clamps and a thick stainless-steel skin was developed to preload brittle Nb_3Sn coils and support large Lorentz forces. The maximum field for this design is limited by 15 T due to mechanical considerations. The first magnet assembly was done with lower coil pre-load to achieve 14 T and minimize the risk of coil damage during assembly.

This paper presents the MDPCT1 design and its parameters and reports the results of magnet training and magnetic measurements in the first test run.

MAGNET DESIGN AND PARAMETERS

The design concept of the 15 T Nb_3Sn dipole demonstrator and the details of magnet fabrication are presented in [2, 3]. The magnet design consists of a 60-mm aperture 4-layer shell-type coil, graded between the inner and outer layers, a cold iron yoke, a thick stainless steel shell, and a coil axial support structure.

The cable in the two innermost coil layers has 28 strands 1.0 mm in diameter, whereas the cable in the two outermost layers has 40 strands 0.7 mm in diameter. Both cables were fabricated at Fermilab using RRP Nb_3Sn composite wires produced by Bruker-OST. The 0.7 mm RRP-108/127 wire and the 1.0 mm RRP-150/169 wire have 41 and 52 μm sub-elements respectively to reduce the persistent current effect and improve cable stability with respect to flux jumps. The 0.025-mm thick and 11-mm wide stainless steel core is used in both cables to suppress the inter-strand eddy currents induced by the varying magnetic field in coils. The cables were insulated with two layers of 0.075-mm thick and 12.7-mm wide E-glass tape.

After winding, heat treatment at high temperatures in Argon to create superconducting Nb_3Sn phase, and impregnation with epoxy resin, the magnet coils were wrapped with four layers of 0.125-mm thick Kapton film and two 316L stainless steel sheets, each 2-mm thick, and placed inside the vertically-split iron yoke. The yoke is made of 1020 iron laminations with 587-mm outer diameter, connected by strong 7075-T6 aluminum I-clamps, and surrounded by a 12.5-mm thick 316 stainless-steel skin. The coils were supported axially by two 50-mm thick end plates made of 304L stainless steel connected by 8 stainless steel rods 30 mm in diameter.

The coil pre-stress at room temperature is provided by the mid-plane and coil-yoke shims, the yoke-clamp interference, and the yoke-skin shims. During and after magnet cooling-down, pre-stress is controlled by the size of the vertical gap between the yoke blocks. The transverse mechanical rigidity of the structure is provided by the rigidity of the iron laminations, aluminum clamps and skin.

Figure 1 shows the view of MDPCT1 from the magnet non-lead end.

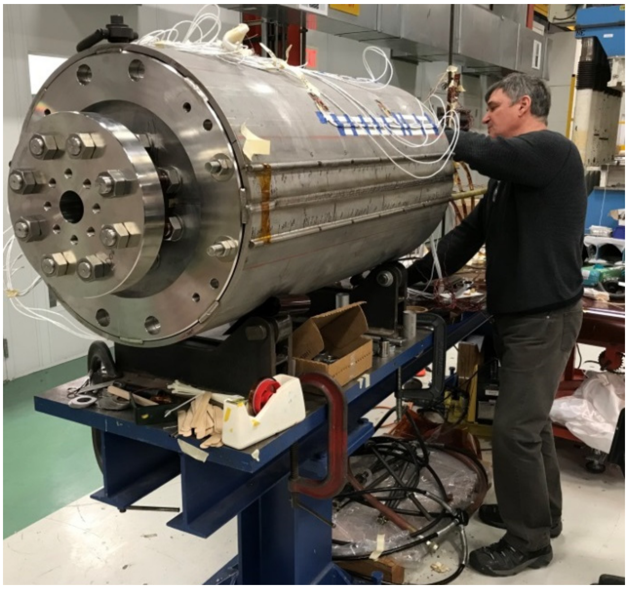

Figure 1: 15 T dipole demonstrator MDPCT1.

---

* This work supported by Fermi Research Alliance, LLC, under contract No. DE-AC02-07CH11359 with the U.S. DOE and the U.S. Magnet Development Program (MDP).

† zlobin@fnal.gov

ISBN: 978-3-95450-223-3 ISSN: 2673-7000 doi:10.18429/JACoW-NAPAC2019-MOPLO23

INVESTIGATION OF VARIOUS FABRICATION METHODS TO PRODUCE A 180GHz CORRUGATED WAVEGUIDE STRUCTURE IN 2MM DIAMETER 0.5m LONG COPPER TUBE FOR THE COMPACT WAKEFIELD ACCELERATOR FOR FEL FACILITY

K. Suthar*, D.S. Doran, W. Jansma, A. Siy[1], S. Sorsher, E. Trakhtenberg,
G. J. Waldschmidt, and A. Zholents, Argonne National Laboratory, Lemont, IL, USA
[1]also at University of Wisconsin, Milwaukee, WI, USA

Abstract

Argonne National Laboratory is developing a 180 GHz wakefield structure that will house in a co-linear array of accelerators to produce free-electron laser-based X-rays. The proposed corrugated waveguide structure will be fabricated on the internal wall of 0.5m long and 2mm nominal diameter copper tube. The estimated dimensions of these parallel corrugations are 200 μm in pitch with 100 μm side length (height and width). The length scale of the structure and requirements of the magnetic field-driven dimensional tolerances have made the structure challenging to produce. We have employed several method such as optical lithography, electroforming, electron discharge machining, laser ablation, and stamping to produce the initial structure from a sheet form. The successive fabrication steps, such as bending, brazing, and welding, were performed to achieve the long tubular-structure. This paper discusses various fabrication techniques, characterization, and associated technical challenges in detail.

BACKGROUND

Free-electron laser (FEL) sources have a tremendous potential to advance scientific research in the fields of material science, medical applications, biophysical, surface science, and the broad range of condensed matter physics [1]. The lasing medium of an FEL consists of moving electrons passing through a radiation generating sources such as magnetic undulator [2, 3] or a compact accelerator such as Čerenkov wakefield [4] at nearly the speed of light. The current FELs are large, expensive, and complex systems that are not practical for the industrial or the consumers' use at this time. There is an immediate need for FEL facilities with compact, tunable, and multi-user accelerator. Reduction in size of the accelerator is a key for making affordable FEL facilities for material characterization, industrial or medical purposes. Argonne National Laboratory (ANL) is leading an effort to develop a compact, broadly tunable, high repetition rate, multi-user, and yet cost-effective accelerator for the X-ray FEL source [4, 5] based on the Čerenkov wake-field. A conceptual diagram for a high repetition rate multi-user FEL facility based on a CWA concept that is currently under development is shown in figure 1 in the reference [4]. The electrical design and particular challenges are discussed elsewhere [5]. In this paper, we are going to discuss the challenges in the fabrication of CWA structure.

Compact Collinear Wakefield Accelerator

To produce Čerenkov radiation at 180 GHz, it requires corrugated copper waveguide with dimensions in micrometric regime that can sustain ~100 MV/m accelerating field for the ~ 0.3 nC electron charge witness-bunch. The accelerating field is created by ~ 10 nC charge drive-bunch that was passed at center of the structure near the speed of light. The image in figure 2 in the reference [6] illustrates the Čerenkov wakefield concept.

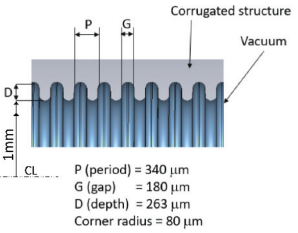

Figure 1: Schematic of corrugation inside of the copper tube.

The Schematic of the corrugation is shown in Figure 1 that is designed to produce 180 GHz wakefield Čerenkov radiation. The corrugation is created on the inside wall of the cylindrical copper (Cu) pipe with a 2 mm internal diameter. The electron bunch repetition rate is 10 - 50 kHz that is limited by the heat deposition on the interior wall due to the interaction of the electromagnetic field with the surrounding material. Strong quadrupole magnets with a 3 mm aperture control the electron beam trajectories. The field polarity of the quadrupoles is repeating at every 25-40 cm. Alignment tolerances for the quadrupoles are about 1 μm over 500mm, and the straightness requirement for the corrugated structure is 10 μmm.

Corrugated Waveguide

The structure of corrugation is being fabricated on the inner wall of a 2mm-inner-diameter copper tube with ridges facing inward. The corrugation has a period of 340 μm, the gap 180 μm, depth 263 μm, and the corner radius of 80 μm. All dimension are designed and optimized using finite element analysis and reported herein [5]. It is challenging to fabrication these 1472 repetitive corrugation structures

---

* suthar@anl.gov

ISBN: 978-3-95450-223-3 ISSN: 2673-7000 doi:10.18429/JACoW-NAPAC2019-MOPL024

A NOVEL TECHNIQUE FOR PULSED OPERATION OF MAGNETRONS WITHOUT MODULATION OF CATHODE VOLTAGE*

G.M. Kazakevich†, R.P. Johnson, Muons, Inc, Batavia, IL USA
T.N. Khabiboulline, V.A. Lebedev, G.V. Romanov, V.P. Yakovlev, Fermilab, Batavia, IL USA

Abstract

Modern pulsed superconducting accelerators of megawatt beams require efficient RF sources controllable in phase and power. It is desirable to have an individual RF power source with power up to hundreds of kW in the millisecond range for each Superconducting RF (SRF) cavity. The efficiency of the traditional RF sources (klystrons, IOTs, solid-state amplifiers) in comparison to magnetrons is lower and the cost of a unit of RF power is higher. The magnetron-based RF sources would significantly reduce the capital and operation costs in comparison with the traditional RF sources. A recently developed kinetic model describing the principle of magnetron operation and subsequent experiments resulted in an innovative technique producing the pulsed "stimulated" generation of magnetrons powered below the self-excitation threshold voltage. This technique does not require pulse modulators to form RF pulses. The magnetron operation in this regime is stable, controllable in phase and power, and provides higher efficiency than other types of RF power sources. It allows operation in pulsed modes with large duty factor. The developed technique and its experimental verification are discussed here.

INTRODUCTION

Magnetrons are presently used in normal conducting compact accelerators as efficient and inexpensive RF self-exciting generators. For superconducting accelerators, the magnetron generators must provide phase and power control with the rates necessary to stabilize the accelerating voltage in SRF cavities [1]. The use of a phase-modulated injected signal to control the phase of the magnetron was first described in [2]. Methods for control of the magnetron phase and power, with the required rates, by injecting resonant (injection-locking) RF signals have been developed recently [3-5]. These methods would provide stabilization of accelerating voltage in a cavity in both phase and amplitude. The phase control is provided via controlling the resonant injected phase-modulated RF signal. The amplitude control is performed via the phase control using vector methods [3, 4] or via the magnetron current control [5]. The last method provides higher transmitter efficiency over a range of power control of ≈10 dB with a bandwidth (presently feasible) about of 10 kHz.

For evaluation of properties of the RF-driven magnetrons and substantiation of the innovative technique, an analytical kinetic model [6] has been developed. The model considers the basic principle of magnetron generation - the resonant interaction of the flow of the phase-grouped Larmor electrons with a synchronous wave. This interaction results in an energy exchange between the wave and the electrons. The developed model enables evaluation of the necessary and sufficient conditions for the coherent generation of the magnetron and predicts and substantiates pulsed coherent generation of the tube driven by a pulsed injected resonant signal and powered without a pulsed modulation of the cathode voltage if it is below the self-excitation threshold.

As follows from the kinetic model, RF generation below the self-excitation threshold enables the maximizing of the efficiency of the magnetrons in a wide range of power control, a reduction of the magnetron noise by the injected signal and looks to be a promising way to extend the magnetron lifetime. A brief description of the advantages of "stimulated" pulsed coherent generation of magnetrons for modern superconducting accelerators with megawatt beams is discussed.

SETUP TO TEST THE STIMULATED GENERATION OF MAGNETRONS

The proof of the principle of this technique was demonstrated with a CW, 2.45 GHz microwave oven magnetron type 2M219G with nominal output power of 945 W and a measured magnetron self-excitation threshold voltage of 3.69 kV. The magnetron was powered by a pulsed High Voltage (HV) source using a partial discharge of the storage capacitor [7], providing a pulse duration of ≈5 ms. The HV source provided negligibly small ripple thus avoiding magnetron start-up caused by the ripple. The pulsed HV source was powered by a charging Glassman 10 kV, 100 mA switching power supply with voltage control.

Pulsed "stimulated" generation of the magnetron was realized by the injection of a pulsed locking signal into the magnetron RF system. This has been studied with the setup shown in Fig. 1. The CW signal of an HP-8341A generator was converted to RF pulses by a mixer (ZEM-4300MH from Mini-Circuits) controlled by a pulsed generator (type 100A). Then the RF pulses were amplified by solid-state and TWT amplifiers which provided a pulsed RF signal with power up to 160 W to drive the magnetron. Pulse shapes and power levels of the injected signal and the magnetron output signal were measured by the RF detectors with Schottky zero-bias diodes calibrated to better than ±0.5%. The magnetron pulse current was measured by a current transducer (type LA 55-P) with a circuit integration time of about 50 μs.

---

* Supported by scientific collaboration of Muons, Inc and Fermilab, Fermi Research Alliance, LLC under CRADA-FRA-2017-0026.

†gkazakevitch@yahoo.com; grigory@muonsinc.com

ISBN: 978-3-95450-223-3 ISSN: 2673-7000 doi:10.18429/JACoW-NAPAC2019-TUXBA3

ROBUST THERMOACOUSTIC RANGE VERIFICATION FOR PULSED ION BEAM THERAPY

S. K. Patch†, UW-Milwaukee, Milwaukee, WI USA
B. Mustapha, D. Santiago-Gonzalez, Argonne National Laboratory, Lemont, IL USA

Abstract

Particle therapy is a high-risk option compared to conventional x-ray radiation because dose is concentrated near the Bragg peak. Patient misalignment can cause greater damage to healthy tissue and failure to completely treat the tumour. Therefore, relatively few tumour sites are deemed appropriate for particle therapy.

Thermoacoustic range verification is enabled by intense pulsed beam delivery and might enable treatment of soft tissue tumors, but range estimates are shifted by soundspeed variations within the patient.

Soundspeed errors dilate and acoustic heterogeneities deform ultrasound images. When thermoacoustic receivers are co-located with the ultrasound imaging array, the same transformations shift thermoacoustic range estimates. Therefore, thermoacoustic range verification is robust relative to ultrasound images of underlying anatomy and could be directly used when the treatment target is visible in ultrasound.

INTRODUCTION

Range verification is currently the weak link in ion therapy. Range verification techniques such as prompt gamma, positron emission tomography, and cone beam computerized tomography (CBCT) lack direct correlation to live images of underlying anatomy. CBCT exposes organs at risk (OARs) to ionizing radiation and the primary benefit of ion therapy is to spare OARs.

Thermoacoustics could provide online range verification with direct correlation to underlying morphology as depicted in ultrasound images (Fig. 1), and without exposing OARs to ionizing radiation. However, thermoacoustic range estimates in absolute (room) coordinates are skewed by acoustic heterogeneities, and even by assuming an incorrect soundspeed in a homogeneous target. Incorrect soundspeed settings and acoustic heterogeneities dilate and deform ultrasound images respectively. We demonstrate that thermoacoustic estimates of the Bragg peak location (Fig. 1(b)) are subject to the same transformations as ultrasound images when thermoacoustic receivers are co-located with ultrasound imaging arrays.

Thermoacoustic signals were detected in national laboratories [1, 2] and proposed for range verification during particle therapy [3, 4] decades ago. Synchrocyclotrons deliver stress-confined pulses that may enable thermoacoustic range verification [5], as will linacs designed for therapy [6]. A resurgence in thermoacoustic research, generating too many papers to cite is described in recent reviews [7, 8]. A brief overview of results that correlate range estimates with ultrasound follows.

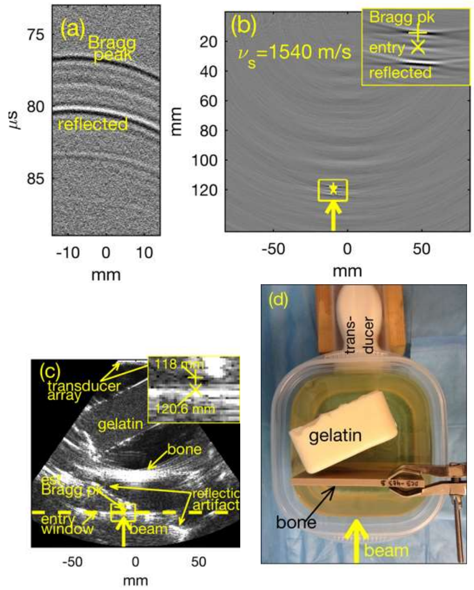

Fig. 1. Thermoacoustic range verification despite acoustic heterogeneity. Thermoacoustic emissions from a single 4He pulse (a) and thermoacoustic image (b) from which Bragg peak location, range, and beam entry point are estimated. (c) Ultrasound image of acoustic scatterers in an oil target with thermoacoustic estimates overlaid. Bragg peak and ion entry locations are overlaid as yellow '+' and 'x'. Estimated beam entry window plotted in dashed yellow. (d) Aerial photo depicting the experimental setup.

A linear array was used to generate ultrasound images that were co-registered to images reconstructed from thermoacoustic emissions measured by a curved array, requiring digital co-registration [9]. To our knowledge, our previous work [10] is the only one that provides inherent co-registration of thermoacoustic range estimates with ultrasound images of underlying anatomy, by using the same ultrasound array to detect thermoacoustic emissions and generate ultrasound images. Thermoacoustic emissions in this report were tailored to the ultrasound array's frequency band, reducing the required dose by three orders of magnitude. 2.3 Gy produced thermoacoustic emissions in Fig. 1(a) from which accurate range estimates were generated. Additionally, in this work we estimate Bragg peak locations from thermoacoustic emissions that traveled through a strongly scattering bone sample (Fig. 1(c)). Finally, we demonstrate robustness and accuracy of thermoacoustic range estimates relative to ultrasound images with fields of view exceeding 60 mm, despite acoustic heterogeneity and incorrect soundspeed settings on the scanner.

ISBN: 978-3-95450-223-3 ISSN: 2673-7000 doi:10.18429/JACoW-NAPAC2019-TUXBA4

RAPID RADIO-FREQUENCY BEAM ENERGY MODULATOR FOR PROTON THERAPY*

X. Lu[†], G.B. Bowden, V.A. Dolgashev, Z. Li, E.A. Nanni, A.V. Sy, S.G. Tantawi
SLAC National Accelerator Laboratory, Menlo Park, CA 94025, USA

Abstract

We present the design for a rapid proton energy modulator with radio-frequency (RF) accelerator cavities. The energy modulator is designed as a multi-cell one-meter long accelerator working at 2.856 GHz. We envision that each individual accelerator cavity is powered by a 400 kW low-voltage klystron to provide an accelerating / decelerating gradient of 30 MV/m. We have performed beam dynamics simulations showing that the modulator can provide ± 30 MeV of beam energy change, with an energy spread of 3 MeV for a 7 mm long (full length) proton bunch. A prototype experiment of a single cell is in preparation at the Next Linear Collider Test Accelerator (NLCTA) at SLAC. The energy modulator is optimized for 150 MeV cyclotron proton beam, while this approach can work with different energies.

INTRODUCTION

Proton therapy has the advantage of a narrow range of proton energy deposition over other types of radiotherapy methods. The radiation dose of a proton beam can be precisely deposited at the tumor location, so healthy organs nearby can receive much less dosage. To deliver the radiation dose to varied depths in human bodies, a beam energy modulation system is needed. In current proton therapy machines, beam energy modulation is performed by a mechanical energy degrader; as a result, the modulation process is slow, reduces beam current and degrades emittance. Use of the mechanical degrader limits the capabilities of the proton source and beam delivery system and increases the treatment time so that the treatment results are more susceptible to organ motion [1]. Here we present a new approach for rapid energy modulation and scanning by radiofrequency (RF) cavities.

A schematic of the rapid proton beam delivery system using RF cavities is shown in Fig. 1. The proton beam is generated by a source such as a cyclotron, and then gets transported to the gantry comprised of permanent or superconducting magnets to bend the beam. The gantry is designed to have an energy acceptance of ±3 MeV, but the actual energy spread of the initial proton beam is an order of magnitude smaller. After the gantry, the beam enters the RF energy modulator to change the beam energy, and the RF deflector to scan the beam transversely. The goal of such a system is to deliver a proton beam which covers a scanning area of 25 cm × 25 cm with a depth variation of 12 cm within 1 second for a dose of 50 Gy/L/s.

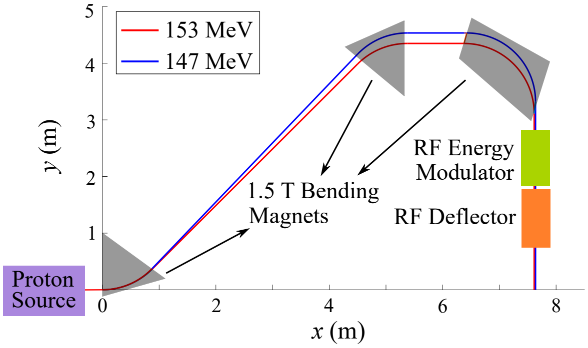

Figure 1: Schematic of the rapid proton beam delivery system, including a proton source, a gantry with three 1.5 T permanent magnets to transport the beam, an RF energy modulator and an RF beam deflector. The beam trajectories are shown for 153 MeV and 147 MeV.

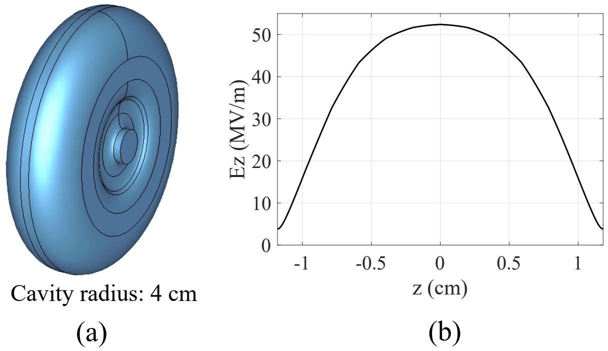

Cavity radius: 4 cm

(a)

(b)

Figure 2: Single cavity of the energy modulator. (a) Vacuum space of a single cell. (b) Longitudinal electric field E_z on axis with 160° phase advance per cell. The field amplitude is normalized for an accelerating gradient of 30 MV/m for a 150 MeV proton beam.

This paper is focused on the design and fabrication of the proton beam energy modulator at 2.856 GHz. The design is optimized for a 150 MeV beam from a cyclotron provided by the Varian Medical Systems, Inc, but the general approach can be adapted to other proton beam sources.

ENERGY MODULATOR DESIGN

Cavity RF Design

The energy modulator is built from multiple accelerator cavities at 2.856 GHz. The geometry of a single cavity (vacuum space) is shown in Fig. 2 (a). The geometry is optimized to achieve a high shunt impedance while keeping

---

* Work supported by US Department of Energy (DOE) Contract No. DE-AC02-76SF00515.

[†] xylu@slac.stanford.edu

ISBN: 978-3-95450-223-3 ISSN: 2673-7000 doi:10.18429/JACoW-NAPAC2019-TUYBA3

BENCHMARKING THE LCLS-II PHOTOINJECTOR

N. Neveu*, T. Maxwell, C. E. Mayes, SLAC, Menlo Park, CA, USA

Abstract

Commissioning of the LCLS-II photoinjector started in late 2018. Efforts to accurately model the gun and laser profiles are ongoing. Simulations of the photoinjector and solenoid are performed using IMPACT-T, OPAL-T, and ASTRA. This work includes efforts to use the laser profile at the virtual cathode as the initial transverse beam distribution, and effects of 2D and 3D field maps. Beam size results are compared to experimental measurements taken at the YAG screen located after the gun.

EARLY INJECTOR COMMISSIONING

Construction of a high repetition rate superconducting (SC) Free Electron Laser (FEL) at SLAC has begun. This beam line will deliver X-ray energies up to 25 keV at a rate of 1 MHz. Once completed, the normal conducting Linac (original LCLS), and the SC Linac will operate simultaneously and provide X-rays to multiple users.

The LCLS-II Early Injector Commissioning (EIC) area consists of a 187 MHz quarter cell gun cavity followed by solenoids, a 1.3 GHz two cell buncher, a YAG screen, correctors, BPMs, and current monitors; see Fig. 1 for detailed layout. This gun is based on the APEX gun work done at LBNL [1]. Some commissioning goals include dark current characterization, production of electron beams with a CsTe cathode, beam based alignments, radiation safety surveys, and continued testing of beam measurement GUIs.

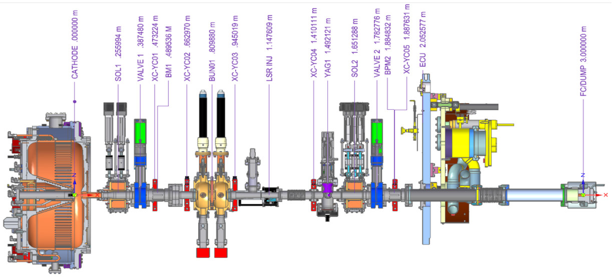

Figure 1: EIC layout, which includes the gun, buncher solenoids and diagnostics.

All simulations and measurements hereafter were preformed with the EIC area as the model. While the buncher has been successfully operated, recent runs have kept the buncher turned off. Therefore the buncher is also off in the following simulations.

SIMULATIONS

Table 1: Simulation Inputs for Code Comparison

Parameter	Value
Charge	20 pC
Laser radius	0.5 mm
Laser FWHM	20 ps
Gun phase	Max energy gain
Field on the cathode	20 MV/m
Buncher	Off
Solenoid Strength	0.06 T

Several particle-in-cell codes are freely available and able to simulate the physics present in photoinjectors. While they do not share exactly the same features, typical beam dynamics of interest are included. In this fashion, LCLS-II beam lines are simulated in a variety of codes. For the injector, IMPACT-T [2], ASTRA [3], and OPAL [4] are used. For higher energies or X-ray generation, codes such as Bmad [5], ELEGANT [6], Genesis 1.3 [7], and SRW [8] are used. Often times it is desirable to switch between codes, or use output from one code as input to another. This is usually difficult to accomplish, as each code can have a unique convention.

The Lightsource Unified Modeling Environment (LUME) is an effort to reduce the start up time associated with using various simulations codes. In addition, emphasis is placed in forming standards for saving simulation data, with the goal of simplifying hand off from one code to another. This work comes in the form of Python 3 wrappers, of which three are currently being developed on GitHub: lume-astra [9], lume-impact [10], and lume-genesis [11]. Lume-astra was used heavily for this work.

Code Comparison

As a quick check to ensure the EIC area was being simulated correctly, two codes were used and results compared. The transverse laser profile was set to a circular and a uniform distribution. The longitudinal profile was Gaussian. Typical EIC commissioning gradient and solenoid strength values were used. Simulation parameters can be found in Table 1. For these settings, good agreement is shown between OPAL and ASTRA in Figs. 2 and 3. This confirms some understanding of how to simulate the gun. Future work will include IMPACT-T in comparisons.

3D Field Maps

It is commonplace for most accelerator design work and optimization to use 1D or 2D field maps at the start of a project. This reduces the time to simulation, and allows for analysis of results quickly. Often the accuracy is adequate depending on the project goals. Such maps were used for the simulations in the previous section (Fig. 3), with no asymmetries in the traverse fields assumed.

---

[*] nneveu@slac.stanford.edu

OPTIMIZATION OF AN SRF GUN DESIGN FOR UEM APPLICATIONS*

A. Liu†, R. Kostin, Euclid Techlabs, LLC, Bolingbrook, IL, U.S.A.
C. Jing, P. Avrakhov, Euclid Beamlabs, LLC, Bolingbrook, IL, U.S.A.

Abstract

Benefiting from the rapid progress on RF photogun technologies in the past two decades, the development of MeV-range ultrafast electron diffraction/microscopy (UED and UEM) has been identified as an enabling instrumentation. UEM or UED use low power electron beams with modest energies of a few MeV to study ultrafast phenomena in a variety of novel and exotic materials. SRF photoguns become a promising candidate to produce highly stable electrons for UEM/UED applications because of the ultrahigh shot-to-shot stability compared to room temperature RF photoguns. Euclid is developing a continuous wave (CW), 1.5-cell, MeV-scale SRF photogun operating at 1.3 GHz. In order to achieve the optimal beam parameters for the UED/UEM applications, the shape of the back wall is optimized by a heuristic Genetic Algorithm (GA) provided by a Python optimization package pyaopt. In this paper, the technical details of the design and preliminary optimization results are presented.

INTRODUCTION

The Basic Energy Science (BES) Workshop on the Future of Electron Scattering and Diffraction, held in 2014, identifies the objectives of pushing the boundaries of existing UED and UEM instruments, for which the desired electron beam parameters are given in Table 1. Specifically, the aggressive pursuit of sampling rates in the GHz range with extreme space-time resolution (STR) of 1 nm/10 nm and 100 fs/10 ps was strongly recommended. In an UED/UEM, stable femtosecond (fs) electron bunches, synchronized with laser pulses that excite transitions in the materials are needed. UEM/UED also has a stringent requirement on the shot-to-shot stability of beam energy and timing, which is difficult for a room temperature RF photogun to guarantee (typical jitter is on the order of 100 fs) [1].

Table 1: Desired Beam Parameters for Future UED/UEM

	UED	UEM
Charge	10 fC - 0.5 pC	0.5-1 pC
Bunch length	10 fs	ns - ps
Energy spread	10^{-4}	10^{-5}
Repetition rate	up to MHz	up to 100 Hz

The photogun in an UEM needs to minimize the energy spread (dE/E) and emittance (ϵ) to eliminate chromatic effects in the strong magnetic lenses, where a large dE/E introduces a spread in focal length. Ultimately a single-shot UEM requires the electron pulse to have $\epsilon_n \sim 10$ nm and $dE/E < 10^{-5}$. The state-of-the-art high-gradient S-band RF photoinjector can offer ~ 0.1 pC, ~ 10 nm emittance and ~ 10^{-4} dE/E, however the MW-level pulsed RF source driving the photogun limits its application. This can be easily solved by using an SRF photogun. It operates at an ultrahigh Q in a CW mode, but only dissipates a few watts of RF power.

The R&D of SRF guns has made significant progress since first proposed [2,3]. Tens of MV/m axial electric field has been achieved at the superconducting cathode. One of the biggest "showstoppers" for using an SRF photogun is that it introduces high fabrication and operation costs. On the one hand, to date, the application of SRF technologies to UEM has mainly focused on the superconducting objective lens [4]. On the other hand, The UED group at SLAC recently successfully initiated the use of an SRF electron source to upgrade the facility performance [5].

Euclid is developing a CW, 1.5-cell SRF gun operating at 1.3 GHz for UED/UEM applications. The project is funded by the DoE SBIR Phase II program. The design is being optimized and finalized for fabrications. In the following sections, the concept of the design, technical approach and the recent optimization results from running a GA on the shape of the back wall are presented.

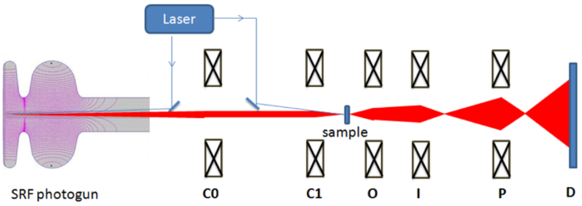

Figure 1: Schematic layout of the SRF photogun-based UEM system.

DESIGN CONCEPT

Figure 1 shows the schematic drawing of an SRF photogun-based UEM system. Besides the SRF cavity, it also includes a high repetition-rate laser system that generates both the pump and photoemission laser pulses, and magnetic lenses for the electron optics. A low-level RF (LLRF) control system manages the amplitude of the accelerating fields in the SRF cavity, which will operate in a phase-locked loop mode. It also synchronizes the laser with the SRF gun and monitors the arrival time of the e-beam at the beam dump/diagnostics. Benefiting from the CW operation, the RF amplitude and phase can be accurately

---

* Work supported by the SBIR program of the U.S. Department of Energy, under grant DE-SC0018621

† a.liu@euclidtechlabs.com

North American Particle Acc. Conf. NAPAC2019, Lansing, MI, USA JACoW Publishing
ISBN: 978-3-95450-223-3 ISSN: 2673-7000 doi:10.18429/JACoW-NAPAC2019-TUYBB2

MANIPULATING H^- BEAMS WITH LASERS*

A. Rakhman[†], A. Aleksandrov, S. Cousineau, T. Gorlov, Y. Liu, A. Shishlo
Oak Ridge National Laboratory, Oak Ridge, TN, USA

Abstract

In recent years lasers have been playing a vital role in many H^- beam measurements and experiments. This talk will review current state of development of various applications using lasers for manipulating H^- ion beams in accelerators. A wide range of applications will be reviewed such as beam diagnostics, laser-assisted charge-exchange injection, generation of arbitrary H^0 pulse patterns and others. An overview of ongoing developments and prospects for other laser H^- beam interactions will also be given.

INTRODUCTION

Laser systems have been routinely in use at many H^- beam facilities around the world since the last four decades. At the early stage of their application with H^- beams, lasers were mainly used for non-invasive diagnostics of low-energy H^- beams [1, 2]. Over the last two decades, significant advancement of laser technology accompanied with increasing demands of H^- beam manipulation with lasers have enabled a wider use of lasers at such facilities. Nowadays, laser manipulations of the H^- beams are an important subject for the state-of-the-art high-intensity proton accelerators with many purposes such as, laser assisted charge exchange injection [3-5], laser notcher (H^- beam chopper) [6] and extraction [7, 8], phase space sculpting [9], etc.

The basic principles of H^- beam manipulation with lasers is based on photodetachment processes [1] by either removing a loosely bound outer electron or exciting the ground state second electron to a higher energy state to completely remove it from the H^- ions. The former is producing neutral H^- (H^0) and therefore called H^- neutralization and the latter is called laser charge exchange injection or laser stripping. For the neutralization process, the energy required for photodetaching an electron is about 0.75 eV, and the interaction cross section is about $4x10^{-17}$ cm^2 for photons of about 1.17 eV (1064 nm). Therefore, a significant fraction of the ion beam can be neutralized by focusing a1064 nm laser beam, for example, with pulse energy on the order of 100 mJ. However, depending on the ion beam energy, photodetaching the second inner bound electron would require much higher laser energy and power and difficult to achieve.

In this paper, we review current state of development of various topics such as non-invasive beam diagnostics, beam chopping and extraction, and laser assisted charge exchange using lasers for manipulating H^- ion beams in accelerators. An overview of ongoing new developments at various H^- facilities and prospects for H^- manipulation will be discussed.

NON-INVASIVE BEAM DIAGNOSTICS

Laser-based diagnostics for H^- beams work by using a laser beam to neutralize some of the ions in the ion beam. The secondary particles produced (electrons and H^0) are separated from the remaining H^- ions using a simple dipole magnet and are then used to diagnose the ion beam. To use the electrons for beam diagnosis, a Faraday Cup (FC) is used to measure the amount of charge that has been detached; to use H^0, typically a scintillator and a Photo Multiplier Tube (PMT) are used to detect the scintillating photons [10]. The scheme used at the Spallation Neutron Source (SNS) is shown in Fig. 1.

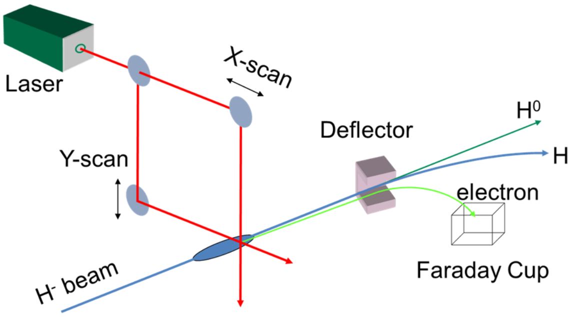

Figure 1: A layout of the laser wire beam profile monitor in SNS HEBT.

In the photodetachment process, the neutralized beam (H^0) maintains nearly the original phase-space parameters of the H^- beam from which it was extracted. The transverse spatial profile, transverse divergence, emittance, energy, energy spread, and phase spread characteristics of the H^0 and H^- beams are nearly identical and can be deduced. During the process, neither the laser photon nor the photodetached electron transfer significant momentum to the H^0 atom. Therefore, the whole process is non-invasive. Three types of laser-based diagnostics (Transverse beam profile, emittance and longitudinal bunch shape monitors) have been developed and operational at SNS for measuring H^- beam.

The system called HEBT (High Energy Beam Transport) laser wire beam profile monitor consists of 9 measurement stations that covers 23 cryomodules in the Super Conducting Linac (SCL) section of the SNS. A 250 meter free space transport line sends a single Q-switched Nd:YAG laser

---

[*] Notice: This manuscript has been authored by UT-Battelle, LLC, under contract DE-AC05-00OR22725 with the US Department of Energy (DOE). The US government retains and the publisher, by accepting the article for publication, acknowledges that the US government retains a nonexclusive, paid-up, irrevocable, worldwide license to publish or reproduce the published form of this manuscript, or allow others to do so, for US government purposes. DOE will provide public access to these results of federally sponsored research in accordance with the DOE Public Access Plan (http://energy.gov/downloads/doe-public-access-plan).

[†] rahim@ornl.gov

ISBN: 978-3-95450-223-3 ISSN: 2673-7000 doi:10.18429/JACoW-NAPAC2019-TUYBB3

FINAL DESIGN OF THE APS-UPGRADE STORAGE RING VACUUM SYSTEM*

J.A. Carter†, B. Billett, B. Brajuskovic, M.A. Lale, A. McElderry, O.K. Mulvany, J. R. Noonan,
M. O'Neill, R.R. Swanson, K.J. Wakefield, D.R. Walters, G.E. Wiemerslage, J. Zientek,
Advanced Photon Source, Argonne National Laboratory, Lemont, IL, USA

Abstract

The Advanced Photon Source Upgrade (APS-U) project is progressing from its final design phase into production for the future 6 GeV, 200 mA upgrade of the existing APS. The storage ring arc vacuum system will include over 2500 vacuum chambers made from a variety of custom designs ranging from 70 mm to 2.5 meters in length and typically feature a narrow 22 mm inner diameter aperture. The scope of NEG coatings was increased to 40% of the length along the e-beam path to ensure efficient conditioning and low pressure requirements can be met.

The final design phase required advancing previous work to a procurement-ready level and to address local and system level challenges. Local challenges include designing thin-walled vacuum chambers with carefully controlled lengths and outer profiles and also mitigating significant radiation heat loads absorbed along vacuum chamber walls. System level challenges include planning for the complex machine assembly, networking components to utilities, managing the quality of upcoming procurements. This presentation will highlight the major design challenges and solutions for the storage ring vacuum system and also plans for production and installation.

VACUUM SYSTEM REQUIREMENTS

APS-U will retrofit the existing 1.1 km circumference APS storage ring with a new 6 GeV, 200 mA multi-bend achromat storage ring. The new magnet lattice brings magnet poles closer to the electron beam and dictates a new storage ring vacuum system featuring thin-walled vacuum chambers with a nominal 22 mm ID circular aperture. Figure 1 compares the typical APS storage ring arc chamber profile to a typical new 22 mm ID APS-U chamber profile. The new profile represents about 40% of the length of each sector. Some chambers along the electron beam path feature antechambers as part of the pumping and photon extraction scheme but all these chambers feature a 22 mm inner diameter beam-side aperture.

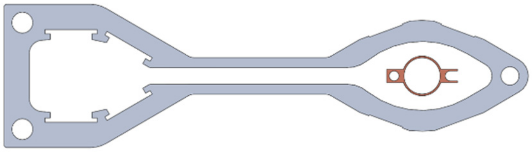

Figure 1: Cross section comparison of 318 mm wide APS chamber profile to 22 mm ID APS-U chamber profile.

APS consists of 40x sectors of a mostly uniform arc design with straight sections in between. This paper covers the scope of only the arc vacuum system design and not the straight sections. Each sector will be first built outside of the tunnel as five separate modules, each containing magnets, vacuum components, and supports. Modules will be connected by individual beam position monitors (BPMs) units featuring bellows on two sides. A project goal is to achieve the tunnel installation and accelerator and vacuum commissioning in no more than one year of dark time. The vacuum conditioning goal is to achieve good beam lifetimes at full 200 mA current by reaching 2 nTorr average pressures at full current by 1000 A*hrs of conditioning.

INTERFACES & DESIGN CHALLENGES

APS-U vacuum system chambers typically span narrow magnet pole gaps with ~26 mm inner diameter and are mounted to compact BPM units as shown in Fig. 2. A BPM design was developed with welded electrode feedthroughs and bellows on each end to accommodate thermal expansion. The BPM mounts to a rigid support base with thin support arms to mount and align the chambers while decoupling the BPMs from chamber vibrations. The integrated BPM, support, and vacuum-sealing chain clamp span fit within access gaps between magnets with minimum spans of 125 mm.

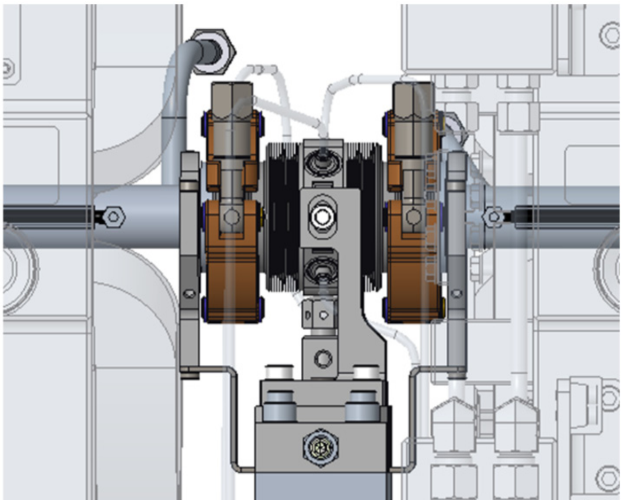

Figure 2: Central BPM support with extended supports for mounting and aligning neighboring vacuum chambers.

Uncooled components like the BPMs and flange gaps are shadowed by upstream components such as vacuum

---

*Work supported by the DOE under contract No. DE-AC02-06CH11357
† jacarter@anl.gov

ONLINE MODELLING AND OPTIMIZATION OF NONLINEAR INTEGRABLE SYSTEMS*

N. Kuklev†, Y.K. Kim, University of Chicago, Chicago, IL, USA
A. Valishev, Fermilab, Batavia, IL, USA

Abstract

Nonlinear integrable optics was recently proposed as a design approach to increase the limits on beam brightness and intensity imposed by fast collective instabilities. To study these systems experimentally, a new research electron and proton storage ring, the Integrable Optics Test Accelerator, was constructed and recently commissioned at Fermilab. Beam-based diagnostics and online modelling of nonlinear systems presents unique challenges - in this paper, we report on our efforts to develop optimization methods suited for such lattices. We explore the effectiveness of neural networks as fast online surrogate estimators, and integrate them into a beam-based tuning algorithm. We also develop a method of knob dimensionality reduction and subsequent robust multivariate optimization for maximizing key performance metrics under complicated lattice optics constraints.

INTRODUCTION

High intensity accelerators with strong space charge effects often exhibit current-limiting collective instabilities. A novel mitigation approach proposed by Danilov and Nagaitsev [1] is to suppress these with nonlinear integrable optics (NIO) lattices, which produce strong amplitude-dependent tune-shifts and hence, via Landau damping, prevent resonantly coupling energy into the beam. Previously, such tune-shifts were achieved with standalone elements like octupoles [2] at the cost of dynamic aperture degradation [3], a disadvantage that NIO mitigates. However, NIO lattices impose a number of linear and nonlinear optics constraints that must be carefully met and maintained, making conventional tuning techniques insufficient or difficult to apply. In this paper, we present several exploratory efforts to design more suitable methods, and study applicability of recently proposed machine learning approaches [4, 5].

Integrable Optics

An ideal strong-focusing lattice is a linear system that has no amplitude-dependent tune shifts and is fully integrable. Due to misalignments, field errors, and the need to correct chromaticity and induce tune spread, real accelerators have significant nonlinearities which break integrability. Their set of initial conditions with regular motion is limited to a finite region, called the dynamic aperture (DA) - preserving its size is critical for achieving good accelerator performance. Mathematically, the Hamiltonian for transverse particle dynamics is

$$H = \frac{1}{2}\left(K_x(s)x^2 + K_y(s)y^2 + p_x^2 + p_y^2\right) + V(x, y, s)$$

with $K_{z=x,y}$ being the linear focusing strength, and $V(x, y, s)$ containing any nonlinear terms (in general dependent on time ($\equiv s$) and transverse (x, y) position). DN approach is to seek solutions for V that yield two invariants of motion and are implementable with conventional magnets. First invariant comes from appropriate time scaling of $V(x, y)$, such that it becomes a time-independent potential $U(x_N, y_N)$ in normalized coordinates. It is furthermore possible to derive a specific form of $U(x_N, y_N)$ that yields second invariant of motion I, which we omit for brevity. Such system is both nonlinear and fully integrable, with ideally infinite DA.

Practical Implementation

Above derivation implicitly imposed several lattice constraints - such as the need to remove chromaticity, which in turn introduces unaccounted sextupolar nonlinearities. Within the nonlinear region, there should be no dispersion and β-functions must be equal. Finally, the rest of the ring must have phase advance be a multiple of 2π and have a first-order transport matrix of a thin, axially symmetric lens. For fully integrable case, these conditions must be met with high precision (i.e. 1% β-beat) to maintain integrability [6], but are relaxed by about an order of magnitude for a system with only 1 invariant [7]. Such a lattice, as implemented in IOTA, is shown in Fig. 1.

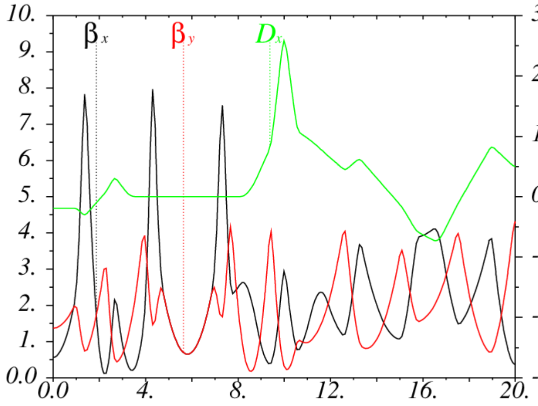

Figure 1: Half of IOTA lattice at working point $Q_{x,y}$=5.3. All units in meters, $\beta_{x,y}$ on the left, D_x on the right. Lattice is mirror symmetric across 20m marker.

Realistically, due to field imperfections, magnet misalignments, and the unavoidable approximation of continuous

---

* This work was supported by the U.S. National Science Foundation under award PHY-1549132, the Center for Bright Beams. Fermi Research Alliance, LLC operates Fermilab under Contract DE-AC02-07CH11359 with the US Department of Energy.

† nkuklev@uchicago.edu

DESIGN AND ANALYSIS OF A HALO-MEASUREMENT DIAGNOSTICS*

C. J. Marshall, P. Piot[1], Northern Illinois University, DeKalb, IL, USA
S. V. Benson, J. Gubeli,
Thomas Jefferson National Accelerator Laboratory, Newport News, VA, USA
J. Ruan, Fermi National Accelerator Laboratory, Batavia, IL, USA
[1]also at Fermi National Accelerator Laboratory

Abstract

A large dynamical-range diagnostics (LDRD) design at Jefferson Lab will be used at the (Fermilab Accelerator Science and Technology-Integrable Optics Test Accelerator) FAST-IOTA injector to measure the transverse distribution of halo associated with a high-charge electron beam. One important aspect of this work is to explore the halo distribution when the beam has significant angular momentum (i.e. is magnetized). The beam distribution is measured by recording radiation produced as the beam impinges a YAG:Ce screen. The optical radiation is split with a fraction directed to a charged-couple device (CCD) camera. The other part of the radiation is reflected by a digital micro-mirror device (DMD) that masks the core of the beam distribution. Combining the images recorded by the two cameras provides a measurement of the transverse distribution over a large dynamical range $O(10^5)$. The design and analysis of the optical system is discussed.

INTRODUCTION

A beam halo is generally considered to be the low intensity of particles that surround the main core of the beam. Particle within the beam halo do not generally participate in the front-end application of the beam but can limit the overall performances of an accelerator. For instance, a particle in the beam halo can be lost and results in beamline-component radiological activation or damaged hardware. Particle loss could especially hinder the operation of high-average current electron accelerator such as needed for electron-beam cooling [1] in the foreseen Electron-Ion Collider (EIC). Therefore understanding the source of halo formation could help its mitigation which ultimately improves accelerator performances. Consequently developing a reliable halo-measurement beam diagnostics is critical.

Over the years, the beam halo distribution is often measured using a coronographic technique where a mask block the beam core and a charged-coupled device (CCD) detector measured the unlock distribution. Such a technique supported the exploration of halo formation in high-duty-cycle photoinjector [2]. Given the advances in micro-fabrication, the coronographic method was improved to use dynamical mask employing digital micro-mirror device (DMD) [3, 4].

This paper discusses the implementation of a flexible halo diagnostics using a DMD similar to Ref. [4]. We detail the optical design of such a system and develop numerical simulation to explore its performances. Ultimately, the system will be tested on an electron-beam test accelerator and support the investigation of halo formation in magnetized electron beams such as required for magnetized electron cooling.

OVERVIEW

A diagram of the optical setup associated with the large-dynamical range diagnostics (LDRD) appears in Fig. 1. In brief, the optical radiation emitted as an electron beam impinges on a YAG:Ce screen is collected and imaged by a pair of lenses on the DMD surface which is further imaged on the CCD chip of the camera. The DMD (development kit from DLP model LightCrafter 6500 1080p) consists of an array of 1920 × 1080 mirrors and is set up so mask the central part of the beam before imaging on CCD#2. In our setup, a 50-50 beam splitter is placed upstream of the DMD to direct half of the light to another CCD camera (CCD#1). This dual-CCD approach was first adopted in Ref. [5]. Images from both of these CCDs (operated with different gains) are simultaneously recorded and combined to reconstruct the beam profile.

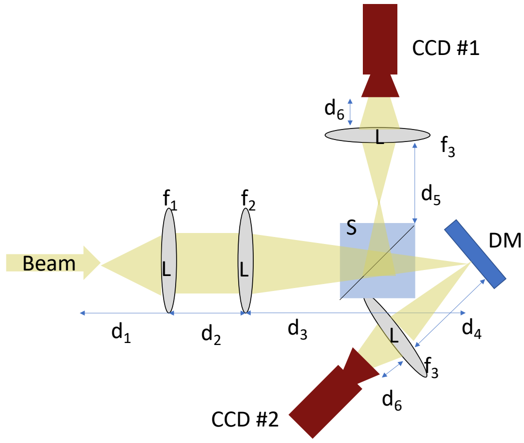

Figure 1: Diagram of the optical setup used in the LDRD. The labels “L”, “S” correspond to the locations of the lenses and splitter.

OPTICAL SYSTEM

We first consider the optical function of the setup shown in Fig. 1 and note that both arms of the diagnostics are identical. They can be represented by an unfolded configuration

---

* This work is supported by the U.S. Department of Energy, Office of Science, Office of Nuclear Physics, under contracts DE-AC05-06OR23177 and DE-AC02-07CH11359.

BEAM DYNAMICS IN A HIGH-GRADIENT RF STREAK CAMERA*

A. Landa, V.A. Dolgashev, F. Toufexis†, SLAC, Menlo Park, CA, USA

Abstract

Traditionally, time-resolved experiments in storage ring synchrotron light sources and free-electron lasers are performed with short x-ray pulses with time duration smaller than the time resolution of the phenomenon under study. Typically, storage-ring synchrotron light sources produce x-ray pulses on the order of tens of picoseconds. Newer diffraction limited storage rings produce even longer pulses. We propose to use a high-gradient RF streak camera for time-resolved experiments in storage-ring synchrotron light sources with potential for sub-100 fs resolution. In this work we present a detailed analysis of the effects of the initial time and energy spread of the photo-emitted electrons on the time resolution, as well as a start-to-end beam dynamics simulation in an S-Band system.

INTRODUCTION

The motivation for this work is twofold: to enable measurement of x-ray pulse structure in Free-Electron Lasers (FELs) and sub-picosecond time-resolved experiments in storage-ring synchrotron light sources. There is currently no practical method of directly instrumenting the time structure of the x-ray pulse in an FEL; this measurement is performed indirectly by streaking the electron beam after the undulators with an rf deflector [1–3]. Storage-ring synchrotron light sources typically produce x-ray pulses on the order of tens of picoseconds that allow for time-resolved experiments with sub-nanosecond resolution. Newer diffraction limited storage rings produce even longer pulse lengths. An ultrafast streak camera would enable sub-picosecond intensity-based time-resolved experiments with long x-ray pulses. It is also possible that diffraction-based experiments could be performed using the 2D movie reconstruction techniques discussed in [4–7].

Streak cameras are instruments for measuring the variation in a pulse of light's intensity with time. The time structure of the incident light pulse is encoded onto an electron beam through a photocathode. The photo-electrons are accelerated and then streaked producing a 2D image on a screen, from which the intensity versus time of the light pulse can be inferred. Streak cameras have been used in particle accelerators for a variety of instrumentation tasks including bunch length measurements, longitudinal instability measurements, characterization of FEL performance, and synchronization in pump-probe experiments [8]. They have also been used for plasma diagnostics [9–11]. The 2D image of visible light streak cameras was used to create a 2D movie of the propagation of a light pulse [4–6] and a similar concept has been studied for an X-ray streak camera [7].

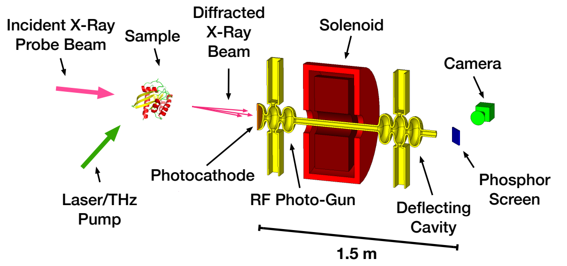

Figure 1: High-gradient rf streak camera concept, adapted from Toufexis *et al.* [25].

The typical time resolution of X-ray streak cameras is on the order of a few ps, primarily dominated by the bunch lengthening due to the initial energy spread of the photo-electons and low accelerating field on the photocathode. With photocathode fields on the order of 10 kV mm^{-1}, single-shot sub-picosecond streak cameras have been demonstrated with 600 fs Full Width Half Max (FWHM), 350 fs rise time, and 50 fs timing jitter [10, 12–14]. In accumulation mode, time resolution down to 233 fs was achieved [15, 16]. However, all these experiments used Ultraviolet (UV) light instead of an X-ray beam. It was shown in simulation that using low-power accelerating RF fields may improve the resolution down to 100 fs [17, 18]. Experiments using THz radiation [19] and laser light [20, 21] have shown resolution of 10 fs and 100 as, respectively. RF deflectors have been used to capture ultrafast processes in a single shot in ultrafast electron diffraction with 150 fs FWHM temporal resolution [22–24].

In this work we propose the use of a high-gradient RF photo-injector and RF deflector as an ultra-high-resolution X-ray streak camera operating in either single-shot or accumulation mode. This concept is shown in Fig. 1. Our initial work was reported in [25]. Here we show a detailed analysis of the effects on the time resolution of the initial time and energy spread of the photo-emitted electrons both analytically and numerically, using the beam dynamics code ASTRA [26]. Finally, we show a start-to-end beam dynamics simulation of the system; the S-Band photo-gun and deflector are discussed in detail in [25].

DEFINITION OF RESOLUTION

Typically the FWHM of one pulse is used as a measure of the time resolution in streak cameras [10, 12–14]. In this work we define the X time resolution Δt^X as the spacing between two photon pulses at the cathode that results in $\frac{N_V}{N_{LP}} = X$, as shown in Fig. 2. This approach is a similar to what is used in optics [27]. We will report the FWHM, the 50 %, and the 80 % resolution below.

If we have two photon pulses with some overlap in time then the combined distribution will have two peaks and a val-

---

* This project was funded by U.S. Department of Energy under Contract No. DE-AC02-76SF00515.

† ftouf@slac.stanford.edu

COMMISSIONING OF THE ELECTRON ACCELERATOR LEReC FOR BUNCHED BEAM COOLING*

D. Kayran†, Z. Altinbas, D. Bruno, M.R. Costanzo, K.A. Drees, A.V. Fedotov, W. Fischer, M. Gaowei, D.M. Gassner, X. Gu, R.L. Hulsart, P. Inacker, J.P. Jamilkowski, Y.C. Jing, J. Kewisch, C.J. Liaw, C. Liu, J. Ma, K. Mernick, T.A. Miller, M.G. Minty, L.K. Nguyen, M.C. Paniccia, I. Pinayev, V. Ptitsyn, V. Schoefer, S. Seletskiy, F. Severino, T.C. Shrey, L. Smart, K.S. Smith, A. Sukhanov, P. Thieberger, J.E. Tuozzolo, E. Wang, G. Wang, W. Xu, A. Zaltsman, H. Zhao, Z. Zhao, Brookhaven National Laboratory, Upton, New York, USA

Abstract

The brand-new state of the art electron accelerator, LEReC, was built and commissioned at BNL. LEReC accelerator includes a photocathode DC gun, a laser system, a photocathode delivery system, magnets, beam diagnostics, a SRF booster cavity, and a set of Normal Conducting RF cavities to provide sufficient flexibility to tune the beam in the longitudinal phase space. Electron beam quality suitable for cooling in the Relativistic Heavy Ion Collider (RHIC) was achieved, which lead to the first demonstration of bunched beam electron cooling of hadron beams. This presentation will discuss commissioning results, achieved beam parameters and performance of the LEReC systems. The layout of LEReC is shown in Fig. 1.

INTRODUCTION

A new, state of the art, electron accelerator for cooling low energy RHIC hadron beams (LEReC) was built and commissioned at BNL [1]. The purpose of LEReC is to provide luminosity improvement for the RHIC operation at low energies to search for the QCD critical point (Beam Energy Scan Phase-II physics program) [2-3].

Unlike all electron coolers to date, LEReC uses bunched electron beams accelerated to the required energies using RF cavities [4]. To achieve efficient cooling, the electron beam must not only be optimized for low transverse emittance but, more importantly, for low energy spread.

The LEReC accelerator includes a photocathode DC gun with a high power laser system, magnets, beam diagnostics, an SRF booster cavity, and a set of normal conducting RF cavities to provide sufficient flexibility to tune the beam in the longitudinal phase space. LEReC is designed to provide electron beam for cooling RHIC Ions at energy 3.85-5.75 GeV/nucleon.

LEReC uses a DC photocathode gun similar to the one used at Cornell University [5]. The gun itself was built by Cornell University. The gun tests with beam started in 2017 when the gun delivered up to 10 mA average current [6]. Electron beams are generated by illuminating a multi-alkali (CsK2Sb or NaK2Sb) photocathode [7] with green light (532 nm) from a high-power fiber laser [8] by utilizing sophisticated laser transport and stabilization [9-10].To optimize operational time and minimize the cathode exchange time three multi-cathode carriers were built. Each cathode carrier, which can hold up to 12 pucks of photocathodes, is attached to the gun in a 10^{-11} Torr-scale vacuum (for details of design see [11]). For initial gun tests in 2017-2018 we used large cathode active are 12 mm. Later, in order to reduce cathode QE degradation due to ion back bombarding during high current operation, we used small 6 mm diameter active area cathodes deposited 4 mm off the puck center (see Fig. 2).

The 350-400 keV electron beam from the gun is transported via a 704 MHz SRF booster cavity and a 2.1 GHz 3rd harmonic linearizer normal conductive cavity.

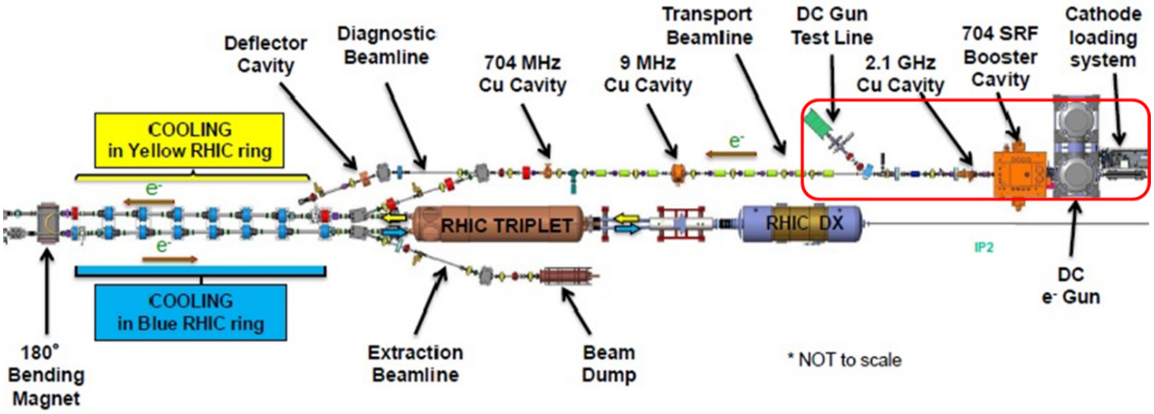

Figure 1: Layout of the LEReC accelerator. The red contour box indicates DC gun test area.

---

* Work supported by Brookhaven Science Associates, LLC under Contract No. DE-AC02-98CH10886 with the U.S. Department of Energy

† dkayran@bnl.gov

ELECTRON ION COLLIDER MACHINE DETECTOR INTERFACE*

B. Parker†, E.C. Aschenauer, A. Kiselev, C. Montag, R. B. Palmer, V. Ptitsyn, F.J. Willeke, H. Witte,
Brookhaven National Laboratory, Upton, Long Island, NY, USA
M. Diefenthaler, Y. Furletova, T.J. Michalski, V.S. Morozov, D. Romanov, A. Seryi, R. Yoshida,
Thomas Jefferson National Accelerator Facility, Newport News, VA, USA
C. Hyde, Old Dominion University, Norfolk, VA, USA
M.K. Sullivan, SLAC National Accelerator Laboratory, Menlo Park, CA, USA

Abstract

Here we review the major physics requirements, accelerator challenges and some magnet design issues for the Machine Detector Interface (MDI) of an Electron Ion Collider (EIC) Interaction Region (IR). In order to fully exploit the rich physics potential of an EIC, an IR MDI team must balance a complex interplay that arises when combining hadron and electron collider accelerators in an optimized IR. The work described in this paper results from ongoing close collaboration between many people at BNL, JLab and other institutes to realize an EIC as the next, highest priority, future nuclear physics project.

EIC MDI CONSIDERATIONS

HERA at DESY, which collided unpolarized protons with a self-polarized electron beam, was the only ep-collider built so far. HERA opened new areas of investigation and gave new questions to explore; subsequent studies led to establishing an EIC Physics White Paper as a guide for future EIC physics requirements [1-4]. Some EIC detector and accelerator requirements taken from the White Paper are outlined in Table 1, where we also compare the existing state of the art LHC and RHIC physics parameters to the EIC design requirements [5-7].

HERA experience, especially from the HERA-II upgrade, shows that hadronic beam gas and synchrotron radiation (direct and backscatter) backgrounds can significantly impact the physics data taking; such backgrounds are do not a dominate background source at other hadron colliders.

Further compounding EIC measurement difficulty is the need to detect particles traveling very close to the circulating beams due to the kinematics of the physics process. Also, the natural optimization path for providing the highest possible EIC luminosity leads to colliding many bunches at high frequency (i.e. short bunch spacing) and at much larger total crossing angles than considered for the LHC. Reaching a high EIC luminosity, obtainable with a Crab Crossing scheme, is essential do a wide range of precision physics and is especially critical for studies involving polarization dependent observables.

While the rapid beam separation enabled via a large crossing angle allows colliding bunches at high frequency, the short bunch spacing is a significant factor for choosing appropriate EIC detector technologies. Finally, we will see that some aspects of the EIC physics program favor using a crossing angle instead of depending upon beam separation dipoles as was done at HERA.

In the idealized EIC detector shown in Fig.1, we see events where the scattered electron, #1, and particles associated with the struck parton, #3, are detected in the central solenoid region; however, sometimes particles associated

Table 1: Some ways that EIC challenges are different from other colliders. Here we compare EIC to the LHC and RHIC. The differences impact both EIC detector acceptance and the choice of possible detector technologies that can be used.

EIC	LHC / RHIC
Collide different beam species: ep and eA	**Collide the same species: pp, pA and AA**
→ Hadron beam backgrounds, i.e. beam gas events	→ Hadron backgrounds, i.e. beam gas and high pile up
→ Synchrotron radiation related backgrounds	
Asymmetric Beam Energies	**Symmetric Beam Energies**
→ Boosted kinematics → high activity at high $\lvert\eta\rvert$	→ Not boosted → Most activity at mid rapidity
High Repetition Rate	**Moderate Repetition Rate**
→ 2 – 9 ns spacing between bunches	→ 25 ns spacing between bunches
Large Crossing Angle	**No crossing Angle…Yet**
→ Crab Crossing: 25 – 50 mrad	→ Any future LHC angle would be very much smaller
Wide Range of Center of Mass Energies	**Limited Range of Center of Mass Energies**
EIC → Factor 7	LHC → Factor 2
	RHIC → Factor 26 in AA and 8 in pp
EIC Both Beams Are Polarized	**LHC No Beam Polarization / RHIC Polarized pp**
→ Polarized Stat. Uncertainty: $\sim 1/(P_1P_2\,(\int L\,dt)^{1/2})$	→ LHC Unpolarized Stat. Uncertainty: $\sim 1/(\int L\,dt)^{1/2}$

---

* Work supported by U.S. Department of Energy, Office of Nuclear Physics under contracts: DE-SC0012704 and DE-AC05-06OR23177.

† email address : parker@bnl.gov

ISBN: 978-3-95450-223-3 ISSN: 2673-7000 doi:10.18429/JACoW-NAPAC2019-TUZBA3

A HIGH-ENERGY DESIGN FOR JLEIC ION COMPLEX*

B. Mustapha† and J. Martinez-Marin
Argonne National Laboratory, Lemont, IL USA
V. Morozov, F. Lin, Y. Zhang and Y. Derbenev
Thomas Jefferson National Accelerator Facility, Newport News, VA, USA

Abstract

A recent assessment of the scientific merit for a future Electron Ion Collider (EIC) in the US, by the National Academy of Sciences (NAS), found that such a facility would be unique in the world and that it would answer science questions that are compelling, fundamental, and timely. This assessment confirmed the recommendations of the 2015 Nuclear Science Advisory Committee (NSAC) for an EIC with highly polarized beams of electrons and ions, sufficiently high luminosity and sufficient, and variable, center-of-mass energy. The baseline design of Jefferson Lab Electron-Ion Collider (JLEIC) has been recently updated to 100 GeV center-of-mass (CM) collision energy, corresponding to 200 GeV proton energy. We here present a high-energy design for the JLEIC ion complex, as part of the alternative design approach. It consists of a 150 MeV (~ 40 MeV/u for Pb) injector linac, a 6-GeV (~ 1.5 GeV/u for Pb) non figure-8 pre-booster ring and a 40-GeV proton (~ 16 GeV/u for Pb) large ion booster which could also serve as electron storage ring (e-ring). The energy choice in the accelerator chain is beneficial for future upgrade to 140 GeV center of mass energy. The large ion booster is designed with the same shape and size of the original e-ring and does not preclude the option of having separate electron and ion rings by stacking them in the same tunnel as the ion collider ring. The ion collider ring design is the same as for the baseline design, which was updated to 200 GeV proton energy with 6 Tesla superconducting magnets.

INTRODUCTION

As discussed in previous work [1], the main motivation for the alternative design approach for the JLEIC ion complex is not to replace the baseline design. It is rather to investigate alternative options for the different components of the ion complex that have the potential of lowering the cost, mitigating a risk, and to prepare for possible staging or future upgrades of the project. For example, we list the options we investigated for the low-energy design (65-GeV CM), which we are now updating for the high-energy design (100-GeV CM and higher):

- Reducing the footprint and cost of the ion complex
  i. A more compact injector linac: ~ 135 MeV instead of 280 MeV
  ii. A small pre-booster ring: 3 GeV circular ring instead of 8-GeV figure-8 booster
  iii. Consolidate the electron storage ring as large booster for the ions
- Lowering the overall risk
  i. Use room-temperature (RT) magnets whenever possible
  ii. Avoid transition crossing for all ions, which is an operational risk
- Staging or upgrading the project
  i. Design an ion injector system compatible with 65, 100 and 140 GeV CM energies
  ii. Upgrade only the ion collider ring with stronger magnets

ALTERNATIVE 65-GEV DESIGN REVIEW

As part of the 65-GeV alternative design, a shorter more compact lower energy injector linac was designed with higher performance superconducting cavities [2]. This was possible due to the recent development at ANL for quarter-wave (QWR) and half-wave (HWR) resonators operating at high voltage (~ 3 MV per cavity) in CW mode [3, 4]. The JLEIC linac requires pulsed mode operation, where 50% higher voltage can be achieved. Similarly, a design for a 3-GeV pre-booster ion ring with RT magnets [5], was developed to serve as pre-booster before injecting the beam into the large booster, which is nothing but the electron storage ring modified to also serve as ion accelerator [6]. Spin preservation and correction schemes were investigated for both protons and deuterons in the 3-GeV pre-booster [7], which is circular and not figure-8. Finally, an ion beam formation scheme through the alternative accelerator chain, from the ion source to the collision point, was proposed and carefully studied in order to ensure the high beam collision luminosity of 10^{34} cm^{-2} s^{-1} or higher [8]. In summary, the lower energy linac seems reasonable for both protons and heavy-ion injection into a small lower-charge pre-booster ring. However, a higher energy pre-booster of ~ 5-GeV maybe needed to lower the space charge tune shift for heavy ions in the large booster (e-ring). The e-ring as large ion booster seems feasible from space and beam optics point of view.

CURRENT 100-GEV BASELINE

A schematic layout of the current high-energy baseline line design [9] is shown in Fig. 1.

---

* This work was supported by the U.S. Department of Energy, Office of Nuclear Physics, under Contract No. DE-AC02-06CH11357 for ANL and by Jefferson Science Associates, LLC under U.S. DOE Contract No. DE-AC05-06OR23177

† corresponding author: brahim@anl.gov.

ISBN: 978-3-95450-223-3 ISSN: 2673-7000 doi:10.18429/JACoW-NAPAC2019-TUZBA4

INTERACTION REGION MAGNETS FOR FUTURE ELECTRON-ION COLLIDER AT JEFFERSON LAB *

Renuka Rajput-Ghoshal†, Chuck Hutton, Fanglei Lin, Tim Michalski,
Vasiliy Morozov and Mark Wiseman
Thomas Jefferson National Accelerator Facility (TJNAF), Newport News, VA, USA

Abstract

The Jefferson Lab Electron Ion Collider (JLEIC) is a proposed new machine for nuclear physics research. It uses the existing CEBAF accelerator as a full energy injector to deliver 3 to 12 GeV electrons into a new electron collider ring. An all new ion accelerator and collider complex will deliver up to 200 GeV protons. The machine has luminosity goals of 10^{34} cm^{-2} sec^{-1}. The whole detector region including forward detection covers about 80 meters of the JLEIC complex. The interaction region design has recently been optimized to accommodate 200 GeV proton energy using conventional NbTi superconducting magnet technology. This paper will describe the requirements and preliminary designs for both the ion and electron beam magnets in the most complex 34.5 m long interaction region (IR) around the interaction point (IP). The interaction region has over thirty-four superconducting magnets operating at 4.5K; these include dipoles, quadrupoles, skew-quadrupoles, solenoids, horizontal and vertical correctors and higher order multipole magnets. The paper will also discuss the electromagnetic interaction between these magnets.

INTRODUCTION

The Jefferson Lab Electron Ion Collider (JLEIC) is a proposed new machine that uses the existing CEBAF (Continuous Electron Beam Accelerator Facility) as an electron injector, ion source linac, figure of eight low energy ion booster, figure of eight high energy ion booster and a unique figure of eight shape for the collider rings [1]. The machine design was updated recently in order to achieve higher energy and reduce the risk in the superconducting magnets [2, 3]. The original machine design was to deliver between 15 and 65 GeV center of mass energy collisions between electrons and nuclei. The updated design is to deliver up to 100 GeV center of mass energy collisions. The electron and ion rings intersect at the interaction point (IP) and the region around IP is called the interaction region (IR). The interaction region contains a full acceptance detector built around a detector solenoid. This paper focuses only on the magnets in the IR (and excludes the central solenoid and detector dipoles). The IR layout is shown in Fig. 1. A preliminary design was done for all the IR magnets for the earlier machine design parameters [4]. Some of the quadrupoles in that design had high peak fields in the coils, and the coil design assumed Nb_3Sn conductor. The new improved machine design reduces the risk for the IR magnets by lowering the peak field in the coils thereby allowing use of NbTi superconductor for the magnet designs.

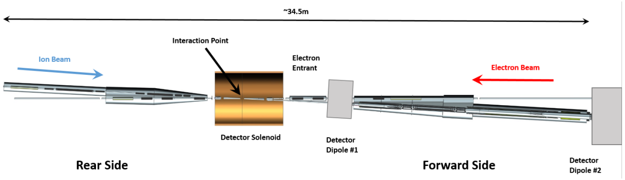

Figure 1: Interaction region layout.

MAGNET REQUIREMENTS AND DESIGN

The IR magnet design specifications are given in Table 1. Preliminary designs have been completed to the first order for all the IR magnets. The main purpose of this initial design work is to optimize the coil geometry to calculate the peak field in the coils and to make sure all the magnets fit within the available longitudinal space. The magnet geometry has not yet been optimized to minimize higher order harmonics. Magnet-magnet interactions for the most challenging locations have been studied; this will be extended to all the magnets in the next phase of the project. The peak field in the coils is less than 7 T for all magnets, which is within the limit for NbTi magnets operating at 4.5K. All magnets for both ion and electron beam lines are based on cold bore designs. This is done to lower the peak field in the coils and reduce radial space requirements. The design summary for all the magnets is also summarized in Table 1. The higher order multipole corrector magnets are not included in this table, as the requirements for these magnets are still being finalized. SIMULIA Opera FEA by Dassault Systemes [5] is used for all electromagnetic simulations, and the optimizer module is used for optimizing the coil geometry.

Electron Beam IR Quadrupole

The electron quadrupole and skew quadrupole have reduced field strength in the new layout; therefore, the electron quadrupole design has been kept the same. All the electron quadrupoles and skew quadrupoles have the same design as of now with a main quadrupole strength of 45 T/m and 9.5 T/m for the skew quadrupole strength. The peak field in the electron quadrupole is approximately 3.5 T [4]. These quadrupoles will be optimized further for longitudinal space requirements and the peak field in the coils.

---

* Work supported by Jefferson Science Associates, LLC under U.S. DOE Contract No. DE-AC05-06OR23177.

†Corresponding author: renuka@jlab.org

ISBN: 978-3-95450-223-3 ISSN: 2673-7000 doi:10.18429/JACoW-NAPAC2019-TUZBA5

ALGORITHMS USED IN ACTION AND PHASE JUMP ANALYSIS TO ESTIMATE CORRECTIONS TO QUADRUPOLE ERRORS IN THE INTERACTION REGIONS OF THE LHC

J. F. Cardona[*], Universidad Nacional de Colombia, Bogotá, Colombia

Abstract

Action and phase jump analysis has been used to estimate corrector strengths in the high luminosity interaction regions of the LHC. It has been proven that these corrections are effective to eliminate the beta-beating that is generated in those important regions and that propagates around the ring. More recently, it was also shown that the beta-beating at the interaction point can also be suppressed by combining *k*-modulation measurements with action and phase jump analysis. Applying this technique to the re-commissioning of the LHC in 2021 requires a good knowledge of the software developed for action and phase jump analysis over the years. In this paper a detailed description is made of all the modules that are part of this software and the corresponding algorithms.

INTRODUCTION

A one-turn particle trajectory in a linear lattice is conventionally described by

$$z(s) = \sqrt{2J_c\beta_r(s)}sin(\psi_r(s) - \delta_c), \qquad (1)$$

where z represents the distance between the transverse position of the particle respect to the design trajectory, s is the the longitudinal position of the particle around the ring, J_c and δ_c are the action constants, and finally β_r and ψ_r correspond to the lattice functions with errors. These lattice functions can also be expressed as

$$\begin{aligned} \beta_r &= \beta_n + \Delta\beta, & (2)\\ \psi_r &= \psi_n + \Delta\psi, & (3) \end{aligned}$$

where β_n and ψ_n are the nominal lattice functions while $\Delta\beta$ and $\Delta\psi$ correspond to the beating produced by the magnetic errors in the accelerator. A one-turn particle trajectory can also be described by

$$z(s) = \sqrt{2J(s)\beta_n(s)}sin(\psi_n(s) - \delta(s)) \qquad (4)$$

In this case, J and δ change along the axial coordinate in accordance with the magnetic errors present around the ring, resulting in what is called Action and Phase Jump (APJ) Analysis [1]. This approach has proven to be effective in estimating magnetic errors in the Interaction Regions (IRs) of high energy accelerators [1–3]. Under APJ analysis, actions and phases are inferred from one-turn beam trajectory and the nominal lattice functions. Plots of these action and phases as function of the longitudinal coordinate s reveals significant jumps at the IRs. These jumps can be used to estimate how the strength of some of the quadrupole of the Interaction Region should be changed to suppress the jump. This is done by first estimating the equivalent magnetic deflection or kick that all the quadrupole errors of the IR would make in the beam trajectory. Then, analytical expressions are used to find the corresponding corrections. The IRs are mainly formed by two sets of three quadrupoles called triplets, one located to the left of the IP and the other to the right. The first scheme of correction estimated with APJ analysis used only two quadrupoles of the IR, one for each triplet [3]. The effectiveness of this correction was tested verifying that the jumps in action and phase were significantly reduced after applying the correction. The effectiveness of this correction was also tested through the beta-beating. This test revealed that the 2-corrector scheme is effective in suppressing the beta-beating around the ring but not at the Interaction Point (IP). This problem was solved with a new scheme of correction that uses the variables associated to *k*-modulation measurements as shown in [4]. Different to the previous scheme of correction, this new scheme of correction uses four quadrupoles per IR. Description of *k*-modulation measurements and their associated variables can be found in [5].

BEAM TRAJECTORIES FROM TURN-BY-TURN DATA

Beam used for APJ analysis consist of only one bunch, which has been excited to large amplitude oscillations with a special device called the AC dipole. The bunch centroid is measured with the 500 dual Beam Position Monitors (BPMs) of the LHC for 6600 turns. All this data is stored in an ASCII file called a Turn-By-Turn (TBT) data set, which allows to draw a trajectory for every turn (simple trajectory) as seen in Fig. 1. In this paper, average trajectories are used rather than simple trajectories. The average trajectories are obtained by averaging simple trajectories of certain selected turns. The most common average trajectory is the closed orbit, which is obtained after averaging all the 6600 simple trajectories stored in a TBT data set. Other average trajectories are built so that they have maximum values of at specific points of the accelerator where the errors want to be estimated. Those average trajectories are called average max trajectories.

MODULES OF THE APJ SOFTWARE

The software is divided in several modules, which are executed according to the flowchart shown in Fig. 2. Each module performs a specific task as explained below.

---

[*] jfcardona@unal.edu.co

REACHING LOW EMITTANCE IN SYNCHROTRON LIGHT SOURCES BY USING COMPLEX BENDS*

G.M. Wang†, J. Choi, O.V. Chubar, Y. Hidaka, T.V. Shaftan, S.K. Sharma, V.V. Smaluk,
C.J. Spataro, T. Tanabe, Brookhaven National Laboratory, Upton, NY, USA
N.A. Mesentsev, Budker Institute of Nuclear Physics, pr. Lavrentyeva 30, Novosibirsk, Russia

Abstract

All modern projects of low-emittance synchrotrons follow Multi-Bend Achromat approach. The low emittance is realized by arranging small horizontal beta-function and dispersion in the bending magnets, the number of which varies from 4 to 9 magnets per cell. We propose an alternative way to reach low emittance by use of a lattice element that we call "Complex Bend", instead of regular dipole magnets. The Complex Bend is a new concept of bending magnet consisting of a number of dipole poles interleaved with strong alternate focusing so as to maintain the beta-function and dispersion oscillating at very low values. The details of Complex Bend, considerations regarding the choice of optimal parameters, thoughts for its practical realization and use in low-emittance lattices, are discussed.

INTRODUCTION

Modern synchrotron lattice sources are competing intensively to increase X-ray brightness and, eventually, approach the diffraction limit, which sets the final goal of lattice emittance. The trend of minimizing the emittance in modern synchrotrons translates into the reduction of dispersion and beta-functions in their lattice dipoles. Most recent facility upgrades employ MBA lattices [1-5], i.e., introduce a number of dipoles with strong focusing quadrupoles interspersed, which helps maintain lattice functions at smaller values, compared with conventional (Double-Bend) DBA or (Triple-Bend) TBA lattice solutions. The number of dipoles per machine period may vary between 5 (MAX-4) to 19 (MAX-4 upgrade) for the latest designs [6].

In this paper we propose another optics solution to reach ~20 pm-rad low emittance, using a lattice element that we named "Complex Bend" [7, 8] and its evolution "Complex Bend II" [9, 10], which reduces its overall length, lower the quadrupole strength and, therefore, to free up more space in the storage ring lattice available for installing lattice magnets, diagnostics and Insertion Devices. With these solutions we designed the Complex Bend element, which is about the same length as conventional dipole at a lower gradient (we constrained ourselves to stay at or below 250 T/m and the bore diameter of not less than 1 cm). Then we applied the developed solution to a model ring lattice with 18.7 pm-rad emittance, taking NSLS-II ring geometry as the reference.

COMPLEX BEND

It is customary to relate ring emittance with the number of ring dipoles as:

$$\varepsilon_x = F\frac{E^2}{J_x N_d^3} \tag{1}$$

where F is a function of ring lattice, E is the beam energy, J_x is horizontal partition number and N_d is the number of dipoles in the ring. In MBA lattice, many facilities increase N_d and distribute dipoles along arc.

We propose to substantially decrease the beam emittance by converting number of dipoles with the same field polarity, N_p, into "one element" and keep the bending element, N_d, the same as 3rd generation synchrotron light source ring. Overall, the total number of dipole poles becomes $(N_d N_p)$. This will preserve substantial room for insertion devices and associated lattice elements.

Figure 1 shows the concept of the Complex Bend. It is a bending element consisting of dipole poles, interleaved with strong focusing and defocusing quadrupole poles.

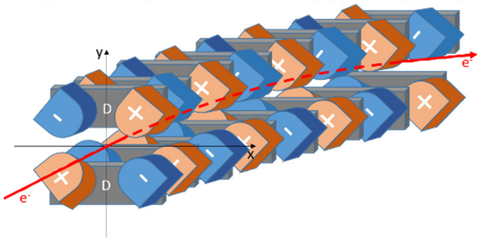

Figure 1: Cartoon illustrating the concept of Complex Bend.

The element provides distributed focusing and bending of the particle beam (Fig. 2). A single cell is featured by the betatron phase advance, which depends on the combination of field gradients in quadrupole and field in the dipole magnets, their lengths and the distance between the consecutive poles.

We approximated the beta function β_x and dispersion η for one cell of Complex Bend with the following expression:

$$\begin{bmatrix}\beta_x(s)\\ \eta(s)\end{bmatrix} \approx \begin{bmatrix}\bar{\beta}_x\\ \bar{\eta}\end{bmatrix} + \begin{bmatrix}\Delta\beta_x\\ \Delta\eta\end{bmatrix}\cdot\cos(k_{CB}s), \tag{2}$$

which is quite accurate for the relatively small phase advances that we consider in our cases of interest. Here $L_{CB} = 2(L_Q + L_B + 2L_D)$ is the length of the cell,

---

*This manuscript has been authored by Brookhaven Science Associates, LLC under Contract No. DE-AC02-98CH10886 with the U.S. Department of Energy

† gwang@bnl.gov

PRECISE BEAM VELOCITY MATCHING FOR THE EXPERIMENTAL DEMONSTRATION OF ION COOLING WITH A BUNCHED ELECTRON BEAM *

S. Seletskiy †, M. Blaskiewicz, K.A. Drees, A.V. Fedotov, W. Fischer, D. M. Gassner, R.L. Hulsart, D. Kayran, J. Kewisch, K. Mernick, R.J. Michnoff, T.A. Miller, G. Robert-Demolaize, V. Schoefer, H. Song, P. Thieberger, P. Wanderer
Brookhaven National Laboratory, Upton, USA

Abstract

The first ever electron cooling based on the RF acceleration of electron bunches was experimentally demonstrated on April 5, 2019 at the Low Energy RHIC Electron Cooler (LEReC) at BNL. The critical step in obtaining successful cooling of the Au ion bunches in the RHIC cooling sections was the accurate matching of average longitudinal velocities of electron and ion beams corresponding to a relative error of less than 5e-4 in the e-beam momentum. Since the electron beam kinetic energy is just 1.6 MeV, measuring the absolute e-beam energy with sufficient accuracy and eventually achieving the electron-ion velocity matching was a nontrivial task. In this paper we describe our experience with measuring and setting the e-beam energy at LEReC.

LEREC DESCRIPTION

LEReC [1, 2] is the world's first electron cooler utilizing RF based acceleration of electron bunches. It is the first cooler applied directly to the ions in the collider at top energy and it is the first cooler that utilizes the same electron beam to cool ion bunches in two collider rings.

The LEReC accelerator consists of a 400 keV photo-gun followed by the SRF Booster, which accelerates the beam to 1.6-2.6 MeV, the transport beamline, the merger that brings the beam to the two cooling sections (in the Yellow and in the Blue RHIC rings), the cooling sections (CSs) separated by the 180° bending magnet and the extraction to the beam dump. The LEReC also includes two dedicated diagnostic beamlines: the DC gun test line and the RF diagnostic beamline. The LEReC layout is schematically shown in Fig. 1.

The friction force acting on the ion in the cooling section is given by [3, 4]:

$$\vec{F} = -\frac{4\pi n_e e^4 Z^2}{m_e} L_C \int \frac{\vec{v_i}-\vec{v_e}}{|\vec{v_i}-\vec{v_e}|^3} f(v_e) d^3 v_e \qquad (1)$$

where e and m_e are electron charge and mass, n_e is electron bunch density in the beam frame, Z is ion charge number, L_C is Coulomb logarithm, which for LEReC is ~10, v_e and v_i are respectively electron and ion velocities in the beam frame and $f(v_e)$ is the electron bunch velocity distribution.

LEReC design parameters are chosen so that electron bunch transverse and longitudinal root mean square (rms) velocity spread is equal to respective ion velocity spread. For such a choice, ions on average experience linear cooling force in both transverse and longitudinal dimensions.

Requirements to electron bunch relative momentum spread and angular spread in the laboratory frame are [1]:

$$\sigma_\delta = 5 \cdot 10^{-4}; \quad \sigma_\theta = 130\ \mu\text{rad} \qquad (2)$$

It is also important to match electron relativistic γ-factor relative to ion γ with accuracy better than 5e-4 to observe and optimize the cooling of ion bunches.

Electron bunches satisfying conditions (2) were obtained during LEReC accelerator commissioning in 2018 [5].

Longitudinal component of force (1) has a relatively weak dependence on electron angular spread, which is affected by the presence of the ion beam in the CS. Since the electron bunch momentum spread is satisfying (2) regardless of ions presence, it was enough to match the electron and ion beam γ-factors to observe the longitudinal cooling.

The lowest e-beam energy required for LEReC operation is 1.6 MeV, which means that electron beam absolute energy must be measured and set with an accuracy of 0.8 keV.

We had planned and implemented a three-step process for electron beam γ-matching to the ion beam.

First, to set the absolute energy of the electron beam with an accuracy better than 5·10-3 we utilized the 180° bending magnet as a spectrometer.

Second, to check and fine-tune γ-matching we used the recombination monitor and e-beam energy scan performed with small steps.

Finally, we performed the energy scan with even finer steps to obtain and optimize the longitudinal beam cooling.

LOW ENERGY HIGH ACCURACY SPECTROMETER

The 180° bend is located between the first and the second LEReC cooling sections.

It is designed to have a bending radius $\rho_0 = 0.35$ m. The entrance to the magnet is equipped with two beam position monitors (BPMs) and its exit is equipped with one BPM.

The field of the U-turn bending magnet was mapped in +/-20 mm range around the design beam trajectory at 200 G, 240 G and 300 G flat-top fields corresponding respectively to 1.6 MeV, 2 MeV and 2.6 MeV electron beam energies [6]. The field was measured with a probe combining Hall sensor and a customized high-accuracy NMR probe capable of measuring fields as low as 140 G [7]. The resulting field map had a required accuracy of 0.02 G.

In the final U-turn bend setup at its destination in the RHIC tunnel the same probe was installed at a known, and well-mapped, fixed location in the uniform region of the

---

* Work supported by the US Department of Energy under contract No. DE-SC0012704

† seletskiy@bnl.gov

SPACE CHARGE STUDY OF THE JEFFERSON LAB MAGNETIZED ELECTRON BEAM*

S.A.K. Wijethunga†[1], J.R. Delayen[1], F.E. Hannon[2], G.A. Krafft[1,2], M.A. Mamun[2], M. Poelker[2],
R. Suleiman[2], S. Zhang[2],
[1]Old Dominion University, Norfolk, VA 23529, USA
[2]Thomas Jefferson National Accelerator Facility, Newport News, VA 23606, USA

Abstract

Magnetized electron cooling could result in high luminosity at the proposed Jefferson Lab Electron Ion Collider (JLEIC). In order to increase the cooling efficiency, a bunched electron beam with high bunch charge and high repetition rate is required. We generated magnetized electron beams with high bunch charge using a new compact DC high voltage photo-gun biased at -300 kV with alkali-antimonide photocathode and a commercial ultrafast laser. This contribution explores how magnetization affects space charge dominated beams as a function of magnetic field strength, gun high voltage, laser pulse width and laser spot size.

INTRODUCTION

The proposed Jefferson Lab Electron Ion Collider (JLEIC) must provide ultra-high collision luminosity ($10^{34}\ \mathrm{cm}^{-2}\mathrm{s}^{-1}$) to achieve the promised physics goals and this necessitates small transverse emittance at the collision point. Emittance growth can be reduced by the process called electron cooling, where the electron beam with temperature T_e is co-propagated with the ion beam traveling at the same velocity but with temperature T_i where $T_i > T_e$. The ion beam is “cooled” as a result of the Coulomb collisions and the transfer of thermal energy from ions to the electrons. Thermal equilibrium is reached when both the particles have the same transverse momentum.

The cooling rate can be significantly improved using a “magnetized electron beam” where this process occurs inside a solenoid field which forces electrons to travel with small helical trajectories that help to increase the electron-ion interaction time while suppressing the electron-ion recombination [1, 2]. However, the fringe radial magnetic field at the entrance of the solenoid creates a large additional rotational motion which adversely affects the cooling process inside the solenoid. In order to overcome this effect, the electron beam is created inside a similar field but providing a rotating motion in the opposite direction, so that the fringe field effects at the exit of the photo-gun and at the entrance of the cooling solenoid exactly cancel.

In order to have efficient cooling at JLEIC, the cooling electron beam must have high bunch charge, high repetition rate, and low temperature (low emittance and low energy spread). The high bunch charge requirement results in large space charge forces. In this paper, we present systematic measurements designed to study the space charge effect in magnetized electron beam especially, how magnetization affect the space charge current limitations as a function of gun high voltage, laser pulse width and laser spot size.

EXPERIMENTAL SETUP

The experimental beamline consists of gun high voltage chamber, photocathode preparation chamber, cathode solenoid, green laser, three fluorescent YAG screens, harp, few focusing solenoids and beam dump. A schematic diagram of the beamline is shown in Fig. 1.

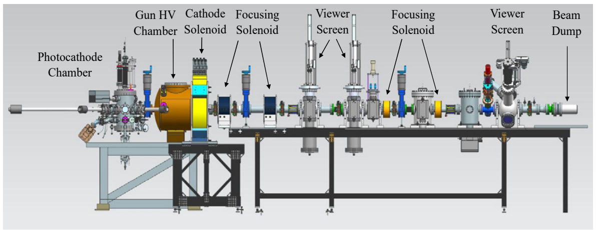

Figure 1: The diagnostic beamline.

The compact gun high voltage chamber includes an inverted insulator and spherical cathode electrode operating at or below -300 kV. The cathode-anode gap is 9 cm and the anode aperture is 2 cm. A load-lock type photocathode deposition chamber was installed behind the gun high voltage chamber to manufacture the photocathodes. For this experiment a bialkali-antimonide (K_2CsSb) photocathode made on GaAs substrate was used. The active area was limited to 3 mm radius and the typical quantum efficiency (QE) was in the range of 5-8% with 523 nm laser. A commercial ultrafast laser with pulse duration less than 0.5 ps, 20 µJ pulse energy, operating at 50 kHz pulse repetition rate and 1030 nm wavelength (NKT Origami) was used as the laser source for the experiment. The IR beam was converted to 515 nm using a BBO crystal. The laser spatial and temporal profiles were Gaussian. To explore parameter space, the laser beam size at the photocathode was varied and the temporal pulse width was varied using a pulse stretcher built with diffraction gratings. The magnetic field at the photocathode was provided by a solenoid magnet designed to fit at the front of the gun chamber, 0.2 m from the

---

* Authored by Jefferson Science Associates, LLC under U.S. DOE Contract No. DE-AC05-06OR23177. Additional support comes from Laboratory Directed Research and Development program. The U.S. Government retains a non-exclusive, paid-up, irrevocable, world-wide license to publish or reproduce this manuscript for U.S. Government purposes.
† wwije001@odu.edu

TRANSVERSE ION BEAM EMITTANCE GROWTH DUE TO LOW FREQUENCY INSTABILITIES IN MICROWAVE ION SOURCE PLASMA

C. Mallick[1, 2, †] M. Bandyopadhyay[1,2,3] and R.K. Kumar[1,2]
[1]Institute for Plasma Research (IPR), Gandhinagar, Gujarat, India
[2]Homi Bhabha National Institute (HBNI), Anushaktinagar, Mumbai, Maharashtra, India
[3]ITER-India, Institute for Plasma Research, Gandhinagar, Gujarat, India

Abstract

The microwave ion source plasma is accompanied by the generation of low frequency (LF) plasma instabilities (PI). The signature of it can also be visible in high current ion beam required for any accelerator applications. These LFs may affect the profile of the ion beam in transverse phase-space. These issues are investigated by measuring the emittance of beam. The beam oscillations are extracted from the transverse emittance data by carrying out Fast Fourier Transform (FFT) analysis of it. The PI frequencies are identified in the measured electromagnetic emission from the plasma by a microwave spectrum analyzer, in which these frequencies appeared as sidebands around the launched frequency 2.45 GHz. The PI components are also visible in the FFT spectra of an Allison beam emittance scanner data. The oscillations in the extracted beam may be generated because of the plasma perturbations (or instabilities) by drift wave frequency and due to the presence multiple closely-spaced cavity modes around 2.45 GHz. The measured beam emittance (rms-normalized) in horizontal and vertical phase-space varies from 0.002-0.098 π mm mrad and 0.004-0.23 π mm mrad respectively due to increase of MW power from 250 W-700 W. The PI induced beam oscillation may be the reason behind such broad transverse emittance growth.

INTRODUCTION

Maintaining a least emittance growth of the ion beam during its transport through a low energy beam (LEBT) transport system is essential to minimize the beam loss at the mouth of an accelerator. One of the initial starting sources of beam emittance growth may hails from the plasma perturbations of drift wave frequency range, present in the ion source itself. In addition, multiple close-frequency heating (MCFH) in the Electron Cyclotron Resonance (ECR) ion source can also perturb plasma that may cause more growth in the beam emittance compared to the previous case. The MCFH is a well-established method in terms of production of highly intense and stable higher-charge-state ion beams [1-3]. This type of heating is also useful in mitigating the plasma instability [4]. The dynamics of perturbed plasma particles (electron and ion) is two-dimensional in their velocity phase-space if the frequency gap between the different combinations of heating frequency pairs is more than 1 GHz [4]. Under this condition, the particles' diffusion becomes similar to the case of single frequency heating (SFH). Hence, the MFH in which the frequency differences are in the GHz range shows no significant impacts on the ion beam emittance [5]. On the other hand, in the case of MCFH, (frequency gap ~ few 100's of MHz), the plasma may be perturbed significantly mainly in the sheath region. The dynamics of perturbed plasma particles is described by its diffusion under four-dimensional velocity phase-space [4 and 6]. As a result, the perturbed particles' distribution in four dimensional phase-spaces may affect the transverse beam emittance. In case of SFH, the electron's diffusion in velocity phase-space is remained as two dimensional in velocity phase-space [4]. It was demonstrated experimentally that two close-frequency heating (TCFH) is capable of suppressing the plasma kinetic instabilities and improving the confinement time of plasma electrons [4-7]. Recently, a less intense but stable ion beam compared to the SFH was produced experimentally [4 and 7] using MFH. The study related to the dependence of ion beam emittance on the instabilities generated due to the plasma perturbations is still relatively unexplored in the research community. In the present study, the impacts of plasma instabilities on the ion beam oscillations and its transverse emittance growth is investigated.

The present MW ion source supports multiple cavity dependent resonant modes [8]. Some of them are excited in plasma having equivalent intensity with respect to launched MW 2.45 GHz. The presence of these multiple close frequency modes around the launched one in this plasma filled cavity may perturb the MW E-field distributions due to the shifting of MW E-fields corresponding to one mode to another mode or vice versa [9]. This can yield a different steady state features of plasma. The physics associated with multiple closely-spaced excited modes may be considered as similar to the case of MCFH in an ion source. During the propagation of those excited MW modes, a fraction of every MW's energy is reflected off their corresponding critical plasma density layers. The reflected MW mode may change its polarization and convert into another mode near a mode conversion layer. The presence of excited closely-spaced MW modes may also perturb the E-field profiles within the sheath region. It is well known through analytics and experiments that the existence of strong inhomogeneous electric field within the plasma-sheath layer is associated

---

[†] Chinmoy.mallick@ipr.res.in

ISBN: 978-3-95450-223-3 ISSN: 2673-7000 doi:10.18429/JACoW-NAPAC2019-TUZBB6

NONLINEAR TUNE-SHIFT MEASUREMENTS IN THE INTEGRABLE OPTICS TEST ACCELERATOR*

S. Szustkowski†, S. Chattopadhyay[1], Northern Illinois University, DeKalb, IL, USA
A. Romanov, A. Valishev, Fermi National Accelerator Laboratory, Batavia, IL, USA
N. Kuklev, The University of Chicago, Chicago, IL, USA
[1]also at Fermi National Accelerator Laboratory, Batavia, IL, USA

Abstract

The first experimental run of Fermilab's Integrable Optics Test Accelerator (IOTA) ring aimed at testing the concept of nonlinear integrable beam optics. In this report we present the preliminary results of the studies of a nonlinear focusing system with two invariants of motion realized with the special elliptic-potential magnet. The key measurement of this experiment was the horizontal and vertical betatron tune shift as a function of transverse amplitude. A vertical kicker strength was varied to change the betatron amplitude for several values of the nonlinear magnet strength. The turn-by-turn positions of the 100 MeV electron beam at twenty-one beam position monitors around the ring were captured and used for the analysis of phase-space trajectories.

INTRODUCTION

In Ref. [1], V. Danilov and S. Nagaitsev proposed a nonlinear accelerator lattice, which leads to integrable and stable nonlinear motion. This introduces large betatron tune spread where bounded motion can fill a large phase space. The nonlinear element has a special elliptic-potential, that is time-independent, which can be expressed in elliptic coordinates (ξ, η) as:

$$U(\xi,\eta) = \frac{f(\xi) + g(\eta)}{\xi^2 - \eta^2}, \tag{1}$$

where f and g are arbitrary functions. In order for the potential to satisfy the Laplace equation these functions are expressed as:

$$\begin{aligned} f_2(\xi) &= \xi\sqrt{\xi^2 - 1}[d + t\,\mathrm{acosh}(\xi)], \\ g_2(\eta) &= \eta\sqrt{1 - \eta^2}[b + t\,\mathrm{acos}(\eta)], \end{aligned} \tag{2}$$

where b, d, and t, are arbitrary constants. In order to have the lowest multipole expansion term to be a quadrupole, $d = 0$ and $b = \frac{\pi}{2}t$. The constant t is then the nonlinear potential strength. To determine the maximum attainable betatron tune spread at small amplitudes, a multipole expansion of the potential can be done. The small amplitude betatron tune can then be expressed as [2]:

$$\begin{aligned} Q_x &= Q_0\sqrt{1 + 2t}, \\ Q_y &= Q_0\sqrt{1 - 2t}, \end{aligned} \tag{3}$$

where Q_0 is the unperturbed, linear-motion, working point tune. Thus for small amplitude, stable linear motion, the range of strength values need to be $-0.5 < t < 0.5$. There are regions of the phase space that exhibit bounded nonlinear motion for larger t values as well [3].

The IOTA ring, see Fig. 1, was specifically built to experimentally demonstrate integrable nonlinear optics predicted by Danilov and Nagaitsev. The experiment will use a 150 MeV, 'pencil-like', electron beam of RMS emittance 40 nm. The beam will map out the dynamic aperture by kicking the beam at various amplitudes. The key goal of the experiment is to demonstrate large betatron tune spread of $\Delta Q_y > 0.10$, with using a special elliptic-potential magnet, without beam loss and degradation of dynamical aperture [4].

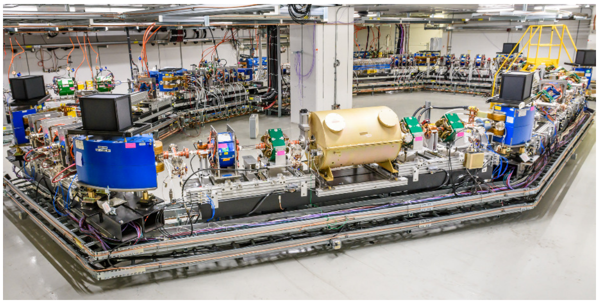

Figure 1: The Integrable Optics Test Accelerator (IOTA) ring.

EXPERIMENTAL SETUP

Nonlinear Magnet

The nonlinear magnet and vacuum chamber were designed and manufactured by RadiaBeam Technologies. Due to the complexity of having a varying aperture, there are eighteen individual magnets that scales as the square root of β-function along the beam path. All eighteen magnets were required to have a 50 μm alignment of the magnetic axes. Each element magnetic field is also required to be within one percent of the theoretical model [5].

The magnetic centers of each of the 18 magnets were aligned to ±50 μm using a stretch copper-beryllium wire [6]. To verify the alignment of the nonlinear elements, beam

---

* Fermilab is operated by the Fermi Research Alliance, LLC, under Contract No. DE-AC0207CH11359 with the US Department of Energy. This work is supported by the Office of High Energy Physics General Accelerator Research and Development (GARD) Program.

† sszustkowski1@niu.edu

ISBN: 978-3-95450-223-3 ISSN: 2673-7000 doi:10.18429/JACoW-NAPAC2019-TUPLM01

EXPERIMENTAL STUDIES OF RESONANCE STRUCTURE DYNAMICS WITH SPACE CHARGE*

L. Dovlatyan†, T.M. Antonsen Jr., B.L. Beaudoin, S. Bernal , I. Haber, D. Sutter, G.D. Wyche
University of Maryland, College Park, MD, USA

Abstract

Space charge is one of the fundamental limitations for next generation high intensity circular accelerators. It can lead to halo growth as well as beam loss, and affect resonance structure in ways not completely understood. We employ the **U**niversity of **M**aryland **E**lectron **R**ing (UMER), a circular 10 keV storage machine, to experimentally study the structure of betatron resonances for beams of varying degrees of space charge intensity. A grid based tune scan experimental technique is employed and results are compared to computer simulations using the WARP code.

INTRODUCTION

In conventional circular accelerators the design goal of a focusing magnet system is to have a restoring force that varies linearly with the distance from the system center. In actuality several resonances will be driven by imperfections in the machine. The resonances excite other degrees of freedom of the beam motion which can cause instabilities, amplitude growth, and ultimately particle loss. Many of these resonances limit the beam intensity and luminosity that can be physically achieved.

As new machines aim to go to ever higher space charge intensity [1], it is clear that impacts of coulomb interactions on resonance structure dynamics must be better understood. Work has been done in generating theories and simulations of potential behavior, but not much in the way of experimental verification on an accelerator [2–5].

An ongoing experimental program at the University of Maryland Electron Ring (UMER) is focused on studying resonance behavior over a broad range of space charge intensities. UMER has the unique ability to inject a beam with a range of intensities varying from an emittance dominated 150 µA beam up to a space charge dominated 80 mA beam with a typical tune depression of 0.2. Using a set of numerical and hardware tools, we scan and map a large range of tune space revealing nonlinear resonance structure with different beam intensities.

EXPERIMENTAL SETUP AND TOOLS

Assuming a simple hard edge model of a FODO lattice, a set of equations can be derived through matrix multiplication that relate the change in phase advance to the focusing and defocusing strengths of the quadrupoles [6]. Expanding these equations to second order gives an approximate form relating the tunes to quadrupole strengths:

$$(Q_x, Q_y) = C_0 \pm C_x k_x \mp C_y k_y + k_x k_y C_{xy} = f(k_x, k_y) \quad (1)$$

where the constants C_x, C_y, C_{xy} are functions of the effective length of quadrupoles, k_x is the strength of focusing quadrupoles (QF), and k_y is the strength of defocusing quadrupoles (QD). By varying the magnet strengths by Δk, tune space can be measured and mapped over a range of values. See visual representation in Figure 1.

$$\begin{aligned}(Q_x, Q_y)_{ij} &= f(k_x + i\Delta k, k_y + j\Delta k)\\ i,j &= 1,2,\dots,M,\ \ 1,2,\dots,N\end{aligned} \quad (2)$$

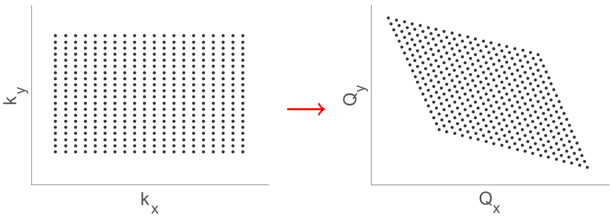

Figure 1: Visual example of mapping from quadrupole strengths to tune space using Eq. (1).

UMER's lattice consists of a FODO design (see Figure 2) which allows the ability to experimentally run a quadrupole scan, where each focusing and defocusing quad is independently controllable. Although measurements can take a long time to complete, the gridded scans can be done in parts over different runs.

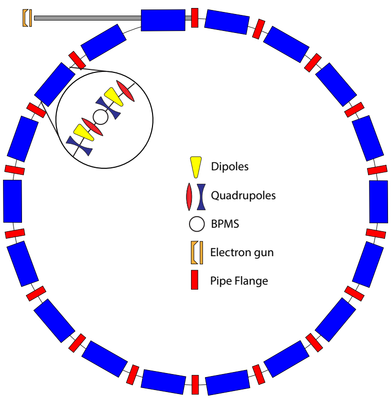

Figure 2: UMER lattice consists of 36 FODO cells around the 11.52 m circumference ring. Each cell contains two quadrupoles and one bending dipole.

---

* Funding for this project provided by DOE-HEP

† Levondov@umd.edu

ADJOINT APPROACH TO ACCELLERATOR LATTICE DESIGN*

T. M. Antonsen†, B. L. Beaudoin, L. Dovlatyan, I. Haber
University of Maryland, College Park, MD, USA

Abstract

Traditionally, accelerator lattices are designed using computer codes that solve the equations of motion for charged particles in both prescribed and self-consistent fields [1, 2]. These codes are run in a mode in which particles enter a lattice region and travel through the lattice for a finite distance. Various figures of merit (FoMs) are evaluated, and the lattice is then optimized by varying the positions and strengths of the focusing elements. [3, 4] This optimization is done in a high dimensional parameter space, requiring multiple simulations of the particle trajectories. We propose to alter the design process using "adjoint" techniques [5]. Incorporation of an "adjoint" calculation of the trajectories and self-fields can, in several runs, determine the gradient in parameter space of a given FoM with respect to all lattice parameters. It includes naturally self-fields and can be embedded in existing codes. The theoretical basis for the method and an application will be presented.

LATTICE OPTIMIZATION

Design and optimization of accelerator lattices is carried out using sophisticated numerical models. [3, 4] The current state of the art codes follow a large number of simulation particles through the combined magnetic fields of the focusing magnets and the electric and magnetic self-fields of the charged simulation particles [1,2]. Typically, particles are followed for a finite distance, their ending coordinates are recorded, and a figure of merit (FoM) quantifying the quality of confinement is assessed. To optimize the FoM the strengths and locations of the focussing magnets are varied and the gradient of the FoM in parameter space is determined. The parameters are then adjusted to increase the FoM and the process is repeated. As there are many parameters describing the lattice, direct determination of the gradient of the FoM is computationally expensive. We present here an alternative (adjoint) approach that reduces dramatically the number of simulations needed to determine the gradient.

ADJOINT APPROACH

The adjoint approach is based on a form of reciprocity implicit in Hamilton's equations and is associated with the symmetry of the governing equations under time reversal [5]. We describe briefly a paraxial, model system here in which charged particles move in a four-dimensional phase space ($\mathbf{x}_\perp, \mathbf{p}_\perp$) in time-independent fields with distance along the path acting as time. After a canonical transformation, the motion is governed by Hamilton's equations with axial momentum serving as the Hamiltonian,

$$\frac{d\mathbf{x}_\perp}{dz} = -\frac{\partial P_z}{\partial \mathbf{p}_\perp}, \quad \frac{d\mathbf{p}_\perp}{dz} = \frac{\partial P_z}{\partial \mathbf{x}_\perp}, \tag{1}$$

where

$$P_z(\mathbf{x}_\perp, \mathbf{p}_\perp, z) = P_{z0} - q\Phi_{eff}(\mathbf{x}_\perp, z)/v_{z0} - \frac{1}{2}|\mathbf{p}_\perp|^2 / P_{z0}. \tag{2}$$

Here $\Phi_{eff}(\mathbf{x}_\perp, z) = \Phi - v_{z0}A_z/c$ includes both electrostatic and magnetic contributions and satisfies the Poisson equation $-\nabla_\perp^2 \Phi_{eff} = 4\pi\gamma_{z0}^{-2}\rho$, where $\rho(\mathbf{x}_\perp, z)$ is the beam charge density. We assume for simplicity that all particles have the same axial velocity. The portion of the potential due to the focussing magnets is imposed through A_z as a boundary condition on the solution for the effective potential.

Let us assume that we have solved the self - consistent nonlinear equations for beam propagation over a distance L. This is our reference solution for which we evaluate the FoM. We now consider two perturbations of this solution. One perturbation, which we label with a superscript 1, is the true solution to the case in which the effective potential at the wall is changed by a small amount reflecting a small change in the focusing magnets. The other perturbation, which we label with superscript 2, is the adjoint solution. The change in symplectic area entering and leaving the region $0<z<L$, for these two perturbations is then expressed (see Ref. 5),

$$\begin{aligned} &\sum_j I_j \left(\delta\mathbf{p}_{j\perp}^{(1)} \cdot \delta\mathbf{x}_{j\perp}^{(2)} - \delta\mathbf{p}_{j\perp}^{(2)} \cdot \delta\mathbf{x}_{j\perp}^{(1)}\right)_0^L \\ &= \frac{q\gamma_{z0}^2}{4\pi} \int dl\, dz \left[\left(\mathbf{n} \cdot \nabla_\perp \delta\phi_{eff}^{(1)}\right) \delta\phi_{eff}^{(2)} - (1 \leftrightarrow 2) \right] \end{aligned}. \tag{3}$$

Here I_j is the current associated with particle j, and the integral on the right is carried out over the transverse boundary where the effective potential is specified. Relation (3) can be regarded as an extension of Green's theorem to include the effect of dynamic charge.

The approach now is to pick conditions on the adjoint solution, with superscript 2, such that Eq. (3) becomes an evaluation of the change in the figure of merit associated with the true solution, the one with superscript 1. As an example, consider a figure of merit based on the coordinates of the particles at the exit plane, $z = L$, $F = \sum_j I_j f(\mathbf{x}_{\perp j}, \mathbf{p}_{\perp j})\big|_{z=L}$ The change in this quantity for the true solution is given by

$$\delta F = \sum_j I_j \left[\delta\mathbf{x}_{\perp j}^{(1)} \cdot \partial f / \partial \mathbf{x}_\perp + \delta\mathbf{p}_{\perp j}^{(1)} \cdot \partial f / \partial \mathbf{p}_\perp \right]_{z=L}. \tag{4}$$

---

* US DoE under DESC0010301
† antonsen@umd.edu

FIRST EXPERIMENTAL OBSERVATIONS OF THE PLASMA-CASCADE INSTABILITY IN THE CeC PoP ACCELERATOR

I. Petrushina[1], Y. Jing[1], V. N. Litvinenko[1], J. Ma, I. Pinayev, K. Shih[1], G. Wang[1] Y.H. Wu[1]
Brookhaven National Laboratory, Upton, NY, USA
[1]also at Stony Brook University, Stony Brook, NY, USA

Abstract

Preservation of the beam quality is important for attaining the desirable properties of the beam. Collective effects can produce an instability severely degrading beam emittance, momentum spread and creating filamentation of the beam. Microbunching instability for beams traveling along a curved trajectory, and space charge driven parametric transverse instabilities are well-known and in-depth studied. However, none of the above include a microbunching longitudinal instability driven by modulations of the transverse beam size. This phenomenon was observed for the first time during the commissioning of the Coherent electron Cooling (CeC) Proof of Principle (PoP) experiment [1, 2]. Based on the dynamics of this instability we named it a Plasma-Cascade Instability (PCI). PCI can strongly intensify longitudinal micro-bunching originating from the beam's shot noise, and even saturate it. Resulting random density and energy microstructures in the beam can become a serious problem for generating high quality electron beams. On the other hand, such instability can drive novel high-power sources of broadband radiation. In this paper we present our experimental observations of the PCI and the supporting results of the numerical simulations.

PLASMA-CASCADE INSTABILITY

The PCI is a microwave instability occurring in beams which propagate in a straight line, and is driven by modulation of the electron beam density via transverse focusing. The resulting modulation of the frequency of the plasma oscillations can result in a strong exponentially growing longitudinal instability.

Let us consider a cold, homogeneous infinite electron beam of density n. A small perturbation of the beam density, $\delta n \ll n$, will cause oscillations within the beam with plasma frequency $\omega_p = \sqrt{\frac{4\pi n e^2}{m}}$, which can be described by the equation of plasma oscillations:

$$\frac{d^2\tilde{n}}{dt^2} + \omega_p^2 \tilde{n} = 0, \text{ with } \tilde{n} = n + \delta n \tag{1}$$

Assume that the beam is propagating through a periodic focusing lattice consisting of 5 solenoids, or 4 focusing cells (see Fig. 1). We will denote the period of this lattice to be $2l$, and the solenoid strengths are defined such that it supports a periodic nature of the beam envelope a. The system of solenoids provides a periodic transverse beam size modulation, which causes a periodic modulation of the beam density. This density modulation will be inversely proportional to the square of the beam radius a, which would lead to a corresponding modulation of the plasma frequency. Modulation of the plasma frequency is shown in green, and its maxima fall onto the minima (waist) of the transverse beam envelope. These plasma oscillations will lead to the subsequent modulation of the longitudinal density of the beam.

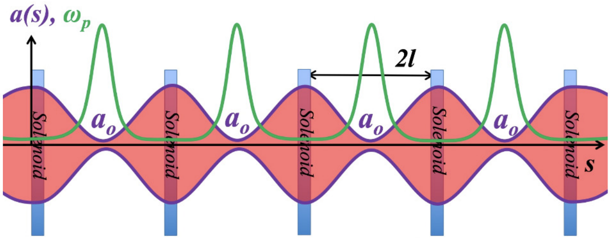

Figure 1: A sketch of four focusing cells with periodic modulations of beam envelope, $a(s)$ (purple with red shading), and the plasma frequency, ω_p (green). Beam envelope has waists, a_0, in the middle of each cell where plasma frequency peaks. Scales are adjusted for illustration purpose.

When the oscillator frequency is modulated with a period close to a half of oscillation period, it results in an exponential growth of oscillation amplitude: the phenomenon known as parametric resonance, which leads to an instability.

The set of two coupled second order differential equations (see Eq. 2) gives a complete description of the PCI: the transverse envelope equation and the equation for the longitudinal density modulation $\tilde{q}_k$.

$$\begin{cases} \dfrac{d^2\hat{a}}{d\hat{s}^2} - \dfrac{k_{\mathrm{sc}}^2}{\hat{a}} - \dfrac{k_\beta^2}{\hat{a}^3} = 0, \\ \dfrac{d^2\tilde{q}_k}{d\hat{s}^2} + \dfrac{2k_{\mathrm{sc}}^2}{\hat{a}^2}\tilde{q}_k = 0 \end{cases} \tag{2}$$

Here we utilize a set of dimensionless parameters inherited from [3], with normalized beam envelope $\hat{a} = \frac{a}{a_0}$, where a_0 is the beam waist; $\hat{s} = \frac{s}{l}$ is the longitudinal distance s normalized to the half of the lattice period. The beam envelope inside the cell is fully determined by the two dimensionless parameters: the space charge, $k_{\mathrm{sc}} = \sqrt{\frac{2}{\beta^3\gamma^3}\frac{I_0}{I_a}\frac{l^2}{a_0^2}}$, and the geometric (or emittance), $k_\beta = \frac{\varepsilon l}{a_0^2}$. Here we denote the beam current as I_0, and $I = \frac{mc^3}{e}$ is the Alfven current.

North American Particle Acc. Conf. NAPAC2019, Lansing, MI, USA JACoW Publishing
ISBN: 978-3-95450-223-3 ISSN: 2673-7000 doi:10.18429/JACoW-NAPAC2019-TUPLM08

EXPERIMENTAL STUDIES OF SINGLE INVARIANT QUASI-INTEGRABLE NONLINEAR OPTICS AT IOTA*

N. Kuklev†, Y.-K. Kim, University of Chicago, Chicago, IL, USA
S. Nagaitsev, A. Romanov, A. Valishev, Fermilab, Batavia, IL, USA

Abstract

The Integrable Optics Test Accelerator is a research electron and proton storage ring recently commissioned at the Fermilab Accelerator Science and Technology facility. Its research program is focused on testing novel techniques for improving beam stability and quality, notably the concept of non-linear integrable optics. In this paper, we report on run 1 results of experimental studies of a quasi-integrable transverse focusing system with one invariant of motion, a Henon-Heiles type system implemented with octupole magnets. Good agreement with simulations is demonstrated on key parameters of achievable tune spread, dynamic aperture, and invariant conservation. We also outline current simulation and hardware improvement efforts for run 2, planned for fall of 2019.

INTRODUCTION

One of key factors limiting beam intensity in modern circular accelerators are collective instabilities, which can be suppressed by amplitude-dependent tune shift through Laundau damping, or in case of slow instabilities by an external damper. Tune spreads are conventionally produced with standalone octupoles distributed around the ring, as is the case for LHC [1]. The disadvantage of using octupoles, and most other nonlinear elements, is the appearance of resonant behavior, leading to chaotic and unbounded motion, and eventual particle loss [2]. Recently, a new nonlinear focusing system was proposed by Danilov and Nagaitsev (DN) [3] that can achieve significant tune spreads without such detrimental effects. To test this concept, the Integrable Optics Test Accelerator (IOTA) storage ring was constructed at Fermilab, and has recently finished its year 1 commissioning and scientific run [4]. In this paper, we discuss the obtained results as well as plans for run 2, scheduled for fall of 2019.

INTEGRABLE OPTICS

The basis of all strong-focusing lattices is a linear system that has no amplitude-dependent tune shifts and is fully integrable - that is, it has the same number of conserved dynamic quantities (Courant-Snyder invariants) as degrees of freedom, and so particle motion is regular for any initial conditions. Due to misalignments, field errors, and the need to correct chromaticity and induce tune spread, real accelerators have significant nonlinearities which break exact CS invariant conservation. Their set of initial conditions with regular motion is limited to a finite region, called the dynamic aperture (DA) - preserving its size is critical for achieving good accelerator performance. Mathematically, transverse particle dynamics can be described by the Hamiltonian

$$H = \frac{1}{2}\left(K_x(s)x^2 + K_y(s)y^2 + p_x^2 + p_y^2\right) + V(x, y, s)$$

with $K_{z=x,y}$ being the linear focusing strength, and $V(x, y, s)$ containing any nonlinear terms (in general dependent on time ($\equiv s$) and transverse (x, y) position). DN approach is to seek solutions for V that yield two invariants of motion and also are implementable with conventional magnets. First invariant comes from appropriate time scaling of $V(x, y)$, such that it becomes a time-independent potential $U(x_N, y_N)$ in normalized coordinates, namely

$$z_N = \frac{z}{\sqrt{\beta(s)}} \qquad p_N = p\sqrt{\beta(s)} - \frac{\beta'(s)}{2\sqrt{\beta(s)}}$$

It is furthermore possible to derive a specific form of $U(x_N, y_N)$ (DN solution) that yields another invariant of motion. Such system is both nonlinear and fully integrable, and its experimental demonstration is the ultimate goal of IOTA. However, this is a difficult task due complex field shape, and extremely small tolerances on optics and field errors [5]. Conveniently, the first nonlinear term in the DN potential multipole expansion is that of a spatially varying octupole, which produces tune shift ΔQ_z quadratic with particle oscillation amplitude, and has potential of the form

$$V(x, y, s) = \frac{\alpha}{\beta(s)^3}\left(\frac{x^4}{4} + \frac{y^4}{4} - \frac{3x^2y^2}{2}\right)$$

where $\alpha(\mathrm{m}^{-1})$ is the strength parameter. Using only this multipole component instead of full DN potential gives a system of so-called Henon-Heiles type [6], first studied in the context of galaxy dynamics, and known to have rich dynamical behavior. It has a single invariant of motion, and is hence only quasi-integrable, with finite DA. However, even a single invariant is highly beneficial for particle stability, and unlike the DN potential, this system is easily implementable with conventional magnet designs and predicted to be highly robust to misalignments and other lattice errors [7], making it the perfect first nonlinear optics system to test at IOTA.

EXPERIMENTAL SETUP

IOTA is a research electron and proton storage ring recently commissioned at Fermilab's Accelerator Science and

---

* This work was supported by the U.S. National Science Foundation under award PHY-1549132, the Center for Bright Beams. Fermi Research Alliance, LLC operates Fermilab under Contract DE-AC02-07CH11359 with the US Department of Energy.

† nkuklev@uchicago.edu

ISBN: 978-3-95450-223-3 ISSN: 2673-7000 doi:10.18429/JACoW-NAPAC2019-TUPLM09

A FAST METHOD TO EVALUATE TRANSVERSE COUPLED-BUNCH STABILITY AT NON-ZERO CHROMATICITY*

R. R. Lindberg[†], Argonne National Laboratory, Lemont, IL, USA

Abstract

We present a dispersion relation that gives the complex growth rate for coupled-bunch instabilities at arbitrary chromaticity in terms of its value at zero chromaticity. We compare predictions of the theory to elegant tracking simulations, and show that there are two distinct regimes to stability depending upon whether the zero chromaticity growth rate is smaller or larger than the chromatic tune shift over the bunch. We derive an approximate expression that is easily solved numerically, and furthermore indicate how the formalism can be extended to describe arbitrary longitudinal potentials.

INTRODUCTION

The standard theory of coupled-bunch instabilities expands the distribution function in orthogonal synchrotron modes [1–3], which are typically then simplified by assuming that the modes do not couple. However, assuming that the modes are independent becomes poor at high chromaticity. We present a dispersion relation that is valid at arbitrary chromaticity and wakefield strength that is relatively easy to solve.

OUTLINE OF THE DERIVATION

Our theory begins with the single particle dynamics including the (linear) transverse betatron motion, the longitudinal focusing, and the chromatic coupling between the two. Our first step is to choose a new set of coordinates that approximately eliminates the chromatic coupling; this coordinate change involves the well-known "head-tail" (or chromatic) phase [4, 5]

$$\frac{\omega_0 \xi}{\alpha_c c} z = \frac{2\pi \xi}{\alpha_c c T_0} z \equiv k_\xi z, \tag{1}$$

where $\omega_0 = 2\pi/T_0$ is the revolution frequency, ξ is the chromaticity, and α_c is the momentum compaction. The head-tail phase arises because the betatron frequency depends linearly on the energy for $\xi \neq 0$, which in turn leads to the betatron phase accumulating a shift that is proportional to the longitudinal coordinate z as it performs synchrotron oscillations. Hence, the quantity $k_\xi \sigma_z$ encapsulates the chromatic tune-shift across a bunch of length σ_z.

Next, we add the long-range transverse wakefield, whose effect we will describe using the distribution function of bunch j $F_j(\mathscr{Z}; s)$, where the phase-space coordinates $\mathscr{Z} = (z, p_z, \Psi, \mathscr{J})$, and $\int d\mathscr{Z}\ F_j = 1$ for N_b bunches (i.e., $0 \leq j \leq N_b - 1$). The dipolar wakefield gives a kick to trailing particles that is proportional to the displacement of the leading particle, and the total kick is obtained by summing the wakefields over all bunches in the ring and over all previous turns. Defining the equilibrium centroid spacing between bunch n and j to be $L_{n,j}$ with $L_{n,j} > 0$ if $j > n$ and $L_{n,j} = -L_{n,j}$ if $j \leq n$, the potential due to the dipole wakefield is

$$\mathscr{V}_D = y \sum_{j=0}^{N_b-1} \frac{e^2 N_j}{\gamma m c T_0} \sum_{\ell=0}^{\infty} \int d\mathscr{Z}'\ y' F_j(\mathscr{Z}'; s - \ell c T_0)$$
$$\times W_D[z - (z' + \ell c T_0 + L_{n,j})].$$

We expand the long-range wakefield W_D assuming it varies slowly over the bunch,

$$\begin{aligned} &\approx \sqrt{\mathscr{J}} \cos(\bar{\Psi} - k_\xi z) \sum_{j=0}^{N_b-1} \frac{2e^2 N_j}{\gamma m c T_0} \\ &\quad \times \sum_{\ell=0}^{\infty} W_D^\beta(-\ell c T_0 - L_{n,j}) \qquad (2) \\ &\quad \times \int d\mathscr{Z}'\ \sqrt{\mathscr{J}'} \cos(\bar{\Psi}' - k_\xi z') F_j(\mathscr{Z}'; s - \ell c T_0) \\ &= \sqrt{\mathscr{J}} \cos(\bar{\Psi} - k_\xi z) \sum_{j=0}^{N_b-1} \mathscr{W}_{n,j}(s), \qquad (3) \end{aligned}$$

where $\mathscr{W}_{n,j}$ is proportional to the kick that particles in bunch n receive due to the centroid displacement of bunch j.

In terms of the transverse and longitudinal actions $(\mathscr{J}, \mathscr{I})$ and their respective angles (Ψ, Φ), the single particle Hamiltonian is

$$\begin{aligned} \mathscr{H} = {}& \mathscr{H}_z(\mathscr{I}) + \frac{\omega_\beta}{c} \mathscr{J} \\ & + \sqrt{\mathscr{J}} \cos[\bar{\Psi} - k_\xi z(\Phi, \mathscr{I})] \sum_{j=0}^{N_b-1} \mathscr{W}_{n,j}(s), \end{aligned} \tag{4}$$

where, the dependence on $\Psi - k_\xi z$ comes from the coordinate change using Eq. (1), $\mathscr{W}_{n,j}$ is the dipolar kick defined by (2)-(3), and $\mathscr{H}_z$ and $z(\Phi, \mathscr{I})$ depends on the rf potential.

The Hamiltonian (4) specifies the particle equations of motion within our model, and to determine multi-bunch collective stability we will consider the coupled set of Vlasov equations associated with $\mathscr{H}$. Each bunch satisfies its own Vlasov equation, and for bunch n we have

$$\begin{aligned} 0 = {}& \frac{\partial F_n}{\partial s} + \frac{\omega(\mathscr{I})}{c} \frac{\partial F_n}{\partial \Phi} + \frac{\omega_\beta}{c} \frac{\partial F_n}{\partial \Psi} \\ & + \sum_{j=0}^{N_b-1} \mathscr{W}_{n,j} \frac{\cos(\Psi - k_\xi z)}{2\sqrt{\mathscr{J}}} \frac{\partial F_n}{\partial \Psi} \\ & + \sum_{j=0}^{N_b-1} \mathscr{W}_{n,j} \sqrt{\mathscr{J}} \sin(\Psi - k_\xi z) \frac{\partial F_n}{\partial \mathscr{J}}, \end{aligned} \tag{5}$$

---

[*] Work supported by U.S. Dept. of Energy Office of Science under Contract No. DE-AC02-06CH11357.

[†] lindberg@anl.gov

ISBN: 978-3-95450-223-3 ISSN: 2673-7000 doi:10.18429/JACoW-NAPAC2019-TUPLM11

BEAM-BEAM DAMPING OF THE ION INSTABILITY*

M. Blaskiewicz, BNL, Upton, NY USA

Abstract

The electron storage ring of the proposed Electron Ion Collider at BNL (BNL EIC) has bunch charges as large as 50 nC and bunch spacings as small as 10 ns. For molecules like carbon monoxide (CO) a dangerous buildup of positive ions is possible and a significant fraction can survive allowable clearing gaps. This beam ion instability (BII) is thus multi-turn and the weak damping required to stop the ion instability with an ideal clearing gap is ineffective here. The beam-beam force is highly nonlinear and a potent source of tune spread. Simulations employing several macro-particles per electron bunch and several ion macro-particles are used to estimate maximum gas densities for CO and H2. A simplified model is introduced and compared with simulations.

INTRODUCTION

Ions have always been a source of difficulty in electron rings [1–15]. As an electron bunch passes through the vacuum, positive ions are generated which act upon subsequently passing electron bunches. During gaps in the electron bunch train ions are partially cleared. In the approximation that ions are cleared to the point of irrelevance the instability is referred to as the fast beam ion instability (FBII). In this approximation the first electron bunch in the train undergoes a free betatron oscillation. It creates ions that act upon following bunches. The second bunch is driven by the first and acts upon subsequent bunches, and so on. Real bunches always undergo a noiselike betatron oscilation of rms amplitude $A_{rms} = \sqrt{\beta(s)\epsilon/N}$ where $\beta(s)$ is the beta function, ϵ is the rms unnormalized emittance, and N is the number of electrons in the bunch. The inverse correlation time of this random process is the betatron frequency spread. This random noise will lead to residual oscillations that are similar to oscillations created by noise in a feedback system and a similar formalism can be applied [4]. In electron storage rings nonlinearities in the restoring force cause the instability to saturate and the FBII usually manifests as an increased vertical beam size. Such a situation could be devastating in an electron ion collider (EIC).

In an EIC any oscillations of the electron bunches will influence the ion bunches via the beam-beam force [16]. Since ions have no radiation damping this can result in continuous emittance growth. For a simple model consider a proton at the interaction point with vertical offset $y_p(n)$ and angle $y'_p(n)$ on turn n. Let the vertical beta function at the interaction point be β^* and let the electron bunch offset be $y_e(n)$. With a small amplitude beam-beam tune shift of ΔQ_{bb} the one turn map for the proton is

$$z_p(n) = z_p(n-1)e^{-i\psi_p} + 4\pi i\Delta Q_{bb}y_e(n), \qquad (1)$$

where $z_p(n) = y_p(n) + i\beta^* y'_p(n)$ and $\psi_p = 2\pi Q_p$, where Q_p is the vertical proton tune. Assume $y_e(n)$ is a stationary random process with rms amplitude σ_y and correlation function $\rho_e(m)$. This yields a growth rate

$$\frac{d\langle|z_p|^2\rangle}{dn} = (4\pi\Delta Q_{bb}\sigma_y)^2 \sum_{m=-\infty}^{\infty} \rho_e(m)\cos(m\psi_p), \qquad (2)$$

where angular brackets denote expectation value. For white noise the sum in Equation (2) is 1 while for slow closed orbit motion it is very small.

If a feedback system is operating, σ_y will be strongly influenced by the noise level in the feedback system [4] and the correlation time of $\rho_e(m)$ will include the feedback damping time. While it might be possible to build a damping system with adequately low noise we have found that one needs $\sigma_y \lesssim \sqrt{\epsilon\beta^*} \times 10^{-4}$ for the equivalent white noise oscillation, which is extremely challenging.

Therefore, the BNL EIC baseline design is such that BII will be collisionlessly damped by tune spread in the electron beam. The largest source of tune spread is the beam-beam force, which is always present during luminosity production.

MODEL AND SIMULATIONS

The BII simulations use macro-particles for both the electrons and the ions. The ionization happens continuously around the ring but for the purposes of simulation the ions are confined to N_{slice} thin lenses spaced evenly around the ring. Each ion slice corresponds to particular values of β_x and β_y. Ion macro-particles are generated in balanced pairs according to the appropriate two dimensional Gaussian distribution. By using pairs no additional noise is added. These ions are added to the ones already present in the slice. The ions barely move during the passage of a single electron bunch so the momentum kick to the ions is calculated assuming the ions are stationary. To calculate the kick the centroid and rms values for the electron bunch are calculated. The Basetti-Erskine formula is used to calculate the ion kicks. The ion kicks are summed and conservation of momentum is used to get the net kick to the electron bunch. The same kick is given to each electron macro-particle in the bunch. This approximation correctly includes the coherent tune shift due to the ions but neglects the incoherent tune shift due to the ions. In the future we will include the incoherent force from the ions. Next, the ions are time drifted until the next electron bunch arrives, removing any that get outside the aperture. The process repeats over the rest of the bunch train. The electrons are transported, including RF and chromatic effects, to the next ion slice and the process repeats. At the end of the turn a single weak-strong beam-beam kick is applied and the process repeats.

Ion-ion forces are neglected since the electric fields from the electrons are much larger than the electric fields of the

---

* Work supported by United States Department of Energy

METHOD FOR A MULTIPLE SQUARE WELL MODEL TO STUDY TRANSVERSE MODE COUPLING INSTABILITY*

M.A. Balcewicz†, Y. Hao[1], Michigan State University, East Lansing, MI, USA
M. Blaskiewicz, Brookhaven National Laboratory, Upton, NY, USA
[1]also at Brookhaven National Laboratory, Upton, NY, USA

Abstract

In the high intensity limit it can become difficult to simulate intense beams sufficiently within a short time scale due to collective effects. Semi-Analytic methods such as the Square Well Model [1]/AirBag Square Well [2] (SWM/ABS) exist to estimate collective effects within a short time scale. SWM/ABS discretizes the longitudinal confining potential into a single square well enforcing linearity for the case of linear transverse optics. A method is proposed here to extend the Square Well Method to multiple square wells. This method preserves linearity properties that make it easily solvable within a short time scale as well as including nonlinear effects from the longitudinal potential shape.

INTRODUCTION

For the general case of instabilities in the presence of collective Space Charge (SC) and Wakefield effects, an exact solution does not exist except in special cases. To evaluate instabilities with SC and Wakefields, a simulation method must be applied. Unfortunately, many of these methods take a prohibitively long time to reach a solution. In order to reach a rapid solution while including both SC and Wakes, some sort of well founded simplification must be made to the dynamics of the system. Previous work exists where the longitudinal potential is simplified to a single finite square potential well [3]. A single potential well like this confers several useful properties to the longitudinal dynamics that make it easily solvable. This has been applied to the Transverse Mode Coupling Instability (TMCI).

For a single finite square well, there are two synchrotron tunes which correspond to a set of discrete longitudinal velocities in opposing longitudinal directions. These velocities form a single cycle with simple longitudinal particle dynamics. Under linear focusing optics collective particle moments and wakes are a system of linear ordinary differential equations solvable by matrix methods. These methods produce a set of tune shift parameters that indicate the presence of the TMCI instability. Although simple and efficient, the single finite square well underestimates the onset of TMCI compared to many other theoretical methods. [4]

By increasing the number of approximating square wells, the number of discrete longitudinal velocities increases allowing for the introduction of nonlinear chromatic effects as well as well as the introduction of synchrotron tune spread. This increases applicability to realistic systems.

THEORY

To expand upon the SWM/ABS models one should begin with the equations of motion of a particle in a ring undergoing linear transverse motion with chromatic tune shift $\xi(\dot{z})$, linear space charge, and wakes (Eq. (2) from [3]).

$$\begin{aligned}\frac{d^2x}{dt^2} = \frac{dp_x}{dt} &= [-(Q_x^2 + \xi(\dot{z}))x + C_{sc}\rho(z)(x - \overline{x}(t,z)) \\ &+ \int_0^z dz' W(z-z')\rho(z')\overline{x}(t,z')]\omega_0^2 \\ &\equiv [x g_1(z,\dot{z}) + g_2(t,z)]\omega_0^2 \qquad (1)\end{aligned}$$

$\rho(z)$ corresponds to the linear longitudinal particle density. Due to the presence of both single particle motion and collective effects, it is difficult to treat analytically unless the collective effects act as a small perturbation on single particle motion.

To properly consider the collective effects, we shall define collective phase space moments from the Vlasov Equation. Since longitudinal dynamics generally vary slowly compared to transverse dynamics, we assume that the longitudinal dynamics are independent of transverse, while the transverse dynamics are dependent on longitudinal. This indicates that it is possible to construct and use two separate Vlasov Equations, one longitudinal and one transverse. The longitudinal particle density $\psi(t,z,\dot{z})$ can be constructed out of the moments from the transverse particle density $f(t,x,p_x,z,\dot{z})$

$$\int_{-\infty}^{\infty} dx \int_{-\infty}^{\infty} dp_x f \equiv \psi(t,z,\dot{z}) \qquad (2)$$

$$\int_{-\infty}^{\infty} dx \int_{-\infty}^{\infty} dp_x x f \equiv D(t,z,\dot{z}) \qquad (3)$$

$$\int_{-\infty}^{\infty} dx \int_{-\infty}^{\infty} dp_x p_x f \equiv P(t,z,\dot{z}) \qquad (4)$$

In the case of linear optics, these moments converge to a and we can apply ψ to the longitudinal Vlasov.

$$\frac{d\psi}{dt_L} = \frac{\partial\psi}{\partial t} + \dot{z}\frac{\partial\psi}{\partial z} - \frac{1}{m}\frac{dU(z)}{dz}\frac{\partial\psi}{\partial\dot{z}} = 0 \qquad (5)$$

The properties of these collective moments and their respective convective derivatives allow for the creation of collective equations of motion. These equations of motion are analogous to the single particle EOM in Eq. (1).

$$\frac{d^2D}{dt_L^2} = \frac{dP}{dt_L} = [g_1(z,\dot{z})D + g_2(t,z)\psi]\omega_0^2 \qquad (6)$$

---

* Work supported by by Brookhaven Science Associates, LLC under contract number 364776.

† balcewic@nscl.msu.edu

ISBN: 978-3-95450-223-3 ISSN: 2673-7000 doi:10.18429/JACoW-NAPAC2019-TUPLM13

TWO-ENERGY STORAGE-RING ELECTRON COOLER FOR RELATIVISTIC ION BEAMS*

B. Dhital[#1,2], J.R. Delayen[1,2], Y.S. Derbenev[2], D. Douglas[2], G.A. Krafft[1,2], F. Lin[2], V.S. Morozov[2], Y. Zhang[2]
[1]Center for Accelerator Science, Old Dominion University, Norfolk, VA, USA
[2]Thomas Jefferson National Accelerator Facility, Newport News, VA, USA

Abstract

An electron beam based cooling system for the ion beam is one of the commonly used approaches. The proposed two–energy storage-ring electron cooler consists of damping and cooling sections at markedly different energies connected by an energy recovering superconducting RF structure. The parameters in the cooling and damping sections are adjusted for optimum cooling of a stored ion beam and for optimum damping of the electron beam respectively. This paper briefly describes a two cavities model along with a third cavity model to accelerate and decelerate the electron beam in two energy storage ring. Based on our assumed value of equilibrium emittance shows that these models give a bunch length of the order of cm and energy spread of the order of 10^{-5} in the cooling section which are required parameters for the better cooling. Numerical calculations along with elegant simulation are presented.

INTRODUCTION

Recently, in storage ring, it has been realized that several interesting topologies for the multiple beam energies may be possible [1]. Here we focus our study on two energy storage ring where one ring is at higher energy and another ring at lower energy connected by RF cavities as shown in Fig. 1. Recent study shows that longitudinal stability exists in a two-energy storage ring [2]. We are interested to this type of storage ring for electron cooling. Cooling allows small transverse beam sizes at the interaction point and enhanced luminosity. Electron cooling rate will be affected by the bunched electron beam properties such as beam size, energy spread etc [3]. Hence, from the cooling requirement, we can apply two cavities model to get the longer bunch length in the cooling section. This further allows to get smaller energy spread in the cooling section as required for the better cooling.

TWO CAVITIES MODEL

Concept

The schematic diagram for such a storage ring is shown in Fig. 1. We use two groups of RF cavities to accelerate (Acc cav1, Acc cav2) and decelerate (Dec cav1, Dec cav2) the electron beam in the corresponding accelerating and decelerating passes. Two cavities model is in the sense that we use two RF cavities to accelerate and another two RF cavities to decelerate the beam. This arrangement causes the beam to stretch more giving the longer bunch length in the cooling section. In this scheme, each cavity adds or subtracts energy by an equal amount in the corresponding accelerating and decelerating passes.

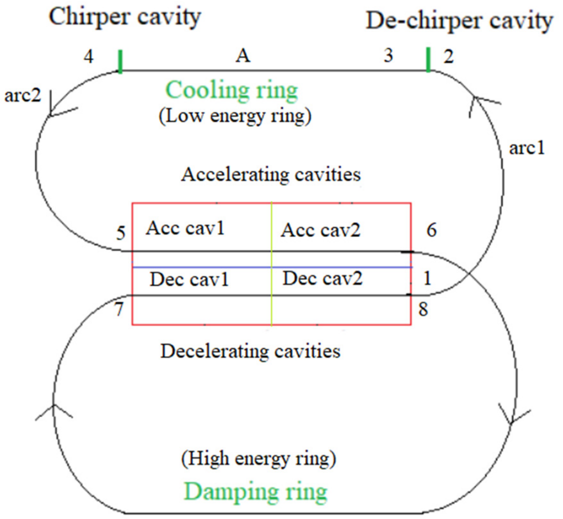

Figure 1: Schematic drawing of a two-energy storage ring with two cavities to accelerate and another two cavities to decelerate electron beam [4].

For simplicity, cooling ring is at 55 MeV and the damping ring is at 155 MeV, so the gain in energy through each cavity during acceleration is 50 MeV, and the total gain through two cavities is 100 MeV. Beam passing through the decelerating cavities lose the energy by an equal amount. We introduce a small phase shift in the accelerating phase of second accelerating cavity (Acc cav2) so that there is no cancelation of total slope in accelerating and decelerating passes.

In energy recovery linac (ERL) mode, one of the accelerating and decelerating passes is longitudinally focusing while the other is defocusing and the small phase shift introduced to second accelerating cavity provides the stability.

We study the longitudinal stability using two cavities model in ERL mode.

Two Cavities Model: Phasor Diagram

The RF phasor diagram is shown in Fig. 2. $\phi_s^{acc}(1)$ is the RF accelerating phase angle for the first accelerating cavity, $\phi_s^{acc}(2)$ is the RF accelerating phase angle for second accelerating cavity. Similarly, $\phi_s^{dec}(1)$ and $\phi_s^{dec}(2)$ are the corresponding decelerating phase angles for first and second decelerating cavities respectively. If we apply

---

* Work supported by U.S. DOE Contract No. DE-AC05-06OR23177 and DE-AC02-06CH11357.

[#] bdhit001@odu.edu

ISBN: 978-3-95450-223-3 ISSN: 2673-7000 doi:10.18429/JACoW-NAPAC2019-TUPLM15

ARBITRARY TRANSVERSE PROFILE SHAPING USING TRANSVERSE WIGGLERS

G. Ha†, M.E. Conde, J.G. Power, Argonne National Laboratory, Lemont, IL, USA

Abstract

Transverse wigglers provide a sinusoidal vertical magnetic field along the horizontal direction. This magnetic field imparts a sinusoidal modulation on the horizontal phase space. Since sine and cosine functions are the basis of periodic function space, the combination of multiple wigglers would be able to impart arbitrary correlation on the horizontal phase space. In this paper, we numerically demonstrate the application of this new method for arbitrary transverse profile shaping.

INTRODUCTION

Argonne Wakefield Accelerator (AWA) group demonstrated arbitrary longitudinal shaping capability of the emittance exchange (EEX) beamline in 2016 [1]. Several different transverse masks were used to shape the beam transversely, and the transmission through the mask was around 40%. The masking is one of the easiest ways to control the profile, but this low transmission would make a significant drop in the beam quality due to a higher charge requirement in the gun, and it can make thermal issues for high repetition rate or high intensity beams.

We recently proposed a scheme to generate a tunable bunch train using an EEX beamline with a transverse wiggler [2]. This wiggler provides a sinusoidal magnetic field which makes a sinusoidal modulation on the transverse phase space. If the beam passes the series of transverse wigglers with different periods and strengths, one can correlate the particle's horizontal position and momentum arbitrarily. This new method can open up a new way to control all longitudinal properties including arbitrary current profile shaping without charge loss. The following sections describe the related theoretical background and numerical demonstration of the method for shaping application.

PRINCIPLE OF ARBITRARY SHAPING USING TRANSVERSE WIGGLERS

Profile shaping using wigglers requires two steps. Firstly, an appropriate correlation function should be defined to generate a desired profile. This correlation function can be found from the relationship with beam parameters and beamline parameters.

Particle transport can be described by the matrix formalism. If the particle's initial coordinate is (x_0, x_0'), its final horizontal position can be written as,

$$x_f = R_{11}x_0 + R_{12}x_0'. \tag{1}$$

If one applies arbitrary correlation (*f*) to the initial horizontal phase space, particle's momentum term (x_0') should be replaced to $x_{0,old}' + f(x_0)$. Here, we ignore the particle's initial momentum to simplify the calculation and only consider newly added arbitrary correlation.

When the particle's final coordinate is (x_f, x_f') and profiles are expressed as *N*, the initial and final profiles have a relationship as below due to the charge conservation.

$$N_f(x_f)\mathrm{d}x_f = N_0(x_0)\mathrm{d}x_0. \tag{2}$$

By substituting the final coordinate (x_f) to Eq. (1), Eq. (2) can be rewritten to,

$$N_f(R_{11}x_0 + R_{12}f)\{R_{11} + R_{12}f'\} = N_0(x_0). \tag{3}$$

If there is a desired final profile, Eq. (3) shows the required correlation function to generate the desired profile in the given system (i.e. beam transport and initial profile are fixed).

The next step is to correlate *x* and *x'*. To generate an arbitrary correlation, we use the concept of Fourier expansion. The summation of cosine functions can approximate an arbitrary function. Here we use transverse wigglers to generate cosine modulation on the horizontal phase space.

The transverse wiggler provides the alternating magnetic field which can be described as,

$$B_y \cong -2B_r \cos\left(\frac{2\pi}{\lambda_w}x\right)\cosh\left(\frac{2\pi}{\lambda_w}y\right)\exp\left(-\frac{\pi}{\lambda_w}g\right), \tag{4}$$

where B_r is the residual induction of the magnet, λ_w is the magnetic period of the wiggler, and g is the gap of the wiggler. Cosine term in this field provides cosine correlation on the horizontal phase space which will be the building block for cosine series constructing the correlation function.

To determine how many wigglers we need and other wiggler parameters such as gap and length, both Fourier expansion and genetic algorithm based optimization are tried.

APPLICATION TO ARBITRARY PROFILE CONTROL

In this section, we provide two simple examples of wiggler based shaping. We derived required correlation functions for each example using Eq. (3). Then, Fourier expansion is applied to the first example to find the wiggler setting while genetic optimization is used for the second example. Particles are generated and correlation is numerically applied to the distribution. This correlated particle

---

† gha@anl.gov

ISBN: 978-3-95450-223-3 ISSN: 2673-7000 doi:10.18429/JACoW-NAPAC2019-TUPLM16

DOUBLE-HORN SUPPRESSION IN EEX BASED BUNCH COMPRESSION

J. Seok† [1,2], M. Chung[1], M. Conde[2], G. Ha[2], J. Power[2]
[1]Ulsan National Institute of Science and Technology, Ulsan, 44919, Korea
[2]Argonne National Laboratory, Lemont, IL, USA

Abstract

Nonlinearities on the longitudinal phase space induce a double-horn current profile when the bunch is compressed strongly. Since this double-horn can degrade the performance of FELs due to the CSR it makes, the suppression of the double-horn is one of important beam dynamics issues. Emittance exchange (EEX) can be interesting option for this issue due to its longitudinal controllability. Since EEX exchanges the longitudinal phase space and transverse phase space, higher order magnets such as octupole can control the nonlinearity. In this paper, we present simulation results on the suppression of the double-horn current profile using EEX based bunch compression. We use a double EEX beamline installed at the Argonne Wakefield Accelerator facility for the simulation.

INTRODUCTION

XFELs require a bunch length of ~10 fs to generate ultrafast X-ray pulses [1-4]. This strong compression sometimes introduces a bad feature called double-horn in the current profile [5, 6]. This double-horn possibly degrades the lasing quality when it generates an intense CSR acting with the core of the bunch [6]. Naturally, how to suppress the double-horn feature is one of important beam dynamics issues to improve the X-ray quality.

Emittance exchange (EEX) is an interesting option to provide a strong bunch compression with a correction on the double-horn profile. EEX exchanges horizontal and longitudinal phase spaces [7, 8], thereby any horizontal manipulation controls longitudinal properties [9, 10]. This means that a horizontal focusing compresses a bunch [1-13] and nonlinear correction on the transverse plane corrects longitudinal nonlinearities. Similarly, this exchange based compression has two advantages compared to chicane compressors. The first advantage is that the compression does not require a specific longitudinal chirp. It releases a constraint on the operating phase of accelerating cavities. On-crest operation would be more efficient to operate the machine. Secondly, the EEX compressor can control the longitudinal chirp at the downstream of the beamline using quadrupole magnets due to the exchange again [10].

Although the exchange of phase space enables a new way to compress the bunch, it also increases the transverse emittance due to an exchange with an initially large longitudinal emittance. We use a double-EEX (DEEX) beamline to avoid this issue. DEEX beamline consists of two EEX beamlines pointing opposite directions and transverse manipulation section in between. The first EEX beamline exchanges longitudinal and horizontal phase spaces and following manipulation section control the transverse phase space using quadrupole magnets. The second EEX beamline exchanges these phase space and the transverse manipulation from quadrupoles becomes longitudinal control.

In this paper, we present progress on simulation work to support upcoming experimental demonstration of the concept. We firstly describe a possible source of double-horn formation. Next, we introduce a simple method to suppress the double-horn formation from this source using a single octupole magnet. Finally, we demonstrate the concept using IMPACT-T [14] simulation.

SOURCE OF DOUBLE-HORN FORMATION

Particle's longitudinal position and momentum usually have a correlation due to both external field applied to the bunch and self-field such as space-charge field. One of the possible source of double-horn formation is included in this longitudinal correlation. To confirm this source, we need to understand how the correlation affect on the final profile.

Bunch's final profile can be written as below due to the charge conservation

$$g(z_i) = f(z_i)\ (dz_i/dz_f), \tag{1}$$

where $f(z_i)$ and $g(z_i)$ are initial and final current profiles, respectively. Here the derivative term can be derived from the particle transport through the beamline. In the DEEX beamline, the particle's final longitudinal position can be written as

$$z_f = R_{55}z_i + R_{56}\delta_i\ , \tag{2}$$

where R_{55} and R_{56} are elements of the linear transfer matrix of a DEEX beamline. Note, quadrupoles in between two EEX beamlines control these linear coefficients.

If δ and z do not have any correlation, dz_i/dz_f term will be a constant and there will be no double-horn. However, correlations can make denominator zero which generates a spike on the profile. If we expand the longitudinal correlation using polynomial, the fractional momentum (δ) and longitudinal position (z) can be written as

$$\delta_i = h_1 z_i + h_2 z_i^2 + h_3 z_i^3, \tag{3}$$

where index of i corresponds to particle's initial location, and fourth order or higher are ignored in this discussion since the first three terms dominantly determine the correlation in most of case. By plugging in Eq. (2) and Eq. (3) to Eq. (1), denominator can be written as

ISBN: 978-3-95450-223-3 ISSN: 2673-7000 doi:10.18429/JACoW-NAPAC2019-TUPLM18

IMPROVING ENERGY RESOLUTION AND COMPENSATING CHROMATIC ABERRATION WITH A TM010 MICROWAVE CAVITY

C. J. R. Duncan*, P. Cueva, J. M. Maxson, D. A. Muller,
Cornell University, Ithaca, NY, USA

Abstract

The intrinsic energy spread of electron sources limits the achievable resolution of electron microscopes in both spectroscopic and spatially resolved measurements. We propose that the TM010 mode of a single radio frequency (RF) cavity be used to dramatically reduce this energy spread in a pulsed beam. We show with analytic approximations, confirmed in simulations, that the non-linear time-energy correlations that develop in an electron gun can be undone by the RF cavity running near-crest. We derive an expression that gives the required RF field strength as a function of accelerating voltage. We explore multiple applications, including EELS and SEM. By pulsing a photocathode with commercially available, high repetition-rate lasers, our scheme could yield competitive energy spread reduction at higher currents when compared with monochromated continuous-wave sources for electron microscopes.

INTRODUCTION

Motivated by the demands of ultrafast electron diffraction (UED), progress in photoelectron sources over the last decade now makes it possible to produce sub-picosecond electron pulses with femtosecond timing precision. Beyond UED, ultrafast pulses could yield improved beams for microscopy applications that do not aim to make time resolved measurements. Improvement is possible because the pulsed structure gives a handle on the energy-time dimensions of phase-space for experimental manipulation.

The history of attempts to use time dependent fields to correct lens aberrations in electron microscopes date back to the 1940s and the pioneering work of Scherzer [1, 2]. Common to all proposals is the *phase condition*: that the electron pulses be much shorter than the period of the RF wave [3]. Having in mind the use of time dependent fields as transverse lenses, this historical work formulated the phase condition in terms of the lens aberration introduced by a time dependent focal length. Letting ω be the angular RF frequency, the change in focal length during the transit of an electron pulse from its optimal value $f_{\min}$ has the effect of blurring a point focus into a disc of radius r,

$$r = \frac{1}{2}\omega^2 \Delta t^2 f_{\min}\alpha + O\left(\Delta t^4\right), \qquad (1)$$

where α is the angular aperture of the beam and Δt is the pulse length. A suitable criterion for the feasibility of using RF fields as a microscope lens is that the right-hand-side of Eq. (1) be less than the aberration of the uncorrected microscope, something never achieved in the 20th century [4]. Considering hypothetical but realistic numbers today, a 100 fs r.m.s. pulse transiting a 3 GHz cavity with an aperture of 100 mrad gives a blur $r/f_{\min} = 9 \times 10^{-9}$, smaller than even the best corrected transmission electron microscopes, which get $r/f \approx 10^{-7}$ [5]. The possibility today of reliably producing pulses shorter than 100 fs is thus a reason to reconsider the use of microwave cavities in electron microscopy, as was done in [6], a work which inspired the line of though that we pursue in this proceeding.

An important metric of beam quality is energy spread. An energy spread of around 10 meV is necessary to resolve phonon spectra [7]. Moreover, chromatic aberration is the leading lens aberration after correcting for spherical aberration. Scanning Transmission Electron Microscopy (STEM) typically uses a probe beam with a 1 eV energy spread; while for Transmission Electron Microscopy, the best monochromated microscopes have an energy spread of 10 meV [7]. Monochromation using an energy filtering slit is not an option in STEM or in Scanning Electron Microscopy (SEM) because of the attendant loss of beam current. At the lower voltages at which SEM and STEM operate compared with TEM, higher current is needed to overcome the signal to noise of particle detectors.

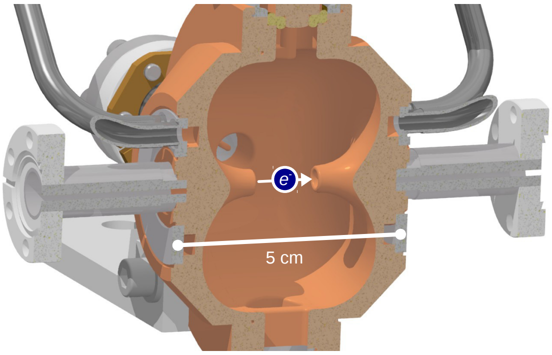

Figure 1: This reentrant cavity design contains a TM010 mode at 3 GHz . The high field gap across which electrons transit is 1 cm long; powered at ~ 50 W the cavity amplitude is 2 MVm^{-1}. The short gap makes the design ideal for time-of-flight based energy correction. The optical properties of a cavity of similar design are studied in [6].

In reducing energy spread, RF cavities are a potential alternative or complementary technology to monochromation using energy filtering slits. When a TM010 mode is operated such that the maximum accelerating phase coincides with the arrival of the lowest energy particle in a pulse, the effect of the cavity is to reduce the overall energy spread of the pulse. By *pulse* in this context is meant an ensemble of single-particle shots: the low emittance required in mi-

---

[*] cjd257@cornell.edu

ISBN: 978-3-95450-223-3 ISSN: 2673-7000 doi:10.18429/JACoW-NAPAC2019-TUPLM20

GENERATION OF HIGH-CHARGE MAGNETIZED ELECTRON BEAMS CONSISTENT WITH JLEIC ELECTRON COOLING REQUIREMENTS*

A. T. Fetterman, P. Piot[1], Northern Illinois University, DeKalb, IL 60115, USA
S.V. Benson, F. E. Hannon, S. Wang
Thomas Jefferson National Accelerator Laboratory, Newport News, VA 23606, USA
D. Crawford, D. Edstrom, J. Ruan, Fermi National Accelerator Laboratory, Batavia, IL 60510, USA
[1]also at Fermi National Accelerator Laboratory, Batavia, IL 60510, USA

Abstract

The proposed Jefferson Lab Electron-Ion Collider (JLEIC), currently under design, relies on electron cooling in order to achieve the desired luminosity. This includes an electron beam with >55 Mev, 3.2 nC bunches that cools hadron beams with energies up to 100 GeV. To enhance cooling, the electron beam must be magnetized with a specific eigen-emittance partition. This paper explores the use of the Fermilab Accelerator Science and Technology (FAST) facility to demonstrate the generation of an electron beam with parameters consistent with those required in the JLEIC high-energy cooler. We demonstrate via simulations the generation of the required electron-beam parameters and perform a preliminary experiment to validate FAST capabilities to produce such beams.

INTRODUCTION

The Jefferson Laboratory Electron-Ion Collider (JLEIC) is a proposed facility to support experiments in nuclear physics with designed energies for ion or proton of up to 100 GeV. Cooling these beams will require an electron beam with energy >55 MeV [1]. Producing such an electron beam requires a radio-frequency (RF) accelerator. Given the stringent demand on the relative energy spread and beam emittances combined by the 3.2 nC bunch charge, the beam will likely need to be produced with a photoinjector. Lastly, to improve cooling efficiency, the electron beam needs to be magnetized, i.e., have significant canonical angular momentum (CAM).

The specifications for the JLEIC high-energy electron cooler in Table 1 are close to beam parameters attainable at the FAST facility, Fig. 1, at Fermilab. The attainable beam parameters at FAST (either experimentally verified or simulated) match most of the requirements except for the peak-to-peak fractional energy spread which is substantially higher at FAST due to RF-induced curvature on the longitudinal phase space. The uncorrelated fractional energy spread is however comparable to the one required in the JLEIC electron cooling. Thus experiments aimed at exploring the generation of magnetized beams [2] with eigen-emittance partition relevant to JLEIC can be performed at the FAST facility. Magnetized beams have been produced at FAST previously in support for generation of flat beams with high transverse-emittance ratios [3].

Table 1: Comparison for the electron-cooling beam requirements for the JLEIC parameters [1] and corresponding value (inferred from simulations) achievable at FAST. All values are RMS quantities and the emittances are normalized.

Parameter	Unit	JLEIC	FAST
Beam Energy	MeV	[20,55]	45
Beam Charge	nC	3.2	>3.2
cath. spot size	mm	1.1	1
B field on cath.	T	0.05	< 0.09
cyclotron emitt.	μm	≤ 19	< 5
drift emitt.	μm	36	37
δp/p (uncor.)	-	3.10^{-4}	$< 4.10^{-4}$
δp/p (pk-to-pk.)	-	$<6.10^{-4}$	$O(10^{-4})$
bunch length σ_z	cm	2	0.2

GENERATION & ACCELERATION OF MAGNETIZED BUNCHES AT FAST

The magnetization sets the eigen-emittance partition that can ideally be achieved. It is given by $\gamma\mathcal{L} = \frac{eB_c}{2mc}\sigma_c^2$, where we refer to $\gamma\mathcal{L}$ as the *normalized* magnetization. B_c is the axial magnetic field on the photocathode surface and σ_c the rms transverse size (assumed to be identical within the two transverse directions). Here we should note that $\gamma\mathcal{L}$ plays the role of an emittance and the effective emittance associated with a beam with significant CAM is $\varepsilon_{n,\text{eff}} = [(\gamma\mathcal{L})^2 + \varepsilon_{n,u}^2]^{1/2}$. Assuming a CAM-dominated beam $\gamma\mathcal{L} \gg \varepsilon_{n,u}$ the eigen-emittances $\varepsilon_{n,\pm}$ are given by

$$\varepsilon_{n,+} = 2\gamma\mathcal{L} \equiv \varepsilon_{n,d} \text{ and } \varepsilon_{n,-} = \frac{\varepsilon_{n,u}^2}{2\gamma\mathcal{L}} \equiv \varepsilon_{n,c} \qquad (1)$$

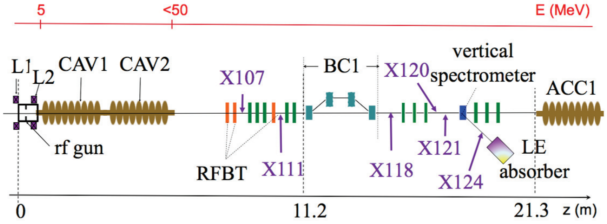

Figure 1: Layout of the FAST injector. The red quads labeled RFBT are the skew quads that form the transformation lattice for the conversion of round magnetized beam to flat beams.

---

* This material is based upon work supported by the U.S. Department of Energy, Office of Science and the Office of Nuclear physics under contracts DE-AC05-06OR23177 and DE-AC02-07CH11359.

ISBN: 978-3-95450-223-3 ISSN: 2673-7000 doi:10.18429/JACoW-NAPAC2019-TUPLM21

OPTICAL STOCHASTIC COOLING PROGRAM AT FERMILAB'S INTEGRABLE OPTICS TEST ACCELERATOR*

J.D. Jarvis†, S. Chattopadhyay[1], V.A. Lebedev, H. Piekarz, P. Piot[1], A. L. Romanov, J. Ruan,
Fermi National Accelerator Laboratory, Batavia, IL, USA
[1]also at Northern Illinois University, DeKalb, IL, USA

Abstract

Beam cooling enables an increase of peak and average luminosities and significantly expands the discovery potential of colliders. Optical Stochastic Cooling (OSC) is a high-bandwidth cooling technique that will advance the present state-of-the-art, stochastic-cooling rate by more than three orders of magnitude. A proof-of-principle demonstration with protons or heavy ions involves prohibitive costs, risks and technological challenges; however, exploration of OSC with electrons is a cost-effective alternative for studying the beam-cooling physics, optical systems and diagnostics. The ability to demonstrate OSC was a key requirement in the design of Fermilab's Integrable Optics Test Accelerator (IOTA) ring. The IOTA program will explore the physics and technology of OSC in amplified and non-amplified configurations. We also plan to investigate the cooling and manipulation of a single electron stored in the ring. The OSC apparatus is currently being fabricated, and installation will begin in the fall of 2019. In this contribution, we will describe the IOTA OSC program, the upcoming passive-OSC experimental runs and ongoing preparations for an amplified-OSC experiment

INTRODUCTION

The precise control of a relativistic charged particle using its own spontaneous radiation may have broad implications ranging from the science reach of future colliders to a deeper understanding of radiative processes in storage rings. The necessary capabilities for a research program in this area are provided by the physics and technology of Optical Stochastic Cooling (OSC), a high-bandwidth, beam-cooing technique that represents a more than three-order of magnitude advance in the state-of-the-art stochastic-cooling rate [1,2]. The physics of the OSC principle does not depend on the type of charged particle in any fundamental way, engineering challenges notwithstanding; therefore, the physics results, and some technology elements, of a cost-effective research program with electrons are universal and could be readily applicable to future systems for protons, heavy ions or muons [3,4].

Van der Meer's Nobel-winning Stochastic Cooling (SC) was vital in the accumulation of antiprotons and in the delivery of the beam quality required for the discovery of the W and Z bosons [5,6]. In a SC system, signals from electromagnetic pickups, operating in the microwave regime with a bandwidth on the order of several GHz, are used in negative feedback systems to reduce the phase-space volume of a circulating beam in all degrees of freedom [5-10]. SC systems have been successfully implemented at a number of facilities around the world, most recently at the Relativistic Heavy Ion Collider, where bunched-beam cooling was used to boost the collider's luminosity [11,12].

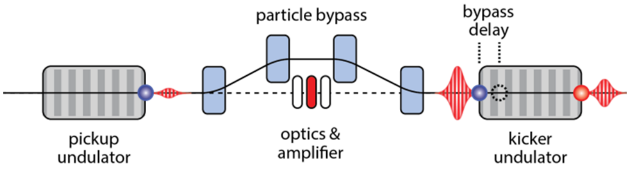

Figure 1: Simplified conceptual schematic of a transit-time OSC insertion.

Optical Stochastic Cooling

Extension of the SC principle to optical frequencies could increase cooling rates by three to four orders of magnitude and would be a significant advance in beam-cooling physics. OSC was first suggested in the early 1990s by Zolotorev, Zholents and Mikhailichenko, and replaced the microwave hardware of SC with optical analogs, such as wigglers and optical amplifiers [1,2]. OSC's greatest strength, its high-bandwidth phase-space sampling, also presents a challenge; very stringent tolerances must be met in design, engineering and experimental execution due to the short wavelength of the radiation. Several variations on the original OSC concept have been proposed, and its use has been suggested for hadron, heavy-ion, electron-ion and muon colliders and also controlling emittance growth in electron storage rings [13-19]. Simplified proof-of-principle demonstrations have also been proposed at several facilities over the last decade or so [4,18-20].

In the transit-time method of OSC, shown schematically in Fig. 1, a particle's deviations from the reference particle are encoded in its arrival time at the kicker system by transiting a magnetic bypass [2]. The particle (an electron for purposes of discussion) first emits a radiation packet while traversing a pickup undulator (PU). The radiation packet is transported with or without amplification to a kicker undulator (KU) where it interacts with the same electron. Between the pickup and kicker, the electron traverses a bypass (chicane), which is designed such that a reference particle at the design energy will arrive at the KU simultaneously with the head of its radiation packet. The energy of the reference particle is unchanged by its interaction with the radiation field in the KU; however, in the linear approximation, all other particles will have a delay change that is proportional to their momentum deviation $\Delta p/p$, and will receive corresponding corrective kicks towards the design

---

* Fermi National Accelerator Laboratory is operated by Fermi Research Alliance, LLC under Contract No. DE-AC02-07CH11359 with the United States Department of Energy.

† jjarvis@fnal.gov

ISBN: 978-3-95450-223-3 ISSN: 2673-7000 doi:10.18429/JACoW-NAPAC2019-TUPLM22

OFF AXIS DEPENDENCE OF CURRENT DEPENDENT COHERENT TUNE SHIFTS IN THE UMER RING*

D.F. Sutter, B.L. Beaudoin, L. Dovlatyan,
Institute for Research in Electronics and Applied Physics,
University of Maryland, College Park, MD, USA

Abstract

The University of Maryland Electron Ring (UMER) was built to explore space charge effects in the extreme – beyond the space charge limit of most existing storage rings. At the nominal operating kinetic energy of 10 keV, the beam is also non relativistic. We have experimentally verified that the current dependent coherent tune shift obeys the Laslett formula over a wide current range for a cylindrical geometry and non-penetrating magnetic fields when the beam is on axis; i.e. the average closed orbit displacement around the ring is essentially zero. In the current experiment this measurement is extended to the change in current dependent coherent tune shift as the average closed orbit is moved off axis. It can be displaced over approximately ± 5 mm of the vacuum pipe diameter of 50 mm. without loss of beam. Because the 36 bending magnets in UMER are very short, we treat each of them as a local kick and then increment each by a calculated small amount to achieve the desired, global closed orbit displacement. Experimental results are compared to predictions by Laslett and others.

INTRODUCTION

Space charge dependent incoherent and coherent tune shifts are of primary interest and very well studied for synchrotrons and storage rings operating with relativistic beams, but there is a lack of experimental studies for very non relativistic beams where $\gamma < 2$. The University of Maryland electron ring, UMER, operates in the very nonrelativistic regime, with a $\gamma = 1.02$.

Of particular interest is the coherent tune shift because coherent beam centroid motion is what beam position monitors measure; they cannot directly measure incoherent tune. Moreover, there is a well-established theoretical model developed by L. J. Laslett and others [1-3]. In 2011 the UMER group measured the space charge induced coherent tune shift at beam currents ranging from 0.6 to ~ 70 mA, showing very good agreement with the Laslett predictions [4]. The important restriction for that measurement is that the beam be centered in the beam pipe around the ring; equivalently the average equilibrium orbit displacement must be zero. To gain a feeling for how well the restriction was met, it was planned to measure the change in tune as the beam was scanned off center. Unfortunately, the alignment of the ring was not adequate. A complete disassembly, remounting and precision alignment in 2017, has finally enabled the measurement.

EXPERIMENTAL CONFIGURATION

A recent detailed description of UMER can be found in references [5, 6]. Recent upgrades include a system of Helmholtz coils to cancel out the horizontal ambient magnetic field, a combination of the earth's field and building iron, and a small ferrite loaded rf cavity that can keep the beam bunched for up to 10^4 turns. Importantly, the Helmholtz coils enable vertical centering of the equilibrium orbit.

The space charge driven tune shift is strongly dependent on vacuum chamber geometry and fabrication. The chamber is round over essentially the entire 11.52 m circumference and is made of low permittivity stainless steel (316N) tubing. Discontinuities in the vacuum chamber include bellows (18), BPM's (14), glass gaps (3) and 24 cm of the injection section with an inner diameter of 8.0 cm, compared to 5.0 cm for all the rest. The ring is injected with a 50% fill, square pulse of length 580 cm. The physical simplicity of the vacuum chamber and the fact that the bunch is very much longer than any of the discontinuities allows treating the entire circumference as an identical, cylindrical boundary structure in the experiment. A list of the experiment's key parameters is given in Table 1.

Table 1: Parameters for the coherent tune shift versus beam current experiments. The characteristic current, I_0, is related to the classical radius of the electron, r_0, through $I_0 r_0 = ec$, e is the electronic charge and c is light velocity.

Circumference	1152 cm	Beam pipe radius, b	2.489 cm
Average radius, R	183.3 cm	Beam pipe wall, d	0.0508 cm
Kinetic energy, T	10 keV	Wall resistivity, ρ	7.4 x 10^7 Ω–cm
Relativistic, β	0.1950	Wall magnetization, μ_r	1.0
Relativistic, γ	1.0196	Characteristic current, I_0	17.05 x 10^6 mA

To ensure that the tune shifts are only a function of beam current, it is essential to use exactly the same optical parameters – steering and focusing strengths – for all the beam currents.

COMPUTING THE TUNE SHIFTS

Coherent tune shifts of the betatron oscillation of the beam centroid (the first moment of the beam) are a function of the interaction of the current in the beam with the image current in the chamber wall. The defocusing force is, therefore, the Lorentz force between the beam and the induced image current. A particularly good summary of the physics can be found in chapter 8 of reference [7].

---

* Work supported by US Department of Energy Office of High Energy Physics, Grant No. DE-SC0010301.

ISBN: 978-3-95450-223-3 ISSN: 2673-7000 doi:10.18429/JACoW-NAPAC2019-TUPLM24

ELECTRON HEATING BY IONS IN COOLING RINGS*

H. Zhao†, M. Blaskiewicz
Brookhaven National Laboratory, Upton, NY, U.S.A.

Abstract

Hadron beam cooling at high energy is a critical technique for Electron-Ion Colliders (EIC). We consider using an electron storage ring for the EIC at BNL. For such a cooler, the electron beam quality plays an important role since it directly determines the cooling rate. Besides the effects of IBS, space charge and synchrotron damping, which are calculable with well known methods, the heating effect by ions also needs to be carefully considered in electron beam dynamics. In this paper, we present an analytical model to calculate the heating rate by ions and give some example calculations. In addition, this model was benchmarked by applying it on the IBS calculation.

INTRODUCTION

Brookhaven National Laboratory (BNL) is proposing an electron ion collider (EIC), based on the existing and highly optimized RHIC ion-ion collider [1]. In order to achieve the full luminosity of eRHIC some beam cooling is required. We will consider an electron cooler based on a storage ring designed to balance emittance growth rates due to intrabeam scattering (IBS). The challenges of such a cooler include long cooling section without solenoids, bunched electron beam cooling at high energy and keeping the low temperature of electron beam for a long time. Recently, the LEReC project has successfully demonstrated hadron cooling using a bunched electron beam at RHIC with no magnetic field in the cooling section [2, 3]. In our design we use a series of wiggler magnets to keep the low temperature of electron beam. The electron beam dynamics are dominated by IBS, radiation damping and heating due to ions. The first two effects have well known models to make estimates [4, 5]. The electron heating by ions is a newer effect [6, 7] which has largely been estimated using conservation of energy arguments.

In this paper we review the conservation of energy approach by applying the Landau/Spitzer formula for thermal equilibration. Next we develop a gas model based on the full Landau collision integral that allows for different temperatures in all three-dimensions. The two models are compared using a beam tracking simulation, and the heating effect by ions is estimated based on eRHIC design. We also applied the gas model to IBS calculation and compared it with the Bjorken-Mtingwa IBS model. The results of the two IBS calculation show a good agreement.

HEATING MODELS

Spitzer formula

This model is based on the energy exchange between two charged particles during encounter [8]. Considering both the electron and ion beam have Maxwellian velocity distribution but with different kinetic temperatures T_e and T_i, the heating or cooling rate for electron beam can be obtained by

$$\frac{dT_e}{dt} = \frac{T_i - T_e}{\tau_{eq}} \tag{1}$$

where τ_{eq} is the time of equipartition

$$\tau_{eq} = \frac{3 m_i m_e (4\pi\varepsilon)^2}{8\sqrt{2\pi} n_i Z^2 e^4 ln\Lambda} \left(\frac{kT_e}{m_e} + \frac{kT_i}{m_i}\right)^{3/2}. \tag{2}$$

This formula gives the average temperature changes of a beam, but it is just a one-demensional formula. So, it cannot accurately estimate the energy change in real conditions. Generally, this formula is perfect for the beam with the same or similar temperatures in each dimension, but not correct when the beam has different temperatures in three-dimensions. In order to get a more accurate formula, we developed a new model called gas model that considered the three-dimensional distribution of beams.

Gas model

We start with the Boltzmann transport equation [9]

$$\frac{\partial f}{\partial t} + \vec{v} \cdot \nabla f + \frac{\vec{F}}{m} \cdot \frac{\partial f}{\partial \vec{v}} = C(f) \tag{3}$$

where $f = f(\vec{x}, \vec{v})$ is the beam distribution function in phase space, $\vec{F}$ is the external force on particles and $C(f)$ is the collision integral. From Eq. (3), we know that the evolution of the beam distribution depends on particle diffusion, external force and the collisions between particles. Our cooling is in a drift section so only coulomb collisions are relevant. We include electron-electron collisions in the IBS rates and only consider electron-ion collisions here [10],

$$\frac{\partial f_e}{\partial t} = C_{ei} \tag{4}$$

where

$$C_{ei} = \frac{\gamma_{ei}}{2} \frac{\partial}{\partial v_\alpha} \int U_{\alpha,\beta} \left(f_i' \frac{\partial f_e}{\partial v_\beta} - \frac{m_e}{m_i} f_i \frac{\partial f_i'}{\partial v_\beta'}\right) d^3 v' \tag{5}$$

and the scattering tensor $U_{\alpha,\beta}$ and constant γ_{ei} are

$$U_{\alpha,\beta} = \frac{u^2 \delta_{\alpha,\beta} - u_\alpha u_\beta}{u^3}, \quad \gamma_{ei} = \frac{e_e^2 e_i^2 ln\Lambda}{4\pi \varepsilon_0^2 m_e^2} \tag{6}$$

---

* Work supported by States Department of Energy

† hezhao@bnl.gov

North American Particle Acc. Conf. NAPAC2019, Lansing, MI, USA JACoW Publishing
ISBN: 978-3-95450-223-3 ISSN: 2673-7000 doi:10.18429/JACoW-NAPAC2019-TUPLM25

CONNECTING GAS-SCATTERING LIFETIME AND ION INSTABILITIES*

B. Podobedov, M. Blaskiewicz, Brookhaven National Laboratory, Upton, NY, USA

Abstract

Recently there is a renewed interest in fast ion instability (FII) which is of concern for future low-emittance electron storage rings, such as MBA light sources and colliders, i.e. eRHIC. While analytical theories and numerical codes exist to model the effect, due to various assumptions and limitations, accurate experimental verification is often desirable. Unfortunately, one of the most critical parameters for FII (as well as the classical "trapped-ion" instability), the residual ion concentration, is usually the most uncertain. Vacuum gauges and residual gas analyzers (RGAs) provide some useful data, but they are often not accurate enough, and, more importantly, they cannot directly probe the ion concentration along the beam orbit. In this paper we show how one could use gas-scattering lifetime measurements to infer the residual gas concentration suitable for ion instability experiment modelling.

INTRODUCTION

The theory of fast ion instability and its first observations were reported more than 20 years ago [1-3]. As recent machine developments push for even lower emittances and higher currents, the instability is becoming more important for modern light sources and colliders. More recent observations at newly constructed light sources and low emittance storage rings can be found, for example in [4-9]. Several codes are reported to reproduce well the essential features of the instability [10-12]. Another code [13] is presently being developed for eRHIC [14], where ion instabilities could be of significant concern, because any coherent motion of the electrons will, via the beam-beam force, drive ion emittance growth. The goal of benchmarking this code at NSLS-II is what partially motivated this work.

A major difficulty in making quantitative comparison of the experimental results with the theory or with the tracking codes' predictions, is that one of the most critical parameters for the instability (as well as its classical, multiturn, counterpart, "trapped-ion" instability), the residual ion concentration, is usually the most uncertain. For instance, theoretical predictions of FII based on linear response [1-2] predict transverse beam oscillation growth with time as $y \sim e^{\sqrt{t/t_c}}$ where the time constant is inversely proportional to the residual gas density. In a real machine, for a given vacuum system configuration, this density changes a lot along the beam path (due to varying magnetic fields, local pumping speed, local desorption rates, etc.), as well as with beam parameters and machine conditions.

Modern rings are equipped with a large number of vacuum gauges, but, by design, they cannot directly probe ion concentrations along the beam orbit. Finally, while elevated vacuum pressures at the gauge locations can generally be measured quite accurately, if the machine is well-conditioned, and the pressures are below ~1e-10 Torr, the accuracy often becomes much worse.

This is why we are investigating an alternative method to get an independent assessment of the residual gas pressure under conditions that are most relevant to FII experiments at NSLS-II. Gas-scattering is a relatively simple and well-understood process with the scattering rate directly proportional to the integral of residual gas density along the beam path. Our idea is to estimate these column densities from the gas-scattering lifetime. This is a work in progress and our initial goal is to show that the gas-scattering lifetime can be measured non-invasively, accurately and reliably under the conditions most relevant for FII experiments, and, in particular, when this lifetime is much longer than the Touschek lifetime.

BEAM LIFETIME BASICS

The mechanisms leading to lifetime losses in storage rings are well-known. Usually only two mechanisms need to be accounted for, gas-scattering and (typically dominant) Touschek scattering.

For constant gas pressure, gas-scattering lifetime results in the exponential time dependence of the total beam current,

$$I(t) = I(0)e^{-t/\tau_{gas}}, \tag{1}$$

where two separate processes are responsible for the decay. Elastic gas-scattering lifetime is given by [15]

$$\frac{1}{\tau_{gas\_el}} = \frac{2r_e^2 Z^2 \pi n c}{\gamma^2}\left[\frac{\langle\beta_x\rangle}{A_x} + \frac{\langle\beta_y\rangle}{A_y}\right], \tag{2}$$

where $A_{x,y} = \min_s(a_{x,y}(s)^2/\beta_{x,y}(s))$ are the horizontal and vertical acceptances, given by the minimum value of the aperture, $a(s)$, squared and divided by the beta function at that location, n and $Z \gg 1$ are the concentration and the atomic number of the residual gas ions, γ is the relativistic factor, and r_e is the classical radius of electron.

Lifetime due to inelastic gas-scattering, or Bremsstrahlung, is given by [15]

$$\frac{1}{\tau_{gas\_brem}} = \frac{16r_e^2 Z^2 n c}{411}\ln\left[\frac{183}{Z^{1/3}}\right]\left[-\ln\varepsilon_{acc} - \frac{5}{8}\right], \tag{3}$$

where ε_{acc} is the limiting momentum acceptance.

Both gas-scattering lifetimes are inversely proportional to the ion density, and their effect can be combined in Eq. (1) by adding the rates,

$$1/\tau_{gas} = 1/\tau_{gas\_el} + 1/\tau_{gas\_brem}. \tag{4}$$

---

* Work supported by DOE under Contract No. DE-SC0012704.
† boris@bnl.gov

PROGRESS TOWARD A LASER AMPLIFIER FOR OPTICAL STOCHASTIC COOLING*

A.J. Dick, P. Piot[1], Northern Illinois Center for Accelerator & Detector Development
and Department of Physics, Northern Illinois University, DeKalb, IL, USA
M.B. Andorf, Cornell University, Ithaca, NY, USA
[1] also at Fermi National Accelerator Laboratory, Batavia, IL, USA

Abstract

Optical Stochastic Cooling (OSC) is a method of beam cooling using optical frequencies which compresses the phase space of the beam by correcting the deviation of each particle's momentum. A particle bunch passing through an undulator produces radiation which is amplified and provides the corrective energy kick. In this project, we are testing a method of amplifying synchrotron radiation (SR) for the eventual use in OSC. The SR is amplified by passing through a highly-doped Chromium:Zinc Selenide (Cr:ZnSe) crystal which is pumped by a Thulium fiber laser. The SR will be produced by one of the bending magnets of the Advanced Photon Source. The first step is to detect and measure the power of SR using a photo-diode. The gain is then determined by measuring the radiation amplified after the single-pass through the crystal. This serves as a preliminary step to investigate the performance of the amplification of beam-induced radiation fields. The planned experiment is an important step towards achieving active OSC in a proof-of-principle demonstration in IOTA.

INTRODUCTION

In the optical stochastic cooling (OSC) scheme, radiation produced by the particle bunch in the pickup undulator will pass through the crystal and be amplified [1, 2]. The amplified radiation is fed back into the kicker undulator and coupled back onto the same beam in such a way to produce a net corrective kick. The process is repeated multiple time in a storage ring leading to a gradual cooling of the beam. With proper lattice design, the cooling can be distributed over all 6-degrees of freedom in the phase space of the beam. The optical amplifier plays a crucial role in the cooling process and the selected amplification medium needs to provide the necessary gain but also provide amplification over a large bandwidth as the cooling time is inversely proportional to the optical-signal bandwidth. One potential lasing medium for the OSC proof-of-principle experiment at Fermilab's IOTA ring [3,4] is a thin Cr:ZnSe crystal pumped by a thulium fiber laser operating at 1908 nm [5]. The choice of the medium was dictated by its broadband in the mid-infrared which have a large overlap with the undulator radiation emitted from a 7-period undulator [6]; see Fig. 1.

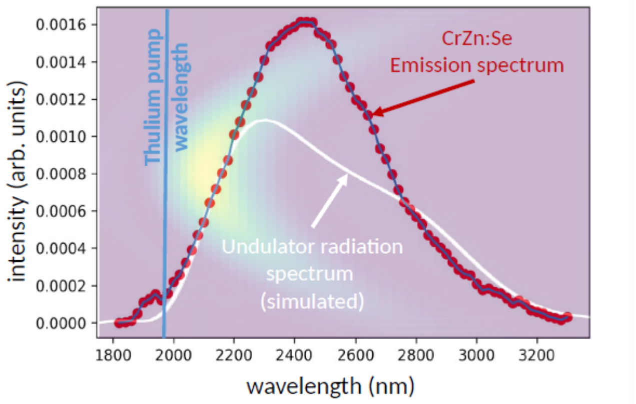

Figure 1: Measured CrZn:Te emission spectrum (red symbols) superimposed with the simulated on-axis undulator radiation (white trace). The false color image gives the angle (vertical axis)-wavelength intensity distribution associated with the undulator radiation; see Ref. [6] for the undulator radiation calculation.

To investigate the amplifier performances, we plan to use synchrotron radiation (SR) produced by one of the bending magnets at the Advanced Photon Source (APS). Specifically, our experiment will be installed in the 35BM beamline hutch. The amplifier setup comprises a Cr:ZnSe crystal which is pumped by a thulium fiber laser operating at 1908 nm. The experiment will guide the final design of the amplifier that will ultimately be incorporated in the active-OSC demonstration in IOTA. The topic discussed in this paper is a continuation of the work initiated in Ref. [7] and aimed at demonstrating amplification of electromagnetic radiation generated by an electron beam at the APS facility.

AMPLIFICATION OF RADIATION

Amplification is produced in the crystal through stimulated emission caused by the broadband SR. The energy levels in the Cr:ZnSe crystal can be modeled as a four-level system. The pumping laser is responsible for populating the third excited state. From there, a radiation-free decay occurs to the second excited state. There are two main processes by which the second excited state falls back to the ground state. It may fall first to the first excited state then to ground or it may fall directly to ground. In the first case, emission from 2 to 1 can be stimulated by the signal SR. Then, like states 3 to 2, the decay from the first excited state to the ground state is radiation-free. In the second case, the wavelength

---

* This work is supported by U.S. Department of Energy under award No. DE-SC0013761 with Northern Illinois University and by the U.S. National Science Foundation under award PHY-1549132, the Center for Bright Beams.

CURRENT STATUS AND PROSPECTS OF FRIB MACHINE PROTECTION SYSTEM*

Z. Li[†], D. Chabot, S. Cogan, S.M. Lidia
Facility for Rare Isotope Beams, East Lansing, Michigan, USA

Abstract

The Facility for Rare Isotope Beams (FRIB) is designed to accelerate beam up to 400 kW power with kinetic energy ≥ 200 MeV/u. Fast response of the machine protection system is critical for FRIB beam commissioning and operation to prevent damage to equipment. The beam commissioning of the first LINAC segment, including fifteen cryomodules, has been completed. Four ion species were accelerated to a beam energy of 20.3 MeV/u with duty factors from 0.05 percent to continuous wave. The peak beam current exceeded 10 percent of the final requirements. This paper summarizes the status of the machine protection system deployed in the production, Machine interlock response time of ~8 µs was achieved. Incentives for future development include being able to achieve smooth and reliable beam operation, faster machine protection response time and real time data analysis of failure mode.

INTRODUCTION

The Facility for Rare Isotope Beams (FRIB) is designed to accelerate beam up to 400 kW power with kinetic energy ≥ 200 MeV/u. Fast response of the machine protection system is critical for FRIB beam commissioning and operation to prevent damage to equipment. The beam commissioning of the first LINAC segment (LS1), including fifteen cryomodules, has been completed. Four ion species were accelerated to a beam energy of 20.3 MeV/u with duty factors from 0.05 percent to continuous wave. The peak beam current exceeded 10 percent of the final requirements [1]. Room temperature and cryogenic button-style BPMs, AC current transformers (ACCTs), halo monitor rings, fast thermometry sensors on the cryomodule beam pipe, scintillator-based neutron monitors for beam loss detection, LLRF controllers and PLCs of front end, LS1 and its folder section are connects to MPS [2].

The machine protection system safeguards the cryomodules and ensures that beam will be tripped off in case of any fault and violation of presetting beam parameters. During the beam commissioning, from the ACCT network detecting a fault of over-power or power-loss-over-threshold conditions, or from fast events detected by the LLRF controllers, to the moment when beam is inhibited, the response time of MPS is within 35 µs [1, 2]. This paper will focus on MPS system structure and its FPGA logics currently implemented in the production line for LS1 commissioning and discussion of its future improvements.

MPS CURRENT IMPLEMENTATION

FRIB MPS is built with master and slave structure [2], where slave nodes collect OK/NOK status from MPS sensor devices [2] and pass to the master through optical fibre daisy chain which uses Time-division multiplexing technique to carry sensor information of each slave node. MPS master processes the information of each sensor received and also the machine status of its own to decide the operation state. It requires 33 slave nodes and 6 master-slave daisy chains to fully cover FRIB front end and LS1 area for machine protection. Since the MPS master can only handle two daisy chains due to limitation of FGPDB [2] board, displayed in Figure 1, a "reptile" structure of MPS was deployed in the production line where we have multiple master nodes consisting of "head", "body" and "tail". Each master node can hold 2 daisy chains with maximum of 16 slave nodes. Master nodes communicate with each other the operation states through RS422 serial state links and also are connected to the EPICS IOC through individual Ethernet cables to be able to configure mask bits [2] of sensor devices simultaneously. Master FPGA logics is designed such that only the master head can accept the EPICS process variable (PV) command to change the operation state. The rest can synchronize their operation states to master head through RS422 links in µs scale and broadcast the synchronized operation state to each slave node on their daisy chains. Each master node can make the decision to enter fault state based on its sensor inputs and machine status and lock up the rest nodes through a dedicate fault link.

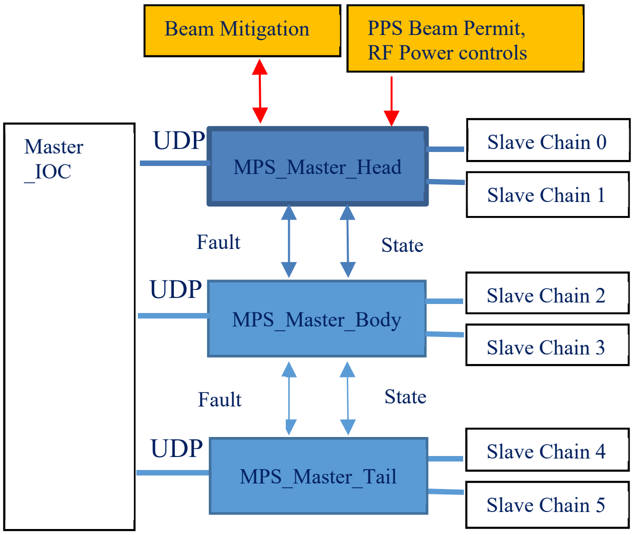

Figure 1: MPS of reptile structure deployed in production.

---

*Work supported the U.S. Dept. of Energy Office of Science under Cooperative Agreement DE-SC0000661.

[†] liz@frib.msu.edu

OPTIMIZATION OF BEAM PARAMETERS FOR UEM WITH PHOTO-EMISSION S-BAND RF GUN AND ALPHA MAGNET

H.R. Lee*[1], P. Buaphad[1], I.G. Jeong[1], Y.J. Joo[1], Y. Kim†[1],
University of Science and Technology, Daejeon, Korea
M.Y. Han, J.Y. Lee, S. Lee, Korea Atomic Energy Research Institute, Daejeon, Korea
B.L. Cho, Korea Research Institute of Standards and Science, Daejeon, Korea
H. Suk, Gwangju Institute of Science and Technology, Gwangju, Korea
[1]also at Korea Atomic Energy Research Institute, Daejeon, Korea

Abstract

Ultrafast Electron Microscopy (UEM) is a powerful tool to observe ultrafast dynamical processes in sample materials at the atomic level. By collaborating with KRISS and GIST, the future accelerator R&D team at KAERI has been developing a UEM facility based on a photo-emission S-band (= 2856 MHz) RF gun. Recently, we have added an alpha magnet in the beamline layout of the UEM to improve beam qualities such as emittance, divergence, energy spread, and bunch length. To achieve high spatial and time resolutions, we have been optimizing those beam parameters and other machine parameters by performing numerous ASTRA and ELEGANT code simulations. In this paper, we describe our ASTRA and ELEGANT code optimizations to obtain high-quality beam parameters for the UEM facility with a photo-emission S-band RF gun and an alpha magnet.

INTRODUCTION

UEM is a powerful tool to visualize atomic or molecular dynamic processes at sample materials [1]. To visualize the atomic bond breaking or making, the spatial and temporal resolutions of sub-angstrom and femtoseconds are required. The spatial and temporal resolutions strongly depend on the electron beam parameters. To achieve the higher spatial and temporal resolutions, the beam parameters such as the transverse beam emittance, beam size, and divergence should be smaller, and the bunch length should be shorter while keeping a higher bunch charge [2]. However, the higher bunch charge makes the space charge force stronger, which can deteriorate the beam quality. Therefore, it is important to optimize those beam parameters by performing beam dynamics simulations under various conditions. Recently, Osaka University has developed a MeV UEM with a photoemission S-band RF gun. By obtaining a bunch length of about 100 fs (rms), they have achieved the temporal resolution of about 170 fs (rms) better than conventional UEMs with a DC gun [3]. The future accelerator R&D team at KAERI has also been studying to develop a MeV UEM to obtain the bunch length shorter than 100 fs (rms). To do so, we have recently added an alpha-magnet to compress the bunch length further. In this paper, we describe our design concepts and beam dynamics simulation results of the MeV UEM with a photoemission S-band RF gun and an alpha-magnet.

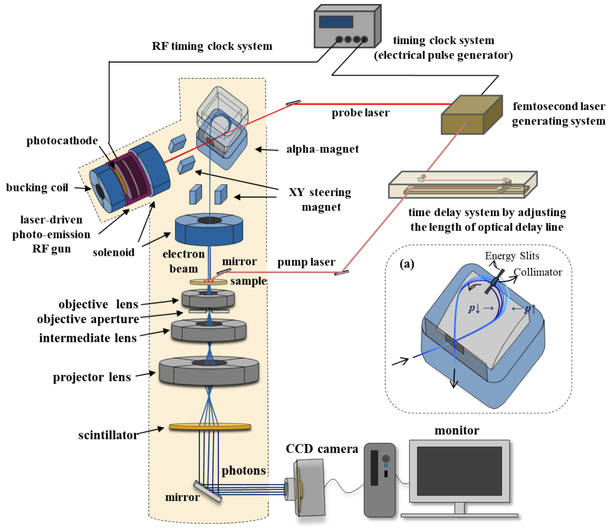

Figure 1: A schematic of the UEM with an alpha-magnet.

REQUIRED BEAM PARAMETERS

Generally, a conventional UEM consists of an electron gun, a beam transport system, a laser system, a sample, and an imaging system. Among them, beam qualities are mainly determined by the electron gun and beam transport system. To determine the beamline component and its lattice, the requirements of the beam parameters, summarized in Table 1, have been investigated as follows.

- The atomic bond breaking and making occur at femtoseconds time domain. Therefore, a femtosecond long bunch length is required for a high temporal resolution at the atomic level.
- If electron beam is accelerated up to 3 MeV, the electron speed is close to that of light, and de Broglie wavelength of electron beam becomes shorter than 0.01 angstrom. For a high spatial resolution, a small transverse beam emittance of 100 nm is chosen [4].
- Considering the number of pixel sensors (1000 × 1000) of the imaging system, at least 10^6 electrons are required to obtain bright images. Therefore, a single bunch charge should be much higher than 0.16 pC at the sample.

---

* hrlee18@kaeri.re.kr
† yjkim@kaeri.re.kr

TEMPERATURE MEASUREMENTS OF THE NSLS-II VACUUM COMPONENTS*

A. Blednykh[†], G. Bassi, C. Hetzel, B.N. Kosciuk,
D. Padrazo Jr, T.V. Shaftan, V.V. Smaluk, G.M. Wang
Brookhaven National Laboratory, Upton, NY, USA

Abstract

This paper is dedicated to the analysis of our recent experience from ramp-up of operating current at NSLS-II from 25 mA at the end of commissioning in 2014 to 475 mA achieved in studies today. To approach the design level of the ring intensity we had to solve major problems in overheating of the chamber components. Since the beginning of the NSLS-II commissioning, the temperature of the vacuum components has been monitored by the Resistance Temperature Detectors (RTDs) located predominantly outside of the vacuum chamber and attached to the chamber body. A several vacuum components were designed with the possibility for internal temperature measurements under the vacuum as diagnostic assemblies. Temperature map helps us to control overheating of the vacuum components around the ring especially during the current ramp-up. The average current of 475mA has been achieved with two main 500MHz RF cavities and w/o any harmonic cavities.

INTRODUCTION

The experimental data collected with $M = 1000$ number of bunches for the regular operational lattice with all IDs magnet gap closed at $V_{RF} = 3MV$. It corresponds to $\sigma_s(I_0 \to 0) = 4.4mm$ bunch length at low current. The RF voltage is induced by two superconducting 500MHz CESR-B RF cavities installed back-to-back in Cell 24. Up to 4 RF cavities are planned to be used for a maximum deliverable RF voltage $V_{RF} = 4.5MV$, corresponding to $\sigma_s(I_0 \to 0) = 3.6mm$. With all IDs installed, a voltage of $4.5MV$ will guarantee a momentum acceptance larger than 3%. The rms bunch length is short compared to the standard half-aperture of the vacuum chamber, i.e. $\sigma_s \ll b$.

BELLOWS

The internal RF contact fingers of the NSLS-II bellows are designed to follow the octagonal profile of the standard vacuum chamber and to minimize impedance contribution due to the outer bellows convolution. The 3D rendered picture of the NSLS-II bellows is shown in Fig. 1. The simplified internal connection of the RF contact fingers relative to the vacuum chamber is shown in Fig. 2, where $b = 12.5mm$ is the chamber radius, $L = 42mm$ is the length of the cavity type joint and $\Delta = 0.4mm$ is the sleeve thickness. The RF contact fingers are able to slide longitudinally with a good contact on the top of the octagonal sleeve under the RF spring force. Three individual bellows in NSLS-II were designed for internal temperature measurements by the Resistance Temperature Detectors (RTDs). A couple of RTDs were fixed on the top of the GLIDCOP RF contact fingers as it is shown in Fig. 3a. The experimental internal temperature measurements are shown in Fig. 3b. The measured temperature (blue dots) has a quadratic dependence on the average current, $T \sim I_{av}^2$, where the dark cyan trace is the experimental data fit. The RF contact fingers heats up to $T = 65°C$ at $I_{av} = 400mA$ with $\sigma_s(I_0 \to 0) = 4.4mm$.

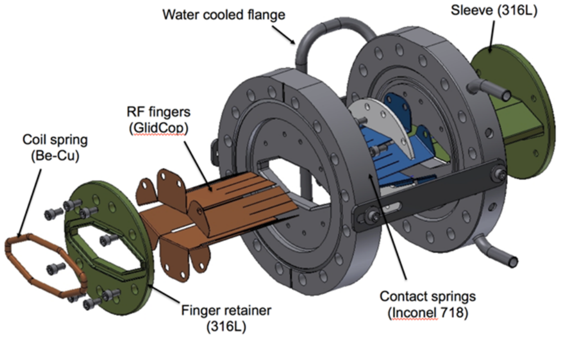

Figure 1: 3D rendered picture of the bellows geometry.

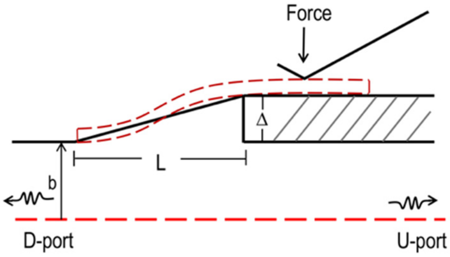

Figure 2: Simplified 2D model of the bellows.

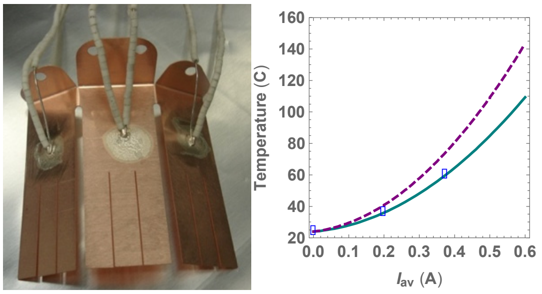

a) b)

Figure 3: a) GLIDCOP RF fingers of the bellows with attached RTDs for internal temperature measurements. b) Internal temperature measurements at $V_{RF} = 3MV$ (blue dots) and the data fit (dark cyan solid line). The dashed purple line is the predicted data at $V_{RF} = 4.5MV$.

To estimate the temperature rise for a shorter bunch length, the numerical simulations of the bellows geometry with a perfect contact of the RF contact fingers have been performed by the GdfidL code [1]. The real part of the longitudinal impedance $\mathrm{Re}Z_{||}$ is shown in Fig. 4. Several

HIGH ENERGY BEAM TRANSPORT ALONG THE 68-m LANSCE 1L BEAMLINE TO OPTIMIZE NEUTRON PRODUCTION *

P. K. Roy[†], R. J. Macek, C. E. Taylor, C. Pillai, E. L. Kerstiens
Los Alamos National Laboratory, LANSCE, AOT-AE/OPS, Los Alamos, NM, USA

Abstract

An 800 MeV proton beam of up to 150 μA is accumulated in the LANCSE Proton Storage Ring (PSR) for 1800 turns and delivered to the Lujan Center, one of five user facilities at the LANSCE linear accelerator center, to generate an intense beam of pulsed neutrons for studies in academia, national security and industry. The Lujan Center beam transport line, known as 1L beamline, is over 68 meters in length, starting from a wire scanner ROWS01 in the extraction line of PSR. The beamline consists of several bending and focusing elements and ends at the 1L target where the beam spot size is nominally 3 cm (2RMS). The next 1L target, Mark IV target, has been designed to optimize the neutron production for the Lujan center to improve high energy flux and resolution. As part of the safety review of this design, it is necessary to know the beam intensity and size on the new target. Alignment data of the beam line was measured with a laser tracking system and was compared with legacy measurements. Using the new measurement of the beamline, calculated beam sizes using the LANL version of the beam envelope code TRANSPORT and CERN code MAD-X are compared. The input beam parameters for the codes were extracted from an ORBIT code [1] analysis of the proton storage ring beam. The beam envelope measurements were made at various locations throughout the beamline using wire scanners. The predicted beam envelopes and measured data agree within expected errors.

INTRODUCTION

An 750 keV H$^-$ beam is accelerated using a Drift Tube Linac (DTL) and a Couple Cavity Linac (CCL) to an energy of 800 MeV and transported to user facilities [2–4]. One of the facilities is the Lujan Center (1L) that utilizes 800 MeV proton beam for neutron production. The 1L beam transport line, starting from wire scanner ROWS01, is composed of many bending and focusing elements before it reaches the 1L target system, where the beam spot size is nominally 3 cm (2RMS). Small field variation of the beamline quadrupoles and/or bending magnets from the standard tune can frequently lead to significant radiation from beam spill, beamline elements damage, and beam-time loss, etc. Therefore, simulation of the beam envelope throughout the length is crucial in understanding the beam bunch distribution during transport. Once the envelope is in good agreement with diagnostics measurements, this information will significantly improve our ability to predict how each optical element responds with various beam conditions. Though the 1L beam transport line was studied previously using the code TRANSPORT [5], many updates have been conducted over the years. Moreover, it is a good opportunity to utilize the modern MAD-X [6] code that is used across the accelerator community for accelerator design at present. Comparison of the measured beam envelope and the prediction from codes is important.

In this report, we present the beam sizes obtained using the Fermilab modified version of the TRANSPORT beam envelope code, modern accelerator design code MAD-X, and beam size measurements along the beamline. The input beam parameters for the codes were extracted from an ORBIT [1] analysis of the proton storage ring beam. The input parameters utilized in the codes are discussed. Measured data are compared to models and the results are extracted to have an estimate of the beam size at the 1L target.

1L BEAMLINE

The 1L beamline starting at ROWS01, consists of 20 quadrupole, 8 bending magnets, 5 wire scanners for beam profile measurements, 11 beam position monitors (BPMs), current monitors, vacuum system, and associate mechanical and electrical systems. The effective lengths of each quadrupole vary from 0.56 m to 0.7 m with half aperture 0.05 m to 0.077 m. These magnets are powered for 1.7 kG to 3.88 kG field. Three 30° beam bending magnets are located upstream of the target, and used to bend the beam a total of 90° to place the beam on target which is surrounded by a safety shielding. Detail of the 1L beamline is not addressed in this report.

Table 1: Basic Relationship of Twiss Parameters

	Parameters	
Beam	Horizontal (x)	Vertical (y)
Beam size (cm)	$x = \sqrt{\sigma_{11}} = \sqrt{\varepsilon_x \beta_x}$	$y = \sqrt{\sigma_{33}} = \sqrt{\varepsilon_y \beta_y}$
Divergence (mr)	$x' = \sqrt{\sigma_{22}} = \sqrt{\varepsilon_x \gamma_x}$	$y' = \sqrt{\sigma_{44}} = \sqrt{\varepsilon_y \gamma_y}$
x- x' correlation	$\alpha_x = \frac{r_{12}}{\sqrt{1-r_{12}^2}}$	$\alpha_y = \frac{r_{34}}{\sqrt{1-r_{34}^2}}$
Twiss parameter	$\beta_x = \frac{\sqrt{\sigma_{11}}}{\sqrt{\sigma_{22}}} \sqrt{\left(1 + \alpha_x^2\right)}$	$\beta_y = \frac{\sqrt{\sigma_{33}}}{\sqrt{\sigma_{44}}} \sqrt{\left(1 + \alpha_x^2\right)}$

---

* LA-UR-19-28531. Work supported by the United States Department of Energy, National Nuclear Security Agency, under contract DE-AC52-06NA25396.

[†] pkroy@lanl.gov

APS UPGRADE INSERTION DEVICE VACUUM CHAMBER DESIGN*

J.E. Lerch†, T.J. Bender, O.K. Mulvany, M.E. Szubert
Argonne National Laboratory, Advanced Photon Source, Lemont, IL, USA

Abstract

A straight section vacuum system (nominally 5.363 meters long) has been designed for the APS upgrade project. This vacuum system will be used in straight sections equipped with hybrid permanent magnet undulators (HPMU). The vacuum system assembly consists of the insertion device vacuum chamber (IDVC), the vacuum chamber distributed support, and the photon absorber. Numerous functional requirements constrained the IDVC design. These constraints included incorporation of the beam aperture transition into the end of the aluminum vacuum chamber extrusion (storage ring aperture to IDVC aperture), thin walls (~600 microns) surrounding the beam aperture to allow for as small a magnetic gap as possible, and complicated weld paths to ensure a continuous beam surface to minimize impedance. Additionally, extensive finite element analysis (FEA) and ray tracing was performed to ensure that the chamber would not fail due to structural or thermal perturbations.

INTRODUCTION [1]

The APS-Upgrade (APS-U) project plan calls for the cur-rent APS 40-sector storage ring (SR) to be retrofitted with a new 6 GeV, 200 mA storage ring optimized for bright-ness above 4 keV. Thirty-one of the forty sector straight sections will be dedicated to Hybrid Permanent Magnet Undulators (HPMU) which will produce photons at various energies to ID beamline users based on their needs. Each HPMU straight section requires a vacuum system to ensure UHV continuity between the upstream and downstream sector arc vacuum systems.

The IDVC design must accommodate many functional requirements. Externally, the IDVC is spatially constrained by the HPMU's in all three directions (see Fig. 1). In the vertical direction (Y-axis), the chamber must fit within a minimum ID magnetic gap of 8.0 mm. In the longitudinal direction (Z-axis) the chamber must provide 5050 mm of space for the HPMU magnetic structures, phase shifters, and canting magnets (for canted HPMU configurations). In the transverse direction (X-axis), the chamber must provide adequate clearance for the width of the largest magnet structure. Internally, accelerator physicists limits the internal beam aperture height to a minimum of 6.0 mm and the aperture surface finish must have an RMS surface finish of <1 micron. The chamber must also provide an adequate antechamber so that enough pumping can be used to meet pressure requirements. Additionally, there must be a slot between the beam aperture and the antechamber to provide adequate vacuum conductance and avoid scraping synchrotron radiation from the upstream bending magnet, but not so large that the material in the wall yields while under vacuum due to wall thinning. The machine physics group also desires as few flanged connections as possible along the beam path to limit impedance during operation. Finally, the small difference between the minimum magnetic gap height and the minimum beam aperture height require the beam aperture to be aligned vertically (Y-axis) within a +/- 50 microns tolerance band and the chamber straightness to be +/- 100 microns across the length of the IDVC. The following is an overview of the IDVC design process with an emphasis on the design challenges encountered.

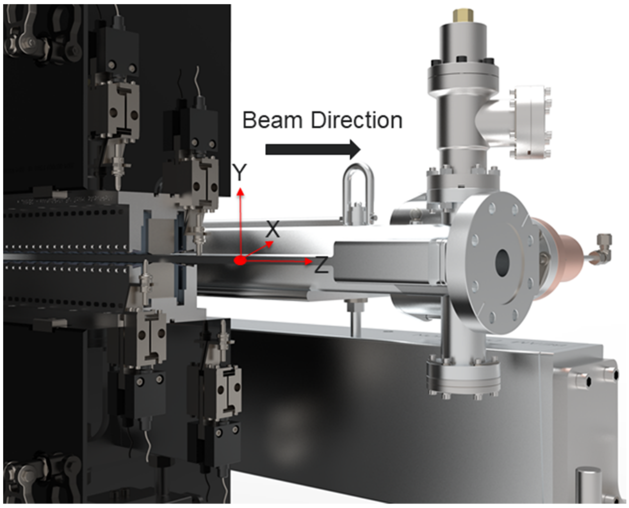

Figure 1: IDVC Assembly within HPMU structure. Coordinate system shown in red for reference.

IDVC EXTRUSION DESIGN

The IDVC is designed to be machined from a single 5.4-meter-long aluminum extrusion. The extrusion geometry (shown in Fig. 2) has three critical features: beam aperture, pumping slot, and antechamber.

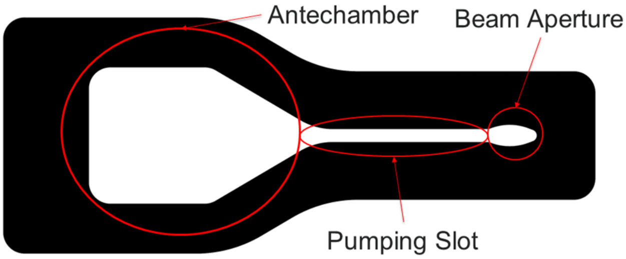

Figure 2: IDVC extrusion cross-section with critical features noted.

---

* Sponsor: Argonne National Laboratory
† Author Email: Jlerch@anl.gov

ISBN: 978-3-95450-223-3 ISSN: 2673-7000 doi:10.18429/JACoW-NAPAC2019-TUPLS03

THE DESIGN OF THE ADVANCED PHOTON SOURCE UPGRADE (APS-U) SUPERCONDUCTING UNDULATOR (SCU) VACUUM SYSTEM*

M.E. Szubert†, E.R. Anliker, T.J. Bender, J.E. Lerch
Advanced Photon Source-Upgrade, Argonne National Laboratory, Lemont, IL, USA

Abstract

The Advanced Photon Source Upgrade (APS-U) includes four straight sections equipped with full length Superconducting Undulators (SCUs). These sections require vacuum systems that must span 5.383 meters at nominal length, accommodate the SCU device, and accommodate additional magnets for the canted configurations. In the direction of the beam, the upstream portion of the vacuum system is a copper chamber doubling as a photon absorber with a design that is manufactured to allow a 13.5 mm canting magnet gap. This portion of the vacuum system operates at room temperature and shadows the length of the vacuum chamber that operates within the cryostat at 20K. The vacuum chamber inside the cryostat is a weldment including a machined aluminum extrusion allowing for an 8mm magnetic gap, stainless steel thermal insulators, copper shields, and bellows/flange assembly. The vacuum system includes another room temperature copper chamber and absorber on the downstream end of the straight section. The vacuum system provides Ultra-high Vacuum (UHV) continuity through the straight section, connecting the storage ring vacuum systems.

INTRODUCTION

The APS-U project plan calls for the current APS 40 sector storage ring (SR) to be retrofitted with a new 6 GeV, 200 mA storage ring optimized for brightness above 4 keV. Superconducting Undulators (SCUs) equip 4 of the 40 sector straight sections which produce photons at various energies to Insertion Device (ID) beamline users based on their needs [1].

Each ID layout requires a vacuum system to ensure UHV continuity between SR vacuum systems. The SCU vacuum system interfaces with the SR vacuum systems at the up and downstream BPMs, and needs to span a nominal distance of 5.383 meters. At these locations, the SCU aperture matches the $\emptyset 22\,mm$ SR aperture. During operation, the vacuum system is fixed at the center of the straight section, and its length contracts 14 mm on each side; therefore, its operating length is 5.355 meters.

The straight sections equipped with SCUs accommodate two configurations, canted and inline. The sectors equipped with canted SCUs impose the most limitations for the vacuum system design. One vacuum system was designed to accommodate both canted and inline sectors. Having a uniform design aids in the production of these systems.

OVERVIEW

The SCU Vacuum System consists of 3 assemblies: (1) upstream out-of-cryo vacuum assembly, (2) in-cryo vacuum assembly that resides inside the cryostat, and (3) downstream out-of-cryo vacuum assembly (Fig. 1). Within the straight section, the aperture varies between a 22 mm diameter round aperture, a 10.3 mm (H) x 49 mm (W) racetrack aperture, and a semi-elliptical aperture (Fig. 2). A transition feature is machined into both ends of the extrusion, blending the racetrack aperture and the internal extrusion geometry, and keeping any weld under-bead from impeding on the aperture. The smooth transitions are seamless to reduce beam impedance and occur in both the in-cryo and out-of-cryo systems.

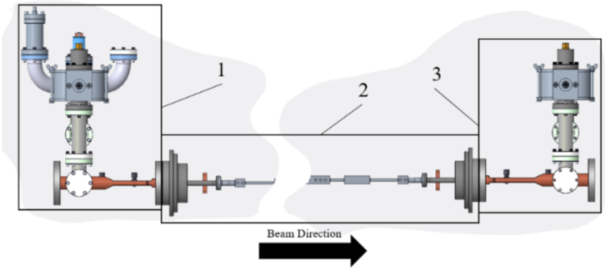

Figure 1: Vacuum sub-systems breakdown.

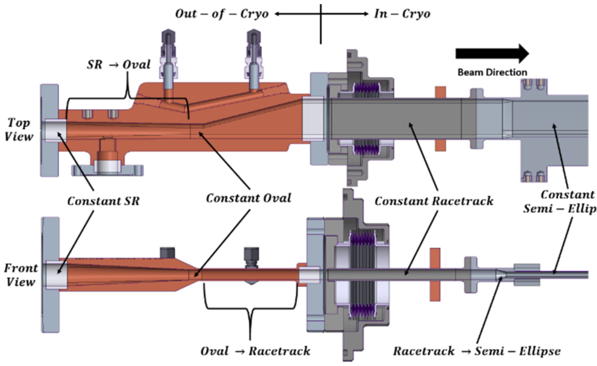

Figure 2: Aperture breakdown.

The aperture geometries are the result of the varying magnetic gaps and the requirement to prevent beam incidence on the in-cryo system. The out-of-cryo OF-Copper vacuum chambers act as photon absorbers; the upstream absorber protects the in-cryo vacuum system and the downstream absorber shadows 1.2 meters of downstream equipment.

The in-cryo chamber is supported as a part of the cold-mass inside the cryostat. The two out-of-cryo vacuum systems require supports external to the cryostat, using standoffs and threaded rods (Fig. 3).

---

* Work supported by the U.S. Department of Energy, Office of Science, under Contract No. DE-AC02-06CH11357.
† mszubert@anl.gov

ISBN: 978-3-95450-223-3 ISSN: 2673-7000 doi:10.18429/JACoW-NAPAC2019-TUPLS04

RE-EVALUATION OF THE NSLS-II ACTIVE INTERLOCK WINDOW*

R.P. Fliller, III†, C. Hetzel, Y. Hidaka, T. Tanabe, Brookhaven National Laboratory, Upton, USA

Abstract

The NSLS-II Active Interlock is the system which protects the NSLS-II Storage Ring vacuum chamber from damage due to synchrotron radiation. The Active Interlock measures the beam position and angle at all insertion devices and issues a beam dump if the beam is outside of the pre-defined window. The window is determined by thermal analysis of vacuum apertures and considers the effects of local magnets such as canting magnets, etc. Recently, it was realized that the insertion device correction coils where not considered in the initial evaluation of the envelope. The purpose of these coils is to correct for the orbit deviations caused by imperfections in the insertion devices that steer the beam. The usual effect is to negate any angle induced by the device, however, if the coil is not set properly the beam may have a larger angle than permitted by the Active Interlock even though the angle calculation does not show it. In this paper we discuss the effect of the insertion device coils on the electron beam and the steps taken to account for this effect in the Active Interlock.

INTRODUCTION

The NSLS-II Active Interlock System (AI) protects the NSLS-II Storage Ring vacuum chamber from damage caused by mis-steered synchrotron radiation. The ring vacuum chamber, absorber apertures and possibly front end components may be damaged by errant steering of the x-ray beam[1]. Part of the AI is to measure the beam position and angle within the insertion devices to ensure that the beam is appropriately located, that is to say it is within the AI envelope. When the beam is outside of the envelope the AI trips the RF system.

All of the insertion devices have correction coils that are used to correct for steering induced by the devices as the gap is closed. The appropriate strength of these coils as a function of gap is measured and subsequently controlled via feedforward tables. It was realized that the influence of these coils was not considered in the analysis of synchrotron radiation protection and the active interlock system. Even though the purpose of the coils of to correct for steering induced by the insertion device, for whatever reason these coils may not have the proper current and therefore the beam may have additional steering. If the beam is measured to be close to the edge of the envelope, the beam may exceed it, and cause damage to the vacuum chamber.

In this paper we recall the requisite functionality of the AI System, and the previous analysis that was performed. Then we discuss the strategy for including the correction coils in the analysis and then the results of the analysis and its incorporation in the AI system.

AI SYSTEM BASICS

The AI system protects the storage ring vacuum chamber from synchrotron radiation damage by controlling the electron beam location and angle through the insertion device. In insertions with one or two uncanted devices, two beam position monitors (BPMs) are used. In canted insertions, three or four BPMs are used. Figure 1 shows a typical canted insertion. The data from the BPMs is sent through a dedicated link to a FPGA which calculates the beam position and angle within the insertion. This result is compared to the AI envelope, if the position or angle is outside of this envelope, then the AI delivers a beam dump signal to the RF system.

The AI envelope is determined by calculations of where the synchrotron radiation strikes various objects in the storage ring (vacuum chambers, flanges, RF fingers, absorbers, etc.) and what the temperature rise is for various missteerings of the beam. This sets ultimately sets the safe limits of the electron beam and angle at the center of the insertion device [2]. The most stringent limits come from the dipole chamber immediately downstream of the insertion device. As with most synchrotron light source chambers, the vertical aperture is very small and the horizontal aperture is large, especially when the antechamber for pumping is included.

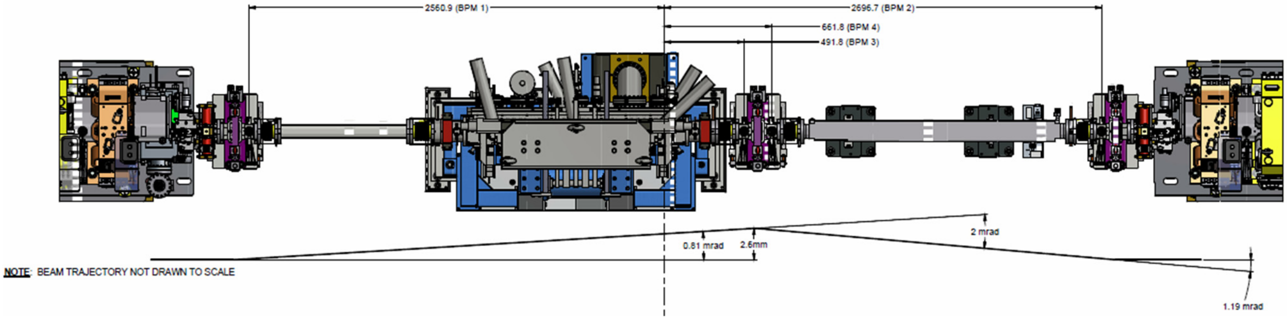

Figure 1: Layout of the 19 ID Straight section. This is a typical canted beamline with one undulator. Taken from [3].

The beam position and angle calculation assume that the distance between the BPMs is a drift. The one exception is a three BPM canted beamline which takes into account the

---

* This manuscript has been authored by Brookhaven Science Associates, LLC under Contract No. DE-SC0012704 with the U.S. Department of Energy

† rfliller@bnl.gov

ISBN: 978-3-95450-223-3 ISSN: 2673-7000 doi:10.18429/JACoW-NAPAC2019-TUPLS05

HIGH-LEVEL PHYSICS APPLICATION FOR THE EMITTANCE MEASUREMENT BY ALLISON SCANNER*

T. Zhang†, S. M. Lund, T. Maruta, J. C. Wong
Facility for Rare Isotope Beams, Michigan State University, East Lansing, MI, USA

Abstract

On the ion accelerator, transverse emittance diagnostics usually happens at the low-energy transportation region, one device named 'Allison scanner' is commonly used to achieve this goal. In this contribution, we present the software development for both the high-level GUI application and the online data analysis, to help the users to get the beam emittance information as precise and efficient as possible, meanwhile, the entire workflow including the UI interaction would be smooth and friendly enough. One soft-IOC application has been created for the device simulation and application development. A dedicated 2D image data visualization widget is also introduced for the general-purposed GUI application development with PyQt5.

INTRODUCTION

The driver LINAC of Facility for Rare Isotope Beams (FRIB) is designed to be able to accelerate a range of stable ions from Oxygen to Uranium to the kinetic energy > 200 MeV/u, with a final delivered beam power at the target of up to 400 kW, which is more than two orders advancement in the heavy ion accelerators regime [1, 2].

The transverse beam emittance is usually diagnosed at the lower beam energy transportation line (LEBT), the projected two-dimensional phase space distribution could be sampled by moving the step motor on which is mounted with an open slit to capture the beam at the different transverse location, at the meantime, sweeping the deflection voltage applied onto the parallelly displaced electric plates to figure out the incident angle. The voltage sweeping (V_0) could map the transverse divergence x' information, by the simple formula $x' = \frac{qV_0L}{2dE_k}$, where V_0 is the voltage applied onto the upper ($+V_0$) and bottom ($-V_0$) plates, L is the effective horizontal displacement of the deflection and E_k is the kinetic energy of the incidental ion. Such kind of emittance measurement device is so-called 'Allison scanner', which was proposed in early last 80's [3].

Reference [4] investigates the details about the data analysis about the emittance measurement by Allison scanner at FRIB LEBT beamline. And also presents the developed Python routine for quick data post-processing. In this paper, we present the continued software development for Allison scanner, the deployed high-level control software application features the core data analysis algorithm developed (see the appendix section of ref [4]), and more user-friendly interactive data processing is introduced, as well as other subtle improvement that can boost the efficiency and user experience.

ALLISON SCANNER APPLICATION

The physics high-level applications for FRIB are systematically designed and developed. Started from the Python interactive scripting environment, to the higher-level GUI applications, various techniques are utilized to make the development robust and efficient, as well as the deployment to FRIB's controls network [5].

Allison scanner is one of the 'slow' devices used by FRIB LINAC, 'slow' means the response of the data for process from the device usually happens a few seconds or minutes after the trigger command is sent out. The EPICS [6] hardware input output controller (IOC) is developed by diagnostic engineers, which is responsible for the device controls, that is to make the step motor and the voltage sweeping as requested by controlling specific controls process variables (PVs). At FRIB, there also comes with a dedicate CS-studio OPI for the user to operate the Allison scanner device, rather than typing the tedious commands to talk to the IOC.

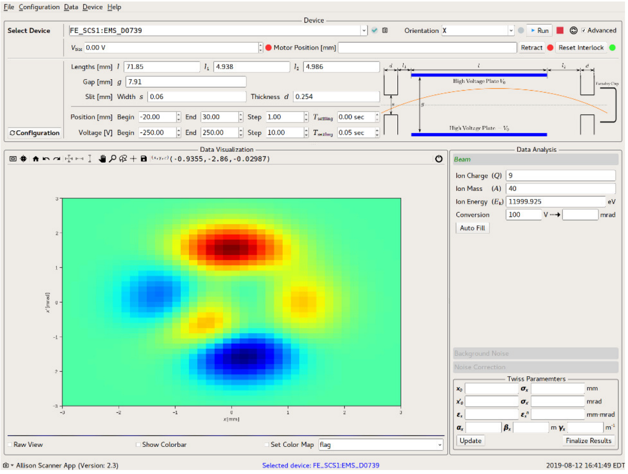

Select Device: FE_SCS1:EMS_D0739
Orientation: X
V_{bias}: 0.00 V
Lengths [mm] l: 71.85 l_1: 4.938 l_2: 4.986
Gap [mm] g: 7.91
Slit [mm] Width s: 0.06 Thickness d: 0.254
Position [mm] Begin: -20.00 End: 30.00 Step: 1.00 $T_{settling}$: 0.00 sec
Voltage [V] Begin: -250.00 End: 250.00 Step: 10.00 $T_{settling}$: 0.05 sec
(-0.9355,-2.86,-0.02987)
Ion Charge (Q): 9
Ion Mass (A): 40
Ion Energy (E_k): 11999.925 eV
Conversion: 100 V → mrad
Set Color Map: flag
Allison Scanner App (Version: 2.3)
Selected device: FE_SCS1:EMS_D0739
2019-08-12 16:41:49 EDT

Figure 1: Main window of Allison scanner application developed by PyQt5*.
*The image shown here is just a place holder from the widget

While after the data acquisition (DAQ) of the beam transverse phase space, post data analysis is the most important part to get the beam Twiss parameters [7], say α, β, γ, ϵ, as well as projected beam sizes and center positions. To accomplish this goal, another dedicated GUI application is developed within the software framework addressed in ref [5].

Figure 1 shows the main window of Allison scanner app, from which, the user could have the controls to the device,

---

* Work supported by the U.S. Department of Energy Office of Science under Cooperative Agreement DE-SC0000661, the State of Michigan and Michigan State University.

† zhangt@frib.msu.edu

HELICAL TRANSMISSION LINE TEST STAND FOR NON-RELATIVISTIC BPM CALIBRATION [*]

C. Richard[†], Michigan State University, East Lansing, MI, USA
S. Lidia, Facility for Rare Isotope Beams, East Lansing, MI, USA

Abstract

Measurements of non-relativistic beams by coupling to the fields are affected by the properties of the non-relativistic fields. The authors propose calibrating for these effects with a test stand using a helical line which can propagate pulses at low velocities. Presented are simulations of a helical transmission line for such a test stand which propagates pulses at 0.033c. A description of the helix geometry used to reduce dispersion is given as well as the geometry of the input network.

INTRODUCTION

Measurements of beam properties using devices that couples to the fields generated by the beam, such as beam position monitors, are made easier if the beam is assumed to be relativistic. For slow beams, such as in the front end of heavy ion accelerators, the measured fields will be traveling non-relativistically, $v < 0.1c$, causing the measured results will be distorted. The measurements can be corrected using analytic solutions of the fields [1] and simulations [2]. However, the authors are unaware of any test stand used to calibrate beam-line devices for non-relativistic perturbations.

A test stand for this purpose will be strung through the device under test to replicate the structure and velocity of the bunch. Such test stands have been created using Goubau lines to replicate the fields from electron beams [3]. However, Goubau lines cannot propagate pulses slow enough to simulate non-relativistic beams. The authors propose using a helical transmission line. These lines can theoretically propagate pulses at arbitrarily low phase velocities based on the pitch of the helix [4]. In order to use helical transmission lines in a test stand, the impedance and dispersion must be characterized to ensure reasonable matching and pulse propagation.

DISPERSION

In order to produce the specific pulse shape at the device under test, it is ideal to have a constant phase velocity so any pulse input into the transmission line will maintain the pulse shape throughout propagation. To calculate the phase velocity of a helical transmission line, the sheath helix model was used. This model approximates the helix as a thin cylinder where the current is forced to travel in a helical path along the surface with pitch angle, ψ. The boundary conditions at the sheath helix in polar coordinates are [4]

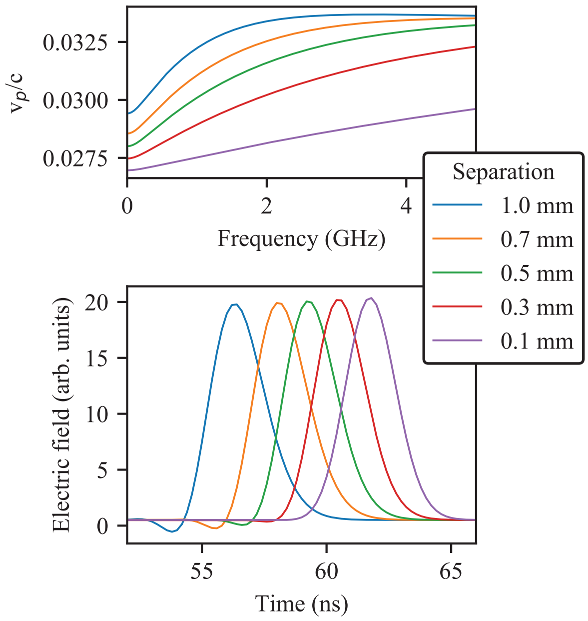

Figure 1: Top: phase velocities with varying separation (s). All other dimensions are given in Table. 1. Bottom: the corresponding pulse deformation of a 1 ns rms pulse after propagating 0.5 m.

$$E_z^i = E_z^e \tag{1}$$

$$E_\theta^i = E_\theta^e \tag{2}$$

$$E_z^{i,e} = -E_\theta^{i,e} \cot(\psi) \tag{3}$$

$$H_z^i + H_\theta^i \cot(\psi) = H_z^e + H_\theta^e \cot(\psi). \tag{4}$$

where the superscripts i and e denote the interior and exterior regions of the helix. This model of the helical transmission line uses a sheath helix centered inside a conducting pipe. From these boundary conditions it was found the dispersion from a helix has large variation with frequency causing the pulse shape to deteriorate. For example, a 5 mm radius helix with $\psi = 0.05$ rad will have the phase velocity reduced from 0.085c to 0.05c over 0.25 GHz. While the input pulse can be tailored to evolve under dispersion to the correct profile at the device under test [5], the generation of such pulses is complicated.

A more practical solution is to add a conducting rod inside of the helix to increase the capacitance of the system. Increasing the capacitance lowers the phase velocity at low frequency while leaving the high frequency limit unchanged

---

[*] Work supported by the US Department of Energy, Office of Science, High Energy Physics under Cooperative Agreement award number DE-SC0018362 and Michigan State University.

[†] richard@nscl.msu.edu

North American Particle Acc. Conf. NAPAC2019, Lansing, MI, USA JACoW Publishing
ISBN: 978-3-95450-223-3 ISSN: 2673-7000 doi:10.18429/JACoW-NAPAC2019-TUPLS08

ANALYSIS OF ALLISON SCANNER PHASE PORTRAITS USING ACTION-PHASE COORDINATES [*]

C. Richard[†], Michigan State University, East Lansing, MI, USA
J.P. Carneiro, L. Prost, A. Shemyakin, Fermilab, Batavia, IL, USA

Abstract

Allison scanners provide detailed information on the beam transverse phase space. An effective way for analyzing the beam distribution from these measurements is to use action-phase coordinates, where beam propagation in a linear lattice is reduced to advancing the phase. This report presents such analysis for measurements performed with a 2.1 MeV, 5 mA H^- beam in the MEBT of the PIP2IT test accelerator at Fermilab. In part, with the choice of calculating the Twiss parameters over the high intensity portion of the beam, the beam core is found to be phase-independent with intensity decreasing exponentially with action, while the beam tails exhibit a clear phase dependence that is stable over the beam line.

INTRODUCTION

To improve comparisons of beam phase space measurements performed with different focusing, the phase portraits can be viewed in action-phase coordinates where the action J and phase ψ are defined as

$$J = \frac{1}{2}\left(\gamma x^2 + 2\alpha x x' + \beta x'^2\right) \tag{1}$$

$$\psi = \arctan\left(\frac{\alpha x + \beta x'}{x}\right) \tag{2}$$

where α, β, and γ are the Twiss parameters and x and x' are the position and angle coordinates.

Table 1: PIP2IT MEBT Allison Scanner Dimensions

Parameter	Value
Slit size	0.2 mm
Slit separation	320 mm
Slit thickness	0.04 mm
Plate voltage	±1000 V
Plate length	300 mm
Plate separation	5.6 mm

The benefit of using this coordinate system that is the intensity distribution over action does not change assuming negligible non-linear effects [1]. Also, the phase is proportional to the betatron phase advance. Thus under linear optics, beam transport results in only a shift in phase. Distributions can therefore be compared even between measurements with different beamline configurations resulting in different Twiss parameters. This allows for measurements of distortions and tail growth due to non-linear forces.

This approach is detailed below and illustrated by measurements of the phase space of a 2.1 MeV H^- beam in the PIP2IT beamline [2]. The measurements were taken using an Allison scanner [3] with dimensions given in Table 1. The measured 2D distributions, called phase portraits, were converted to action-phase coordinates by calculating the action and phase for each pixel in the scan based on the measured ensemble.

DISTRIBUTION OVER ACTION

For negligible space charge, the beam density is expected to be Gaussian in position and angle [4]. In this case the intensity follows a Boltzmann distribution in action

$$I = I_0 e^{-J/\epsilon_c} \tag{3}$$

where ϵ_c is referred to as the central slope. At higher actions, it was found that the intensities deviate from the distribution in Eq. (3). The action where the intensities deviate significantly from Eq. (3) is found by binning the intensities by action, typical bin size of 0.05 mm mrad, and calculating the mean and standard deviation of the intensity in each bin. The 'transition action' J_t is defined as the action where the average intensity deviates from Eq. (3) by more than three times the standard deviation of the mean.

$$I(J_t) - I_0 e^{-J_t/\epsilon_c} = 3\sigma_{\text{int}}(J_t) \tag{4}$$

The transition action defines the separation of the Gaussian core from the non-Gaussian beam tails. The fraction of the beam in the core is typically between 70-90%.

At larger actions the beam becomes phase dependent and splits in phase into two 'branches' separated by approximately π (Fig.1 middle). Currently, no satisfactory description or source of the phase dependent tails has been found, and the tails are only characterized by the average phase of the 'upper' branch, $\psi \in (0, \pi]$, and the maximum action.

In the initial attempts to transform the measured $x - x'$ phase portraits into $J - \psi$ coordinates two issues were found. The first issue was the distributions over action were not constant under changes to the optics. The second peculiarity was the distributions showed a phase dependence even at low actions which was not believed to accurately describe the beam. To address these issues, special care must be taken when defining the central slope and Twiss parameters used to determine J and ψ. The corrections for these complications are described below.

---

[*] Work supported by the US Department of Energy, Office of Science, High Energy Physics under Cooperative Agreement award number DE-SC0018362 and Michigan State University.

[†] richard@nscl.msu.edu

PRECISION INSERTION DEVICE CONTROL AND SIMULTANEOUS MONOCHROMATOR FLY SCANNING FOR NSLS-II

D.A. Hidas*, P.L. Cappadoro, T.M. Corwin, J. Escallier, A. Hunt, M. Musardo, J. Rank, C. Rhein, J. Sinsheimer, T. Tanabe, I. Waluyo, Brookhaven National Laboratory, Upton, NY, USA

Abstract

Beginning in January of 2019, eight of the 10 In-Vacuum Undulators installed in the NSLS-II storage ring underwent in-house in-situ control system upgrades allowing for control of the magnetic gap during motion down to the 50 nanometer level with an in-position accuracy of nearly five nanometers. Direct linking of Insertion Devices and beamline monochromators is achieved via a fiber interface allowing precise, simultaneous, nonlinear motion of both devices and providing a fast hardware trigger for real-time accurate insertion device and monochromator fly scanning. This presentation will detail the accuracy of motion and its effect on the produced spectra as well as the variation of flux when both insertion device and monochromator are in simultaneous motion.

INTRODUCTION

Between January and April of 2019, eight of the 10 In-Vacuum Undulators (IVUs) installed in the NSLS-II storage ring underwent in-house in-situ control system development and replacement. The motivation for this was to correct the underperforming and unreliable operation of the vendor supplied systems, speed up step-scanning, and lay the proper groundwork for Insertion Device (ID) and monochromator synchronization for fast fly scanning of photon energy while maintaining peak photon flux. Step scanning speeds were improved by a factor of nearly five and all eight IVUs are currently running with extremely high reliability. The first real-time synchronization of an ID and monochromator has been achieved with one of the out-of-vacuum Elliptically Polarizing Undulators (EPUs) for the In situ and Operando Soft X-ray Spectroscopy (IOS) beamline with another IVU and EPU to follow shortly.

IVU CONTROL SYSTEMS UPGRADE

The eight IVUs that underwent a complete software overhaul are three 2.8 [m] long 23 [mm] period (IVU23), three 1.5 [m] long 21 [mm] period (IVU21), and two 3 [m] long 20 [mm] period (IVU20) devices. The simplest with regard to the control system among them are the two IVU20s which have one motor to control the magnetic gap and one for device elevation. This type device will not be discussed in detail, but can be thought of as the single-axis (gap) analog of the more complicated systems discussed herein. The remaining six IVUs (IVU21s and IVU23s) each have four motor axes which we denote TU, TD, BU, and BD (where: T - Top, B - Bottom, U - Upstream, D - Downstream). The simple linear transformation shown in Eq. (1) gives the useful coordinates of gap, elevation, taper, and tilt of the device. This transformation and its inverse are used to form the forward and inverse kinematics for device motion. The IVU21 devices have an additional jack elevation motor axis which is used for alignment and not used in normal operation which is of little interest here and not discussed further.

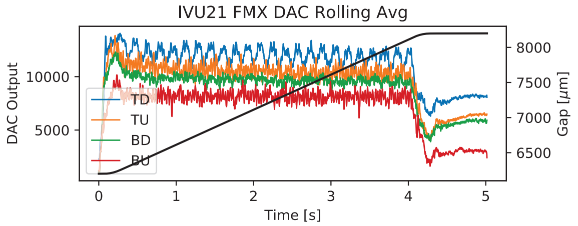

Figure 1: DAC output rolling average showing output during motion for each motor with notable oscillatory behavior of the TD output possibly indicating component misalignment or wear as an example of diagnostic plots used at NSLSII.

The DeltaTau Brick Controller is used for motion control. Renishaw 1 [nm] linear encoders are used for position feedback on the four girder gap axes while the rear mounted motor rotary encoders are used for velocity feedback. Proportional Integral Derivative (PID) tuning is performed separately for top-girder and bottom-girder drives. The DeltaTau drives external servo amplifiers with a ± 10 [V] analog signal (here referred to as DAC output). It is noted here that from this output one may glean insight into mechanical misalignment or wearing, possibly preventing damage or failure if monitored occasionally. An example of this this is shown in Fig. 1. It is also noted that in these systems the linear encoders are not mounted in line with the drive shafts and may suffer from a dual feedback cantilever resonance effect. This effect has been witnessed in less massive devices [1].

$$\begin{bmatrix} gap \\ elevation \\ taper \\ tilt \end{bmatrix} = \begin{bmatrix} \frac{1}{2} & \frac{1}{2} & \frac{1}{2} & \frac{1}{2} \\ \frac{1}{4} & \frac{1}{4} & -\frac{1}{4} & -\frac{1}{4} \\ 1 & 1 & -1 & -1 \\ \frac{1}{2} & -\frac{1}{2} & -\frac{1}{2} & \frac{1}{2} \end{bmatrix} \begin{bmatrix} TU \\ TD \\ BU \\ BD \end{bmatrix} \tag{1}$$

IVU CONTROL PERFORMANCE

It is highly desirable to have well behaved ID gap movement during operations, not only as a prerequisite to simultaneous ID-monochromator scanning, but also to minimize any effect on the electron beam that would which would normally be compensated by an active feed-forward corrector

---

* dhidas@bnl.gov

ISBN: 978-3-95450-223-3 ISSN: 2673-7000 doi:10.18429/JACoW-NAPAC2019-TUPLS10

TROUBLESHOOTING AND CHARACTERIZATION OF GRIDDED THERMIONIC ELECTRON GUN

M. Stefani[*], Old Dominion University, Dept. of Electrical & Computer Engr., Norfolk, VA, USA
F. Hannon, Thomas Jefferson National Accelerator Facility, Newport News, VA, USA

Abstract

Jefferson National Laboratory has, in collaboration with Xelera research group, designed and built a gridded thermionic election gun with the potential for magnetization; in an effort to support research towards electron sources that may be utilized for the electron cooling process in the Jefferson Laboratories Electron Ion collider design. Presented here is the process and result of troubleshooting the electron gun components and operation to ensure functionality of the design.

OVERVIEW OF GUN CONFIGURATION AND OPERATION

The overall design goals were to build a gridded thermionic gun, operating at 125 kV with a frequency of 500 MHz, and a variable bunch charge with the nominal bunch charge being 130 pC. The gun must also be able to macro pulse the bunch train to control the average current. The standard operation of a gridded thermionic gun produces electron bunched by heating the cathode emitting surface via a current producing resistive heating, applying a sufficient bias voltage to the nearby grid to prevent electron emission and then superimposing a RF voltage to the bias on the grid to periodically reduce the local gradient and allow for electron emission. [1,2]

The design of our gun however superimposes all of these DC and RF signals onto the cathode surface, as well as the high voltage (HV) applied to the cathode electrode. This design requires that the RF components, RF transmission line, bias voltage supply, and heater current supply all be lifted to the 125 kV by an isolation transformer allowing 110 AC power to these components while they have a new local "ground" potential of 125 kV. The controls for these components are then communicated via fiber optic cables. The bias voltage is remotely controlled by an analog fiber optic transceiver that has an output of 0-10 V. The supply then linearly scales this input to a 0-320 V output. This bias supply output is used to float the current supply voltage. The current supply then contacts the electrically isolated cathode heater and emitter via the center conductor of the co-axial RF transmission line; having the effect of allowing resistive heating while also establishing a stable bias voltage on the cathode compared to the grid which is locally grounded via the outer conductor of the co-axial RF transmission line. Therefore, the necessary gradient is present between the grid and cathode to restrict emission. The RF signal is transferred from the RF generator to the components at HV (collectively called the "hot deck") via RF to RF fiber optic transceivers. The RF signal once sent to the hot deck then goes through a low noise amplifier and then must pass through a pin modulator which allows the macro pulsing. The pin modulator is also controlled via fiber optic signal. A 5V signal is sent to the pin modulator from a digital fiber optic transceiver and when this 5 V signal is present the pin modulator passes the 500MHz RF signal to a 50-Watt amplifier on the hot deck. After the amplifier, a RF isolator is present to protect the amplifier form any reflected power. Then the RF is sent through a Bi-directional coupler used to pick up the reflected power which is needed to match the RF transition line by minimizing the reflected power. The forward power from the bi-directional coupler is then passed through a DC blocker, so that the DC signal on the center conductor do not back-feed into the RF system. Finally, the RF is sent into the co-axial transmission line by a SMA connection that functions as an RF bias-T. Thus, the RF signal, The bias voltage and the heater current are all carried to the cathode via the RF transmission line.

By applying HV to the electrodes, controlling the bias and RF power to produce electron bunches from the gridded cathode, and using the macro pulsing signal to the pin modulator, this design should be able to produce all the design characteristics. The following sections of this paper should clarify the operations of each component mentioned and the method of troubleshooting used to establish functionality.

RF COMPONENTS

This section will more clearly detail the RF transmission line design and functionality. Figure 1 gives a general schematic of the transmission line.

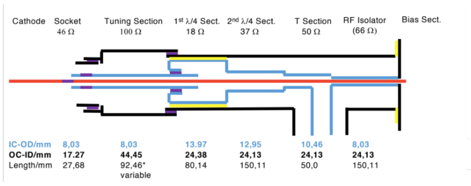

Figure 1: RF transmission line schematic.

An important design feature is the inner conductor diameter increasing in steps from the back of the transmission line where the DC bias and current are introduced. The larger inner diameter will have a lower impedance for the RF signal and therefore channel the RF signal forward towards the cathode. The back plate where the DC bias and current are introduced is electrically isolated from the outer conductor of the transmission line by a kepton gasket. The contact for the grid at the cathode contacts the outer conductor of the co-

---

[*] mstefani@jlab.org

NEG-COATED COPPER VACUUM CHAMBERS FOR THE APS-UPGRADE STORAGE RING VACUUM SYSTEM*

O. K. Mulvany†, B. Billett, B. Brajuskovic, J. A. Carter, A. McElderry, K. J. Wakefield,
Advanced Photon Source, Argonne National Laboratory, Lemont, IL, USA

Abstract

The APS-Upgrade (APS-U) storage ring features a diverse group of vacuum chambers including seven distinctive, non-evaporable getter (NEG)-coated copper vacuum chambers per each of the 40 sectors. These chambers feature a 22-millimeter diameter aperture along the electron-beam path, with two vacuum chambers permitting photon extraction through a keyhole-shaped extension to this aperture. The chambers range from 0.3-meters to 1.7-meters in length and fit within the narrow envelope of quadrupole and sextupole magnets. Six of the seven copper vacuum chambers intercept significant heat loads from synchrotron radiation; five of these designs are fabricated entirely from OFS copper extrusions and are equipped with a compact Glidcop® photon absorber. A hybrid vacuum chamber, fabricated from OFS copper extrusion and a copper chromium zirconium (CuCrZr) keyhole transition, also intercepts synchrotron radiation. The seventh vacuum chamber design features a keyhole aperture across its length and is entirely fabricated from CuCrZr. This paper details the careful balance of vacuum chamber functionality, manufacturability, and the overall design process followed to achieve the final designs.

INTRODUCTION

The APS-U project is designing a storage ring upgrade that will be retrofitted to the current APS storage ring, which is composed of 40 sectors around a 1.1-kilometer circumference. By utilizing narrow aperture magnets and a small aperture vacuum system in a multi-bend achromat (MBA) lattice, the upgrade will produce a 6 GeV, 200 mA beam that is optimized for brightness above 4 keV [1].

Design Constraints

Seven copper alloy vacuum chambers were designed to be strategically placed throughout each of the 40 storage ring sectors. The superior thermal conductivity of copper made copper alloys a straightforward material choice in regions that intercept high-intensity synchrotron radiation from the MBA lattice. Five of the seven vacuum chambers will be fabricated from copper extrusions and feature a Glidcop® photon absorber at their downstream end to shadow subsequent components that are passively cooled. Further, two of the seven designs are fully or partially fabricated from CuCrZr and feature a full or transition keyhole aperture to allow for photon extraction to bending magnet beamlines. An extrusion-based vacuum chamber design and keyhole vacuum chamber design are shown in Fig. 1.

The final assemblies primarily utilize oxygen-free with silver (OFS) copper (UNS C10700), Glidcop® Al-15 (UNS C15715), and/or CuCrZr (UNS C18150) depending on the individual requirements of the vacuum chambers. In addition, each vacuum chamber is also equipped with stainless steel flanges and water fittings.

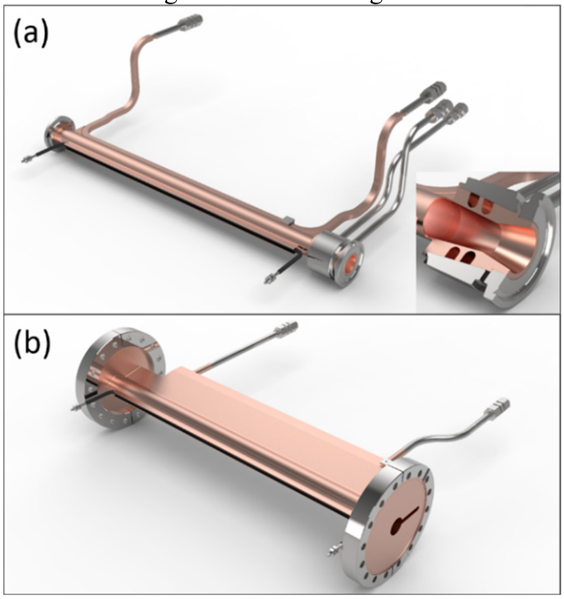

Figure 1: (a) Extrusion vacuum chamber with an inline photon absorber and (b) CuCrZr keyhole vacuum chamber.

Formal interfaces were established early in the design process of the storage ring vacuum system to ensure that the needs of each system were taken into account throughout each design phase. Interfaces with other components in the storage ring include magnets, supports, electrical systems, water systems, and other vacuum system equipment. The MBA lattice, for example, requires magnets with a narrow aperture, as seen in Fig. 2 [1].

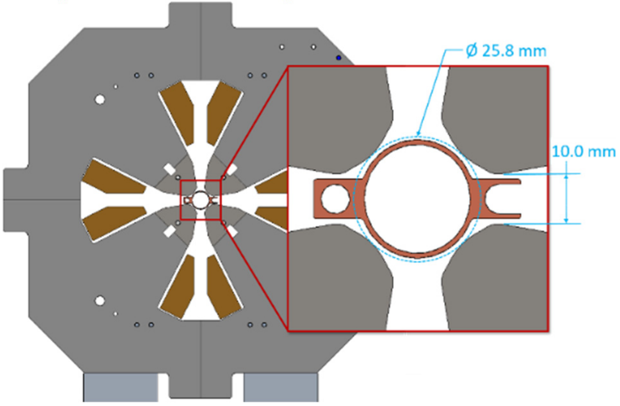

Figure 2: Typical copper vacuum chamber and magnet interface.

---

*Work supported by the DOE under contract No. DE-AC02-06CH11357
† omulvany@anl.gov

ISBN: 978-3-95450-223-3 ISSN: 2673-7000 doi:10.18429/JACoW-NAPAC2019-TUPLS12

FINAL DESIGN OF NEG-COATED ALUMINUM VACUUM CHAMBERS & STAINLESS STEEL KEYHOLE VACUUM CHAMBERS FOR THE APS-U STORAGE RING

A. McElderry[†], B. Billett, J.A. Carter, K.J. Wakefield,
Argonne National Laboratory, Lemont, Illinois, USA

Abstract

The APS-Upgrade storage ring features a diverse group of vacuum chambers which includes eight NEG (non-evaporable getter) coated aluminum chambers and two copper coated stainless steel keyhole-shaped chambers per sector (40 total). Each chamber contains a 22 mm diameter electron beam aperture; the keyhole chambers also include a photon extraction antechamber. The chambers vary in length of approximately 289 – 792 mm and fit within the narrow envelope of quadrupole and sextupole magnets. Each design is a balance of functionality, manufacturability, and installation space. An innovative CAD skeleton model system and ray tracing layout accurately determined synchrotron radiation heat loads on built-in photon absorbers and the internal envelope of the keyhole antechamber. Chamber designs were optimized using thermal-structural FEA for operating and bakeout conditions. The group of chambers require complex manufacturing processes including EDM, explosion-bonded metals, furnace brazing, and welding with minimal space. This paper describes the design process and manufacturing plan for these vacuum chambers including details about FEA, fabrication plans, and cooling/bakeout strategies.

INTRODUCTION

The APS-Upgrade project goal is to replace the 1.1 km circumference APS storage ring with a 6 GeV, 200 mA storage ring with a brightness above 4 keV. The new storage ring features NEG-coated aluminum vacuum chambers and pumping crosses that are a series of straight circular (Ø22 mm) aperture chambers that populate four of the five modules in the APS-U storage ring. An example of a pumping cross is shown in Fig. 1. In total, there are five chambers and three pumping crosses per sector (forty sectors total), varying in length 289 mm – 792 mm.

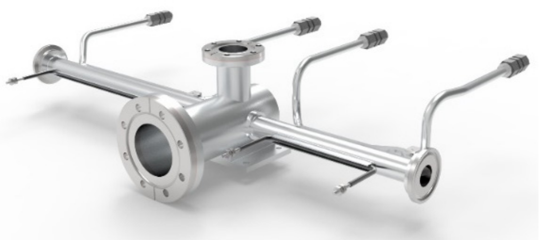

Figure 1: Rendering of the NEG-coated aluminum pumping cross.

The stainless steel (SST) keyhole chambers are a pair of vacuum chambers with extended outboard apertures as part of the overall scheme for extracting photons to the end users. The two chambers are 300 mm and 350 mm long with an example shown in Fig. 2. The NEG-Al chamber and SST keyhole chambers form the majority of the multiplet and double regions of the APS-U magnet lattice [1].

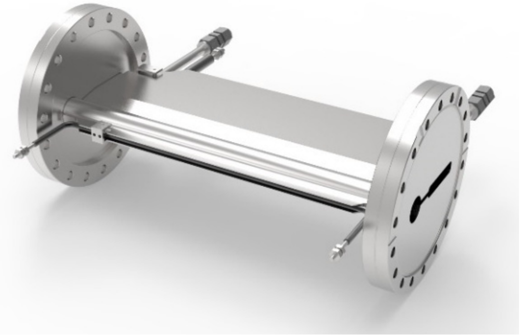

Figure 2: Rendering of a SST keyhole vacuum chamber.

Interfaces

The NEG Al chambers and SST keyhole chambers interface with the following systems: vacuum system, magnets, water system, and the electrical bakeout system. The primary design constraint of the chambers is to fit in the limited space envelope of the quadrupole and sextupole magnets as shown in Fig. 3 and Fig. 4.

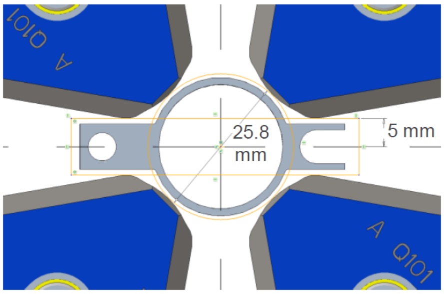

Figure 3: Cross-sectional view of an aluminum chamber within a quadrupole magnet.

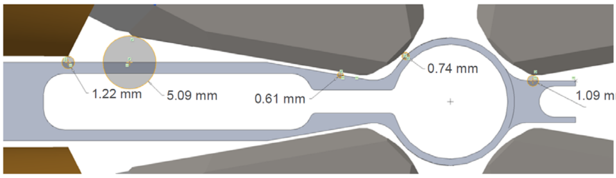

Figure 4: Cross-sectional view of a SST keyhole chamber within a quadrupole magnet.

Furthermore, the vacuum chamber space envelopes are limited axially and transversely as shown in Fig. 5. The water channels have to exit the magnet core and fit over the outboard photon extraction chambers with limited space.

---

† amcelderry@anl.gov

North American Particle Acc. Conf. NAPAC2019, Lansing, MI, USA JACoW Publishing
ISBN: 978-3-95450-223-3 ISSN: 2673-7000 doi:10.18429/JACoW-NAPAC2019-TUPLS13

EVALUATION OF THE XILINX RFSoC FOR ACCELERATOR APPLICATIONS

J.E. Dusatko[†], SLAC National Accelerator Laboratory, Menlo Park, California, USA

Abstract

As electronic technology has evolved, accelerator system functions (e.g. beam instrumentation, RF cavity field control, etc.) are increasingly performed in the digital domain by sampling, digitizing, processing digitally, and converting back to the analog domain as needed. A typical system utilizes analog to digital (ADC) and digital to analog (DAC) converters with intervening digital logic in a field programmable gate array (FPGA) for digital processing. For applications (BPMs, LLRF, etc.) requiring very high bandwidths and sampling rates, the design of the electronics is challenging. Silicon technology has advanced to the state where the ADC and DAC can be implemented into the same device as the FPGA. Xilinx, Inc. has released a multi-GHz sample rate RF System on Chip (RFSoC) device. It presents many advantages for implementing accelerator and particle detector systems. Because direct conversion is possible, RF analog front/back end and overall system design is simplified. This paper presents the results of an evaluation study of the RFSoC device for accelerator and detector work, including test results. It then discusses possible applications and work done at SLAC.

INTRODUCTION AND MOTIVATION

Many applications in particle accelerators [1,2] and detectors involve the sampling of an analog signal, conversion to a digital quantity, processing in the digital domain, presentation of the processed measurement (e.g. beam position data), and in some cases, conversion back to the analog domain to drive an actuator. The architecture of such systems is very similar in many instances.

Figure 1 shows the block diagram of a generic accelerator instrumentation and/or control system with digital processing. It should be noted that important differences may exist in the analog front- and back-ends as well as the required system sampling rates. The implementation of such a system has traditionally involved using discrete ADC and DAC components tied to an FPGA. With the hardware interconnects between components involving many parallel wires, or in more modern high-speed devices, medium to very high-speed serial data paths utilizing such interface standards as JESD204B [3]. The disadvantage of this configuration is the added hardware for supporting electronics in the ADC & DAC (power supply, clocking, auxiliary SPI control interfaces, etc) as well as the firmware complexity in the ADC/DAC digital interfaces. All of which, in turn, drives up power consumption, increases board space and ultimately system cost and reliability. For systems requiring many processing channels, these costs can be prohibitive.

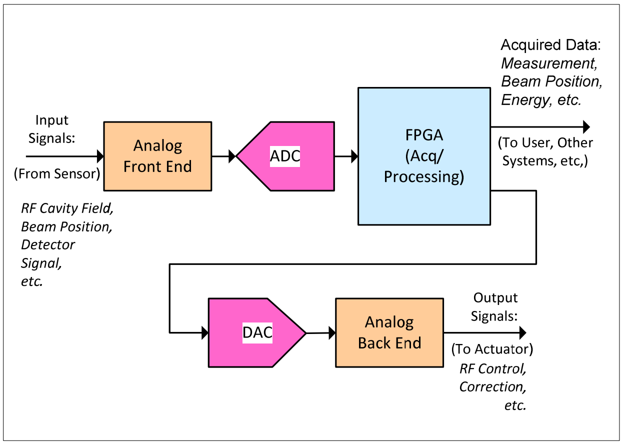

Figure 1: Generic control/instrumentation system.

With the introduction of the RFSoC device, the size, power consumption and hardware complexity issues are reduced to the point where it makes this device becomes an attractive candidate for certain accelerator applications. Added advantages include simplified RF front and back end design (via direct conversion at higher BW and sampling rates) and reduced system latency, which is critical for feedback applications.

THE XILINX RFSOC

The Xilinx RFSoC device [4], part of its Zync System On Chip product line, integrates multiple channels of high-speed ADCs and DACs onto the same silicon as the FPGA fabric. The fabric itself contains digital logic elements, static RAM blocks and DSP Multiply-Accumulate (MAC) units. Added to this are many peripherals including multi-core ARM CPUs, DDR4 memory interface, high-speed SERDES blocks (for Ethernet, PCIe, etc.). A block diagram [5] of the RFSoC is shown in Fig. 2.

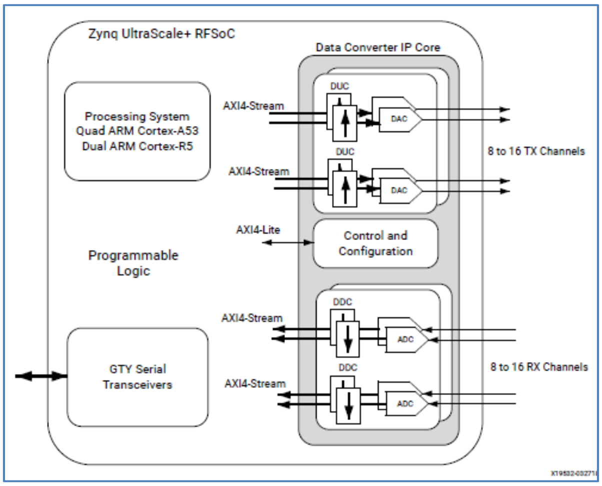

Figure 2: RFSoC device block diagram [5].

[†] jedu@slac.stanford.edu

ISBN: 978-3-95450-223-3 ISSN: 2673-7000 doi:10.18429/JACoW-NAPAC2019-TUPLS14

ANALYZING ACCELERATOR OPERATION DATA WITH NEURAL NETWORKS*

F.Y. Wang†, X. Huang#, Z. Zhang
SLAC National Accelerator Laboratory, Menlo Park, CA, USA

Abstract

Accelerator operation history data are used to train neural networks in an attempt to understand the underlying causes of performance drifts. In the study, injection efficiency of SPEAR3 [1] over two runs is modelled with a neural network (NN) to map the relationship of the injection efficiency with the injected beam trajectory and environment variables. The NN model can accurately predict the injection performance for the test data. With the model, we discovered that an environment parameter, the ground temperature, has a big impact to the injection performance. The ideal trajectory as a function of the ground temperature can be extracted from the model. The method has the potential for even larger scale application for the discovery of deep connections between machine performance and environment parameters.

INTRODUCTION

SPEAR3 is a 3rd generation storage ring based light source. It operates in the top-off mode with frequent fills at the 5-minute interval, keeping the stored beam current within 1.2% percent from 500 mA. It's very import to keep a high injection efficiency in order to minimize the disturbance to the storage beam and the radiation due to the lost beam. Injection efficiency is sensitive to many parameters that affect the injected beam and the storage ring. For SPEAR3, the injected beam is mostly stable as it comes from a 3 GeV Booster, which shields upstream jitters. The injection performance is mainly determined by the Booster-to-SPEAR (BTS) transport line and the storage ring due to mis-steering of the injected beam, optics matching at septum, dynamic aperture and physical aperture in the ring, longitudinal phase space, and so on.

The BTS trajectory is controlled by a feedback that correct the trajectory every 5 minutes during operation. While the trajectory is kept stable, the injection efficiency still varies over time as shown in Fig. 1. During a run, the target trajectory needs to be updated in accelerator physics shifts from time to time.

To understand the cause of the injection performance variation, we are motivated to exam the operation history data. A fully-connected NN model was built to successfully extract the complex dependence of injection efficiency with steering as well as the environment variables.

DATA PREPARATION

We investigated operation history data of SPEAR3, which include injection efficiency, BPM readings, and steering magnet currents in BTS, insertion device gaps, and ambient air and ground temperatures. These parameters are archived at the different time intervals and there were occasionally missing data points. Therefore, some efforts were necessary to clean up the data and align the data points.

Data from three recent runs were used in the analysis, including the 2017, 2018 runs and a fraction of the 2019 run. There are about 60,000 data points in each full run and about 10,000 data points from the 2019 run.

Injection Efficiency

There are three injection efficiency measurements, differing in the monitor used to measure the average intensity of the injected beam (see Fig. 1). Among them, the Booster Q-meter based data are the least noisy and were thus used as the target of NN model. There are still some unrealistic data points due to diagnostic issues. To ensure only valid data enter the analysis, we filtered out data points with injection efficiency above 200%, below 50%, or periodic large fluctuation (~20%) in 5 minutes interval. About 3% of all data sets were removed from the study.

BTS Trajectory

The beam trajectory has very large shifts between different runs, with some BPM readings change by more than 10 mm, as shown in Fig. 2. Accordingly, the downstream steering magnets had to be tuned to compensate. The vertical orbit at two BPMs and the currents on two vertical steering magnets are shown in Fig. 2 as examples.

Environment Parameters

Two of the SPEAR3 insertions devices (ID) can have particularly large effect on the injection efficiency, including the BL5.elliptical polarized unduator (EPU) and BL15 ID, an in-vacuum undulator (IVU). The EPU is a major source of perturbation to the dynamic aperture. The IVU gap changes the physical aperture and could affect the injection beam loss. The gap changes of two devices for the three runs are shown in Fig. 3. The EPU phase is also included in the analysis.

---

* Work supported by DOE contract DE-AC02-76SF00515 (SLAC) and DOE contracts 2018-SLAC-100469 and 2018-SLAC-100469ASCR
† fywang@slac.stanford.edu
# xiahuang@slac.stanford.edu

ISBN: 978-3-95450-223-3 ISSN: 2673-7000 doi:10.18429/JACoW-NAPAC2019-TUPLH01

STATUS OF THE SUPERCONDUCTING UNDULATOR PROGRAM AT THE ADVANCED PHOTON SOURCE*

M. Kasa†, E. Anliker, E. Gluskin, Q. Hasse, Y. Ivanyushenkov, W. Jansma,
I. Kesgin,Y. Shiroyanagi, Argonne National Laboratory, Lemont, IL, USA
J. Fuerst, SLAC National Accelerator Laboratory, Menlo Park, CA, USA

Abstract

Since 2013 there has been at least one superconducting undulator (SCU) in operation at the Advanced Photon Source (APS), currently there are two planar SCUs and one helical SCU. The combined operational experience of SCUs at the APS is more than 11 years and counting. Through all these years, APS SCUs operated with the predicted or better than predicted radiation performance and with 99% availability. With this demonstrated reliability and experimentally confirmed spectral performance, the APS upgrade project is planning on leveraging the advantages of SCU technology. The present planar SCUs are comprised of 1.1-meter long magnets, each operated within a 2-meter long cryostat, while the planar SCUs for the upgrade will have two 1.8-meter long magnets operating within a 5-meter long cryostat. Progress is also being made in other areas of SCU development with work on an arbitrary polarizing SCU, referred to as SCAPE, and a planar SCU wound with Nb_3Sn superconductor. A Nb_3Sn SCU is being designed with two 1.3-meter long magnets within a 5-meter long cryostat, and installation is planned for 2021. Also under development are the alignment and magnetic measurement systems for use with the 4.8-meter long cryostat.

INTRODUCTION

Utilizing the proven advantage of SCUs for generating hard x-rays and building on the success of years of reliable operation of superconducting undulators (SCUs) at the APS [1], the APS upgrade (APSU) project has decided to incorporate SCU technology to leverage the capability of generating higher on-axis magnetic fields at a given magnetic period and gap than other undulator technologies. Combining SCU technology with the upgrade of the storage ring to a multi-bend achromat lattice along with a doubling of the stored beam current, the generated x-rays of the APSU are expected to be two to three orders of magnitude brighter than the APS.

Planar SCUs for APSU will scale the previous design of a single 1.1-meter long undulator housed in a 2-meter long cryostat to two undulators housed in a 4.8-meter long cryostat. Presently, the cryostat and magnets are being fabricated and testing of the first article is planned for 2020. Also under development are a novel magnetic measurement system that will allow the SCU magnetic field to be characterized under normal operating conditions after final assembly in the long cryostat and an alignment system that will provide position data during cooldown of the cryostat.

Development of a superconducting arbitrary polarizing emitter (SCAPE) is also continuing after the testing of a 0.5-meter long prototype. A feasibility study of modulating the undulator field of a SCAPE style magnet using alternating current is on-going.

In advance of the shutdown of the APS for APSU, development of a Nb_3Sn SCU is underway. Two 1.3-meter long SCUs wound with Nb_3Sn superconductor are being prepared to be assembled into a 4.8-meter long cryostat. Installation is planned for 2021 to allow for testing and operation on the APS storage ring.

HISTORY OF SCUs AT THE APS

Installation and subsequent commissioning of the first 0.33-meter long, 16-mm period SCU, SCU0, in sector 6 at the APS occurred in 2013. SCU0 was replaced by a 1-meter long, 18-mm period SCU [2], SCU18-2, in September of 2016. SCU18-1, also 1-meter long with a period length of 18 mm, was installed in sector 1 in May of 2015. And the most recent SCU to be incorporated into sector 7, see Fig. 1, in 2018 was the 1.2-meter long helical SCU with a 31.5-mm period.

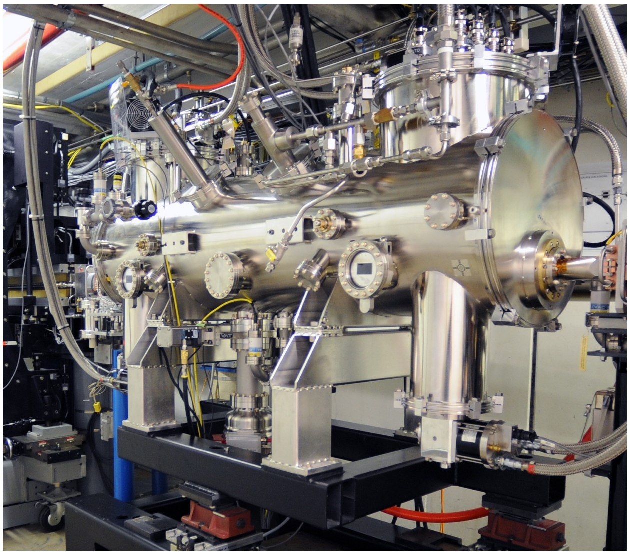

Figure 1: HSCU cryostat installed in sector 7 of the APS storage ring. Photo: R. Fenner.

In each case the undulator was installed on the storage ring during one of the three maintenance periods of the APS. At the end of the mantenance period and before the start of

---

* Work supported by the U.S. Department of Energy, Office of Science, under Contract No. DE-AC02-06CH11357.

† kasa@anl.gov

ISBN: 978-3-95450-223-3 ISSN: 2673-7000 doi:10.18429/JACoW-NAPAC2019-TUPLH03

DOUBLE-BEND ACHROMAT BEAMLINE FOR INJECTION INTO A HIGH-POWER SUPERCONDUCTING ELECTRON LINAC

C. H. Boulware, T. L. Grimm, R. Hipple, Niowave, Inc., Lansing, MI, USA
S. M. Lund, Dept. of Physics and Astronomy and Facility for Rare Isotopes and Beams,
Michigan State University, East Lansing, MI, USA
V. S. Morozov, Jefferson Lab, Yorktown, VA, USA

Abstract

To take advantage of the high duty cycle operation of superconducting electron linacs, commercial systems use thermionic cathode electron guns that fill every radiofrequency (RF) bucket with an electron bunch. For continuous operation, the exit energy of these guns is limited when compared to pulsed systems. The bunch length and energy spreads at the exit of the gun are incompatible with low losses required for the superconducting cavity. To mitigate this issue, an achromatic bend system is used to transport and filter the beam from the gun to the superconducting RF cavities. This achromatic system efficiently exploits symmetries using a minimal combination of two solenoids and two dipoles to map an incident round beam profile into a round beam at the exit. Edge angle focusing of the dipoles is exploited to balance the focusing effects in the two transverse planes. This design also allows beam filtering at the symmetry plane (axial midpoint) where the dispersion is maximal. Additionally, the bend angle positions the electron gun off of the high energy beam axis, allowing multipass operation of the superconducting booster. This study details the optical design of the double-bend achromat along with the design of the magnets and beam chambers. Operational experience with the system is reviewed.

SRF ACCELERATORS FOR RADIOISOTOPE PRODUCTION

National laboratories around the world have developed superconducting radiofrequency (SRF) particle accelerators for both high energy and high average power accelerator systems for a broad variety of research applications. SRF accelerators offer a low-cost pathway to high average power electron beams for a variety of commercial and research applications. These systems are robust and flexible in terms of the beam energy and pulse structure, with duty cycles up to and including continuous (CW) operation.

Niowave designs use ~20 MeV, >10 kW electron beams to produce high-energy X-rays and neutrons for commercial applications. Medically and industrially relevant radioisotopes are made by fissioning of uranium or by knocking out protons or neutrons to transmute targets [1, 2]. A two-pass machine with a three-cell SRF cavity is shown in Fig. 1. These machines exploit an efficient solenoid double-bend achromat (DBA) to transport the beam from the gun to a multi-cell SRF cavity and recirculate the beam through the cavities a second time. Here we describe in detail the low-energy DBA, but the concepts involved in the design of the recirculating arc are analogous.

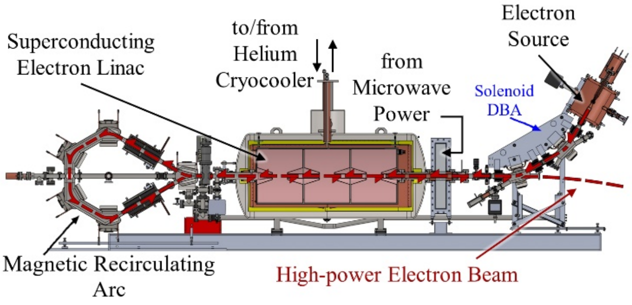

Figure 1: Annotated CAD model of a two-pass linac.

THERMIONIC-CATHODE RF ELECTRON GUN

The electron source for Niowave linacs is a normal conducting RF electron gun with a thermionic cathode. These cathodes are robust, with lifetimes upwards of 10,000 hours at the current densities required. With stable emission densities of 20 A/cm^2, small cathodes (~1 mm in diameter) provide the needed tens of mA to inject into the cryomodule for acceleration. These guns can operate CW, but the beam energy at the gun exit is low (~100 keV). The beam is only weakly relativistic until it reaches the first gap of the SRF booster cavity.

The requirement on the quality of the electron bunches (beam brightness) produced by the gun is simply that they are accelerated in a superconducting structure with low losses. The principal issue is the long bunch length. The bunch length at the gun exit is controlled by a combination of a DC reverse bias and two RF frequencies at the cathode surface. These same fields also mitigate back-bombardment of the cathode by preventing electron emission at phases that would not pass the accelerating gap of the gun. The gating design does not intercept any part of the electron beam. This design allows long cathode lifetime at high current with high beam brightness.

SOLENOID-BASED DOUBLE-BEND ACHROMAT

In order to use the SRF cavity twice as shown in Fig. 1, the electron source must be moved away from the high-energy beam path. The beam is bent onto the SRF cavity axis with a DBA bend. The bend section also provides beam dispersion (transverse separation of different energy electrons) which makes it possible to further filter the energy spread and the accompanying bunch length by using a scraping aperture in the axial midplane (point of maximal dispersion). Classic Chasman-Green type DBAs were first

FEASIBILITY STUDY OF FAST POLARIZATION SWITCHING SUPERCONDUCTING UNDULATOR

I. Kesgin†, Y. Ivanyushenkov, M. Kasa, Argonne National Laboratory, Lemont, IL, USA

Abstract

Polarization switching in an undulator relies on modulating the undulator magnetic field. This, however, inevitably incurs losses in superconductors, which need to be mitigated for safe operation of the device. In this study, feasibility of fast polarization switching has been investigated through fabricating and testing several short prototype magnets wound with different superconductors and new design concepts. The losses at different frequencies and field amplitudes are measured and details are presented. It has been found that by design optimization the losses can be reduced by about 40% at 2 Hz.

INTRODUCTION

Introduction of superconducting wire to undulators has increased their performance significantly and has introduced new opportunities for building various types of undulators. The Superconducting Arbitrary Polarization Emitter (SCAPE) is a new 4-magnet concept for a universal undulator, that offers linear, elliptical, or circular polarization states in one device [1, 2]. In investigation of the magnetic properties of materials, polarization switching capability i.e., horizontal linear polarization to vertical linear polarization or circular left to circular right, is a powerful tool. One way of achieving polarization switching is the complete reversal of current; however, this is accompanied by huge losses making it impractical. In order to avoid complete current reversal while switching between different polarization states, a SCAPE device composed of two modules in series—one for each polarization state—has been envisioned (see Fig. 1) [3]. This dual-SCAPE will enable fast polarization switching via fast current modulations by a rather small amount (~2.5-3.5% of the operating current). The corresponding modulation in x-ray energy is, nevertheless, large enough such that the desired polarization (left and right circular or horizontal and vertical linear) can be selected by a monochromator. Even this small current modulation might generate enough losses to exceed the available cooling capacity and it is important to characterize them.

AC LOSS MEASUREMENTS

In order to characterize the losses, an experimental setup is designed as shown in Fig. 2. Simulations indicated that only one cryocooler is enough to characterize the prototype magnets. A 2-stage Sumitomo cryocooler was used in the test stand. The thermal shield is connected, not shown in the figure, to the 1st stage that runs at about 55 K. The room temperature connections are thermally sunk to the shield or 1st stage before connecting to the second stage. The shield also acts as the radiation barrier. Magnets connected to the 2nd stage runs at about 3.2 K in the static case.

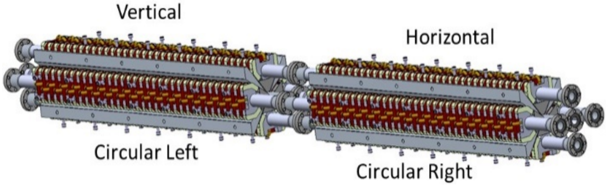

Figure 1: Dual SCAPE concept. Flux from each device can be selected by a monochromotor with the energy shifts by the current bumps.

AC losses are typically measured by two methods—electrical and thermal. The designed test setup allows measurements of both. The cold head can be calibrated by the heat deposited through the heater and AC losses generated during the field modulations can be found using this calibration. In addition, the measured voltage multiplied by the measured current can be integrated over a cycle to find the losses.

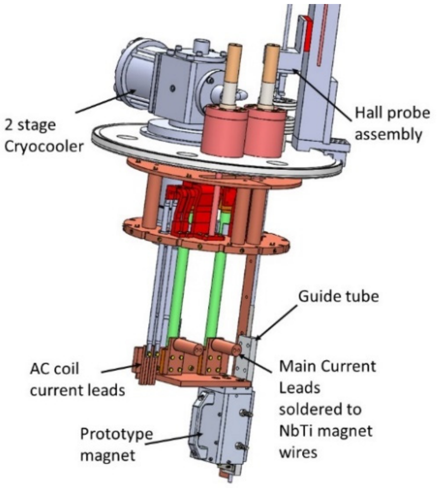

Figure 2: AC loss measurement setup.

A Hall probe is assembled to the system to measure the field. It stands off from the pole face of the magnet by a copper guide tube, as shown in Fig. 2. This guide tube is connected to the 2nd stage copper block with four low thermal conductivity peak washers. NbTi main and AC coil current leads are soldered to copper terminals at the end of the HTS current leads. Then these are routed to room temperature current terminals via copper chromium rods. The prototype magnets are attached to the bottom of the 2nd stage Cu block. The magnet is equipped with voltage taps and two heaters located at the bottom for calibration.

---

* Work supported by the U.S. Department of Energy, Office of Science, through Laboratory Directed Research and Development program (LDRD) under Contract No. DE-AC02-06CH1135.

† ikesgin@anl.gov

ISBN: 978-3-95450-223-3 ISSN: 2673-7000 doi:10.18429/JACoW-NAPAC2019-TUPLH07

HIGH-GRADIENT SHORT PULSE ACCELERATING STRUCTURES

S.V. Kuzikov†, S.P. Antipov, E. Gomez, Euclid Techlabs LLC, Bolingbrook, IL, USA
A.A. Vikharev, Institute of Applied Physics of Russian Academy of Sciences,
Nizhny Novgorod, Russia

Abstract

High gradients are necessary for many applications of electron accelerators. Since the maximum gradient is limited by effects of RF breakdown, we present the development of an electron accelerating structure operating with a short multi-megawatt RF pulse. The structure exploits the idea to decrease the breakdown probability due to RF pulse length reduction. This concept requires distributing RF power so that all accelerating cells are fed independently of each other. This implies the waveguide net system, which allows delay and to properly distribute RF radiation along the structure, to keep synchronism of particles and waves. We have designed an X-band pi-mode structure including the RF design, optimization, and engineering. The structure will be tested as an RF power extractor at the Argonne Wakefield Accelerator Facility for two-beam acceleration experiments. In this regime we anticipate obtaining 10 ns, gigawatt power level RF pulses generated by a train consisting of eight 25-50 nC relativistic bunches.

INTRODUCTION

Accelerating gradient is a key parameter for many acceleration applications [1]. In X-band, the best results have been achieved at SLAC and CERN, which provide 100-120 MV/m pulses of 200 ns duration [2]. RF breakdown and pulse heating are the greatest obstacles to increasing gradient. Numerous experiments carried out have shown that the RF breakdown threshold depends on structure exposure time [2]. Also, the pulse heating temperature decreases with shorter pulse length [3]. In this paper, we propose to reduce the pulse duration to ~1 ns scale. This proposed short pulse operation requires new accelerating structures. Such structures must be broad band, possessing low loaded Q-factors to accommodate short pulses. These structures become comparable to THz single cycle structures developed in several labs [4-5]. For low-Q structures, a high shunt impedance could be reached using a side-coupling design. On the other hand, short pulse structure design can be simplified. This is because possible reflection does not spoil operation, if the distance between the RF source and the acceleration structure is larger than the pulse duration. There are appropriate high-power (~1 GW) X-band RF sources based on relativistic electron beams [6] for such short pulse accelerating structures.

A SHORT PULSE ACCELERATING STRUCTURE WITH SIDE-COUPLING

A side-coupled design is the natural solution for a low-Q, short pulse, accelerating structure. In this case, all accelerating cells could be independent of each other (Fig. 1). This principle helps to reduce the breakdown influence and to increase shunt impedance, due to the smaller than usual beam pipe diameter of the structure. It is assumed that each accelerating cell has an individual coupler. This design is also appealing due to a low sensitivity to a cell's fabricated size. This is because a field in a given low-Q cell does not depend on the fields in all the other cells.

Necessary Cerenkov synchronism could be provided by utilizing a feeding antenna - combiner with a special bent design (Fig. 2). In this design, the radiation is distributed among 5 cells as a result of the bent blades. Figure 3 shows combiner antenna simulated together with accelerating structure at 11.7 GHz frequency. Key parameters of the structure are shown in the Table. 1. The S_{11} parameter for the feeding antenna without the structure is plotted in Fig. 4. An RF source, delivering 1 GW peak power in 1.4 ns pulses, can create a 300 MV/m accelerating field at axis.

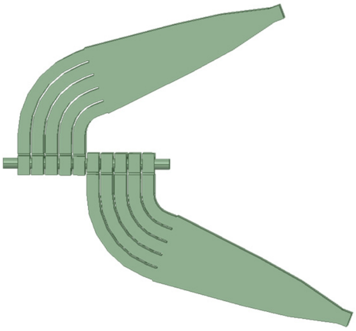

Figure 1: 5-cell side coupled accelerating structure.

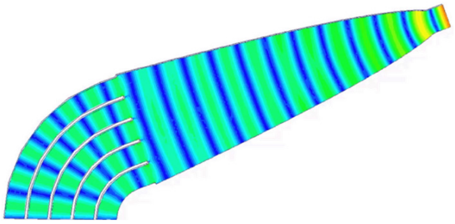

Figure 2: Instant E-field structure in feeding antenna.

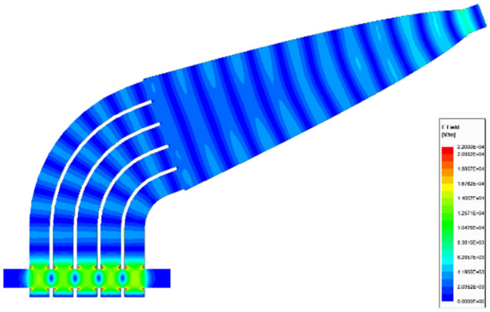

Figure 3: E-field distribution of the operating mode.

---

† s.kuzikov@euclidtechlabs.com

X-RAY AND CHARGED PARTICLE DETECTION BY DETUNING OF A MICROWAVE RESONATOR*

S.P. Antipov†, P.V. Avrakhov, E. Dosov, E. Gomez, S.V. Kuzikov,
Euclid Techlabs LLC, Bolingbrook, IL, USA
A.A. Vikharev, Institute of Applied Physics, Nizhny Novgorod, Russia
S. Stoupin, Cornell Laboratory for Accelerator-Based Sciences and Education, Ithica, NY, USA

Abstract

Charged particle detection is important for beam alignment, beam loss, and background control. In case of halo detection, traditional wire scanner measurement utilizing carbon or tungsten wires is limited by the damage threshold of these materials. In this paper, we present an electrodeless method to measure halo with a diamond scraper. This measurement utilizes a microwave resonator placed around the diamond scraper, which is sensitive to charged particle-induced conductivity. Due to this transient induced conductivity in the dielectric, a microwave coupling to the resonator changes. Diamond in this case is chosen as a radiation hard material with excellent thermal properties. The absence of electrodes makes the device robust under the beam. The same measurement can be done for x-ray flux monitoring, which is important for measurement feedback and calibration at modern x-ray light sources. In this case, x-rays passing through the diamond sensing element enable a photo-induced conductivity and in turn detunes the cavity placed around the diamond. Diamond being a low-Z material allows for in-line x-ray flux measurements without significant beam attenuation.

INTRODUCTION

In 1944, The Soviet physicist Yevgeny Zavoisky discovered, that a single crystal CuCl2 placed in a 4 mT magnetic field absorbs a 133 MHz signal, resonantly. That was the first electron paramagnetic resonance measurement [1]. Since that time, the EPR measurement has been used to study metal complexes and organic radicals. The measurement is based on the change in microwave coupling to a high quality factor resonator due to miniscule changes in the microwave properties of sample inside.

While the EPR signal appears due to the change in the sample's magnetic permeability, we propose to measure the changes to resonator properties caused by variation of the electromagnetic properties of a thin diamond film that absorbs a small portion of the incoming x-ray radiation or high energy charged particles. In contrast to existing solid-state x-ray flux monitoring, the EPR-like measurement does not require electrodes and a high-voltage bias across the diamond. In such measurements, x-rays or charged particles will promote bounded electrons from valence zone to cross the band gap into the conduction band, changing the electromagnetic properties of the sensing element (diamond). This change will detune the resonator producing a signal correlated to the incoming radiation.

LASER PULSE ENERGY METER

We have a 515 nm laser (60 kHz rep-rate, 200 fs pulse length, 3W average power), which has high enough energy photons to excite electrons across the band gap of silicon. We used this laser beam to produce photoconductivity and measure signals from the resonator. We used a network analyzer to measure the reflection in a range of frequencies, producing standard reflection curves. The setup is shown in Fig. 1 and the measurement results are shown in Fig. 2. When the laser was off, we tuned the resonator coupling to achieve a tiny, -30 dB reflection. Once the laser was on, we increased the power and observed that the resonance became weaker (resonator decouples), until at 592 mW, it seemed that the resonance was gone. Note that the resonance was not really gone—what was gone was sufficient RF coupling to observe the resonance. We could keep the laser running at 592 mW and move the tuning pin until the critical coupling is restored.

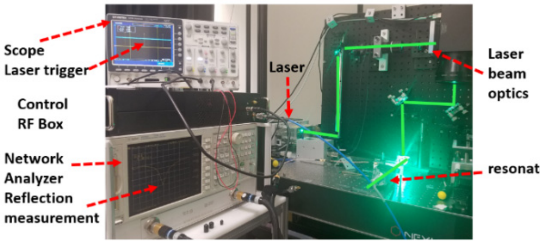

Figure 1: Laser flux monitoring experiment long relaxation time sample (high resistivity silicon) measurement with network analyzer.

We built a single frequency RF circuit to measure microwave detuning (proxy to laser flux) in the time domain. We set the oscillator at the resonant frequency, turned on the laser, and measured a time-domain signal at the laser repetition rate. The resulting signal had a large quasi-constant component proportional to the incoming laser flux, and then a ripple on top of it, with repetition rate of laser. In Fig. 3, we zoom in to obtain the time structure of the signal. This time structure includes the quality factor of the resonator effect paired with the relaxation times, that strongly depends on the sensing element composition. For practical applications, these effects can be calibrated. Sensitivity of the detector is determined by the quality factor of the resonator. There is a tradeoff between the time resolution of the measurement and the sensitivity, since both depend on the quality factor.

---

* Work supported by DoE SBIR grant
† s.antipov@euclidtechlabs.com

ISBN: 978-3-95450-223-3 ISSN: 2673-7000 doi:10.18429/JACoW-NAPAC2019-TUPLH09

THERMAL EFFECTS ON BRAGG DIFFRACTION OF XFEL OPTICS*

Z. Qu, Y. Ma[†], University of California, Merced, Merced, CA, USA
B. Yang, Western Digital, Milpitas, CA, USA
G. Zhou, J. Wu[‡], SLAC National Laboratory, Menlo Park, CA, USA

Abstract

Crystal optical devices are widely used in X-ray free electron laser (XFEL) systems, monochromators, beam splitters, high-reflectance backscattering mirrors, lenses, phase plates, diffraction gratings, and spectrometers. The absorption of X-ray in these optical devices can cause increase of temperature and consequent thermal deformation, which can dynamically change in optic output. In self-seeding XFEL, the thermal deformation and strain in monochromator could cause significant seed quality degradation: central energy shift, band broadening and reduction in seed power. To quantitatively estimate the impact of thermomechanical effects on seed quality, we conduct thermomechanical simulations combined with diffraction to evaluate the seed quality with residual temperature field in a pump-probe manner. With our results, we show that a critical repetition rate could be determined, once the criteria for deviation of the seed quality are selected. This tool shows great potential for the design of XFEL optics for stable operation.

INTRODUCTION

The performance of the optics in synchrotron and XFEL applications has long been limited by the thermal load. To understand and relieve the thermal loading effects, many studies [1.2] have been performed. Different designs of the optics [3] have been proposed to improve their thermal performance. On the other hand, cooling and cryogenic operation [4, 5] are also reported to overcome the thermal difficulties. These technologies, unfortunately, have not been well adapted for some XFEL operating modes, such as the self-seeding mode.

In the self-seeding mode [6], one monochromator is implemented to separate the undulators into two segments. The self-amplified spontaneous emission (SASE) generated in the first segment of undulators passes through the monochromator to produce a coherent seed, which will then be amplified in the second segment of undulators. In this way, the coherence and brightness of the final XFEL can be significantly improved. However, the system performance can be severely undermined if the thermal load of the key component, the monochromator, exceeds the critical point. Bushuev [7, 8] demonstrated the thermal distortion of the rocking curves and indicated the possible degradation of the seed quality. Unfortunately, a quantitative description of the criterion, as well as a direct evaluation of the seed quality, is not yet clear.

In present study, we perform numerical simulation to quantitatively evaluate the seeding behaviour. This comprehensive thermal-mechanical-diffraction simulation is carried out in a pump-probe manner, but it can also be applied for quasi-steady multi-pulse situation. Our results provide insights to determine the critical parameters (such as repetition rate and single pulse dose) and implementation of the appropriate cooling techniques.

METHOD

The physical situation is illustrated by Fig. 1 below.

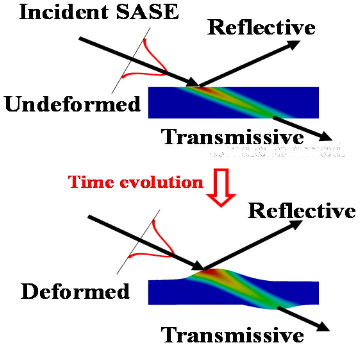

Figure 1: Schematic illustration of FEL induced thermal loads on crystal monochromators.

The incident SASE pulse from the first segment of the undulators interacts with the monochromator and splits into three parts: the reflected, transmitted and absorbed part. Among these parts, the reflected component contains the seed for reflective monochromator, while the transmitted part contains the seed for transmissive monochromator. The absorbed part, however, deposits energy into the monochromator, resulting in non-uniform temperature increase, which further develops into the strain field through thermal expansion. Next, when the second incident SASE pulse arrives, the interplanar distance between atoms in crystal monochromator deviates from the original status. This deviation causes the disturbance in wavelength of the seed, as governed by Bragg condition, thus undermines the seed quality.

Therefore, it is necessary to obtain the temperature and strain evolution in crystal monochromator. We employ 3D finite element analysis by ANSYS Mechanical APDL solver for thermal and mechanical simulation. On the other hand, to obtain the diffraction behavior (rocking curve) under thermal loads, Shvyd'ko's method [9] is employed. In this work, we only consider the first two FEL pulses in a pump-probe manner, but further investigation will be carried out to study the thermal loading effects at quasi-steady state.

---

* Work is supported by National Science Foundation (#1637370), the US Department of Energy (DOE) under contract DE-AC02-76SF00515 and the US DOE Office of Science Early Career Research Program grant FWP-2013-SLAC-100164

[†] yma5@ucmerced.edu
[‡] jhwu@slac.stanford.edu

North American Particle Acc. Conf. NAPAC2019, Lansing, MI, USA JACoW Publishing
ISBN: 978-3-95450-223-3 ISSN: 2673-7000 doi:10.18429/JACoW-NAPAC2019-TUPLH10

FABRICATION PROGRESS OF A SUPERCONDUCTING HELICAL UNDULATOR WITH SUPERIMPOSED FOCUSING GRADIENT FOR HIGH EFFICIENCY TAPERED X-RAY FELs*

S. M. Lynam†, R. Agustsson, I. I. Gadjev, A. Y. Smirnov, RadiaBeam, Santa Monica, CA, USA
F. H. O'Shea, Elettra-Sincrotrone Trieste S.C.p.A., Basovizza, Italy

Abstract

The Advanced Gradient Undulator (AGU) represents a potentially significant advancement in x-ray conversion efficiency for x-ray FELs. This increase in efficiency would have broad implications on the capabilities of x-ray light sources. To achieve this high conversion efficiency, the inner diameter of the undulator coil is a mere 7 mm, even with the use of superconducting coils. To accommodate the beamline at the Advanced Photon Source this yields in a chamber with a wall thickness of 0.5 mm fabricated from Aluminum. With a period of 2 cm and a conductor position tolerance of 100 µm over a length of 80 cm at 4.2 K, the engineering and fabrication challenges for the undulator alone are substantial. We will discuss these fabrication challenges and present solutions to meet the tolerances required for desired performance, and provide an update on current progress of the construction of a section of the AGU insertion device.

BACKGROUND

One of the largest difficulties facing self-amplified spontaneous emission (SASE) free electron lasers (FELs) is that of efficiency; because amplification must occur in a single pass of the electron bunch, radiation amplification is limited by the FEL parameter ρ. Current conversion efficiencies of beam power to radiation are approximately 0.1%, limiting x-ray brightness and creating a requirement for expensive high brightness electron sources to be used [1]. To reduce the requirement for immense beam power at FEL facilities, insertion devices must be made more efficient.

As noted above the AGU uses a combination of extremely small bifilar helical undulator design with an overlaid quadrupole field, both wound with He-cooled Nb-Ti superconducting wire. The quadrupole is critical to the design, supplying the 26.6 T/m gradient field which allows the conversion efficiency to surpass the FEL parameter.

ENGINEERING DESIGN

Strongback

The strongback will serve as both the structural member for the mandrel, as well as the epoxy mold. Once the mandrel has been wound, it will be placed in the strongback and epoxied in place. Once epoxied the mandrel will not be removed from the strongback, so cryogenic considerations must be made for its design. The passages delivering liquid Helium (LHe) will be gun drilled along the length of the strongback.

Mandrel Beam Pipe and Vacuum Chamber

A significant concern in manufacturing is the surface roughness of the beam pipe through the centre of the mandrel, as well as wall thickness of the vacuum vessel which will be on the beam line. Gun drilling the beam pipe was considered, however this approach was discarded due to unpreferable cutting fluids required as well as inability to reliably achieve the required geometric tolerancing. The mandrels will be extruded as raw stock from a preferred vendor, with several samples destructively tested to ensure proper beam pipe straightness and concentricity relative to the outer diameter [2]. See Fig. 1 for sample cross section of a segment of the undulator assembly.

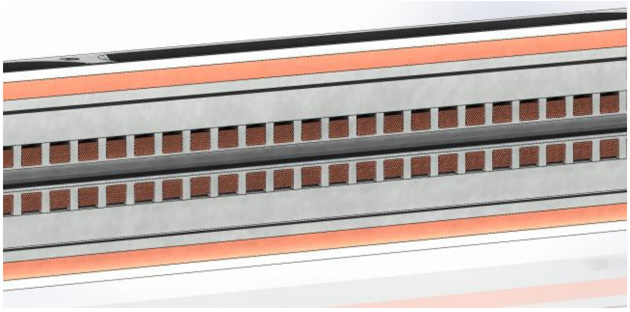

Figure 1: Cross section of bifilar undulator assembly with conductor, quadrupole, and strongback.

Conductor Pitch Angle and Grooves

Early in the design phase of the mandrel it was realized that the pitch angle of the conductor would play a major factor in the geometry of the mandrel. Due to the extremely small diameter of the inner conductor on the helix, and high aspect ratio between the inner diameter and the outer diameter, there is a significant change in pitch angle of the conductor as it is wound from the inner layer to the outermost layer. As a result the overall width of the filament layers changes significantly, by approximately 0.12 mm from inner conductor layer to outer as seen in Fig. 2. Failure to account for this change would result in considerable difficulty in conductor packing, as each location error compounds in the winding above it, causing the undulator to fail to meet its tolerance budget.

---

* Work supported by DOE grant no. DE-SC0017072, "Superconducting Helical Undulator with Superimposed Focusing Gradient for High Efficiency Tapered X-Ray FELs"

† slynam@radiabeam.com

DESIGN STUDY OF LOW-LEVEL RF CONTROL SYSTEM FOR CW SUPERCONDUCTING ELECTRON LINEAR ACCELERATOR IN KAERI

S.H. Lee[1], P. Buaphad[1,2], M.-H. Chun[3], I.G. Jeong[1,2], Y.J. Joo[1,2], Y. Kim[1,2†],
H.R. Lee[1,2], J.Y. Lee[1], I.H. Yu[3]
[1]Korea Atomic Energy Research Institute, Daejeon, Korea
[2]University of Science & Technology, Daejeon, Korea
[3]Pohang Accelerator Laboratory, Pohang, Korea

Abstract

Korea Atomic Energy Research Institute (KAERI) has been operating a 20 MeV superconducting RF linear accelerator (SRF LINAC) to conduct research on atom/nuclear reaction using neutron Time-of-Flight (nTOF). It can accelerate electron beams up to 20 MeV with 1 kW continuous wave (CW) operation mode. Unfortunately, this machine has been aged over 15 years that brings about considerably difficulty in normal operation due to the performance degradation of sub-systems. To normalize the operation condition of 20 MeV SRF LINAC, we have been carrying out an upgrade project with replacement and repair of old sub-systems from 2018. This paper describes a design study of Low-Level RF (LLRF) control system to improve the stability and acceleration efficiency of the electric field generated in the superconducting RF cavity structure of 20 MeV SRF LINAC.

INTRODUCTION

The nTOF method is generally used to measure and verify the neutron cross-section data of major actinides, minor actinides, and photo nuclear reaction library [1]. To produce neutron cross-section data from keV up to MeV range, construction of KAERI nTOF experimental building was started from early 2016. It will be mainly used to measure nuclear data [2].

To produce neutron beams in KAERI nTOF facility, we apply the photonuclear reactions in a target filled with liquid lead (Pb). An incident electron beam produces bremsstrahlung photons, and then bremsstrahlung photons bring about photonuclear chain reaction (γ,n) in the target. It can generate neutrons with a white spectrum [3]. Finally, neutrons go through nTOF experimental building with 10 m flight-path to analyze experiment results. Overview of KAERI nTOF facility is shown in Fig. 1.

To generate electron beam in the facility, SRF LINAC is used as an injector. It can accelerate electrons up to 20 MeV kinetic energy with 1 kW continuous operation mode. Two 352 MHz SRF cavities with a cryomodule were fabricated by CERN for the Large Electron-Positron Collider (LEP) facility [4]. To operate those SRF cavities, we installed a RF generator, a Helium refrigerator, a vacuum stage, a control system and a cooling system collaborating Budker Institute of Nuclear Physics (BINP), Russia in 1996.

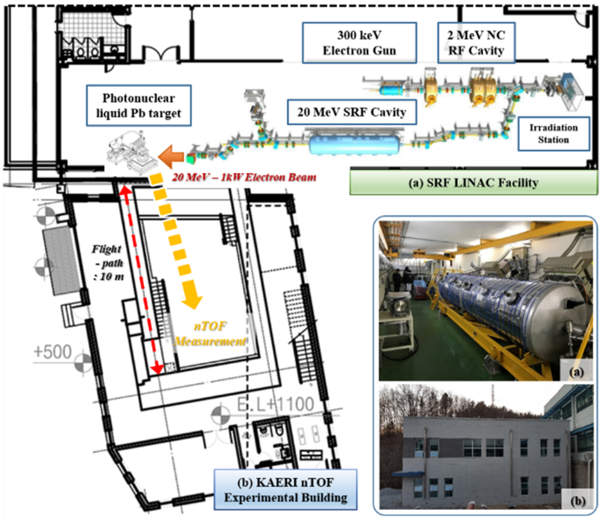

Figure 1: Overview of KAERI nTOF facility.

Unfortunately, a fire accident occurred at 2003, so subsystems of RF generator and Helium refrigerator were broken or malfunctioned. In addition, many components of SRF LINAC outdated due to 15 years operating duration.

To solve those problems, we have been carrying out an upgrade project by replacing or repairing old RF sub-systems since 2018. In this paper, we review RF sub-systems of the SRF LINAC and design a new LLRF system based on digital signal processing to improve beam stability and accelerating efficiency.

SYSTEM OVERVIEW

The schematic of SRF LINAC for KAERI nTOF facility is shown in Fig. 2. At first, electron beams are generated from electron gun tank with 300 kV kinetic energy. They move to normal conducting (NC) RF cavities which accelerate electron beams up to 2 MeV. Continuously, SRF LINAC accelerates electron beams around 20 MeV.

SRF LINAC system is composed of two identically same RF stage. Each RF stage consists of SRF cavity, RF generator, and LLRF control system. SRF cavity has the amplitude of accelerating voltage around 9 MV per one stage with 352 MHz resonance frequency. To make high-intensity electric field (E-field) in SRF cavity, RF generator transmits 45 kW RF power signal to each stage. To raise the stability and acceleration efficiency of SRF LINAC, LLRF control system is essential. The operating parameters of SRF LINAC is summarized on Table 1.

NSLS-II INJECT LINAC RF CONTROL ELECTRONICS UPGRADE*

Hengjie Ma, Brookhaven National Laboratory, Upton, NY, USA

Abstract

The electron injection LINAC of NSLS-II Synchrotron Light Source is designed to operate in both single-bunch and multi-bunch beam mode (MBM). In the MBM operation, the beam bunch train length varies from 40 to 150 bunches which translates a beam loading time of 80~300ns in time. That requires that the LINAC rf control front-end module (FE RFM) have a sufficient control bandwidth (estimated 100 MHz min.) to be able to effectively perform the necessary adaptive feed forward control (AFF) for the beam loading compensation. The RFM from the LINAC OEM has successfully supported the commissioning and the operation to the date. However, the issues in its performance, reliability and support pose the need to develop an upgraded rf control in-house to better support NSLS-II operation. The RFM electronics upgrade is designed with the emphasis on meeting the specific operation needs of NSLS-II injector LINAC, and the capability of being best integrated in the existing accelerator control infrastructure. The implementation strategy is to use the modern digital rf components and designs to achieve the best result, while leveraging the built-in digital radio IP to minimize the amount of required IP development effort, and thus reduce the development costs and risk.

NSLS-II INJECTOR LINAC OVERVIEW

NSLS-II LINAC is a 2.998MHz, 200MeV Pre-Injector to the following Booster Synchrotron which in turn serves as the injector to the final Storage Ring. It delivers minimum 0.5nC of charge in Single-Bunch Mode, and up to 15 nC in Multi-Bunch Mode (or MBM). The length of an MBM varies from 40 to 150 beam bunches, or 80~300nS in time. The basic parameters are listed in the Table 1 below. The LINAC rf chain starts with the rf modulating grid PA for a YU-171 Electron Gun, followed by a 500MHz Sub-Harmonic Buncher, a 3GHz Pre-Buncher and a Final Buncher as the LINAC Front-end, and a following four traveling-wave structure LINAC powered by two 45MW klystrons to bring the beam energy to the required 200 MeV [1].

RF TRANSMITTER DOWN-STREAM PA'S

The NSLS-II LINAC down-stream RF power plant is shown in the system diagram in Fig. 1. In the LINAC front-end, a 500MHz/2.5kW Solid-State RF Power Amplifiers (or SSA) is used to drive the Electron Gun modulating grid (500MHz/500W) for MBM beam, a 500MHz/500W SSA to drive the Sub-Harmonic Buncher; and a 3GHz/1.2kW SSA to drive the Pre-Buncher (PB, 3GHz, 1.2kW). The following 3GHz, 4-section LINAC is rf-powered with three 45MW klystrons (Toshiba E37302A). The two klystron stations in position #1 and 3 are needed in the normal operation, while the Klystron in Station #2 is in standby and can be switched in to back up Klystron #1 or # 3 should either one fail.

The high-performance, compact solid-state switching modulators that support the klystrons are a commercial product. The details about these SS switching modulators are reported in a companion paper [2]. The rf drives for the rf PA and klystrons are provided by the rf modulator front-end, its electronics and functions are described in the following section.

Table 1: NSLS-II LINAC Parameters

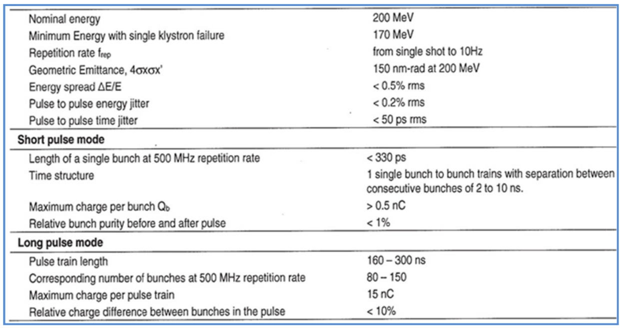

Nominal energy	200 MeV
Minimum Energy with single klystron failure	170 MeV
Repetition rate f_{rep}	from single shot to 10Hz
Geometric Emittance, 4σxσx'	150 nm-rad at 200 MeV
Energy spread ΔE/E	< 0.5% rms
Pulse to pulse energy jitter	< 0.2% rms
Pulse to pulse time jitter	< 50 ps rms
Short pulse mode	
Length of a single bunch at 500 MHz repetition rate	< 330 ps
Time structure	1 single bunch to bunch trains with separation between consecutive bunches of 2 to 10 ns.
Maximum charge per bunch Q_b	> 0.5 nC
Relative bunch purity before and after pulse	< 1%
Long pulse mode	
Pulse train length	160 – 300 ns
Corresponding number of bunches at 500 MHz repetition rate	80 – 150
Maximum charge per pulse train	15 nC
Relative charge difference between bunches in the pulse	< 10%

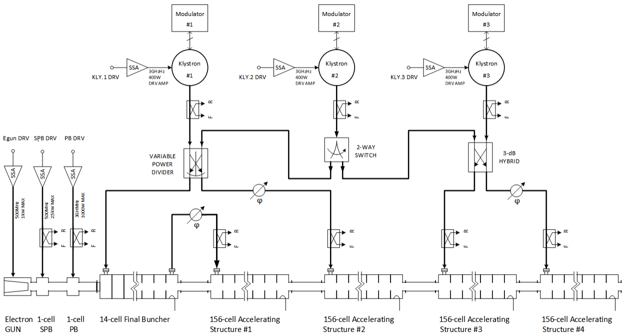

Figure 1: The NSLS-II LINAC rf power plants are comprised of three Solid-State RF PA's for the beam bunchers in the front-end and three 45MW klystrons for the following 4-section 3GHz accelerating structures.

RF MODULATOR FRONT-END

The LINAC rf control front-end electronics is a digital rf modulator (RFM). Its first primary function is to performs the phase and amplitude control of the rf drive to the down-stream high-power rf plants. The second primary function of the RFM is the beam-loading compensation in MBM operation to order to keep the beam energy dispersion within the tolerance over the beam bunch train.

In the 500MHz sub-harmonic buncher, the beam-loading effect shows up on both the phase and amplitude of the buncher cavity field, while the effect is only on the rf amplitude in the following 3GHz LINAC section.

The magnitude of the effect gradually grows over the beam bunch train, and the cavity field is consequently distorted. To counteract this cavity field distortion by the

---

* Work supported by US Department of Energy, Office of Basic Science.
† hengjie@bnl.gov

UPGRADE AND OPERATION EXPERIENCE OF SOLID-STATE SWITCHING KLYSTRON MODULATOR IN NSLS-II LINAC*

H. Ma[†], J. Rose, Brookhaven National Laboratory, Upton, NY, USA

Abstract

The NSLS-II synchrotron light-source at BNL uses three S-band, 45MW klystrons in its injection LINAC. At the core of each klystron station design is a novel solid-state switching modulator (or SSM). Compared to the conventional PFN klystron modulators, the main advantages of the SSM include the compact size requiring a smaller footprint in the LINAC gallery, and a very flat top in the produced klystron HV pulse waveforms. The flatness of the HV pulses is very important to NSLS-II LINAC that runs multi-bunch beams for keeping the beam energy dispersion within the tolerance. The principle of the SSM is fairly simple. It uses a large number of relatively low-voltage switched charging capacitor cells (or SU's) in parallel. A specially designed, high step-up ratio, pulse transformer in the oil-tank with the same number of primary windings (as that of SU's) combines the power from all the SU's, and steps up to the required ~300kV klystron beam voltage. The operation experience at NSLS-II has proven the performance and reliability of the SSM's. The BNL Model K2 SSM's are currently being upgraded to Model K300 to run more powerful, and more cost-effective Canon's E37302A klystrons.

KLYSTRON RF POWER PLANTS

To achieve the designed 200 MeV beam energy, the required rf power level would be in 70~100 MW range. For the S-Band rf power of this level, Klystron is still the only feasible choice, despite of the progress in cost/Watt ratio being made for the solid-state rf amplifiers in recent years.

As previously mentioned, NSLS-II Injector LINAC was designed to have the capability of filling up to 150 Booster rf buckets in one shot with the long multi-bunch beam patterns. That requires that the LINAC pulsed rf maintain a constant flat top in its amplitude/phase waveform envelope for about 1 us period (for 150 bunches/300nS beam) to allow the long bunch trains to pass through the LINAC with the energy dispersion within the designed tolerance. For this reason, the rf pulse compression device SLED cannot be considered for gaining extra rf peak power as the severely distorted and lopsided waveform that a SLED outputs is inherently incompatible with the multi-bunch beam operation. The long bunch train length in MBM operation also poses an additional issue of beam-loading on the rf fields. NSLS-II LINAC design adopted a digital rf modulator in the rf transmitter front-end (or RFM) to generate a Pre-distortion waveform for the beam-loading compensation. The details about the digital RFM is reported in a companion paper [1]. The photos in Fig. 1 show the high-power LINAC rf equipment, while the block diagram in Fig. 2 shows the function blocks of the system.

Figure 1: NSLS-II Injector LINAC tunnel (left) and Klystron Gallery (right).

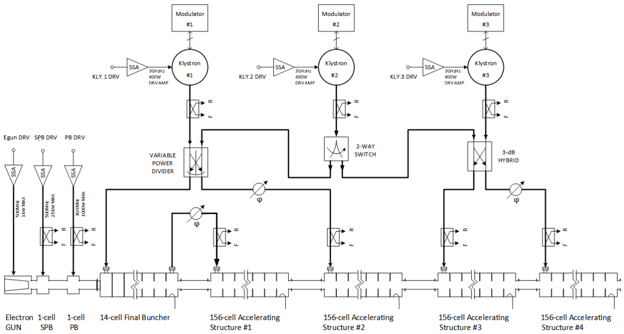

Figure 1: The NSLS-II LINAC rf power plants is comprised of three Solid-State RF PA's and three 45MW klystrons for the following 4-section 3GHz accelerating structures. The klystron in position #1 and 3 are for normal operation, while the one in #2 is a backup station.

The NSLS-II Injection LINAC was manufactured by Research Instruments, GmbH per NSLS-II-BNL's specifications, with its design consideration emphasized on achieving the highest operation reliability while using the new technology where it is feasible [2, 3].

SOLID-STATE SWITCHING KLYSTRON MODULATORS

The choices for the NSLS-II LINAC modulators were also carefully examined. The traditional approach for the short-pulsed klystron modulators is to use a single lump-sum Pulse Forming Network (or PFN) with hard-tube (Thyratron) switches to produce HV pulses between 2 and 4 microseconds long. The diagram in Fig. 3 depicts a typical design of the traditional PFN modulator.

---

* This manuscript has been authored by Brookhaven Science Associates, LLC under Contract No. DE-SC0012704 with the U.S. Department of Energy.

[†] hengjie@bnl.gov

ISBN: 978-3-95450-223-3 ISSN: 2673-7000 doi:10.18429/JACoW-NAPAC2019-TUPLH20

COMMISSIONING OF THE CESR UPGRADE FOR CHESS-U

J. Shanks*, G. Codner, M. Forster, D.L. Rubin, S. Wang, L. Ying
CLASSE, Cornell University, Ithaca NY, USA

Abstract

The Cornell Electron Storage Ring (CESR) was upgraded in the second half of 2018 as a dedicated synchrotron light source, CHESS-U. The upgrade is by far the largest modification to CESR in its 40-year history, replacing one-sixth of the storage ring with six new double-bend achromats, increasing beam energy from 5.3 GeV to 6.0 GeV, and switching from two counter-rotating beams to a single on-axis positron beam. The new achromats include combined-function dipoles, a first in CESR, and reduce the horizontal emittance at 6.0 GeV by a factor of four. Eight compact narrow-gap undulators (4.6mm vacuum chamber aperture) and one high-energy 24-pole wiggler feed a total of six new and five existing x-ray end stations from a single positron beam. Commissioning of CHESS-U took place in the first half of 2019. We report on the results of beam commissioning, including optics correction and characterization.

CHESS-U OVERVIEW

The accelerator design for the CHESS-U upgrade is documented elsewhere [1]. Parameters before and after the CHESS-U upgrade are summarized in Table 1.

Table 1: Design Lattice Parameters for CESR Before and After CHESS-U Upgrade

Parameter	CHESS	CHESS-U
Circumference [m]	768.438	768.438
Energy [GeV]	5.289	6.0
Species	e^+ and e^-	e^+
Current [mA]	120/120	200
ϵ_x [nm·rad]	98	29.6
Emittance coupling	1%	1%
$\beta_{x,y}$ at IDs [m]	7.9, 3.1	11.2, 2.6
η_x at IDs [m]	0.42	0
IDs	3	9
End Stations	11	11
$Q_{x,y}$	11.28, 8.78	16.55, 12.63
$Q'_{x,y}$	−16.0, −14.2	−25.6, −26.8
α_p	9.2×10^{-3}	5.7×10^{-3}
σ_z [mm]	16	17
I_{bunch} [mA]	7	2.2
τ_{Touschek} [hrs]	>24	40
V_{RF} [MV]	5.2	6.0

Four of the seven straights (Sectors 2, 3, 4, and 7) house a pair of CHESS Compact Undulators [2,3], split by a 2 mrad canting angle (1 mrad in Sector 7). Sector 1 uses an existing 24-pole wiggler [4]. The geometry of the remaining two sectors is not conducive to end stations at this time. Removal of the old sextant of CESR and installation of the six new achromats was completed from June 2018 to January 2019.

Table 2: Commissioning Timeline

Date	Milestone
1/30/19	CESR gun, linac, and synchrotron on
2/22/19	First attempt at e^- injection
3/6/19	First turn achieved – e^- at 5.289 GeV
3/11/19	Recover e^- accumulation at 5.289 GeV Time in CBPM system and correct optics.
4/8/19	Recover e^+ accumulation. Store 50 mA e^+ at 5.289 GeV.
4/24/19	First turn achieved – e^+ at 6.0 GeV
4/26/19	Recover e^+ accumulation at 6.0 GeV
4/27/19	Establish 100 mA e^+ conditions at 6.0 GeV
5/9/19	Sector 1 wiggler gap closed First canted IDs installed in Sector 7
5/16/19	First light in Sector 7
5/17/19	First light in Sector 1
6/27/19	All five front-ends illuminated

The digital CESR Beam Position Monitor (CBPM) system requires timing in to the peak of a bunch passage to around 10 ps. Details on the CBPM system are available in [5]. Timings for the new sextant of the ring were initially unknown, therefore the first turns in the storage ring were observed using an older analog BPM system with diode stretcher and higher sensitivity. Roughly every tenth set of buttons in CESR is permanently connected to the relay system, though it is possible to "steal" buttons from the CBPM system for use in the relay system. For threading the first turn, relay BPMs in the new sextant were set up in a "cow" configuration, where all four button signals are summed to provide a dead-or-alive intensity signal. Once beam was stored, the digital bunch-by-bunch system was restored.

COMMISSIONING

The CHESS-U commissioning timeline is summarized in Table 2. Positron operation is in the clockwise direction, compatible with CHESS operation. Electron operation is in the counter-clockwise direction, which although incompatible with the polarity of x-ray beam lines, allows for approximately 10 times higher charge per injection pulse, improving BPM signal amplitude prior to accumulation.

---

* js583@cornell.edu

ISBN: 978-3-95450-223-3 ISSN: 2673-7000 doi:10.18429/JACoW-NAPAC2019-TUPLH24

PERFORMANCE OF CeC PoP ACCELERATOR*

I. Pinayev†, Z. Altinbas, J.C. Brutus, A.J. Curcio, A. Di Lieto, T. Hayes, R.L. Hulsart, P. Inacker, Y.C. Jing, V. Litvinenko, J. Ma, G.J. Mahler, M. Mapes, K. Mernick, K. Mihara, T.A. Miller, M.G. Minty, G. Narayan, I. Petrushina, F. Severino, K. Shih, Z. Sorrell, J.E. Tuozzolo, E. Wang, G. Wang, A. Zaltsman, Brookhaven National Laboratory, Upton, NY, USA

Abstract

Coherent electron cooling experiment is aimed for demonstration of the proof-of-principle demonstration of reduction energy spread of a single hadron bunch circulating in RHIC. The electron beam should have the required parameters and its orbit and energy should be matched to the hadron beam. In this paper we present the achieved electron beam parameters including emittance, energy spread, and other critical indicators. The operational issues as well as future plans are also discussed.

INTRODUCTION

An effective cooling of ion and hadron beams at energy of collision is of critical importance for the productivity of present and future colliders. Coherent electron cooling (CeC) [1] is a novel cooling method which would outperform existing techniques by orders of magnitude.

A dedicated experimental set-up, shown in Fig. 1, has been under design, manufacturing, installation, and finally commissioning during last few years [2-5]. The CeC system is comprised of the SRF accelerator and the CeC section followed by a beam dump system. It is designed to cool a single bunch circulating in RHIC's "yellow" ring (indicated by yellow arrow in Fig. 1). A 1.5 MeV electron beam for the CeC accelerator is generated in a 113 MHz SRF quarter-wave photo-electron gun and first focussed by a gun solenoid. For beam compression energy chirp is provided by two 500 MHz copper RF cavities, and bunch is ballistically compressed in 9-meter long low energy beamline comprising five focusing solenoids. A 5-cell 704 MHz SRF linac accelerates the compressed beam to 15 MeV. Accelerated beam is transported through an achromatic dogleg to merge with ion bunch circulating in RHIC's yellow ring. The design and demonstrated beam parameters are shown in Table 1.

In CeC interaction between ions and electron beam occurs in the common section: in the modulator, each hadron induces density modulation in electron beam that is amplified in the high-gain FEL; in the kicker section, the hadrons interact with the self-induced electric field of the electron beam and receive energy kicks toward their central energy. The process reduces the hadron's energy spread, i.e. cools the hadron beam. Fourteen quadrupoles are used to optimize the e-beam interaction with the ion beam and FEL performance.

Table 1: CeC System Parameters

Parameter	Design	Achieved
Kinetic energy, MeV	21.95	15
Bunch charge, nC	0.5-5	9.0
Peak current, A	100	50
Bunch length, ps	10	12
Beam current, μA	400	120

Finally, the used electron beam is bent towards an aluminium high-power beam dump equipped with two quadrupoles to over-focus the beam.

COMMISSIONING OF THE CeC SYSTEM

The CeC accelerator superconducting RF system uses liquid helium from RHIC refrigerator system, which operates only during RHIC runs, typically from February till end of June every year. Hence, the commissioning and operation of CeC accelerator is synchronized with RHIC runs.

The commissioning of the CeC accelerator was accomplished during three RHIC runs: Runs 15, 16 and 17.

During the run 15, only SRF gun and a part of the low energy beam line had been installed and commissioned. The installation of the equipment was continued during the RHIC maintenance days. We went through a steep learning curve of how to condition and operate an SRF gun with CsK_2Sb photocathode and how to prevent its QE degradation. The run was very successful and the SRF gun generated electron bunches with 1.15 MeV kinetic energy and 3 nC charge per bunch.

The major installation of the CeC system, including all common section with FEL, occurred during RHIC shutdown in 2016. We had received and installed 5-cell SRF linac cryostat from Niowave Inc, and three helical wigglers for our FEL amplifier from Budker INP, Novosibirsk, Russia [6].

We encountered strong multipacting zone in the range from 28 kV to 40 kV of the gun accelerating voltage, which was hard to pass. This zone multipacting was spoiling the gun vacuum and was ruining photocathode's QE, more details about can be found in [7-8]. As the result of our experiences we increased the power of our transmitter to 4 kW and also developed a dedicated LLRF procedure providing for a single-shot pass through the most dangerous 40-kV multipacting barrier. After the passing the barrier, the gun was kept at operational voltage all the time and was intentionally turned down only for access to the RHIC IP2, where the gun is located.

---

* Work supported by Brookhaven Science Associates, LLC under Contract No. DE-AC02-98CH10886 with the U.S. Department of Energy, DOE NP office grant DE-FOA-0000632, and NSF grant PHY-1415252.

† pinayev@bnl.gov

ISBN: 978-3-95450-223-3 ISSN: 2673-7000 doi:10.18429/JACoW-NAPAC2019-TUPLO01

DUAL-FUNCTION ELECTRON RING-ION BOOSTER DESIGN FOR JLEIC HIGH-ENERGY OPTION

J.L. Martinez-Marin[1], B. Mustapha, Argonne National Laboratory, Lemont, IL, USA
L.K. Spentzouris, Illinois Institute of Technology, Chicago, IL, USA
[1]also at Illinois Institute of Technology, Chicago, IL, USA

Abstract

As part of the alternative design approach for the Jefferson Laboratory Electron-Ion Collider (JLEIC) ion complex, the electron storage ring (e-ring) is consolidated to also serve as a large booster for the ions. The goal of reaching 16 GeV/u or higher for all ions using only room-temperature magnets forces the re-design of the e-ring because of magnetic field and lattice limitations. The new design is challenging due to several imposed constraints: (1) use of room-temperature magnets, (2) avoiding transition crossing, and (3) maintaining the size and shape of the original e-ring design as much as possible. A design study is presented for a 16 GeV/u large ion booster after analyzing different alternatives that use: (1) combined-function magnets, (2) long quadrupoles or (3) quadrupole doublets in the lattice design. This design boosts the injection energy to the collider ring from 8 GeV (proton-equivalent) in the original baseline design to 16 GeV/u for all ions which is beneficial for the high-energy option of JLEIC of 200 GeV or higher. A scheme for adapting the new large ion booster design to also serve as electron storage ring is presented. The new booster design does not preclude the possibility of separate e-ring and ion booster ring stacked in the same tunnel as the ion collider ring.

INTRODUCTION

The most recent high-energy design for the ion complex of Jefferson Laboratory Electron-Ion Collider (JLEIC) [1] consists of a 150 MeV linac, an 8 GeV figure-8 low-energy booster, a 12 GeV figure-8 high-energy booster and a 200 GeV collider ring. Several changes have been adopted in the baseline design [2] from the alternative design approach [3], such as the lower-energy shorter linac, two boosters before injection to the collider ring and room-temperature magnets in the boosters, with superconducting magnets only in the collider ring. A schematic layout of the JLEIC baseline design is shown in Fig. 1.

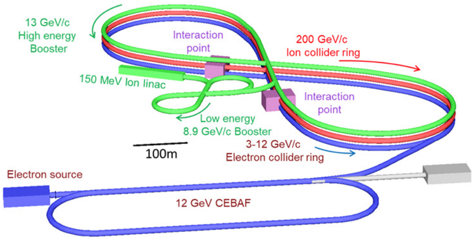

Figure 1: A schematic layout of JLEIC baseline design.

The alternative design approach was proposed in an effort to lower the risk and reduce the footprint of the JLEIC ion complex. As the baseline and alternative designs are converging, the essential part of the current alternative approach is to use a more compact non-figure-8 lower energy first booster (~ 6 GeV pre-booster) followed by a higher energy second booster (~ 16 GeV/u large booster) that could also be used as electron storage ring. However, the requirement to go to higher large booster energy presented further challenges. The main consequence is that the existing electron ring design cannot work as an ion booster up to 16 GeV/u and a new ion booster design is needed, which will be retro-fitted to serve as electron ring.

The first studies for a dual-function electron-ion booster were made for a medium energy option in the alternative design approach. There, the e-ring was adapted to be used also as a large ion booster. The rf sections for ion acceleration were successfully added to the e-ring lattice and the beam optics were re-matched for 11 GeV proton-equivalent with room-temperature magnets [4].

This medium energy option has recently been upgraded to high energy following the National Academy of Sciences (NAS) review [5].

High Energy Option for the Alternative Ion Complex Design

The high-energy option for the alternative design approach (see Fig. 2), consists of:

- A more compact 150 MeV Linac that has also been adopted for the JLEIC baseline design.
- A more compact 6 GeV racetrack pre-booster using room-temperature magnets. At this energy, the figure-8 shape is not required, different mechanisms with reasonable magnetic fields could be used for spin corrections [6].
- A large booster, up to 16 GeV/u for all ions with room-temperature magnets, adapted to also work as e-ring.

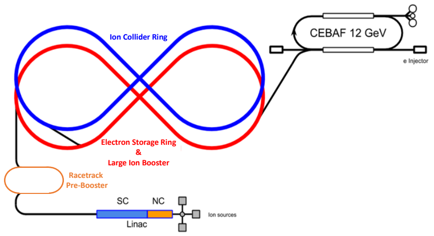

Figure 2: A schematic layout of the high-energy option for the alternative approach JLEIC design.

ISBN: 978-3-95450-223-3 ISSN: 2673-7000 doi:10.18429/JACoW-NAPAC2019-TUPLO02

SPIN DYNAMICS IN THE JLEIC ION INJECTOR LINAC*

J.L. Martinez Marin†[1], B. Mustapha, Argonne National Laboratory, Chicago, IL, USA
L.K. Spentzouris, Illinois Institute of Technology, Chicago, IL, USA
[1]also at Illinois Institute of Technology, Chicago, IL, USA

Abstract

One of the requirements for the future Electron Ion Collider (EIC) is to collide polarized electrons and light ions with at least 70% polarization for each beam. For light ions, polarized ion sources are used for injection to a linac, which is usually the first accelerator in the collider chain. The Jefferson Lab EIC (JLEIC) ion injector linac consists of a low-energy room-temperature section with quadrupole focusing followed by a superconducting linac with solenoid focusing inside long cryomodules. These two sections have different effects on the spin. Spin dynamics simulation studies are carried out for the JLEIC injector linac in order to preserve and maintain a high degree of polarization for light ion beams for delivery to the booster. The different options to maintain and restore the spin in the different sections of the linac for hydrogen, deuterium and helium ions are presented and discussed. Results from both the Zgoubi and COSY-Infinity codes are presented and compared for every section of the ion linac but the radio-frequency quadrupole (RFQ). Currently, a method to simulate the RFQ using Zgoubi is being investigated.

INTRODUCTION

The Jefferson Lab Electron Ion Collider (JLEIC) is based on a ring-ring collider design [1]. It consists of two intersecting accelerators, one producing an intense beam of electrons, the other a beam of protons, light or heavier atomic nuclei, which are steered into head-on collisions.

One of the accelerator challenges is to produce and maintain a high degree of polarization to be able to get insight into the nucleon spin. Around ~70% polarization is needed for both beams, the electron and the light ion beams [2].

A high energy option for JLEIC's ion complex was recently presented [3], consisting of a 150 MeV ion linac, an 8-GeV figure-8 low-energy booster, a 12-GeV figure-8 high-energy booster and a 200 GeV collider ring. See Fig. 1 for a schematic layout of the current JLEIC ion complex design.

The more compact 150 MeV ion linac [4] was adopted from the alternative design approach [5], and consists of a low-energy room-temperature section with quadrupole focusing followed by a superconducting linac with solenoid focusing inside long cryomodules. See Fig. 2 for a schematic layout of JLEIC ion injector linac.

A spin dynamics study was carried out in the ion linac to ensure a high degree of polarization of the beam. Two different codes, Zgoubi [6] and COSY-Infinity [7], were used for this study. Code-code benchmarking was one of the recommendations of the Community Review Report [8], which is especially important where beam measurement data is not available.

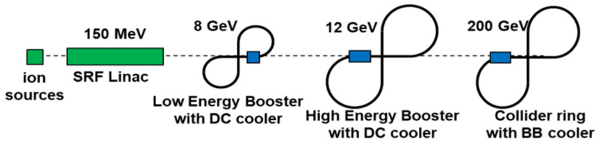

Figure 1: A schematic layout of JLEIC ion complex [3].

SPIN DYNAMICS IN SRF LINAC

The two different sections of the ion linac are analysed separately. The room-temperature section and the superconducting section have different effects on the spin because of the different focusing and beam energy in each section.

Room-temperature Section

The room-temperature section consists of a Low Energy Beam Transport line (LEBT), a radio-frequency quadrupoles (RFQ) and a drift tube linac (DTL). The LEBT section is from the source to the RFQ. The DTL section connects the RFQ to the superconducting radio-frequency (SRF) section.

Spin tracking simulations for both proton and deuteron beams have been performed using both the Zgoubi and COSY-Infinity codes. Unfortunately, none of the codes have a special element for the RFQ, therefore the simulations have been done only for the LEBT and the DTL. Currently, a method to simulate the RFQ using Zgoubi is being investigated.

Figure 3 shows the evolution of different spin components along the LEBT for both proton and deuteron beams. The simulation was performed for a beam of 100 particles starting with vertical spin in both Zgoubi and COSY-Infinity. The agreement between the two codes is almost perfect.

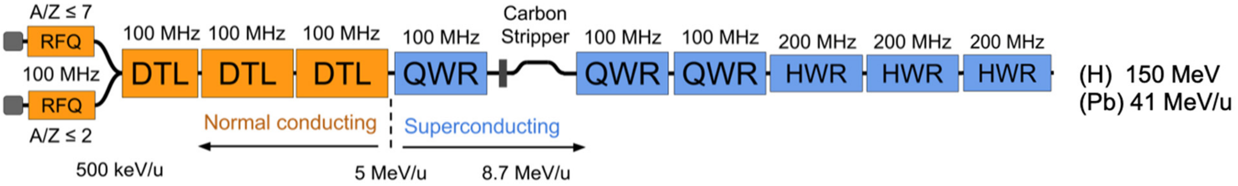

Figure 2: A schematic layout of JLEIC ion injector linac [4].

RHIC BEAM ABORT SYSTEM UPGRADE OPTIONS*

W. Fischer†, M. Blaskiewicz, M. Mapes, M. Minty, C. Montag, S. Nayak, V. Ptitsyn,
J. Sandberg, P. Thieberger, N. Tsoupas, J. Tuozzolo, K. Yip,
Brookhaven National Laboratory, Upton, NY, USA

Abstract

The RHIC ion (polarized proton) beam intensity has increased to 4x (1.1x) of the original design specifications. For heavy ions the beam dump window has limited the beam intensity. In 2014 the beam dump vacuum window was changed from stainless steel to a titanium alloy and the adjacent beam diffuser block carbon material was changed to allow for higher ion intensities. A thicker beam pipe was installed to prevent secondaries from quenching the adjacent superconducting quadrupole. For high intensity proton operation heating of the abort kicker ferrites had limited the intensity, leading to a reduction in kicker strength. Also in 2014, the abort kicker ferrites were changed, the eddy current reduction design was upgraded, and an active ferrite cooling loop was installed to prevent heating. With these upgrades the intensity was raised to new records for Au+Au operation in 2016, and for p+p operation in 2015 (100 GeV) and 2017 (255 GeV). A further increase in the beam intensity is planned for the RHIC program with the sPHENIX detector, and the Electron-Ion Collider eRHIC. We evaluate the need for upgrades and upgrade options for the beam abort system to accommodate these intensity increases.

INTRODUCTION

The current focus of the RHIC physics program is the Beam-Energy Scan II (BES-II) in search of a critical point in the nuclear physics phase diagram. This requires collisions at and below the nominal injection energy [1]. After completion of the BES-II in 2021 RHIC is expected to return to high-energy operation with the sPHENIX detector [2], presently under construction. With sPHENIX Au+Au, p+p and p+Au collisions with higher intensity beams are planned [3]. Higher beam intensities are also planned for the Electron-Ion Collider eRHIC [4, 5]. Table 1 list the main parameters relevant for the abort system design. For the beam dump design the heavy ion beams are more demanding, and for the abort kicker ferrite heating the polarized proton beams are more demanding. Shown are values achieved and planned for RHIC and eRHIC, for Au and polarized p beams.

BEAM DUMP UPGRADES

The RHIC beam dump is an internal dump inside the tunnel but outside the vacuum, separated from the beam vacuum by a Ti alloy vacuum window. It was originally designed for 60 Au bunches with 1.0×10^9 intensity (0.12 MJ) and upgrades several times. The last upgraded in 2014 to allow for higher Au intensity with a new Ti alloy vacuum window [6, 7] and new carbon-carbon blocks that disperse the energy of the extracted beam (Fig. 1). A thicker beam pipe was installed to shield the adjacent superconducting Q4 quadrupole from secondary particles. The beam dump is surrounded by marble slabs. During an abort the beam is swept in the horizontal plane across the window but not in the vertical plane. With these upgrades RHIC operated at 100 GeV/nucleon with Au bunch intensities of up to 2.0×10^9 in 2016 (Table 1).

(a) Existing dump with vacuum window

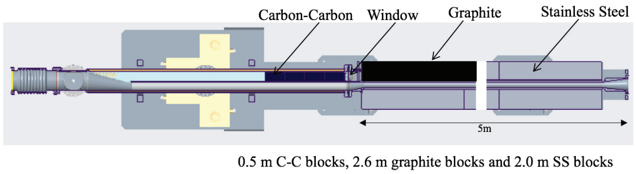

(b) Dump without vacuum window

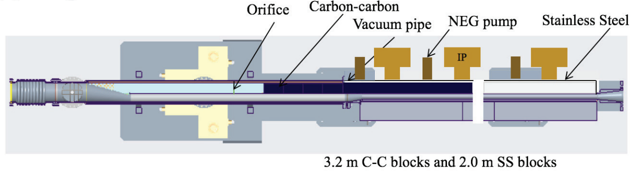

Figure 1: (a) Existing RHIC beam dump with vacuum window. (b) Possible upgrade without a vacuum window. The external marble shielding is not shown and may affect the location of the vacuum pumps. In both cases the view is from the top and the beam enters from the left.

For a further intensity increase the following upgrades are under consideration for the beam dump:

- a different Ti alloy window
- the addition of a vertical kicker
- a beam dump in vacuum without a window

The first two options have been previously considered [7], and the first option was implemented in the last upgrade.

Ti window upgrade. The energy deposition in the vacuum window was calculated with the MCNP6.2 code [8], which simulates the heavy ions directly, not approximated by protons multiplied by the charge number Z. It must be possible to abort the beam at any energy safely. In the RHIC energy range the highest energy deposition in the window is at the highest beam energies. Figure 2 shows the calculated energy density profiles in the horizontal (a) and vertical (b) plane for the case of the planned RHIC upgrade with Au beams (Table 1).

---

* Work supported by Brookhaven Science Associates, LLC under Contract No. DE-AC02-98CH10886 with the U.S. Department of Energy.

† Wolfram.Fischer@bnl.gov

ISBN: 978-3-95450-223-3 ISSN: 2673-7000 doi:10.18429/JACoW-NAPAC2019-TUPLO04

THE LATEST CODE DEVELOPMENT PROGRESS OF JSPEC*

H. Zhang#, S. Benson, Y. Zhang, Y. Roblin
Jefferson Lab, Newport News, VA, USA

Abstract

The JLab Simulation Package on Electron Cooling (JSPEC) is an open source software developed at Jefferson Lab for electron cooling and intrabeam scattering (IBS) simulations. IBS is an important factor that leads to the growth of the beam emittance and hence the reduction of the luminosity in a high density ion collider ring. Electron cooling is an effective measure to overcome the IBS effect. Although JSPEC is initiated to fulfil the simulation needs in JLab Electron Ion Collider project, it can be used as a general design tool for other accelerators. JSPEC provides various models of the ion beam and the electron beam. It calculates the expansion rate and simulates the evolution of the ion beam under the IBS and/or electron cooling effect. In this report, we will give a brief introduction of JSPEC and then present the latest code development progress of JSPEC, including new models, algorithms, and the user interface.

INTRODUCTION

JLab simulation package for electron cooling (JSPEC) is an efficient C++ program for intrabeam scattering (IBS) effect and electron cooling simulations. It is developed at JLab to fulfil the requirements of JLab Electron-Ion Collider (JLEIC) [1] cooling scheme and cooler design. It provides various models and tools for IBS expansion rate and/or electron cooling rate calculations and cooling process simulations. JSPEC has been thoroughly benchmarked with BETCOOL [2]. For a typical JLEIC IBS and cooling simulation, the two programs agree and JSPEC has been observed to achieve a noticeable improvement in efficiency. Now JSPEC is being actively used in JLEIC design. JSPEC is open source, with the source code and the documents available on the github repository [3]. A cloud version has been developed by Radiasoft in their SIREPO platform [4]. We have reported the development of JSPEC in the IPAC conference in Busan, Korea, 2016 [5]. In this report, we will concentrate on the latest development of JSPEC, including a turn-by-turn model for IBS and/or cooling process simulation, a model for user-defined arbitrary electron beam, and the input file for JSPEC.

TURN-BY-TURN MODEL

JSPEC originally had the RMS dynamic model and the particle model for IBS and/or electron cooling process simulation. The RMS dynamic model assumes the ion beam always maintains the Gaussian distribution so that the ion beam can be represented by the macroscopic parameters, *i.e.* emittance, momentum spread, and bunch length (for bunched beam). The particle model uses sample particles to represent the ion beam, hence the beam does not necessarily maintain the Gaussian distribution. In each time step, each particle receives a random phase advance for betatron and synchrotron oscillations. The turn-by-turn model is a development of the particle model. Instead of the random phase advance, the betatron and synchrotron motion is simulated by a linear one-turn map, which currently is generated from the tunes, but could be replaced by a high-order transfer map generated by an accelerator design/simulation program, *e.g.* MAD-X [6] and COSY Infinity [7], for more accurate modeling. The algorithm of the turn-by-turn model could be descibed as follows: (1) Create particles w.r.t. the original emittances of the ion beam; (2) Calculate the friction force on each ion, which leads to a momentum change (a kick); (3) Calculate the IBS rate and apply the IBS kick to each ion; (2) Apply the one-turn map on all particles; (5) Emittances are calculated statistically from the 6D phase space coordinates of all the particles; and (6) Repeat from step (2).

Comparing with the other models, the turn-by-turn model is much slower and may not be suitable as a design tool for a long cooling process. But it is considered more fundermental and hence more accurate. It can be used to benchmark the other models.

We have compared the turn-by-turn model with the RMS model, trying to figure out what is the proper particle number and step size for the RMS simulations. Take a typical JLEIC cooling case, perform the simulation of a 10-second cooling using the turn-by-turn model with 10,000 or 100,000 particles. Then repeat the same simulations again using the RMS dynamic model with the step size of 1 second and 10 seconds. Comparing the result, we can see the relative error of the emittances for one time step, listed in Table 1. The accumulated relative error for one hour can be estimated, which is listed in Table 2. We can see that more particles with smaller step

Table 1: Relative Error of Emittance in One Step

Step size (s)	N=10,000	N=100,000
1	1.54×10^{-5}	2.42×10^{-6}
10	3.06×10^{-4}	1.04×10^{-4}

Table 2: Relative Error of Emittance in One Hour

Step size (s)	N=10,000	N=100,000
1	5.70%	0.88%
10	11.65%	3.81%

---

* Work supported by the Department of Energy, Laboratory Directed Research and Development Funding, under Contract No. DE-AC05-06OR23177.

#hezhang@jlab.org

North American Particle Acc. Conf. NAPAC2019, Lansing, MI, USA JACoW Publishing
ISBN: 978-3-95450-223-3 ISSN: 2673-7000 doi:10.18429/JACoW-NAPAC2019-TUPLO05

FIXED TARGET OPERATION AT RHIC IN 2019

C. Liu*, I. Blacker, M. Blaskiewicz, D. Bruno, K.A. Brown, K.A. Drees, A.V. Fedotov, W. Fischer, C.J. Gardner, C. Giorgio, X. Gu, T. Hayes, H. Huang, R. Hulsart, D. Kayran, N. Kling, Y. Luo, D. Maffei, B. Martin, G. Marr, A. Marusic, C. Naylor, K. Mernick, R. Michnoff, M. Minty, C. Montag, J. Morris, S. Nemesure, I. Pinayev, S. Polizzo, V. Ranjbar, D. Raparia, G. Robert-Demolaize, T. Roser, J. Sandberg, V. Schoefer, F. Severino, T. Shrey, K. Smith, S. Tepikian, P. Thieberger, A. Zaltsman, K. Zeno, I. Zhang, W. Zhang, Brookhaven National Lab, Upton, NY, USA

Abstract

RHIC operated in fixed target mode at beam energies 4.59, 7.3, and 31.2 GeV/nucleon in 2019 as a part of the Beam Energy Scan II program. To scrape beam halo effectively at the fixed target which is 2.05 m away from the center of the STAR detectors, lattice design with relative large beta function at STAR was implemented at the two lower energies. The kickers of the base-band tune (BBQ) measurement system were engaged to dilute the beam transversely to maintain the event rate except for 31.2 GeV/nucleon. In addition, beam orbit control, tune and chromaticity adjustments were used to level the event rate. This paper will review the operational experience of RHIC in fixed target mode at various energies.

INTRODUCTION

Beam Energy Scan (BES) at RHIC [1] was aiming to investigate the first-order phase transition and location of the possible critical point [2–4]. The luminosity drops significantly with decreased center-of-mass (CoM) energy in colliding mode. It is extremely difficult to accumulate enough statistics with colliding beams at CoM energy as low as 3 GeV/nucleon. Therefore, the fixed target experiments [5] were proposed as a part of BES to extend the energy range. At the same time, the fixed target experiments also compliment the physics data taken in colliding mode at the same CoM energy. The operation of fixed target experiments at some beam energies has already been tested or conducted in recent years at RHIC [6, 7].

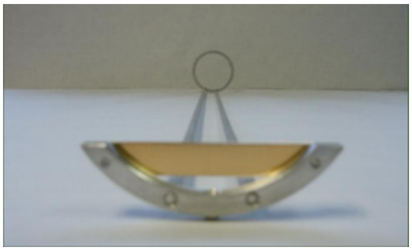

Figure 1: Picture of the STAR gold fixed target. The target was inserted in the lower part of the 75 mm beam pipe.

The fixed target is located 2.05 m west of the center of the STAR detectors. Figure 1 shows the fixed target, which is 1 mm thick gold foil with the edge 2 cm away from the center of the beam pipe. The shortest distance from the center of the beam pipe to the edge of the fixed target is identical to the radius of the beryllium pipe.

Only 12 Yellow bunches were injected into equally distributed buckets for the fixed target experiments. The beam were lowered vertically using local orbit bump to scrape beam halo on the target. A variety of measures have been employed to keep a more or less constant rate around 1.6 kHz, which is the upper limit for the rate without increasing significantly detector dead time. The operation of fixed target experiment at 4.59, 7.3 and 31.2 GeV/nucleon are presented in this report.

4.59 GeV/NUCLEON

The 9 MHz cavities were used at 4.59 GeV/nucleon for the fixed target experiment. This contributed to good lifetime therefore the long store length. A typical store and the event rate at STAR for fixed target experiment at 4.59 GeV/nucleon is shown in Fig. 2.

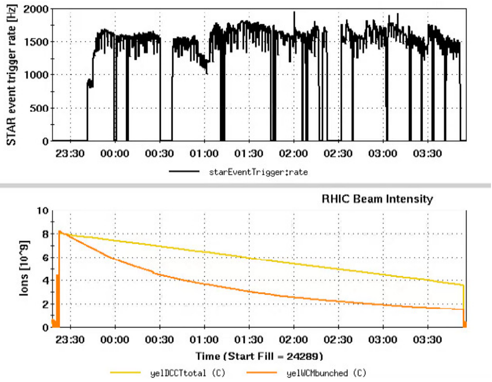

Figure 2: The upper plot shows the fixed target event rate over the time period of a physics store. The lower plot shows the beam intensity evolution during the store, DC beam intensity in light yellow and bunched beam intensity in dark yellow.

The beta function at STAR collision point is 10 m. With 1.5 µm normalized beam emittance, the rms beam size at the fixed target location is 1.8 mm. At the same time, the beta function/beam size at the final focusing quadrupole is reduced by ~40% with a 10 m beta star compared to that with a 2 m beta star used in colliding mode [1]. Therefore, the background was well under control during the store (the upper plot in Fig. 3). For this particular store shown in Fig. 2, only orbit control (the lower plot in Fig. 3) was applied to level the event rate at about 1.6 kHz. For another store at

---

[*] cliu1@bnl.gov

ISBN: 978-3-95450-223-3 ISSN: 2673-7000 doi:10.18429/JACoW-NAPAC2019-TUPLO06

WEAK-STRONG BEAM-BEAM SIMULATION FOR eRHIC*

Y. Luo†, G. Bassi, M. Blaskiewicz, W. Fischer, C. Montag, V. Ptitsyn, F. Willeke
Brookhaven National Laboratory, Upton, NY USA
Y. Hao, D. Xu Facility for Rare Isotope Beams, Michigan State University, East Lansing, MI USA
J. Qiang, Lawrence Berkeley National Laboratory, Berkeley, CA USA

Abstract

To compensate the geometric luminosity loss due to the crossing angle in eRHIC, crab cavities are to be installed on both sides of the interaction point. When the proton bunch length is comparable to the wavelength of its crab cavities, protons in the bunch head and tail will not be perfectly tilted in the x-z plane. In the article, we employ weak-strong beam-beam interaction model to calculate the proton beam size growth rates and the luminosity degradation rate. The goal of these studies is to optimize the beam-beam related machine and beam parameters of eRHIC.

INTRODUCTION

In the present eRHIC design, a crossing angle of 25 mrad between the proton and electron closed orbits in the interaction region is adopted. To compensate the geometric luminosity loss, crab cavities are to be installed to tilt the proton and electron bunches by 12.5 mrad in the x-z plane so that the two beams collide head-on at the interaction point (IP).

A local crabbing scheme is adopted for both beams. One set of crab cavities are placed on either side of IP. The horizontal phase advance between the crab cavities and IP is exactly $\pi/2$. The total voltage for crab cavities on one side is determined by the particle energy, crossing angle, and the crab cavity frequency. The higher crab cavity frequency is, the lower cavity amplitude is required.

To evaluate the effects of beam-beam interaction with crab cavities, both strong-strong and weak-strong simulation methods are used [1]. In this article, we present the results with weak-strong model. The eRHIC machine and beam parameters v5.1 are used. Table 1 shows the beam-beam interaction related parameters. Figure 1 shows the particle distributions of both beams at IP. Here the proton crab cavity frequency is 394 MHz. The final choice is to be decided.

Table 1: Beam-beam Interaction Related Machine and Beam Parameters Used in this Article

quantity	unit	proton	electron
Beam energy	GeV	275	10
Bunch intensity	10^{11}	1.05	3.0
β^* at IP	cm	(90, 5.9)	(63, 10.4)
Beam sizes at IP	μm	(112, 22.5)	
Bunch length	cm	7	1.9
Energy spread	10^{-4}	6.6	5.5
Transverse tunes		(0.31, 0.305)	(0.08, 0.06)
Longitudinal tune		0.01	0.069

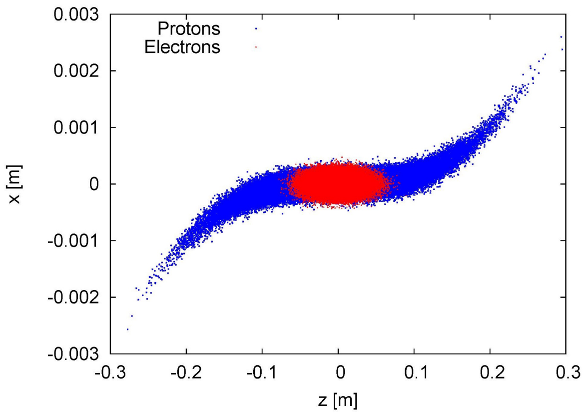

Figure 1: Proton and electron distributions at IP.

SIMULATION METHOD

In the weak-strong simulation with the code SimTrack [2], we focus on the long-term stability of the protons. In the code, the proton bunch is represented by 10,000 macro-particles with 6-d Gaussian distribution. The electron bunch is assumed to be a rigid 6-d Gaussian charge distribution and is assumed perfectly crabbed. In the simulation, only 1 interaction point per turn is considered. The proton macro-particles are transported around the ring using a 6×6 uncoupled linear matrix. The betatron tunes will be adjusted each turn according to the particle's relative momentum deviation and the settings of linear chromaticities.

So far beam-beam interaction is the only source of nonlinear force in our current weak-strong simulation code. For the beam-beam interaction at IP, we split the electron bunch into 5 slices longitudinally. At IP, each macro-proton interacts with these 5 electron slices one-by-one in a time order. At each encounter, the beam-beam force is calculated with Hirata's synchro-beam mapping [3]. There is no cross-talk between the proton macro-particles.

We track protons up to 2 million turns. On each turn, we calculate the RMS beam sizes of the protons and the luminosity. The luminosity is calculated by overlapping the proton macro-particle onto the transverse Gaussian charge distribution of electron slices. Figure 2 shows one example of calculated turn-by-turn proton RMS beam sizes in 2 million turns. Figure 3 shows the raw data of calculated turn-by-turn luminosity.

---

* Work supported by Brookhaven Science Associates, LLC under Contract No. DE-AC02-98CH10886 with the U.S. Department of Energy.

† yluo@bnl.gov

ISBN: 978-3-95450-223-3 ISSN: 2673-7000 doi:10.18429/JACoW-NAPAC2019-TUPLO07

CALCULATION OF ACTION DIFFUSION WITH CRABBED COLLISION IN eRHIC*

Y. Luo†, G. Bassi, M. Blaskiewicz, W. Fischer, C. Montag, V. Ptitsyn, F. Willeke
Brookhaven National Laboratory, Upton, NY USA
Y. Hao, D. Xu, Facility for Rare Isotope Beams, Michigan State University, East Lansing, MI USA
J. Qiang, Lawrence Berkeley National Laboratory, Berkeley, CA USA

Abstract

To compensate the geometric luminosity loss due to the crossing angle in eRHIC, crab cavities are to be installed on both sides of the interaction point. When the proton bunch length is comparable to the wavelength of the crab cavities, protons in the bunch head and tail will not be perfectly tilted in the x-z plane. This may cause synchro-betatron resonance and even coherent beam-beam instability. In the article, we develop a simulation method to calculate the transverse action diffusion rate and study its dependence on the beam-beam related machine and beam parameters.

INTRODUCTION

The 2015 Nuclear Science Advisory Committee Long Rang Plan identified the need for an electron-ion collider (EIC) facility as a gluon microscope with capabilities beyond those of any existing accelerator complex. To reach the required high energy, high luminosity, and high polarization, the eRHIC design, based on the existing heavy ion and polarized proton collider RHIC, adopts a very small β-function at the interaction points (IPs), a high collision repetition rate, and a novel hadron cooling scheme.

The maximum beam-beam parameters for the electron and proton beams in eRHIC are targeted at $\xi_e = 0.1$ and $\xi_p = 0.015$, respectively. These choices of beam-beam parameters are based on the successful operational experiences of KEKB and RHIC. However, such high beam-beam parameters have never been demonstrated in the any previous proton-electron colliders. Especially, due to lack of the radiation damping, the long-term stability of protons with beam-beam interaction and crab cavities is one of the most important concerns we have to pay attention to.

In the present eRHIC design, a full crossing angle of 25 mrad at the interaction regions is adopted. To compensate the geometric luminosity loss due to the crossing angle, crab cavities are to be installed to tilt the proton and electron bunches by 12.5 mrad in the x-z plane at the IPs so that the two beams collide head-on in the head-on collision frame.

In the early weak-strong and strong-strong simulations, we observe proton beam size growth and luminosity degradation. Their change rates show strong dependences on the crab cavity frequency, the proton longitudinal and transverse tunes, the proton bunch length, and so on. All of them indicates that there is coupled motion between the transverse and longitudinal motions through beam-beam interaction.

Table 1: Beam-beam Interaction Related Machine and Beam Parameters Used in this Article

quantity	unit	proton	electron
Beam energy	GeV	275	10
Bunch intensity	10^{11}	1.05	3.0
β^* at IP	cm	(90, 5.9)	(63, 10.4)
Beam sizes at IP	μm	(112, 22.5)	
Bunch length	cm	7	1.9
Energy spread	10^{-4}	6.6	5.5
Transverse tunes		(0.31, 0.305)	(0.08, 0.06)
Longitudinal tune		0.01	0.069

In this article, instead of time-consuming direct massive calculation of beam size growth and luminosity degradation rates in million-particle and million-turn tracking [1, 2], we evaluate the so-called action diffusion rate in a relatively short-term tracking and with a much smaller number of macro-particles. This method had been previously used to SSC, LHC, and other colliders to determine the long-term stability of protons with beam-beam interaction. However, the direct connections between the action diffusion rate and the real emittance growth is not straightforward. We still need direct tracking to confirm in the end to confirm the findings from action diffusion rate calculation. In this article, we use the lattice and beam parameters described in the eRHIC design parameters v5.1 as shown in Table 1.

SIMULATION SETUP

In the action diffusion rate calculation, we use the weak-strong code SimTrack [3]. We assume that the electron bunch is rigid and the electron bunch is perfectly crabbed in the head-on collision frame. For each simulation case, we track 200 protons with identical initial transverse actions $J_{x,y}$. However, their phases in the phase space (x, p_x, y, p_y) are randomly assigned between 0 and 2π. We track these particles up to 100,000 turns.

In the code, the proton ring is represented by a 6×6 linear matrix. There is no coupling between the horizontal, vertical, and longitudinal planes. However, the particle's transverse tunes are adjusted turn-by-turn based on the settings of linear chromaticities and the particle's relative momentum deviation. The beam-beam interaction takes place at the interaction point (IP). The calculation of beam-beam

---

* Work supported by Brookhaven Science Associates, LLC under Contract No. DE-AC02-98CH10886 with the U.S. Department of Energy.

† yluo@bnl.gov

ELECTRON-ION COLLIDER PERFORMANCE STUDIES WITH BEAM SYNCHONIZATION VIA GEAR-CHANGE *

I. Neththikumara†, G. A. Krafft[1], B. Terzić, Old Dominion University, Norfolk, Virginia, USA
Y. Roblin, Thomas Jefferson National Accelerator Facility, Newport News, Virginia, USA
[1]also at Thomas Jefferson National Accelerator Facility

Abstract

Beam synchronization of the future electron-ion collider (EIC) is studied with introducing different bunch numbers in the two colliding beams. This allows non-pairwise collisions between the bunches of the two beams and is known as 'gear-change', whereby one bunch of the first beam collides with all other bunches of the second beam, one at a time. Here we report on the study of how the beam dynamics of the Jefferson Lab Electron Ion collider concept is affected by the gear change. For this study, we use the new GPU-based code (GHOST). It features symplectic one-turn maps for particle tracking and Bassetti-Erskine approach for beam-beam interactions.

INTRODUCTION

The Proposed Jefferson Lab Electron – Ion Collider (JLEIC) [1] is designed to accommodate a wide range of center of mass energies, from 21.9 GeV to 98 GeV. The ion beam energy varies in a range of 40-200 GeV and for electron beam it is 3-12 GeV. The figure-8 shaped electron and ion storage rings have nearly identical circumferences and intersect at two interaction points along two long straights, as shown in Fig. 1 [2].

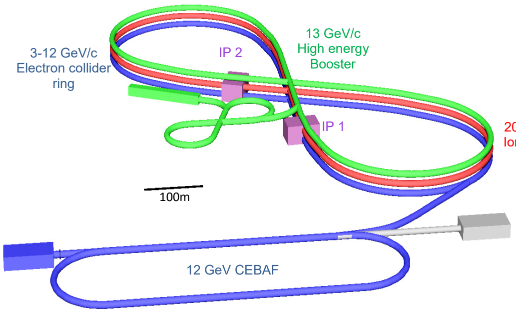

Figure 1: JLEIC layout for 200 GeV ion ring.

The electron beam is ultra-relativistic even for 3 GeV with a velocity of 0.99999971c, where c is the speed of light. But ion beam is not fully relativistic for low energy. This velocity difference in two beams causes a large difference of path lengths in the rings.

Both electron and ion rings are designed to match the revolution times of both beams at a specific center of mass energy (63.3 GeV). Then a particular ion bunch in ion-beam will collide with a same electron bunch at the interaction point (IP) for every turn.

This matching condition maintenance is impossible for the proposed large energy range due to non-relativistic ion velocities. Therefore, for lower energy values, bunches could miss each other at the IP due to different path lengths. This issue is known as beam synchronization and becomes more complicated if there is more than one IP in the machine as JLEIC [3].

Changing ring circumference is cumbersome and expensive. Other implementations to resolve this issue involve variation of bunch numbers, variation of ion path length, variation of electron path length and rf frequency. As the difference of revolution time is equal to ion-bunch spacing, synchronization between beams can be achieved when ion ring accommodates additional bunches. This implementation allows non-pairwise collisions between bunches of two beams at the IR and is known as 'gear-changing' of bunches. In order to avoid parasitic collisions, bunch numbers should satisfy the following relation.

$$N_0 \beta_0 = N\beta \quad (1)$$

where, N_0 is bunch number at the matched energy, N bunch number at the new energy, β_0 relativistic beta at matched energy and β relativistic beta at new energy.

For JLEIC, reference beam path lengths are defined for medium energy (E_{CM} = 63.3 GeV) where, $E_{\text{e-beam}}$ = 5 GeV and $E_{\text{p-beam}}$ = 100 GeV. The electron ring circumference is 2336.00336 m [3]. Relation between path lengths is,

$$L_{0-ions} = L_{0-elec}\, \beta_{0-ions} \quad (2)$$

SIMULATION TOOLS

For this study GPU accelerated Higher Order Symplectic Tracking (GHOST) code was used [4]. In this code, particle tracking through a storage ring in six-dimensional phase space is carried out with arbitrary order symplectic Taylor maps. These maps were generated as in COSY Infinity [4] with omitting zero-coefficient terms to speed up calculations and coeffients are found by

$$x = \sum_{\alpha\beta\gamma\eta\lambda\mu} M(x|\alpha\beta\gamma\eta\lambda\mu)\, x^{\alpha} x'^{\beta} y^{\gamma} y'^{\eta} z^{\lambda} \left(\frac{dE}{E_0}\right)^{\mu}. \quad (3)$$

For initial and final coordinates (q_i, p_i) and (q_f, p_f) the second kind of generating function satisfies the following relations : $(q_f, p_i) = J\, \nabla F_2\, (q_i, p_f)$. Beam-beam kick calculation for both 'strong-strong' and 'strong-weak' modes is based on Bassetti–Erskine approximation [6]. It enables solving Poisson equation, assuming collision of infinitely short bunches. This thin-bunch model is used by dividing

---

* This material is based upon work supported by the U.S. Department of Energy, Office of Science, Office of Nuclear Physics under contracts DE-AC05-06OR23177 and DE-AC02-06CH11357.

† ineth001@odu.edu

ISBN: 978-3-95450-223-3 ISSN: 2673-7000 doi:10.18429/JACoW-NAPAC2019-TUPLO12

OFF-MOMENTUM OPTICS CORRECTION IN RHIC*

G. Robert-Demolaize†, A. Marusic, V. Ptitsyn, Brookhaven National Laboratory, Upton, NY, USA

Abstract

Future operations of the electron-hadron collider eRHIC [1] call for beams circulating off of the magnetic center of all arc elements. In order to ensure that both stable beam conditions and the desired circumference changes can be achieved, dedicated experiments were conducted during the 2018 RHIC Run, which included the first off-momentum linear optics correction. This article reviews the experimental setup and the offline modeling predictions, then presents the measured radial excursions and corresponding residual off-momentum β-beat.

INTRODUCTION

The eRHIC electron-hadron collider project is currently being designed with the goal of repurposing one of the two existing RHIC beamlines for circulating hadron bunches and aiming them at electron bunches inside of the interaction region (IR6) currently hosting the STAR detector. Collisions are planned for a range of center of mass energies $\sqrt{s_{e-h}}$ = 29-140 GeV, with the corresponding energies for each species as listed in Table 1.

The top energies listed for the hadrons are different enough that not all species will be able to travel through the magnetic center of the RHIC arc dipole magnets [2]: the central orbit reference is therefore taken as the one for 133 GeV protons with the requirement to be synchronous with the electron beam at IP6 to achieve collisions, giving a revolution time of τ_p = 12.78865 μsec for a standard RHIC circumference C_0 = 3833.845 m. For proton energies 100 GeV and above, all RHIC Yellow arcs are used: the required revolution time is achieved by manipulating the circumference C via a closed orbit shift in the arcs (radial shift ΔR), within a range of ±14 mm for all energies between 100-275 GeV. As for proton energies below 100 GeV, C needs a large change, forcing the design to switch to a shorter, inner (Blue) arc between two of the non-colliding RHIC straight sections, IR12 and IR2 in this particular case. This shrinks the circumference by ΔC = 942 mm (C = 3832.903 m) without requiring any radial shift. Table 1 reviews the circumference and arc radius changes for all eRHIC species, including heavy ions.

Having the beams circulating off-center in the arcs must be taken into account when designing the linear optics. This is particularly critical when considering the ramp in energy from injection to flattop, during which the beams will shift from one radius to the next as they get accelerated. To that end, the lattice design process must account for the momentum offset $\delta p/p$ that generates the required radial shit ΔR for each energy, which can be handled using programs like MAD-X [3] or Bmad [4].

Table 1: Design beam energies and circulating radii for the electrons and hadron species planned for eRHIC operations at $\sqrt{s_{e-h}}$ = 29-140 GeV [2].

Species	**Energy** [GeV/u]	C [m]	ΔR [mm]
Polarized electrons	5-18	3833.867	0.0
Polarized protons	41	3832.903	0.0
	100	3833.772	−14.0
	133	3833.845	0.0
	275	3833.981	14.0
Heavy ions *Au*	41	3832.903	0.0
	100	3833.803	−8.0

EXPERIMENTAL SETUP

Dedicated beam time was allocated during the 2018 RHIC Run to determine the largest achievable radial shift in the Yellow arc dipole magnets for Au ions at injection energy E = 10 GeV/u. The goal is to try and push the circulating beam as far as possible while maintaining the linear optics "constant", i.e. correct the off-momentum optics to match the on-momentum settings.

The experiment is performed at injection energy for practical reasons, mainly the convenience of repeatability in the face of limited machine time rather than going through the lengthier process of injection/acceleration/down ramp. There is no limitation from operating with larger transverse beam sizes: the mechanical aperture in the RHIC arcs is assumed circular with a radius r_{arc} = 34.5 mm (taking an arc quadrupole magnet as reference) while the maximum beam size at injection energy $\hat{\sigma}_{x,y}$ is calculated as:

$$\hat{\sigma}_{x,y} = \sqrt{\frac{\hat{\beta}_{x,y}\epsilon_{x,y}}{\gamma_{inj}}} = \sqrt{\frac{55.96\text{ m}\cdot 1.50\ \mu\text{m}}{10.52}} = 2.83\text{ mm}, \tag{1}$$

where $\hat{\beta}_{x,y}$ is the peak betatron function in the arcs, $\epsilon_{x,y}$ is the transverse *rms* emittance in each plane and γ_{inj} the relativistic gamma at injection energy. Assuming a circulating round beam with $\pm 6\hat{\sigma}_{x,y}$ transverse size, the remaining space for radial shifts A_{inj} is therefore:

$$A_{inj} = r_{\text{arc}} - 6.0\cdot\hat{\sigma}_{x,y} = 17.55\text{ mm}. \tag{2}$$

Since the off-momentum closed orbit actually oscillates based on the value of the dispersion function D_x, one has to make sure that the peak orbit excursion still fits within A_{inj}.

---

* Work supported by Brookhaven Science Associates, LLC under Contract No. DE-AC02-98CH10886 with the U.S. Department of Energy.

† grd@bnl.gov

ISBN: 978-3-95450-223-3 ISSN: 2673-7000 doi:10.18429/JACoW-NAPAC2019-TUPLO15

MULTIPOLE EFFECTS ON DYNAMIC APERTURE IN JLEIC ION COLLIDER RING*

B.R. Gamage[†], F. Lin, T.J. Michalski, V.S. Morozov, R. Rajput-Ghoshal, M. Wiseman,
Jefferson Lab, Newport News, VA, USA
G.L. Sabbi, LBNL, Berkeley, CA, USA
Y. Cai, Y.M. Nosochkov, M.K. Sullivan, SLAC, Menlo Park, CA, USA

Abstract

In a collider, stronger focusing at the interaction point (IP) for low beta-star and high luminosity produces large beams at final focusing quadrupoles (FFQs). To achieve the high luminosity requirement in the Jefferson Lab Electron-Ion Collider (JLEIC), the interaction region (IR) beta functions peak at ~4.2 km in downstream FFQs. These large beta functions and FFQ multipoles reduce the dynamic aperture (DA) of the ring. A study of the multipole effects on the DA was performed to determine limits on multipoles, and to include a multipole compensation scheme to increase the DA and beam lifetime.

INTRODUCTION

The Jefferson Lab Electron-Ion Collider (JLEIC) [1] is a high-luminosity high-polarization facility based on the existing CEBAF facility. The JLEIC design was recently updated to have a center-of-mass energy of 100 GeV, with an ion collider ring (ICR) maximum energy of 200 GeV. An aggressive final focus for high luminosity of 10^{34} cm^{-2} s^{-1} produces maximum IR beta functions of ~4.2 km in both planes. Beam parameters are $\varepsilon^{\mathrm{N}}_{\mathrm{x,y}} = 0.5/0.1$ µm, and rms $\Delta p/p = 3 \times 10^{-4}$.

JLEIC IR OPTICS

The JLEIC IR schematic layout is shown in Fig. 1 [2]. At small angles with respect to the beam directions, the detection regions extend 30 m to 40 m in either direction from the central detector. The central detector is designed around a 4 m solenoid with maximum field of 2 T extending 2.4 m on the outgoing ion side, and 1.6 m on the opposite side. The solenoid field is adjustable independent of the beam energies to optimize the detection for various processes. The electron beam is aligned with the detector solenoid axis to avoid local synchrotron radiation generation.

The IR optics must be flexible enough to support the β-squeeze and optimization of the luminosity and detection in different collider configurations, including different beam energies, ion species, and detector solenoid strengths. The ion IR optics designed to support these requirements is shown in Fig. 2. There are three physical quadrupoles on each side of the IP. Their lengths and apertures have been optimized to meet the conditions:

- Downstream angular acceptance of ±10 mrad,
- Integrated field gradients sufficient to provide focusing at the IP up to 200 GeV/c, and
- Maximum field less than 4.6 T at the aperture limit.

The parameters for the IR quadrupoles are shown in Table 1.

Table 1: JLEIC Ion Ring IR Quadrupoles

Name	length [m]	Aperture [cm]	Gradient [T/m]
iQUS2	2.1	4	94.07
iQUS1b	1.45	3	-97.88
iQUS1a	1.45	3	-97.88
iQDS1a	2.25	9.2	-37.23
iQDS1b	2.25	12.3	-37.23
iQDS2	4.5	17.7	25.96

Chromaticity Correction

With the upgrade to the 200 GeV proton ring, the ICR was optimized to attain the proper phase advance between sextupoles and IR which was necessary for local chromaticity correction.

The momentum acceptance for the optimized lattice is about $\Delta p/p = \pm 3 \times 10^{-3}$ as shown in Fig. 3. With the design momentum spread of about 3×10^{-4}, this gives about $\pm 10\sigma_p$ which is adequate for the ICR.

Fig. 4 shows the DA found for this momentum acceptance with a step size of ($2\sigma_{\mathrm{p}}$). The aperture size is about $\pm 60\,\sigma$ (shown by the dotted black line) for the largest momentum offset. This sets the basis for the development of the EIC IR magnet requirements and tests of whether the demonstrated magnet parameters satisfy them.

DA WITH MULTIPOLES

In a collider the dominant effect from multipoles comes from magnets located in areas with high beta function which occurs in the final focus quads. To better understand the limits imposed on the DA from multipoles we use multipole data from existing magnets by scaling them to JLEIC design parameters [3]. The relation for the magnetic field components containing the non linear elements is,

$$B_{\mathrm{y}} + iB_{\mathrm{x}} = 10^{-4} B_{\mathrm{Q}} \times \Sigma_{n=1}^{\infty} (b_n + i a_n) \left(\frac{x + iy}{r_0} \right)^n , \quad (1)$$

where a_n and b_n are the relative values of skew and normal multipoles determined at a reference radius r_0 (typically

---

* This material is based upon work supported by the U.S. DoE under Contracts No. DE-AC05-06OR23177, DE-AC02-76SF00515, and DE-AC03-76SF00098.

[†] randika@jlab.org

PYTHON SCRIPTS FOR RF COMMISSIONING AT FRIB*

H. Maniar, E. Daykin, D. Morris, A. Plastun, H. Ren, S. Zhao
Facility for Rare Isotope Beams, Michigan State University, East Lansing, MI, USA

Abstract

RF commissioning at FRIB involves QWR cavities (β=0.085 and β=0.041), HWR cavities (β=0.29 and β=0.53) and few room temperature devices. Each RF system has many process variables for LLRF and amplifier control located on different pages of CS-Studio. Efficient handling of all these PVs can be challenging for RF experts. Several scripts using Python have been developed to facilitate this process. User interface application has been developed using Qt Designer and PyQt package of Python, for ease of access of all scripts. These scripts are useful for mass actions (for multiple systems) including turning on/ off LLRF controllers and amplifiers, resetting interlocks/ errors, changing a PV value, etc. Python scripts are also used to quickly prototype the auto-start procedure for QWR cavities, which eventually is implemented on IOC driver. The application sends commands to IOC driver with device name, PV name and value to be changed. Future developments can be converting to state-notation language on IOC to add channel access security. This application intends to reduce time and efforts for RF commissioning at FRIB.

INTRODUCTION

The Facility for Rare Isotope Beams (FRIB) at MSU will be a scientific user facility for nuclear physics research and will enable scientists to make discoveries about the properties of rare isotopes [1]. The FRIB linac consists of room temperature front end devices such as Low Energy Beam Transport (LEBT), Multi-Harmonic Buncher (MHB), Radio Frequency Quadrupole (RFQ) and Medium Energy Beam Transport (MEBT) bunchers. It also includes 104 Quarter-Wave Resonators (QWR) and 220 Half-Wave Resonators (HWR). Table 1 shows parameters of SRF cavities at FRIB. Figure 1 shows the layout of FRIB linac [2].

Table 1: FRIB Resonator Parameters

Resonator	QWR1	QWR2	HWR1	HWR2
β	0.041	0.085	0.29	0.53
f (MHz)	80.5	80.5	322	322
No. of cavities	12	92	72	148
Tuner type	Stepper	Stepper	Pneumatic	Pneumatic

CS-Studio screens have been developed for users to access all RF parameters related to Low Level Radio Frequency (LLRF) Controller and Amplifier. Each RF system contains around 400 process variables (PV) including parameters for interlocks, control parameters, cavity conditioning, calibration, attenuation, system configuration etc. All these PVs are accessible using Experimental Physics and Industrial Control System (EPICS) channels. Input/ Output Controller (IOC) driver handles read/ write actions to these PVs.

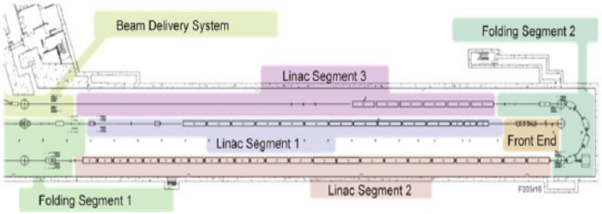

Figure 1: FRIB linac.

PYTHON

Python offers several convenient features for scientific and engineering programming [3]. The Python EPICS package (PyEpics) is useful to interact with EPICS channel access PVs. The PyEpics package contains several function, modules and classes to interact with EPICS channel access [3]. Multiple Python scripts have been developed using PyEpics channel for RF commissioning. GUI framework has been also developed using PyQt library from Python.

Python GUI

Qt Designer is the Qt tool helpful in designing and building graphical user interfaces. It allows user to use built-in widgets and forms to develop designs. It uses eXtensible Markup Language (XML) *'.ui'* format to store design files. Typically, Qt designer stores GUI files in XML format and does not generate C++ or Python code. PyQt is a library that includes *uic* Python module. Qt Designer's '*uic'* utility is useful in creating C++ code, whereas PyQt's *'pyuic'* utility is useful to generate Python files [3]. Any user interface files *'.ui'* can be converted to Python files *'.py'* using this command in terminal

'pyuic5 filename.ui –o filename.py '

Python EPICS

This package can be called in any Python script using '*import epics'*

The main components of this module include functions such as *caget (), caput (), camonitor ()* to simply read, write, monitor PVs. It also includes a *ca* module, useful for low-level epics channel access and a PV object, useful for higher–level epics channel access [4]. The get functions ask for data to be transferred over the network. For large data array, it can take a significant amount of time. Also for disconnected PVs, function will not return any value. For these reasons, *get* functions should be used with *timeout* or *wait* options. It also has options of *count* and *numpy* to return number of elements for array data.

---

* Work supported the U.S. Dept. of Energy Office of Science under Cooperative Agreement DE-SC0000661.

ISBN: 978-3-95450-223-3 ISSN: 2673-7000 doi:10.18429/JACoW-NAPAC2019-TUPLE04

AN IRIS DIAPHRAGM BEAM DETECTOR FOR HALO OR PROFILE MEASUREMENTS*

A. Liu†, on behalf of the project, Euclid Techlabs, LLC, Bolingbrook, U.S.A.

Abstract

Non-Gaussian beam distributions around the Gaussian core can be formed in an accelerator in both the transverse and longitudinal directions. Since there are no clearly defined criteria to distinguish the halo from the core, the measurement of the halo structure without affecting the core is challenging. Both destructive and non-destructive techniques have been developed and tested at various accelerator facilities. Most of these techniques require complex and expensive setups, like in a gas sheet monitor, or a digital micromirror array. In this paper, a novel device that adopts an iris diaphragm structure for transverse beam halo measurement is presented. The iris diaphragm detector can also work as an adjustable collimator. It also has advantages such as high-portability, cost-effectiveness, high-configurability and more. A proof-of-principle version-alpha of the detector has been successfully tested at the ACT beamline of AWA at ANL. The design of a version-beta is also discussed in the paper.

INTRODUCTION

There are multiple mechanisms to form a beam halo structure. It can be from the dark current in an accelerator, or from beam scattering with residual gas molecules in the vacuum chambers, and so forth. Although the halo formation mechanisms may differ, the hazards it presents to the machine operation and the users (such as those light source users) are common concerns for the facilities. The halo beam can deposit overwhelming energy and generate radiations that impacts the detector lifetime or even destroy the detector in a short time window.

Researchers have been exploiting methods to measure the beam halo, using non-destructive, partially-destructive, or completely-destructive techniques. Among the non-destructive methods, the usage of synchrotron radiation light with a digital micromirror array [1, 2], gas sheets monitor are novel techniques that are actively investigated. Among the destructive methods, the use of a Wire Scanner (WS) [3] is one of the most commonly adopted. Most of the methods, however, require complex and expensive setups.

Inspired by the structure of an iris diaphragm for a camera lens, Euclid Techlabs, LLC started developing an iris diaphragm beam transverse halo or profile detector (referred to as iris detector hereafter) from Feb, 2019. The iris detector uses metal iris blades to stop and absorb the charged particles, for which the current is extracted from each blade as an independent signal. The iris closes to intercept the beam, and opens to stop intercepting. Each blade is insulated from the others and generates an independent signal. The pulsed current signals are transported to outside the vacuum through an SMA feedthrough port mounted onto a CF flange. The open-and-close motion of the iris blades can be controlled and driven by a linear actuator. The whole apparatus can be contained in a six-way 6" CF cross. It has the advantages to be *cost-efficient*, *highly-configurable*, *dual-purposed*, and *linearly-responsive*. Furthermore, it can be designed to work *both as a transverse profile detector, and as a movable collimator*, simultaneously.

PROOF-OF-PRINCIPLE VERSION-ALPHA

The version-alpha of the iris detector (referred to as version-alpha hereafter) is a prototype to demonstrate the following proofs-of-principle:

- Pulsed current signals can be generated and sent from an iris blade, which works as a beam collector when being bombarded by an electron beam, through the SMA ports and be read by an oscilloscope.
- When the beam energy is high, or when the stopping power of the iris blade is small, such that a fraction of the charged particles penetrate the blades, the blades can work properly with the partial beam current deposited onto the blades.
- The signal isolation between iris blades can be achieved by using ceramic plates, on which the blades translate in opposition, while the signal on each blade is independent of the other.

The 3D design of the version-alpha is shown in Fig. 1. A metallic holder that has multiple slots for holding iris blades of different materials and different thickness is mounted to a UHV-compatible linear actuator on the top. A 45°-angle YaG screen is attached to an adapter, which is then mounted to the bottom of the holder. The holder and YaG adapter are conductive with each other, and a coax cable is used to connect the holder and one of the SMA ports (upper brown line in the figure). A metallic contactor with two vertical pillars is mounted on but insulated from a rotary feedthrough on the bottom. Ceramic sheets can be mounted on the side faces of the pillars. The purpose of the design is to touch the YaG adapter from different faces, thus providing either a metal-to-metal contact, or a metal-ceramic-metal contact to test ceramic insulation. Another coax cable connects the contactor and the other SMA port (lower brown line). Both top and bottom signals are insulated from either of the feedthrough shafts, thus only go through the SMA ports. The cables are guided by a structure, which is mounted on the 6" to 2.75" zero-length reducer for the SMA ports. The structure guides the cables to slide through the two holes in

---

* Work supported by the SBIR program of the U.S. Department of Energy, under grant DE-SC0019538, PI: A. Liu

† a.liu@euclidtechlabs.com

ISBN: 978-3-95450-223-3 ISSN: 2673-7000 doi:10.18429/JACoW-NAPAC2019-TUPLE05

OPTICAL SYSTEM FOR OBSERVATION OF FRIB TARGET*

I.N. Nesterenko†[1], G. Bollen, M. Hausmann, A. Hussain, S.M. Lidia, S. Rodriguez
Facility for Rare Isotope Beams, Michigan State University, East Lansing, USA
[1]also at Budker Institute of Nuclear Physics, Novosibirsk, Russia

Abstract

Facility for Rare Isotope Beams (FRIB) is a next-generation rare-isotope research facility under construction at Michigan State University (MSU). FRIB will produce rare-isotope beams of unprecedented intensities by impinging a 400 kW heavy-ion beam on a production target and by collecting and purifying the rare isotopes of interest with a fragment separator. A thermal imaging system (TIS) has been developed to monitor the beam spot on the production target. The main features and characteristics of optical system is presented. The prototype of optical system has been tested.

MAIN REQUIREMENTS FOR TIS

- To provide measurement of a temperature distribution in a hot spot with accuracy ± 20 K.
- To observe position of a hot spot on a graphite target with spatial resolution 0.1 mm. Hot spot size is about 1mm.
- Field of view (FOV) should be about 30 mm.
- To provide output signal for Machine Protection System (MPS) if target temperature exceeds allowable threshold. The system of fast thermometry shall have a time response about 10 µs.
- Optical elements of the system should be compatible to high radiation environment. Due to darkening and luminescence of transparent materials it means in optical system only mirrors should be used.
- For suppressing of neutron streaming the optical system shall have a bend ("dog-leg") inside of radiation shielding.

DESCRIPTION OF OPTICAL SYSTEM

Base on the main requirements for TIS, we decided to split of the optical system into two parts. The first part is placed in vacuum vessel near to the production target and before of radiation shielding and it consists from mirrors exclusively. This part of optical system has design of relay lens with scale factor of transformation equal to 1:1. The relay lens is performed by scheme with mirror symmetry and consisting of two identical Cassegrain type telescopes (see Fig. 1).

Main feature of chosen optical design of the relay lens is possible to use a spherical surface in telescopes. In this case, residual spherical aberration allows use of numerical apertures up to 0.03 at diffraction quality. With our parameters of optical system for completely suppressing of spherical aberration the conic factor on primary mirrors should be -0.055 (aspheric deviation corresponds to about 0.1 µm). The secondary mirrors still have spherical surfaces. Another important feature of this design is that mirror-arrangement of telescopes to each other suppresses a coma.

The optical board of relay lens, mounting board with two telescopes and the telescopes themselves are made from invar. This material was used to prevent uncontrollable extension in presence of radiation heating. Due to the relay lens parameters is very sensitive to distances between main elements.

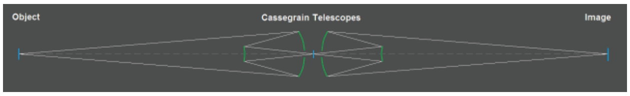

Figure 1: An optical layout of relay lens.

The second part of optical system is placed outside of the vacuum vessel and after of the radiation shielding. This part is realized in form of 2D optical breadboard, where light is distributed between different devices (see Fig. 2).

Usually, a camera sensor has smaller size than the requested field of view. We use Sill Optics telecentric lens to match the image size to the sensor size.

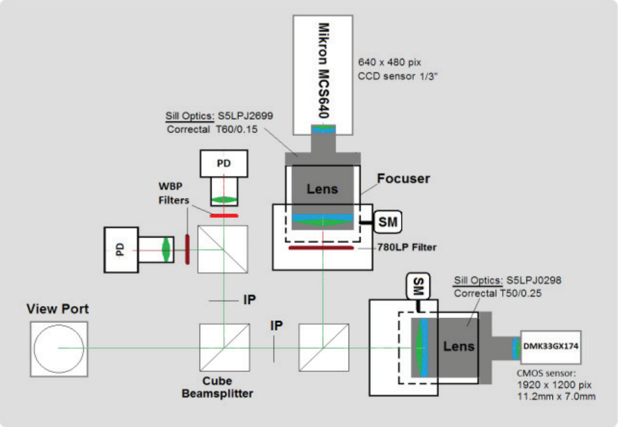

Figure 2: An optical breadboard diagram. The cube beam splitters have 50% by 50% ratio. Here is IP – image plane; SM – stepper motor; PD – photodiode; WBP – wide bandpass filter. 780LP – longpass filter with cut of wavelength 780 nm.

In system of fast thermometry for MPS will be used the method of two-color pyrometry. Base on using of two photodiode modules which will be supplied through two bandpass filters for a different wavelength range. This method of measuring temperature was selected due to its weak dependence from the values of reflection and transmission coefficients, which can significantly vary in presence of high radiation and sublimation of graphite target.

---

* Work supported by the U.S. Department of Energy Office of Science under Cooperative Agreement DE-SC0000661

† email address: nesterenko@frib.msu.edu

North American Particle Acc. Conf. NAPAC2019, Lansing, MI, USA JACoW Publishing
ISBN: 978-3-95450-223-3 ISSN: 2673-7000 doi:10.18429/JACoW-NAPAC2019-TUPLE06

SKIMMER–NOZZLE CONFIGURATION MEASUREMENTS FOR A GAS SHEET BEAM PROFILE MONITOR*

S. Szustkowski[†1], S. Chattopadhyay[1,2], D. J. Crawford[2], B. T. Freemire[‡1]
[1]Northern Illinois University, DeKalb, IL, USA
[2]Fermi National Accelerator Laboratory, Batavia, IL, USA

Abstract

Understanding the characteristics of the gas sheet being produced and optimal configuration of the gas injection system is essential to the the performance of a gas sheet beam profile monitor. A gas injection system test stand has been built at Fermilab to test various nozzle and slit configurations. The distance between the nozzle and slit can be changed to find an optimal configuration. Using a moveable cold cathode gauge the gas profile is measured.

INTRODUCTION

Various diagnostic systems are desired in the accelerator community. Traditional transverse profile monitors are destructive to the beam, such as multiwires and scintillator screens. Residual gas monitors only measure one dimension of the beam and have a slow read back. If the gas is forced into a sheet and injected at an angle with respect to the beam direction, then a two-dimensional transverse profile can be measured.

The premise of a gas sheet beam profile monitor is as follows. A compressed gas is forced through a nozzle. As the gas travels downstream, it exhibits molecular flow due to a high Knudsen number [1]. It then reaches a skimmer, which removes any gas molecules with significant divergence and provides the final shape. The resulting sheet is then injected at an angle transversely to the direction of the particle beam. The beam ionizes the gas, after which the ions are extracted by a series of annular electrodes. A single or series of microchannel plates (MCPs) convert the ions to electrons and allow for an amplification factor of 10^3–10^6, typically. The electrons impinge on a scintillator screen, and the image is recorded by a high speed CCD camera. This allows the transverse beam distribution to be reconstructed. The amplification provided by the MCP allows for single pass readback, or the sparsely-populated tails of the beam to be imaged.

Understanding the injection system is crucial in order to have an appropriate sheet thickness and uniform distribution, as these two parameters directly impact the measured signal [2]. Simulations have also shown that if the distance between the nozzle and skimmer decreases, the distribution of the gas sheet tails become more prominent [3]. A test stand will give insight into the optimal configuration of the injection system, as well as a direct measurement of the sheet thickness and uniformity.

APPARATUS

Figure 1 depicts how the internal layout of the test stand. Figure 2 shows the test stand located at Fermi National Accelerator Laboratory. The test stand footprint is 4×8 ft.

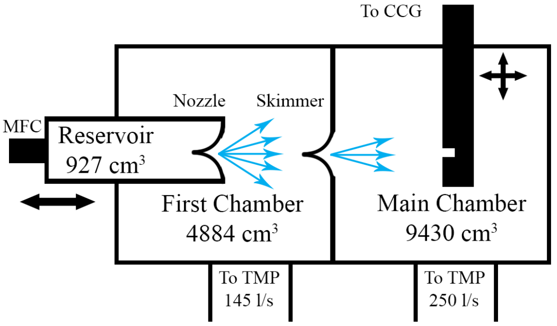

Figure 1: Sketch of apparatus setup.

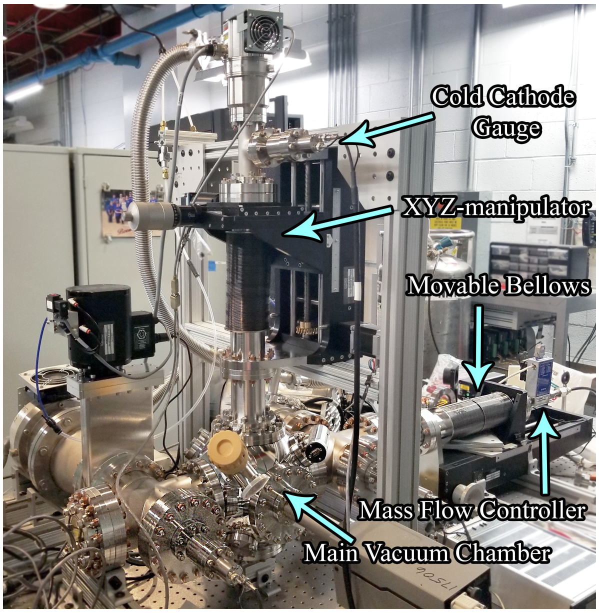

Figure 2: Gas Sheet Profile Monitor Test Stand.

The test stand is constructed as follows. A compressed nitrogen gas bottle is connected to a mass flow controller that can vary the flow up to 10,000 sccm. The gas is injected into a cylindrical reservoir of 927 cm^3. The reservoir is

---

[*] Fermilab is operated by the Fermi Research Alliance, LLC, under Contract No. DE-AC0207CH11359 with the US Department of Energy. This work is supported by the Office of High Energy Physics General Accelerator Research and Development (GARD) Program.

[†] sszustkowski1@niu.edu

[‡] now at Euclid Techlabs, LLC

ISBN: 978-3-95450-223-3 ISSN: 2673-7000 doi:10.18429/JACoW-NAPAC2019-TUPLE07

OVERVIEW OF FRIB'S DIAGNOSTICS CONTROLS SYSTEM*

B. S. Martins†, S. Cogan, M. Konrad, S. M. Lidia, D.O. Omitto, P. J. Rodriguez,
Facility for Rare Isotope Beams, Michigan State University, East Lansing, MI, USA

Abstract

In this work we will present an overview of the diagnostic systems put in place by FRIB's Beam Instrumentation and Measurements department. We will focus on the controls and integration aspects for different kinds of equipment, such as picoammeters and motor controllers, used to drive and readback the devices deployed on the beamline, such as profile monitors, Faraday cups, etc. In particular, we will discuss the controls software used in our deployment and how we make use of continuous integration and deployment systems to automate certain tasks and make the controls system in production more robust.

INTRODUCTION

The Beam Instrumentation and Measurements department is responsible for a myriad of devices used in FRIB's beamline for data collection and monitoring of operational parameters, such as Allison Scanners, Profile Monitors, Cameras, Beam Position Monitors, Beam Current Monitors, among many others. This variety of devices poses a challenge for the controls system, which must accommodate a considerable amount of different software pieces necessary to drive and read these devices.

In order to achieve this goal, FRIB builds on the EPICS [1] ecosystem and a number of commercial technologies for its controls system that will be described in this paper.

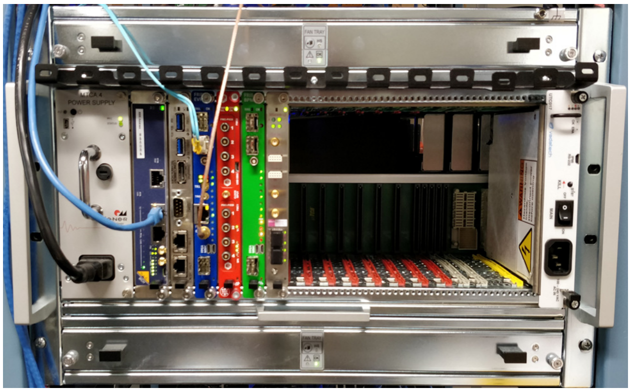

Figure 1: A µTCA crate with MCH, CPU, Event Receiver, Pico8, BPM and BCM cards.

DEVICES OVERVIEW

Diagnostics devices in the controls system can be categorized in a number of different ways. From the controls system infrastructure point of view, they can be divided into fast, medium and slow devices, according to the type and amount of data they generate per unit of time or how quickly they must signal for machine protection purposes. The category of a particular device guides where the device's EPICS IOC (Input/Output Controller) will be hosted, which can be one of the following: µTCA CPUs, Dedicated Server, Embedded or Virtual Machine.

µTCA CPUs

µTCA crates, as the one seen in Fig. 1, are typically used to host fast acquisition cards. We utilize a mix of commercial, off-the-shelf cards and in-house developed ones, with three acquisition card models in use:

- CAENels Pico8 picoammeter cards [2] for Faraday Cups, Profile Monitors, Neutron Detectors and Ion Chambers;
- FGPDB (FRIB General Purpose Digital Board, developed in-house) cards for Beam Position Monitors;
- Struck SIS8300 digitizer [3] for Beam Current Monitors.

In addition to any combination of the aforementioned acquisition cards, every µTCA crate also has one CPU card to host EPICS IOCs and one FGPDB card configured as an Event Receiver, used for timestamping acquisition data.

Dedicated Server Machines

There are a number of Gigabit Cameras in use at FRIB and each, if operated at full rate, can saturate a Gigabit Ethernet link, since frames are transferred without compression. Therefore, these cameras are considered fast acquisition devices. They are segregated into their own subnet and communicate exclusively with the respective EPICS IOC hosted on a dedicated server in order to alleviate network traffic for the rest of the controls system.

Embedded

Some of the Diagnostics devices have their IOC hosted by the device itself, either as a feature provided by their vendors or as a custom IOC developed by the Diagnostics group.

- Cryocon temperature monitors [4] for fast temperature measurements;
- Iseg modular power supplies [5];
- UEI Cubes [6] for standalone A/D and D/A converters.

While embedded IOCs are convenient use, they are harder to maintain since their software run on the device's custom hardware and depend on the vendor's ability and willingness to provide timely updates both for their own software and for the underlying operating system. In order to address this issue, there is a plan to develop new IOCs to control these devices from Virtual Machines, which can

---

* This material is based upon work supported by the U.S. Department of Energy Office of Science under Cooperative Agreement DE-SC0000661, the State of Michigan and Michigan State University.

† martins@frib.msu.edu

ISBN: 978-3-95450-223-3 ISSN: 2673-7000 doi:10.18429/JACoW-NAPAC2019-TUPLE08

COMMISSIONING UPDATE ON RF STATION #5 OF AWA*

W. Liu †, M. E. Conde, D. S. Doran, G. Ha, J. G. Power, J. H. Shao, C. Whiteford,
E. E. Wisniewski, Argonne National Lab, Argonne, IL, USA
C. Jing, Euclid TechLabs LLC, Bolingbrook, IL, USA

Abstract

The RF system of Argonne Wakefield Accelerator (AWA) facility has grown over the years from one RF power station into 4 RF power stations. The demanding for RF power keeps growing as the capability of AWA continues to grow. Now the 5th RF station is needed to fulfill the RF power needs of AWA facility. Some details regarding the construction and commissioning of the 5th RF station of AWA facility are documented in this paper.

INTRODUCTION

Argonne wakefield accelerator facility is a small accelerator research facility setup in the 1980s to explore advanced accelerator concept. It started out with one RF station driving a photoelectron RF electron gun and a linac with few beam diagnostics. It has successfully demonstrated the electron beam driven wakefield acceleration with plasma, dielectric and metallic structures. As the scientific quest continues, AWA has grown. As shown in Fig. 1, AWA currently has 4 RF stations powering 4 beamlines: a 65MeV drive beamline, a 15MeV witness beamline, a cathode test stand and one L-band 20MW RF power station for testing novel RF cavity designs. The drive beam line itself has one 8MeV photoelectron RF electron gun, 6 linacs and a double emittance exchange beamline attached to it. There are 4 transverse deflecting cavities on this double emittance exchange beamline that need RF power. In order to power up all needed cavity for double emittance exchange beamline, the 5th RF power station is a must have.

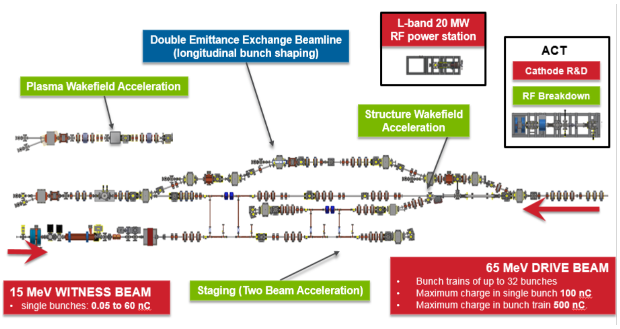

Figure 1: AWA facility beamline layout.

For cost efficiency reason, we decided to build the 5th RF station the same as our 3rd and 4th RF station. As showing in Fig. 2, the klystron we used is a TV2022F ordered from Thales Electronic Device [1]. The maximum power is 25MW with klystron voltage of 273kV and klystron current of 248A. The pulse length is 10us. The focusing solenoid and oil tank/high voltage pulse transformer assembly is ordered from Stangenes [2]. The high voltage pulse transformer turns ratio is 1:15.3 while the filament heater transformer turns ration is 120:28.

Due to some unexpected issues, the order for the transformer tank assembly was delayed and caused delays in the whole project. We are now expecting to power up this RF station in late October.

Figure 2: Picture of klystron, focusing solenoid & High voltage transformer tank assembly.

LLRF AND INTERLOCK CONSIDERATION FOR RF STATION 5

As showing in Fig. 3, except for RF Station #2, the LLRF for all AWA RF stations consist of one NI-PXI5404 to generate the 10MHz IF and a mixer to mix the 10MHz IF with 1.29GHz LO signal to generate the phase controlled 1.3GHz LLRF signal. This phase controlled LLRF signal will be gated and then amplified using a 500W pulsed amplifier before it is used to drive the klystron. We only need to add one NI-PXI5404, one mixer, one RF gate and a 500W RF amplifier to existing system for RF station 5. To feedback control the output of RF station 5, we will need another mixer to mix the signal picked up from RF cavities driven by RF station 5 with 1.29GHz LO to make the 10MHz IF signal. This 10MHz IF signal will be I/Q sampled using one of the 8 channels on NI-PXI5105 to obtain the phase and amplitude information.

---

* Work supported by DOE Office of HEP and Office of BES under Contract No. DE-AC02-06CH11357.

† wmliu@anl.gov

ISBN: 978-3-95450-223-3 ISSN: 2673-7000 doi:10.18429/JACoW-NAPAC2019-TUPLE11

PROPOSED ENHANCED IMAGING STATION IN THE 6-GeV BOOSTER-TO-STORAGE RING TRANSPORT LINE FOR APS UPGRADE*

A.H. Lumpkin†[1], Fermi National Accelerator Laboratory, Batavia, IL USA
W. Berg, J.C. Dooling, K.P. Wootton, C. Yao[1], Argonne National Laboratory, Lemont, IL USA
[1]also Argonne Associate at Argonne National Laboratory, Lemont, IL USA

Abstract

The high charge per micropulse of up to 17 nC in the booster to storage ring transport line for APS Upgrade will necessitate changes in the imaging station used to evaluate beam emittance in this key region. The original Chromox screen has recently been replaced by a YAG:Ce single crystal for immediate screen spatial resolution improvement down to <10 μm. However, the optical system also needs an upgrade with lenses and a digital camera to take full advantage of this. In addition, at the high areal charge densities expected, the YAG:Ce scintillator mechanism will saturate, or quench, leading to images larger than the actual beam size. To circumvent this effect, optical transition radiation (OTR) screens will be implemented. A proposed longer-range goal of a non-intercepting beam-size monitor using optical diffraction radiation techniques during top-up injection will also be addressed.

INTRODUCTION

One of the challenges of the injector for the Advanced Photon Source Upgrade (APS-U) [1] is the measurement and monitoring of the required high charge beam at 6 GeV between the booster synchrotron and the storage ring in the transport line (BTS). In APS-U, charges of up to 17 nC per micropulse are specified with a beam geometric emittance of 80 nm rad. One issue is the possibility of transverse emittance blow up at these high charges, and evaluations of this at station BTS:FS3 using a quadrupole field scan with downstream beam size measurements has been initiated. The anticipated lattice will result in vertical beam sizes at the imaging station BTS:FS3 of ~80 μm (sigma) so system resolutions of <30 μm are warranted. To address this need, a phased approach to enhance the imaging station performance has been initiated.

Recently, a 20-year-old Chromox screen oriented at 45 degrees to the beam was replaced by a 100-μm thick YAG:Ce screen with the surface orientation normal to the beam followed by a 45-degree backing mirror which resulted in an estimated screen resolution of <10 μm (σ). The optical magnification of the system still needs to be increased to take full advantage of this screen resolution, however. In addition, the high areal charge densities of APS-U are expected to exceed the scintillator mechanism's saturation threshold so an optical transition radiation (OTR) screen will be added to the station for high-charge studies. A final implementation phase under consideration is the use of an optical diffraction radiation (ODR) screen configuration as a non-intercepting beam-size monitor during top-up injections. Evaluations of the different imaging techniques will be presented.

EXPERIMENTAL ASPECTS

The APS Linac and Injector Rings

The APS linac is based on an S-band thermionic cathode (TC) rf gun which injects beam into an S-band linear accelerator with acceleration capability currently up to 450 MeV. This is an S-band pulse train with about 10 ns macropulse duration and 28 micropulses, presently delivering 1 to 1.5 nC per macropulse. Beam diagnostics in the linac include imaging screens, rf BPMs, loss monitors, and coherent transition radiation (CTR) autocorrelators [2].

The linac beam is injected into the particle accumulator ring (PAR) at 375 to 425 MeV at up to 30 Hz, and the macropulse is damped to about 300 ps pulse length at 3 nC normally. For APS-U however, up to 20 nC are stacked in the PAR, which in turn results in bunch lengthening, and some instabilities occur [3]. The beam is extracted and injected into the booster synchrotron which ramps the beam energy from the injection energy to 7 GeV currently, but 6-GeV for APS-U and machine injector studies. The beam is extracted from the booster and then enters the booster to storage ring transport line (BTS) as schematically shown in Fig. 1. The beam is then injected into the storage ring at full energy. One wishes to characterize the beam transverse emittance in normal conditions and at the high charges of APS-U in this transport line. Our injector studies are on the path to measure these beams with sufficient spatial resolution even at high charge. This objective has motivated the upgrade of the imaging station BTS:FS3 from the Chromox screen oriented at 45° to the beam direction to a YAG:Ce single crystal oriented with its surface normal to the beam and with a 45° mirror behind it (to redirect the light to the optical system). This crystal is a good solution for spatial resolution at low charge, but we address the potential saturation [4], or quenching [5], of the scintillator mechanism which occurs at charge areal densities of ~10 fC/μm^2. Note one reaches this regime with a 1 nC charge focussed in a 100 μm by 100 μm sigma-x,y beam size. We will show that APS-U parameters will exceed this value in the BTS line.

---

* This manuscript has been authored by Fermi Research Alliance, LLC under Contract No. DE-AC02-07CH11359 with the U.S. Department of Energy, Office of Science, Office of High Energy Physics. Work supported by the U.S. Department of Energy, Office of Science, Office of Basic Energy Sciences, under Contract No. DE-AC02-06CH11357.
† lumpkin@fnal.gov

ANALYTICAL THERMAL ANALYSIS OF THIN DIAMOND IN HIGH-INTENSITY HIGH-REPETITION-RATE APPLICATIONS*

Y. Hong†, B. Yang[1], University of Texas at Arlington, Arlington, Texas, USA
G. Zhou[2], J. Wu, SLAC National Accelerator Laboratory, Menlo Park, California, USA
[1]currently working at Western Digital Company, Milpitas, California, USA
[2]also at Institute of High Energy Physics, and UCAS, Chinese Academy of Sciences, Beijing, China

Abstract

Thin diamond plates are used in monochromator for X-ray Free-Electron Laser (XFEL) self-seeding scheme. To function properly, they must endure high-intensity and high-repetition-rate XFEL pulses without crossing thresholds set by various adverse effects, such as thermal strain-induced diffraction distortion and graphitization. In this work, a theoretical model is developed, and an analytical solution is derived to elucidate potential thermal runaway under edge cooling condition. It is shown that the crystal edge cooling can effectively mitigate the issue to a certain extent. The analytical solution can be used as an efficient tool for XFEL operation parameter setup.

MANUSCRIPTS

X-ray free-electron laser (XFEL) can generate high peak-power pulses with atomic and femtosecond scale resolution, impacting cutting-edge scientific research [1, 2]. Thin diamond layers are used in spectrometer and monochromator for XFEL self-seeding [3, 4, 5]. When an X-Ray pulse passes through a thin diamond layer, a part of its energy is deposited into the diamond lattice. This process thermalizes the crystal lattice causing temperature buildup within the crystal [6]. In high-repetition rate applications, such temperature buildup may reach a thermal runaway condition, alongside with considerable lattice deformation and local permanent damage, such as local graphitization on the surface and internally at the grain boundary of a diamond plate [7, 8, 9]. Graphitization happens when the absorbed energy is greater than the activation energy of the crystal [10].

In the present paper, an analytical steady-state solution for continuous-wave (CW) laser input is derived to address potential thermal issues in thin diamond. The temperature-dependent thermal properties of diamond, i.e., thermal conductivity [11] and specific heat capacity [12], valid for temperature in the range from 100 K to 3000 K, are used in the calculation. The objective of this study is to provide a quick estimation tool for determining operational guideline based on thin-diamond material properties and cooling condition under focused laser heating at high repetition rates. From the steady-state solution, by setting the central temperature $T_0^* \to \infty$, the (definite) thermal runaway condition can be defined. A relaxed thermal runaway condition can also be defined by setting T_0^* equal to a finite value, for instance, graphitization temperature, to address a particular effect of concern. The relationships between dimensionless terms of cooling edge distance to laser waist size ratio R/a, edge cooling temperature T_R, and critical (allowed) laser heating power fI are discussed. It shows that the critical heating power fI is higher with smaller R/a, and lower T_R. However, when it comes to design of an edge cooling system, there are limits such as the size of the working area and the size of the cooling device.

Problem Formulation

Consider a train of X-Ray pulses impinging perpendicularly at the center of a circular, thin diamond crystal at repetition rate f, as illustrated in Fig. 1. The circumferential sink temperature is held constant via a cooling system. The pulses are assumed to be Gaussian, and extremely short compared to all other time scales under consideration. The heat is deposited instantaneously while a laser pulse passes through the crystal. The problem is axisymmetric with radial axis r set from the center. The temperature field is assumed to be uniform in the through-thickness direction. The deposited energy is dissipated by conduction inside the plate only; any radiative heat transfer is assumed to be negligible.

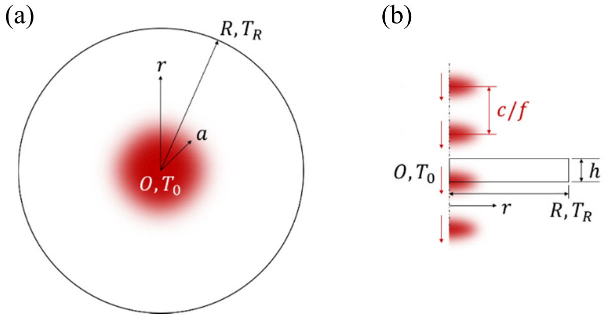

Figure 1: Schematic show of high repetition rate laser heating in a thin crystal: (a) top view and (b) side view. The cylindrical coordinate system is established for reference.

The flux of laser heat deposition from the top surface is expressed as,

$$i(r,t) = i_0 e^{-2(r/a)^2} \delta(t-n/f) \qquad (1)$$

---

* Work supported by the US Department of Energy (DOE) under contract DE-AC02-76SF00515 and the US DOE Office of Science Early Career Research Program grant FWP-2013-SLAC-100164.

† ye.hong@mavs.uta.edu

ISBN: 978-3-95450-223-3 ISSN: 2673-7000 doi:10.18429/JACoW-NAPAC2019-TUPLE15

BPM PROCESSOR UPGRADES AT SPEAR3*

F. Toufexis†, S. Condamoor, J. Corbett, SLAC, Menlo Park, CA, USA
L. Lai, Shanghai Synchrotron Radiation Facility, Shanghai, China
P. Leban, Instrumentation Technologies, Solkan, Slovenia

Abstract

We are upgrading the BPM processors in the SPEAR3 accelerator complex as several of the existing systems have reached end of life. To reduce the resources required for maintenance we have evaluated and installed several commercial BPM processors from the SPARK series of Libera/Instrumentation Technologies. In SPEAR3 we evaluated the SPARK-ERXR turn-by-turn BPM processor as a replacement to the in-house developed/commercially built Echotek processors that are used for a range of accelerator physics studies. We show measurements of the orbit dynamics with another SPARK-ERXR in the booster synchrotron from beam injection up to ejection. We have further evaluated a Spark-EL in the transport lines to replace the in-house built uTCA-based single-pass BPM processors. In this paper we show measurements and discuss our experience with the Libera SPARK series of BPM processors and comment on the software integration.

INTRODUCTION

SPEAR3 is a 3 GeV, 500 mA, 3rd generation synchrotron light source, commissioned in 2004 [1]. It operates with beam current distributed in four bunch trains and a single isolated timing bunch for pump-probe experiments. Top-up occurs at 5-minute intervals. Each top-up event requires about 50 single-bunch charge pulses into targeted SPEAR3 buckets at a 10 Hz rate. The SPEAR3 storage ring contains 18 lattice cells each with 6 button-style Beam Position Monitors (BPMs). Three BPMs per cell are connected to Bergoz processors for fast orbit control and beam inter-lock purposes. Approximately 10 more BPMs are connected to the Echotek processors [2] to provide turn-by-turn orbit information at discrete locations. The Echotek processors were developed in-house and produced commercially when SPEAR3 was commissioned; they are used for accelerator physics programs and not for operations. The Echotek have reached their and of life and we have evaluated commercial alternatives for replacement. A Libera Brilliance+ was first tested in SPEAR3 in 2017 [3]. Since turn-by-turn studies for accelerator physics programs do not require the long-term stability capability of the Brilliance+, and additionally the fast orbit feedback is implemented in the Bergoz BPM system, a SPARK-ERXR processor [4] was purchased and installed for further testing.

The SPEAR3 injector was commissioned in 1990 [5], and includes the 120 MeV linac injector with a thermionic RF gun [6], the booster synchrotron [7] and the transport lines. The entire injector, including the transport lines, is equipped with stripline-style BPMs. The original booster synchrotron BPM electronics used a commercial multiplexer to switch between several BPM signals into an in-house built analog BPM processor electronics [8].

In the Linac-To-Booster (LTB) and Booster-To-SPEAR (BTS) transport lines 1990's-era Bergoz BPM processors have provided reliable shot-by-shot single-pass data at 10 Hz with limited resolution [8]. As an upgrade to the original transport line BPM processors, two smaller-diameter stripline BPMs connected to two SLAC-built uTCA-based BPM processors replaced the last two BPMs at the end of the BTS in 2015 (BTS BPMs 8 and 9). This systems has proven hard to maintain and we have evaluated the single-pass SPARK-EL processor as a replacement. The unit was tested in the BTS and LTB transport lines demonstrating comparable position resolution to the uTCA processors at the small-diameter striplines, as well as substantially improved resolution at the large-diameter striplines.

In this work we report on the operation of the SPARK series BPM processors across the SPEAR3 accelerator complex. The overall operational experience has been satisfactory and the software configuration provides a single, uniform working environment.

SPARK-ERXR IN SPEAR3

Figure 1 shows a direct comparison between the SPARK-ERXR (right) and Echotek (left) processors following a horizontal impulse to the beam. The impulse was generated using the SPEAR3 injection kickers with the data acquired on the same event using a synchronized 10 Hz trigger distribution system [9]. The beam current at the time was 1.9 mA in a single bunch and the motion fully damps after 10 ms, or about 12,000 turns.

Figure 2 shows a magnified view of the first 75 turns in the horizontal plane immediately following the impulse. Although the initial phase of the motion is different due to different BPM positions in the storage ring, both systems clearly resolve the turn-by-turn betatron motion with an amplitude difference proportional to square root of beta fuction values at the BPM sites. Using the numerical analysis of fundamental frequency algorithm [10] to evaluate the betatron tunes at $t = 4$ ms, the algorithm yields the expected values for the tunes for both processors.

Processor noise figures can be evaluated from data acquired after the damping event is complete, in this case from vertical data at points of zero dispersion. Note that phase oscillations are present in the horizontal plane and are difficult to remove for rms noise analysis. Figure 3 shows the verti-

---

* Work sponsored by US Department of Energy Contract DE-AC02-76SF00515.

† ftouf@slac.stanford.edu

RFA MEASUREMENT OF E-CLOUD GENERATION PROCESS AT FERMILAB MAIN INJECTOR

Y. Ji*, L. Spentzouris, Illinois Institute of Technology, Chicago,IL,USA
R. M. Zwaska, Fermilab, Batavia, IL,USA

Abstract

Electron cloud (E-cloud) refers to generation of unwanted electrons inside the beam pipe of a high intensity accelerator. The E-cloud could cause degradation of vacuum, beam pipe heating and beam instabilities [1]. The E-cloud generation mechanism consists of three steps: 1) passing beam bunches accelerate existing electrons, 2) accelerated electrons hit the beam pipe and knock out more electrons and 3) generated electrons are accelerated by the next bunch and the process is repeated. The mechanism generates the electron population exponentially and this eventually saturates when the space charge forces of the E-cloud cancel the beam kicks.

For accelerators that may be affected by E-cloud, it is important to monitor the E-cloud generation to study and possibly mitigate E-cloud related problems. In case of the Fermilab Main Injector (MI), while E-cloud is not causing instabilities or other operational problems at this time, E-cloud is observed in the MI, and may be a problem in the future due to planned increases in beam intensity. Since E-cloud is already present in the MI, there is an opportunity to study the build-up process of the E-cloud.

A Retarding Field Analyzer (RFA) is a device that collects electrons incident on a portion of the vacuum chamber wall of an accelerator [2, 3]. The RFA will generate a signal that measures the E-cloud bombardment rate at the collector. Systematic studies of the E-cloud generation process in the Fermilab Main Injector (MI) are presented.

THE RETARDING FIELD ANALYSER

Table 1: MI Parameters

Beam energy [GeV]	8-120
Intensity [protons]	50×10^{12}
revolution frequency [kHz]	90
Harmonic number	588
RF frequency [Mhz]	53
Total RF bucket filled	492
SEY	1.2-1.4
Bunch length [ns]	0.5-4

The MI RFA is located at the MI-10 area because the area's E-cloud generation parameters are well known [4, 5]. There is Secondary Electron Yield (SEY) measurement capability there, and E-cloud generation is sensitive to this parameter. Table 1 shows the general MI parameters. The RFA used is a copper collector cup with a metal grid on top. As electrons enter the collector cup a current signal proportional to the E-cloud bombardment rate is generated. Figure 1 shows the RFA, and a schematic of the RFA. There is a screen electrically isolated from the collector cup. By applying a negative bias voltage on the screen, electrons that pass the screen will be forced into the collector and all secondary electrons that are generated inside the collector cup will be recaptured. The screen also stops electrons with energy below the screen bias voltage from entering the collector. By controlling the screen bias voltage, the RFA can be used to measure the E-cloud wall collision energy distribution.

The Equipment

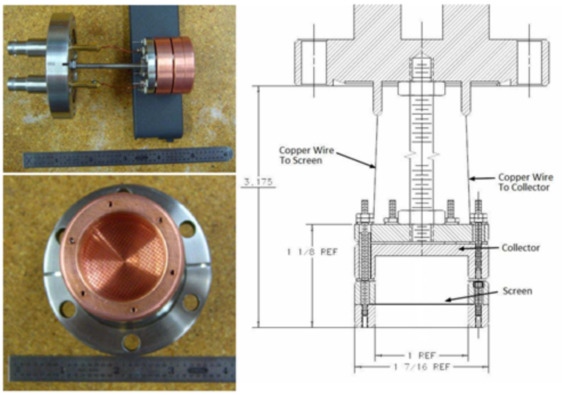

Figure 1: The Retarded Field Analyzer.

The RFA is connected to a SONOMA 310b Broadband Amplifier. The amplifier has a 30dB gain or 31 fold increase in the output signal ($\frac{V_{out}}{V_{in}}$). The bandwidth is 9 kHz to 1 GHz and the input impedance is 50 Ω (Z_{in}). The signal is monitored directly a TBS2000 oscilloscope. A grid of 0.04 diameter holes are drilled above the RFA. Based on the design of the RFA system, the total surface area exposed to the RFA is roughly 0.82 cm^2 (A_{RFA}) and about 50% of the electrons pass through the holes based on POSINST simulation ($P(\theta)$). The RFA capture efficiency was measured to be around 90% (P_C) [6]. Based on this information the RFA signal to E-cloud bombardment rate conversion factor can be calculated by the following equation

$$V_{RFA} = eR_{Brate}P_CP(\theta)A_{RFA}Z_{in}(\frac{V_{out}}{V_{in}}) \qquad (1)$$

Where V_{RFA} is the measured RFA voltage, R_{Brate} is the E-cloud bombardment rate and e is electron charge. Plugging in the numbers, the conversion factor is calculated to be

$$R_{Brate}\left[\frac{N_e}{\text{s cm}^2}\right] = V_{RFA}[\text{volts}] \times 1.128 \times 10^{16}\left[\frac{N_e}{\text{s cm}^2}\right]$$

---

[*] yji11@hawk.iit.edu

RECENT RESULTS AND OPPORTUNITIES AT THE IOTA FACILITY *

A. Romanov†, D. R. Broemmelsiek, K. Carlson, D. J. Crawford, N. Eddy, D. R. Edstrom,
J. Jarvis, V. Lebedev, S. Nagaitsev, J. Ruan, J. K. Santucci, V. Shiltsev, G. Stancari,
A. Valishev, A. Warner, Fermilab, IL, USA
Y.-K. Kim, N. Kuklev, I. Lobach, University of Chicago, IL, USA
S. Chattopadhyay, S. Szustkowski, Northern Illinois University, IL, USA

Abstract

The Integrable Optics Test Accelerator (IOTA) was recently commissioned as part of the Fermilab Accelerator Science and Technology (FAST) facility. The IOTA ring was briefly operated with electrons at 47 MeV followed by a 6-months run with 100 MeV electrons. The main goal of the first run was to study beam dynamics in the integrable lattices with elliptical nonlinear magnets and in the quasi-integrable case with profiled octupole channel. The flexibility of the IOTA ring allowed a wide range of complementary studies, such as experiments with a single electron; studies of fluctuations in undulator radiation and operation with low emittance beams. Over the next year the proton injector will be installed and two runs carried out. One run will be dedicated to the refinement of nonlinear experiments and another will be dedicated to the proof-of-principle demonstration of Optical Stochastic Cooling.

INTRODUCTION

The Integrable Optics Test Accelerator (IOTA), together with the FAST superconducting linac, is an accelerator research facility dedicated to the accelerator science studies for future intensity-frontier machines. IOTA is a storage ring with perimeter of 40 meters, which can operate with beams at momentum between 50 and 200 MeV/c. The main goal of IOTA is to demonstrate the advantages of nonlinear integrable lattices [1] for high-intensity beams and to demonstrate new beam cooling methods [2]. The first experiments were conducted with readily available electrons from the FAST superconducting linac [3–12]. The high flexibility of the linac made it easy to adjust the energy and intensity of the electron beam and match the beam envelope with IOTA. Another advantage of the electron beam in IOTA is its small transverse size and natural cooling due to synchrotron radiation. This allows the use of a wider range of diagnostic tools and provides more accurate measurements compared to proton beams. Research with high intensity proton beams will begin after the completion of the proton source and the corresponding injection line.

The main parameters of the IOTA ring are listed in Table 1. Figure 1 and Figure 2 show the schematic structure and panoramic view of the ring.

Table 1: IOTA Parameters with e-beam

Parameter	Value
Perimeter	39.97 m
Momentum	50-200 MeV/c
Electron current	0-4.8 mA
Proton current	10 mA
RF frequency	30 MHz
RF voltage	1 kV
ν_x, ν_y, ν_s	$(0.3, 0.3, 5.7 \times 10^{-4})$
τ_x, τ_y, τ_s	(2.0, 0.7, 0.3) s
$\epsilon_x, \epsilon_{x,ycoupled}$, RMS	(96.3, 25.3) nm
$\Delta p/p$, RMS	1.26×10^{-4}

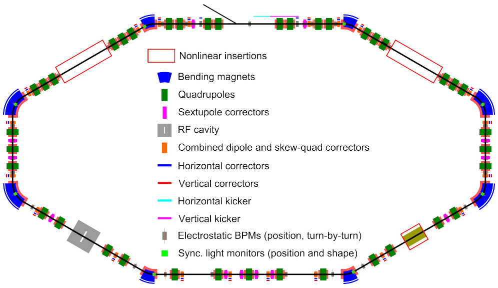

Figure 1: Schematic diagram of the IOTA ring.

IOTA COMMISSIONING

Activities during the commissioning of IOTA can be divided into two groups. Firstly, the general mechanical integrity was checked and live tests of the main subsystems were carried out. During the initial period, special attention was paid to verifying the correct integration of IOTA equipment with the controls system, the correct timing of the kickers and the phasing of the RF generator with respect to the injected beam, basic BPM performance tests and minor operational improvements. The second group covers tuning the magnetic lattice of IOTA using beam-based methods and improvements to the corresponding subsystems that were necessary for the precise control of the beam dynamics.

The first IOTA run started with electron beams with momentum of 47 MeV/c and without an RF cavity in the ring due to issues with the FAST linac and ring RF. The goal of the 47 MeV program was to verify that all key IOTA subsystems are working properly by demonstration of beam circulation in the ring. Shortly after achieving these goals, both problems were resolved and run continued with electrons with a momentum of 100 MeV/c.

---

[*] Work supported by the DOE under contract No. DE-AC02-07CH11359 to the Fermi Research Alliance LLC., the U.S. National Science Foundation under award PHY-1549132 (the Center for Bright Beams) and by the University of Chicago.

[†] aromanov@fnal.gov

CSR PHASE SPACE DILUTION IN CBETA*

W. Lou, G. H. Hoffstaetter, D. Sagan, CLASSE, Ithaca, NY, USA
C. Mayes, SLAC, Menlo Park, CA, USA

Abstract

CBETA, the Cornell BNL Energy-Recovery-Linac (ERL) Test Accelerator [1], will be the first multi-turn ERL with SRF accelerating cavities and Fixed Field Alternating gradient (FFA) lattice with a range of energy acceptance. While CBETA gives promise to deliver very high beam current with simultaneously small emittance, Coherent Synchrotron Radiation (CSR) can cause detrimental effects on the beam bunches at high bunch charges. To investigate the CSR effects on CBETA, the established simulation code Bmad is used to track a bunch with different parameters. We found that CSR causes phase space dilution, and the effect becomes more significant as the bunch charge and recirculation pass increase. Potential ways to mitigate the CSR effects, including adding vacuum chamber shielding and increasing bunch length, are being investigated.

INTRODUCTION

Synchrotron radiation occurs when an electron traverses a curved trajectory, and the radiation emitted can give energy kicks to the other electrons in the same bunch. While the high frequency components of the radiation spectrum tend to add up incoherently, the low frequency part, with wavelength on the order of the bunch length, can add coherently. These are termed incoherent and coherent synchrotron radiation respectively (ISR and CSR). While the total intensity for ISR scales linearly with the number of charged particles (N_p), it scales as N_p^2 for CSR. For an ERL which aims for high beam quality like CBETA, CSR can pose detrimental effect on the beam, including energy loss, increase in energy spread, and potential micro-bunching instability. Therefore it is important to run CSR simulation for CBETA, and investigate potential ways for mitigation. Fig. 1 shows the design layout of CBETA. Note that with adjustment on the time of flights, CBETA can operate as a 1-pass or 4-pass ERL.

CSR SIMULATION OVERVIEW

Cornell Wilson Laboratory has developed a simulation software called Bmad to model relativistic beam dynamics in customized accelerator lattices [2], and subroutines have been established to include CSR calculation [3]. As Fig. 2 shows, a bunch of particles is divided into a number of bins (N_b) in the longitudinal direction. During beam tracking, N_b is constant, and the bin width is dynamically adjusted at each time step to cover the entire bunch length. The contribution of a particle to a bin's total charge is determined by the overlap of the particle's triangular charge distribution and the bin. With Δz_b denoting the bin width and ρ_i denoting the total charge in the i^{th} bin, the charge density (λ_i) at the bin center is taken to be $\rho_i/\Delta z_b$. In between the bin centers, the charge density is assumed to vary linearly.

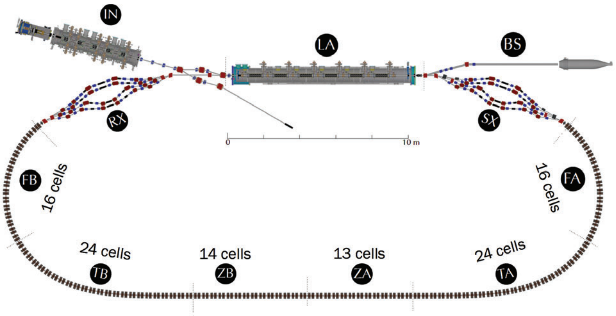

Figure 1: Layout of the CBETA accelerator. The section labeled (LA) is the accelerating LINAC. The sections labelled (SX) and (RX) are the splitters which control the beam optics and time of flights of each recirculation pass. The sections labeled (FA), (TA), (ZA), (ZB), (TB), and (FB) form the FFA beamline which can accommodate four recirculating orbits with an energy range from 42 MeV to 150 MeV.

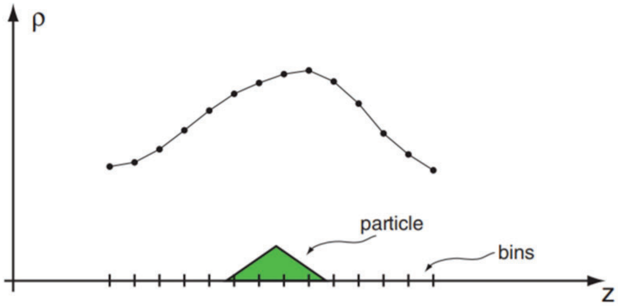

Figure 2: Bmad implementation of CSR. The bunch is divided into N_b bins in the longitudinal direction for calculation of CSR kicks.

In theory the CSR wakefield can be written as [3]:

$$\left(\frac{d\mathcal{E}}{ds}\right) = \int_{-\infty}^{\infty} ds' \frac{d\lambda(s')}{ds'} I_{\mathrm{CSR}}(s-s'), \tag{1}$$

in which $\lambda(s)$ is the longitudinal charge density, and I_{CSR} comes from solving the Liénard-Wiechert retarded field with two charged particles on a curved trajectory. In Bmad the energy kick received by a particle centered at the j^{th} bin, after travelling for a distance ds, is modelled in Bmad as [3]:

$$d\mathcal{E} = ds \sum_{i=1}^{N_b} (\lambda_i - \lambda_{i-1}) \frac{I_{\mathrm{CSR}}(j-i) + I_{\mathrm{CSR}}(j-i+1)}{2}, \tag{2}$$

with $I_{\mathrm{CSR}}(j) \equiv I_{\mathrm{CSR}}(z = j\Delta z_b)$.

---

* This work was performed with the support of NYSERDA (New York State Energy Research and Development Agency).

ADAPTIVE MACHINE LEARNING AND AUTOMATIC TUNING OF INTENSE ELECTRON BUNCHES IN PARTICLE ACCELERATORS*

A. Scheinker†, Los Alamos National Laboratory, Los Alamos, NM, USA

Abstract

Machine learning and in particular neural networks, have been around for a very long time. In recent years, thanks to growth in computing power, neural networks have reshaped many fields of research, including self driving cars, computers playing complex video games, image identification, and even particle accelerators. In this tutorial, I will first present an introduction to machine learning for beginners and will also touch on a few aspects of adaptive control theory. I will then introduce some problems in particle accelerators and present how they have been approached utilizing machine learning techniques as well as adaptive machine learning approaches, for automatically tuning extremely short and high intensity electron bunches in free electron lasers.

Introduction

Precise control of bunch lengths, current profiles, and energy spreads of increasingly shorter electron beams at femtosecond resolution is extremely important for all advanced particle accelerators, including free electron lasers (FEL). FEL X-ray bursts with tunable wavelength are generated by tuning the energies of extremely short electron bunches (~fs). Two of the most advanced FELs are the Linac Coherent Light Source (LCLS) and the European XFEL (EuXFEL). The LCLS provides users with photon energies of 0.27 keV to 12 keV based on electron bunches with energies of 2.5 GeV to 17 GeV with electron bunch charges ranging from 20 pC to 300 pC and the bunch duration from 3 fs to 500 fs [1–3]. The EuXFEL, utilizes electron bunches with energies of up to 17.5 GeV, with charges ranging from 0.02 to 1 nC per bunch, and photon energies of 0.26 keV up to 25 keV [4]. Both the LCLS and the EuXFEL face challenges in quickly tuning between different beam types and achieving precise control for desired current and energy profiles and complex experiments such as two color mode and self seeding [5–8].

Machine Learning

Recently, powerful machine learning (ML) techniques have been studied for various particle accelerator applications. ML-based tools, such as neural networks (NN), can be trained to automatically tune and control large complex systems such as particle accelerators [9–12]. In a preliminary simulation study for a compact THz FEL, a NN control policy was trained to provide suggested machine settings to switch between desired electron beam energies while preserving the match into the undulator and a fast surrogate model was also trained from PARMELA simulation results in order to facilitate the training of the control policy [13].

For mapping inputs to outputs of an analytically unknown, but sampled system, a standard linear regression approach assumes a noise corrupted linear model of the form

$$f(\mathbf{x}) = \mathbf{x}^T \mathbf{w}, \quad y = f(\mathbf{x}) + \epsilon, \quad \epsilon \sim N\left(0, \sigma_n^2\right), \tag{1}$$

where ϵ is a identically distributed Gaussian distribution with zero mean and variance σ_n^2. The goal here is to determine an approximation of the weights, $\mathbf{w}$, in order to learn the mapping $\mathbf{x} \longrightarrow y$. Given a collection of measurements, $M = (X, \mathbf{y})$, where the matrix X has rows given by m sets of input parameters $\mathbf{x}_i = (x_{i1}, \ldots, x_{in})$, $i \in [1, m]$, and the vector $\mathbf{y} = (y_1, \ldots, y_m)$ is a collection of outputs, a Bayesian approach gives the following approximation for the weights $\mathbf{w}$, based on the assumption that they are mean 0 with covariance matrix Σ:

$$\hat{\mathbf{w}} = \sigma_n^{-2}\left(\sigma_n^{-2} X X^T + \Sigma^{-1}\right)^{-1} X\mathbf{y}. \tag{2}$$

This approach works extremely well and is the least squares-based optimal solution for (1) given a set of measurements X, but fails once nonlinearities are introduced in the mapping $f(\mathbf{x})$. The most straight forward way to extend this approach to nonlinear systems is to choose a set of functions, such as polynomials, project an input x into a higher dimensional space, of the form $\mathbf{g}(x) = (1, x, x^2, \ldots)$, and then perform a similar approach as above on an assumed model of the form $f(\mathbf{x}) = \mathbf{g}(\mathbf{x})^T \mathbf{w}$. Another approach is to work directly in function space, utilizing Gaussian processes, which are collections of random variables with joint Gaussian distributions, with mean $m(\mathbf{x}) = \mathbb{E}[f(\mathbf{x})]$ and covariance

$$k(\mathbf{x}, \mathbf{x}') = \mathbb{E}\left[(f(\mathbf{x}) - m(\mathbf{x}))(f(\mathbf{x}') - m(x'))\right]. \tag{3}$$

The choice of covariance function determines the shapes of response functions and their smoothness. A typical choice for a smooth covariance function is given by an exponential:

$$k(\mathbf{x}, \mathbf{x}') = \exp\left(-\left|\mathbf{x} - \mathbf{x}'\right|^2 / 2\right), \tag{4}$$

which corresponds to a Bayesian linear regression model with an infinite number of basis functions. A thorough overview of Gaussian processes is available in [14].

Neural networks are another class of extremely powerful ML tools for learning input-output relationships for complex, many parameter systems. In particular, convolutional neural networks (CNN) are very useful for images, for example to map 2D LPS measurements to accelerator component values, because they take into account spacial relationships. Mathematically, a convolutional layer can be written as

$$h^l_{(i,j),c} = \sum_{m=-s}^{s} \sum_{n=-s}^{s} \sum_{c'} w_{(m,n),c,c'} h^{l-1}_{(i-m,j-n),c} + b_{c,c'} \tag{5}$$

---

[*] Work supported by Los Alamos National Laboratory

[†] ascheink@lanl.gov

TOLERANCES FOR PLASMA WAKEFIELD ACCELERATION DRIVERS*

G. R. White, T. O. Raubenheimer
SLAC National Accelerator Laboratory, Menlo Park, CA, USA

Abstract

Transverse jitter tolerances are considered for beam-driven plasma accelerators. A simple model for jitter transfer from the drive to witness beam was developed and concrete examples were studied for: high-brightness witness bunch injectors; high-energy boosters for FELs; and future Linear Colliders. For the LC application, we consider a superconducting Linac designed to minimize the jitter conditions of the drive beam. We use a start-to-end tracking model to simulate expected jitter performance. The tolerances on each subsystem of the driver Linac are found to be very tight, especially for magnet vibration which must be controlled at the sub-nm level.

OVERVIEW

The electron beam-driven Plasma Wakefield Acceleration (PWFA) concept has been actively pursued in the past two decades with multi-GeV accelerating gradients demonstrated [1, 2]. Other test facilities are under construction and aim to demonstrate preservation of the accelerated beam quality [3, 4] and research practical applications such as FEL drivers. As the community moves towards progressing the PWFA concept into a viable engineering solution for a practical accelerator, it is timely to consider requirements for the required supporting infrastructure.

We consider here the jitter requirements on the main particle beams (henceforth referred to as “witness” beams) used in future accelerators powered by PWFA acceleration cells and the contribution from the jitter of the “drive” beams used to form the PWFA acceleration plasma bubble. The drive beam is usually mismatched to the accelerated bunch in terms of its geometric emittance, frequently having order-of-magnitude larger emittance; this is true for laser-driven as well as beam-driven plasmas. The stability requirements of the drive beam are dictated by the phase-space of the higher-quality witness beam.

We consider here the specific examples of high-brightness witness bunch injectors (HBI), a high-energy “doubler” application for FEL’s (ED), and future Linear Colliders (LC). For each, we investigated the transverse tolerance requirements on the drive beam and the conventional accelerator component tolerances (RF, magnet, alignment etc.) necessary to meet these. The calculated tolerances were compared to an existing PWFA driver facility [2, 3] in a previous report [5] and were found to be 18 to 170 times tighter than achievable. This report summarizes work done to calculate the expected jitter performance of a purpose designed superconducting drive beam accelerator.

Typical requirements for a beam driven PWFA application are to drive the plasma cell with a multi-nC electron bunch which is highly compressed (>10 kA peak current) and tightly focused (<<100μm rms transverse size at plasma entrance). State-of-the-art high-brightness electron accelerators utilizing rf photo-injectors with conventional rf acceleration cavities and magnetic bunch compression systems can meet these requirements, but the achievable bunch emittances are necessarily in the multi μm-rad range. This should be compared with the nm-rad scale of required vertical emittance for the witness beam in a LC application. The acceleration channel seen by the witness bunch in the PWFA cells is formed by the drive beam and by design strongly focuses the witness beam within the plasma channel. It will therefore steer the witness beam according to any misalignment of the driver bunch. Given the large disparity between drive and witness bunch emittances, one would a-priori expect very tight fractional tolerances on the allowable drive beam jitter.

To investigate the magnitude of the driver jitter tolerance challenge, we put forward a simple analytic model of jitter transfer between the drive and witness beams in [5] which we also tested using a particle tracking model. Note that this jitter model does not include collective effects in the plasma which will further amplify any jitter. Using this jitter transfer model, we describe the jitter amplification of a physically realizable plasma cell and calculate the drive beam jitter tolerances implied by the witness bunch jitter requirements. We then compare these requirements to a simulated model of a real drive beam accelerator.

WITNESS BUNCH JITTER REQUIREMENTS

The allowable jitter of the witness bunch as it is delivered to either the undulators of an FEL or the collision point of a collider are shown in Table 1 below. The required jitter tolerances for an FEL application are dependent on the design of the undulators; typically the beam jitter must be a small fraction of the beam size in the undulators for useful lasing and a value of 0.1σ is used here for reference. The LC requirements are more complicated and are explained further below.

The combined effect of all jitter sources (i.e. multiple PWFA stages) must sum to beneath the requirements stated below.

Table 1: Required Delivered Witness Beam Jitter to FEL Undulator Section or Collision IP

Application	Horizontal Jitter Requirement / σ_x	Vertical Jitter Requirement / σ_y
PWFA LC	Insensitive	0.3
HBI	0.1	0.1
ED	0.1	0.1

---

[*] Work supported by the Department of Energy under Contract Number: DE-AC02-76SF00515.

DIAMOND FIELD EMITTER ARRAY CATHODE EXPERIMENTAL TESTS IN RF GUN [*]

K. E. Nichols[†], H. L. Andrews, D. Kim, E. I. Simakov,
Los Alamos National Laboratory, Los Alamos, NM, USA
M. Conde, D. S. Doran, G. Ha, W. Liu, J. F. Power, J. Shao, C. Whiteford, E. E. Wisniewski,
Argonne National Laboratory, Lemont, IL, USA
S. P. Antipov, Euclid Beamlabs LLC, Bolingbrook, IL, USA
G. Chen, IIT, Chicago, IL, USA

Abstract

Diamond Field Emitter Array (DFEA) cathodes are arbitrarily shaped arrays of sharp (50 nm tip size) nano-diamond pyramids with bases on the order of 3 to 25 microns and pitches 5 microns and greater. These cathodes have demonstrated very high bunch charge in tests at the L-band RF gun at the Argonne National Laboratory (ANL) Advanced Cathode Test Stand (ACT). Intrinsically shaped electron beams have a variety of applications, but primarily to achieve high transformer ratios for Dielectric Wakefield Accelerators (DWA) when used in conjunction with an Emittance Exchange (EEX) system. Here we present preliminary results from a number of recent cathode tests including bunch charge and YAG images. We have demonstrated shaped beam transport down the 2.54-meter beamline.

INTRODUCTION

Transversely shaped beams are currently produced in a number of ways, including using a photocathode excited by a transversely shaped laser beam [1], by use of a transverse mask to intercept a portion of the beam [2], [3], and [4]. The mask method has beam loss of up to 80%, the intercepted beam produces hazardous X-rays, and the beam shape is often inconsistent due to jitter. These disadvantages can be nullified by making an intrinsically shaped beam. Further, use of a field emission cathode significantly reduces the expense and cost of the beam source.

Diamond field emitter tips have been studied for a number of years, [5], [6] mostly in a small direct current test stands. Los Alamos National Laboratory has recently developed the capability to produce these cathodes completely in-house [7]. An SEM image of one of the sharp emitter tips can be seen in the inset in Fig. 1. We are able to produce the cathodes with a flat diamond base, and any number of ultra-sharp pyramidal emitters with base sizes ranging from 3 μm to 25 μm, with pitches of 5 μm and greater. This fabrication flexibility allows us to produce emitter arrays with nearly any macro shape we wish, in principle, arrays as large as two inches in diameter can be fabricated. Here we present results from both sparse and dense array cathodes that were tested in the rf gun at ACT. We demonstrated shaped beam production from the diamond field emission tips, and were able to transport the shaped beam down to the end of the beamline, approximately 2.54 meters from the cathode.

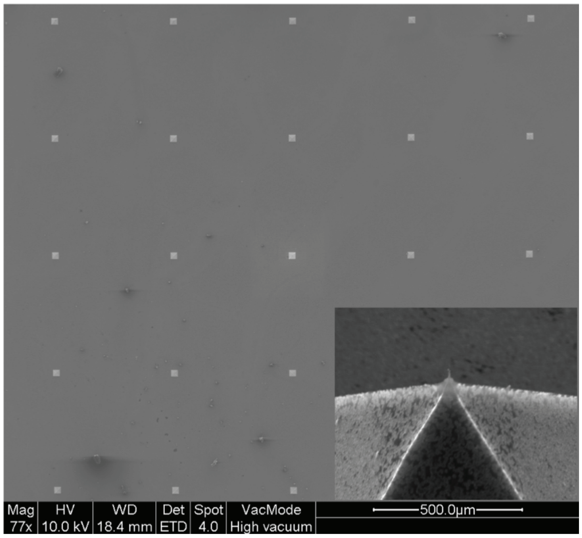

Figure 1: An SEM image of a 5x5 array and close up of a single diamond pyramid tip (insert).

EXPERIMENTAL TEST SETUP

A schematic of the experimental set-up can be seen in Fig. 2. The ACT at ANL consists of a half-cell L-band RF gun, followed by several beamline diagnostics consisting of: gun solenoids, Gsol1 and Gsol2, a beam solenoid, Bsol, two Faraday cups, FC1 and FC2, and three YAG screens, YAG1, YAG2, and YAG3. The rf field in the gun cavity is measured by rf pickup, and the field at the cathode is extrapolated from simulations. In the experiments, the vacuum level was at or below $2x10{-}8$ Torr, the rf was 1.3 GHz, and the rf power level was slowly increased to observe cathode behavior. The I-V curves were measured with decreasing power levels, with the charge during a macro-pulse being collected and reported at FC2. Images were taken on all the YAG screens at various

---

[*] The authors gratefully acknowledge the support of Los Alamos National Laboratory (LANL) Laboratory Directed Research and Development (LDRD) program. This work was performed, in part, at the Center for Integrated Nanotechnologies, an Office of Science User Facility operated for the U.S. Department of Energy (DOE) Office of Science by Los Alamos National Laboratory (Contract DE-AC52-06NA25396) and Sandia National Laboratories (Contract DE-NA-0003525). The work at AWA is funded through the U.S. Department of Energy Office of Science under Contract No. DE-AC02-06CH11357.

[†] knichols@lanl.gov

A HIGH-PRECISION EMISSION COMPUTATIONAL MODEL FOR ULTRACOLD ELECTRON SOURCES

A.J. Tencate[*], B. Erdelyi,
Northern Illinois University, DeKalb, IL, USA

Abstract

The high-intensity, high-brightness and precision frontiers for charged particle beams are an increasingly important focus for study. Ultimately for electron beam applications, including FELs and microscopy, the quality of the source is the limiting factor in the final quality of the beam. It is imperative to understand and develop a new generation of sub-Kelvin electron sources, and the current state of PIC codes are not precise enough to adequately treat this ultracold regime. Our novel computational framework is capable of modelling electron field emission from nanoscale structures on a substrate, with the precision to handle the ultracold regime. This is accomplished by integrating a newly developed Poisson integral solver capable of treating highly curved surfaces and an innovative collisional N-body integrator to propagate the emitted electron with prescribed accuracy. The electrons are generated from a distribution that accounts for quantum confinement and material properties and propagated to the cathode surface. We will discuss the novel techniques that we have developed and implemented and show emission characteristics for several cathode designs.

INTRODUCTION

Broadly speaking, the current state of the art in low emittance electron sources fall into two categories: cold atom sources, and single nanotip emitters. In the former, atomic gasses are typically suspended in a magnetic trap, and optically cooled to sub-Kelvin temperatures. Emitted electrons exhibit the low temperatures of the source when photoionized near the threshold energy. The second category of emitter utilize an electric field enhancing sharp tip, which leads to highly localized emission. Such emitters have been shown to produce electrons with a normalized emittance only one order of magnitude above the quantum degeneracy limit [1], however such sources are limited to low emission currents. An array of nanometer sharp tip emitters (see Fig. 1) would lead to higher emission currents, and also allows for spatial patterning of the emitted beams.

Large arrays of nanotip emitters present a significant computational challenge. Specifically, they require both a precise description of physical processes on the scale of the sharp tip, which is highly curved and at $O(1\,\text{nm})$, and consideration of the interaction of the geometrically arranged array of emitters on a scale of $O(1\text{-}10\,\mu\text{m})$. Moreover, collisional particle dynamics become relevant for beams near the quantum degeneracy limit (the ultracold regime), so the relevant time scales of the simulation exhibit a similar, if not more significant range ($> 10^4$). Conventional simulation tools use particle-in-cell (PIC) and other finite-element methods (FEM), which involve a full three dimensional volume discretization. Additionally, these methods typically represent the charged particle beam as a continuous density or using macroparticles, which become increasingly inaccurate in the ultracold regime (as space-charge effects become more significant). In order to overcome those challenges, we are developing a high-precision emission (HiPE) computational model which includes particle-particle interactions directly and implements an adaptive, high-order boundary element method (BEM) to include the boundary conditions accurately and efficiently (Fig. 1c illustrates the decrease in surface element size near the sharp tip).

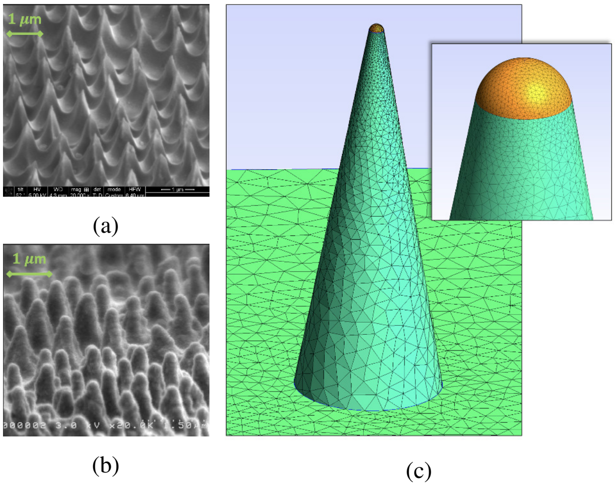

(a)

(b)

(c)

Figure 1: Images of nanotip array developed in collaboration with the engineering department. Shown are the fabricated Si nanotips (a), the tips after UNCD deposition (b), and the discretized boundary of a single nanotip model (c).

This model is being created using the Fortran based COSY Infinity, developed at MSU [2]. This gives HiPE access to a robust suite of beam physics routines and procedures (including map analysis/manipulation, and standard electromagnetic and optical accelerator components), and a language-level differential algebra (DA) implementation which HiPE utilizes on many levels. Nanotip boundary models are discretized using Gmsh [3], though any software capable of generating high-order surface discretizations could be used.

CODE MODULES AND INTEGRATION

Accurate simulation of electron emission from a nanotip array cathode requires considering three fundamental processes (see Fig. 2). Electrons have some initial state within

---

[*] atencate@niu.edu

ISBN: 978-3-95450-223-3 ISSN: 2673-7000 doi:10.18429/JACoW-NAPAC2019-WEYBB1

ELENA COMMISSIONING*

D. Gamba†, M.E. Angoletta, P. Belochitskii, L. Bojtar, F. Butin, C. Carli, B. Dupuy, Y. Dutheil,
T. Eriksson, P. Freyermuth, C. Grech[1], M. Hori[2], J.R. Hunt, M. Jaussi, L. V. Joergensen, B. Lefort,
S. Pasinelli, L. Ponce, G.A. Tranquille, CERN, Espl. des Particules 1, 1211 Meyrin, Switzerland
R. Gebel, Jülich Institute for Nuclear Physics, Jülich 52425, Germany,
[1]also at University of Malta, MSD 2080 Msida, Malta,
[2]also at Max Planck Institute Quantenopt., Munich D-80799 Germany

Abstract

The Extra Low ENergy Antiproton storage ring (ELENA) is an upgrade project at the CERN AD (Antiproton Decelerator). ELENA will further decelerate the 5.3 MeV antiprotons coming from the AD down to 100 keV. ELENA features electron cooling for emittance control during deceleration thus preserving the beam intensity and allowing to extract bright bunches towards the experiments. The lower energy will allow for increasing the antiproton trapping efficiency up to two orders of magnitude, which is typically less than 1% with the present beam from AD. The ring was completed with the installation of the electron cooler at the beginning of 2018. Decelerated beams with characteristics close to the design values were obtained before the start of CERN Long Shutdown 2 (LS2). During LS2 electrostatic transfer lines from the ELENA ring to the experimental zones will be installed, replacing the magnetic transfer lines from the AD ring. The latest results of commissioning with H^- and antiprotons and the first observation of electron cooling in ELENA will be presented, together with an overview of the project and status and plans for LS2 and beyond.

INTRODUCTION

The Antimatter Experiments hosted at CERN [1] presently take antiproton beams from the AD [2]. The AD provides about 3×10^7 antiprotons per pulse with 5.3 MeV kinetic energy to experiments typically capturing them in traps. The experiments have to further decelerate the beam to an energy of a few keV to be able to trap them. This further deceleration is typically obtained by sending the beam through several thin foils (one experiment uses a RadioFrequency Quadrupole Decelerator (RFQD) [3,4]). During the process most of the beam is lost, and the final trapping efficiency is of the order of 0.5%. Instead, ELENA [5] allows for controlled deceleration of the antiproton beam down to 100 keV with high transmission efficiency (nominal 60%) and keeping low transverse and longitudinal emittances thanks to the use of the electron cooling technique. It is expected that this will allow for increasing the experiments trapping efficiency by up to two orders of magnitude. ELENA has also the flexibility to produce up to four bunches of equal intensity and emittances which can be used to serve several experiments at the same time.

The ELENA project was approved at CERN in June 2011 and construction began two years later [6]. The first circulating H^- beam was observed in November 2016 [7], even though the ring installation was completed at the beginning of 2018 with the final installation of the electron cooler. The results presented in this proceedings have mainly been obtained in 2018, before the start of LS2.

ELENA OVERVIEW

Details of the ELENA design can be found in [5]. The ELENA ring has an hexagonal shape and its circumference is about 30 m. Figure 1 shows a picture of the ELENA ring after its complete installation, with the main components highlighted. Two slightly longer straight sections host the injection and the electron cooling. The other four straight sections host two fast deflectors [8] to extract the beam toward the experimental areas, one wide-band RF cavity and one wide-band longitudinal diagnostics, among three families of quadrupoles for optics control. The three quadrupole families allow for the adjustment over a certain range of the transverse tunes to avoid resonances and of the dispersion at the electron cooler in order to optimise the cooling process. Additionally, two families of skew quadrupoles and two families of sextupoles are installed for coupling and chromaticity correction, as well as two solenoids to compensate for the effect of the main solenoid of the electron cooler.

The 5.3 MeV pbar beam from AD is injected into ELENA from a 20 m long magnetic transfer line. Due to the low

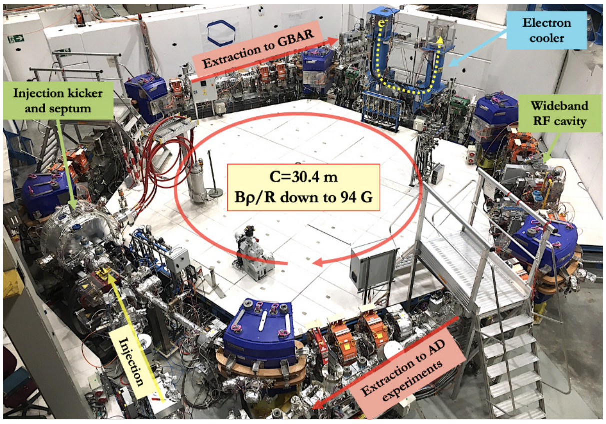

Figure 1: Picture of the ELENA Ring after installation. The main components are highlighted.

---

* Work supported by the ELENA Project

† davide.gamba@cern.ch

ISBN: 978-3-95450-223-3 ISSN: 2673-7000 doi:10.18429/JACoW-NAPAC2019-WEYBB3

FOIL SCATTERING MODEL FOR FERMILAB BOOSTER*

C.M. Bhat†, S. Chaurize, J.S. Eldred, V.A. Lebedev, S. Nagaitsev, K. Seiya, C.Y. Tan, R. Tesarek
Fermi National Accelerator Laboratory, Batavia, IL, USA

Abstract

At the Fermilab Booster, and many other proton facilities, an intense proton beam is accumulated by multi-turn injection of an H^- beam through a stripping foil. The circulating beam scatters off the injection foil and large-angle Coulomb scattering leads to uncontrolled losses concentrated in the first betatron period. We measure the foil scattering loss rate in the Fermilab Booster as a function of LINAC current, number of injection turns, and time on the injection foil. We find that current Booster operation has ~1% foil scattering loss and we make projections for the Proton Improvement Plan II (PIP-II) injector upgrade. Here we present the results from our recent beam measurements and a foil scattering model analyses.

INTRODUCTION

The Fermilab Booster's near-term improvement plan includes a 20% increase in intensity from 4.5×10^{12} protons to 5.4×10^{12} protons per Booster batch (ppBc) which would be enabled by a commensurate reduction in beam loss radio-activation. The quantification and accurate identification of Booster loss mechanisms forms an integral part of the loss reduction strategy. In this paper we examine the subset of Booster injection losses which are directly attributable to scattering of the incoming and circulating beam off the injection foil.

Large-angle Coulomb scattering from the injection foil is an operational reliability concern for the Fermilab Booster. The Booster has about a 0.57 π phase-advance per period and consequently particles with extreme divergence at the injection foil will primarily be lost in the downstream long straight section. That straight section includes extraction kickers which have had shortened service lifetimes due to severe radiation damage.

The study will also inform a later PIP-II intensity upgrade [1], in which the Booster will use a new 800 MeV injection region with a transversely painted foil-injection process. The PIP-II injection region design is actively being optimized to minimize and control the localized injection losses. Not only at Fermilab, at other proton facilities – such as SNS, J-PARC, and Los Alamos, including the current injection region in the Fermilab Booster – where the highest radio-activation levels are observed at the injection region [2–4]. We find foil-scattering injection loss to be a subject of broad interest.

SCATTERING MEASUREMENTS

Many scintillator and photo-multiplier tube (PMT) detectors were installed early 2015 around the collimation region of the Booster to identify and monitor beam loss mechanisms [5]. The response time of the PMT detectors is a few nanoseconds, allowing fast-loss mechanisms such as injection foil scattering to be visualized in detail. After three years of operation, several PMT detectors were non-operational due to radiation damage and are in the process of being replaced. The PMT detector attached to the "5-1 downstream dipole magnet" is operational however and provides a clear sample of the injection foil scattering loss.

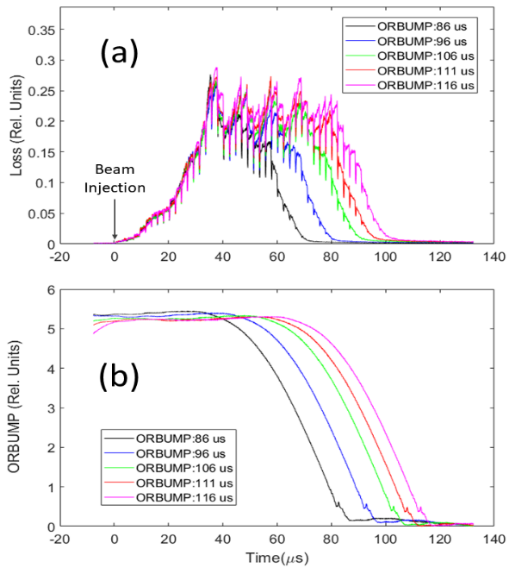

Figure 1: (a) PMT signal for first 140 μs at 14-Booster turn beam injection with LINAC current of 24 mA. The black curve with legend "ORBUMP:86 μs" corresponds to beam on foil for ≈70 μs and so on. (b) ORBUMP data.

The PMT foil-scattering signal was studied under varying injection conditions. The PMT foil-scattering signal was measured with the number of revolutions injected into the Booster at 10-turns and 14-turns (3.3×10^{12} ppBc and 4.7×10^{12} ppBc at nominal current of 25mA). To obtain data at reduced current of 10 mA and 1 mA, the LINAC beam is collimated downstream of the RFQ. The PMT foil-scattering signal was also measured by varying the duration that the circulating beam is on the foil from $2.2BT$+40 μs (nominal) to $2.2BT$+70 μs. The quantity BT is number of turns during multi-turn injection. For each case, the PMT signal for 64 consecutive accelerator cycles are averaged to minimize the impact of cycle-to-cycle variation.

Figure 1(a) shows averaged PMT signals for nominal beam current of 14-turn injection. The losses are associated with foil scattering, rising when the beam is injected and falling as the circulating beam moves off the injection foil. The rise of the scattering signal is not simply linear, which is consistent with ripple in the Booster corrector magnet power supplies. The periodic sudden decreases in the foil-

---

* This manuscript has been authored by Fermi Research Alliance, LLC under Contract No. DE-AC02-07CH11359 with the U.S. Department of Energy, Office of Science, Office of High Energy Physics.

† cbhat@fnal.ogv

PROGRESS OF LIQUID LITHIUM STRIPPER FOR FRIB *

T. Kanemura†, J. Gao, M. LaVere, R. Madendorp, F. Marti, Y. Momozaki[1]
Facility of Rare Isotope Beams, Michigan State University, East Lansing, USA
[1]also at Argonne National Laboratory, Lemont, USA

Abstract

The Facility for Rare Isotope Beams (FRIB) at Michigan State University is building a heavy ion linear accelerator (linac) to produce rare isotopes by the fragmentation method. At energies between 16 and 20 MeV/u ions are further stripped by a charge stripper increasing the energy gain downstream in the linac. The main challenges in the stripper design are high power deposited by the ions in the stripping media and radiation damage to the media itself. To overcome these challenges, self-recovering stripper media are the most suitable solutions. The FRIB baseline choice is a high-velocity thin film of liquid lithium. Because liquid lithium is highly reactive with air, we have implemented rigorous safety measures. Since May 2018, the lithium stripper system has been operated safely at an offline test site to accumulate operational experience. We successfully completed a 10-day long unattended continuous operation without any issue, which proved the reliability of the system. We present in this paper that the recent progress of the liquid lithium stripper for FRIB.

INTRODUCTION

Michigan State University was charged by the Office of Science of the Department of Energy of the US to design and build the Facility for Rare Isotope Beams (FRIB) at the end of 2008. The facility is funded by the Office of Nuclear Physics with contributions and cost share from the State of Michigan and Michigan State University. The goal of the facility is the production of rare isotopes produced by the in-flight separation method. This method provides fast development time for any isotope and allows short lived isotopes to be available. The facility will provide fast, stopped and reaccelerated beams of secondary ions.

One of the main components of the facility is a driver linac capable of producing beams of ions from the low mass region up to U at energies above 200 MeV/u and with a total beam power on target of 400 kW [1]. The linac is folded in three segments running parallel to each other with two 180 degree bends in between. After the first linac segment and before the first bend a charge stripper is located to increase the Q/A of heavy ions by more than a factor two. The FRIB baseline choice of the charge stripper is a high-velocity thin film of liquid lithium. For beam commissioning (low intensity, lighter ion beams), however, a conventional carbon stripper is used.

This paper describes the current status of the liquid lithium stripper commissioning.

DESIGN OF LITHIUM STRIPPER

Design and Construction

Figure 1 shows the layout of the FRIB liquid lithium stripper at the offline test site. The module consists of a liquid lithium loop including a main vacuum chamber, a secondary confinement vessel, an argon safety subsystem, a vacuum subsystem, and an electron gun (E-gun) diagnostics subsystem. The lithium loop is completely contained by the secondary confinement vessel.

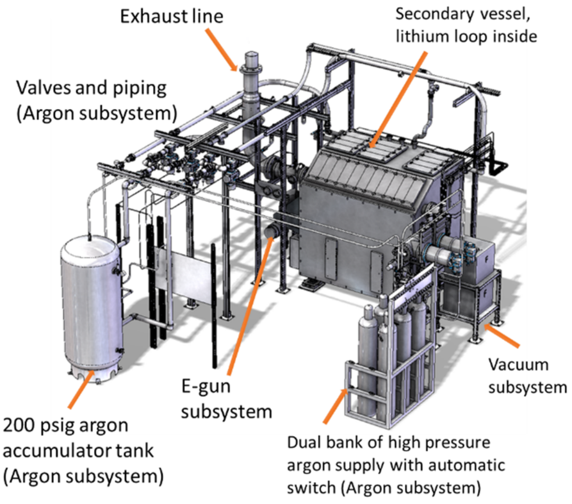

Figure 1: Liquid lithium stripper module at offline test site.

Lithium Loop

The liquid lithium loop (Figure 2) consists of an electromagnetic pump (EMP), particulate filter, nozzle assembly, vacuum chamber, lithium charge tank, and plumbing. The EMP can produce a high pressure flow of more than 1380 kPa (200 psi) at a flow rate of 10 cc/s. In the vacuum chamber, there are a nozzle and a deflector to produce a lithium film, which is formed by hitting a round lithium jet emerging from the nozzle onto the deflector (Figure 3). This film formation scheme was established in Argonne National Laboratory (ANL) [2], and the film stability and capability of removing high-power heat deposition were demonstrated under a collaboration work between FRIB and ANL [3, 4].

Secondary Confinement Vessel

This serves as a safety component. The vessel is filled with argon during operation to provide an inert environment blanket around the lithium loop so that in case lithium leaks out of the loop, it is still able to be confined in an inert atmosphere and will not catch a fire.

---

* This work is supported by the U.S. Department of Energy Office of Science under Cooperative Agreement DE-SC0000661
† email address: kanemura@frib.msu.edu

ISBN: 978-3-95450-223-3 ISSN: 2673-7000 doi:10.18429/JACoW-NAPAC2019-WEYBB5

A CRAB-CROSSING SCHEME FOR LASER-ION BEAM APPLICATIONS*

A. Aleksandrov†, S. Cousineau, T. Gorlov, Y. Liu, A. Rakhman, A. Shishlo,
Oak Ridge National Laboratory, Oak Ridge, Tennessee, USA

Abstract

Lasers have recently been used in many applications to H- beams, including laser charge exchange, laser wire scanners, and laser temporal pulse patterning [1]. The H- beam in these applications has a wide variation of micro pulse length dependent on the focusing of the RF cavities, the energy spread of the beam, and the space charge forces. Achieving the required laser pulse length for complete overlap with the H- beam can be challenging in some scenarios when available laser power is constrained. The scheme proposed here utilizes a crab-crossing concept between the laser and the ion beam to achieve overlap of a short laser pulse with an arbitrarily long H- beam pulse. An experiment to test the hypothesis in the context of H- charge exchange is described.

INTRODUCTION

Lasers have recently been used in many applications to H- beams, including laser charge exchange, laser wire scanners, and laser temporal pulse patterning [1]. The details of the applications differ from case to case, but all require efficient interaction between ions and photons. The technique described below is being developed for the laser assisted charge injection at SNS but can be used for other applications as well.

The charge exchange injection is the technology of choice for injecting beam of protons in circular accelerators. Typically, a thin foil is used to convert accelerated negative ions of hydrogen to protons. Passing a high intensity high power beam through the foil leads to foil heating and particle loss through scattering. Eventually, the foil performance and lifetime can be the limiting factor for further increase of the injected beam power [2].

An alternative charge exchange injection scheme, so called laser-assited charge exchange, or in short laser stripping, is being developed at the Spallatoin Neturon Source (SNS) [2]. The scheme uses two magnets to remove two electrons from the ion. A laser is used to excite the second electron from the ground state to one of upper levels in order to reduce the required magnetic field strength of the second magnet. The required laser power is the main limiting factor of the method. A number of laser power reducing techniques have been proposed and some tested experimentally [3,4]. With all the advances in laser stripping development, practical implementation seems feasible for the SNS accumulator ring after the upcoming linac energy upgrade to 1.3GeV [5].

One of the reamining problems to be resolved is mitigation of the ion bunch longitudinal expansion in the long beam line between the linac exit and the laser-ion interaction point. In this paper we propose a simple method of providing efficient temporal overlapping of short laser pulse with long ion bunch using a crab-crossing collision scheme.

BUNCH SIZE COMPRESSION

The efficiency of the laser-ion beam interaction is proportional to the laser power density $\frac{Q}{a_x a_y a_z}$, where Q is the laser pulse energy and a_i are the laser spot size in horizontal, vertical and longitudinal dimensions. The power density can be increased by increasing the pulse energy or by reducing the spot sizes. The laser spot size cannot be smaller than the ion bunch size to ensure good overlap for efficient interaction. In practice, the ion bunch size is the limiting factor. The SNS accelerator layout is shown in Fig.1.

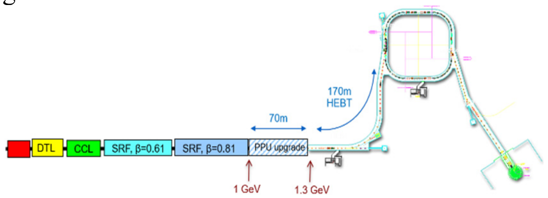

Figure 1: A layout of the SNS accelerator.

The transverse bunch size can be compressed to the limit determined by the ion bunch emittance using the quadrupole magnets in the transport line. A vertical RMS size of 100um was achieved during the laser stripping demonstration experiment [4].

Unfortunately, there are no longitudinally focusing elements between the linac exit and the interaction point. The energy spread of the particles causes the longitudinal bunch size to increase in the ~240m long drift. The longitudinal bunch size evolution for the nominal linac tune is shown by the blue line in Fig.2. The SNS superconducting linac has independently powered and controlled RF cavities. Several RF cavities in the end of the linac can be tuned to focus the bunch longitudinally at the interaction point, as shown in Fig.2 by the red line.

This solution works only for low beam current because the space charge effect does not allow the bunch to remain compressed over a long distance. The bunch size profile evolutions for the zero-beam current and the nominal beam

---

*This manuscript has been authored by UT-Battelle, LLC, under contract DE-AC05-00OR22725 with the US Department of Energy (DOE). The US government retains and the publisher, by accepting the article for publication, acknowledges that the US government retains a nonexclusive, paid-up, irrevocable, worldwide license to publish or reproduce the published form of this manuscript, or allow others to do so, for US government purposes. DOE will provide public access to these results of federally sponsored research in accordance with the DOE Public Access Plan (http://energy.gov/downloads/doe-public-access-plan).

† sasha@ornl.gov

DESIGN CONSIDERATIONS AND OPERATIONAL FEATURES OF THE COLLIMATORS FOR THE FERMILAB MAIN INJECTOR AND RECYCLER *

B. Brown†, P. Adamson, R. Ainsworth, D. Capista, K. Hazelwood, I. Kourbanis, N.V. Mokhov,
D.K. Morris, V.S. Pronskikh, I. Rakhno, I.S. Tropin, M. Xiao, M.-J. Yang
Fermilab, Batavia, IL, USA

Abstract

The Fermilab Main Injector system delivers 700 kW of 120 GeV Proton beam for neutrino experiments. Since 2013 this has been achieved using slip stacking accumulation in the Recycler with up to 12 batches from the Fermilab Booster per Main Injector Ramp Cycle. To control activation from beam loss, collimation systems in the Booster to Recycler transfer line, in the Recycler and in the Main Injector are employed. Residual radiation measurements around the ring with detailed studies at the collimators are required to maintain adequate loss control. We will review design considerations, operational parameters and activation results for more than ten years of operation. Simulations with MARS15 are used to explore the activation rates and the isotopic composition of the resulting activation.

OVERVIEW

Since preparations began in 2004 for high intensity operation of the Fermilab Main Injector for the neutrino program, an intensive effort has been required to control activation and radiation damage to devices in the accelerator tunnel. An overview of the efforts through the Tevatron era is provided in [1]. Peak power delivered in that era reached 400 kW using slip stacking in the Main Injector. By using the Recycler as a stacking ring [2] [3] beam power of 700 kW of 120 GeV protons have been delivered. These have been achieved with about 1% loss at collimators in the MI8 Booster to Recycler transfer line, >97% transmission in the Recycler and >97% transmission in the Main Injector. A gap-clearing kicker system [4] delivers some unwanted beam to the abort while collimators in the MI8 line [5], in the Main Injector [6], and in the Recycler [7] localize most of the remaining losses. Acceleration from 8 GeV to 120 GeV with very low losses is normally achieved.. Residual radiation at some critical locations are now ten times lower than their peak. Table 1 introduces these collimation systems.

Examination of the residual radiation for the Main Injector found patterns which suggested [8] that the transverse emittance of Booster beam was not cleanly accepted into the Main Injector aperture. At the same time, plans for higher intensity using slip stacking [9] assured that a few percent of the injected beam would not be captured into rf buckets for acceleration. A modest collimation system for the MI8 Booster to Main Injector Transfer Line [5] was developed quickly (installed in Spring 2006) while we designed and built a collimation system for the Main Injector [6] which would capture the beam from Main Injector slip stacking which was not accelerated and also define aperture limits to localize transverse losses from either injected beam or emittance growth from any source. This system was installed in Fall 2007 and commissioned in 2008.

Plans to employ the Recycler Ring for proton stacking [10] deferred collimation considerations. It was understood that the uncaptured beam from slip stacking would transfer cleanly to the Main Injector where the existing collimation system would contain the loss. Although other improvements solved many problems, the usefulness of a collimation system for localizing transverse emittance issues (injection, beam growth, and instabilities) was determined to demand a Recycler Collimation system. It was installed in the 2016 Facility Shutdown [7]. We will describe some features of these systems and report various issues which remain.

COLLIMATOR DESIGN

Collimation is achieved with thick-wall stainless steel vacuum boxes with a taper on the upstream end. Beam starts interacting downstream at the end of the taper. Welded vacuum bellows permit the required motion. This is surrounded by a massive steel shield to absorb the interaction products. Since the stainless and steel becomes highly radioactive, a layer of marble surrounds the steel to shield the outside from the residual gamma radiation. Marble is highly resistant to activation. This design allows the motion control and readout to be placed in low radiation areas near the floor for MI8 and MI Collimators.

Simulations for the energy deposition design of these collimators employed MARS [11]. The MI8 and Main Injector tunnel depth is sufficient to reduce concerns about prompt dose on the surface. Considerations for hands-on maintenance, radiation damage to accelerator components, air activation and activation of ground water (important) were explored [12].

Transfer Line Collimation

Collimation of the Booster beam halo was achieved using a 2” x 2” collimation aperture with horizontal and vertical motion. A pair of collimators provides scraping of four sides of the beam in a half cell. After a 90^o phase advance

---

* This manuscript has been authored by Fermi Research Alliance, LLC under Contract No. DE-AC02-07CH11359 with the U.S. Department of Energy, Office of Science, Office of High Energy Physics.

† bcbrown@fnal.gov

ISBN: 978-3-95450-223-3 ISSN: 2673-7000 doi:10.18429/JACoW-NAPAC2019-WEZBA2

EXPERIENCE AND LESSONS IN FRIB SUPERCONDUCTING QUARTER-WAVE RESONATOR COMMISSIONING*

S. Kim[†], H. Ao, F. Casagrande, W. Chang, C. Compton, A. Facco[1], R. Ganni, E. Gutierrez, N. Hasan, W. Hartung, P. Knudsen, T. Larter, H. Maniar, S. Miller, D. Morris, P. Ostroumov, A. Plastun, J. Popielarski, L. Popielarski, H. Ren, K. Saito, M. Thrush, D. Victory, J. Wei, M. Xu, T. Xu, Y. Yamazaki, C. Zhang, S. Zhao,
Facility for Rare Isotope Beams, Michigan State University, East Lansing, MI, USA
[1]also at INFN - Laboratori Nazionali di Legnaro, Legnaro, Padova, Italy

Abstract

The superconducting (SC) linear accelerator (linac) for the Facility for Rare Isotope Beams (FRIB) has one quarter-wave resonator (QWR) segment and two half-wave resonator (HWR) segments. The first linac segment (LS1) contains twelve β = 0.041 and ninety-two β = 0.085 QWRs operating at 80.5 MHz, and thirty-nine SC solenoids. Superconducting radiofrequency (SRF) commissioning and beam commissioning of LS1 was completed in April 2019. The design accelerating gradients (5.1 MV/m for β = 0.041 and 5.6 MV/m for β = 0.085) were achieved in all cavities with no multipacting or field emission issues. The cavity field met the design goals: peak-to-peak stability of ±1% in amplitude and ±1° in phase. We achieved 20.3 MeV/u ion beams of Ar, Kr, Ne, and Xe with LS1. In this paper, we will discuss lessons learned from the SRF commissioning of the cryomodules and methods developed for efficient testing, conditioning, and commissioning of more than 100 SC cavities, each with its own independent RF system.

INTRODUCTION

The FRIB SC driver linac is designed to accelerate stable ion beams, from hydrogen to uranium, to 200 MeV/u. The linac is divided into three segments with two 180º bending sections. The first segment, LS1, contains twelve β = 0.041 QWRs and ninety-two β = 0.085 QWRs operating at 80.5 MHz, house in 15 cryomodules along with 39 SC solenoids. Table 1 shows details of the LS1 cryomodules. The next two segments, LS2 and LS3, contain seventy-two β = 0.29 HWRs and one hundred forty-eight β = 0.53 HWRs operating at 322 MHz, housed in 31 cryomodules along with 30 SC solenoids [1]. In the phased commissioning of the FRIB driver linac, we completed commissioning of all LS1 cryomodules with beam and achieved 20.3 MeV/u ion beams with four different ion species (Ne, Ar, Kr, and Xe) [2, 3]. The design operating temperature of the LS1 cavities is 2 K but they were operated at 4.5 K at this stage of the phased commissioning.

Commissioning of QWR cryomodules in LS1 will be discussed in this paper. The status of HWR cryomodule production for LS2 and LS3, offline bunker testing, and tunnel installation is presented elsewhere [2,4-6].

Table 1: Configuration of LS1 Cryomodules. All Cavities are QWRs Operated at 80.5 MHz

Cryomodule type	CA	CB	CH
Number of cryomodules	3	11	1
β	0.041	0.085	0.085
Cavities per cryomodule	4	8	4
Design accelerating gradient E_a (MV/m)	5.1	5.6	5.6
SC solenoids per cryomodule	2	3	0
Design solenoid magnetic field (T)	8	8	N/A

CAVITY PERFORMANCE

Accelerating Gradients

Figure 1 shows the average accelerating gradient (E_a) reached in each cryomodule. The measured gradients exceeded the design goals in all 104 cavities. For this stage of linac commissioning, the highest operating E_a was limited to 5-10% higher than the design E_a by an administrative decision; in offline cryomodule bunker tests, many cavities were tested to approximately 20% higher than the design E_a [4].

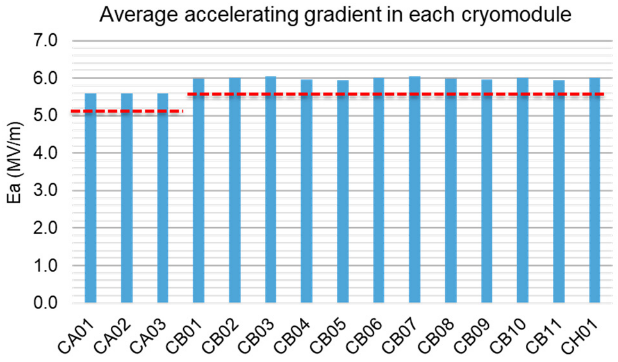

Figure 1: Accelerating gradients achieved in LS1. Solid blue bars: average accelerating gradient in each cryomodule. Dashed red lines: design gradients.

---

*Work supported by the U.S. Department of Energy Office of Science under Cooperative Agreement DE-SC0000661 and the National Science Foundation under Cooperative Agreement PHY-1102511.

[†] kims@frib.msu.edu

ISBN: 978-3-95450-223-3 ISSN: 2673-7000 doi:10.18429/JACoW-NAPAC2019-WEZBA3

NO BEAM-LOSS QUADRUPOLE SCAN FOR TRANSVERSE PHASE SPACE MEASUREMENTS *

K. Fukushima†, T. Maruta, P. N. Ostroumov, T. Yoshimoto,
Facility for Rare Isotope Beams, Michigan State University, East Lansing, MI USA

Abstract

Facility for Rare Isotope Beams (FRIB) at Michigan State University is based on a high power heavy ion linac and beam commissioning is under way. For evaluation of beam Twiss parameters and rms emittance, we routinely use multiple profile measurements while the strength of an upstream quadrupole is varied. The change of the quadrupole strength results in a beam mismatch downstream of the profile monitor which can cause beam losses. This is not acceptable in a high energy beamline. To avoid this transverse mismatch, we developed a beam matching procedure by optimization of quadrupoles' setting downstream of the profile monitor. Using this procedure we were able to eliminate beam losses during the quadrupole scan, and evaluate beam Twiss parameters and rms emittance. Examples of using this procedure in the folding segment of the FRIB linac are reported.

INTRODUCTION

The driver linac of the Facility for Rare Isotope Beams (FRIB) is designed to accelerate stable ions from oxygen to uranium above 200 MeV/u [1]. Figure 1 shows the layout of the FRIB linac in the tunnel.

The linac segment 1 (LS1) was tuned for acceleration of argon beam up to 20.3 MeV/u [2, 3]. Other ion species such as Ne, Kr and Xe were accelerated to the same energy by simple scaling of all electromagnetic fields. The accelerated beams were stripped to higher charge states using the carbon foil and transported to the beam dump. The emittance growth on the stripping foil depends on the beam size and the beam phase space ellipse orientation on the stripper. Therefore, the transverse phase space measurements are necessary upstream of the stripper to optimize beam Twiss parameters on the stripper. A quadrupole-scan (Q-scan) method was applied to measure the beam Twiss parameters and emittance. Assuming a thin-lens model and a linear field beam optics, the root mean squared (rms) beam size at the downstream profile monitor can be written as a quadratic function of the upstream quadrupole strength and the transfer matrix elements between the quadrupole and the profile monitor. Even if we use a thick-lens beam optics model, we can obtain the beam σ-matrix by fitting the quadrupole strength to match the measured rms beam size. To achieve high accuracy of the Q-scan method the measured beam rms size as a function of the quadrupole strength should have downward-convex shape. The change of the quadrupole strength in the Q-scan procedure causes a significant beam mismatch in the downstream section and can result in beam losses. The latter can produce unnecessary radio-activation of the accelerator equipment. To avoid these beam losses, we developed a "Twiss recovery" procedure by optimization of the quadrupoles' setting downstream of the profile monitor.

RMS ENVELOPES DURING Q-SCAN

Typically, the beam commissioning was performed using argon beam and Table 1 lists the design beam parameters at the exit of the last cryomodule in LS1.

Table 1: Design Beam Parameters at the Exit of the Last Cryomodule in LS1

Ion species	$^{40}\mathrm{Ar}^{9+}$	
Beam energy [MeV/u]	20.3	
	x	y
Normalized rms emittance [π mm-mrad]	0.10	0.10
Twiss parameter β [m]	5.0	5.0
Twiss parameter α	0.0	0.0

Figure 2 shows the layout of the optical elements and the design beam envelopes from the last cryomodule in the LS1 to the beam dump in the folding segment 1 (FS1). There are 16 quadrupoles upstream of the stripper, and last 4 quadrupoles are used for the beam matching to the stripper. The aperture radii are 25 mm at the quadrupoles and 17 mm at the rf bunchers. The first profile monitor is the most suitable for the quadrupole scan to obtain the downward-convex plot with a small range of the quadrupole strength variation.

Figure 3 presents the simulation results of the rms beam envelopes during the Q-scan for the 30 % variation of the quadrupole strength with respect to the design setting. The rms size difference in the vertical plane is large enough compared to the profile monitor accuracy. However, the rms beam envelopes downstream of the profile monitor are mismatched from the design envelopes especially in the vertical plane.

Figure 4 shows the rms beam envelope when we apply the "Twiss recovery" procedure downstream of the profile monitor. In this case, 4 quadrupoles between the profile monitor and the recovery point are optimized to reproduce the same Twiss parameters for each step of the Q-scan. As a consequence, the beam envelopes for each Q-scan quadrupole setting are recovered to match the design envelopes.

In operation, total 5 quadrupoles (1 for the Q-scan and 4 for the Twiss recovery) settings are pre-calculated using

---

* Work supported by the U.S. Department of Energy Office of Science under Cooperative Agreement DE-SC0000661, the State of Michigan and Michigan State University.

† fukushim@frib.msu.edu

North American Particle Acc. Conf. NAPAC2019, Lansing, MI, USA JACoW Publishing
ISBN: 978-3-95450-223-3 ISSN: 2673-7000 doi:10.18429/JACoW-NAPAC2019-WEZBA5

DEVELOPMENT OF A MARX MODULATOR FOR FNAL LINAC*

T. A. Butler†, F. G. Garcia, M. R. Kufer, K. S. Martin, H. Pfeffer,
Fermi National Accelerator Laboratory, Batavia, IL, USA

Abstract

A Marx-topology modulator has been designed and developed at the Fermi National Accelerator Laboratory under the Proton Improvement Plan (PIP). This modulator replaces the previous triode hard-tube design, increasing reliability, lowering operational costs, and maintaining waveform accuracy. The Marx modulator supplies the anode of the 7835 VHF power triode tube with a 35 kV, 375 Amp, 460 µs pulse at 15 Hz. It consists of 54 individual Marx cells, each containing a 639 µF capacitor charged to 900 Volts, combined in series with IGBT switches to create the desired output waveform. This requires variable rise and fall times, flattening of capacitive droop, and feedforward beam loading compensation. All five 201.25 MHz RF systems have been upgraded to Marx modulators to ensure continued operation of the linear accelerator.

INTRODUCTION

The specification and design of a new anode modulator for the 7835 triode [1] have culminated in the development and installation of a new design, shown in Fig. 1. This new modulator uses the solid-state Marx generator technique of charging individual cells, each consisting of main storage and control power capacitors, in parallel via a charging switch in each cell, and then, after the charging cycle has completed, erecting the high voltage output by turning on separate firing switches in each cell. The modulator output amplitude is controlled by the voltage of the main storage capacitors in each cell and the number of cells fired at a time. This modulator is distinguished by the addition of a multi-cell interleaved pulse width modulation (PWM) regulator that sits on top of the main cells. The main cells run the voltage up to the flattop and back down while the PWM cells flatten and regulate the voltage during the flattop.

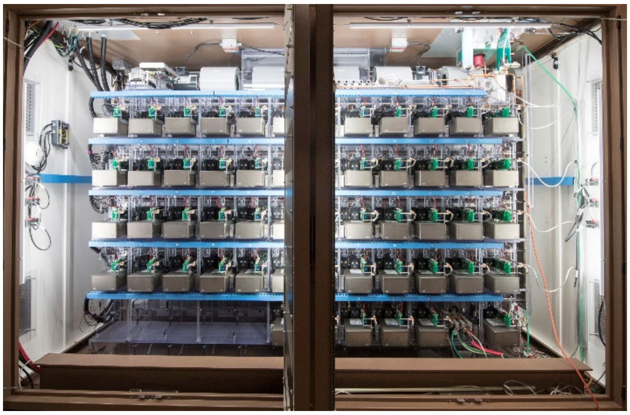

Figure 1: Photograph of the Marx modulator.

MARX MODULATOR DESIGN

Marx modulator topologies can be used to create any desired waveform since each cell can be independently fired. However, the fixed step size and undesired capacitive voltage sag of each cell creates a challenge in designing a modulator that has a smooth flattop plus the desired slow rising and falling edges as well as the high dV/dt beam step slew rate needed to match the rising edge of the incoming beam. To overcome the limitations of the standard Marx topology, this modulator design was broken up into three groups as shown in Fig. 2, consisting of 41 Main cells, shown in black, which are used to create the overall rising and falling edges of the modulator pulse, 12 PWM cells, shown in blue, which are filtered to reduce the ripple created from the PWM process and used to compensate for capacitive droop along with providing the beam top tilt, and one special cell, shown in orange, that uses an adjustable voltage charging power supply to create a voltage step of any desired value to match various beam intensities.

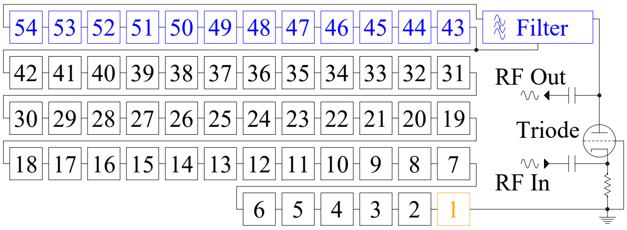

Figure 2: Marx modulator cell layout.

Marx Cell Design and Operation

The selection of the voltage per cell is critical in determining the cost, performance, and reliability of any Marx design. With the desire to reduce the power reflected from the accelerating cavity back to the tube, the operation of 900 V per cell was selected. The main storage capacitor is a 639 µF, 1.8 kV power film capacitor, which limits voltage sag to < 15%. Dual 5.6 µF snubber capacitors are added to reduced transients across the main storage capacitor. The solid-state insulated-gate bipolar transistors (IGBT) half-bridge configuration switches have a collector-to-emitter rating of 1.7 kV and peak collector current rating of 600 A, providing the overhead required for reliable operation.

The Marx cells main storage capacitors are charged by nineteen 6 A, 1 kV capacitor charging power supplies fed through 120 A, 1.8 kV fast recovery diodes to the Marx cells. To power the gate control circuitry, each cell also receives 300 V through a separate power supply. The gate circuity uses the same charging IGBT's as the main capacitors but use a different set of charging diodes. The cell outputs are interconnected by parallel plate stripline, used to limit the Marx inductance to 10 µH. The high voltage wiring for the capacitor charging and gate power supply are

---

* This manuscript has been authored by Fermi Research Alliance, LLC under Contract No. DE-AC02-07CH11359 with the U.S. Department of Energy, Office of Science, Office of High Energy Physics.

† tbutler@fnal.gov

A 100 kW 1.3 GHz MAGNETRON SYSTEM WITH AMPLITUDE AND PHASE CONTROL

M.E. Read, T. Bui, G. Collins, R.L. Ives, D. Marsden,
Calabazas Creek Research, Inc., San Mateo, CA, USA
J.R. Conant, C.M. Walker, Communications & Power Industries LLC, Beverly, MA, USA
B.E. Chase, J. Reid, Fermilab, Batavia, IL, USA

Abstract

Calabazas Creek Research, Inc., Fermilab, and Communications & Power Industries, LLC, developed a 100 kW peak, 10 kW average, 1.3 GHz, magnetron-based, RF system for driving accelerators. Efficiency varied between 81% and 87%. Phase locking uses a novel approach that provides fast amplitude and phase control when coupled into a superconducting accelerator cavity [1]. The system was successfully tested at Fermilab and produced 100 kW in 1.5 ms pulses at a repetition rate of 2 pps. A locking bandwidth of 0.9 MHz was achieved with a drive signal of 269 W injected through a 4 port circulator. The phase locking signal was 25 dB below the magnetron output power. The spectrum of the phase locked magnetron was suitable for driving accelerator cavities. Phase modulation was demonstrated to 50 kHz (the limit of the available driver source). The average power was limited by available conditioning time. Scaling indicates 42 kW of average power should be achievable. Estimated cost is less than $1/Watt of delivered RF power. System design and performance measurements will be presented.

INTRODUCTION

The magnetron is a highly efficient and relatively inexpensive source of RF power. Magnetrons with efficiencies exceeding 85% are available at 915 MHz and are commonly used in industrial RF heating systems. These are free-running oscillators and are not suitable where control of the frequency and phase are critical, including many accelerator systems. While one can control the amplitude by varying the beam current, this cannot be achieved on a sufficiently fast time scale for systems requiring feedback control. Calabazas Creek Research, Inc., Fermilab and Communications and Power Industries, LLC developed a phase-locked, 1.3 GHz magnetron-based RF system with fast amplitude control for accelerator applications.

The system provides 10o kW of peak power with a 10% duty cycle. The magnetron is phase-locked using a technique developed by Fermilab [1] that employs phase modulation of the locking signal to produce sidebands that are rejected by a high Q load, such as a superconducting cavity. Power in the sidebands effectively reduces the power delivered to the cavity and provides amplitude modulation on a very fast time scale.

SYSTEM DESCRIPTION

The magnetron and its driver and ancillary equipment are enclosed in a support frame, as shown in Figure 1. The magnetron and its solenoid, shown in Fig. 2, is driven by a klystron capable of 5 kW. The high driver power was chosen to explore a wide parameter space, but, much lower power iss required for locking. A 4-port circulator was used to inject the locking signal. For these experiments, the output of the system was shorted to reflect the power from the magnetron into the circulator load.

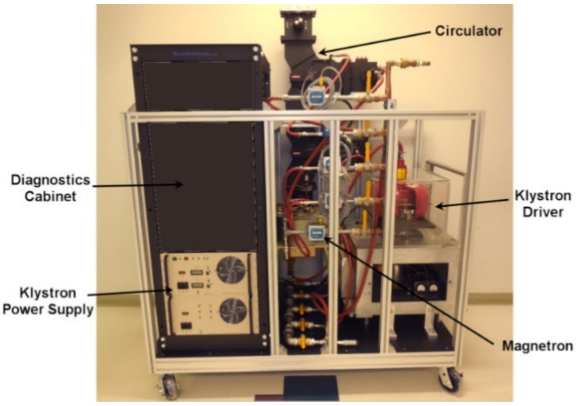

Figure 1: Photograph of magnetron system

AMPLITUDE CONTROL

While phase control has been available for many years, the approach developed by Fermilab also provides amplitude control on a fast time scale, Phase modulation of the phase locking signal shifts power into side bands. For very

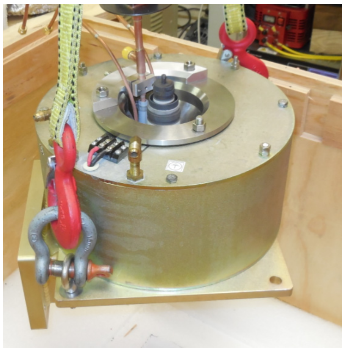

Figure 2: Photograph of magnetron inside solenoid

North American Particle Acc. Conf. NAPAC2019, Lansing, MI, USA JACoW Publishing
ISBN: 978-3-95450-223-3 ISSN: 2673-7000 doi:10.18429/JACoW-NAPAC2019-WEPLM01

STUDIES IN APPLYING MACHINE LEARNING TO RESONANCE CONTROL IN SUPERCONDUCTING RF CAVITIES*

J. A. Diaz Cruz, S. G. Biedron, M. Martinez-Ramon, S. I. Sosa,
Department of Electrical and Computing Engineering,
University of New Mexico, Albuquerque, NM, USA
R. Pirayesh, Department of Mechanical Engineering,
University of New Mexico, Albuquerque, NM, USA,

Abstract

Traditional PID, active resonance and feed-forward controllers are dominant strategies for cavity resonance control, but performance may be limited for systems with tight detuning requirements, as low as 10 Hz peak detuning (few nanometers change in cavity length), that are affected by microphonics and Lorentz Force Detuning. Microphonic sources depend on cavity and cryomodule mechanical couplings with their environment and come from several systems: cryoplant, RF sources, tuners, etc. A promising avenue to overcome the limitations of traditional resonance control techniques is machine learning (ML) due to recent theoretical and practical advances in these fields, and in particular Neural Networks (NN), which are known for their high performance in complex and nonlinear systems with large number of parameters and have been applied successfully in other areas of science and technology. In this paper we introduce ML to LLRF control. An LCLS-II superconducting cavity type system is simulated using the *Cryomodule-on-Chip* (CMOC) model developed by LBNL and is used to produce data for future training of NN. Future work based on the experience and results of the present research will be performed for resonance control systems to overcome microphonics detuning of SRF cavities.

INTRODUCTION

Low Level Radio Frequency (LLRF) control systems aim to control the amplitude and phase of the electric field used in driving the cavities of particle accelerators. For X-ray Free Electron Lasers (FELs), such as the Linac Coherent Light Source II (LCLS-II), the quality of the X-rays produced at the undulators is directly affected by the quality of the electron beam accelerated with Superconductive RF cavities (SRF). Therefore, tight stability requirements for the cavity field's amplitude and phase have to be achieved by the LLRF control system [1].

Typically, amplitude and phase are controlled by the LLRF through Proportional-Integral (PI) controllers implemented in FPGAs. The goal of our research is to explore alternative control techniques based on ML, specifically a Neural Network (NN) based controller, to further improve the performance of the LLRF system. We present simulations of how amplitude stability is impacted by several sources of noise, which are modelled by the *CMOC* software developed at LBNL. The data obtained from these simulations will then be used as training data for a NN-based controller.

Applying ML and controls have been developed in different applications by members of this research team. Reza developed control systems to keep formation between 2 CubeSats [2–4]. He also developed, different ML frameworks to increase the efficiency of the formation control [5–7], similar techniques can be applied to the control of accelerator components.

LLRF FOR LCLS-II

The LCLS-II upgrade includes a scheme for higher beam energy, this is achieved with the addition of 35 cryomodules, each with 8 superconducting accelerating cavities. The cavities are driven under a Single Source Single Cavity (SSSC) topology, where 280 Solid State Amplifiers (SSA) will deliver RF power to 280 cavities [8].

A LLRF for LCLS-II has been designed and tested. It has proven the ability to regulate the RF amplitude and phase under the aforementioned stability requirements. This system is now in a production phase, and installation will begin at the SLAC gallery soon. The LLRF system is based on a basic PI controller [9], and is depicted in Fig. 1.

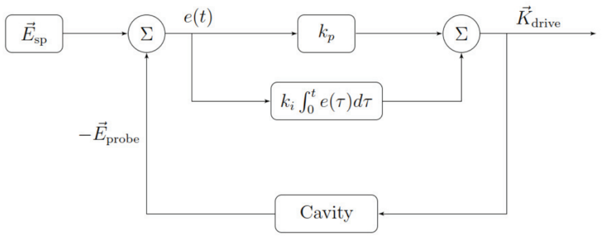

Figure 1: Diagram of a PI Controller.

The proportional gain, k_p, increases the gain of the closed loop and the integral gain, k_i, minimizes the steady state error. A nominal configuration with $k_p = 1200$ and $k_i = 3.8\times10^7$ has been chosen for the control system [10].

Cavity Model

A model of the system encompassing the superconducting cavity, the LLRF control system and the cryomodule was developed by the LLRF team at LBNL and has been used to study the performance of electrodynamic system. For a

---

[*] The study at the University of New Mexico was supported by DOE Contract DE-SC0019468

FINDING BEAM LOSS LOCATIONS IN A LINAC WITH OSCILLATING DIPOLE CORRECTORS*

A. V. Shemyakin†, R. Prakash[1], K. Seiya, Fermilab, Batavia, IL, USA
[1]also at RRCAT, Indore, India

Abstract

The paper proposes a method of finding the beam loss locations in a linac. If the beam is scraped at an aperture limitation, moving its centroid with two dipole correctors located upstream and oscillating in sync produces a line at the corresponding frequency in spectra of current-sensitive devices, loss monitors, and BPMs downstream of the loss point. The phase of this signal contains information about the location of the beam loss. Proof-of-principle measurements performed at the Fermilab Linac are presented.

INTRODUCTION

Transporting a beam with low losses is important requirement for beam lines or linear accelerators. While a large accidental loss can be detected by comparing the beam current in different parts of the linac [1], small chronic losses are usually identified using radiation monitors. An alternative solution proposed by V. Lebedev and used in CEBAF [2], employs that a beam loss caused by beam scraping on a physical aperture is typically associated with a sharp dependence of the loss signal on the beam position at that location. In this case, oscillating a dipole corrector current at the beginning of the linac produces a signal at that frequency in the beam current signal measured at the end of the linac. Such measurement does not provide an absolute value of the loss but rather the difference in the loss over the range of the beam oscillation. While the latter is lower than the total loss, the synchronous detection allows to greatly improve the overall sensitivity. For sufficiently long measurement time, the oscillations resulting in a detectable effect can be made small enough so that the emittance growth is negligible. What follows below is a development of this idea, with a more detailed derivation presented in [3].

FORMULAE

Trajectory deviation excited by a dipole kick turns zero in the locations where the betatron phase advance $\varphi(z)$ counted from the corrector is πn. Hence, a loss is such location remains unidentified. To address this, the procedure can be repeated with another corrector shifted from the first one by the betatron phase advance of $\varphi_x \neq \pi n$. To speed the process up, both correctors can be oscillated simultaneously with the same frequency ω and a phase difference in time of φ_t. Corresponding trajectory deviation downstream is

$$x_0(z,t) = \theta_1\sqrt{\beta_x(z)\beta_{x1}}\sin\varphi(z)\sin\omega t + \\ +\theta_2\sqrt{\beta_x(z)\beta_{x2}}\sin(\varphi(z)+\varphi_x)\sin(\omega t+\varphi_t), \quad (1)$$

where θ_i is the deflection amplitude, $\beta_x(z)$ and β_{xi} are the beta-functions along the line and in the location of i-th corrector, and *i*= 1, 2 is the corrector number. In all locations, the beam position oscillates at the same frequency but with amplitude and phase dependent on z:

$$x_0(z,t) = A(z)\sin(\omega t + \varphi_1(z)) \quad (2)$$

In the model where the aperture limitation is a flat-edge "scraper" separated from unperturbed central trajectory by the offset d, the current intercepted by the scraper is

$$I_s = \int_d^\infty j(x-x_0)dx = \int_d^\infty j(x)dx + j(d)x_0 - \\ \frac{dj}{dx}(d)\frac{{x_0}^2}{2} + \cdots. \quad (3)$$

For the perturbations much smaller than the beam size, only first terms are significant. Using Eq. (2) and Eq. (3),

$$I_s \approx \int\limits_d^\infty j(x)dx + j(d)A(z)\sin\big(\omega t+\varphi_1(z)\big) - \\ -\frac{dj}{dx}(d)\frac{1}{2}\Big(A(z)\sin\big(\omega t+\varphi_1(z)\big)\Big)^2 \equiv \\ \equiv I_{s0} + I_{s1}\sin(\omega t+\varphi_1(z)) + \\ +I_{s2}\Big(1-\cos\big(2\cdot(\omega t+\varphi_1(z))\big)\Big). \quad (4)$$

Let assume that the spatial current density distribution is scaled along the beam line as the beam rms size σ_b:

$$j(x) = \frac{I_0}{\sigma_b}J\left(\frac{x}{\sigma_b}\right),\ \ \sigma_b = \sqrt{\beta_x(z)\varepsilon_0}, \quad (5)$$

where ε_0 is the rms beam emittance, I_0 is the total beam current, and the dimensionless function $J\left(\frac{x}{\sigma_b}\right)$ does not change along the beam line. In this model, the loss linear component is determined by the scraper position and oscillation amplitude, both normalized by the rms beam size:

$$\frac{I_{s1}}{I_0} = \frac{A(z)}{\sigma_b}J\left(\frac{d}{\sigma_b}\right). \quad (6)$$

At the specific choice of deflection amplitudes and the time delay between correctors waveforms,

$$\theta_2\sqrt{\beta_{x2}} = \theta_1\sqrt{\beta_{x1}}\ ,\quad \varphi_t = \pi \pm \varphi_x, \quad (7)$$

Eq. (2) is simplified [3] to

$$x_0(z,t) = \theta_1\sqrt{\beta_x(z)\beta_{x1}}\sin\varphi_x\sin\big(\omega t+\varphi_1(z)\big) \quad (8)$$

with the phase changing linearly with the betatron phase:

$$\varphi_1(z) = \pm(\varphi(z)+\varphi_x). \quad (9)$$

The amplitude of the current first harmonic becomes dependent only on the relative penetration of the scraper:

$$\frac{I_{s1}}{I_0} = \frac{\theta_1\sqrt{\beta_{x1}}}{\sqrt{\varepsilon_0}}J\left(\frac{d}{\sigma_b}\right). \quad (10)$$

---

* This manuscript has been authored by Fermi Research Alliance, LLC under Contract No. DE-AC02-07CH11359 with the U.S. Department of Energy, Office of Science, Office of High Energy Physics

†shemyakin@fnal.gov

ISBN: 978-3-95450-223-3 ISSN: 2673-7000 doi:10.18429/JACoW-NAPAC2019-WEPLM03

THE LLRF CONTROL DESIGN AND VALIDATION AT FRIB*

S. Zhao†, W. Chang, S.H. Kim, H. Maniar, D.G. Morris, P.N. Ostroumov, J.T. Popielarski, H.T. Ren,
N.R. Usher[1], Facility for Rare Isotope Beams, Michigan State University, East Lansing, MI, USA
[1] also at Ionetix Corporation, Lansing, MI, USA

Abstract

One of the challenges in designing the low level radio frequency (LLRF) controllers for the Facility for Rare Isotope Beams (FRIB) is the various types of cavities, which include 5 different frequencies ranging from 40.25 MHz to 322 MHz, and 4 different types of tuners. In this paper, the design strategy taken to achieve flexibility and low cost and the choices made to accommodate the varieties will be discussed. The approach also allowed easy adaptation to major design changes such as replacing two cryo-modules with two newly designed room temperature bunchers and the addition of high-voltage bias to suppress multi-pacting in half-wave resonators (HWRs). With the successful completion of the third accelerator readiness review (ARR03) commissioning in early 2019, most of the design has been validated in the real accelerator system, leaving only HWRs which are constantly undergoing tests in cryo-module bunker. The integrated spark detector design for HWRs will also be tested in the near future.

INTRODUCTION

The Facility for Rare Isotope Beams (FRIB) is a scientific user facility for nuclear physics research being built at Michigan State University (MSU). The folded linear accelerator (LINAC) at FRIB consists of a front end (FE), three linear segments (LS1/2/3) and two folding segments (FS1/2). Four types of superconducting radio-frequency (SRF) cavities spread out in the linear and folding segments, namely β=0.041 and β=0.085 quarter-wave resonators (QWR041/085) and β=0.29 and β=0.53 half-wave resonators (HWR29/53). Most of the room temperature (RT) cavities including the multi-harmonic buncher (MHB), radio-frequency quadruple (RFQ) and medium energy beam transport (MEBT) buncher are in the FE, with the exception of multi-gap buncher (MGB) in FS1 [1]. Table 1 summarizes different types of cavities in the FRIB LINAC.

As shown in the table, the various types of cavities run at five different frequencies from 40.25 MHz to 322 MHz and have four different tuner types. Designing a low level radio frequency (LLRF) controller to support all those cavity types is a challenging task.

LLRF DESIGN

As stated earlier, the FRIB LLRF design has to be flexible to support various cavity types. The flexibility also means that the design should be able to accommodate possible design changes in a later stage. For any engineering design, cost is also a major factor to be considered. Time wise, it is critical to integrate the LLRF controller with other systems as early as possible to identify potential issues and fix them in the next iteration.

Table 1: FRIB Cavity Types

System	Area	Frequency (MHz)	Type	Tuner
MHB F1	FE	40.25	RT	N/A
MHB F2	FE	80.5	RT	N/A
MHB F3	FE	120.75	RT	N/A
RFQ	FE	80.5	RT	temperature
MEBT	FE	80.5	RT	2-phase stepper
QWR	LS1 FS1	80.5	SC	2-phase stepper
MGB	FS1	161	RT	5-phase stepper
HWR	LS2/3 FS2	322	SC	pneumatic

Hardware

FRIB General Purpose Digital Board A common digital board based on the Xilinx Spartan-6 field programmable gate array (FPGA) was designed at FRIB to serve different applications including LLRF, beam position monitor (BPM) and machine protection system (MPS). The cost of the FRIB General Purpose Digital Board (FGPDB) is reduced due to the combined high volume. For the LLRF application, some unused and expensive parts are not populated to further reduce the cost. The FGPDB is compatible with the µTCA standard and can be used either in a µTCA crate (BPM case) or in a chassis (LLRF and MPS cases). The FGPDB has 512 MB onboard double data rate memory which can be used for waveform storage.

RF Board Trying to reduce the temperature dependency of some RF devices, e.g. mixers and local oscillator, the FRIB LLRF control adopts direct-sampling / under-sampling approach, which means that the analog-to-digital converter (ADC) samples the RF signal directly without mixing it to an intermediate frequency at a frequency lower than the Nyquist frequency of the signal. This makes sharing the same RF input chain across all five frequencies possible, and allows the ADC to use the same sampling frequency which greatly simplifies the board design. Non-In-Phase/Quadrature (non-IQ) sampling is also adopted to reduce the effect of harmonics.

No mixer is used in the RF output chain as well. The digital-to-analog converter (DAC) generates four points (I, Q, −I, −Q) per waveform. The band-pass filters pick up the fundamental or higher harmonics of interest. By carefully choosing the parts to be footprint compatible, three variations of the RF board were designed to have the same

---

* Work supported by the U.S. Department of Energy Office of Science under Cooperative Agreement DE-SC0000661
† Email address: zhaos@frib.msu.edu

ISBN: 978-3-95450-223-3 ISSN: 2673-7000 doi:10.18429/JACoW-NAPAC2019-WEPLM04

PRECISION CAVITY HIGHER-ORDER MODE TUNING SCHEME FOR STABILIZING THE STORED BEAM IN THE ADVANCED PHOTON SOURCE UPGRADE*

L. Emery†, P. Kallakuri, U. Wienands, Argonne National Laboratory, Lemont, IL USA
D. Teytelman, Dimtel, Inc., San Jose, CA, USA

Abstract

The Advanced Photon Source Upgrade will suffer longitudinal multi-bunch instability because of the presence of several monopole higher-order mode (HOMs) of the 12 352-MHz rf cavities. Even with a feedback system, it would be good to mitigate any driving terms with conventional means such as tuning HOM frequencies with temperature. However the latter is problematic because there will be 90 or so HOMs that are potentially harmful. A scheme is developed, utilizing the measured spectrum of HOMs, to find the best temperature setting for each cavity. We present measurements of 30 or so HOMs, and a thermal model of HOM frequencies using cavity wall power and cooling water temperature as inputs to maintain the optimum tuning condition with sufficient accuracy. The newly acquired Dimtel iGp12 processor box is central to the HOM frequency measurements.

INTRODUCTION

Experience at the Advanced Photon Source (APS) storage ring has indicated that the monopole high-order mode (HOM) frequencies of the sixteen 352-MHz accelerating rf cavities, rather than drifting randomly with time by unknown causes, actually follow a reproducible function of cavity temperature. The temperature of a cavity, in turn, depends on two primary operational parameters, namely cooling water temperature and power absorbed into the cavity wall, both of which are well controlled. This leads to the idea mentioned in [1] that if the frequencies of the relevant HOMs and their dependence on temperature are determined precisely enough, then the multi-bunch stability of the beam in the APS Upgrade (APS-U) ring can be assessed immediately. This is particularly important because the new rf frequency of APS-U will be 110 kHz higher than in APS, changing the set of problematic HOMs. Cavity temperature settings that optimize HOM placement, which we call "smart" tuning, can be known in advance of the APS-U beam commissioning. Even though a longitudinal feedback system will cure multi-bunch instabilities, any mitigation of instability growth rate will help.

This paper will present the HOMs that have been characterized so far, and the thermal model of the HOM frequency change.

First we review the motivation for temperature tuning the cavities. Figure 1 show the spectrum of the APS cavity monopole HOMs from an URMEL model along with curves comparing the longitudinal instability thresholds for APS and APS-U. The thresholds are calculated from the simple formula of longitudinal growth rate assuming one HOM in resonance. There are a total of 96 HOMs from different cavities, some of which will certainly overlap to produce higher growth rates when cavity temperatures have no particular setting. For the APS-U an additional assumption is that the high-harmonic cavity (HHC) is off. With HHC turned on the growth increases by factor 2-3 and the threshold will drop proportionately, a worsening of the situation.

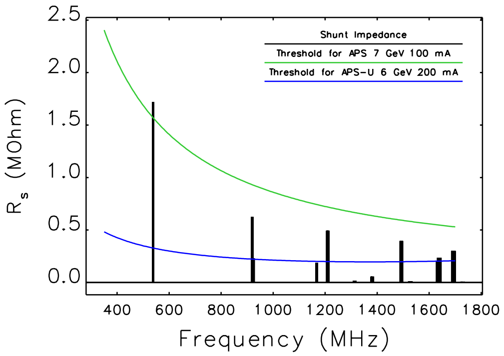

Figure 1: Thresholds of longitudinal instability for APS and APS-U.

MODELING OF HOM FREQUENCY

Each of the APS cavities have slightly different dimensions of its central body segment for the purpose of spreading the HOM frequencies. The spread varies with the particular HOM family and is typically 10 MHz. These HOM frequencies can be measured from cavity antenna probes with a spectrum analyzer reading revolution harmonic lines from a single-bunch stored beam. The resolution is only 271 kHz resolution, but is useful information when combined with beam mode detection with the iGp12 mentioned later, resulting in a very good picture of the HOM spectrum.

The frequency of the HOM proved to be very reproducible with temperature. The cavity temperatures correlated with just two other physical parameters, the cooling water circuit and the cavity power probe signal.

Reference [1] puts forth a thermal model of HOM frequency that change with cavity temperature along with a

---

* Work supported by the U.S. Department of Energy, Office of Science, Office of Basic Energy Sciences, under Contract No. DE-AC02-06CH11357.

† lemery@anl.gov

CONTINUOUS MONITORING OF SPECTRAL FEATURES OF ELECTRON BEAM ORBIT MOTION AT NSLS-II*

B. Podobedov[†], A.A. Derbenev, K. Ha, T.V. Shaftan,
Brookhaven National Laboratory, Upton, NY 11973

Abstract

NSLS-II ring is equipped with state-of-the art beam position monitors (BPMs) which are indispensable in all aspects of machine studies and operations. Among other data, they can provide, on demand, up to 10 seconds of fast-acquisition (FA) data, sampled at ~10 kHz. Analysis of these data in time, frequency and spatial domains provides valuable insights into orbit stability, locations of residual noise sources, performance of feedback systems, etc. In addition, changes in FA signal spectral features are often the earliest indicators of potential equipment problems. This is why we recently implemented an Input / Output Controller (IOC) software that runs during regular user operation, and, once a minute, acquires 10 second buffers of FA data from 180 BPMs around the ring. These buffers are processed to determine the amplitudes and frequencies of the strongest spectral peaks as well as some other measures of fast beam orbit noise. Processed results can be monitored in real time and are also archived for offline analysis and troubleshooting. In this paper we discuss the implementation of this system and the insights we gained from it over about two years of operations.

INTRODUCTION

NSLS-II is the latest third-generation light source in the United States, located at Brookhaven National Laboratory [1,2]. Since the storage ring commissioning in 2014, the stored beam current for routine user operation was gradually raised to 400 mA, with top off injection. Because beam stability is of paramount importance for the users, from the very beginning of NSLS-II meticulous attention was paid to all aspects of machine design and operation that have potential impact on beam stability. State-of-the-art RF BPM receivers were designed and built in-house [3,4] to provide the capability to monitor beam orbit with unprecedented resolution. Among other data streams, BPMs provide 10-kHz sampled orbit FA data to another state-of-the art system, Fast Orbit Feedback (FOFB) [5], which currently suppresses orbit noise up to 200 Hz to the level below 10% of the beam size in the vertical and ~1 % in the horizontal plane. Together with other active stabilization systems, such as RF-frequency feedback [2] and local bump agent [6], FOFB also maintains long-term drifts at the ID source points at the few micron / few microradian peak-to-peak over a 24-hour period.

While monitoring long-term orbit drifts is conceptually simple (10-Hz data from all BPMs are routinely archived), the case of fast orbit motions is not straightforward. First of all, FA data rates all but prohibit efficient archiving. Second, the sheer volume of data calls for some automated data processing, which extracts some key stability metrics that are suitable for human analysis. For fast orbit motions, these metrics are most conveniently constructed in the frequency domain, i.e. noise line peak amplitudes and frequencies. Reducing FA data from hundreds of BPMs to a handful of metrics inevitably requires data decimation or averaging in space, frequency or time domains. In this paper we present the solution we arrived at and implemented in the so-called “Orbit Monitor IOC”.

IOC IMPLEMENTATION

Check run current cutoff 300.000
Live current value - must be above cutoff 375.351
Master shutter status - must be 'ENABLE' ENABLE
Operation status - must be 'Operations' Operations
Check run condition based on all above Permitted
Delay, sec 60

Figure 1: Orbit Monitor IOC control menu.

The IOC runs continuously, unless it is disabled (which is uncommon) from the lead Operator console using the control menu shown in Fig.1. However, since the IOC is mainly geared for characterization of fast orbit stability during user operations, it only saves the data when the ring is in operations, shutters are enabled, and the beam current is above certain threshold (typically set at 300 mA). Under these conditions, every minute, all 180 “regular” BPMs are triggered, and a 10-second buffer of synchronized FA data is acquired. The buffer is subsequently converted to the frequency domain, and the resulting spectra are averaged over three groups of BPMs, horizontal dispersive (a total of 60), horizontal non-dispersive (120), and vertical (179). An example of these averaged spectra (PSD) for the horizontal plane is presented in Fig. 2.

Each of the three resulting spectra is then processed by the IOC to find the amplitudes and frequencies of the 10 highest spectral peaks (separated by at least 10 Hz from each other and from zero). The resulting amplitudes and frequencies are written into corresponding EPICS Process Variables (PVs), which could be monitored (alongside any

---

* Work supported by DOE under Contract No. DE-SC0012704.

† boris@bnl.gov

ISBN: 978-3-95450-223-3 ISSN: 2673-7000 doi:10.18429/JACoW-NAPAC2019-WEPLM06

NuMI BEAM MUON MONITOR DATA ANALYSIS AND SIMULATION FOR IMPROVED BEAM MONITORING[*]

Y. Yu[†], P. Snopok, Illinois Institute of Technology, Chicago, IL, USA
A. Wickremasinghe, K. Yonehara, Fermilab, Batavia, IL, USA
A. Bashyal, Oregon State University, OR, USA
T. Rehak, Drexel University, Philadelphia, PA, USA

Abstract

The NuMI muon monitors (MMs) are a very important diagnostic tool for monitoring the stability of the neutrino beam used by the NOvA experiment at Fermilab. The goal of our study is to maintain the quality of the MM signal and to establish the correlations between the neutrino and muon beam profile. This study could also inform the LBNF decision on the beam diagnostic tools. We report on the progress of beam scan data analysis (beam position, spot size, and magnetic horn current scan) and comparison with the simulation outcomes.

NuMI BEAM AT FERMILAB

NOvA uses Fermilab's NuMI neutrino beam [1]. The beam is created by 120 GeV protons from the Main Injector striking a 1.2-m-long graphite and beryllium target. Two magnetic horns focus pions and kaons produced in the target. The focused mesons decay in a 675-m-long decay pipe to produce muons and muon neutrinos. This muon neutrino beam is delivered to neutrino experiments such as NOvA. The layout of the beamline is shown schematically in Fig. 1.

MUON MONITORS

Three muon monitors (MM1, MM2, MM3) are located downstream of the hadron absorber and separated by 12 and 18 m of rock, hence sensitive to muons of different momenta. Each muon monitor consists of a 9×9 array of ionization chambers, see Fig. 2. Each ionization chamber consists of two parallel plate electrodes separated by a 3-mm gap. The chambers are filled with He gas. A typical muon signal on MM1 is shown in Fig. 3.

BEAM SCANS: DATA AND SIMULATION

To understand the behavior of the NuMI beam and be able to predict the effect of the changes in the key beam parameters, multiple beams scans are carried out. The beam position on target, beam spot size, and focusing horn currents are changed in a controlled fashion. The results of such scans (beam horizontal and vertical position scan, horn current scan) are shown in Figs. 4, 5. The two left plots in Fig. 5 show the change in the horizontal position of the proton beam on target (top) and the change in the position of the horizontal centroid of the beam on the three muon monitors (bottom). Similarly, the two right plots show the change in the vertical position of the proton beam on target and the change of the vertical centroid of the beam on the muon monitors.

Beam scans demonstrate that each MM responds to beam position and horn current variation. Consolidated diagnostic plots similar to the beam scan plots will be eventually incorporated in the NOvA shifter routine to monitor the MM data.

The results of the simulations using the g4numi software package and reproducing the beam position and horn current scans are shown to be consistent with the data. One example of such an analysis is illustrated in Fig. 6. As can be seen from the graph, the centroids of the muon beam on MM1 and MM3 have the opposite slopes as a function of the beam

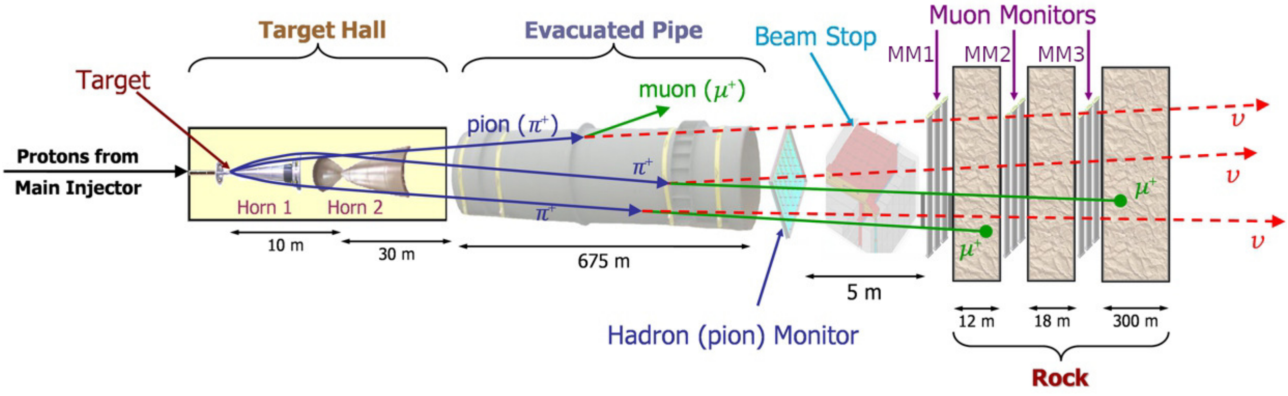

Figure 1: Schematics of the NuMI beamline.

---

[*] Work supported by Fermilab Research Alliance, LLC under contract No. DE-AC02-07CH11359 and US DOE grants No. DE-SC019264 and DE-SC0017815

[†] yyu79@hawk.iit.edu

LOW LEVEL RF TEST SYSTEM FOR THE COMPACT X-RAY LIGHT SOURCE AT ARIZONA STATE UNIVERSITY

H.S. Marks †, W.S. Graves, M.R. Holl, L.E. Malin, Arizona State University, Tempe, AZ, USA

Abstract

A compact femtosecond X-Ray Light Source (CXLS) for time-resolved scientific and medical studies is being constructed at Arizona State University. The CXLS X-rays will be generated by the inverse Compton scattering (ICS) collision of 200 mJ, 1 ps, IR laser pulses with 300 fs electron bunches with energy up to 35 MeV. The electron beam is accelerated via a photoinjector and three standing-wave 20-cell linac sections driven by two klystrons delivering up to 6 MW 1 µs pulses at 9.3 GHz with a pulse repetition rate of 1 kHz. For initial testing of the CXLS klystrons a hybrid digital-analog low-level RF (LLRF) driver has been developed which allows for inter-pulse phase and amplitude corrections based on feedback from waveguide-couplers. The micro-controller based system can also be programmed to adjust continuously in advance of predictable drifts.

INTRODUCTION

The CXLS being constructed at Arizona State University is the first stage of a multi-year plan which will culminate with the world's first truly compact x-ray free electron laser (CXFEL). Generating x-rays via ICS the CXLS will be an incoherent source of ~10^8 photons per interaction of a relativistic electron bunch and an IR laser at 1 kHz. Here we report on development of the LLRF system, whose purpose is to both provide the initial drive signals which are amplified by two klystrons, before being fed into the RF-cavities to accelerate the electron beam, and to receive feedback from different points in the beamline to enable control to ensure the correct phase and power relationships are maintained between the different accelerating sections. The LLRF system presented here produces 700 ns pulses of 9.3 GHz RF that are amplified to 10 W by an X-band solid-state power amplifier (SSPA) (Microwave Amps, Ltd., AM73-06-001RB) and then up to 6 MW by the klystron (L3 Electron Devices, model L6145) powered by a modulator (ScandiNova, model K100). CXLS is powered by two modulator/klystron systems. Klystron 1 drives 2 RF structures. The first is a 4.5 cell photoinjector [1] accelerating the beam to 4 MeV. Electrons are generated at the photocathode using a UV laser which also triggers the ICS IR-laser. Klystron 1 also powers the first linear accelerator (Linac L1), a 0.35 m, 20 cell, standing wave RF-cavity [2] which is capable of accelerating the e-beam from 4 to 12 MeV. A second set of two linacs (L2 and L3) similar to L1 are powered by Klystron 2 resulting in a final beam energy of 35 MeV.

The LLRF system described here will be upgraded to a fully digital system based on the LCLS upgrade [3] in collaboration with SLAC.

RF DRIVE CONTROL

The modulation scheme employed in the test-LLRF control system is Amplitude/Phase, as opposed to I/Q or Direct Digital Synthesis [4]. That is, our seed signal proceeds in series through electronic components which in turn modulate as required the amplitude and phase in response to feedback. The main controls element are microcontroller chips which are pre-programmed to run in a number of different control modes. This is in contrast to say systems controlled by Labview and commercial PXI systems [5] or ultra-fast FPGA based systems on more complex machines such as that for the International Linear Collider [6].

Seed Signals

The LLRF system provides the 9.3 GHz seed signal for the klystrons, which amplify these signals and fill the accelerating cavities. The initial 9.3 GHz driving master oscillator (MO) signal comes from a Wenzel Golden-Frequency Source which provides outputs at 76.65625 MHz, 2.325 GHz, 6.975 GHz, and 9.3 GHz.

The greatest noise beyond the carrier of the 9.3 GHz channel of the MO from 10 MHz to 13 GHz, are two sidebands at -81 dBc, their origin likely mixing with the 76.66 MHz frequency. The next highest noise peak -91 dBc, is at 6975 MHz, leaked from one of the other channels. The phase noise of the 9.3 GHz driving signal is shown in Fig. 1, the signal has single-sideband noise figures of, -116, -122, -126, and -136 dBc/Hz, at 1, 10, 100, and 1000 kHz.

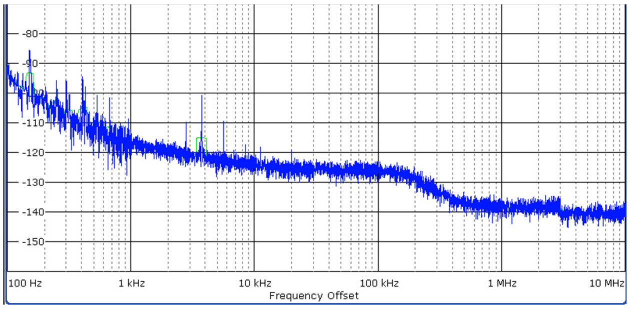

Figure 1: Single sideband phase noise plot of the 9.3 GHz seed signal.

Most of the noise seen in the plot of Fig. 1 is likely of mechanical/acoustic origin that has been mixed up to the carrier frequency. That the origin is most likely vibrational can be demonstrated simply. In Fig. 2 the spectrum around the carrier has been plotted with a 3.7 kHz tone from a laptop speaker either on or off. One way to overcome some of the microphonic disturbances is with piezoelectric devices in a feedback loop [7].

---

† hsmarks@asu.edu

CLOSED LOOP MODELING OF THE APS-U ORBIT FEEDBACK SYSTEM*

P. Kallakuri†, J. Carwardine, A. Brill, and N. Sereno
Argonne National Lab, Lemont, USA

Abstract

Orbit stabilization to 10% of the expected small beam sizes for Advanced Photon Source Upgrade (APS-U) requires pushing the state of the art in fast orbit feedback (FOFB) control, both in the spatial domain and in dynamical performance. We are building a Matlab/Simulink fast orbit feedback system model to guide decisions about APS-U fast orbit feedback system implementation and to provide a test bench for optimal-control methodologies and orbit correction algorithms applicable to the APS-U. A transfer function model was built from open-loop frequency-response and step-response measurements of the present APS and subsequently validated against closed-loop measurements. A corresponding model for APS-U fast orbit feedback was generated by substituting measured responses of APS-U prototype corrector magnets and power supplies into this same model. Stabilizing PID gains are designed using model, and simulated dynamic performance of the new controller is validated through experiments.

INTRODUCTION

A new orbit feedback system is under development for the APS Upgrade, where the expected beam sizes are 13 μm and 2.8 μm for horizontal and vertical planes respectively. This new system will use a distributed array of DSPs to compute orbit corrections at 22.6 kHz (12x faster than the present system) and a matrix of 560 bpms and 160 correctors. The target unity-gain bandwidth is 1 kHz. Orbit stability requirements for the upgrade are considerably more stringent than the present APS where the regulator uses just the integral term (K_i) of a classical PID, and is tuned for minimum residual broad-band rms orbit motion [1]. A higher K_i than optimal gives better attenuation at lower frequencies but comes at the expense of amplifying residual motion at higher frequencies. Also, once the correctable modes have been reduced below the level of the noise floor, there is little to be gained from further increasing K_i gain. We need to investigate control design methods (beyond classical PID tuning) in advanced control theory that are applicable to electron beam stabilization to learn the performance benefits.

We are building a Matlab/Simulink fast orbit feedback system model to provide a test bench for optimal-control methodologies and orbit correction algorithms. First step is to model the open loop dynamics of the prototype feedback system developed in APS Sector 27/28 for beam stability studies [2]. This system uses present storage ring corrector magnets. The modeling results are tested and validated against this prototype before developing the predictive model for APS-U [3]. Next step is to develop a closed loop model using estimated dynamics and accelerator response matrix, and validate model performance with measurements. Since the model application in our case is to use it for control design, it is important to verify how close our model based controller design results match the actual system performance. We design PID gains for stabilizing the model and compare the predicted performance with designed gains against measurements.

FAST ORBIT FEEDBACK SYSTEM CLOSED LOOP MODEL

Layout of the closed loop Fast Orbit FeedBack (FOFB) dynamic model developed in matlab/simulink is shown in Fig. 1. Main components included are open loop dynamic model, spatial response matrix, and DSP controller schematic. Significant elements of the controller model are IRM, and the regulator with LPF, HPF and digital PID controller. Four input - Four output closed loop configuration (4 fast correctors to 4 P0 bpms in S27/28) is used for results shown in this paper. Open-loop dynamic model $H[z]$ is estimated using beam based time and frequency measurements (system identification process is detailed in [3]). It includes the dynamics of the power supply, magnet, vacuum chamber and bpms. Based on a-priori knowledge of the physical components, $H[z]$ is separated into 2 components. Transfer function of the present corrector magnet with vacuum chamber $H_M[z]$, and rest of the open loop dynamics $H_1[z]$ (dominated by power supply).

$$H[z] = H_1[z] \cdot H_M[z] \qquad (1)$$

$$\begin{aligned} H_M[z] &= \frac{-0.000112(1-14.78z^{-1})(1-0.97z^{-1})}{(1-0.73z^{-1})(1-0.98z^{-1})(1-0.82z^{-1}+0.40z^{-2})} \\ H_1[z] &= \frac{(1+2.11z^{-1}+6.12z^{-2})}{(1+0.75z^{-1}+0.36z^{-2})} \end{aligned}$$

Time Domain Response Validation

The closed loop model is first validated by comparing the model step responses against measurements with integral gain (K_i). Step bump of 50 μm is given to BPM set points of 2 P0 bpms using AFG 1, output measured is *BPM Readback* signal. Model responses are in good agreement with measurements in both planes, horizontal response comparisons are as shown in Fig. 2. Measured horizontal BPM response has small perturbation in steady state which is not present in

---

[*] Work supported by the U.S. Department of Energy, Office of Science, under Contract No. DE-ACO2-O6CH11357.

[†] pkallakuri@anl.gov

ISBN: 978-3-95450-223-3 ISSN: 2673-7000 doi:10.18429/JACoW-NAPAC2019-WEPLM13

MULTIPACTOR ELECTRON CLOUD ANALYSIS IN A 17 GHz STANDING WAVE ACCELERATOR CAVITY*

H. Xu†, M.A. Shapiro, R.J. Temkin, Massachusetts Institute of Technology, Cambridge, MA, USA

Abstract

Theoretical predictions of single-surface one-point multipactor modes have been confirmed in experiments with a 17 GHz standing wave single cell disk-loaded waveguide accelerator structure operating in the gradient range of 45-90 MV/m. Theoretical calculations were performed of the frequency detuning introduced by the multipactor electron cloud on the cell side wall for different electron cloud thicknesses and densities. We found that the detuning ($\Delta\omega/\omega$) due to the electron cloud was too small to cause significant power reflection in room temperature copper cavities, but may be significant in cavities cooled to cryogenic temperatures. A similar cavity design with the central cell taking an elliptical axial profile was tested under high power, and the results showed that the multipactor modes observed previously in a cell with a straight axial profile were eliminated under this elliptical design. We used a dc-biased current monitor to study the side dark current energy spectrum, and the result is presented.

INTRODUCTION

Internal dark current refers to the electrons that are generated and then terminated inside an accelerator cavity. It is differentiated from the conventional dark current that exits the accelerator at the upstream or downstream ends. Much information regarding the origin and formation of the internal dark current cannot be retrieved since, as has been observed in multiple particle-in-cell (PIC) simulations, only a small portion of the total dark current generated can eventually exit the accelerator structure and be captured by the Faraday cups upstream or downstream. The study of internal dark current emphasizes on understanding the sources of the dark current, especially those in addition to the field emission, the termination of the dark current inside the accelerator cavity, and the subsequent physical processes that can potentially affect the cavity performance.

Apart from the field emission of electrons at the locations where the metal surface witnesses intense rf electric field, e.g. the irises forming the beam aperture, one important mechanism of dark current generation is multipactor. In one of our previous experiments testing a standing wave single cell disk-loaded waveguide (DLWG) accelerator structure at 17 GHz, we observed two single surface one-point multipactor modes, the $N = 1$ and $N = 2$ modes, on the side wall of the central cell in the acceleration gradient range of 45 MV/m to 90 MV/m [1]. In a recent theoretical study of the dark current inside travelling wave accelerator structures designed for CLIC prototype testing, electron trajectories for multipactor modes were identified at a gradient of 100 MV/m [2].

In our DLWG structure, when the multipactor resonances are excited, CST [3] PIC simulations indicate that a layer of electron cloud is formed over the cylindrical side wall, marking a state of equilibrium by multipactor secondary electron emission and space-charge suppression of the emission. It is of interest to understand the effect of the electron cloud loading inside the accelerator cavity, whether or not this layer of electrons can cause cavity detuning or microwave breakdown. The dependence of these effects on the accelerator operating frequency is also of great interest.

DETUNING BY ELECTRON CLOUD

We consider that the side wall multipactor forms a uniform electron cloud that can be represented by a dielectric layer with thickness l and constant relative permittivity ϵ_r:

$$\epsilon_r = 1 - \frac{\omega_{p,e}^2}{\omega^2} \tag{1}$$

where the electron cloud plasma frequency $\omega_{p,e}$ is calculated from the electron cloud density n_e using $\omega_{p,e}{}^2 = n_e e^2/(\epsilon_0 m_e)$. CST eigenmode solver was used to calculate the resonant frequencies of the accelerator cell loaded with such a dielectric layer. We are interested in the resonant frequency detuning ($\Delta\omega/\omega$) introduced by the electron cloud.

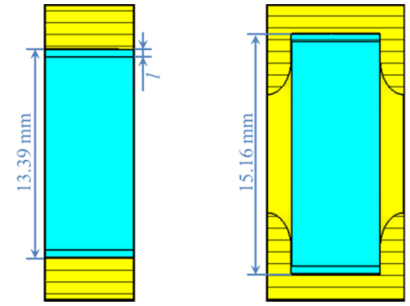

Figure 1: CST eigenmode solver 17.136 GHz models for pillbox TM_{010} mode (left) and the accelerator cavity TM_{01} mode (right) with 180 degree phase advance in the direction of the beam axis between the boundaries (π-mode).

Two types of models were used in the calculation, as shown in Fig. 1. The calculation for the basic case of a pillbox TM_{010} mode serves as the benchmark of the calculation for the realistic accelerator cavity operating at TM_{01} mode and π-mode.

For the pillbox case, the detuning can be given conveniently by the Slater perturbation theorem:

$$\frac{\Delta\omega}{\omega} = \frac{p_{0,1}^2}{3} \cdot \frac{\omega_{p,e}^2}{\omega^2} \cdot \left(\frac{l}{R}\right)^3 \tag{2}$$

where $p_{0,1}$ denotes the first zero point of Bessel function $J_0(x)$, and R the cell radius. The detuning is proportional to

---

* Work supported by the U.S. Department of Energy, Office of High Energy Physics, under Grant No. DE-SC0015566.

† haoranxu@mit.edu

HIGH-QUALITY RESONATORS FOR QUANTUM INFORMATION SYSTEMS

S.V. Kuzikov†, S.P. Antipov, P.V. Avrakhov, E. Gomez
Euclid Techlabs LLC, Bolingbrook, IL, USA
A. Bezryadin, Department of Physics
University of Illinois at Urbana-Champaign, Urbana, IL, USA

Abstract

We analyze ultra-high-quality factor resonators for quantum computer architectures. As qubit operation requires external DC fields, we started our study with a conventional closed copper cavity, which naturally allows external magnetic fields. In order to increase quality factor and to keep DC magnetic field control at a level less than critical field, an open SRF resonator promises much higher quality. The next step resonator is a photonic band gap (PBG) resonator. This resonator allows easy external control for either magnetic or electric field. It consists of a periodic 3D set of sapphire rods assembled between two superconducting plates. The PBG resonator exploits unique properties of the crystalline sapphire. Tangent delta for sapphire in X-band is reported at 10^{-9} - 10^{-10} at 4 K. That is why, the Q-factor of the sapphire PBG resonator can be expected as high as 10 billion at mK temperatures which provides long relaxation times (dephasing etc.). The established PBG design implies obtaining a large Purcell factor, i.e. large ratio of quality to mode volume which is an important parameter to establish strong interaction of a qubit with the cavity mode, rather than RF noise.

INTRODUCTION

Quantum computing is one of the most ambitious goals in modern physics [1]. Many developed concepts of quantum computer architectures imply interaction of qubits with microwave photons. These concepts require high-quality (SRF) resonators [2-5]. A more particular requirement is an opportunity to provide an efficient qubit control, which includes RF field control and DC field control as well. In this paper, we describe two ideas for X-band resonators to be used in Quantum Information Systems (QIS). The first idea involves a normal conducting copper resonator with tunable couplers to be operated at cryogenic temperatures, the second one is a PBG sapphire resonator with SRF end cups.

A COPPER RESONATOR FOR MEISSNER TRANSMON QUBIT

The resonator functions at the TM_{110} mode and has a thin hole in the center for qubit installation (Fig. 1). This resonator design includes two coaxial couplers with tuning bolts, in order to vary the external Q-factor. Figure 2 shows the eigen mode field structure. The couplers have SMA connectors in each of their ends (Fig. 3). In Fig. 4 one can see a photograph of the tested resonator. This resonator was designed for a frequency 8 GHz, so that the intrinsic quality, Q_0, equals 3×10^4 (OFHC cavity, RRR=300, T= 4.2°K).

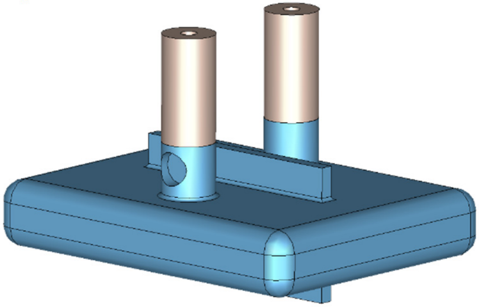

Figure 1: X-band copper resonator for Meissner qubit.

In Table 1, one can see the key parameters and dimensions of the resonator. The external Q-factor could be tuned in a broad band. The mentioned flexibility in tuning range allowed for the testing of various qubits with different sizes, eigen frequencies and insertion losses. The resonator was tested at room temperature, the measured characteristics were in good agreement with calculated ones.

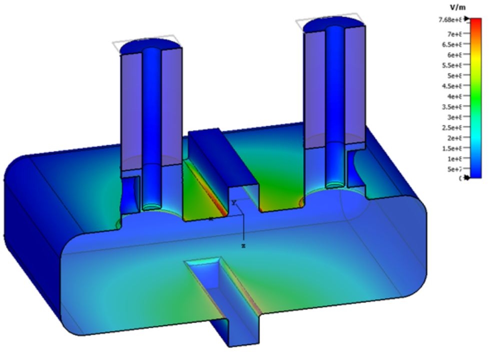

Figure 2: Surface electric field of the eigen mode.

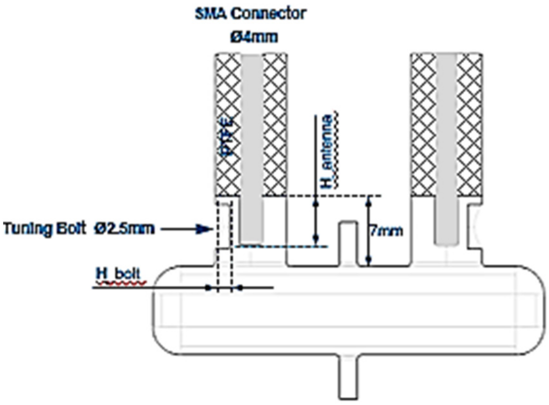

Figure 3: Drawing of X-band copper cavity.

---

† s.kuzikov@euclidtechlabs.com

UPDATED APPLICATIONS OF ADVANCED COMPACT ACCELERATORS

M. Uesaka†, University of Tokyo, Tokyo, Japan

Abstract

We are working for downsizing of RF linacs from room-size to portable and table-top sizes and applying them to medical, industrial and social uses. Recently, we have proposed and designed a new S-band 35 MeV/35 kW linac γ-ray source for ^{99}Mo/^{99m}Tc (γ-emitter for medical diagnosis) production from ^{100}Mo target. Its construction will be finished within two years and the domestic production and even export will start then. The same system can be used for ^{225}Ac (α–emitter for cancer therapy) from ^{226}Ra target. We are proposing making the Mo/^{226}Ra target from nuclear wastes from nuclear power plants and fuel production plants. Next, we have developed portable 950 keV / 3.95 MeV X-band (9.3 GHz) electron linacs to on-site non-destructive inspection of industrial and social infrastructures such as chemical reaction chambers and bridges following the radiation safety law and regulation in Japan. By using the portable 950 keV / 3.95 MeV X-band electron linac based X-ray sources for on-site bridge inspection, we visualize inner reinforcement iron structure. The information of the iron states is used for the structural analysis of a bridge to evaluate its residual strength and sustainability. Table-top micro electron / ion beam sources using laser dielectric accelerating techniques are under development. The beam energy is ~ 1 MeV, the beam size is ~1 µm. We aim to apply them to 3D dynamic observation of radiation-induced DNA damage / repair for basic research of radiation therapy and low dose effect.

INTRODUCTION

We have been continuing developing and operating S-band linacs (35 / 18 MeV, room-size), X-band linacs (9.3 / 11.424 GHz , portable size) and laser accelerator dielectric accelerators (Yb laser of 1 mm, one-table-top size) at Nuclear Professional School, University of Tokyo for these 40 years as shown in Fig. 1.

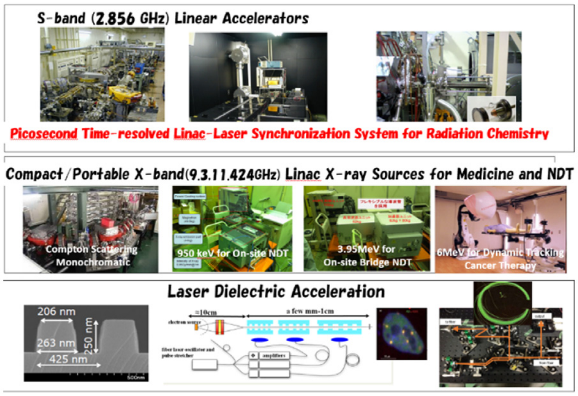

Figure 1: Three-staged downsizing of RF linac at University of Tokyo.

This activity is really three-staged downsizing of RF linac.

S-BAND 35 MEV / 35 KW LINAC FOR MEDICAL RI PRODUCTION

Currently, the medical RI of ^{99}Mo/^{99m}Tc (γ-emitter for medical diagnosis) are produced by 6 research reactors in the world. Three out of the six are aged so that they are planned to be shut-downed within a few years. In Japan we are perfectly import them from the two countries. Since the two reactors are inspected at the same time, almost all supply was suspended last November. Thus, the supply is rather fragile so that we have to solve this problem by using accelerators. There are the two ways to use accelerators, namely cyclotron and electron linac [1]. There must be advantages and drawbacks in the both ways. Then, our group has decided to choose the latter based on the advantage of the overall performance of the system. We have proposed and designed the optimized S-band 35 MeV/35 kW linac γ-ray source for domestic and stable production and supply. About five / fifty systems are estimated to meet the whole demands in Japan and the world, respectively. We have chosen 100 keV thermionic electron gun, buncher system two traveling-wave type acceleration tubes and the 5 MW / 770 Hz clystrons of CANNON E37307. The power of 35 kW is determined based on the consideration of beam loading. The system layout is depicted in Fig. 2. The left / right-hand sides correspond to the linac and Mo target irradiation areas, respectively.

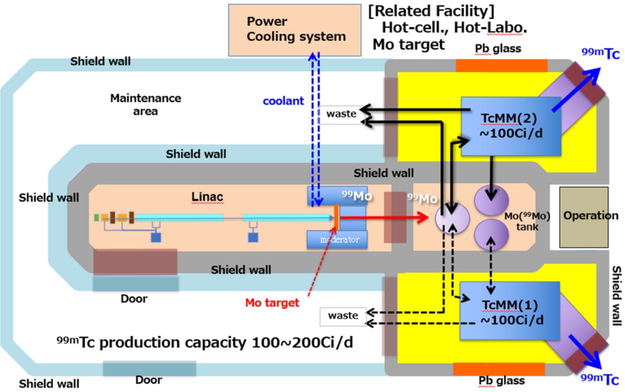

Figure 2: Layout of S-band 35 MeV / 35 kW linac and chemical processing devices for ^{99}Mo /^{99m}Tc.

Although the linac and chemical processing devices become home-made, solid targets of extremely high impurity ^{100}Mo and ^{226}Ra for ^{99}Mo/^{99m}Tc and ^{225}Ac are manufactured by using the centrifuge technique. Now we are proposing an alternative methodology to solve the above issue. We plan to use nuclear wastes from U fuel production and spent fuels in nuclear power generation. We chemically extract Mo of chemically extremely high purity from U mine wastes and ^{226}Ra of extremely high impurity from high

---

† uesaka@tokai.t.u-tokyo.ac.jp

ANALYSIS OF HIGH FIELD Q-SLOPE (HFQS) CAUSES AND DEVELOPMENT OF NEW CHEMICAL POLISHING ACID*

D. Luo†, K. Saito, S.M. Shanab
National Superconducting Cyclotron Laboratory, Michigan State University, East Lansing, MI, USA
E.S. Metzgar, L. Popielarski, G.V. Simpson
Facility for Rare Isotope Beams, Michigan State University, East Lansing, MI, USA
T. Nakajima, I. Nasu, J. Taguchi, Nomura Plating Co, Ltd., Osaka, Japan

Abstract

In our previous studies of High Field Q-slope (HFQS) we have concluded that nitrogen contamination from the nitric acid is the main cause of the degradation of the Q in buffered chemical polished cavities. Our conclusion is made based on previously unresolved phenomena which are found from huge amount of published cavity test data, including fine grain, large grain and single crystal cavities treated with EP and BCP. According to this analysis, we have started developing new nitrogen-free chemical polishing acid. Hydrogen peroxide with HF mixture was reported able to react with Nb, and there's no extra element contamination in it, so we replace the conventional BCP with this mixture to start our study. In this paper, some Nb coupon sample results with new acid will be reported. We completed the first step of developing the new acid and we got the Nb finish roughness no worse than conventional BCP.

INTRODUCTION

Demand for New Acid

For superconducting Nb cavities, chemical polishing or electropolishing (EP) is required to remove defects and the contaminated surface layer. It is an important process that leads to much better performance. One commonly used method – Buffered Chemical Polishing (BCP) – always suffers from cavity High Field Q-slope (HFQS) which seriously limits the cavity performance at high operating field. The other method – EP [1] – can recover the cavity HFQS by an extra 120 °C low temperature baking (LTB) post EP [2]. However, EP is not always applicable to low/medium β cavities because of their complicated shapes. Therefore, a new chemical polishing process is in demand, especially for low/medium β cavities which are used in heavy ion accelerators.

HFQS is the phenomenon where Q_0 (unloaded Q) performance of the SRF cavity begins to drop exponentially when the magnetic field increases beyond 80 - 100 mT (corresponding to an accelerating gradient E_{acc} of 20 - 25 MV/m for ILC elliptical shape cavity [3]). The Q_0 drop is caused by pure heating at RF high magnetic field region (equator area) on the SRF surface [4–6], and it ultimately limits the magnetic field to below 130 mT (E_{acc} is 30 MV/m for ILC elliptical shape cavity).

Low to medium β cavities evolved in many areas and are becoming one of the most widespread types in LINACs. FRIB is an example of a heavy ion accelerator project whose cavities suffer from HFQS. All FRIB cavities are treated with BCP. Statistically, the performance of ~ 35% of the cavities at FRIB is limited by pure HFQS (HFQS without X-rays) [7]. An example is shown in Fig. 1, the FRIB cavities experience Q_0 drop starting from $B_{\mathrm{p}} \sim 85$ mT in $\beta = 0.041$ Quarter Wave Resonators (QWRs).

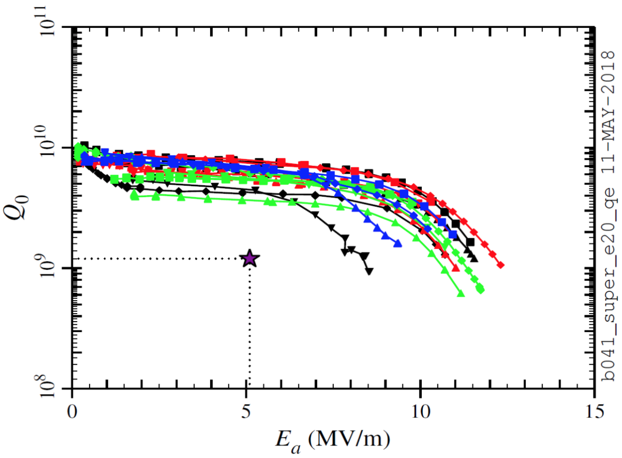

Figure 1: FRIB cavity performance at 2 K in Vertical Test, $\beta = 0.041$ QWRs, $B_{\mathrm{p}}/E_{\mathrm{acc}} = 10.71$ [mT/(MV/m)].

Alternative Acid Treatment

It is highly probable from our recent analysis that the HFQS under BCP arises from nitrogen contamination, which is introduced by nitric acid in the commonly used BCP acid. Thus, the replacement of the nitric acid by an alternative is a promising way to mitigate this issue. For this purpose, past experiment results that are relevant to this study are summarized as follows [8]:

1. If nitric acid (1500ppm) is added to EP, subsequent LTB can no longer always eliminate the HFQS [9].
2. BCP HFQS has a deep memory effect which cannot be explained only by surface smoothness changes [1, 8].
3. Large grain/single crystal cavities have very smooth surface after etching by BCP ($R_z \sim 0.2$ µm), but their

---

* Work supported by the U.S. DOE Office of Science under Cooperative Agreement DE-SC0000661 and the NSF under Grant No. PHY-1565546.

† Luo@frib.msu.edu

ISBN: 978-3-95450-223-3 ISSN: 2673-7000 doi:10.18429/JACoW-NAPAC2019-WEPLM49

NEW RF SYSTEM FOR FIRST DRIFT TUBE LINAC CAVITY AT LANSCE*

J.T.M. Lyles[†], R.E. Bratton, G. Roybal, M. Sanchez Barrueta, G.M. Sandoval, D.J. Vigil, J.E. Zane,
Los Alamos National Laboratory, Los Alamos, NM, USA

Abstract

From 2014-2016, the three highest power 201 MHz power amplifier (PA) systems were replaced at the Los Alamos Neutron Science Center 100 MeV DTL. The initial DTL cavity provides 4.25 MeV of energy gain and has been powered by a Photonis (RCA) 4616 tetrode driving a 7835 triode PA for over 30 years. It consumes 110 kW of electrical power for tube filaments, power supplies and anode modulator. The modulator is not required with modern tetrode linear amplifiers. In 2020 we plan to replace this obsolete 6 tube transmitter with a design using a single tetrode PA stage without anode modulator, and a 20 kW solid-state driver stage. This transmitter needs to produce less than 400 kW, and will use a coaxial circulator. Cooling water demand will reduce from 260 to 70 gal/min of pure water. High voltage DC power comes from the same power supply/capacitor bank that supplied the old system. The old low-level RF controls will be replaced with digital LLRF with learning capability for feedforward control, I/Q signal processing, and PI feedback. All high-power components have been assembled in a complete mock-up system for extended testing. Installation of the new RF system is to begin in January of 2020.

PRESENT RF POWER SYSTEM

Since LANSCE (and LAMPF before that) was commissioned in 1972, the 201.25 MHz RF PAs used a triode vacuum tube, the 7835 developed in 1958 by RCA. This was similar to the RF amplifiers for injector linacs at Fermilab and at Brookhaven National Laboratory. Amplitude modulation for pulse formation and for field (gradient) regulation was provided with a HV modulator consisting of a chain of pulse amplifiers using four more tubes. Another RF tube, a Photonis (RCA) 4616 tetrode, was incorporated as a driver for the triode. Low level rf control used a split function analog system, where the large pulse modulator controlled the RF amplitude, with an electronic phase shifter inserted before the power amplifiers for phase modulation. Installation of new RF amplifiers using high power tetrodes (Diacrodes®) was completed for DTL cavities 2-4 in 2016 [1]. At this time, digital low level (dLLRF) controls were installed for those systems. The new RF amplifiers are linear, like solid state PAs (SSPA) and IOTs, and use I/Q low level RF control topology. This simplified the design of the amplifier systems and reduced the number of tubes used by 50%, with only two types remaining.

The first DTL cavity at LANSCE continues to operate using the old RF amplifier cascade (Fig. 1) operating with reduced voltages. It was not replaced in the earlier upgrade. This RF system continues operating using old components remaining from the prior upgrades. This “orphan” amplifier system has several lingering problems for long-term sustainability. The working condition of legacy spare tubes is uncertain except for recorded hours of service. The high-power test set was removed in 2017 to make space for other projects. The triode amplifier requires over 18 hours for a tube change. Finally, this RF amplifier cascade continues to operate using the split-function analog LLRF and lacks the advanced capabilities of dLLRF. Reduced bandwidth of the anode modulator limits the effectiveness of LLRF controls in this system, affecting beam quality throughout LANSCE.

Figure 1: Legacy triode and tetrode RF amplifiers.

REPLACEMENT RF SYSTEM

Amplifiers

The block diagram in Fig. 2 represents the new chain of amplifiers with a circulator for DTL cavity 1.

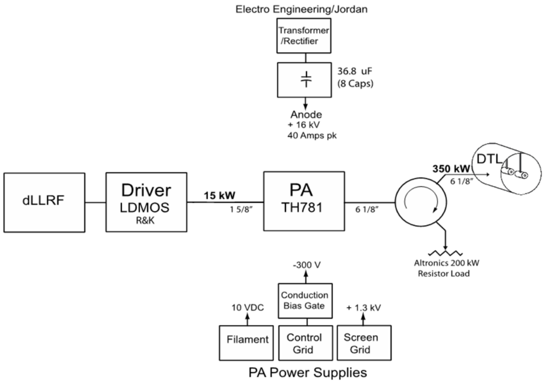

Figure 2: New RF amplifiers: SSPA and tetrode stage.

In 2004, the first TH781 tetrode and a matching Thales cavity amplifier were tested up to 510 kW at 20% DF [2]. This pushed the amplifier and tube beyond the manufacturers recommendations but proved that there was sufficient headroom. Typical power at module 1 (with beam) has

---

* Work supported by the United States Department of Energy, National Nuclear Security Agency, under contract 89233218CNA000001

† jtml@lanl.gov

BEAM DRIVEN BIMODAL CAVITY STRUCTURE FOR HIGH GRADIENT ACCELERATION*

X. Chang[1,†], J. L. Hirshfeld[1,2], Y. Jiang[1], S. V. Shchelkunov[1]
[1]Yale University, New Haven, CT, USA ; [2]Omega-P R&D, Inc., New Haven, CT, USA

Abstract

Research aiming to increase the RF breakdown threshold in electron/positron accelerators is being conducted at the Yale University Beam Physics Laboratory. Our two-beam accelerator approach employs a beam driven bimodal cavity structure. This cavity includes (i) two modes excited by the drive beam, with the higher mode frequency three times that of the fundamental TM010 mode; (ii) a low-current accelerated beam and high-current drive beam traversing the same cavity structure. This approach has the potential advantages of (a) operating at higher acceleration gradient with lower breakdown and pulsed heating rates than that of a single-mode cavity structure at the same acceleration gradient, due to the spatiotemporal field distribution properties in the bimodal cavities; and (b) obtaining high accelerating gradient with a low energy drive beam. Recent progress in simulations and work towards an experimental test stand are presented.

INTRODUCTION

Surface RF pulsed heating is considered as one of the major causes of RF breakdown which limits the acceleration gradient to be less than about 150 MV/m in conventional metallic X-band accelerator structures. A higher breakdown threshold would be desirable for a multi-TeV machine. One novel cavity design we proposed for this application is the electron beam driven bimodal cavity structure, using a superposition of multi-harmonic modes to suppress pulsed heating and RF breakdown [1-4].

The RF electromagnetic field distributions in a multi-harmonic cavity with fundamental TM-010 mode and its 3rd harmonic TM-012 mode are shown in Fig. 1. Its RF properties and features in RF breakdown suppression is described in Refs. [3-4]. The superposition of fields from these two modes introduces a possible mechanism to suppress RF breakdown.

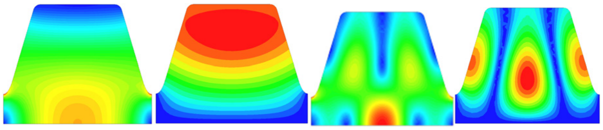

(a) (b) (c) (d)

Figure 1: (a) Bimodal cavity electric and (b) magnetic field distributions for TM010 mode; (c) electric and (d) magnetic field distributions of its 3rd harmonic TM012 mode.

Our drive beam test stand under development to test bimodal cavities has a maximum beam energy of 500 keV. Consequentially, drive beam particles would be reflected at sufficiently high field gradient in the test cavity were both beams to move collinearly. Therefore our design has the drive and test beams not moving collinearly, even as the beams are essentially in the same composite cavity. This approach allows evaluation of RF breakdown results predicted by our theory as would apply to collinear beams in a bimodal cavity with a higher energy drive beam that would not experience particle reflections.

EXPERIMENTAL DESIGN AND SIMULATION

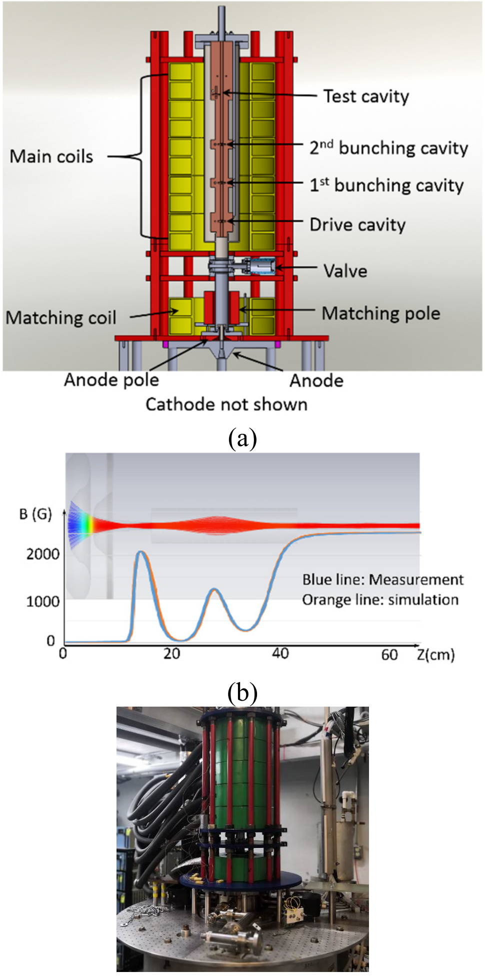

(a)

(b)

(c)

Figure 2: (a) Engineering design of the test stand setup. (b) End-to-end tracking simulation of beam and magnetic field distribution along axis. (c) Assembled test stand, showing magnetic system on top of 500kV/218A gun tank.

---

* Supported by US National Science Foundation, Award #1632588.
† xychang6666@gmail.com

North American Particle Acc. Conf. NAPAC2019, Lansing, MI, USA JACoW Publishing
ISBN: 978-3-95450-223-3 ISSN: 2673-7000 doi:10.18429/JACoW-NAPAC2019-WEPLM51

Ka-BAND HIGH POWER HARMONIC AMPLIFIER FOR BUNCH PHASE-SPACE LINEARIZATION*

X. Chang†,[1], J. L. Hirshfield[1,2], Y. Jiang[1], S. V. Shchelkunov[1],
[1]Yale University, New Haven, CT, USA; [2]Omega-P R&D, Inc., New Haven, CT, USA

Abstract

A future European light source CompactLight is being proposed to extend FEL operation further into the x-ray region than other light sources by using a linac operating at X-band (12 GHz) with a short Ka-band (36 GHz) section for linearizing bunch phase space. The Ka-band system requires a high-power RF amplifier, synchronized with the main X-band source. We report here on design of a third-harmonic klystron amplifier for this application. Our design employs a four-cavity system with a multi-cell extended interaction output cavity. Initial simulation results indicate that more than 10 MW of 36-GHz power can be obtained with an efficiency exceeding 20%, and with 12-GHz drive power of 30 W. A preliminary design for a proof-of-principal experimental test of this concept is described.

INTRODUCTION

European scientists are proposing an advanced light source CompactLight [1] which aims to extend FEL operation into the hard X-ray region and thus beyond present state-of-the-art. CompactLight is to employ advanced concepts for bright electron photo injectors, high-gradient X-band structures at 12 GHz, and innovative compact short-period undulators. The proposed facility will enjoy lower electrical power demand and a smaller footprint than would a comparable C- or S-band system.

To correct the longitudinal phase space non-linearity as arises in the X-band (12 GHz) linac, a Ka-band, third-harmonic (36 GHz) short linac is proposed, which requires a high RF power source, of the order of 10 MW [2]. Such a power level is generally achieved using a klystron, but is difficult to realize at Ka-band. A main reason is that a large diameter beam pipe is required to transport a high current beam, so spurious modes could easily be excited in the beam pipe. Furthermore, the radius of TM010 mode Ka-band cavities (4.7 mm) is comparable to the beam pipe radius; this lowers beam transit time factors significantly due to field leakage from the cavities into the beam pipe.

The Yale University Beam Physics Lab operates a pulsed electron gun and associated DTI Marx-band modulator, with a peak voltage and current of 500 kV and 218 A, as pictured in Fig.1. We present here a preliminary design for a klystron amplifier that employs this gun and embodies an X-band bunching system and a third-harmonic Ka-band output cavity to supply a total output power of more than 10 MW for initial tests of the CompactLight Ka-band linac.

Figure 1: 500 kV, 218 A electron gun tank (at left) connected to the 500 kV, 250 A Marx modulator (at right) in the Beam Physics Lab at Yale University.

3RD HARMONIC KLYSTRON DESIGN AND SIMULATION

A design of the test stand for a related experiment (beam driven bimodal cavity [3] for raising acceleration gradient) has been realized, as shown in Fig. 2. The design for the 3rd harmonic klystron we are proposing is similar to that: it embodies a beam matching system, X-band bunching cavities, output cavity, and magnetic field system. The main differences are that the main magnetic field is taken to be 3.0 kG instead of 2.3 kG; and the frequencies of the drive and bunching cavities are 12 and 36 GHz instead of 11.424 and 34.272 GHz.

Beam tracking simulations indicate that a 500 keV, 218 A beam can be confined within a 6 mm diameter pipe with a solenoid magnetic field of 2.3 kG or higher, as shown in Fig. 2(b). We designed our klystron with a conservative beam voltage of 350 kV, with a corresponding current of our 0.62 μperv gun of 128 A. With a 3.0 kG magnetic field, the beam can be compressed to propagate within a 5.5 mm diameter beam pipe.

The bunching cavities and output cavity are designed to be in two split copper pieces for suppressing excitation of spurious modes, simplified machining, avoiding brazing, and tuning, as shown in Fig. 3. For the 5.5 mm diameter beam pipe, the cutoff frequency for the TM010 mode is 41.7 GHz, so a 36 GHz TM010 mode cannot propagate in the pipe. The distances between the drive cavity and first bunching cavity, and between the two bunching cavities, are 10 cm; while the distance between the 2nd bunching cavity and the output cavity is 7 cm.

---

* Supported by USA National Science Foundation, Award #1632588

† xychang6666@gmail.com

ISBN: 978-3-95450-223-3 ISSN: 2673-7000 doi:10.18429/JACoW-NAPAC2019-WEPLM52

RECENT DEVELOPMENTS OF Nb_3Sn AT JEFFERSON LAB FOR SRF ACCELERATOR APPLICATION*

U. Pudasaini[1]†, G. Eremeev[2]#, M. J. Kelley[1,2], C. E. Reece[2]
[1]Applied Science Department, The College of William and Mary, Williamsburg, VA, USA
[2]Thomas Jefferson National Accelerator Facility, Newport News, VA, USA

Abstract

The desire to reduce the construction and operating costs of future SRF accelerators motivates the search for alternative, higher-performing materials. Nb_3Sn (T_c ~ 18.3 K and H_{sh} ~ 425 mT) is the front runner. However, tests of early Nb_3Sn-coated cavities encountered strong Q-slopes limiting the performance. Learnings from studies of coated materials related to cavity performance prompted significant changes to the coating process. It is now possible to routinely produce slope-free single-cell cavities having $Q_0 \geq 2\times10^{10}$ at 4 K and $> 4\times10^{10}$ at 2 K up to the accelerating gradient in excess of 15 MV/m at its best. Obtaining similar results in five-cell cavities is a current goal to test them under an accelerator environment. This contribution discusses recent developments at Jefferson Lab.

INTRODUCTION

Nb_3Sn (T_c ~ 18.3 K and H_{sh} ~ 425 mT) is a prospective alternative material to replace Nb (T_c ~ 9.2 K and H_{sh} ~ 220 mT) in SRF cavities [1]. It promises more powerful, economical, and simplified SRF accelerators. Its potential for SRF accelerators was recognized early, and it has been researched since the 1970s. Because of extreme brittleness and low thermal conductivity, Nb_3Sn can be used only as a thin-film or coating. So far, the most successful technique that can deposit Nb_3Sn coating on the interior surface of a cavity is vapor diffusion. The basic premise is to create tin vapor and transport it to the interior surface of a Nb-cavity at about 1200 °C, where Nb_3Sn exclusively forms. The process was adopted at JLab in 2012 with the Nb_3Sn deposition system, which was designed to coat 1.3-1.5 GHz single-cell cavities [2]. Several single-cell cavities were coated and tested. They consistently attained quality factors (Q_0) as high as $> 1\times10^{10}$ at 4 K at low field, but the maximum gradient was limited by a precipitous Q-slope. The slope was very similar to the "Wuppertal-slope," seen in early cavities coated there. Although [3] several laboratories reported the Wuppertal-slope, its origin is still not known completely. Researchers here pointed to Ti contamination of the Nb_3Sn layer from Ti-parts residing inside the deposition chamber during the coating process. Almost all cavities at that point had Nb-Ti flanges, known to contaminate the Nb_3Sn layer [4, 5]. The issue was addressed during the recent upgrade of the coating system to allow a multi-cell (CEBAF 5-cell) cavity coating. We were now able to produce almost a Q-slope free Nb_3Sn cavity for the first time, but Q was below 1×10^{10} at 2 K [6]. Since then, several single-cell and 5-cell cavities were systematically coated and tested. This paper presents results from recent cavities coated here and gives an overview of Nb_3Sn development.

SINGLE-CELL CAVITY COATINGS

Following the coating system upgrade, several new (all niobium) cavities were added to the Nb_3Sn program in hope of avoiding the strong Q-slope by adopting a Ti-free coating protocol. Though the first cavity coated after the coating system upgrade was a success, several cavities coated afterward exhibited typical Q-slopes (Fig. 3). The witness samples coated with each of those cavities were analyzed with SEM/EDS revealing several issues. Although the coating was excellently uniform, the coated surface appeared to have nano-residues of Sn at the surface, Fig. 1, possibly contributed to the Q-slope which we observed in several cavity coatings. Those residues were believed to be the result of Sn-vapor condensation at the end of the coating process.

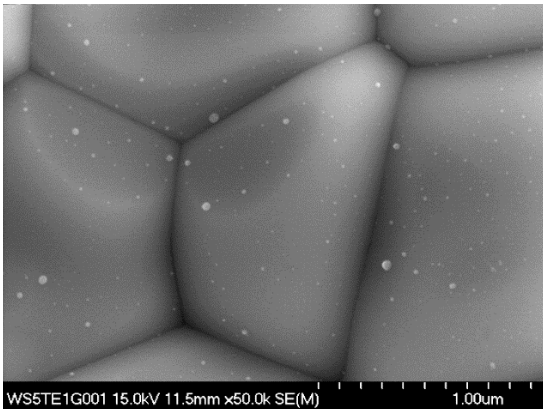

Figure 1: SEM image showing Sn nano-residues observed in a witness sample coated with a single-cell cavity. The bright circular features are Sn residues. EDS examination of larger residue showed that these features are Sn-rich.

Some cavities that have visible non-uniformity, as shown in Fig. 2 [right], usually had Q-slopes. Analysis of corresponding witness samples often showed patchy regions, e.g., Fig. 2 [left], which are thin film regions in the Nb_3Sn coating. They are often attributed to low tin flux during the coating. It indicates that an undersupply (or oversupply) of Sn during the process can lead to patchy

---

*Partially authored by Jefferson Science Associates under contract no. DEAC0506OR23177. This material is based upon work supported by the U.S. Department of Energy, Office of Science, Office of Nuclear Physics.
†uttar@jlab.org
#Presently at Fermilab.

ISBN: 978-3-95450-223-3 ISSN: 2673-7000 doi:10.18429/JACoW-NAPAC2019-WEPLM53

50 kW CW MULTI-BEAM KLYSTRON*

S. V. Shchelkunov[†,1], J. L. Hirshfield[1], V. E. Teryaev,
Omega-P R&D, Inc.,New Haven, CT, USA
[1]also at Yale University, New Haven,CT, USA

Abstract

This klystron has been designed to deliver 50 kW CW at 952.6 MHz and to serve as a microwave power source for ion acceleration in the Electron Ion Collider (EIC) being developed at Thomas Jefferson National Accelerator Facility. The main components of a novel klystron, which are the electron gun, cavity-chain, magnetic system, and partially-grounded depressed four-stage collector, were conceptually designed. The efficiency is 80%, a number in which the power consumption by the solenoid and filament is already factored. The tube is a combination of proven technologies: it uses multiple beams to have its perveance low to boost beam-power to RF-power efficiency. It uses a partially-grounded depressed collector to recover energy, thereby increasing the overall efficiency. A low operating voltage of 14kV makes the tube more user-friendly, avoiding need for costly modulators and oil insulation. A sectioned solenoid is used to insure superb beam-matching to all components downstream from the electron gun, increasing the tube performances.

INTRODUCTION

The tube, described above, is to serve as an efficient microwave source [1] for the Electron-Ion Collider (EIC) as developed at Thomas Jefferson National Accelerator Facility (TJNAF). The tube [2] is to operate at 952.6 MHz, producing 50kW continuously with an efficiency of 80%. We must point out that VKL7811, the present microwave source (klystron) at TJNAF, at this time can deliver only 10kW, with a low efficiency of 32% only.

The parameters of our tube are given in Table 1, and its general layout is shown in Fig. 1. As of this writing, the tube is fully developed; that is to say, all of its main components—the magnet, the gun, cavity structure, and the partially-grounded depressed four-stage collector—are designed. The simulated performances of the tube are illustrated in Fig. 2 and Fig. 3.

COMPONENT DESIGN AND PERFORMANCES

Figure 4 shows a few details of the gun and cathode geometries. The gun's total perveance is 3.26 $\mu AV^{(-3/2)}$. The cavity chain geometry is illustrated in Fig. 1. The distance between the anode and the middle plane of the gap of the first cavity is 40±2mm. The distances between the cavity gaps (the middle planes) are 88, 94, 120, 172, and 56 mm, respectively. The gap sizes are 12, 12, 10, 12, 12, and 10 mm, respectively. Figure 6 shows a geometry of the second harmonic cavity. Our Final Technical Report to the U.S. Department of Energy (DoE) describes all details and dimensions of the cavity chain (herein, we do not reveal them for the sake of certain proprietary information). The beam dynamics in the cavity chain has already been presented elsewhere [2].

Table 1: Klystron Parameters

Parameter Name	Value
Operating Frequency	952.6 MHz
Bandwidth at 3dB	4.5 MHz
Output power	54-55kW
Output style	one WR975
Input power	45W
Saturated gain	31 dB
Beam voltage	14 kV
Total beam current	5.4 A
Total beam power	75.6 kW
Number of beams	6
Overall efficiency	80%
Filament power	0.135 kW
Power for magnets	0.5 kW
Total length	1630 mm
Depressed voltage for stage 1	1.1 kV
... for stage 2	2.25 kV
... for stage 3	3.4 kV
... for stage 4	4.55 kV
Water flow for collector	60 l/min
Max. average collector power	75 kW
Peak loading of collector	125 W/cm^2
Average collector loading	<50 W/cm^2
Cathode loading	0.8 A/cm^2
Diameter of a cathode	12 mm
Beam common circle	52 mm
Diameter of drift tubes	20 mm
Peak of electric field in gun	16 kV/cm
Peak of electric field in output cavity	22 kV/cm
Max. magnetic field	400 Gs
Power recovered by collector	8.1 kW
Necessary efficiency of the HV-circuit for power recovery	93 %

---

* Work supported by the U.S. Department of Energy, grant #DE-SC0018471

† sergey.shchelkunov@gmail.com

ISBN: 978-3-95450-223-3 ISSN: 2673-7000 doi:10.18429/JACoW-NAPAC2019-WEPLM56

DEVELOPMENT OF HELIUM GAS CHARGE STRIPPER WITH PLASMA WINDOW*

J. Gao†, F. Marti, Facility for Rare Isotope Beams,
Michigan State University, East Lansing, MI, USA
A. LaJoie, National Superconducting Cyclotron Laboratory,
Michigan State University, East Lansing, MI, USA

Abstract

The cascade arc discharge, also called "plasma window", was proposed to be used as an interface to provide an effective separation between atmosphere and vacuum. As suggested by Thieberger and Hershcovitch at Facility for Rare Isotope Beams (FRIB) workshop in 2009, helium plasma window offers an alternative to a large pumping system used in helium gas charge stripper for high intensity heavy ion beam accelerator facilities. In this report, we present the recent progress on the development of helium plasma window with 10 mm diameter apparatus. The sealing performance of helium plasma window has been investigated. Various diagnostics tools have been developed to improve our understanding of underlying physics. Over 140 hours continuous unattended operation of helium plasma window in recirculating gas system has been achieved, which suggests our system to be a feasible charge stripper solution for heavy ion beam accelerators. We also discuss anticipated future developments of plasma window.

INTRODUCTION

For intense heavy ion beam accelerators, helium gas can be a good candidate for stripping, although offering lower charge states than liquid lithium [1]. The advantages are the helium gas has less safety concerns and contributes no contamination to superconducting cavities afterwards. The work at RIKEN has showed that a recirculating helium gas stripper with a large differential pumping system can be used for stripping U beam at an energy of approximately 11 MeV/u [2]. The pressure at the helium target is around 7 kPa and a final pressure of 5 x 10 $^{-6}$ Pa is achieved after five stages pumping system. Compared to RIKEN, the stripping energy at FRIB is about 16.5 MeV/u. A thicker stripper is required in order to achieve an equilibrium charge state distribution. According to the approximation [1], a 30 cm long with a cell pressure P_{cell} of 40 kPa can produce an average charge state of 71+, starting from 33+.

As suggested by Thieberger at 2009 Facility for Rare Isotope Beams Facility (FRIB) workshop on high power strippers and targets, plasma window contained helium cell can be used as an alternative to a large pumping system in gas charge stripper applicable for high intensity heavy ion beam accelerator facilities. The novel apparatus of plasma window used as an interface to provide an effective separation between atmosphere and vacuum was first proposed by Hershcovitch [3]. Many applications of such an effective vacuum seal device have been demonstrated [4–8].

The basic idea is to install a pair of plasma windows on both sides of helium gas chamber, so that the gas leakage to the beamline which is under high vacuum can be significantly reduced [1]. A 10 mm diameter arc flow channel is desired due to the intense beam at FRIB. Argon cascade arc with high pressure up to 9 atm and diameter from 2 mm to 10 mm has been studied previously [3–12]. However, the helium cascade arc has rarely been investigated, especially with high flowrate and large aperture. In order to develop a vacuum-atmosphere interface for the high intensity heavy ion beam at around 16 to 20 MeV/u, a recirculating plasma window test stand was developed.

In this report, we summarize recent development of helium gas charge stripper with plasma window. In Experimental Setup, a new diagnostic plate design is presented. The sealing performance of 10 mm plasma window under various experimental conditions is shown in Results. Over 140 hours long term operation of helium plasma window in recirculating gas system has been achieved for the first time. The last section discusses the future plan and concludes the results.

EXPERIMENTAL SETUP

A schematic diagram of the experiment is shown in Fig.1(a). The plasma window consisting of three cathodes, a series of eight copper disks and an anode, is inserted between a high-pressure gas cell and a low-pressure chamber. The arc can be generated between the cathodes and the anode. The whole system is cooled by water. An Omega flowmeter (not shown in Fig.1(a)) is connected to the high pressure gas cell in series. The cathode tip is made of 2% thoriated tungsten, 2.5 mm diameter and shaped into a 40-degree cone. Each floating disk is electrically insulated by G10 spacers and sealed by Kalrez made O-rings which have high temperature resistance up to 600 K. In order to better confine the cascade arc and restrict the gas flowrate, a disk with 6mm bore size is attached near the cathodes. The rest of the disks have 10 mm diameter hole. The total length is around 8 cm. After pumping through the low-pressure chamber, the gas can be recirculated in the system. The setup is similar to that described in Ref [12].

Figure 1(b) shows a newly fabricated diagnostic plate with a side viewport. A 2 mm diameter hole inside the viewport is selected so that the flow pattern disturbance can

---

* Work supported by NSF Award PHY-1565546

† gaoj@frib.msu.edu

ISBN: 978-3-95450-223-3 ISSN: 2673-7000 doi:10.18429/JACoW-NAPAC2019-WEPLM57

200 kW, 350 – 700 MHz RF SOURCES USING MULTIPLE BEAM TRIODES

R.L. Ives, T. Bui, D. Marsden, M.E. Read,
Calabazas Creek Research, Inc., San Mateo, CA, USA
B. Henderson, L. Higgins, R. Ho,
Communications & Power Industries, Palo Alto, CA, USA

Abstract

Calabazas Creek Research, Inc. and Communications & Power Industries, LLC are developing multiple beam triodes to produce more than 200 kW of RF power at extremely low cost and efficiencies exceeding 80%. RF power is achieved by installing the triode inside coaxial input and output cavities at the desired frequency. The multiple beam triodes developed in this program will provide RF power from 350 MHz to 700 MHz using the appropriate, tuned, resonant cavities.

This program is using eight grid-cathode assemblies to achieve 200 kW with a target efficiency exceeding 80%. A 350 MHz RF source would be approximately 36 inches high, 18 inches in diameter and weigh approximately 150 pounds. This is significantly smaller than any other RF source at this frequency and power level.

The gain is limited to approximately 14 dB, so a single beam triode-based source will serve as a driver. The combined cost and efficiency will still exceed the performance of other comparable RF sources, including solid state sources. Design issues, include grid cooling, uniformity of RF electric fields on the grids, and efficiency, will be discussed.

TRIODE RF SOURCE BASICS

The triode provides an electron beam source when driven by appropriate RF fields. The device uses a grid driven by an axial electric field to generate a pulsed electron stream at the desired RF frequency. Power from this stream is transferred to RF fields using an output cavity resonant at the pulsed frequency of the electron stream.

Figure 1 provides the basic geometry, exemplifying the simplicity of these devices. RF drive power from the input cavity enters the triode through a ceramic insulator and creates an axial electric field between the cathode and control grid. The electron beam is emitted during the positive portion of the RF cycle. Consequently, the efficiency of these sources is approximately 90%.

The pulsed electron stream excites RF fields in the output cavity at the pulse frequency, and electron beam power is transferred to these fields. This power is extracted through a capacitive or inductive coupler to the external transmission line. Tuners allow frequency control of both the input and output cavities. The spent beam power is deposited on the collector (anode) and dissipated with air or liquid cooling, depending on the average power.

A single triode can drive a multiplicity of RF sources. The triode provides its own vacuum envelope and can be plugged into appropriate cavities for the frequency desired.

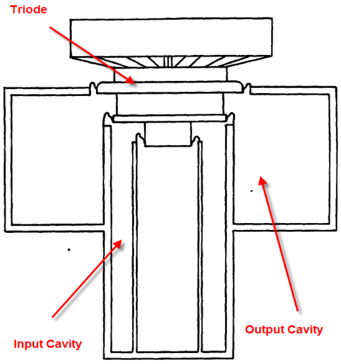

Figure 1: Schematic configuration of triode-base RF source.

MULTIPLE BEAM TRIODE

Single beam triodes were developed more than fifty years ago and are still in production. The device primarily consists of a cathode and one or more grids surrounded by a vacuum envelope. Figure 2 shows the YU-176 triode, which operates from 300 MHz to 1. 2 GHz and provides sufficient beam power to generate 25 kW of RF power.

The YU-176 grid-cathode assembly is shown in Fig. 3. The cathode consists of a flat, nickel surface coated with barium oxide. The grid is cut from commercially available tungsten screen and brazed to tungsten supports. A vacuum ceramic isolates the grid from the cathode. The assembly costs less than $1,500 in production quantities.

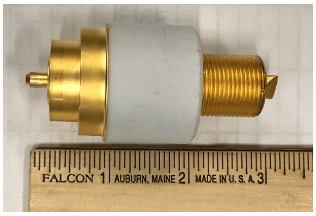

Figure 2. YU-176 triode produced by Communications & Power Industries, LLC.

This program is using eight YU-176 grid-cathode assemblies to increase the available beam power to 250 kW. Figure 4 shows the eight beam array, and Fig. 5 shows the size and configuration of complete devices, including their integral vacuum envelopes and insulating ceramics.

RF power is produced by installing the triode into a set of input and output cavities. Each is typically a single, coaxial resonator with integral tuners and couplers. Figure 6 shows solid models for a 350 MHz and 600 MHz RF source using the water-cooled (CW) multiple beam triode. Note that the sizes are dramatically smaller than comparable klystron, inductive output tube, or solid-state sources.

FAST Sn-ION TRANSPORT ON Nb SURFACE FOR GENERATING Nb_xSn THIN FILMS AND XPS DEPTH PROFILING*

Z. Sun†, M. Liepe, J. T. Maniscalco, T. Oseroff, and R. D. Porter,
CLASSE, Cornell University, Ithaca, NY, USA
D. Zhang, Mechanical Engineering, Cornell University, Ithaca, NY, USA
X. Deng, Chemical Engineering, University of Virginia, Charlottesville, VA, USA

Abstract

In this work, we propose and demonstrate a fast and facile approach for Nb_xSn thin film deposition through the ion exchange reaction. By simply dipping a tin precursor on the Nb substrate surface, a ~600 nm thin film is generated due to the electronegativity difference between Sn and Nb. Through X-ray photoelectron spectroscopy (XPS) depth profiling, the compositional information as a function of film thickness was obtained. Results showed a Sn layer on the film surface, Sn-rich and Nb-rich Nb_xSn layers as the majority of the film, and a ~60 nm Nb_3Sn layer at the film/substrate interface. Quantitative analysis confirmed stoichiometric Nb/Sn ratio for the Nb_3Sn layer. This deposition method is demonstrated to be an alternative choice for Nb_3Sn film growth.

INTRODUCTION

Nb_3Sn thin film growth has drawn increased attention recently due to the potential of this material for replacing niobium (Nb) in superconducting radio frequency (SRF) cavities [1, 2]. Nb_3Sn can lead to superior RF performance owing to its high critical temperature (twice that of Nb) and also a higher superheating field. Considerable efforts have been made to explore Nb_3Sn film deposition on Nb substrate. The state-of-the-art approach relies on a tin (Sn) vapor diffusion process under >1000 °C high temperature in a high vacuum furnace [3]. Electroplating [4], sputtering [5], and chemical vapour deposition [6] are also actively being developed to coat Nb_3Sn-based cavities.

In this paper, we report an alternative method for generating Nb_xSn films based on fast Sn-ion transport on a Nb surface. Fast ion transport is a fast and facile approach which takes advantage of ion exchange reactions [7, 8]. As illustrated in Fig. 1a, the Nb-Sn alloy can be formed at room temperature when the Sn^{2+} cation containing organic electrolyte is exposed to a sufficiently polarized Nb surface. This fast reaction is enabled by the electronegativity difference between Nb and Sn [7]. Accordingly, the half reactions of Sn^{2+} reduction and Nb oxidation,

$$Sn^{2+} + 2e^- \rightarrow Sn \ (-0.14\ V), \qquad (1)$$

$$Nb \rightarrow Nb^{3+} + 3e^- \ (1.099\ V), \qquad (2)$$

yield a positive electrochemical potential, so the reaction

$$x\,Nb + Sn^{2+} + 2e^- \rightleftarrows Nb_xSn, \qquad (3)$$

is able to proceed spontaneously. Fig. 1b shows the grey-color Nb_xSn film from this Sn-ion transport process.

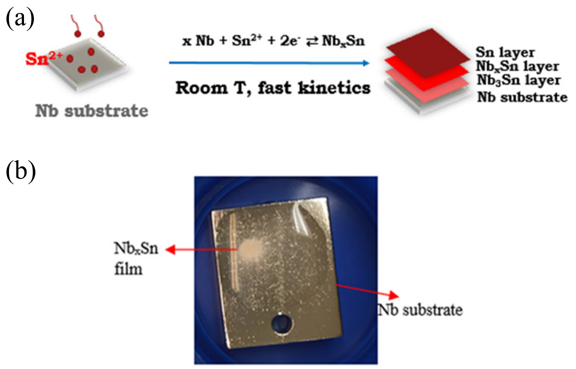

Figure 1: (a) Schematic showing the process of fast Sn-ion transport to the Nb surface. (b) Image of the generated Nb_xSn film on the Nb substrate.

In order to further improve the Nb_xSn film to a pure-stoichiometric Nb_3Sn film, the compositional characteristics are of great interest. The use of X-ray photoelectron spectroscopy (XPS) is specialized to characterize the composition at nano-scale (3-5 nm electron mean free path for Sn and Nb elements). By exploiting argon ion sputtering on the film surface and softly etching the film for a few nanometer, the depth profile of the film composition is analyzed in this study.

EXPERIMENTAL PROCEDURES

The Sn precursor, tin bis(trifuoromethanesulfonyl) imide (SnTFSI), was obtained from Alfa Aesar. 10 mM concentration solution was prepared by dissolving the precursor in DI water. 0.1 mL SnTFSI solution was dropped on the Nb substrate and then dried for 30 min. All these treatments were done in a glove box at room temperature. The film was observed immediately after the drying step.

XPS spectra were collected using a PHI Versaprobe III system with a sensitivity of < 0.1% atomic percentage. The system used monochromatic Al k-alpha X-rays with energy of 1486.6 eV and beam size of 200 µm. Ion sputtering was performed for 5.5 min in between each scan for data acquisition. In total, scans 1-35 were taken from the film surface to the film/substrate interface after each sputtering process. The etching rate of 3.6 nm/min was determined from standard SiO_2 films [9]. This work assumes the same sputter rate for Nb_xSn films. Thus, each scan probed the film with a step in depth of ~20 nm.

---

*This work was supported by the U.S. National Science Foundation under Award PHY-1549132, the Center for Bright Beams. Also, this work made use of the Cornell Center for Materials Research Shared Facilities which are supported through the NSF MRSEC program (DMR-1120296).

† zs253@cornell.edu

ISBN: 978-3-95450-223-3 ISSN: 2673-7000 doi:10.18429/JACoW-NAPAC2019-WEPLM62

FIRST COLD TEST RESULTS OF MEDIUM-β 644 MHz SUPERCONDUCTING 5-CELL ELLIPTICAL CAVITY FOR THE FRIB ENERGY UPGRADE*

K.E. McGee,† B.W. Barker, K. Elliott, A. Ganshyn, W. Hartung, S.H. Kim, P.N. Ostroumov,
J.T. Popielarski, A. Taylor, C. Zhang, FRIB/MSU, East Lansing, MI, U.S.A.
M.P. Kelly, T. Reid, Argonne National Laboratory, Argonne, IL, U.S.A.

Abstract

The CW superconducting linac for the Facility for Rare Isotope Beams (FRIB) will accelerate ions to 200 MeV per nucleon of uranium, with the possibility of a future energy upgrade to 400 MeV per nucleon via additional cavities. The design study [1] concluded that the 644 MHz 5-cell $\beta_{opt} = 0.65$ cavity is a superior option, maximizing accelerating gradient [E_{acc}] to meet the target energy upgrade while minimizing the additional cryogenic load, cryomoduls, and real estate. Two bare niobium [Nb] cavities, S65-001 and S65-002, have been fabricated. The first, S65-001, underwent 150 µm bulk electropolishing [EP], hydrogen degassing at 600°C for 10 hours, 20 µm light EP, and in-situ baking at 120°C for 48 hours following high-pressure water rinsing and clean assembly. In the first cold-test, S65-001 achieved a Q_0 of $2{\cdot}10^{10}$, equivalent to $R_s = 10$ nΩ, at its design E_{acc}, 17.5 MV/m ($V_{acc} = 12.4$ MV). The cavity was tested in a newly refurbished FRIB test dewar, equipped with a variable input coupler driven by a stepper motor. The second cavity, S65-002, has undergone a buffer chemical polish [BCP] and will be tested soon to compare against S65-001's performance. S65-002 was also used to investigate mechanical modes and passband/higher order modes at room temperature. This work is in preparation for S65-001 to undergo nitrogen doping/infusion at FNAL, to compare its nitrogen-doped performance against its EP performance detailed here.

INTRODUCTION

The upgraded linac will be able to deliver 400 MeV/u for the heaviest uranium ions and up to 1 GeV for protons, including a variety of light ions with energies higher than 400 MeV/u, which will increase the yield of rare isotopes from the targets. Further benefits of this upgrade include providing the same 400 kW of power on target but at a reduced dissipation power density at the beam-dump. The baseline design of the FRIB conventional facilities incorporated an 80-meter space reserved in the linac tunnel for energy upgrade cryomodules. In the past two years, several technical solutions have been studied to find the best option for the energy upgrade within this available real estate. Several types of superconducting [SC] cavities operating at different frequencies were investigated, and it was concluded that a 5-cell 644 MHz cavity with $\beta_{opt} = 0.65$ is optimal for the energy upgrade. The design parameters are described in [1]. Essentially, this design meets energy upgrade targets while minimizing heat load, number of additional cavities, and number of additional cryomodules.

RF SURFACE PROCESSING

The initial surface treatment of S65-001 was based on the standard ILC recipe for EP with a slightly modified hydrogen degassing step. The 150 µm bulk EP was carried out at Argonne National Laboratory [ANL], then baked FRIB's high-vacuum furnace for hydrogen degassing: first at 350°C for 12h, then at 600°C for 10 hours. The cavity was then moved to a bead-pull test stand at FRIB, and mechanically squeezed/stretched with tuning cuffs to achieve uniform cell-by-cell field distribution. After field-flatness tuning, the cavity was shipped to ANL for the final 20 µm EP, followed by high pressure water rinse and clean assembly. Final clean assembly of the variable coupler and vacuum fittings to the refurbished test-insert occurred at the FRIB clean-room facilities. After clean assembly, S65-001 was baked in-situ at 120°C for 48 hours, assembled to the dewar insert. This long, low-temperature bake was undertaken in order to ameliorate the potential for a high-field Q-slope, a practice common in 1.3 GHz TESLA cavities [2]. Cold test #1 (with high-power RF) was then conducted on S65-001. In preparation for cold test #2, S65-001 underwent another 20 µm EP at ANL, followed by HPR and clean assembly at FRIB facilities. A 60°C, 12 hour bake was then included to remove any remaining water from the cavity surface, and cold test #2 was conducted on S65-001.

BEAD PULL MEASURMENTS

Figure 1 shows a schematic of the FRIB bead-pull test stand. An 8mm brass bead is threaded onto nylon monofilament, and mounted on pulleys above and below the cavity. The bottom end is attached to the stepper motor, and the top is weighted over a third pulley. Jigs attached to the beam ports ensure that the bead is drawn precisely along the center of the beam axis. As the bead traverses the cavity, it perturbs the cavity's resonant frequency. This perturbation is treated formally with the Slater perturbation theorem [3]. The resonant frequency shift is related to the phase shift, $\frac{\tan\phi}{2Q_L} = \frac{\Delta\omega}{\omega_0}$, where $\Delta\omega$ is the difference between the unperturbed (ω_0) and perturbed resonant frequencies, and ϕ is the measured phase change from resonance [4]. A vector network analyser provided 10 dBm to the input coupler, and measured the change in the phase at the pickup port at the unperturbed π-mode frequency. A Labview program was created [5] to step the bead through

---

* Work supported by the Michigan State University and US Department of Energy, Office of Science, High Energy Physics under Cooperative Agreement award number DE-SC0018362.

† mcgee@frib.msu.edu.

ISBN: 978-3-95450-223-3 ISSN: 2673-7000 doi:10.18429/JACoW-NAPAC2019-WEPLM63

DEVELOPMENT OF A SECONDARY Sn SOURCE FOR Nb3Sn COATING OF HALF-WAVE COAXIAL RESONATOR*

J. K. Tiskumara†, J. R. Delayen, H. Park, Old Dominion University, Norfolk, VA, USA
G.V. Eremeev, Thomas Jefferson National Accelerator Facility, Newport News, VA, USA
U. Pudasaini, College of William and Mary, Williamsburg, VA, USA

Abstract

Superconducting thin films have the potential of reducing the cost of particle accelerators. Among the potential materials, Nb_3Sn has a higher critical temperature and higher critical field compared to niobium. Sn vapor diffusion method is the preferred technique to coat niobium cavities.

Although there are several thin-film-coated basic cavity models that are tested at their specific frequencies, the Half-wave resonator could provide us data across frequencies of interest for particle accelerators. With its advanced geometry, increased area, increased number of ports and hard to reach areas, the half-wave resonator needs a different coating approach, in particular, a development of a secondary Sn source. We are commissioning a secondary Sn source in the coating system and expand the current coating system at JLab to coat complex cavity models.

INTRODUCTION

In the field of Accelerator science, most of the superconducting cavities are made out of bulk Niobium. For reduced cost and increased quality factor, thin-film coated cavities are investigated in modern research. Not only the niobium thin film, but also other substances as magnesium diboride, niobium nitride, and niobium-tin are also used in the experiments. Among these, Nb_3Sn has shown the promising T_c close to 18 K. [1]. This gives a lower dissipation than that of the niobium at the same temperature. Its superheating field of about 400 mT gives a higher breakdown field.

Many methods have been used to coat thin films on Niobium cavities, but here at Jefferson Lab, the vapor diffusion technique is being used to deposit Nb_3Sn thin layers on SRF cavities. The technique has been used since the 70's. Although there are several basic cavity models are coated and tested at their specific frequencies using this method, it has not yet applied to coat the cavities with complex geometries with hard to reach areas, increased area with more number of ports.

Half-wave resonator is one of such a complex cavity, which could provide us data across frequencies of interest for particle accelerators [2] and at the same time it is an investigation of coating Nb3Sn on complex geometries.But with its differences from the basic cavity models, the current coating system, which is initially designed for basic cavity types, needed some modifications. An addition of a secondary Sn-source with an independent heater to control its temperature is realized to be the primary modification needed to coat a half-wave resonator. This is expected to supply higher vapor pressure of tin during the coating, along with primary Sn-source, in order to deposit a uniform coating. This paper discusses the development of the secondary Sn source for Nb3Sn coating of Half-wave coaxial resonator at Jefferson Lab.

CAVITY DEPOSITION SYSTEM AT JLAB

The Nb_3Sn deposition system at JLAB as shown in Fig. 1, contains two main parts: the coating chamber that hosts a cavity to be coated and the furnace that provides the desired heating to the coating chamber [1]. The coating chamber was built out of niobium as a 40" long x 16" diameter cylinder, and the furnace is commissioned to reach 1250 ^{0}C with the furnace vacuum in 10^{-7} Torr range.

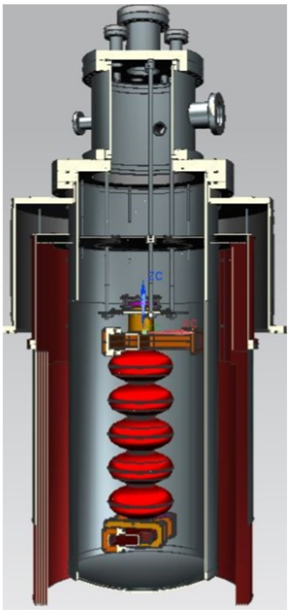

Figure 1: A sketch of the Jlab Nb3Sn coating system with a 5-cell cavity [3].

Figure 2 shows the typical coating process at JLab consists of a nucleation step that involves the tin chloride evaporation at 500 ^{0}C for 1-hour. Nucleation is followed by a deposition step which involves the evaporation of tin for 3-hours at 1200 ^{0}C, which is favorable to form Nb_3Sn phase on substrate niobium [4].

---

* Research supported by DOE Office of Science Accelerator Stewardship Program Award DE-SC0019399. Partially authored by Jefferson Science Associates under contract no. DEAC0506OR23177. This material is based upon work supported by the U.S. Department of Energy, Office of Science, Office of Nuclear Physics.

† jtisk001@odu.edu

ISBN: 978-3-95450-223-3 ISSN: 2673-7000 doi:10.18429/JACoW-NAPAC2019-WEPLM64

HIGH DYNAMIC VOLTAGE RANGE STUDIES OF PIEZOELECTRIC MULTILAYER ACTUATORS AT LOW TEMPERATURES

C. Contreras-Martinez[†,1], Y.M. Pischalnikov, J.C. Yun, Fermilab, Batavia, Illinois, USA
[1]Michigan State University, East Lansing, Michigan, USA

Abstract

Piezoelectric actuators are used for resonance control in superconducting linacs. In high accelerating gradients linacs, such as those operated in a pulsed mode, require a large operating piezo voltage. This is due to the Lorentz forced detuning which causes a large frequency shift and is compensated with an active piezo-tuning system. In this high dynamic voltage range the piezo is expected to warm up drastically due to it being in an insulated vacuum The capacitance, dielectric losses, piezo stroke (based on geophone), and thermal properties such as heating are obtained in the temperature range of 20K to 300K of the piezo actuator P-844K075 that was developed at Physik Instrumente will be presented and discussed.

INTRODUCTION

Piezoelectric (piezo) actuators are used for resonance control of superconducting radio frequency (SRF) cavities in linacs. Linacs with cavities of narrow bandwidth caused by low beam current are especially dependent on the reliability and lifetime of piezo actuators. The reliability and lifetime of the encapsulated piezo stacks PICMA P-844K075 were tested under a continuous wave (CW) operation for the LCLS-II project. During these tests it was shown that the piezo sustained 2×10^{10} cycles (equivalent to 20 years of LCLS-II operation) with a peak-to-peak voltage (V_{pp}) of 2 V on the piezo [1]. During this study the temperature rise of the piezo was on the order of 5 K. In the case of a linac in pulsed operation a larger voltage is needed to compensate the detuning of the cavities.

Piezo actuators use the piezoelectric effect which occurs when an electric field creates a mechanical deformation on the crystal. The opposite effect is also possible where a mechanical deformation of the crystal will induce an electric field. For resonance control a voltage is applied to the piezo to deform the cavity which results in a change of frequency. The amount of frequency shift depends on the voltage that is applied, a higher voltage will lead to a larger frequency shift of the cavity. The amount of voltage needed for resonance control depends on the linac operation. During CW operation the main source of vibration noise is caused by microphonics which can results in a detuning of the cavity of ~10-20 Hz and in the worst-case scenario 100-150 Hz [2]. The frequency of the microphonics vibration sources is found to be less than 100 Hz [2]. This level of detuning can be compensated with a low voltage on the piezo and by driving it at frequency less than 100 Hz. For a linac in pulse operation the main source of detuning is caused by radiation pressure known as Lorentz force detuning (LFD). This can result in a frequency shift of -500 Hz. In order to compensate for this type of detuning a larger voltage must be used. The RF pulse will also excite the mechanical frequencies of the cavity which can be greater than 100 Hz. In order to compensate for pulse linac operation detuning a larger V_{pp} on the order of 120 V-200V and frequencies of 200-300 Hz is needed.

The piezo actuators are made from lead zirconate titanate (PZT). PZT has a thermal conductivity of 4 $W/(m \cdot K)$ at room temperature and this drops to 0.02 $W/(m \cdot K)$ at 20 K [3] which makes heat transfer difficult. At large V_{pp} and high driving frequency the piezo actuator is expected to heat up dramatically. The majority of the SRF linacs such as SNS, Eu-XFEL, LCLS-II, and ESS employ tuner system with piezo-actuators located inside a cryomodule (CM) at insulated vacuum. In this configuration the stroke of the piezo is maximized by being closer to the cavity. Additionally, a humid free environment increases the overall lifetime of the piezo by preventing voltage breakdown due to water creeping into the ceramic. In order to increase overall lifetime of the piezo actuators for a pulsed linac this study will characterize the piezo heating at large V_{pp} values at cryogenic temperatures and in an insulated vacuum.

THEORY

Self-heating Generation Model

The temperature dependence of the piezo with respect to time can be model with a 1-D self-heating equation based on the first law of thermodynamics. The behaviour of the temperature rise for different voltages and frequencies shows that the rise is proportional to $\left(1 - e^{-\frac{t}{\tau}}\right)$ [4]. Additionally, this model can be used to estimate the internal heat generation of the piezo when an empirical formula is not known. For this derivation a uniform temperature distribution and isotropic material is being assumed, the equation then can be written as

$$\dot{Q}_G - \dot{Q}_d = \mathrm{m}C_\mathrm{p}\frac{dT}{dt} \quad (1)$$

where $\dot{Q}_G$ is the internal heat generation due to dielectric losses and $\dot{Q}_d$ is the heat dissipation; m is the mass; and C_p is the specific heat capacity of PZT. At low electric field (voltage) the heat generation can be approximated by

$$\dot{Q}_G = \frac{\pi}{4}(C \tan\delta) f V_{pp}^2 \quad (2)$$

where C is the capacitance of the piezo; tan δ is the dissipation factor; f is the driving frequency of the piezo; and

---

This manuscript has been authored by Fermi Research Alliance, LLC under Contract No. DE-AC02-07CH11359 with the U.S. Department of Energy, Office of Science, Office of High Energy Physics. Additional support provided by award number DE-SC0018362 and Michigan State University.

† contrera@frib.msu.edu

North American Particle Acc. Conf. NAPAC2019, Lansing, MI, USA JACoW Publishing
ISBN: 978-3-95450-223-3 ISSN: 2673-7000 doi:10.18429/JACoW-NAPAC2019-WEPLM66

MICROPHONICS STUDIES AT STC IN FERMILAB*

C. Contreras-Martinez†,[1], Y.M. Pischalnikov, W. Schappert, A.I. Sukhanov, J.C. Yun,
Fermilab, Batavia, IL, USA
[1]Michigan State University, East Lansing, MI, USA

Abstract

The spoke test cryostat is used to qualify the 325 MHz single spoke resonators at Fermilab (FNAL). During these tests a large detuning on the cavity was observed. The data acquisition for continuous captures were based on measurements from the piezoelectric actuators. A comparison of the cavity vibrations measured with RF signal from the cavity and piezoelectric actuator signals are shown. The effects of microphonics on the cavity are discussed.

INTRODUCTION

Fermilab's Proton Improvement Plan (PIP)-II is an 800 MeV superconducting H^- linac which will consist of 5 different types of radio frequency (RF) cavities [1]. One of these cavities is a 325 MHz single spoke resonator (SSR1) of $\beta_{opt} = 0.22$. These "dressed" cavities can be tested in a cryomodule-like environment at the spoke test cryostat (STC) facility located in Fermilab's meson detector building (MDB). This facility shown in Fig. 1 is used to test the performance of the cavities such as the cavity's accelerating gradient, Q_o, field emission, and other ancillaries such as the tuner system used for resonance control.

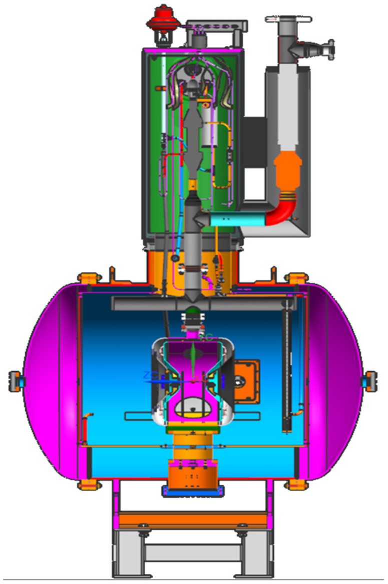

Figure 1: Schematic of SSR1 cavity inside the cryostat in STC.

Microphonics are vibrational noise that can couple to the cavity causing it to detune from its nominal frequency. These noise sources include pumps, internal and external vibration, pressure in the helium bath, and thermal acoustic oscillations (TAOs) in the helium supply lines. The calculated longitudinal frequency sensitivity of this cavity is 520 Hz/μm and the pressure sensitivity is 4.45 Hz/Torr [1]. A large detuning of the cavity will require more RF power to keep the desired accelerating gradient. Additionally, the RF power source has a limit, if the detuning is large enough the RF power source will not be able to provide sufficient power to the cavity and this will cause the cavity to trip.

In order to compensate for the detuning caused by microphonics a double lever tuner system is used. The design and figure of merit of the tuner are described elsewhere [2]. The slow/coarse frequency tuning component of the tuner is driven by a stepper motor with a tuning range of 135 kHz. This component is only used after cooldown to put the cavity at 325 MHz and is rarely used during the beam operation. The fast/fine tuner component uses piezoelectric (piezo) actuators which have a tuning range of 1 kHz. A control algorithm is used to drive the piezo actuators to compensate for microphonics [3].

For the control algorithm to reach the required PIP-II specifications of 20 Hz peak detuning for the 325 MHz SSR1 cavity the level of microphonics must be small. Fig. 2 shows a histogram for the detuning comparing the distribution when the active compensation algorithm is on versus when it's off. The level of observed microphonics noise is too high in order to compensate with the existing fast tuning system. This figure also compares the level of noise in the LCLS-II cryomodules to the one in the cryostat in this current study. The level of microphonics is 20 times larger than those in LCLS-II [4].

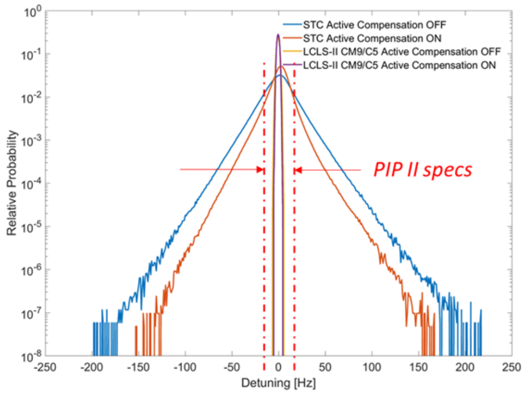

Figure 2: Histogram of detuning with active compensation on or off. For comparison the level of detuning in the LCLS-II is shown.

---

*This manuscript has been authored by Fermi Research Alliance, LLC under Contract No. DE-AC02-07CH11359 with the U.S. Department of Energy, Office of Science, Office of High Energy Physics. Additional support provided by award number DE-SC0018362 and Michigan State University.

† contrera@frib.msu.edu

OPTIMIZATION OF A SINGLE-CELL ACCELERATING STRUCTURE FOR RF BREAKDOWN TEST WITH SHORT RF PULSES

M.M. Peng*[1], M.E. Conde, G. Ha, C. Jing[2], W. Liu, J.G. Power, J. Seok, J.H. Shao†,
E.E. Wisniewski, Argonne National Laboratory, Lemont, IL, USA
J. Shi, Tsinghua University, Beijing, People's Republic of China
[1]also at Tsinghua University, Beijing, People's Republic of China
[2]also at Euclid Techlabs, Bolingbrook, IL, USA

Abstract

RF breakdown is one of the major limitations to achieve high gradient acceleration for future structure-based normal conducting linear colliders. Previous statistic research shows that the breakdown rate is proportional to $E_a^{30} \times t_p^5$, which indicates that the accelerating gradient (E_a) could be improved by using shorter RF pulses (t_p). An X-band 11.7 GHz metallic single-cell structure has been designed for RF breakdown study up to 273 MV/m using short pulses (~3 ns) generated by a 400 MW power extractor at Argonne Wakefield Accelerator (AWA) facility. The structure has also been scaled to 11.424 GHz for the long pulse (100-1500 ns) breakdown study driven by a klystron and a pulse compressor at Tsinghua X-band High Power Test-stand (TPoT-X), with the gradient up to 246 MV/m with 200 MW input power.

INTRODUCTION

High gradient acceleration is one of the key technologies to reduce the cost of future TeV-scale linear colliders. A major limiting factor to improve the accelerating gradient is the RF breakdown phenomenon [1, 2] which will lead to structure damage, reduced energy gain, or even beam loss. Intense experimental research has been conducted worldwide led by CERN-SLAC-KEK collaboration to study the RF breakdown dependence on accelerating structure properties, from which it has been observed that the breakdown rate (BDR) is sensitive with the accelerating gradient and the RF pulse length as $BDR \propto E_a^{30} \times t_p^5$ [3].

Argonne Flexible Linear Collider (AFLC) [4] has therefore been proposed to significantly improve the state-of-the-art gradient by applying short RF pulses. The baseline design applies the two-beam acceleration approach in which ~20 ns GW level RF pulses are generated from 26 GHz power extractors driven by short trains of high charge drive bunches. The corresponding accelerating gradient is above 250 MV/m in the main beam accelerators.

This research aims to study RF breakdown with a wide range of RF pulse lengths to verify the short pulse high gradient concept. It contains two parts: 1) short pulse (~3 ns, up to 400 MW) test driven by an X-band 11.7 GHz power extractor [5] at AWA; 2) long pulse (100-1500 ns, up to 200 MW) test driven by an X-band 11.424 GHz klystron with a pulse compressor [6] at TPoT-X [7]. A single-cell accelerating structure has been optimized at 11.7 GHz to obtain the maximum accelerating gradient using the short RF pulses and then scaled to 11.424 GHz. In both parts, the maximum gradient is designed to be ~250 MV/m with the available input power.

ACCELERATING GRADIENT ANALYSIS

Figure 1 illustrates the layout of the high gradient accelerating structure for high power test, including a single high gradient accelerating cell, two matching cells, and two RF couplers.

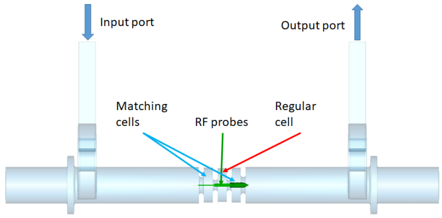

Figure 1: The simulation model of the single-cell structure for transit accelerating gradient analysis.

Detailed analysis of the structure response has been conducted in this section to determine the accelerating gradient driven by long and short RF pulses. In this section, the structure is assumed to be a N-cell traveling-wave metallic disk-loaded one with cell length of L.

On-axis longitudinal electric field

When driven by an RF pulse with finite length (bandwidth), several TM_{01} modes with various phase advances could be excited within the bandwidth. Their space harmonics [8] also exist to satisfy the longitudinal period boundary condition at the iris.

When ignoring the structure attenuation, the on-axis longitudinal electric field can therefore be express as

$$E_z(z,t) = \sum_{k=0}^{N-1} \sum_{n=-\infty}^{\infty} E_{k,n} e^{j(\omega_k t - \beta_{k,n} z)} \qquad (1)$$

where the subscript k, n denotes the nth harmonic of the kth mode, ω_k denotes the frequency of the kth mode and its harmonics, and β denotes the longitudinal wave number as $\beta_{k,n} = k\pi/NL + 2\pi n/L$. The 0th harmonic is referred as the fundamental mode in this manuscript.

---

* mpeng@anl.gov
† jshao@anl.gov

North American Particle Acc. Conf. NAPAC2019, Lansing, MI, USA JACoW Publishing
ISBN: 978-3-95450-223-3 ISSN: 2673-7000 doi:10.18429/JACoW-NAPAC2019-WEPLM68

DESIGN OF A DIELECTRIC-LOADED ACCELERATOR FOR SHORT PULSE HIGH GRADIENT RESEARCH

M.M. Peng*[1], M.E. Conde, G. Ha, C. Jing†[2], W. Liu, J.G. Power, J. Seok, J.H. Shao,
E.E. Wisniewski, Argonne National Laboratory, Lemont, IL, USA
J. Shi, Tsinghua University, Beijing, People's Republic of China
[1]also at Tsinghua University, Beijing, People's Republic of China
[2]also at Euclid Techlabs, Bolingbrook, IL, USA

Abstract

The short-pulse two-beam acceleration approach is a promising candidate to meet the cost and luminosity requirements for future linear colliders. Dielectric-loaded structure has been intensely investigated for this approach because of its low fabrication cost, low RF loss, and potential to withstand GV/m gradient. An X-band 11.7 GHz dielectric-loaded accelerator (DLA) has been designed for high power test with short RF pulses (~3 ns) generated from a power extractor driven by high charge bunches at Argonne Wakefield Accelerator (AWA) facility. The gradient is expected to be over 100 MV/m with the maximum input power of 400 MW.

INTRODUCTION

Structure wakefield acceleration (SWFA) is one of the Advanced Accelerator Concepts aiming to significantly reduce the cost of future TeV-scale linear colliders [1]. In this scheme, high charge drive bunches traveling through a structure exist wakefields which are used to accelerate the low charge main beam in either the same structure (collinear wakefield acceleration, a.k.a. CWA) or a parallel structure (two-beam acceleration, a.k.a. TBA). Based on current understanding, the TBA approach is favored over CWA due to the less challenging beam transportation as well as the flexibility of independent accelerating/decelerating structures optimization [1].

RF breakdown is a potential limitation to reach high accelerating gradient in the SWFA scheme. To improve the gradient, the short pulse (~20 ns) TBA method has been proposed [2] based on the experimental observation of the exponential dependence of RF breakdown rate on pulse length [3]. Various advanced structures with high group velocity and relatively high shunt impedance are under study to efficiently accelerate the main beam with such short RF pulses [4–6]. The dielectric-loaded accelerator, in which the electromagnetic wave is slowed by a uniform dielectric layer, is attractive due to its low fabrication cost, low RF loss, and the potential to withstand high gradient [1]. Although various key technologies of DLA have been successfully tested, its high gradient performance in the short-pulse TBA approach is yet to be demonstrated.

In this study, an X-band 11.7 GHz traveling-wave DLA structure has been designed to be tested with power extractors capable to generate over 100 MW RF pulses at AWA [1, 7, 8]. In our recent study of a tunable metallic power extractor, ~3 ns ~400 MW rf pulses are expected when driven by 8-bunch high charge drive trains [8]. The corresponding accelerating gradient will be over 100 MV/m in the DLA structure. The design, the fabrication, and the experimental plan will be introduced in this manuscript.

STRUCTURE DESIGN

The high gradient structure consists of a uniform section and two tapered sections at both ends to match the impedance between the uniform section and the dual-feed rf couplers, as illustrated in Fig. 1.

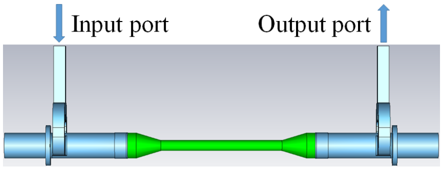

Figure 1: The layout of the X-band DLA structure (green) together with rf couplers (blue).

The uniform section has been optimized so as to achieve over 100 MV/m accelerating gradient with 400 MW input power. The detailed parameters of the DLA structure are listed in Table 1.

Table 1: Parameters of the Uniform Section

Parameters	**Unit**	**Value**
Dielectric material		MCT-16
Dielectric constant		16
Dielectric loss tangent		1×10^{-4}
Dielectric inner diameter	mm	6
Dielectric outer diameter	mm	9.448
Outside metallic material		copper
Metallic conductivity	S/m	5.8×10^{7}
Length	mm	100
Group velocity v_g	c	0.068
Quality factor Q		2468
Shunt impedance r	MΩ/m	23.3

The tapered section has been optimized to obtain a wide coupling bandwidth. The optimized structure has been simulated with the frequency domain solve in CST Microwave

---

* mpeng@anl.gov
† jingchg@anl.gov

ISBN: 978-3-95450-223-3 ISSN: 2673-7000 doi:10.18429/JACoW-NAPAC2019-WEPLM70

FRIB TUNER PERFORMANCE AND IMPROVEMENT*

J. Popielarski#, W. Chang, C. Compton, W. Hartung, S.-H. Kim, E. Metzgar, S. J. Miller, K. Saito, J. Schwartz, T. Xu
Facility for Rare Isotope Beams, Michigan State University, East Lansing, MI, USA

Abstract

The Facility for Rare Isotope Beams (FRIB) is under construction at Michigan State University (MSU). The FRIB superconducting driver linac will accelerate ion beams to 200 MeV per nucleon. The driver linac requires 104 quarter-wave resonators (QWRs, β = 0.041 and 0.085) and 220 half-wave resonators (HWRs, β = 0.29 and 0.53). The cryomodules for β = 0.041, 0.085, and 0.29 have been completed and certified; 38 out of 49 cryomodules are certified via bunker test (as of August 2019). The QWRs have a demountable niobium tuning plate which uses a warm external stepper motor. The HWRs use pneumatically-actuated bellows. Progress on the preparation and performance of the tuners is presented in this paper, along with improvements made to ensure that the resonators meet the frequency requirements.

INTRODUCTION

Frequency tuning characteristics for the FRIB resonators are summarized in Table 1. The FRIB half wave resonators (HWRs) use a pneumatic tuner [1, 2]. As shown in Fig. 1, the tuner is actuated by a bellows which expands and contracts with changes in helium gas pressure. The bellows is linked to a frequency-sensitive area on the cavity (the beam port cups) such that when the helium gas pressure changes, the cavity frequency changes. Bunker testing has shown that stable control can be achieved for single cavities over a span of several hours. Long term testing of multiple HWRs is planned in the next few months.

Table 1: FRIB Frequency Tuning Characteristics

Type	**QWR**		**HWR**	
Deformation	Bottom plate		Beam port cups	
Actuation	Stepping motor		Pneumatic	
Force	±150 lbs		1,000+ lbs	
Frequency	80.5 MHz		322 MHz	
β	**0.041**	**0.085**	**0.29**	**0.53**
Range (kHz)	20	50	62	39

The FRIB quarter wave resonators (QWRs) have a demountable bottom flange with a tuning plate attached. A similar tuner design was used successfully for the MSU reaccelerator [3], though improvements were made to the control system for FRIB. As shown in Fig. 2, the tuning plate has a mechanical link to a stepping motor for actuation. The stepper motor is outside of the cryomodule for ease of maintenance. Most cavities installed in the linac can be tuned by a low-cost stepper motor which provides up to 150 lbs of linear force. Additional space is provided for a warm piezo tuner, which may be added in the future to mitigate microphonics by cancelling disturbances [4].

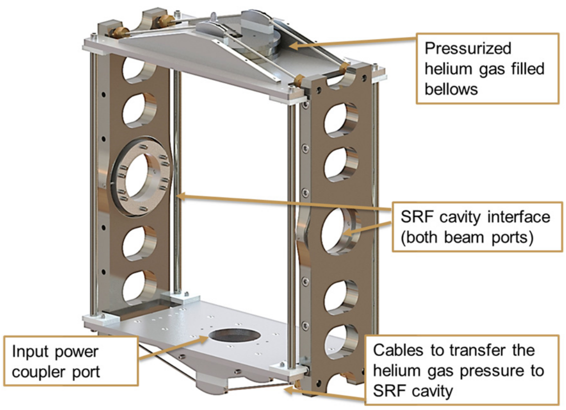

Figure 1: Isometric view of the pneumatic HWR tuner.

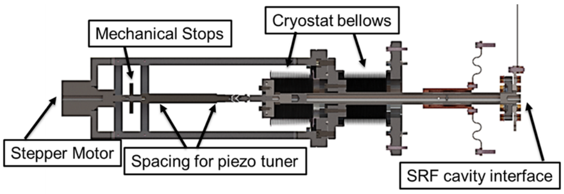

Figure 2: Rotated sectional view of the QWR tuner.

The FRIB team worked with suppliers to develop coarse tuning strategies during the manufacturing steps of the resonators. As a result, the suppliers could ship the resonators within a specified frequency range. During the process workflow to prepare the resonator for installation in the cold mass, frequency data was collected and reviewed before proceeding to the next step.

FREQUENCY CONTROL AND IMPROVEMENTS

The cavity certification test in the vertical test area (VTA) is the final quality assurance check before a resonator is installed onto the cold mass string. One criterion for acceptance is the frequency, which is measured at the operating temperature (~2 K). Statistics were gathered with pre-production resonators on the frequency shift for each preparation step, including the shift between the last room temperature bench measurement and the 2 K test. Some of the shifts are given in Table 2 ("installation" includes attachment of the input coupler and tensioning of the HWR tuner). An unexpected frequency shift may indicate a problem in one of the preparation steps.

---

*Work supported by the U.S. Department of Energy Office of Science under Cooperative Agreement DE-SC0000661.
#popielar@frib.msu.edu

ISBN: 978-3-95450-223-3 ISSN: 2673-7000 doi:10.18429/JACoW-NAPAC2019-WEPLM71

THERMAL PERFORMANCE OF FRIB CRYOMODULES *

M. Xu[†], W. Chang, C. Compton, A. Ganshyn, S. Kim, S. Miller, J. Popielarski, K. Saito and T. Xu,
Facility for Rare Isotope Beams, Michigan State University, East Lansing, USA

Abstract

Now SRF cavity development is advancing high-Q/high gradient by nitrogen doping, infusion, or the new low temperature bake recipe. Once cavity dynamic loss is reduced, the static heat load of the cryomodule will be of concern from the cryogenic plant capability point of view. FRIB gives us a good chance to statistically compare the cryogenic plant design and the measured results, along with a thought for future updated cryomodule design using a low/medium beta cryomodule. FRIB cryomodules have two cooling lines: 4.5 K for solenoids and 2K for cavities. The boil-off liquid helium method was used to measure the cryomodule's heat load. So far, FRIB has completed certification testing (bunker tests) on 39 of 49 cryomodules (80%). This paper reports the static heat load measurement results, which are important for future FRIB upgrades to estimate remaining cryogenic capability. The cryomodule's evolution related to heat load is introduced too.

INTRODUCTION

The Facility for Rare Isotope Beams (FRIB) is a rare isotopes research centre under construction at Michigan State University, USA [1]. A superconducting accelerator is used to produce rare isotopes for energy conservation, as compared to a normal conducting accelerator. There are 15 Quarter-Wave Resonator (QWR) cryomodules and 31 Half-Wave Resonator (HWR) cryomodules that will be deployed in the FRIB tunnel, along with three backup cryomodules that will serve as replacements [2].

The dynamic and static heat load of the cryomodules consumes the most capability of the cryogenic plant. For validating a cryomodule's performance, the dynamic and static heat load of the cryomodules was tested during bunker testing stage. Currently, 39 of 49 cryomodules (80%) have been tested, which is enough to estimate the difference between the cryomodule's total heat load requirements and the cryogenic plant's capability.

To preserve the high clean surface necessary for the cavities, the FRIB cryomodules have two separate vacuum systems - a beam line system and an insulating system. A section view of a cryomodule is shown in Fig. 1. The cryomodule uses a three cooling line system comprising a 38 K helium gas line for thermal shield, a 4.5 K liquid helium for supporting rail and solenoid, and a 2 K liquid helium for cavity.

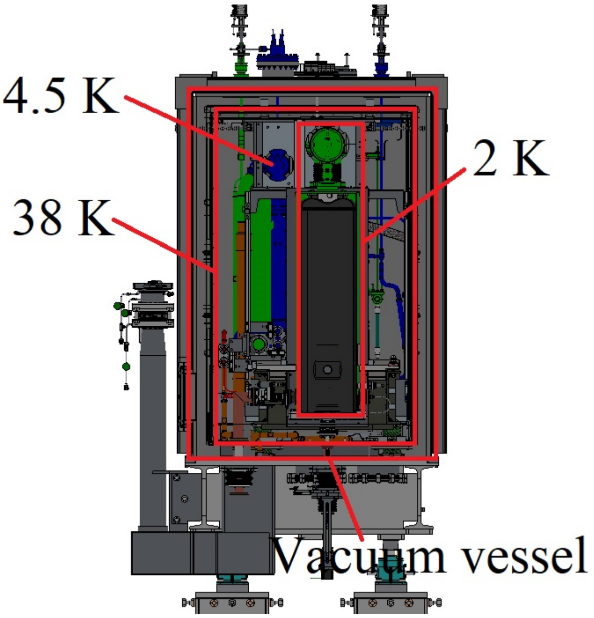

Figure 1: The section view of 0.085 cryomodule of FRIB.

Many methods are applied to reduce heat leaking to the cryogenic temperatures within the cryomodules from the outside. Multilayer insulation is used on both sides of the thermal shield to reduce radiation heat transfer. Copper straps are used for heat interception such as in beam pipe, magnet shield, tuner, and coupler. The G10 material is used for heat insulation. Cold helium gas is used to cool the coupler and solenoid current lead. Attaching the instrument wires to the thermal shield was also used for temperature interception.

MEASUREMENT OF STATIC HEAT LOAD

The cryomodules were designed to operate at 2 K for bulk niobium cavities and 4.5 K for the superconducting solenoids initially. The method of boiling off liquid helium was applied to both the cooling systems for measuring the static heat load of the cryomodule. Helium's phase changing energy is a certain number if keeping a stable pressure in saturated temperature, which is known as the heat of vaporization. From the liquid helium consumption we can deduce how much heat leaks to the low temperature system. The helium volume was indicated by the helium level sensors. The relation between helium level and helium volume was calculated from the cryomodule Solidworks 3D model. During the measurement, pressure change was avoided, as this will cause the results to swing.

---

* Work supported by the U.S. Department of Energy Office of Science under Cooperative Agreement DE-SC0000661 and the National Science Foundation under Cooperative Agreement PHY-1102511.

† xum@frib.msu.edu

ISBN: 978-3-95450-223-3 ISSN: 2673-7000 doi:10.18429/JACoW-NAPAC2019-WEPLM72

DESIGN OF A HIGH-GRADIENT S-BAND ANNULAR COUPLED STRUCTURE*

B. Mustapha[†], A. Abogoda, A. Barcikowski, R. Fischer and A. Nassiri
Argonne National Laboratory, Lemont, IL, USA

Abstract

At Argonne, we have recently developed a conceptual design for a compact linear accelerator for ion beam therapy, named ACCIL. A linac-based ion-beam therapy facility offers many advantages over existing synchrotron based facilities. In addition to the reduced footprint, ACCIL offers more flexibility in beam tuning, including pulse-per-pulse energy and intensity modulation and fast switching between ion species. Essential to the compactness of the ACCIL linac are high-gradient structures for low to intermediate velocity ions, capable of accelerating fields of ~ 50 MV/m. For this purpose, we have designed an S-band annular-coupled structure (ACS). An ACS has the desired qualities of high electric field limit, high shunt-impedance, large area for magnetic coupling and good cooling capacity, making it a very promising candidate for high-gradient operations. We here present the optimized design for a β ~ 0.4 ACS.

INTRODUCTION

High-gradient R&D is well established for velocity-of-light electrons. Recently at the high-power RF Test Facility of the APS, we have demonstrated a gradient of 52 MV/m for a velocity-of-light S-band (2856 MHz) electron beam structure [1]. Such a high gradient is yet to be demonstrated for low velocity ions as R&D in this field started only recently. In the velocity range of β=v/c ~ 0.3, the accelerating cell is short and compact, making electric breakdowns and power dissipation a real challenge to reliably operate these high-gradient structures. R&D in this field is being pursued at CERN [2] and other European institutions, and most recently in the US. In collaboration with RadiaBeam through an SBIR project, we started the development of a β ~ 0.3 traveling-wave structure capable of delivering 50 MV/m [3]. This structure was designed to operate at the negative spatial harmonic which elongates the cell making it more suitable for β ~ 0.3. However, more development is needed to cover the whole β ~ 0.3-0.7 velocity range with the appropriate accelerating structures for the ACCIL linac [4]. Standing wave π/2-mode options such as the annular-coupled structure (ACS) are promising candidates for β ~ 0.4 and higher, capable of similar performance. Standing-wave structures are generally more desirable because they can be more compact and require less power in addition to being simpler to tune and operate. The ACS structure has been employed at lower gradients in the JPARC linac [5], but has not been investigated for high-gradient operation. Here, we developed an optimized design for a 2856 MHz β ~ 0.4 ACS structure. Along with the RF design, the tuning and cooling systems, as well as thermal analysis results and the proposed fabrication procedure are presented.

RF DESIGN

The annular-coupled structure (ACS) is made of alternating accelerating and coupling cells. Coupling cells are annular rings surrounding accelerating cells. Magnetic coupling is ensured by windows cut between each coupling cell and two neighboring accelerating cells. Figure 1 shows the ACS geometry with 3 accelerating cells and two coupling cells.

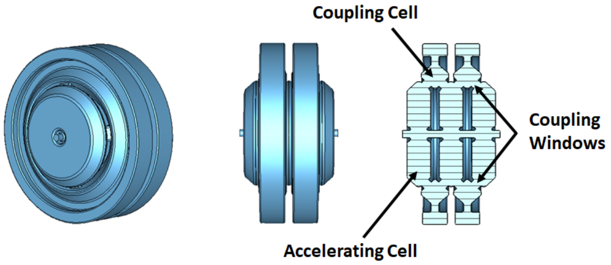

Figure 1: Geometry of an ACS structure with 3 accelerating cells and 2 coupling cells.

Following the RF design optimization of a single cell, a full cavity model with 15 accelerating cells and 14 coupling cells was built. The coupling window size was optimized to provide enough coupling to avoid higher order modes (HOMs) and stabilize the field for the main mode. The geometry of the end cells, especially the gap was adjusted to produce a flat field distribution along the structure. Figure 2 shows the electric field in the 15-cell cavity and the accelerating field along the structure. Table 1 lists the RF design parameters for the single cell and the coupled 15-cell structure. We clearly notice that the cell coupling significantly enhances the peak magnetic field and reduces the shunt impedance. While this is expected, further optimization of the coupling windows may be required to reduce the peak surface field. Two important criteria for pulsed high-gradient operations are also listed, these are the pulsed heating [6] and the modified Poynting vector [7]. While the latter is related to the voltage breakdown rate, the former has to do with the mechanical stability and lifetime of the structure.

TUNER SYSTEM DESIGN

The design frequency for this cavity is 2856 MHz. Machining errors can be controlled down to 5 µm for certain dimensions like the inner cavity radius, while they can be up to 25 µm for other dimensions, especially after assem-

---

* This work was supported by the U.S. Department of Energy under Contract No. DE-AC02-06CH11357 through ANL's LDRD program
[†] corresponding author: brahim@anl.gov.

ISBN: 978-3-95450-223-3 ISSN: 2673-7000 doi:10.18429/JACoW-NAPAC2019-WEPLM73

BUNKER TESTING OF FRIB CRYOMODULES*

W. Chang#, S. Caton, A. Ganshyn, W. Hartung, S.H. Kim, B. Laumer, H. Maniar,
J.T. Popielarski, K. Saito, M. Xu, T. Xu, C. Zhang, S. Zhao,
Facility for Rare Isotope Beams, Michigan State University, East Lansing, MI, USA

Abstract

The Facility for Rare Isotope Beams' (FRIB) superconducting driver linac requires 104 quarter-wave resonators (QWRs, β = 0.041 and 0.085), 220 half-wave resonators (HWRs, β = 0.29 and 0.53), and 74 superconducting solenoid packages (8 packages of length 25 cm, and 66 packages of length 50 cm). The resonators and solenoids are installed onto a cold mass and assembled into a cryomodule. Four accelerating cryomodule types (β = 0.041, 0.085, 0.29, 0.53) and 2 matching cryomodule types (β = 0.085, 0.53) are required. Each cryomodule undergoes cryogenic and RF testing in a bunker prior to installation in the tunnel. The cryomodule test verifies operation of the cavities, couplers, tuners, solenoid packages, magnetic shield, and thermal shield at 4.3 K and 2 K. All of the required cryomodules for β = 0.041, 0.085, and 0.29 have been bunker tested and certified. As of August 2019, eight of the β = 0.53 cryomodules are certified; the remaining cryomodules are being assembled or are in the queue for testing. This paper will present test results for certified cryomodules, including cavity statistics (accelerating gradient, field emission X-rays at operating gradient), solenoid package statistics (operating current, lead flow), and cryomodule 2 K dynamic heat load.

INTRODUCTION

The driver linac for the Facility for Rare Isotope Beams (FRIB) is designed to accelerate ion beams to 200 MeV/u using 46 superconducting cryomodules (SCMs) [1]. The four accelerating SCM types are SCM041 (β = 0.041), SCM085 (β = 0.085), SCM29 (β = 0.29), and SCM53 (β = 0.53). The two matching SCM types are SCM085-matching (β = 0.085) and SCM53-matching (β = 0.53).

Two bunkers in the FRIB complex are used for FRIB cryomodule tests, one in the SRF High Bay (SRF Bunker), the other in the East High Bay (ReA6 Bunker) [2]. They allow us to test and certify up to 2 SCMs per month.

As of August 2019, all SCM041, SCM085, SCM085-matching and SCM29 cryomodules are certified and installed in the FRIB tunnel [3], and ten SCM53 cryomodules are certified. Updated bunker test statistics are shown in the Table 1. Five cryomodules have been certified since the last bunker testing report [4].

CERTIFICATION TESTING

The SCM bunker certification test includes testing of cavities, RF input couplers, tuners [5], and solenoid packages [6]. All of the components must meet the FRIB requirements. Tables 2 and 3 list the main requirements for the cavities and solenoid packages.

Table 1: FRIB Cryomodule Bunker-Test Certification Status

FRIB Cryomodule Type	Certified | Operation Need	Completed
SCM041	3 | 3	100%
SCM085	11 | 11	100%
SCM085-matching	1 | 1	100%
SCM29	12 | 12	100%
SCM53	8 | 18	44.4%
SCM53-matching	0 | 1	0%
Totals	35 | 46	76.1%

Table 2: Main Cavity Requirements (f = resonant frequency, E_a = accelerating gradient; BW = bandwidth)

Parameter	QWR041	QWR085	HWR29	HWR53
f (MHz)	80.5	80.5	322	322
E_a (MV/m)	≥ 5.1	≥ 5.6	≥ 7.7	≥ 7.4
BW (Hz)	43	41.5	57	33.3
2 K Heat Load (W)	≤ 1.32	≤ 3.85	≤ 3.55	≤ 7.9

Table 3: Main Solenoid Package Requirements

Package	Maximum field on axis	Ramp rate	Current
25 cm solenoid	≥ 8 T	≥ 0.3 A/s	≤ 91 A
25 cm dipoles	≥ 0.06 T·m	≥ 0.5 A/s	≤ 20 A
50 cm solenoid	≥ 8 T	≥ 0.3 A/s	≤ 91 A
50 cm dipoles	≥ 0.03 T·m	≥ 0.5 A/s	≤ 20 A

Bandwidth Measurements

Figure 1 shows BW measurements and requirements for 37 FRIB SCMs. Although the results show cavity BWs have some offset relative to the specifications, all of values are acceptable for the beam operation. A few cavities' coupler positions were adjusted to increase the BW to mitigate microphonics issues.

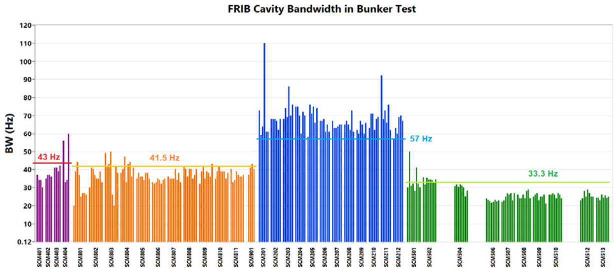

Figure 1: Measured cavity bandwidths.

High-Power Testing

All SCM cavities are tested at high RF power. Initial RF turn-on, calibration verification, and conditioning are done in the self-excited loop mode of the FRIB low-level RF controller (LLRF) [7]. Typically, the high multipacting (MP) barrier is conditioned first, then the middle MP

---

*Work supported by the U.S. Department of Energy Office of Science under Cooperative Agreement DE-SC0000661.

Email address: chang@frib.msu.edu

SIMULATION OF A KLYSTRON INPUT CAVITY USING A STEADY-STATE FULL-WAVE SOLVER

A.R. Gold*, S.G. Tantawi
SLAC National Accelerator Laboratory, Menlo Park, USA

Abstract

The simulation of vacuum electronic radio-frequency (RF) power sources is generally done through semi-analytical modeling approaches. These techniques are computationally efficient as they make assumptions on the source topology, such as the requirement that the electron beam travel longitudinally and interact with cylindrical modes. To simulate more general interactions, transient particle-in-cell (PIC) codes are currently required. We present here simulation results of a 5045 klystron using a newly developed steady state code which does not make assumptions on the beam configuration or geometry of the structure and resonant modes. As we solve directly for the steady-state system dynamics, this approach is computationally efficient yet, as demonstrated through comparison with experimental results, provides similar accuracy.

INTRODUCTION

Modeling the non-linear interaction between intense charged particle beams and electromagnetic fields in beam-based radiation sources, from klystrons to free electron lasers, has historically been addressed using semi-analytical simulation tools. Through recent advances in manufacturing and materials science, we can now realize structures and interaction topologies which are vastly more complex than in current devices – unintuitive configurations with the potential to overcome traditional limits in interaction efficiency and output power. These device concepts lie beyond the assumptions of semi-analytical models and existing large signal codes [1–9], however. Their multi-scale nature, spanning time scales from picoseconds to milliseconds, also renders them computationally intractable to model with more general, transient solvers (particle-in-cell codes) [10–13].

To address this issue, we have developed a steady-state solver which accounts for fully general beam-wave interactions. This approach is also computationally efficient, converging to the steady-state solution in less than ten iterations compared to the thousands to billions of time steps required by a transient solver. We describe this steady-state framework and demonstrate how it works through the example of the SLAC 5045 klystron.

STEADY-STATE FRAMEWORK

The basic concept is to iterate on the steady-state solution for the electromagnetic fields and beam evolution through the vacuum structure, eventually obtaining a self consistent solution. The process begins by meshing the structure geometry spatially, after which the resonant frequencies of the structure are identified through an eigenmode analysis. Once these are known, the amplitude of the fields excited by external pre-defined drivers (RF ports, magnets and applied potentials) are computed.

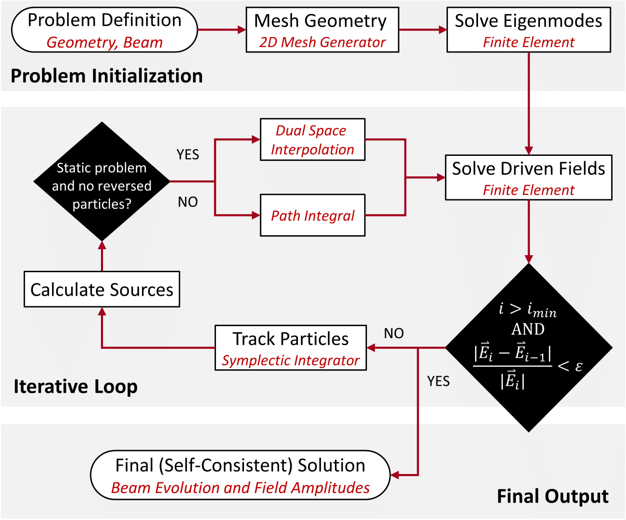

Figure 1: An iterative steady-state beam-wave solver.

In the first iteration, the self-fields of the beam are neglected. Macro-particles, each representing many individual electrons, are tracked through the excited fields to determine the beam evolution. These particles need to be tracked starting from various injection times as the trajectories are dependent on the RF phase at injection. Piece-wise continuous distributions for the charge and current density, ρ and $\vec{J}$ are then calculated from these discrete trajectories. As the fields are computed in the frequency domain, it is in fact the the Fourier transforms, $\tilde{\rho}$ and $\tilde{\vec{J}}$ that are required (in particular, the harmonic content at DC and the resonant frequencies of the structure). Two methods for computing the source terms are used in the solver at present, a dual space interpolation technique for static problems and a path integral (charge deposition) approach for time harmonic problems [14]. The computed distributions become additional driving terms in the next iteration of the field solver.

The process described above is iterated until a self-consistent solution is obtained where the fields produce a beam which generates the same fields. Figure 1 illustrates this process where $i_{min} \geq 1$ is some minimum number of

---

* vrielink@stanford.edu

ANALYTICAL EXPRESSION FOR A N-TURN TRAJECTORY IN THE PRESENCE OF QUADRUPOLE MAGNETIC ERRORS

Y. Rodríguez García,[1]* J. F. Cardona †, Universidad Nacional de Colombia, Bogotá, Colombia
[1] also at Universidad Antonio Nariño, Bogotá, Colombia

Abstract

The action and phase jump method is a technique, based on the use of turn-by-turn experimental data in a circular accelerator, to find and measure local sources of magnetic errors through abrupt changes in the values of action and phase. At this moment, this method uses at least one pair of adjacent BPMs (Beam Position Monitors) to estimate the action and phase at one particular position in the accelerator. In this work, we propose a theoretical expression to describe the trajectory of a charged particle for an arbitrary number of turns when a magnetic error is present in the accelerator. This expression might help to estimate action and phase at one particular position of the accelerator using only one BPM in contrast to the current method that needs at least two BPMs

INTRODUCTION

The Action and Phase Jump Analysis Technique, known as APJ method, is one of the available methods to estimate local magnetic field errors. This method uses as a theoretical argument that the action and phase in betatron oscillations must be preserved in the absence of a magnetic error. This method requires at least two adjacent BPMs to estimate the action and phase variables as described in [1, 2].

In this paper, an analytical expression to describe a N-turn trajectory is proposed considering the presence of a magnetic error, which might provide an alternative way to compute action and phase using only one BPM. First, the betatron oscillations in an arbitrary BPM are described through a first-order approximation for betatron oscillations in that place where a magnetic error is present. Then, an improved expression is obtained using perturbation theory. Finally, the resulting expression is compared with simulated turn by turn trajectories.

TURN BY TURN TRAJECTORY

Reference [1] shows that one-turn trajectory after the particle has passed through a magnetic error can be described by

$$\begin{aligned} z(s) &= \sqrt{2J_{z_0}\beta_z(s)}\sin\left[\psi_z(s)-\delta_{z_0}\right] \\ &\quad + \theta_z\sqrt{\beta_z(s)\beta_z(s_\theta)}\sin\left[\psi_z(s)-\psi_z(s_\theta)\right] \\ &= \sqrt{2J_{z_1}\beta_z(s)}\sin\left[\psi_z(s)-\delta_{z_1}\right] \end{aligned} \tag{1}$$

where z denotes either the x or y axis, β_z represent the nominal beta functions, J_{z_0} (δ_{z_0}) and J_{z_1} (δ_{z_1}) are the actions (phases) before and after the error, while ψ_z represents the betatron function. Both J and δ remain constant except in the error position, represented by s_θ, where they suffer an abrupt jump. The strength of the magnetic error θ_z can be of any order: a dipole, a quadrupole, etc., and it can be estimated by (15) from [1].

For the case in which there is more than one error, say m, the left side of (1) takes the form given by

$$\begin{aligned} z(s) &= \sqrt{2J_{z_0}\beta_z(s)}\sin\left[\psi_z(s)-\delta_{z_0}\right] \\ &\quad + \sum_{i=1}^{m}\theta_{zi}\sqrt{\beta_z(s)\beta_z(s_i)}\sin\left[\psi_z(s)-\psi_z(s_i)\right], \end{aligned} \tag{2}$$

where subscript i denotes the *i-th* magnetic error located at $s = s_i$. It is easy to show that the value of z at any fixed BPM placed in the longitudinal position s for a given number of turns n can be calculated as follows

$$\begin{aligned} z(s,n) &= \sqrt{2J_{z_0}\beta_z(s)}\sin\left[\psi_z(s)-\delta_{z_0}+2\pi Q_z(n-1)\right] \\ &+ \sum_{j=1}^{n}\sum_{i=1}^{m}\theta_{zi,j}\sqrt{\beta_z(s)\beta_z(s_i)} \\ &\qquad \cdot\sin\left[\psi_z(s)-\psi_z(s_i)+2\pi Q_z(n-j)\right], \end{aligned} \tag{3}$$

with Q_z being the nominal tune value and j the subscript indicating the number of the turn. In the following and without loss of generality, the orbit given by Eq. (3) will be referred to the case $z = x$.

APPROXIMATION AT FIRST ORDER

According to equation (19) from [1], θ_{xi} can be written from the multipolar expansion of the magnetic field as follows

$$\begin{aligned} \theta_{xi} &= B_{0i} - B_{1i}x(s_i) + A_{1i}y(s_i) + 2A_{2i}x(s_i)y(s_i) \\ &\quad + B_{2i}\left[-x^2(s_i)+y^2(s_i)\right] + \cdots \end{aligned} \tag{4}$$

where B_{ki} and A_{ki} correspond to the integrated skew and normal quadrupole components of the *i-th* magnetic error, and $x(si)$, $y(si)$ are the transverse coordinates of the orbit at the error location. If only normal quadrupole errors are considered, the Eq. (4) is reduced to

$$\theta_{xi} = -B_{1i}x(s_i). \tag{5}$$

In practice, Eq. (3) could theoretically reproduce the trajectory for n turns if $x(s_i)$ values in Eq. (5) were available,

---

* yrodriguezga@unal.edu.co
† jfcardona@unal.edu.co

ISBN: 978-3-95450-223-3 ISSN: 2673-7000 doi:10.18429/JACoW-NAPAC2019-WEPLS04

SIMULATIONS OF LOW ENERGY Au^{78+} LOSSES IN RHIC*

G. Robert-Demolaize†, A. Drees, Y. Luo, Brookhaven National Laboratory, Upton, NY, USA

Abstract

The 2019 RHIC Run BES-II program [1] features the commissioning of the Low Energy RHIC electron Cooling (LEReC) Project [2, 3], which uses electron cooling techniques to compensate for intra-beam scattering and thus to improve the luminosity lifetime. During RHIC operations at 3.85 GeV/u (beam energy) with LEReC, one needs to ensure that the electron beam energy is properly matched for cooling purposes: if so, some of the circulating Au-79 ions can recombine with an electron, turning into Au-78 and circulating with a large momentum offset. Part of the LEReC commissioning steps is therefore to drive a maximized number of Au-78 ions towards a chosen location of the RHIC mechanical aperture to generate particle showers that can be detected by a Recombination Monitor (RM) outside the cryostat. This article introduces the baseline lattice design, then discusses the few scenarios considered for optimizing Au-78 losses at a given location. Each scenario is then simulated using new tracking tools for generating beam loss maps. Results from operations with the selected lattices are also presented.

INTRODUCTION

With the 2019 RHIC Run, LEReC entered the commissioning phase of the project. The goal at the onset of this run was to demonstrate electron cooling of Au-79 ion beams using RF based acceleration of electron bunches [2]. Figure 1 presents a schematic view of the LEReC layout.

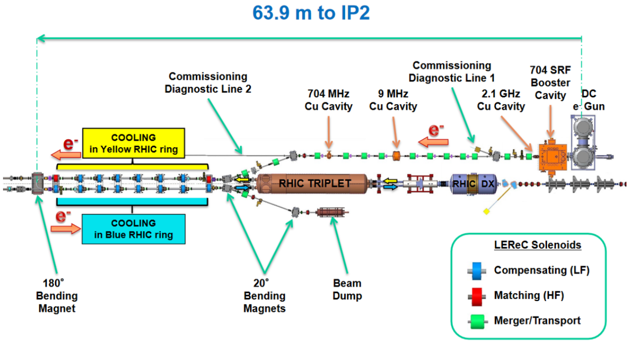

Figure 1: Schematic view of the LEReC layout in and around the RHIC beamlines [2].

On top of the specific lattice requirements for the electron layout, there are prerequisites to the linear optics of the Blue and Yellow ion beam lattices in order to achieve electron cooling: preliminary calculations for LEReC demand that the transverse beam size of the ion bunches matches that of the electron bunches while in the cooling section. Additionally, the electron beam relativistic factor γ_e must be matched to the Au ion beam one γ_{Au} with a precision better than $5.0 \cdot 10^{-4}$ [3]. There is one byproduct of the cooling process that can help fine tune the LEReC RF cavities to that accuracy level: inside of the cooling section, some of the Au-79 ions can recombine with an electron, which turns them into Au-78 ions and gives them a small momentum offset $(\delta p/p)_R = 0.0128$.

Because of this offset, one can design a distortion wave for the dispersion function D_x such that it generates closed orbit oscillations with an amplitude derived from $(\delta p/p)_R$ large enough to drive the recombined Au-78 ions into the physical aperture of the arc downstream of the cooling section for each lattice (Blue or Yellow) but not so large that circulating Au-79 ions with the largest momentum spread at the edges of the bunch length would also get lost. At this location a device (Recombination Monitor, RM) [4] would be installed to detect the resulting particle showers, generating the signal needed to adjust γ_e.

It is relevant to point out that this particular lattice design is only intended to be used as a LEReC commissioning tool to properly set up the electron beam energy for the 2019 program. As such, and for brevity reasons, only the Yellow lattice design will be discussed in the following since it is the one for which the cooling section is closest to a RHIC arc thus presenting the biggest challenge for linear optics manipulation when generating a closed D_x bump for localized orbit excursion. Similar results were achieved for the Blue lattice.

LATTICE DEVELOPMENT

One needs to first establish what the baseline lattice design at 3.85 GeV/u is first. The most straightforward way to do so is to utilize the injection energy ($E = 10$ GeV/u) from the previous RHIC physics run with Au-79 ions and scale the magnet settings to the low energy setpoint, then modify the arc quadrupole magnets to achieve the dedicated working point [1]. Table 1 lists some of the main machine parameters specific to the 3.85 GeV/u setup, and Fig. 2 displays the Yellow linear optics functions at various locations of interest.

For the purpose of electron cooling, the $\beta_{x,y}$ functions for Au-79 would need to be constant along the cooling section, but the matching requirements to the rest of the ring along with a reduced aperture for the beam pipe around IP2 pushes the design towards minimizing the derivative of the parabolic functions $\alpha_{x,y}$ instead. A similar argument applies to the dispersion D_x and its derivative D'_x, and Fig. 2 shows the results of taking both beam size and dispersion into account when matching the linear optics.

---

* Work supported by Brookhaven Science Associates, LLC under Contract No. DE-AC02-98CH10886 with the U.S. Department of Energy.

† grd@bnl.gov

ISBN: 978-3-95450-223-3 ISSN: 2673-7000 doi:10.18429/JACoW-NAPAC2019-WEPLS05

SIMULATION ANALYSIS OF THE LCLS-II INJECTOR USING ACE3P AND IMPACT

D. Bizzozero, J. Qiang, Lawrence Berkeley National Laboratory, Berkeley, CA, USA
L. Ge, Z. Li, C-K Ng, L. Xiao, SLAC National Accelerator Laboratory, Menlo Park, CA, USA

Abstract

The LCLS-II beam injector system consists of a 186 MHz normal-conducting RF gun, a two-cell 1.3 GHz normal-conducting buncher cavity, two transverse focusing solenoids, and eight 1.3 GHz 9-cell Tesla-like superconducting booster cavities. With a coordinated effort between SLAC and LBNL, we have developed a simulation workflow combining the electromagnetic field solvers from ACE3P with the beam dynamics modeling code IMPACT. This workflow will be used to improve performance and minimize beam emittance for given accelerator structures through iterative optimization. In our current study, we use this workflow to compare beam quality parameters between using 2D axisymmetric field profiles and fully 3D non-axisymmetric fields caused by geometrical asymmetries (e.g. RF coupler ports).

OVERVIEW OF ACE3P AND IMPACT

We begin with a brief description of the simulation tools used in our study. The ACE3P code suite [1], developed at SLAC, consists of several tools for various types electromagnetic problems. One such tool, the code Omega3P [2], is a complex eigenmode solver for finding normal modes in RF structures. By using Omega3P with physical design geometries for beamline components, we can export electromagnetic field maps in regions of interest.

Next, the IMPACT code [3–5], developed at LBNL, consists of two particle tracking solvers IMPACT-T (time-coordinate-based) and IMPACT-Z (z-coordinate-based). For our study, we use the IMPACT-T solver to self-consistently track a particle bunch as it propagates through an injector lattice defined by various accelerator structures.

For the analysis in this paper, we use Omega3P to generate high-resolution 3D electric and magnetic field maps for several accelerator components and import them into IMPACT-T for particle tracking as an external field.

In a current configuration, we have implemented a Python script to encapsulate the ACE3P-IMPACT simulation process in a single routine. This script reads-in geometry mesh files, runs Omega3P to compute eigenmodes in various RF cavities, exports the fields into an openPMD hierarchical data structure [6], and runs IMPACT-T on the desired lattice design. In the future, this script will be used as part of a beam optimizer in which the ACE3P-IMPACT workflow is framed as an objective function and optimized by adjusting the geometry and other parameters in an iterative scheme.

PROPOSED LCLS-II INJECTOR DESIGN

In this section, we overview the LCLS-II injector beamline lattice used in our simulation. This design beamline begins with a 186 MHz normal-conducting RF gun, followed by a focusing solenoid, a two-cell 1.3 GHz normal-conducting buncher cavity, a second focusing solenoid, and eight 9-cell 1.3 GHz superconducting boosting cavities for a total length of 14 m, see Figure 1.

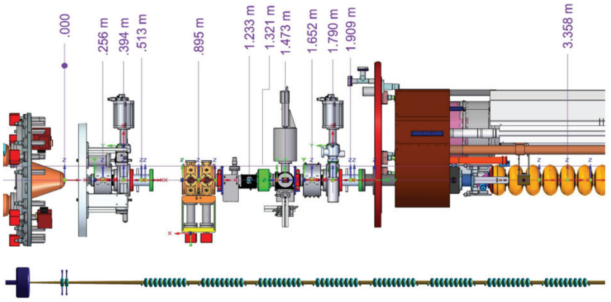

Figure 1: (Top) Schematic layout of the first 3.5 m of the proposed LCLS-II injector (image courtesy of LCLS-II). (Bottom) Full 14 m diagram of the LCLS-II injector RF model (focusing solenoids not shown).

For the beam parameters used in our study, we assume an initial uniform cylindrical electron bunch with charge 100–300 pC, length 34 µm, and radius 0.64 mm. The initial momentum distribution is taken as the product of a zero-mean transverse Gaussian profile with $\sigma_{px,py} = 1.0 \times 10^{-3} m_e c$ and a longitudinal shifted semi-Gaussian profile given by:

$$\rho_{pz}(p_z) = \frac{p_z - p_{z,\min}}{\sigma_{pz}^2} \exp\left[-(p_z - p_{z,\min})^2/(2\sigma_{pz}^2)\right], \quad (1)$$

for $p_z > p_{z,\min} = 2.0 \times 10^{-3} m_e c$ and $\sigma_{pz} = 1.0 \times 10^{-3} m_e c$. This longitudinal distribution ensures all particles have an initial momentum of at least $p_{z,\min}$ for use in simulations.

One important aspect for the LCLS-II injector lattice is to consider the effects of ports and couplers on quantities of interest such as beam emittance. We aim to closely analyze the emittance growth due to the couplers in the boosting cavities through theoretical considerations and numerical simulations.

EMITTANCE GROWTH ESTIMATES

As a reference point for our simulations, we refer to earlier work by Dowell et al [7], which derives an approach to estimate the transverse emittance growth due to the asymmetric couplers. In that study, the couplers in an entire boosting

ISBN: 978-3-95450-223-3 ISSN: 2673-7000 doi:10.18429/JACoW-NAPAC2019-WEPLS09

FAST TWO-DIMENSIONAL CALCULATION OF COHERENT SYNCHROTRON RADIATION IN RELATIVISTIC BEAMS

J. Tang, G. Stupakov*
SLAC National Accelerator Laboratory, Menlo Park, CA, USA

Abstract

Coherent Synchrotron Radiation(CSR) in a relavistic beam during compression can lead to longitudinal modulation of the bunch with wavelength smaller than bunch length and is regarded as one of the main sources of emittance growth in the bunch compressor. Current simulations containing CSR wake fields often utilize one-dimensional model assuming a line beam. Despite its good computation efficiency, 1D CSR model can be inaccurate in many cases because it ignores the so-called 'compression effect'. On the other hand, the existing 3D codes are often slow and have high demands on computational resources. In this paper we propose a new method for calculation of the three-dimensional CSR wakefields in relativistic beams with integrals of retarded potentials. It generalizes the 1D model and includes the transient effects at the entrance and the exit from the magnet. Within given magnetic lattice and initial beam distributions, the formalism reduces to 2D or 3D integration along the trajectory and therefore allows fast numerical calculations using 2D or 3D matrices.

INTRODUCTION

Coherent Synchrotron Radiation(CSR) is one of the main limits to improvements of the brightness of electron beam in storage rings, free electron laser (FEL) light source and high-energy colliders. In a bending magnets, the beam radiates electromagnetic field and experiences a radiation reaction force. 1D model for this forces has been developed [1–4] and implemented in code ELEGANT, which is widely used for the design of bunch compressor in the linac.

Although the 1D models are simple and easy to use, they miss an important part of the total force in relativistic beams moving in a curvilinear trajectory. The attention to this force was attracted by M. Dohlus [5] in 2002, who pointed out that if the beam is compressed (either longitudinally or transversely) the energy of its Coulomb field changes and this should result in a change of the kinetic energy of the beam particles. A force that is responsible for this change can be called the compression force. Note that this force is different from the radiation reaction force, because the compression is a reversible process, and if the beam is decompressed, this force changes sign. It cannot be associated with what is conventionally called the space charge force because the latter typically scales as $1/\gamma^2$ with γ the Lorentz factor. The compression-decompression effect occurs even in the limit $\gamma \longrightarrow \infty$(hence, $v = c$), when the space charge force vanishes. [6]

In this paper, we calculated 2D longitudinal CSR wake based on the integral of retarded potential, which can be very easily extended to three dimensions. The coding is implemented with MATLAB, which enables the fast calculation of the rate of energy change along the beam with 2D matrix. Transient effects at the entrance of the dipole are shown as a benchmark. We also calculated the CSR wake inside a chicane in a configuration studied at the CSR workshop at DESY-Zeuthen in 2002. The differences in longitudinal rate of energy loss compared between 1D and 2D model are discussed .

FORMULAS FOR 3D CSR

Electron beam can be described by its time-dependent charge density $\rho(\boldsymbol{r}, t)$ and velocity $\boldsymbol{v}(\boldsymbol{r}, t)$, where $\boldsymbol{r}$ is the coordinate vector and t is the time. Energy loss per unit time and unit charge due to CSR along the beam can be given by

$$\mathcal{P} = q\, \boldsymbol{v}(\boldsymbol{r}, t) \cdot \boldsymbol{E}(\boldsymbol{r}, t) \tag{1}$$

where the electric field inside the beam can be derived by scalar and vector potential, which are the integrals over retarded space coordinate $\boldsymbol{r'}$ around the beam along the trajectory at proceeding time $t' < t$

$$\begin{aligned}
\phi(\boldsymbol{r}, t) &= \int d^3r' \frac{\rho(\boldsymbol{r'}, t_{ret}(\boldsymbol{r}, t))}{|\boldsymbol{r'} - \boldsymbol{r}|} \\
\boldsymbol{A}(\boldsymbol{r}, t) &= \frac{1}{c} \int d^3r' \frac{\boldsymbol{v}(\boldsymbol{r'}, t_{ret}(\boldsymbol{r}, t))\rho(\boldsymbol{r'}, t_{ret}(\boldsymbol{r}, t))}{|\boldsymbol{r'} - \boldsymbol{r}|} \\
\boldsymbol{E}(\boldsymbol{r}, t) &= -\nabla_r \phi(\boldsymbol{r}, t) - \frac{1}{c}\frac{\partial \boldsymbol{A}(\boldsymbol{r}, t)}{\partial t}
\end{aligned} \tag{2}$$

We made the following assumptions. A cold fluid approximation is applied that at point $\boldsymbol{r}$ the status of particles is determined by density $\rho(r, t)$ and velocity $v(r, t)$. Second, we assume that the spread in velocity due to the angular and energy spread is negligible, which is valid for highly relativistic beams. Third, we assume that the size of the bunch is much smaller that the external scale of the problem under study. With further simplification, the energy loss due along the beam can be given by [6, 7]

$$\begin{aligned}
\mathcal{P} = -c\, q \int & \frac{d^3r'}{|\boldsymbol{r'} - \boldsymbol{r}|}[\boldsymbol{\beta}(\boldsymbol{r}, t) \\
& - (\boldsymbol{\beta}(\boldsymbol{r}, t) \cdot \boldsymbol{\beta}(\boldsymbol{r'}, t_{ret}))\boldsymbol{\beta}(\boldsymbol{r'}, t_{ret})] \cdot \partial_{\boldsymbol{r'}} \rho(\boldsymbol{r'}, t_{ret})
\end{aligned} \tag{3}$$

As in [6], to calculate ρ and $\boldsymbol{v}$ we use use the formalism of the Vlasov equation. In 2D, we use the notation x for the horizontal particle offset relative to the nominal orbit, z

---

* stupakov@slac.stanford.edu

ISBN: 978-3-95450-223-3 ISSN: 2673-7000 doi:10.18429/JACoW-NAPAC2019-WEPLS10

MODELING OF SPACE-CHARGE EFFECTS IN THE ORISS MRTOF DEVICE FOR APPLICATIONS TO FRIB

R. Hipple*[1], S.M. Lund[2], Physics and Astronomy Dept.,
Michigan State University, East Lansing, MI, USA
[1]Also at Niowave Inc., Lansing, MI, USA
[2]Also at Facility for Rare Isotope Beams, Michigan State University, East Lansing, MI, USA

Abstract

The Oak Ridge Isotope/Isomer Spectrometer and Separator (ORISS) is an electrostatic multiply reflecting time-of-flight (MRTOF) mass separator constructed by the University Radioactive Ion Beam Consortium (UNIRIB) and Louisiana State University. The device is now at Michigan State University for use at the Facility for Rare Isotopes and Beams (FRIB). The mass separation process is sensitive to space-charge effects due to the reflection of ions at both ends of the trap, as well as nonlinearities in the optics. In this study, we apply the time-based PIC code Warp [1] to model the effects of intense space-charge during the separation process. We find that the optics can be tuned for operation with many isochronous bounces with focusing in the presence of intense space-charge to enable separation of bunches with high particle counts. This suggests the device may be effectively utilized at FRIB as a separator, spectrograph and spectrometer to provide higher counts of particles on detectors.

INTRODUCTION

ORISS is a 1.43 m long cylindrical ion trap with electrostatic mirrors at each end whereby particles to be separated are repeatedly reflected from end to end. Fig. 1 shows a drawing of the left electrostatic mirror, the on-axis potential and axial field, and the paraxial radial field of a typical operating point. The right mirror geometry is reflection symmetric. There are 8 ring electrodes, and a conical electrostatic lens. All electrodes within each mirror, the conical lens, and the central drift region can each be independently biased. The ring electrodes have a diameter of 146 mm, axial length 32.49 mm, and are separated by thin insulating gaps (ceramic balls) with 12.7 mm diameter. The conical lenses have a smaller aperture of 50 mm and full axial length of 40.51 mm. This is the smallest aperture in the system, and therefore limits radial excursion of the particles. These conical lenses can be removed and replaced with the large-aperture variety [2].

OVERVIEW OF OPERATIONAL TUNING

To analyze the physics of of the reflections we model ORISS as an array of coaxial rings of charge. The on-axis potential of a thin ring of charge Q and radius R at axial position $z = 0$ is [3]

$$\phi(r = 0, z) = \frac{1}{4\pi\epsilon_0} \frac{Q}{\sqrt{R^2 + z^2}} \tag{1}$$

from which we can calculate the off-axis values of the electric field components E_z and E_r to 2nd order in r as [4]

$$\begin{aligned} E_z(r, z) &= -\frac{\partial\phi}{\partial z} \approx -\phi' + \frac{1}{4}\phi''' r^2, \\ E_r(r, z) &= -\frac{\partial\phi}{\partial r} \approx \frac{1}{2}\phi'' r, \end{aligned}$$

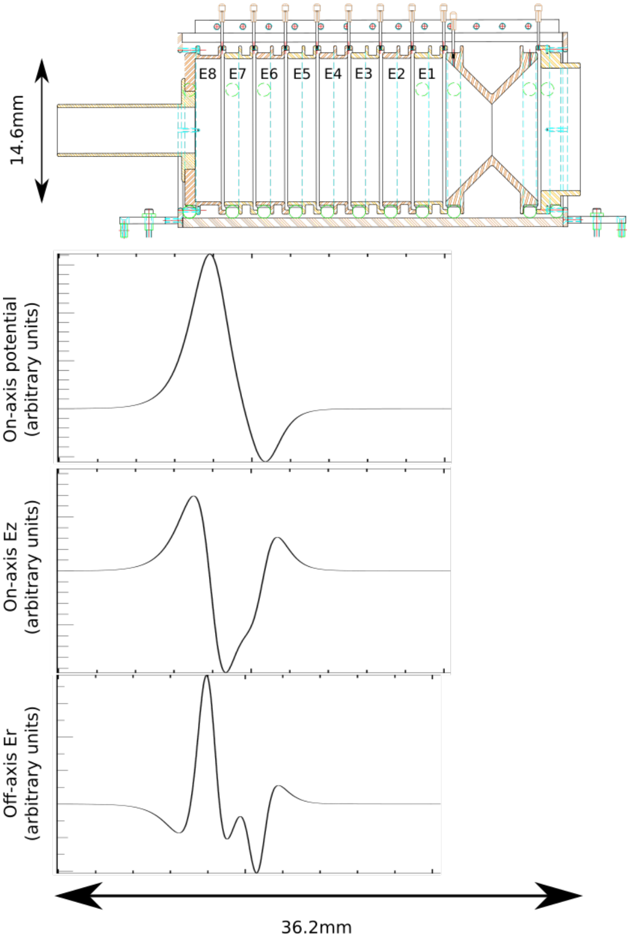

Figure 1: ORISS showing the mechanical structure and relevant electrostatic fields (Mechanical drawing courtesy LSU).

---

[*] hipple@msu.edu

SIMULATION OF TRANSPARENT SPIN EXPERIMENT IN RHIC*

H. Huang[†],Ya.S. Derbenev, F. Lin,V.S. Morozov[†], Y. Zhang,Jefferson Lab., Newport News, USA
A.M. Kondratenko, M.A. Kondratenko, Sci. & Tech. Laboratory Zaryad, Novosibirsk, Russia
Yu.N. Filatov, MIPT, Dolgoprudniy, Moscow Region, Russia
P. Adams, H.X. Huang, F. Méot, V. Ptitsyn, W. Schmidke,
Brookhaven National Laboratory, Upton, NY, USA

Abstract

The transparent spin mode has been proposed as a new technique for preservation and control of the spin polarization of ion beams in a synchrotron. The ion rings of the proposed Jefferson Lab Electron-Ion Collider (JLEIC) adopted this technique in their figure-8 design. The transparent spin mode can also be setup in a racetrack with two identical Siberian snakes. There is a proposal to test the predicted features of the spin transparent mode in Relativistic Heavy Ion Collider (RHIC), which already has all of the necessary hardware capabilities. We have earlier analytically estimated the setup parameters and developed a preliminary experimental plan. In this paper we describe simulation setup and benchmarking for the proposed experiment using a Zgoubi model of RHIC.

MOTIVATION

For Electron Ion Collider (EIC), the high electron and ion polarizations are some of the key requirements [1] that include high polarization (> 70%) of protons and light ions (d, ^{3}He^{++}, and possibly ^{6}Li^{+++}); It also requires both longitudinal and transverse polarization orientations available at all interaction points (IPs), a sufficiently long polarization lifetime, and spin flipping. As a novel technique, the transparent spin (TS) mode makes the ring lattice "invisible" to the spins and allows for polarization control by small magnetic fields just slightly breaking this spin motion degeneracy. In practice, TS mode offers unique opportunities for design of electron and ion polarization dynamics in JLEIC and electron polarization dynamics in Brookhaven's eRHIC [2-5].

In order to further develop the spin dynamics theory and verify TS experimentally, cconsidering all technical capabilities and investigating the current existing colliders, it was proposed to experimentally test in RHIC [5]. RHIC schematically shown in Fig. 1 is a perfect place for an experimental test of the TS mode because it requires no new hardware. Making the snake axes parallel at 0° will set RHIC in the spin transparency mode. This adjustment yields minimum field integral, minimum orbit excursion and requires no flip of the field sign and power supply polarities. The snake currents can be changed dynamically at 1 A/s [6]. The existing polarimeter can provide a fast polarization measurement. Only relative measurement is needed.

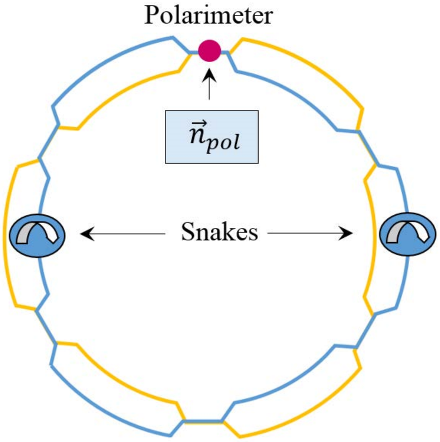

Figure 1: RHIC ring with two helical snakes.

MODEL OF TRANSPARENT SPIN MODE

The total TS resonance strength consists of the coherent and incoherent parts:

$$\omega = \omega_{coh} + \omega_{emitt}. \tag{1}$$

The spin stability criterion is that the spin tune induced by a spin rotator must significantly exceed the TS resonance strength. ω_{coh} can be estimated using a statistical model. Assuming independent random misalignments of machine elements, it is given by

$$|\omega_{coh}| = \sqrt{\frac{1}{4\pi^2} \sum_{elements} \frac{\overline{\Delta B_x^2 L_x^2}}{(B\rho)^2} |F|^2} \tag{2}$$

where $\overline{\Delta B_x^2}$ is the average of an element's error radial magnetic field squared, L_x is the element's length, $B\rho$ is the magnetic rigidity, and F is the spin response function $\overline{\Delta B_x^2 L_x^2}$ arises primarily [4] due to vertical quadrupole misalignments Δy

$$\overline{\Delta B_x^2 L_x^2} = \left(\frac{\partial B_x}{\partial y}\right)^2 \overline{\Delta y^2} L_x^2 \tag{3}$$

and dipole roll $\Delta\varphi$

$$\overline{\Delta B_x^2 L_x^2} = \theta^2 \, \overline{\Delta\varphi^2} \, (B\rho)^2 \tag{4}$$

where θ is the dipole bending angle.

The rms vertical excursion of the closed orbit is

---

* Work supported by the U.S. DOE under Contracts No. DE-AC05-06OR23177 and DE-AC02-98CH10886.

† huang@jlab.org and morozov@jlab,org

ISBN: 978-3-95450-223-3 ISSN: 2673-7000 doi:10.18429/JACoW-NAPAC2019-WEPLS12

A SEMI-ANALYTICAL APPROACH TO SIX-DIMENSIONAL PATH-DEPENDENT TRANSPORT MATRICES WITH APPLICATION TO HIGH-BRIGHTNESS CHARGED-PARTICLE BEAM TRANSPORT*

C.-Y. Tsai†, K. Fan, Huazhong University of Science and Technology, Wuhan, China

Abstract

Efficient and accurate estimate of high-brightness electron beam dynamics is an important step to the overall performance evaluation in modern particle accelerators. Utilizing the moment description to study multi-particle beam dynamics, it is necessary to develop a path-dependent transport matrix, together with application of the drift-kick algorithm. In this paper we will construct semi-analytical models for two typical beam transport elements, solenoid with fringe fields and transverse deflecting cavity. To construct the semi-analytical models for these elements, we begin by formulating the simplified single-particle equations of motion, and apply numerical techniques to solve the corresponding six-by-six transport matrix as a function of the path coordinate. The developed semi-analytical models are demonstrated with practical examples, where the numerical results are discussed, compared with and validated by particle tracking simulations. These path-dependent transport matrix models can be incorporated to the analysis based on beam matrix method for the application to high-brightness charged-particle beam transport.

SEMI-ANALYTICAL MODELS

We note that the mathematical notations follow [1].

Solenoid with Fringe Field

Assuming the longitudinal magnetic field B_s is collinear with z, to first order in the spatial (circular cylindrical) coordinate, we have the radial and azimuthal magnetic field components $B_r \approx -\frac{r}{2}B_s'$ and $B_\varphi = 0$, respectively. Here r is the radial distance from the solenoid axis. Written in Cartesian coordinate, we have $\mathbf{B} = \left(-\frac{1}{2}B_s'x, -\frac{1}{2}B_s'y, B_s\right)$. Neglecting the longitudinal effect of the solenoid, which is of the second order [2], we can write down the single-particle equations of motion in the transverse phase space coordinate $\mathbf{X}_{4D} = (x, x', y, y')$ as [2]

$$x'' = \mathcal{S}(s)y' + \frac{1}{2}\mathcal{S}'(s)y, \tag{1a}$$

$$y'' = -\mathcal{S}(s)x' - \frac{1}{2}\mathcal{S}'(s)x, \tag{1b}$$

where $\mathcal{S}(s) = eB_s(s)/\gamma m\beta c = B_s(s)/[B\rho]$ with $[B\rho]$ the beam rigidity. The formula $[B\rho]$ (T-m) = $3.3356{\times}\beta E$(GeV) can be of practical use.

Here we recommend that the interested reader to [3] for a more detailed discussion of single-particle dynamics in a solenoid magnetic field. For convenience of the subsequent analysis, we perform a coordinate rotation in complex notation and define $\eta_L = x_L + iy_L$, with the subscript L denoting a (complex) quantity in Larmor frame. The solution to Eq. (1) can be generally expressed as

$$\begin{bmatrix}\eta_L\\ \eta_L'\end{bmatrix}_s = \begin{pmatrix} M_{L,11} & M_{L,12}\\ M_{L,21} & M_{L,22}\end{pmatrix}\begin{bmatrix}\eta_L\\ \eta_L'\end{bmatrix}_{s_i}. \tag{2}$$

Note that $M_{L,ij}$ is also a complex quantity in Larmor frame. The evolution equations for $M_{L,ij}$ can be written as [2]

$$\frac{dM_{L,11}}{ds} = M_{L,21}, \frac{dM_{L,12}}{ds} = M_{L,22}, \tag{3a}$$

$$\frac{dM_{L,21}}{ds} = -\frac{i}{2}\mathcal{S}'(s)M_{L,11} - i1\mathcal{S}(s)M_{L,21}, \tag{3b}$$

$$\frac{dM_{L,22}}{ds} = -\frac{i}{2}\mathcal{S}'(s)M_{L,12} - i\mathcal{S}(s)M_{L,22}. \tag{3c}$$

Now we convert η_L to x_L and y_L by taking the real and imaginary parts, respectively. The 2×2 matrix in Eq. (2) now becomes 4×4 with

$$\begin{bmatrix}x_L\\ x_L'\\ y_L\\ y_L'\end{bmatrix}_s = \begin{pmatrix} M_{L,11}^{\mathrm{Re}} & M_{L,12}^{\mathrm{Re}} & -M_{L,11}^{\mathrm{Im}} & -M_{L,12}^{\mathrm{Im}}\\ M_{L,21}^{\mathrm{Re}} & M_{L,22}^{\mathrm{Re}} & -M_{L,21}^{\mathrm{Im}} & -M_{L,22}^{\mathrm{Im}}\\ M_{L,11}^{\mathrm{Im}} & M_{L,12}^{\mathrm{Im}} & M_{L,11}^{\mathrm{Re}} & M_{L,12}^{\mathrm{Re}}\\ M_{L,21}^{\mathrm{Im}} & M_{L,22}^{\mathrm{Im}} & M_{L,21}^{\mathrm{Re}} & M_{L,22}^{\mathrm{Re}}\end{pmatrix}\begin{bmatrix}x_L\\ x_L'\\ y_L\\ y_L'\end{bmatrix}_{s_i}, \tag{4}$$

where the superscripts Re and Im denote the real and imaginary part of a matrix element, respectively. As a final step, we transform the quantities from Larmor frame back to the Lab frame by $\mathbf{R}^{-1}$ (Lab → Larmor), where $\mathbf{R}$ (Lab → Larmor) =

$$\begin{pmatrix} \cos\Delta\theta_L & 0 & \sin\Delta\theta_L & 0\\ -\Delta\theta_L'\sin\Delta\theta_L & \cos\Delta\theta_L & \Delta\theta_L'\cos\Delta\theta_L & \sin\Delta\theta_L\\ -\sin\Delta\theta_L & 0 & \cos\Delta\theta_L & 0\\ -\Delta\theta_L'\cos\Delta\theta_L & -\sin\Delta\theta_L & -\Delta\theta_L'\sin\Delta\theta_L & \cos\Delta\theta_L\end{pmatrix}, \tag{5}$$

with Larmor angle defined as $\Delta\theta_L = -\frac{1}{2}\int\limits_{s_0}^{s}\mathcal{S}(\zeta)d\zeta$. Here positive B_s gives positive Larmor angle (i.e., $e < 0$).

From the above analysis, given the longitudinal magnetic field profile B_s, we can numerically solve Eq. (3) [by using a standard finite difference scheme, for example] to obtain $\mathrm{M}_L(s)$. Multiplying the inverse matrix of Eq. (5) with the obtained $\mathrm{M}_L(s)$ and appending the longitudinal block matrix as a drift section of the length ranging from $s = 0$ to $s = L_{\mathrm{sol}}$ thus gives the 6×6 transport matrix $\mathbf{M}_{\mathrm{sol}}(s)$ for the solenoid. The resulting transport matrix is s-dependent and includes

---

* The work was supported by the Fundamental Research Funds for the Central Universities under Project No. 5003131049.

† jcytsai@hust.edu.cn

ISBN: 978-3-95450-223-3 ISSN: 2673-7000 doi:10.18429/JACoW-NAPAC2019-WEPLS14

A C++ TPSA/DA LIBRARY WITH PYTHON WRAPPER*

H. Zhang#, Y. Zhang
Jefferson Lab, Newport News, VA 23606, USA

Abstract

Truncated power series algebra (TPSA) or differential algebra (DA) is often used by accelerator physicists to generate a transfer map of a dynamic system. The map then can be used in dynamic analysis of the system or in particle tracking study. TPSA/DA can also be used in some fast algorithms, *e.g.* the fast multipole method, for collective effect simulation. This paper reports a new TPSA/DA library written in C++. This library is developed based on Dr. Lingyun Yang's TPSA code, which has been used in MAD-X and PTC. Compared with the original code, the updated version has the following changes: (1) The memory management has been revised to improve the efficiency; (2) A new data type of DA vector is defined and supported by most frequently used operators; (3) Support of inverse trigonometric functions and hyperbolic functions for the DA vector has been added; (4) the composition function is revised for better efficiency; (5) a python wrapper is provided. This library is open-source and the code is published on its github repository.

INTRODUCTION

The truncated power series algebra (TPSA) [1] or differential algebra (DA) [2] is a widely used tool in accelerator physics study. It is often used to generate a transfer map for a section of an accelerator. Once the map is created, it can be used directly to analyse the dynamic property of the section or perform map-based tracking for it. TPSA/DA has also been introduced into the fast multipole method (FMM) [3], which is a fast algorithm to calculate pairwise interactions between particles. The TPSA/DA method has been implemented in many accelerator simulation programs, such as MAD-X [4], COSY Infinity [5], *etc*. However, a library outside the simulation programs is not easily available for developers. The purpose of this work is to provide a stand-alone library with good efficiency for C++ and Python code developers.

THE NEW LIBRARY

The new library is composed of a C++ library that performs the TPSA/DA calculations and a Python wrapper. The C++ code is developed based on Dr. Lingjun Yang's TPSA code [6], which was included in previous versions of MAD-X. Now, our code, Yang's code, and documentations of our code are all available on our github repository[7]. Following the documentation, the users can compile the source code into a static or a shared library. They can also download the source files and use them directly in their projects. In our development, we tried to make minimal changes on the orignal code, but we had to revise or rewrite some functions for better efficiency or consistency.

We added some new features, which are listed as follows. 1. More math functions are supported. 2. Add a DA vector data type and defined the popular math operators for it, so that users can use a DA vector as simple as a normal number in calculations. 3. Revised the function for composition of two DA vectors for better performance. 4. Provide bunch processing of the composition function, since in accelerator studies one usually has to deal with multiple dimensional problems and the composition needs to be carried out on multiple DA vectors. These features will be demonstrated in the flowing sections.

Besides the new features added, one big change is made on the memory management (see Fig. 1). In Yang's code, the pointers to all the DA vectors are stored in a vector. Although the maximum number of DA vectors in the run is defined, the memory is not allocated. Each time when a new DA vector is needed, the program will search in the vector to find the first empty pointer and allocate the memory to it. Once the DA vector is out of scope, the memory is freed. This approach is good enough for a normal usage in accelerator study, which usually only needs a light DA calculation. However, in some cases an intense DA calculation may be needed. For example, when DA is used in FMM, to perform the calculation once, there may be millions of DA vectors created and

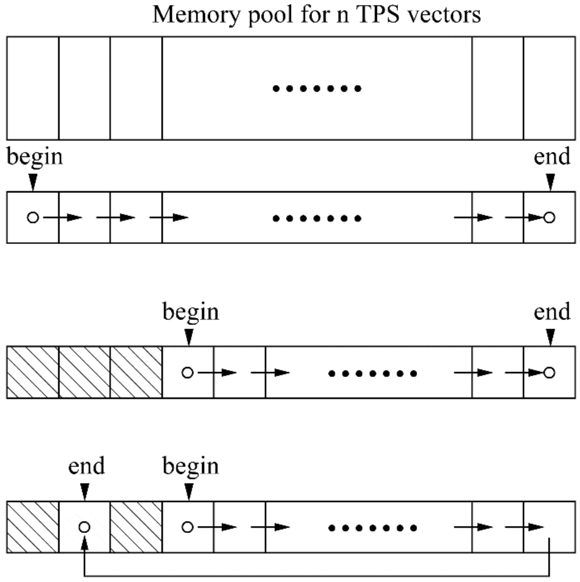

Figure 1: A schematic of memory management.

---

* Work supported by the Department of Energy, Laboratory Directed Research and Development Funding, under Contract No. DE-AC05-06OR23177.

#hezhang@jlab.org

LONGITUDINAL BEAM PROFILE MEASUREMENT BY SILICON DETECTOR IN FACILITY FOR RARE ISOTOPE BEAMS AT MICHIGAN STATE UNIVERSITY*

T. Maruta[†], P.N. Ostroumov, Q. Zhao, Facility for Rare Isotope Beams, East Lansing, MI, USA

Abstract

The silicon detector (SiD) is widely used to precisely measure the kinetic energy of ion beams. In the Facility for Rare Isotope Beams (FRIB) at Michigan State University, a foil scattered type SiD system was installed after the first three superconducting cryomodules to measure the beam energy, energy spread, and longitudinal bunch length. In this paper, the measurement results with the SiD system is reported.

INTRODUCTION

The Facility for Rare Isotope Beams (FRIB) being constructed at Michigan State University [1] is based on a continuous wave (CW) superconducting (SC) linear accelerator which is designed to deliver 400 kW heavy ion beam power to the fragmentation target. The installation of the accelerator equipment is approaching completion and multi-stage beam commissioning activities started in the summer 2017 with expected completion in 2021. The direct current (DC) beam extracted from the electron cyclotron resonance ion source (ECRIS) is transported to the Radio Frequency Quadrupole (RFQ) located in the tunnel. Beam is bunched longitudinally by a multi-harmonic buncher (MHB) and then accelerated to 0.5 MeV/u in the RFQ, followed by three SC linac segments (LS1 to LS3) to deliver beams to the fragmentation target.

The second stage of the beam commissioning took place in the summer 2018 and included acceleration of argon and krypton beams in the first three cryomodules, which contain twelve β_{OPT}=0.041 SC cavities and six SC solenoids [2]. ^{40}Ar and ^{86}Kr beams were successfully accelerated up to 2.3 MeV/u while the design energy for both beams is 1.46 MeV/u in this section of the linac. It should be noted that one resonator was disabled most of the time to stay below the energy threshold for neutrons' generation.

For complete characterization of the beam properties a commissioning diagnostics station (D-station), was developed and installed after the third cryomodules, which included AC-coupled Beam Current Monitors (BCMs), a Faraday Cup (FC), Beam Position Monitors (BPMs), Halo Monitor Rings, a Profile Monitor (PM) and a silicon detector (SiD).

SETUP OF SILICON DETECTOR SYSTEM

The SiD system includes three parts: a head part placed on the beam line, a signal processing circuit, and a signal digitization and analysis. The head part of SiD system is comprised from a gold foil and detector itself as shown in Fig. 1. The detector head is parked off the beam line and inserted only to perform beam measurements. The SiD is placed at 67 mm behind and 30° off-axis vertically to the foil to attenuate counting rate. The counting rate should not exceed 10^3 Hz to avoid signal pileups. The intensity of the beams during the linac commissioning was ~10^{13} ions/sec. Therefore, the attenuation by a factor of 10^{10} was provided in two steps: by using the attenuators in the LEBT and a thin gold foil upstream of the detector head.

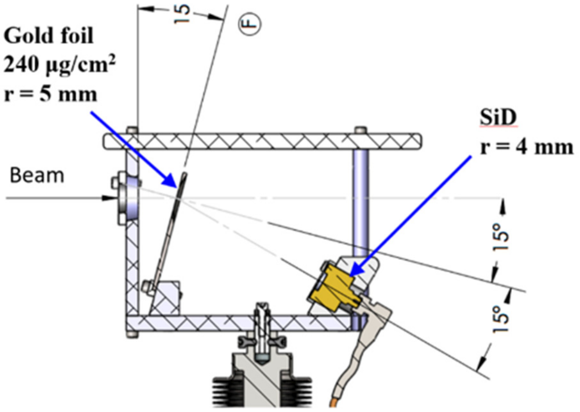

Figure 1: Head part of the silicon detector system.

The 10-mm diameter gold foil of 240 μg/cm^2 thickness is mounted on the aluminium plate that is tilted 15° vertically. The foil thickness was verified by measuring energy loss of alpha particles emitted from ^{241}Am decay.

The silicon detector is a passivated implanted planar silicon detector manufactured by Canberra [3]. Estimated timing resolution by the manufacturer is < 200 psec which corresponds to < 5.8° of the reference RF frequency at 80.5 MHz. The sensitive area's diameter is 8 mm. The sensitive depth is 300 μm that is 10 times more than the penetration depth of 2.3 MeV/u ^{40}Ar ions.

Two signal-processing circuits to measure absolute energy and timing w.r.t RF reference signal were integrated by Nuclear Instrument Modules (NIMs). Both energy and timing information are converted to pulse height and input to a multi-channel analyser (MCA), Lynx [4]. Different electronic circuits are used to process the SiD signal for beam energy or timing measurements. The circuit details are discussed in another paper at this conference [5].

The signal height manipulated by the circuit is digitized by Lynx for these measurements. The pulse height is digitized by a 15-bit (32768 channels) analog-to-digital converter (ADC) and then recorded as corresponding channel number. The Lynx was installed in the same rack of the NIM circuits to mitigate noise contamination. Data-taking

---

* Work supported by the U.S. Department of Energy Office of Science under Cooperative Agreement DE-SC0000661, the State of Michigan and Michigan State University.

† maruta@frib.msu.edu

EXPERIENCE WITH LONG-PULSE OPERATION OF THE PIP2IT WARM FRONT END*

A.V. Shemyakin†, J.-P. Carneiro, A.A. Chen, D. Frolov, B.M. Hanna, R. Neswold, L.R. Prost,
G.W. Saewert, A. Saini, V.E. Scarpine, A. Warner, J.Y. Wu, Fermilab, Batavia, IL, USA
C.J. Richard, Michigan State University, East Lansing, MI, USA

Abstract

The warm front end of the PIP2IT accelerator, assembled and commissioned at Fermilab, consists of a 15 mA DC, 30 keV H^- ion source, a 2 m long Low Energy Beam Transport (LEBT) line, and a 2.1 MeV, 162.5 MHz CW RFQ, followed by a 10 m long Medium Energy Beam Transport (MEBT) line. A part of the commissioning efforts involves operation with the average beam power emulating the operation of the proposed PIP-II accelerator, which will have a duty factor of 1.1% or above. The maximum achieved power is 5 kW (2.1 MeV x 5 mA x 25 ms x 20 Hz). This paper describes the difficulties encountered and some of the solutions that were implemented.

INTRODUCTION

The central part of Fermilab's Proton Improvement Plan, Stage Two (PIP-II) project [1] is an 800 MeV, 2 mA CW-compatible superconducting H^- linac. A prototype of the PIP-II linac front end called PIP-II Injector Test (PIP2IT) is being built to mitigate technical risks associated with acceleration at low energies and to demonstrate a capability to create an arbitrary bunch structure. The PIP2IT Warm Front End (WFE, Fig. 1) comprised of the LEBT, RFQ, and MEBT followed by a 20 kW beam dump has been assembled and commissioned [2]. In 2019, two cryomodules will be installed downstream.

Figure 1: PIP2IT warm front end (top view).

While most of the beam properties were measured with a short pulse length (~10 µs) to minimize the beam's damage potential, stable operation with parameters required for the initial mode of operation of the PIP-II linac with Booster injection only (1.1% duty factor), was demonstrated during the Spring'18 run. In addition, since all major components of PIP-II are being designed to be CW-compatible, the duty factor was pushed significantly higher during a series of dedicated tests.

HIGH DUTY-FACTOR MODE

Ion Source and LEBT

The ion source and LEBT have been commissioned to reliably deliver to the RFQ a 30 keV beam of up to 10 mA with pulse lengths of 1 µs - 50 ms at 20 Hz repetition rate defined by the LEBT chopper, as well as a true DC beam. An atypical LEBT transport scheme [3] minimizes changes of the beam properties throughout the pulse due to neutralization, which allows tuning of the downstream accelerator with a short pulse length of 10 µs or less. Reliability of the ion source [4] and LEBT did not significantly affect the overall performance of the machine in long-pulse operation. During the 3-month period of the Spring'18 run, the ion source experienced only one spark, which was a dramatic improvement (by a factor of ~100 in the rate) in comparison with the beginning of the ion source operation in 2013-2015.

RFQ

While the RFQ has been designed for CW operation [5], it was used mainly in the pulse mode, partly as an additional protection from accidental generation of a long-pulse beam, and partly because of concerns about the power couplers since two out of four initially manufactured ceramic windows developed vacuum leaks after CW operation. In preparation for the Spring'18 run, the window design was modified to use O-ring sealing instead of brazing [6]. The newly designed couplers worked reliably, with the accumulated time of CW operation reaching 350 hours. The time to bring the RFQ to its nominal frequency from a cold state using the resonance control system [7] was ~20 min.

After conditioning the RFQ in CW to 65 kV of inter-vane voltage, the average rate of sparks at the nominal 60 kV was about once per hour, although this varied greatly from day to day. Following a spark, the RF power is recovered by the next beam pulse if the internal trip counter stays below 10. The RFQ then typically remains in resonance, and beam operation can resume quickly. If there are no sparks over a sliding one-minute window, the counter is reset to zero. If the counter reaches 10, the protection system turns the RFQ power off, and recovery requires the intervention of an operator. In such infrequent cases, the recovery time depends on how quickly the recovery starts and varies from minutes to tens of minutes.

One of the unexpected features was short bursts of the RFQ vacuum happening independently on the presence of RF. In the worst cases, the pressure in the RFQ gauges went above 10^{-6} Torr, and ~10% of the beam was lost (Fig. 2). These jumps were eventually traced to excessive grease on the large O-rings of the RFQ vacuum flanges. Air permeating through the O-rings was accumulating in local bubbles created by the grease and released into the vacuum chamber in bursts. The bursts were mostly eliminated after removing the grease.

---

*This manuscript has been authored by Fermi Research Alliance, LLC under Contract No. DE-AC02-07CH11359 with the U.S. Department of Energy, Office of Science, Office of High Energy Physics

†shemyakin@fnal.gov

ISBN: 978-3-95450-223-3 ISSN: 2673-7000 doi:10.18429/JACoW-NAPAC2019-WEPLH03

REDESIGN OF ReA3 4-ROD RFQ*

A.S. Plastun†, P.N. Ostroumov, A.C.C. Villari[1], Q. Zhao[1],
Facility for Rare Isotope Beams, Michigan State University, East Lansing, MI, USA
[1]also at National Superconducting Cyclotron Laboratory, Michigan State University,
East Lansing, MI, USA

Abstract

The present RFQ of ReA3 reaccelerator at Michigan State University (MSU) was commissioned in 2010. This 4-rod RFQ was designed to accelerate the prebunched 80.5 MHz beams with the lowest Q/A = 1/5. However, the lack of proper cooling limited the RFQ performance to the pulsed operation with the lowest Q/A = 1/4. The design voltage for Q/A = 1/5 has never been reached even in a pulsed mode due to the sparking. In 2016 we initiated the upgrade of ReA3 RFQ to support high duty cycle (up to CW) operation with Q/A = 1/5 beams. The upgrade included the new rods with trapezoidal modulation, and new stems with improved cooling. The redesigned 80.5 MHz RFQ will consume only 65% rf power of the present RFQ for Q/A = 1/5 beam. It will provide the transmission up to 78% for 16.1 MHz beams and 86% for 80.5 MHz beams. High reliability and efficiency of the RFQ are very important for the going-on reaccelerator upgrade to ReA6 and for future operation as a part of FRIB.

The electrodes have been fabricated and installed inside the tank. The RF and beam tests started in August 2019.

INTRODUCTION

ReA was commissioned as ReA3 in 2015 [1] and currently accelerates RIBs with Q/A from 1/4 to 1/2 at the energy range from 0.3 to 6 MeV/u. The ongoing ReA3 upgrade includes: (a) replacement of the ReA3 RFQ electrodes to improve the cooling and to provide higher capture efficiency for 16.1 MHz bunches with Q/A down to 1/5, (b) adding another three cryomodules after the ReA3, (c) installation of the new electron beam ion source (EBIS) with 5 Ampere electron gun, (d) new RF controllers.

The ReA3 RFQ was commissioned in 2010, however it has never reached its design voltage for Q/A = 1/5 due to the sparking and operated in pulsed mode due the cooling system limitations.

UPGRADE STRATEGY

In order to provide the reliable CW operation of the 80.5 MHz ReA3 RFQ the electrodes were redesigned to reduce the inter-vane voltage from 86.5 kV to 70 kV, peak fields from 1.6 to 1.45 Kilpatrick units, RF power consumption from 120 kW to 80 kW. The 4-rod RFQ tank and the length of the electrodes remain the same. To gain more energy at reduced voltage we implemented the trapezoidal modulation of the electrodes in the acceleration section of the structure. We reduced the mid-cell aperture radius to keep the focusing strength. Synchronous phase changed from fixed -20° to variable from -60° to -20° to capture the prebunched 16.1 MHz beams essential for time-of-flight measurements in nuclear physics experiments. Output radial matcher of the RFQ was modified as well to provide round beam for the following superconducting linac with solenoidal focusing.

Finally, we modified the RF structure to reduce the peak surface electric fields and improve the cooling design.

MODULATION

Redesign of the modulation included analysis of the existing 4-rod ReA3 RFQ to find the reasons for sparking. Prior to the design of new electrodes we analysed possible causes of sparking in the original electrodes' geometry.

Analysis of the 4-rod Structure

A 4-rod structure is a periodical series of coupled RF cells. The periodicity creates a variation of electrode potential (voltage between the electrode and a tank) along the resonator. The variation of voltage between rods appears to be not very high – a fraction of percent. At the end of the structure we have two opposite rods with low potentials, and two other rods with high potential. The voltage between the last ones and the tank may reach 87% of the rod-to-rod voltage in the case of ReA3 RFQ, which is 1.74 times larger than in longitudinally uniform 4-vane structure. This may significantly increase the peak surface electric fields at the end of the rods (see Fig. 1).

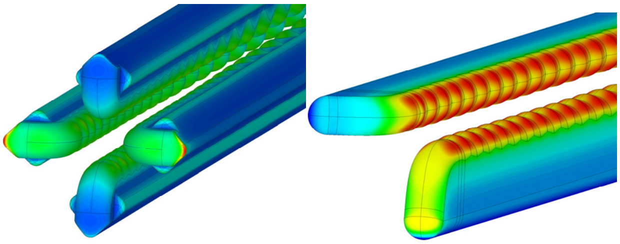

Figure 1: Surface peak electric field at the end of existing ReA3 RFQ (left) and new redesigned ReA3 RFQ (right).

Due to the periodicity, one of the rods is always located close to the stems holding the opposite potential. Peak fields in these areas are usually very high too (see Fig. 2).

Another feature of the 4-rod structure is a lack of quadrupole symmetry. This results in an increase of potentials of top two rods and induction of a dipole electric field component on a geometrical beam axis [2]. Peak fields increase by about 5%.

In the new design of the electrodes we applied proper curvatures and gaps as one can see in Fig. 1 and Fig. 2.

---

* Work supported by the National Science Foundation under Cooperative Agreement PHY-1565546, the State of Michigan and Michigan State University.

† plastun@frib.mdu.edu

ISBN: 978-3-95450-223-3 ISSN: 2673-7000 doi:10.18429/JACoW-NAPAC2019-WEPLH04

BEAM ENVELOPE RECONSTRUCTION FOR FRIB-FS1 TRANSPORT LINE USING BEAM POSITION MONITORS*

T. Yoshimoto†, S. Cogan, J.L. Crisp, K. Fukushima, S.M. Lidia, T. Maruta, P. N. Ostroumov, A.S. Plastun, T. Zhang, Q. Zhao
Facility for Rare Isotope Beams (FRIB), Michigan State University, East Lansing, MI, USA

Abstract

The Facility for Rare Isotope Beam (FRIB) includes a heavy ion superconducting (SC) linac. Recently, we completed beam commissioning of the Linac Segment 1 (LS1) and 45° bend section of the Folding Segment 1 (FS1). Four ion species, $^{40}Ar^{9+}$, $^{20}Ne^{6+}$, $^{86}Kr^{17+}$, and $^{129}Xe^{26+}$ were successfully accelerated to an energy of 20.3 MeV/u. We also explored the possibility of non-invasive beam diagnostics for online beam envelope monitoring based on beam quadrupole terms derived from Beam Positon Monitors (BPMs). In future operations, various ion beam species will be accelerated and minimization of beam tuning time is critical. To address this requirement, it is beneficial to use BPMs to obtain beam Twiss parameters instead of wire scanners. We report the first results of BPM-based beam Twiss parameters measurement [1] in the FS1.

INTRODUCTION

The beam commissioning of the first superconducting (SC) segment of the FRIB linac took place in two stages: the first three cryomodules were commissioned during the summer of 2018 and the whole LS1 including the fraction of the FS1 was commissioned in the spring of 2019 [2-4]. This significant milestone was achieved after acceleration of four ion species, $^{40}Ar^{9+}$, $^{86}Kr^{17+}$, $^{10}Ne^{6+}$ and $^{129}Xe^{26+}$ to 20.3 MeV/u in 14 cryomodules with 99 of two types of SC cavities: $\beta_{opt} = 0.041$ and $\beta_{opt} = 0.085$ [5, 6]. The layout of the FRIB superconductive linac is shown in Fig. 1.

As was noted during the commissioning of LS1 with 20 MeV/u ion beams, the conventional quadrupole scans with wire profile monitors can result to two undesirable effects: increased neutron production due to the beam interaction with the wire scanner and vacuum degradation due to the outgassing. Therefore, a non-invasive beam diagnostic technique for the measurements of the transverse beam parameters would be an attractive approach. We propose an evaluation scheme of quadrupole terms of the BPM signals to reconstruct the beam phase space information. Non-destructive monitoring and control of the beam parameters can maximize beam availability during the routine operation of the facility.

This paper reports initial experimental studies of BPMs' response studies on extraction of the information on beam Twiss parameters and emittances.

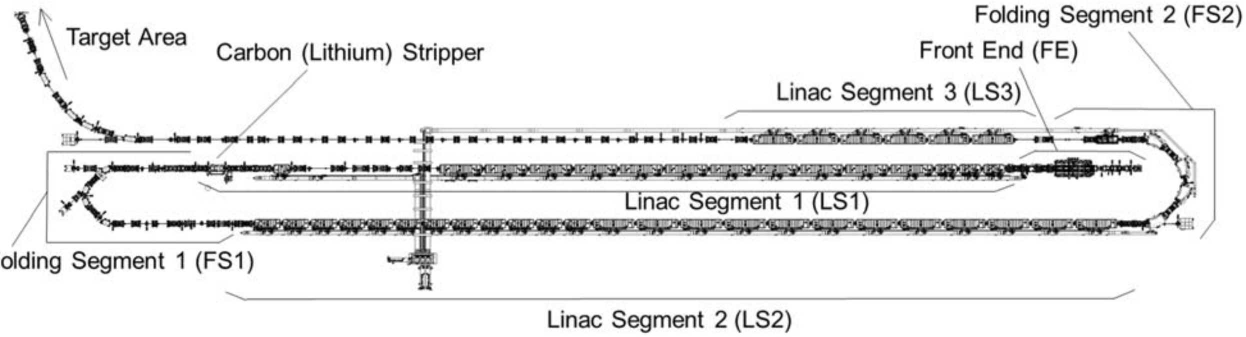

Figure 1: Schematic layout of the FRIB linac which comprises the Front End (FE) (the ion sources and vertical beam transport are not shown in the figure), and three superconductive Linac Segments (LS1, LS2, and LS3).

DIAGNOSTIC SYSTEM OF BEAM POSITION MONITOR

BPMs used in the FRIB linac have four button electrodes (diameter is 20 mm), and are installed in a vacuum pipe (radius R is 20.65 mm) as shown in Fig. 2. The typical beam rms sizes are a few millimetres in longitudinal and transverse directions. The longitudinal beam size is comparable to the button electrode size. Therefore, a conventional approximation that the bunch length is much longer than the size of the electrodes does not apply to FRIB beams. To emulate realistic BPM response, three dimensional electromagnetic calculations based on actual BPM geometries were extensively performed using CST Studio Suite [7] as shown in Fig. 3. The beam energy in the FS1 is 20 MeV/u, corresponding to a relativistic beta β of 0.2.

---

* This material is based upon work supported by the U.S. Department of Energy Office of Science under Cooperative Agreement DE-SC0000661, the State of Michigan and Michigan State University.
† yoshimot@frib.msu.edu

ISBN: 978-3-95450-223-3 ISSN: 2673-7000 doi:10.18429/JACoW-NAPAC2019-WEPLH06

COMMISSIONING STATUS OF THE FRIB FRONT END*

H.T. Ren†, J. Brandon, N.K. Bultman, K.D. Davidson, E. Daykin, T. Elkin, B. Galecka,
P.E. Gibson, L. Hodges, K. Holland, D.D. Jager, M.G. Konrad, B.R. Kortum, S.M. Lidia,
G. Machicoane, I.M. Malloch, H. Maniar, T. Maruta, G. Morgan, D.G. Morris, P. Morrison,
A.C. Morton, P.N. Ostroumov, A.S. Plastun, E. Pozdeyev, X. Rao, S. Renteria, T. Russo,
J.W. Stetson, R. Walker, J. Wei, Y. Yamazaki, T. Yoshimoto, Q. Zhao, S. Zhao,
Facility for Rare Isotope Beams, Michigan State University, East Lansing, MI, USA

Abstract

The FRIB Front End was successfully commissioned in 2017 with commissioning goals achieved and Key Performance Parameters (KPP) demonstrated for both $^{40}Ar^{9+}$ and $^{86}Kr^{17+}$ beams. Two more ion species, $^{20}Ne^{6+}$ and $^{129}Xe^{26+}$, have been commissioned on the Front End and delivered to the superconducting linac during the beam commissioning of Linac Segment 1 (LS1) in March 2019. In August 2019, Radio Frequency Quadrupole (RFQ) conditioning reached the full design power of 100 kW continuous wave (CW) that is required to accelerate Uranium beams. Start-up/shutdown procedures and operational screens were developed for the Front End subsystems for trained operators, and auto-start and RF fast recovery functions have been implemented for the Front End RFQ and bunchers. In this paper, we will present the current commissioning status of the Front End, and performance of the main technical systems, such as the ECR ion source and RFQ.

INTRODUCTION

The Facility for Rare Isotope Beams (FRIB) is a scientific user facility for nuclear physics research [1] being built on the campus of Michigan State University (MSU). The FRIB linac consists of a room-temperature front end and a SRF linac providing stable ion beams to the fragmentation target. The FRIB driver accelerator will accelerate ions with a mass up to Uranium to energies higher than 200 MeV/u and beam power on target up to 400 kW. The FRIB front end includes two Electron Cyclotron Resonance (ECR) ion sources, Lower Energy Beam Transport (LEBT), RFQ, and Medium Energy Beam Transport (MEBT). The front end layout is shown in Fig. 1.

One of the Front End ion sources is a room-temperature ECR ARTEMIS existing in the lab, primarily for commissioning of the FRIB. ARTEMIS is a 14 GHz ECR ion source built at MSU and based on the AECR-U (LBNL). This approach presents a low-risk, low-cost solution for linac commissioning. The other ion source is a 28 GHz superconducting high-power ECR to satisfy ultimate performance requirements for heavy ions. This source is based on the design of VENUS ECRIS developed at LBNL [2]. Source assembly and installation is ongoing in 2019 and conditioning is planned in 2020.

The FRIB RFQ is a 4-vane structure cavity designed to accelerate single and two-charge state ion beams from 12 keV/u to 0.5 MeV/u with estimated transmission efficiency above 80%. Table 1 shows the main RFQ parameters [3]. The RFQ beam physics design is optimized to minimize the longitudinal emittance of the accelerated beam as described in [4,5]. With proper sizing of the vane undercuts, a linear accelerating voltage ramp is implemented on the FRIB RFQ to increase the output energy.

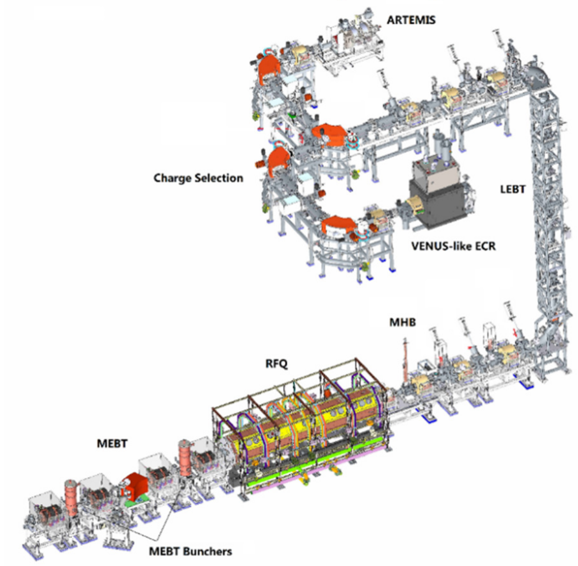

Figure 1: FRIB Front End layout. Two ECR ion sources are located at the ground level. The MHB, RFQ and MEBT are located in the linac tunnel 10 m below grade.

Table 1: FRIB RFQ Principal Parameters

Frequency (MHz)	80.5
Injection/Output energy (keV/u)	12 / 500
Design charge-to-mass ratio	1/7 - 1/3
Accelerating voltage ramp (U, kV)	60 - 112
Surface electric field (Kilpatrick)	1.6
Quality factor	16500
Operational RF power (kW, O-U)	15 - 100
Dipole modes (closest, MHz)	78.3 / 83.2
Length (m)	5.04

DC beam produced by the ECR ion sources is bunched and matched to the RFQ acceptance by an external multi-harmonic buncher (MHB). The accelerated beam from the

---

* This work is supported by the U.S. Department of Energy Office of Science under Cooperative Agreement DE-SC0000661.

† ren@frib.msu.edu

ISBN: 978-3-95450-223-3 ISSN: 2673-7000 doi:10.18429/JACoW-NAPAC2019-WEPLH07

COMMISSIONING OF THE FRIB/NSCL NEW ReA3 4-ROD RADIO FREQUENCY QUADRUPOLE ACCELERATOR

S. Nash[†], J.F. Brandon, D.B. Crisp, P.N. Ostroumov, A.S. Plastun, T. Summers,
A.C.C. Villari, Q. Zhao
Facility for Rare Isotope Beams and National Superconducting Cyclotron Laboratory,
Michigan State University, East Lansing, MI, USA

Abstract

The ReAccelerator facility ReA3 at the National Superconducting Cyclotron Laboratory is a state-of-the-art accelerator for ions of rare and stable isotopes. The first stage of acceleration is provided by a 4-rod radio-frequency quadrupole (RFQ) at 80.5 MHz, which accelerates ions from 12 keV/u to 530 keV/u. The internal copper acceleration structure of the RFQ was re-designed. The goal was to improve transmission while allowing to operate the RFQ in CW and accelerating ions with A/Q from 2 to 5. In this paper, we summarize the steps involved in the disassembly of the existing structure, preparation work on the retrofitted vacuum vessel, installation of the new components, and commissioning of the completed RFQ.

BACKGROUND

The original RFQ was received from the vendor in 2010. After initial commissioning tests, as well as an upgrade completed in 2011 to install improved tuning plates and internal water line clamps, the original structure has been in service to deliver beam to users up until April 2019.

Several issues with the design of the original structure became apparent upon commissioning. RF finger contact failures resulted in damage to stem O-ring vacuum seals. Additionally, clamps designed to create RF contact between the exposed electrode/rod water cooling lines and the stems failed to provide adequate contact, thus causing RF current to pass through the mounting screws vaporizing them [1]. The upgrade in 2011 addressed these two failure modes by replacing all tuning plates with versions with solid silver plates with hammered wedges to improve the stem to tuning plate connection. In addition, the electrode water line clamps were improved to create better surface contact, as well as increasing the mounting screw diameter to allow more torque to be applied to the screws.

After these modifications, average power was limited to 40 kW. This allowed for CW operation of beams with an A/Q of 2. Higher voltages, allowing for beams with an A/Q up to 4 were possible at reduced duty factors. Due to the pulsed nature of EBIT ion source, this did not represent any issue with beam operation, except for the inability to accelerate beams up to an A/Q of 5. Despite the upgrades, additional failure modes resulted in reduced operational reliability. On at least three occasions, electrode/rod water line braze joints failed resulting in in-vacuum cooling water leaks. These required that at least a portion of the structure be disassembled to make repairs to the braze joints.

In the past few years, the original vendor of the RFQ had modified the design of their 4-rod structures with several notable improvements: electrode/rod water lines are now e-beam welded and passed through the stems, so do not see any RF current. The tuning plates no longer use RF finger contacts between plates and stems, but rather more substantial copper L-brackets held in place with screws. After seeing an example of the new design, a contract was made with the company to construct all new internal copper components to retro-fit the existing tank. Design and modelling of the new electrode/rod modulations, including a new trapezoidal design, was handled in-house by NSCL/FRIB staff [2,3,4].

DISASSEMBLY

The planned refurbishment of the RFQ was accelerated due to an in-vacuum cooling water leak which developed through the silver cap of one of the 17 RFQ cell's tuning plates. The leak was identified through helium leak checking, 5 electrode/rod segments were removed in order to access and remove the tuning plate from the RFQ tank, and the leak was repaired with silver solder. However, by this time, the new RFQ components had already shipped from the vendor, so the decision was made to proceed with the refurbishment immediately rather than reassemble the repaired components.

In total, 16 electrode/rod segments, 18 stems, 17 tuning plates, 70 water line vacuum fitting assemblies (each consisting of one Swagelok Ultra-Torr, one Swagelok tube fitting, and one Swagelok NPT O-Seal fitting), nylon tubing for 30 cooling water circuits and their related tube fittings, and 30 return water line temperature sensors were removed. This left only the tank/vacuum vessel with input coupler, two movable tuners, two copper end plates, and vacuum systems attached.

VACUUM VESSEL PREPARATION

Cooling Water Line Vacuum Fittings

After disassembly of the old structure, it was necessary to re-tap the tank with British Standard Parallel Pipe (BSPP) threads to accommodate the new custom vacuum fittings for the cooling water line penetrations. The new fittings are a significant improvement, as only one fitting is required between the tank and water lines, as opposed to the previous assembly of 3 fittings. The tank was previously tapped with shallow National Pipe Taper (NPT) threads to accept the previous Swagelok NPT O-Seal fittings.

---

* Work supported by NSF grant PHY15-65546

† email address: nash@nscl.msu.edu

USE OF THE BASE-BAND TUNE METER KICKERS DURING THE FY18 STAR FIXED TARGET RUN AT 3.85 GeV/u*

P. Adams†, N.A. Kling, C. Liu, G.J. Marr, Brookhaven National Laboratory, Upton, NY, USA

Abstract

The base-band tune meter (BBQ) kickers proved to be a useful tool in managing STAR trigger rates during the RHIC FY18 3.85GeV/u[1] Fixed Target Run. The STAR collected over 3 times their original event goal, since it was possible to optimize the STAR trigger rates throughout the length of the physics store.

INTRODUCTION

STAR fixed target experiments are a recent addition to RHIC heavy ion physics program. The purpose of these runs is to study gold-gold collisions at various low energies [1].

The gold fixed target is mounted at the bottom of the RHIC beam pipe 205cm westwards from the middle of the STAR detector, just at the edge of Time Projection Chamber (TPC) subdetector. The beam closed orbit is moved vertically downwards, in order for transversally large emittance particles of the RHIC beam to reach the fixed target and introduce the collisions. Only "Yellow" beam is used as it interacts with the fixed target before it enters the STAR detector, as shown in Fig. 1.

The STAR experiment requested the trigger rate to be kept constant during data taking. This was soundly achieved with help of the BBQ kickers, which are vertical and horizontal kickers normally used for measuring the betatron tune [2]. At 3.85 GeV these kickers are strong enough to excite particles with lower emittance onto the target and hence provide more ideal control of the trigger rate.

OPERATIONAL SETUP

The FY18 fixed target run at 3.85 GeV/u was the first RHIC fixed target physics run. It took place only over a period of few days, 05/30/2018 - 06/04/2018 [3, 4].

The beam fill pattern was 12 evenly spaced bunches with the beam intensity 0.5e9 ions/bunch. At the beginning of each fill the fresh beam was injected into a flat orbit at STAR, then the vertical bump was inserted. The beam closed orbit had to be moved to approximately -13 mm vertically in order to reach the target, given the beam transverse emittance and the STAR beta function equal to 6 m.

STAR decided to keep their detectors on between the fills in order to minimize the down time, especially since the physics stores were only about 30 minutes long. The collimator positions had to be adjusted during the beam dump and fill time as well as during the vertical bump insertion in order to not trip the detectors.

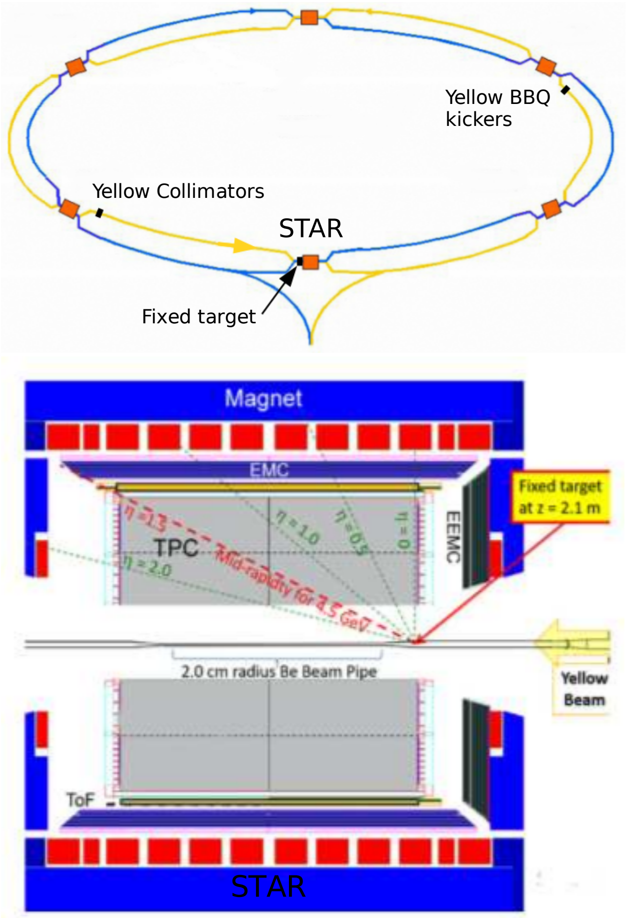

Figure 1: The fixed target layout with respect to the RHIC ring and STAR detector.

The STAR optimal trigger rate was 2000 Hz. It was challenging to maintain this rate throughout the store. Firstly, it was not possible to reach this value at the beginning of each store consistently. Secondarily, the trigger rate was decaying sharply as it is strongly dependent on the bunched beam intensity, as shown in Fig. 2. During FY18 only one 9MHz RF cavity was operational in the Yellow ring, therefore the beam was debunching quickly due to Intra-beam scattering.

Attempts were made to keep the trigger rate leveled by using the orbit control, in other words by changing the size of the STAR vertical orbit bump, as shown in Fig. 3. However, because of the limited control of the corrector power supply setpoints (only 12-bit resolution during FY18), even small orbit changes resulted in large spikes in STAR trigger rate and detector signals (which could cause trips). Additionally the beam position monitors (BPMs), which are needed for the orbit control, would stop reporting data as the bunched beam intensity got too low towards the end of stores (Fig. 4).

---

* Work supported by Brookhaven Science Associates, LLC under Contract No. DE-AC02-98CH10886 with the U.S. Department of Energy.

† padams@bnl.gov

[1] 3.85 GeV/u is the particle beam energy

FRIB DRIVER LINAC INTEGRATION TO BE READY FOR PHASED BEAM COMMISSIONING*

H. Ao†, S. Beher, N.K. Bultman, F. Casagrande, C. Compton, J. Curtin, K.D. Davidson, K. Elliott,
V. Ganni, A. Ganshyn, P.E. Gibson, I. Grender, W. Hartung, L. Hodges, K. Holland, A. Hussain,
M. Ikegami, S. Jones, P. Knudsen, S.M. Lidia, G. Machicoane, S.J. Miller, D.G. Morris,
P. N. Ostroumov, J.T. Popielarski, L. Popielarski, J. Priller, T. Russo, K. Saito, S. Stanley,
D.R. Victory, X. Wang, J. Wei, M. Xu, T. Xu, Y. Yamazaki, S. Zhao
Facility for Rare Isotope Beams, Michigan State University, East Lansing, MI, USA
A. Facco, INFN - Laboratori Nazionali di Legnaro, Legnaro, Italy
R.E. Laxdal, TRIUMF, Vancouver B.C., Canada

Abstract

The driver linac for the Facility for Rare Isotope Beams (FRIB) will accelerate all stable ion beams from proton to uranium beyond 200 MeV/u with beam powers up to 400 kW. The linac currently consists of 104 superconducting quarter-wave resonators (QWR), which is the world largest number of low-beta superconducting radio-frequency (SRF) cavities operating at an accelerator facility. The first 3 QWR cryomodules (CM) (β = 0.041) were successfully integrated with cryogenics and other support systems for the second Accelerator Readiness Review (ARR) in May 2018. The third ARR (ARR3) devices that includes 11 QWR CM (β=0.085) and 1 QWR matching CM (β=0.085) was commissioned on schedule by January 2019. We examine key factors to the successful commissioning, such as component testing prior to system integration, assessment steps of system and device readiness, and phased commissioning. This paper also reports on the current progress on β=0.29 and 0.53 CMs in preparation for the upcoming ARR4 beam commissioning.

INTRODUCTION

Facility for Rare Isotope Beams (FRIB) is a new joint project for a nuclear science facility funded by the Department of Energy (DOE) Office of Science, Michigan State University, and the State of Michigan. The FRIB driver linac will accelerate all stable ion beams from proton to uranium beyond 200 MeV/u with beam powers up to 400 kW. The linac currently consists of 104 superconducting quarter-wave resonators (QWR), which is the largest number of low-beta SRF cavities operating at an accelerator facility in the world [1]. Ion beams (Ne, Ar, Kr, and Xe) were accelerated by cryomodule (CM) 1-14 up to 20.3 MeV/u [2].

FRIB implemented a phased Accelerator Readiness Review (ARR) process to support commissioning (see Table 1). Each commissioning step was preceded by an ARR [3]. Three of seven planned ARRs have been conducted so far. ARR2 was the first SRF commissioning with three β = 0.041 QWR CMs. The systems and devices of ARR3 scope that includes 11 QWR CM (β=0.085) and 1 QWR matching CM (β=0.085) were successfully installed and commissioned on schedule by January 2019 to support ARR3 beam commissioning (see Fig. 1).

Table 1: Phased Beam Commissioning of the FRIB Accelerator

Phase	Area with beam	Energy MeV/u	Date
ARR1	Front end	0.5	7/2017
ARR2	+ LS1 β=0.041 CM	2	5/2018
ARR3	+ LS1 β=0.085 CM	20	2/2019
ARR4	+ LS2 β=0.29, 0.53CM	200	3/2020
ARR5	+ LS3 β=0.53 CM	>200	12/2020
ARR6	+ target and beam dump	-	9/2021
Final	Integration with pre-existing facility	-	6/2022

This paper describes our approach to the phased commissioning from a hardware installation standpoint especially for the SRF system. We examine key factors to the successful system integration to support the beam commissioning including review processes. Finally, we will show our installation progress toward next ARR4 beam commissioning.

INTEGRATE SYSTEMS TO MEET PROJECT MILESTONES

Prototype, Testing, and Validation

Prototype, testing, and validation - these three steps are fundamental engineering approach to develop new systems and devices. Accelerators are highly complex system. Typically, many groups develop each device, e.g. cryomodules, cryogenics, RF, power supplies, diagnostics, controls, vacuum etc., in parallel. To realize prototype, testing, and validation for an integrated accelerator system in early stage is essential to the success of the project especially for large-scale accelerators.

Completed FRIB CMs undergo full system testing in bunkers before being accepted and delivered to the tunnel. There are two test bunkers: one is located in the ReA6 high bay and other is in the SRF high bay (see Fig. 2).

---

* Work supported by the U.S. Department of Energy (DOE) Office of Science under Cooperative Agreement DE-SC0000661.

†ao@frib.msu.edu.

EFFICIENCY ESTIMATION FOR SEQUENTIAL EXCITATION LASER STRIPPING OF H$^-$ BEAM*

T.V. Gorlov, A.V. Aleksandrov, S.M. Cousineau, Y. Liu, A. Rakhman
Oak Ridge National Laboratory, Oak Ridge, TN, USA

Abstract

A new laser stripping scheme for charge exchange injection of H$^-$ beams is considered. The sequential scheme for the planned demonstration experiment includes a two-step excitation that requires much smaller laser power compared to the traditional one-step excitation. The new scheme can be applied to a wider range of H$^-$ beam energies and provides more flexibility on the choice of laser frequency. In this paper we discuss the two-step excitation method and estimate laser stripping parameters and stripping efficiency for the SNS accelerator and for its future H$^-$ energy upgrade to 1.3 GeV.

INTRODUCTION

In this paper we develop laser stripping technology and propose a new laser stripping scheme that would allow the reduction of laser power needed for high efficiency stripping. The standard laser stripping scheme proposed in [1] consists of a three step process where the first electron is Lorentz stripped in a magnetic field (H$^-$ to H^0), the second electron is then excited by a laser from the n=1 to n=3 quantum state, and finally the excited electron is Lorentz stripped by a second identical magnet into protons. The second step excitation is accomplished by a UV laser with 355nm wavelength [1]. A minimum excitation level of n=3 (3p state) is needed for Lorentz stripping of a 1 GeV beam because the electron is strongly bound to the atom in the lower states and cannot be Lorentz stripped by a conventional ≤2T magnet. Thus, for the proof of principle and the proof of practicality experiments at the SNS [2, 3, 4], a 3rd harmonic UV laser with 355 nm wavelength was used for single step excitation (1s→3p) of the 1 GeV H^0 beam. From the standpoint of laser technology, due to nonlinear frequency conversion process, the 3rd harmonic UV laser is often less powerful as compared to 2nd harmonic 532nm laser or to a fundamental 1064 nm laser, and it needs to be enhanced by an optical cavity. In this paper we propose to use sequential excitation to excite the H^0 atom from the ground 1st state to the 2nd state (1s→2p), followed by excitation from the 2nd to the 3rd state (2p →3d) using the same recycled laser (see Fig. 1).

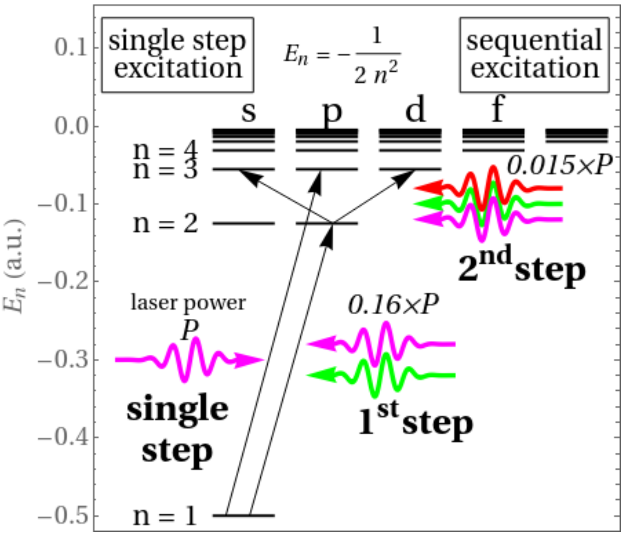

Figure 1: Sequential excitation vs. single step excitation of a hydrogen atom for H$^-$ beam energies below 2 GeV.

As shown in Fig. 1, The sequential scheme allows a wide choice of laser wavelength and requires smaller laser power for excitation compared to the single step excitation. The 1st and the 3rd laser stripping steps of Lorentz stripping in a magnetic field stay the same. The proposed scheme has the following advantages:

- Each step of the sequential excitation 1s→2p and 2p→3d requires smaller laser power due to stronger quantum electric dipole transition of the H atom compared with the single step 1s→3p.
- Alternative laser wavelengths, such as the 2nd harmonic 515nm or 532nm green lasers, are possible. Compared to UV laser, these wavelengths are easier to generate and recycle in a power enhancement optical cavity. The available power is ~5 times higher.

For this reason, for the same excitation efficiency, the sequential excitation scheme with two smaller excitation steps requires roughly 6 times less laser power than the single excitation scheme. This savings can be used to improve the laser system using a low power laser to achieve the same stripping efficiency, or to use the laser power with an optical cavity for stripping H$^-$ beams with larger emittance or energy spread. Also, the sequential scheme gives more flexibility for beam energy by choosing different sequential levels that can be useful for similar projects [5]. In this paper the sequential excitation scheme for SNS beam with 1.0GeV and 1.3 GeV will be estimated. The preliminary design of an experimental implementation of the scheme, utilizing the UV laser configuration already in place at the SNS is also discussed.

---

*This work has been supported by Oak Ridge National Laboratory, managed by UT-Battelle, LLC, under contract DE-AC05-00OR22725 with the U.S. Department of Energy. The United States Government retains, and the publisher, by accepting the article for publication, acknowledges that the United States Government retains a non-exclusive, paid-up, irrevocable, world-wide license to publish or reproduce the published form of this manuscript, or allow others to do so, for United States Government purposes. The Department of Energy will provide public access to these results of federally sponsored research in accordance with the DOE Public Access Plan (http://energy.gov/downloads/doe-public-access-plan).

North American Particle Acc. Conf. NAPAC2019, Lansing, MI, USA JACoW Publishing
ISBN: 978-3-95450-223-3 ISSN: 2673-7000 doi:10.18429/JACoW-NAPAC2019-WEPLH11

RHIC QUENCH PROTECTION DIODE RADIATION DAMAGE*

A. Drees†, O. Biletskyi, D. Bruno, A. DiLieto, J. Escallier, G. Heppner,
C. Mi, T. Samms, J. Sandberg, Brookhaven National Laboratory, Upton, NY, USA

Abstract

Each of RHIC's superconducting magnets is protected by a silicon quench protection diode (QPD). In total, RHIC has over 800 diodes installed inside the cryostat close to the vacuum pipe. After years of operation with high energy heavy ion beams we experienced a first permanently damaged QPD in the middle of our FY2016 Au Au run and a second damaged diode in the following year. In 2016 the run had to be interrupted by 19 days to replace the diode, in 2017 RHIC could still operate with a reduced ramping speed of the superconducting magnets. Both diodes were replaced and examined "cold" as well as "warm". This paper reports on what we have learned so far about the conditions leading up to the damage as well as the damage itself.

INTRODUCTION

At RHIC an average of about 30 beam induced quenches are reported each year, varying between 1 and over 70 depending on the running mode. In most cases, the involved magnets are the triplet quadrupoles of the low beta insertions. Figure 1 shows a QPD and its assembly inside a superconducting magnet. The actual diode, a few millimeter thick silicon wafer at the center of the assembly, is installed at the same height as and next to the beam pipe. This design has the potential to expose the diode to the highest levels of radiation from beam losses if they originate in the area of its host magnet. Y7-D6 is downstream of the yellow ring's collimators, where higher beam loss rates are expected and routine. However, beam losses in the center of an arc, where B10-D19 is located, are unusual unless the beam trajectory is changed significantly.

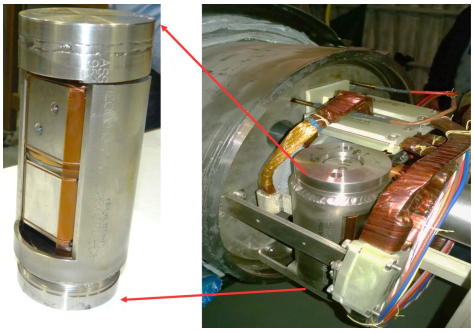

Figure 1: Left: diode assembly, right: installation within a RHIC magnet.

The two diodes were damaged in two consecutive years: one in store 19702, in one of the blue arc dipoles (B10-D19) during a dedicated machine development with 206 10^9 Au ions in the blue ring. Two voltage taps reported a beam induced quench: dipoles D15-20 and quadrupoles Q10-20 in arc 10. In principle, any one or several of the 6 magnets sharing a voltage tap could have quenched. It cannot be known which one. The second event occurred at the end of store 20604, damaging the diode in one of the yellow straight section dipoles (Y7-D6) downstream of interaction region 8 (IP8). In this second instance, the beam abort was caused by a failure of the abort kicker trigger circuit during a normal end-of-store beam dump. An unprecedented total of 31 voltage taps reported beam induced quenches in this event. RHIC had 191 10^{11} protons circulating in the yellow ring at the time of the abort.

Both events were indirectly caused by an ongoing effort of preventing damage to experimental detectors after a so-called prefire and the effort of preventing prefires altogether.

ABORT KICKER PREFIRES AND PROTECTION BUMPS

RHIC abort kicker prefires [1, 2], where one of the five abort kicker modules per ring fires spontaneously and asynchronously, happen with a varying frequency of 0-15 incidents per year and per ring, provided the required abort kicker voltage is above the prefire threshold of about 12 kV. For Au-Au operation at 100 GeV and protons at 255 GeV they are operated at about 26 kV. Figure 2 depicts a scope snapshot of the timing of a typical prefire during run16. Depending on the exact moment, the fill pattern and the total amount of beam circulating at the time of the prefire, up to about 10 bunches, i.e. 20 10^9 Au ions or 20 10^{11} protons, do not receive enough of a kick for a clean dump. Each of these events typically causes a few quenches of triplet quadrupoles and can lead to serious damage in the experimental detectors.

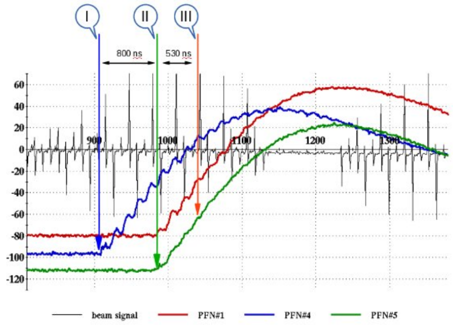

Figure 2: Three abort kicker modules during a prefire of module PFN4 (blue trace). (I) indicates the start time of the prefire, (II) indicates the time the other modules follow suit and (III) indicates the time the sum of all modules reaches default voltage for a clean beam dump. The black trace is the bunched beam.

---

* Work supported by Brookhaven Science Associates, LLC under Contract No. DE-AC02-98CH10886 with the U.S. Department of Energy

† drees@bnl.gov

ISBN: 978-3-95450-223-3 ISSN: 2673-7000 doi:10.18429/JACoW-NAPAC2019-WEPLH15

LIGHT ION INJECTOR FOR NICA

H. Hoeltermann[†], H. Hähnel, B. Koubek, H. Podlech, U. Ratzinger, A. Schempp,
D. Strehl, R. Tiede, BEVATECH GmbH, Frankfurt, Germany
M. Busch, M. Schuett, Goethe Universität, Frankfurt, Germany
A.V. Butenko, D.E. Donets, B.V. Golovenskiy, A. Govorov, V.V. Kobets, A.D. Kovalenko, K.A. Levterov, D.A. Lyuosev, A.A. Martynov, D.O. Ponkin, K.V. Shevchenko, I.V. Shirikov,
A.O. Sidorin, E. Syresin, G.V. Trubnikov, JINR, Dubna, Russia

Abstract

The Nuclotron ring of the NICA project will get a new light ion injector linac (LILac) for protons and ions with a mass to charge ratio up to 3. The LILac will consist of 2 sections: A 600 keV/u RFQ followed by an IH-type DTL up to 7 MeV/u, and a postaccelerator IH cavity for protons only - up to 13 MeV. A switching magnet will additionally allow 13 MeV proton beam injection into a future superconducting testing section. The pulsed Linac up to 7 MeV/u and including the post-accelerator for protons up to 13 MeV will be developed in collaboration between JINR and BEVATECH GmbH. The technical design of that Linac is discussed in this paper.

INTRODUCTION

In the frame of the NICA ion collider upgrade [1] a new light ion frontend Linac (LILac) for polarised particles, protons and ions with a mass to charge ration of up to 3 will be built. Behind the ion source and LEBT, LILac will consist of 3 parts:

1. a normal conducting Linac up to 7 MeV/u
2. a normal conducting energy upgrade up to 13 MeV protons
3. a superconducting section from 13 MeV/u up to a final energy to be determined.

In this paper the Part 1 and Part 2 of LILac up to 7 MeV/u and 13 MeV for protons are discussed. This normal conducting Linac will be built in collaboration between JINR and BEVATECH GmbH.

The Linac will be located in LU20 hall at JINR and provide a beam energy of 7 MeV/u to be injected into the Nuclotron ring for further acceleration as a first stage of the project. Protons and light ions with a mass to charge ratio of up to 3 will be used for either fixed target experiments to study baryonic matter or will be injected into the NICA collider ring for hadron matter and phase transition experiments and to study spin physics on polarised particles [2].

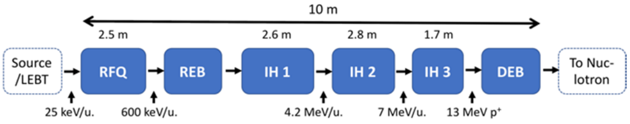

Figure 1: LILac cavity scheme.

The Linac consists of 6 cavities, an RFQ followed by a re- buncher, 3 IH-DTL structures and a de-buncher as shown in Fig. 1. It is operating at 162.5 MHz with a beam repetition rate of 5 Hz and a duty cycle of 0.1% [3]. The main parameters of the LILac are summarised in Table 1. The length of the Linac comprising the cavities, the beam diagnostic devices and focusing magnets but excluding the de-buncher will be realised within a length of below 10 m.

Table 1: LILac Main Parameters

Parameter	Protons	C^{4+}
A/Q	1	3
Injection Energy	25 keV	300 keV
Exit Energy	13 MeV	84 MeV
Beam current	5 mA	15 mA
Rep. Rate Limit	≤ 5 Hz	
Current Pulse Duration	30 µs	
RF Pulse Length	200 µs	
RF Frequency	162.5 MHz	
Transmission	≥ 80%	
Length of the Linac	≤ 10m	

Each cavity will be fed by a dedicated high power solid state amplifier to provide the corresponding power for the accelerating fields in the cavities. The LLRF control soft- and hardware is realized in the MicroTCA.4 standard will be developed together with Bevatech and the MicroTCA Technology Lab at DESY based on the LLRF system from XFEL.

ARCHITECTURE

Ion Source and LEBT

For LILAC two different ion sources, a laser ion source (LIS) and a source of polarized ions (SPI), will be used. From the LIS it is planned to receive light ions, while the SPI will generate polarised and non-polarised protons and deuterons [3]. The ion sources are placed on a high voltage terminal (up to 150 kV) [4]. The LEBT channel with a length of about 1.8 m consists of 2 parts: The first part is an electrostatic section with ion optics and an electrostatic tube, and the second part uses two magnetic solenoids with a maximum magnetic field of 1.2 T. The LEBT channel is currently under redesign.

[†] holger.hoeltermann@bevatech.com

ISBN: 978-3-95450-223-3 ISSN: 2673-7000 doi:10.18429/JACoW-NAPAC2019-WEPLH16

TOLERANCES ON ENERGY DEVIATION IN MICROBUNCHED ELECTRON COOLING*

P. Baxevanis†, G. Stupakov, SLAC National Accelerator Laboratory, Menlo Park, CA, USA

Abstract

The performance of microbunched electron cooling (MBEC) [1] is highly dependent on the quality of the hadron and cooler electron beams. As a result, understanding the influence of beam imperfections is very important from the point of view of determining the tolerances of MBEC. In this work, we incorporate a non-zero average energy offset into our 1D formalism [2, 3], which allows us to study the impact of effects such as correlated energy spread (chirp). In particular, we use our analytical theory to calculate the cooling rate loss due to the electron beam chirp and discuss ways to minimize the influence of this effect on MBEC.

INTRODUCTION

In MBEC, the hadron beam imprints an energy modulation on the co-propagating cooler electron beam in the modulator section of the machine. This energy modulation is then converted into a density modulation (bunching) after the e-beam passes through a dispersive chicane with strength $R_{56}^{(e,1)}$ (Fig. 1). In the meantime, the hadrons go through a separate section of the lattice, which also includes a chicane with strength $R_{56}^{(h)}$. The bunched electron beam then once again interacts with the hadrons in the kicker section, in a way that can ultimately lead to a significant reduction in the hadron energy spread (cooling of the transverse emittance is also possible but, for simplicity, we neglect this effect in this work). In order to accelerate this process and ensure that the cooling timescale is small enough for practical purposes, additional amplification stages are typically required, in which the bunching of the electron beam is boosted through plasma oscillations. Each such plasma stage consists of a drift space followed by a chicane of strength $R_{56}^{(e,j)}$ ($j = 2, ..., M + 1$, where M is the total number of stages). For simplicity, we will assume that all stages have the same length L_d. In Refs. [2, 3] we derived the cooling timescale using a technique that tracks the microscopic fluctuations in the hadron and electron beams. The main results can be summarized as follows: the characteristic cooling time for the energy spread N_c — normalized by the ring revolution period T — is given by $1/N_c = A_0 I$, where

$$A_0 = \frac{4 I_e L_m L_k r_h}{\Sigma^3 \pi \gamma^3 I_A \sigma_e \sigma_h} \times \left(\frac{1}{\sigma_e} \sqrt{\frac{2 I_e}{\gamma I_A}} \right)^M \tag{1}$$

is a pre-factor and the cooling integral I is expressed by

$$\begin{aligned} I = {} & (-1)^M \times 2 q_h q_{e,1} q_{e,2} ... q_{e,M+1} \int_0^\infty d\varkappa \varkappa^2 H^2(\varkappa) \\ & \times \exp(-\varkappa^2 (q_h^2 + q_{e,1}^2 + q_{e,2}^2 + ... + q_{e,M+1}^2)/2) \\ & \times \left(\frac{\varkappa H(r_p \varkappa)}{r_p} \right)^{M/2} \sin^M (r_p \frac{\Omega_p L_d}{c} \sqrt{\frac{2 \varkappa H(r_p \varkappa)}{r_p}}) . \end{aligned} \tag{2}$$

In the expressions given above, γ is the relativistic factor (common for the co-propagating hadron/electron beams), L_m and L_k are the lengths of the modulator and kicker sections, $r_h = (Ze)^2/m_h c^2$ is the classical radius of the hadrons, I_e is the electron beam current and $I_A = m_e c^3/e \approx 17$ kA is the Alfven current. Moreover, σ_h and σ_e are, respectively, the rms energy spread values for the hadron and electron beams (assuming a Gaussian energy distribution for both). As far as the transverse properties of the beams are concerned, we again adopt Gaussian profiles and assume that a) at the modulator and kicker, the interacting beams have an identical, circular cross section characterized by an rms size Σ b) at the plasma stages, the e-beam is also round but with a different rms size $r_p \Sigma$, where r_p is a dimensionless squeeze factor. The latter quantity is also involved in the definition of the plasma oscillation frequency Ω_p, which is given by $\Omega_p = (c/r_p \Sigma)(I_e/\gamma^3 I_A)^{1/2}$. In Eq. (2), $q_h = R_{56}^{(h)} \sigma_h \gamma / \Sigma$ is the scaled hadron chicane strength and $q_{e,j} = R_{56}^{(e,j)} \sigma_e \gamma / \Sigma$ are the normalized strengths of the various electron chicanes. Lastly, the important function $H(\hat{k})$, which is directly related to the Fourier transform of the space charge interaction function, is defined by $H(\hat{k}) = \hat{k} \int_0^\infty d\tau \tau \exp(-\hat{k}^2 \tau^2/4)/(\tau^2 + 4)$.

ENERGY ERROR

In the derivation of Eq. (2), we have assumed a zero central value for the electron energy variable. In what follows, we discuss what would change if we were to remove this assumption. To begin with, we stipulate that the energy deviation of the electron beam, $\Delta\eta$, does not change the interaction between hadrons and electrons in the modulator and the kicker. It does, however, shift the wake generated by a hadron in the electron beam relative to the case when both beams have the same γ. If no plasma stages are present, the longitudinal shift

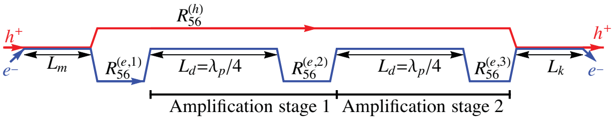

Figure 1: MBEC configuration with two plasma stages (the length L_d is a free parameter but, in practice, its value is $\sim \lambda_p$, where λ_p is the plasma wavelength).

---

* Work supported by the Department of Energy, Contact No. DE-AC02-76SF00515.

† panosb@slac.stanford.edu

ISBN: 978-3-95450-223-3 ISSN: 2673-7000 doi:10.18429/JACoW-NAPAC2019-WEPLH17

DIFFUSION AND NONLINEAR PLASMA EFFECTS IN MICROBUNCHED ELECTRON COOLING*

P. Baxevanis†, G. Stupakov, SLAC National Accelerator Laboratory, Menlo Park, CA, USA

Abstract

The technique of microbunched electron cooling (MBEC) is an attractive scheme for enhancing the brightness of hadron beams in future high-energy circular colliders [1]. To achieve the required cooling times for a realistic machine configuration, it is necessary to boost the bunching of the cooler electron beam through amplification sections that utilize plasma oscillations. However, these plasma sections also amplify the intrinsic noise of the electron beam, leading to additional diffusion that can be very detrimental to the cooling. Moreover, they can exhibit nonlinear gain behavior, which reduces performance and limits the applicability of theory. In this paper, we study both of these important effects analytically with the aim of quantifying their influence and keeping them under control.

INTRODUCTION

In MBEC, the hadron beam first imprints an energy modulation on a co-propagating (cooler) electron beam in a segment of the machine known as the modulator. This energy modulation is then converted into a density modulation (bunching) after the e-beam passes through a dispersive chicane section with strength $R_{56}^{(e,1)}$ (Fig. 1). In the meantime, the hadrons are transported through their own—separate—section of the lattice, which also includes a chicane with strength $R_{56}^{(h)}$. The bunched electron beam then once again interacts with the hadrons in a subsequent section of the machine (the kicker), in a way that can ultimately lead to a significant reduction in the hadron energy spread and transverse emittance, after many passages through the cooling section. In order to accelerate this process and ensure that the cooling timescale is small enough for practical purposes, additional amplification stages are typically required, in which the bunching of the electron beam is boosted through the space charge (or plasma) effect. Each such plasma stage consists of a drift space followed by a chicane of strength $R_{56}^{(e,j)}$ ($j = 2, \ldots, M + 1$, where M is the total number of stages). For simplicity, in this paper we assume that all stages have the same length L_d. In [2–4] we derived the cooling timescales using a technique that tracks the microscopic fluctuations in the hadron and electron beams. The main results can be summarized as follows: the characteristic cooling times for the energy spread and the emittance—normalized by the ring revolution period T and labeled by N_c^η and N_c^ϵ (respectively)—are given by $1/N_c^\eta = A_0' I_\eta'$ and $1/N_c^\epsilon = A_0' I_\epsilon'$, where

$$A_0' = \frac{4 I_e L_m L_k r_h}{\Sigma^3 \pi \gamma^3 I_A \sigma_e \sigma_h} \times \left(\frac{1}{\sigma_e} \sqrt{\frac{2 I_e}{\gamma I_A}} \right)^M \tag{1}$$

is a pre-factor and the cooling integrals I_η' and I_ϵ' are expressed by

$$\begin{aligned} & I_\eta'/(2(q_h - q_s)) = I_\epsilon'/q_s = (-1)^M \times q_{e,1} q_{e,2} \ldots q_{e,M+1} \\ & \times \int_0^\infty d\hat{k} \hat{k}^2 \exp(-\hat{k}^2((q_h - q_s)^2 + q_r^2/2)/2) \\ & \times H^2(\hat{k}, r) \exp(-\hat{k}^2(q_{e,1}^2 + q_{e,2}^2 + \ldots + q_{e,M+1}^2)/2) \\ & \times \left(\frac{\hat{k} H_1(r_p \hat{k})}{r_p} \right)^{M/2} \sin^M (r_p \frac{\Omega_p L_d}{c} \sqrt{\frac{2\hat{k} H_1(r_p \hat{k})}{r_p}}). \end{aligned} \tag{2}$$

In the expressions given above, γ is the relativistic factor (common for the co-propagating hadron/electron beams), L_m and L_k are the lengths of the modulator and kicker sections, $r_h = (Ze)^2/m_h c^2$ is the classical radius of the hadrons, I_e is the electron beam current and $I_A = m_e c^3/e \approx 17$ kA is the Alfven current. Moreover, σ_h and σ_e are, respectively, the rms energy spread values for the hadron and electron beams (assuming a Gaussian energy distribution for both). As far as the transverse properties of the beams are concerned, we again adopt Gaussian profiles and assume that a) at the modulator and kicker, the interacting beams have an identical, elliptical cross section characterized by a horizontal rms size Σ and a size aspect ratio r b) at the plasma stages, the e-beam is round with a common rms size $r_p \Sigma$. The squeeze factor r_p is also involved in the definition of the plasma frequency Ω_p, which is given by $\Omega_p = (c/r_p \Sigma)(I_e/\gamma^3 I_A)^{1/2}$.

In Eq. (1), $q_h = R_{56}^{(h)} \sigma_h \gamma / \Sigma$ is the scaled hadron chicane strength and $q_{e,j} = R_{56}^{(e,j)} \sigma_e \gamma / \Sigma$ are the normalized strengths of the various electron chicanes. In order to describe the mechanism of emittance cooling, we need to take into account the betatron motion of the hadron beam from the modulator to the kicker [4] (for simplicity, we only consider the vertical component of this motion). Including this effect is reflected in the parameters q_s and q_r, which are given by $q_s = S \sigma_h \gamma / \Sigma$ and $q_r = \gamma R \sqrt{\epsilon} / \Sigma$, where

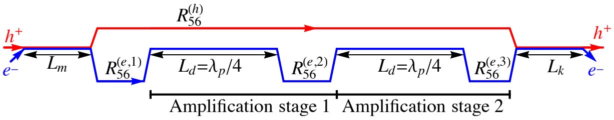

Figure 1: MBEC configuration with two amplification stages (the length L_d is a free parameter but, in practice, its value is ~ λ_p, where λ_p is the plasma wavelength).

---

* Work supported by the Department of Energy, Contract No. DE-AC02-76SF00515.

† panosb@slac.stanford.edu

ISBN: 978-3-95450-223-3 ISSN: 2673-7000 doi:10.18429/JACoW-NAPAC2019-WEPLH19

RECORD FAST CYCLING ACCELERATOR MAGNET BASED ON HIGH TEMPERATURE SUPERCONDUCTOR*

H. Piekarz[†], S. Hays, J.N. Blowers, B. Claypool, V.D. Shiltsev, Fermilab, Batavia, IL, USA

Abstract

We report on the High Temperature Superconductor (HTS) based prototype accelerator magnet capable to operate at 12 *T/s* *B*-field ramping rate with a very low supporting cryogenic cooling power thus indicating a feasibility of its application in the accelerator requiring high repetition rate and high average beam power. The magnet is designed to simultaneously accelerate two particle beams in the separate beam gaps energized by a single conductor. The design, construction and the power test of the prototype fast-cycling HTS based accelerator magnet is presented while the more detailed description and power test data analysis s given in [1]. As example, the measured cryogenic power loss limit is discussed in terms of the feasibility of application of such a magnet for the construction of the 8 GeV dual proton beam Booster.

MOTIVATION

Next generation HEP facilities, such as muon colliders [2], future circular colliders [3, 4], high-intensity proton synchrotrons for neutrino research [5-7] accelerators demand substantially faster beam cycles which in turn require fast-cycling accelerator magnets with *dB/dt* of the order of tens to hundreds of *T/s*. As all these applications require accelerator magnets to operate in the rapid-cycling regime the fast-ramping magnetic field induces possibly very significant power losses in the power cable and in the magnetic core. The use of the superconducting cable instead of the normal conducting one to power accelerator magnets is expected to much reduce the *dB/dt* induced power loses in both magnetic core and cable and thus make accelerator construction more cost effective.

MAGNET DESIGN, CONSTRUCTION AND TEST ARRANGEMENT

The use of the superconductor versus normal conductor significantly reduces the cross-section of the power cable which in turn reduces the cross-section of the magnetic core. In this way the power losses induced by the fast-ramping magnetic field are minimized in both the cable and the magnetic core. In addition, the high current density of the superconductor allows the power cable to be arranged as a narrow slab which with the optimized position within the magnet core cable space allows for strong minimization of cable exposure to the core descending *B*-field. Magnet design with a slab-like conductor is shown in Fig. 1 where the *B*-field crossing cable space is less than 5% of the field in the beam gap. In addition, the HTS superconducting cable can operate within a very wide temperature margin. With the number of strands in the power cable allowing to carry the required transport current at the temperatures up to e.g. 35 K, the cable operational temperature of 4.5 K allows then for the 30 K temperature margin facilitating in this way operation of the quench detection and cable protection systems.

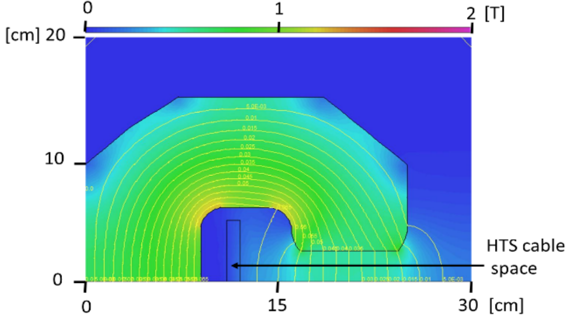

Figure 1: B-field simulation for 40 mm (vertical) x 100 mm (horizontal) gap of 1 T magnet.

For the HTS-based rapid-cycling accelerator magnet design we used the following criteria: (I) A single conductor coil energizes two magnet beam gaps allowing for the simultaneous acceleration of two beams while cutting in half the required accelerator ramping and operation power per beam, (II) The two beam gaps are aligned in the vertical plane allowing for the beam loss and/or beam particle decays to be emitted into the space away from the magnet and thus strongly suppressing potential for the radiation damage of the superconductor. The vertical alignment of the beam gaps also makes orbits of both beams equal and thus eliminating the orbit swapping required to equalize beams circulation periods for the acceleration in the common RF section. The conceptual view of the vertical dual-bore HTS accelerator magnet is shown in Fig. 2. The 0.5 m long test magnet with vertically arranged dual bean gaps of 10 mm (height) x 100 mm (width) and core of 620 mm x 255 mm cross-section is exactly of the shape as shown in Fig. 2. The 3-part core construction allows for simple assembly and installation of the HTS conductor coil. The full 3-turn conductor coil is shown in Fig. 3. The details of the HTS strands and copper tape windings are shown in Fig. 4. The 2 mm wide and 0.1 mm thick, HTS strands (Super-Power, Inc. [8]) are helically wound at 10 cm pitch on the surface of the helium conduit pipes made of 316LN stainless steel, 8 mm OD, 0.5 mm wall thickness. This arrangement makes ~ 1.05 mm averaged exposed width of a single HTS strand to the B-field. A single layer of the 0.1 mm thick, 12.5 mm wide oxygen-free high conductivity copper tape is wound helically over the strands to firmly secure their attachment to the cooling helium conduit pipe.

---

*Work supported by Fermi Research Alliance, LLC under contract No. DE-AC02-07CH1359 with the United States Department of Energy
†hpiekarz@fnal.gov

MODELING OF H^- ION SOURCE AT LANSCE*

N.A. Yampolsky†, I.N. Draganic, and L. Rybarcyk,
Los Alamos National Laboratory, Los Alamos, USA

Abstract

We report on the progress in modelling performance of the H- ion source at LANSCE. The key aspect we address is the lifetime of the tungsten filament. The lifetime depends on multiple parameters of the ion source and can dramatically vary in different regimes of operation. We use the multiphysics approach to model the performance of the ion source. The detailed analysis has been made to recognize key physical processes, which affect the degradation of the filament. The analysis resulted in the analytical model, which includes relevant processes from the first principles. The numerical code based on this model has been developed and benchmarked. The results of the modelling show good agreement with experimental data. As a result, the developed model allows predicting the performance of the ion source in various regimes of operation.

INTRODUCTION

The Los Alamos Neutron Science Center (LANSCE) [1] hosts an 800 MeV linear accelerator, which delivers H^+ and H^- beams to multiple experimental facilities including the Isotope Production Facility (IPF), Lujan Center (neutron spallation source), the Weapon Neutron Research (WNR), the Proton Radiography Facility (pRAD), and the Ultra Cold Neutron (UCN) experiments. The H^- beam is produced be the multicusp surface converter ion source [2, 3]. The lifetime of the ion source is limited by the lifetime of the tungsten filaments, which are used to produce arc and create plasma. Earlier research resulted in models capable of predicting the ballpark of the filament lifetime [4, 5]. However, those models include several empirical factors, introduced to match the experimental observations. It is an indication that earlier models miss key physics and they are not likely to describe significantly different regimes of the ion source operation.

In this paper we describe the progress in development of modeling capabilities of the H^- ion source at LANL. We develop a multiphysics model describing the evolution of the hot filaments from the first principles. We have identified the major physical effects which affect the parameters of the filament and include them into the model.

FILAMENT MODEL

The filament is heated by the current distributed along the filament. The filament is not heated uniformly since the current along the filament is not constant due to presence of arc current. The non-uniform distribution of temperature affects local parameters of the filament material, such as: resistivity, thermal conductivity, evaporation rate, emissivity, thermionic emission, *etc*. These parameters, in turn, define the distribution of current. Such a physics requires a self-consistent model for the filament parameters.

The filament is described as a wire of round cross section. The diameter of the wire, as well as its temperature, vary along the filament. The filament is assumed to have no variation in the cross section.

Ohm's Law

The distribution of current along the filament is described by the Ohm's law. The current is driven by the direct current (DC) voltage applied to the filament ends.

$$\frac{dU}{dz} = I\frac{dR}{dz}, \tag{1}$$

$$\frac{dR}{dz} = \frac{\rho(z)}{\pi d^2(z)/4}, \tag{2}$$

$$\frac{dI}{dz} = (j_e + j_i)\pi d(z), \tag{3}$$

where $U(z)$ is the distribution of electrostatic potential along the filament, $I(z)$ is the distribution of current along the filament, dR/dz is the differential resistance, $\rho(z)$ is the material resistivity which depends on local temperature, $d(z)$ is local diameter of the filament, and j_e and j_i are the electron and ion arc current densities, respectively. Equations (1) – (3) should be solved with the boundary condition of $U(L)-U(0)=U_{DC}$, where L is the filament length and U_{DC} is the applied DC voltage. Equations (1) – (3) should be solved separately for phases of the ion source cycle with and without the arc current. The electron and ion arc current densities can be found from Richardson's law for thermionic emission [6] and plasma sheath problem [7], respectively. The schematics of current flows through the filament is shown in Fig. 1.

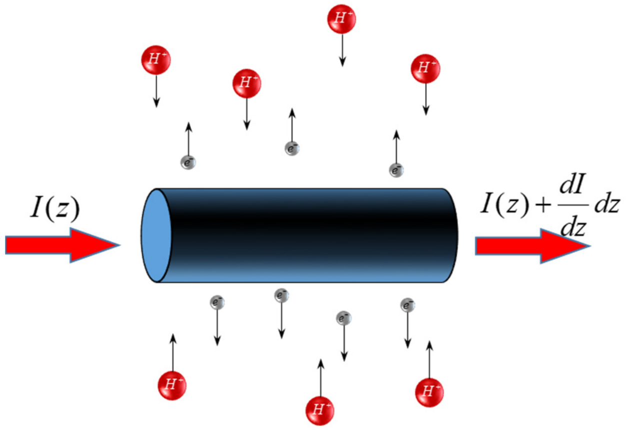

Figure 1: Schematics of currents flow through filament.

---

* Work supported by the US Department of Energy under Contract Number DE-AC52-06NA25396

† Email address: nyampols@lanl.gov

ISBN: 978-3-95450-223-3 ISSN: 2673-7000 doi:10.18429/JACoW-NAPAC2019-WEPLO02

PROGRESS ON MUON IONIZATION COOLING DEMONSTRATION WITH MICE

P. Snopok*, Illinois Institute of Technology, Chicago, IL, USA
on behalf of the MICE collaboration

Abstract

The Muon Ionization Cooling Experiment (MICE) at the Rutherford Appleton Laboratory has collected extensive data to study the ionization cooling of muons. Several million individual particle tracks have been recorded passing through a series of focusing magnets in a number of different configurations and a liquid hydrogen or lithium hydride absorber. Measurement of the tracks upstream and downstream of the absorber has shown the expected effects of the 4D emittance reduction. Further studies are providing more and deeper insight.

INTRODUCTION

Stored muon beams have been proposed as the source of neutrinos at the Neutrino Factory and as the means to deliver multi-TeV lepton-antilepton collisions at the Muon Collider [1]. In such facilities the tertiary muon beam occupies a large volume in phase space. To optimize the muon intensity, while maintaining a suitably small aperture in the muon-acceleration systems, requires that the muon-beam phase space is reduced (cooled) prior to acceleration. The short muon lifetime makes traditional cooling techniques unacceptably inefficient when applied to muon beams. Ionization cooling, in which the muon beam is passed through material (an absorber) and subsequently accelerated, is the technique by which it is proposed to cool the beam [2,3]. The MICE experiment has presented results demonstrating that ionization cooling works and is in agreement with current Monte Carlo simulations [4].

The MICE experiment consists of an upstream beamline [5] to capture pions emitted from the titanium target [6], and focus the produced muons into a cooling channel. The cooling channel (Fig. 1) consists of 12 individually powered solenoid magnets, symmetrically placed up- and downstream of an absorber chamber which could be configured depending on the beam momentum and required beta-function. Upstream and downstream particle ID (PID) detectors [7] are used to improve the reconstruction algorithms and reject pion and electron contamination within the beam. A range of absorbers were used during data-taking including an empty drift space (*No absorber*), a 65-mm lithium hydride disk (*LiH*) and a 22-liter liquid hydrogen vessel (*LH2*).

EMITTANCE AND AMPLITUDE

The experiment's timing, particle identification and tracking detectors allowed individual muon tracks to be identified and reconstructed to a precision better than 1 mm, both upstream and downstream of the absorber module. Each muon candidate was selected based on the time of flight and momentum. The offline combination of the individual muon tracks permitted analysis of the collective beam behavior. A variable-thickness diffuser was included to incrementally increase the initial beam emittance between approximately 3 mm and 10 mm.

The muon beam emittance was calculated by constructing the covariance matrix, Σ, using the covariances, σ_{ab}, of the position and momentum components of the individual muon tracks,

$$\Sigma = \begin{pmatrix} \sigma_{xx} & \sigma_{xp_x} & \sigma_{xy} & \sigma_{xp_y} \\ \sigma_{p_x x} & \sigma_{p_x p_x} & \sigma_{p_x y} & \sigma_{p_x p_y} \\ \sigma_{yx} & \sigma_{yp_x} & \sigma_{yy} & \sigma_{yp_y} \\ \sigma_{p_y x} & \sigma_{p_y p_x} & \sigma_{p_y y} & \sigma_{p_y p_y} \end{pmatrix}. \tag{1}$$

The 4-dimensional normalized transverse emittance, $\epsilon_{4\mathrm{D}}$, of the beam can then be calculated using the determinant of the covariance matrix and the muon mass, m_μ:

$$\epsilon_{4\mathrm{D}} = \frac{1}{m_\mu}\sqrt[4]{|\Sigma|}. \tag{2}$$

The single-particle amplitude, $A_\perp$, can be defined as the Mahalanobis distance between a point in phase space, $v = (x, p_x, y, p_y)$ and the center of the distribution, weighted by the distribution's emittance. It estimates the emittance of a beam which is characterized by an ellipse that passes through that point. It is calculated as

$$A_\perp = \epsilon_{4\mathrm{D}}\ (v - \bar{v})^{\mathrm{T}}\Sigma^{-1}(v - \bar{v}) \tag{3}$$

METHOD

Data were taken with a specific configuration of solenoidal fields, i.e $\beta_\perp \approx 660$ mm at the absorber, with the three different absorber configurations (*No absorber*, *LiH* and *LH2*). The magnitude of the solenoidal field strength along the length of the cooling channel is shown in Fig. 2. Scintillating fiber detectors were installed up- and downstream of the absorber and used to reconstruct individual muon tracks [8]. The data that was collected using an empty channel enabled the observation of optical aberrations and will be used to cross-check for other systematic effects.

Cuts were applied to the raw data to remove electron and pion impurities in the reconstructed beam. The recorded time of flight for each track was required to be consistent with the expected value given the selected muon momentum (140 ± 7 MeV). The trackers must produce a well-reconstructed track in the upstream and, if present, the downstream trackers (χ^2/NDF < 10). Each track must also be

---

* psnopok@iit.edu

ISBN: 978-3-95450-223-3 ISSN: 2673-7000 doi:10.18429/JACoW-NAPAC2019-WEPLO05

DEVELOPING CRITERIA FOR LASER TRANSVERSE INSTABILITY IN LWFA SIMULATIONS

Y. Yan*, L.D. Amorim†, P. Iapozzuto, Y.C. Jing, P. Kumar, V. Litvinenko, V. Samulyak,
N. Vafaei-Najafabadi, Stony Brook University, Stony Brook, NY, USA
M. Babzien, M.G. Fedurin, K. Kusche, M.A. Palmer, M.N. Polyanskiy, I. Pogorelsky
Brookhaven National Laboratory, Upton, NY, USA
M. Downer, J.R. Welch, R. Zgadzaj, University of Texas at Austin, Austin, TX, USA
C. Joshi, W.B. Mori, University of California, Los Angeles, CA, USA

Abstract

Laser-driven plasma wakefield acceleration (LWFA) is considered as a potential technology for future colliders and light sources. To make the best use of a laser's power, the laser is expected to maintain a stable propagation. A transverse instability is observed in our previous simulations when a long, intense CO_2 laser propagates inside a plasma [1]. This unstable motion is accompanied by strong transverse diffraction of the laser power and results in the disruption of the ion channel typically used for radiation generation [2]. We investigated the hosing-like instability using the Particle-in-Cell code OSIRIS [3] by modeling the laser portion where this instability is seeded and then evolves. In this proceeding, a criteria will be described that allows for the characterization of the temporal and spatial evolution of this instability.

INTRODUCTION

Plasma wakefield accelerators can reach an accelerating gradient of 50 GeV/m [4]. This is hundreds of times greater than the gradient in conventional ones. To maximize the efficiency of LWFAs, it is required that the laser propagates stably inside the plasma to maintain the high acceleration gradient. One potential application of these advanced acceleration methods is to build light sources with highly collimated x-rays generated inside the plasma ion channels [2]. These channels, which are generated by the interaction of a pico-second laser pulses with plasma, are the primary motivation for the study of such an interaction.However, recent simulations of a picosecond, intense CO_2 laser propagating in plasma have shown evidence of transverse instability in the laser profile [1]. In these simulations, the laser duration $\tau_c >> \lambda_p$, where λ_p is the plasma wavelength. The laser ionizes neutral hydrogen gas and due to the ponderomotive force, it creates plasma density waves. The local index of refraction, $\eta = \sqrt{1 - \frac{\omega_p^2}{\omega_0^2 \gamma_\perp}}$, is modified by the plasma density. Here, $\gamma_\perp = \sqrt{1 + a_0^2/2}$ and $a_0 = eA/mc^2$ is the normalized vector potential, and ω_o and ω_p are the laser frequency and plasma frequency, respectively [5]. Smaller plasma density n_0 corresponds to a larger η. The laser is self-focused [6] and maintains its spot size as it propagates in the plasma. The laser front part, which interacts with plasma earlier, is dominated by the self-modulation instability [6]. In self-modulation, ω_0 is shifted by ω_p to $\omega_0 \pm \omega_p$ from the plasma wave and the laser gets bunched longitudinally. At the back part, where the interaction starts later, the laser is self-channeled [7]. This occurs when plasma ions follow plasma electrons moving away from the axis, and a hollow plasma ion channel, where significant radiation is generated [2], is formed. In the transition region between laser self-modulation at the front and self-channeling at the back, a transverse instability is observed in the laser envelope which resembles the hosing instability of a particle beam in a particle-driven plasma wakefield accelerator [1]. Under this hosing-like instability, the centroid of each longitudinal laser slice oscillates transversely around its propagation axis with growing amplitude. Saturation is reached when the slices have too large an offset to be restored and just move outward away from the axis. The instability extends backwards from the back of the self-modulation section,the process of which diffracts the laser core and disrupts the plasma channel, thus prematurely terminating electron energy gain or radiation processes. To investigate this seeding, we stimulated the portion of the laser that undergoes self-modulation and the hosing-like motion. The properties of this instability were studied using the OSIRIS code in the two-dimensional (2D) geometry [3]. However, the presence of this instability was also confirmed in 3D geometry, demonstrating that this instability is present regardless of the geometry used in the simulations. In this proceeding, we will first introduce our OSIRIS simulation setups. Then, we will explain the criteria that was developed to characterize the evolution of the hosing-like instability both in time, i.e. at the same position in the frame of the laser, and in space, i.e. the evolution along the laser axis.

SIMULATION SETUP

We launched 2D Cartesian simulations with laser propagation direction (z) longitudinally and laser polarization direction (x) transversely. The CO_2 laser had a transverse Gaussian profile and a longitudinal Gaussian-like profile fitted by a 5th order polynomial.

In the simulation, we model a $\lambda_0 = 9.2\ \mu$m laser with 2 ps duration (τ). The spot size W_0 is 20 μm and its normalized vector potential a_0 is 4.3. The simulation uses a moving window traveling in z. Because $c\tau \gg \lambda$, it is challenging

---

[*] jiayang.yan@stonybrook.edu
[†] Currently at Lawrence Berkley National Labtorary

START-TO-END SIMULATION OF THE DRIVE-BEAM LONGITUDINAL DYNAMICS FOR BEAM-DRIVEN WAKEFIELD ACCELERATION*

W. H. Tan[1]†, P. Piot[1,2], A. Zholents[2]
[1] Northern Illinois University, DeKalb, IL, USA
[2]Argonne National Laboratory, Lemont, IL, USA

Abstract

Collinear beam-driven wakefield acceleration (WFA) relies on shaped driver beam to provide higher accelerating gradient at a smaller cost and physical footprint. This acceleration scheme is currently envisioned to accelerate electron beams capable of driving free-electron laser [1]. Start-to-end simulation of drive-bunch beam dynamics is crucial for the evaluation of the design of accelerators built upon WFA. We report the start-to-end longitudinal beam dynamics simulations of an accelerator beamline capable of producing high charge drive beam. The generated wakefield when it passes through a corrugated waveguide results in a transformer ratio of 5. This paper especially discusses the challenges and criteria associated with the generation of temporally-shaped driver beam, including the beam formation in the photoinjector, and the influence of energy chirp control on beam transport stability.

INTRODUCTION

Collinear beam-driven wakefield acceleration (WFA) schemes, e.g. based on plasmas or structures, strongly benefit from a drive beam with a tailored current distribution. Tailored bunches enhance the efficiency of the acceleration scheme by increasing the transformer ratio $\mathcal{R} = \left|\frac{E_+}{E_-}\right|$, defined as the ratio of the maximum of the accelerating field behind the bunch E_+, to the maximum of the decelerating field within the bunch E_-. Over the years, several beam shaping techniques have been proposed and investigated to enhance the transformer ratio, including photocathode laser shaping techniques [2–4], transverse-to-longitudinal phase-space emittance exchange [5,6], and multi-frequency linacs [7]. In addition to that, similar efforts have been devoted to the practical designs and the study of beam stability in WFA, such as longitudinal-phase-space (LPS) requirements for stability conditions [8], the suppression of transverse wakefields [9], and an overview of WFA development [10]. In this paper, we present our recent efforts in producing the shaped beams required for WFA and addressing beam stability. Building upon efforts in [11], we investigated the generation of required distribution from a low energy electron beam injector, which can be further accelerated and shaped into a drive beam with enhanced transformer ratio ($\mathcal{R} > 5$). The studies were done in beam dynamics simulations where laser profiles and relevant gun parameters were optimized through multi-objective optimization. Consequently, the obtained beam distributions were tracked through longitudinal tracking code Twice to study the evolution of the associated bunch shapes. Finally, we combined both efforts to perform a start-to-end simulation of drive beam longitudinal dynamics to demonstrate a proof of concept of drive beam generation for WFA.

BEAM DYNAMICS SIMULATION

Beam Distribution

The target distribution to be produced at the downstream of an injector is shown in Fig. 1, where its beam parameters are shown in Table 1. It was obtained by reverse tracking simulation of a modified doorstep distribution shown in Fig. 2. Additional details, including accelerator parameters and a description of the reverse-tracking technique, were reported on [11].

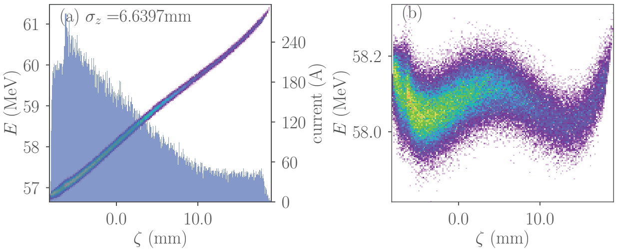

Figure 1: Target bunch LPS to be produced from an electron gun, with its current distribution (a), and its LPS after removing linear chirp (b).

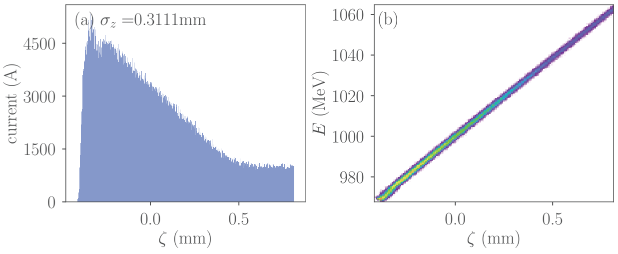

Figure 2: LPS (right) and current (left) distribution used for reverse tracking to obtain target distribution for an injector.

Photoinjector Simulation

In a photoinjector, the laser pulse distribution of a photocathode determines the initial shape of electron bunch

---

* This work is supported by the U.S. Department of Energy, Office of Science under contracts No. DE-AC02-06CH11357 (via a laboratory-directed R&D program at ANL) and No. DE-SC0018656 at NIU.

† z1829753@students.niu.edu

ISBN: 978-3-95450-223-3 ISSN: 2673-7000 doi:10.18429/JACoW-NAPAC2019-WEPLO11

SINGLE CYCLE THz ACCELERATION STRUCTURES*

S.V. Kuzikov†, S.P. Antipov, E. Gomez, Euclid Techlabs LLC, Bolingbrook, IL, USA
A.A. Vikharev
Institute of Applied Physics of Russian Academy of Sciences, Nizhny Novgorod, Russia

Abstract

Recently, gradients on the order of 1 GV/m have been obtained in the form of single cycle (~1 ps) THz pulses produced by the conversion of a high peak power laser radiation in nonlinear crystals (~1 mJ, 1 ps, up to 3% conversion efficiency). These pulses however are broadband (0.1-5 THz) and therefore a new accelerating structure type is required. For electron beam acceleration with such pulses, we propose arrays of parabolic focusing micro-mirrors with common central. These novel structures could be produced by a femtosecond laser ablation system developed at Euclid Techlabs. This technology had already been tested for production of several millimetres long, multi-cell structures which has been tested with electron beams. We also propose use of these structures where necessary GV/m E-fields are excited by a drive bunch travelling in a corrugated waveguide. The radiated by drive bunch sequence of short-range delayed wakes are guided in this case by metallic disks and reflected back being focused exactly at the time when the witness bunch arrives.

BROAD BAND THz ACCELERATING STRUCTURES

High-field single cycle THz pulses are now produced by means of laser light rectification in a nonlinear crystal [1]. Such pulses can potentially provide ~1 GV/m acceleration of sub-picosecond bunches. In [2-6], a new accelerating structure design was proposed, which introduces a set of waveguides with different adjusted lengths.

Concept of Delay Waveguides

Accelerating structure design is based on empty waveguides with different adjusted lengths, in which the synchronism of accelerated particles with transversely propagating picosecond THz pulse is to be sustained (Fig. 1).

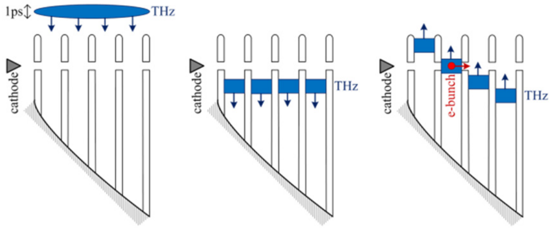

Figure 1: Sketch of particle acceleration in a structure by picosecond THz pulse for three sequent time frames.

Dielectric Delay Concept

This concept exploits inserted dielectric slabs of different lengths, in which the synchronism of accelerated particles with transversely propagating single-cycle THz pulse is sustained (Fig. 2). In the transverse direction, the accelerating structure introduces focusing parabolic mirrors (Fig. 3). These mirrors enhance the accelerating field seen by electrons by a factor of 3-10 times. Such design allows for an overall reduction of losses and mitigation of the negative action of frequency dispersion in the waveguide, because most pathway of THz pulse propagation lies in a wide waveguide. The THz pulse is focused in at the very end of the structure.

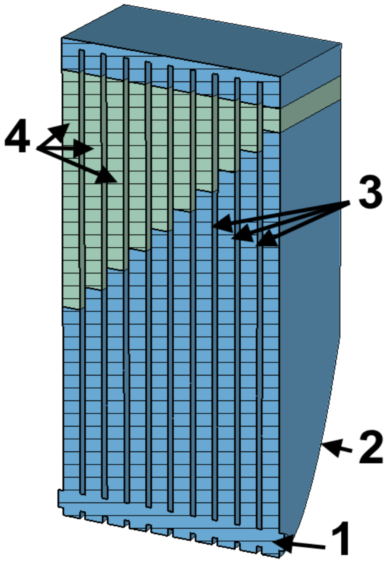

Figure 2: Sketch of broad band THz structure based on dielectric delay waveguides: 1 – beam channel, 2 – mirrors of the parabolic shape, 3 – oversized vacuum waveguides, 4 – delay waveguides filled with dielectrics.

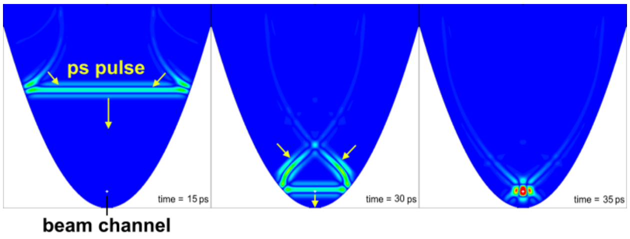

Figure 3: E-field distributions at the parabolic mirror while focusing the short THz pulse, for the time correspondent to beginning of focusing at t=15 ps (left), for time when focusing is close to maximum at t=30 ps (center), and in maximum of focusing (right) at t=35 ps.

---

* This work was supported by the Russian Science Foundation under Grant 19-42-04133 in the part of beam dynamics simulations for THz structures.
† s.kuzikov@euclidtechlabs.com

North American Particle Acc. Conf. NAPAC2019, Lansing, MI, USA JACoW Publishing
ISBN: 978-3-95450-223-3 ISSN: 2673-7000 doi:10.18429/JACoW-NAPAC2019-WEPLO12

DESIGN OF A PIP-II ERA Mu2e EXPERIMENT

M.A. Cummings†, R.J. Abrams, T.J. Roberts, Muons, Inc., Batavia, IL, USA
D.V. Neuffer, Fermilab, Batavia, IL USA

Abstract

We present an alternative Mu2e-II production scheme for the Fermilab PIP-II era based on production schemes we devised for muon-collider and neutrino-factory front ends. Bright muon beams generated from sources designed for muon collider and neutrino factory facilities have been shown to generate two orders of magnitude more muons per proton than the current Mu2e production target and solenoid. In contrast to the current Mu2e, the muon collider design has forward-production of muons from the target. Forward production from 8 GeV protons would include high energy antiprotons, pions and muons, which would provide too much background for the Mu2e system. In contrast, the 800 MeV PIP-II beam does not have sufficient energy to produce antiprotons, and other secondaries will be at a low enough energy that they can be ranged out with an affordable shield of ~ 2 meters of concrete.

INTRODUCTION

The Mu2e experiment at Fermilab will search for evidence of charged lepton flavor violation by searching for the conversion of a negative muon into an electron in the Coulomb field of a nucleus, without emission of neutrinos. The current Mu2e experimental production setup will be capable of producing ~$2\cdot 10^{17}$ negative muons per year. Regardless of the Mu2e outcome, a next generation experiment, Mu2e-II, with a sensitivity extended another factor of 10 or more, has a compelling physics case. This upgrade will require a complete re-design of the muon production and transport, which is the subject of this proposal.

The current Mu2e design is optimized for 8 kW of protons at 8 GeV. The proposed PIP-II upgrade project is a 250-meter-long CW linac capable of accelerating a 2 mA proton beam to a kinetic energy of 800 MeV (total power 1.6 MW). This would significantly improve the Fermilab proton source to enable next-generation intensity frontier experiments. Much of the beam will be utilized for the Fermilab Short Baseline Neutrino and Long Baseline Neutrino Facility neutrino programs, but more than 1 MW of 800 MeV protons will be available for additional experiments. It is expected that Mu2e-II will require about 100 kW.

PREVIOUS WORK

Muons, Inc. software product G4beamline [1] has been widely distributed for HEP projects, and has more than 500 users. It is one of the official software tools of the current Mu2e experiment, illustrated in Fig. 1.

In 2015 Muons, Inc. had a subcontract from Fermilab's Mu2e Project to perform an initial study of how PIP-II would affect the Mu2e experiment, in particular the impact of using 800 MeV protons. This was specifically in the context of the current Mu2e design, with the intent of evaluating minimal changes required to use 800 MeV protons at ~ 10 times the power, to obtain 10 times the rate of stopping muons.

Our first observation was that while 800 MeV protons have 1/10 the kinetic energy of 8 GeV protons, they have 1/6 the momentum. Scaling down all magnet currents by a factor of 6 would make the PIP-II beam follow the same trajectory through the production solenoid, missing the heat and radiation shield (HRS), and hitting the beam absorber. But this would give the transport solenoid too small a field to transport most of the muons, and would give the detector too small a field for the detector to work at all. So the simple and obvious approach does not work.

Muons, Inc. did initial studies of Mu2e in the PIP-II era, looking at three scenarios:

1. No changes (except magnet currents and re-alignments)
2. Minimal changes (leave all coils alone)
    - Modifying the HRS with a new beam hole
3. Modest changes
    - Remove one TS coil
    - Modest changes to HRS, target, and beam absorber

The first two scenarios were quickly dismissed in initial simulations. The third scenario introduced a modest change, removing one TS coil, so two of the gaps between coils would be combined into one gap about 20 cm wide. By putting the proton beam right down the production solenoid axis, it is possible to hit the target and miss the HRS. This would require a re-design of the HRS and target, plus the change to the TS, and the beam absorber must be moved, as shown in Fig. 2. So the "modest change" approach would require:

- Removing one TS coil and drilling a hole for the beam in its cryostat.
- Replace the HRS with one made of tungsten.
- Move the beamline ~100 mm closer to the TS, slight angle.
- Move the target, add active cooling.
- Move the beam dump.

The conclusion of this earlier work was that for Mu2e in the PIP-II era, using the 800 MeV beam requires a redesign of the beamline, target, HRS, production solenoid, and beam absorber. Or perhaps a complete change of concept – the lower-energy proton beam means we can consider using forward production of muons, with potentially a significantly higher number of stopped muons per proton.

---

†macc@muonsinc.com

ENERGY SPREAD MEASUREMENTS FOR 400 MeV LINAC BEAM AT FERMILAB BOOSTER USING A LASER NOTCHER SYSTEM*

C.M. Bhat†, D.E. Johnson
Fermi National Accelerator Laboratory, Batavia, IL, USA

Abstract

To mitigate 8 GeV beam losses at extraction in the Fermilab Booster synchrotron, a LASER chopper system for multi-turn injection that produces a beam free gap, aka “notch” in the LINAC beam pulse at 750 keV is developed. These notches in the LINAC pulse are spaced with the 400 MeV injection revolution period of the Booster. Recently, a dedicated notching pattern that keeps a single 201 MHz LINAC bunch in the middle of a notch is developed to measure the beam energy spread by studying the time evolution of this bunch in the Booster. A method complementary to this has also been realized by injecting <2 Booster turn beam and studying the time evolution of the multiple 201 MHz LINAC bunches. In this paper we present the general principle of the method and results from our measurements.

INTRODUCTION

Recently, Fermilab executed a “Proton Improvement Plan” [1, 2] to upgrade the existing accelerator complex to meet its high intensity proton demand for accelerator-based neutrino experiments. This effort had a baseline goal to extract the beam at a 15 Hz rate from the Booster with about 4.6E12 p/Booster cycle. This allowed the delivery of > 700 kW beam power to the NOvA target while supplying record beam power to the 8 GeV short base-line neutrino program. With the completion of the PIP-II [3], the Booster beam delivery will be upgraded to 20 Hz and the normal conductor 400 MeV injector LINAC will be replaced with an 800 MeV superconducting RF LINAC increasing the injected beam intensity by about 50% allowing the capability to provide 1.2 MW beam power to the new LBNF/DUNE experiment.

Between now and when the PIP-II LINAC comes on line, Fermilab will continue improve the accelerator complex by increasing its reliability and efficiency and, reducing losses with a few modest upgrades to existing accelerators. These upgrades to the Booster and downstream accelerators will increase the beam power to the NOvA long baseline neutrino experiment while providing increased beam power to multiple HEP experiments.

Understanding, monitoring and controlling the beam properties of the injected beam from the current LINAC is an essential part of the upgrades. The beam injection capture and acceleration efficiency in the Booster depends very much on the quality of the LINAC beam. The Booster is a rapid cycling synchrotron which accelerates the beam on a 15 Hz sinusoidal magnetic ramp. The longitudinal acceptance of the Booster is ~5.4 MeV. The jitter in the ramp of main Booster dipole magnet power supplies during injection introduces an error of ~ 0.2 MeV. Also, there are many indications of observed energy variation from head of a long LINAC beam pulse to that of the tail. So, careful attention should be given to the energy error and energy spread of the injected beam and effort should be made to mitigate the energy error.

In the past we have measured the beam energy spread using the “notch method” [4] where a small notch of known width is created in the injected beam. The energy spread is measured by measuring the time required for beam shear and length of beam shear (in time). Although the technique gave us a reliable measurement on the energy spread of the accumulated injected beam, there are two issues which complicate the measurement procedure. In the first place this method was destructive and cannot be used on operational cycles and secondly, it was necessary to turn off the main RF system to get a clear wall current monitor (WCM) signal without RF modulation. In this paper we present an alternative method to measure the energy spread for the LINAC beam which is based on similar physics principle explained in ref. [4].

MEASUREMENTS AND DATA ANALYSIS

During early 2017 a LASER chopper system [5] is brought into operation to mitigate the beam loss in the Booster by producing notches in the LINAC pulse which are synchronized with the revolution period of the beam in the Booster. Each notch is produced by neutralizing about sixteen H^- 201 MHz beam bunch downstream of the 750 keV RFQ. Currently, one can produce up to about 18 notches in the LINAC beam pulse. As beam is stacked in the Booster by multi-turn injection, these notches lineup producing a net gap of ~ 80 ns in the Booster beam. We took advantage of this LASER chopper system and carried out research on energy spread measurements of the injected LINAC beam by two slightly different ways which are complementary to one another. The Booster RF system has little effect on the measured energy spread.

In the first method, we remove all 201 MHz bunches in the notch except one in the middle of the notch. The subsequent notches were left untouched. As this beam arrives at the Booster the single bunch in the notch will be undisturbed. One can observe turn-by-turn bunch length increase as the beam circulates in the Booster. The energy

---

* This manuscript has been authored by Fermi Research Alliance, LLC under Contract No. DE-AC02-07CH11359 with the U.S. Department of Energy, Office of Science, Office of High Energy Physics.

† cbhat@fnal.gov

ULTRASHORT LASER PULSE SHAPING AND CHARACTERIZATION FOR TAILORED ELECTRON BUNCH GENERATION [*]

T. Xu[†], P. Piot[1], Northern Illinois University, DeKalb, IL, USA
M.E. Conde, G. Ha, J.G. Power, Argonne National Laboratory, Lemont, IL, USA
[1]also at Argonne National Laboratory, Lemont, IL, USA

Abstract

Temporally-shaped laser pulse are desirable in various applications including emittance reduction and beam-driven acceleration. Pulse-shaping techniques enable flexible controls over the longitudinal distribution of electron bunches emitted from photocathode. While direct manipulation and measurement of ultrashort pulses can be challenging in the time domain, both actions can be performed in the frequency domain. In this paper, we report investigations toward the development of laser shaper and diagnostics at the Argonne Wakefield Accelerator. Simulations are presented to describe the shaping and measurement process based on a digital mask and a frequency resolved optical gating method.

INTRODUCTION

Collinear wakefield accelerators have driven the demands for electron bunches with tailored current profiles [1]. It has been recognized that longitudinally asymmetric drive bunches produce higher transformer ratios and ultimately enable a larger energy transfer between drive and witness. Therefore bunch shaping techniques to produce asymmetric drive beams are crucial for efficient acceleration. One promising technique that could generate shaped electron bunches is laser shaping where laser pulses are temporally shaped before impinging on a photocathode [2–4] . Laser shaping technique is appealing owing to its simplicity and possible combination with other shaping techniques to produce precisely tailored electron bunches.

In the picosecond regime, laser pulse shaping can be realized by splitting pulses in birefringent crystal and stacking the replicae temporally [5]. This scheme often requires fine-tuning of the orientation of crystals and lacks versatility. Pulses are generated on a femtosecond time scale, providing broader spectral bandwidths compared with picosecond lasers. This allows the manipulation of different spectral components, hence the ability to generate arbitrary optical waveforms [6]. Complementary to laser shaper is the diagnostics for characterizing the pulse temporal distributions. Optoelectronic devices like streak cameras reach temporal resolutions of the order of 100 femtoseconds. Thus a different approach is required to characterize the shaped pulse.

In the present work, we describe our approach to develop a pulse shaper and associated temporal diagnostics at the Argonne Wakefield Accelerator (AWA) facility. The AWA laser system is based on a Titanium-Sapphire system and consists of a phase-locked commercial oscillator (VITARA from COHERENT). The infrared (IR) pulse (λ_0 = 788 nm are stretched and amplified in a regenerative amplifier. In a second stage, a multi-pass amplifier boosts the pulse energy to ~ 100 mJ. The IR pulses are finally compressed and converted to ultraviolet (UV, 263 nm) Fig. 1. The pulse shaper will be installed downstream of the oscillator and two pulse-characterization diagnostics will be implemented in the IR (for both the oscillator and amplifier IR pulse) and the UV. A femtosecond pulse from oscillator is shaped in a dispersive section with a Fourier transform pulse shaping scheme. The desired pulse shape can be obtained by manipulating the amplitudes or phases of different spectral components. For pulse characterization, a Frequency-Resolved Optical Gating (FROG) technique [7] is employed to measure the temporal distribution of the shaped pulses. Possible improvements of the setup are discussed.

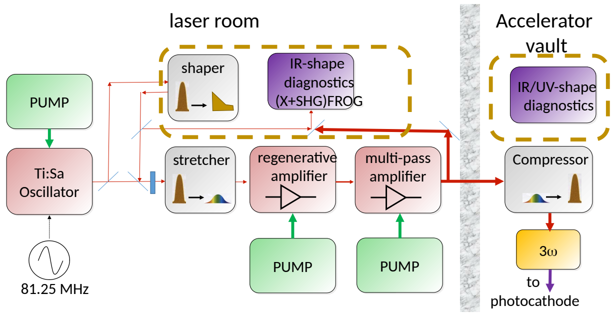

Figure 1: Overview of the AWA laser; see text for details.

LASER PULSE SHAPING

Laser pulse shaping has been an active field of research over the last two decades and has supported various scientific applications [8]. A number of shaping techniques have been implemented for ultrashort pulses [9]. Temporal shaping of a femtosecond pulse can be achieved via manipulation of its optical spectrum $\widetilde{E}(\omega)$. The spectral amplitudes and phases of the input pulse are modified through a programmable digital to generate the desired output waveform $E(t)$.

A straightforward method to shape the spectrum of an ultrashort pulse consists in introducing a local spatial chirp using a dispersive element. A widely used setup is diagrammed in Fig. 2: a grating introduces the needed dispersion and a lens collimates the diverging beam. If the distances $a = b = f$ where f is the focal length associated to

---

[*] This work was supported by the US Department of Energy (DOE) contracts No. DE-SC0018656 with NIU and No. DE-AC02-06CH11357 with ANL.

[†] xu@niu.edu

NUMERICAL STUDY OF COHERENT RADIATION FROM INDUCED PLASMA DIPOLE OSCILLATION BY DETUNED LASER PULSES

P.C. Castillo†, S.D. Rodriguez, D.A. Wan,
SUNY-Farmingdale State College, Farmingdale, NY, USA
K. Yu, Brookhaven National Laboratory, Upton, NY, USA
B. Gross, The City College of New York, NY, USA
D.G. Lee, Stony Brook University, New York, NY, USA
M.S. Hur, S. Kylychbekov, H.S. Song,
Uslan National Institute of Science and Technology, Ulsan, South Korea

Abstract

This research focuses on numerical studies and simulation of interacting counter propagating high-intense short laser pulses inducing strong oscillating dipoles in preformed plasma resulting in novel THz sources. By choosing a suitable frequency detuned colliding laser pulses, a cylindrical spatial plasma column will be established within the laser beam radius regime resulting in a time varying longitudinal ponderomotive field that can drive the charges coherently resulting in the formation of a stable spatially localized plasma dipole oscillation (PDO). This novel excitation approach can then result in emission of terahertz radiation transverse to the laser optic axis. While the general qualitative behavior of the 'released dipole' radiation can be easily modelled as a driven harmonic oscillator, the detailed microphysics during the dipole growth stage requires first principles modelling of the Radiation / Plasma system which can only be accomplished by our proposed 3D Particle in Cell (PIC) time dependent Partial Differential Equation steppers that evolve the simultaneous motions of the plasma charges and the EM fields. In this paper, we focus on a case where the emission is expected to be efficient and use the full 3D capabilities of our simulation environment to observe the radiation structure transverse to the laser induced dipole fields.

INTRODUCTION

The study of intense laser-plasma interactions is an active and growing field of both theoretical and applied research encompassing a variety of disciplines. As discussed in Kwon et. al. [1], there is strong interest in developing potential tunable compact high power-narrow band radiation sources that can be used for a number of applications. Most approaches to the generation of such sources are either expensive and physically large (i.e. Free Electron Lasers) [2-5] or low energy due to material breakdown limits [6]. In addition, the complex nonlinear time varying processes that may be encountered in the interaction of laser irradiation and high concentration plasma make analytical modelling difficult and approximate, and most fundamental studies require sophisticated numerical modelling approaches to account for the complex interactions that charged particle carriers can have with intense EM pulses that can further be focused onto spatial targets [7-9].

This research focuses on developing a suitable computational environment to simulate dense plasma effects during its interaction with high intensity lasers that can be manipulated to provide different laser interaction geometries.

In this paper, we focus on demonstrating through PIC simulations (x-y-z-t) recently discussed spatially modulated plasma dipole oscillation [1, 7, 10-16] induced by detuned counter-propagating laser pulses. Based on approximate 1D modelling and 1D and 2D PIC simulations, such an excitation process can generate a narrow band THz radiation at the Plasma Frequency [17-23]. Because of the high density of particles within the wavelength of the exciting pulses, the abovementioned physical processes require extensive computational simulations in order to process a large amount of data to represent the plasma density (millions of particles) within the Particle-in Cell system. Unlike most previous studies where either 1D or 2D PIC simulations are used, potentially interesting features of the EM-Laser interactions due to cylindrical 3D spatial geometries of the laser beam regime is investigated.

METHODS AND ALGORITHMS

In this numerical study, we adapted the Particle-In-Cell (PIC) method, which is implemented by a code named SPACE. Space is a relativistic and full 3D electromagnetic PIC (EM-PIC) code based on the finite difference time domain (FDTD) [24] being developed at Brookhaven National Laboratory (BNL) [25, 26]. Space has been verified and validated in the studies of a variety of beam-plasma and laser-plasma interaction scenarios such as HPRF at Fermilab [27, 28], CeC at BNL [29, 30], and LWFA at BNL [31, 32].

LASER/PLASMA SYSTEM SETTINGS

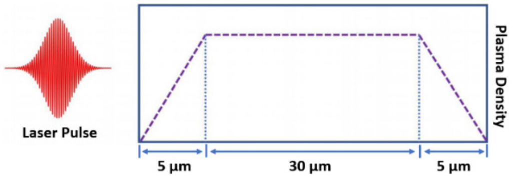

Figure 1: Schematic diagram of the laser pulse and plasma density profile along the pulse propagation direction. The preformed plasma has cilindrical shape of 40 µm length and 5 µm radius. The plasma density ramp up linearly from the both edges and the center part has constant density.

---

† castilp@farmingdale.edu

ISBN: 978-3-95450-223-3 ISSN: 2673-7000 doi:10.18429/JACoW-NAPAC2019-WEPLO19

PROBING MULTIPERIOD PLASMA RESPONSE REGIMES USING SINGLE SHOT WAKEFIELD MEASUREMENTS

R. J. Roussel*, G. Andonian, W. Lynn, J. B. Rosenzweig, UCLA, Los Angeles, CA, USA
J. G. Power, M. E. Conde, S. Doran, G. Ha, J. Seok[1], E. Wisniewski, C. Whiteford,
Argonne National Laboratory, Lemont, IL, USA
[1] also at Ulsan National Institute of Science and Technology, Ulsan, South Korea

Abstract

Systematic differences between the linear and nonlinear regimes of plasma wakefield acceleration from electron beams are manifested in the plasma response. Typically, the ratio of peak beam density to nominal plasma density determines operation in the linear or nonlinear regime. Previous reports have shown that a the cross-over into the nonlinear regime is associated with an increase in the wakefield amplitude, as well as sawtooth-like shape. In this paper, we present preliminary measurements of quasi-nonlinear wakefields driven by a linearly ramped beam, with a maximum charge close to the unperturbed plasma density. We also demonstrate nonlinear wakefield behavior in a probe bunch using a single shot, multi-period wakefield measurement and its dependency on plasma density.

INTRODUCTION

Development of strongly nonlinear plasma wakefield acceleration (PWFA) in the blowout regime is a major focus of the advanced accelerator field. Accelerating gradients up to tens of GeV/m have been have been observed using tightly focused ($k_p\sigma_r \ll 1$), ultra-short ($k_p\sigma_z < 2$) electron bunches to excite highly nonlinear wakefields in plasmas [1]. This gradient is far higher than any conventional accelerating structures and has the potential to shrink accelerator sizes many-fold. Furthermore, the plasma blowout regime has attractive properties due to the complete rarefaction of plasma electrons in the accelerating region.

However, the efficiency of energy exchange in these schemes is often limited by the drive bunch used to excite the plasma wakefield. In order to reach the blowout regime, the drive bunch needs to be more dense then the unperturbed plasma. For the highest reported accelerating gradients, plasma densities on the order of 10^{17} cm^{-3} are used [2]. For an electron beam to reach this density, it must be longitudinally compressed multiple times using magnetic chicanes [2]. Coherent synchrotron radiation in these chicanes leads to unwanted transverse emittance growth that can prevent proper matching into the plasma [3]. This limits the amount of charge in the drive, which in turn limits the non-linearity of the plasma interaction.

A longitudinally ramped beam can be used to excite a similar non-linear wakefield response by slowly building up the longitudinal slice beam charge over several plasma wavelengths and then abruptly cutting off. The plasma electrons will slowly be displaced from the beam region until a rarefied region develops. When the beam current drops off sharply, the electrons will fall back onto the axis in a similar manner to the blowout collapse seen from short beams[4], creating the similarly extreme accelerating gradients as those previously observed. Beam shaping, already experimentally demonstrated using various methods [5–7], would relax the need for strong longitudinal compression.

EXPERIMENTS AT THE ARGONNE WAKEFIELD ACCELERATOR

The Argonne Wakefield Accelerator (AWA) facility provides an ideal environement to investigate key facets of PWFA driven by shaped beams. The AWA incorporates a cesium telluride photocathode based gun to produce electron bunches with a charge of 12 nC and pulse length of 6 ps. These bunches are accelerated to 40 MeV using normal conducting L-band (1.3 GHz) accelerating structures. The beam is then injected into the AWA emittance exchange beamline (EEX). This beamline consists of two dogleg sections, separated by a transverse deflecting cavity oriented such that the time dependent transverse kick is directed along the horizontal (bend) plane. The EEX beamline exchanges the horizontal and longitudinal phase spaces [7], allowing flexible longitudinal bunch shaping through the use of a transverse mask prior to the first EEX dogleg. For this experiment, the mask was shaped such that it produced a linear ramp in current density over roughly 20 ps and a similar length, low charge, witness beam to sample the resulting wakefield. This shaping technique was used previously to measure high transformer ratio wakefields from slab dielectric structures [8].

A hollow cathode arc plasma source [9] was used to produce a plasma column for the experiment. The source contains a set of three concentric tantalum tubes as a cathode and a ring anode. Argon gas flows between the two innermost tubes, which are restively heated to 2000 K and is then ionized by a 150 V, 200 µs capacitive arc discharge. This produces a stable plasma column approximately 8 mm in diameter and 6 cm in length. The plasma density was determined through the use of a triple Langmuir probe [10] and optical imaging of the plasma afterglow. The plasma density is tunable via changing the strength of an external solenoid field used for plasma confinement [9] as well as varying heating power delivered to the cathode tubes. The measured plasma density profiles due to these variations are shown in Fig. 1.

---

* roussel@ucla.edu

ISBN: 978-3-95450-223-3 ISSN: 2673-7000 doi:10.18429/JACoW-NAPAC2019-WEPLO20

HIGH GRADIENT HIGH EFFICIENCY C-BAND ACCELERATOR STRUCTURE RESEARCH AT LANL*

E.I. Simakov†, A.W. Garmon, T.C. Germann, M.F. Kirshner, F.L. Krawczyk, J.W. Lewellen,
D. Perez, G. Wang, Los Alamos National Laboratory, Los Alamos, NM, U.S.A.
A. Fukasawa, J.B. Rosenzweig, University of California Los Angeles, Los Angeles, CA, U.S.A.

Abstract

We report on the status of the new high gradient C-band accelerator project at LANL. Modern applications such as X-ray sources require accelerators with optimized cost of construction and operation, naturally calling for high-gradient acceleration. Our goal is to use a multi-disciplinary approach that includes accelerator design, molecular dynamics simulations, and advanced manufacturing to develop high gradient, high efficiency RF structures for both compact and facility-size accelerator systems. We considered common operation frequencies for accelerators and identified C-band as the optimal frequency band for high gradient operations based on achievable gradients and means to control wakefields. We are putting together a high gradient C-band test facility that includes a 50 MW Toshiba klystron and cryo-coolers for operating normal-conducting copper accelerator cavities at long pulse duration. We plan to conduct high gradient testing of the optimized RF structures made of copper and novel copper alloys. We use LANL modelling capabilities to systematically study the formation of breakdown precursors at high fields to develop basic theoretical understanding of the breakdown.

INTRODUCTION

Particle accelerators are established tools for National Security (NNSA, DoD) and basic science missions. Modern day applications such as X-ray sources require accelerator facilities with optimized cost of construction and operation, naturally calling for high-gradient acceleration. Increasing gradients in normal-conducting radio-frequency (NCRF) copper-based accelerator structures requires innovation in two major areas: understanding of the physics mechanisms of radio-frequency (RF) breakdown, and development of novel copper alloys with increased breakdown limits. At Los Alamos National Laboratory (LANL) we initiated a new project with the major goal to use a multi-disciplinary approach that includes accelerator design, molecular dynamics simulations, and advanced manufacturing of metals to develop high-gradient, high-efficiency radio-frequency (RF) structures for both compact and facility-size accelerator systems.

CHOICE OF THE OPERATIONAL FREQUENCY

At the start of the project we conducted the evaluation of the optimal operational frequency for the high gradient RF structure that could be employed for the future X-ray Free Electron Laser (XFEL), such as for example DMMSC at LANL [1]. RF performance versus frequency was evaluated for otherwise identical structures scaled to the three selected frequencies: 2.856 GHz (S-band), 5.712 GHz (C-band), and 11.424 GHz (X-band). One structure was specifically designed for this effort and one was derived from a high gradient high-performance photo-injector designed at University of California Los Angeles (UCLA) [2]. The designs were compared based on achievable gradients, acceleration-efficiency, given by the shunt impedance, the wakefield loss factors, and the expected ease of fabrication. Table 1 summarizes the performance of one of the structures. For comparison, it also shows typical numbers for an L-band superconducting accelerator cavity.

Table 1: Comparison of the accelerator characteristics of representative structures at different accelerator frequencies. The wakes are computed for an electron bunch with a bunch length of 2 ps and the energy of 1 GeV.

	L-band	**S-band**	**C-band**	**X-band**
Gradient, MV/m	30	50	100	150
Shunt impedance, MΩ/m	$9*10^6$	85	120	170
Longitudinal wake, V/pC	10.2	26.5	36.5	50.4
Energy change due to wake	0.3%	2.5%	3.5%	8.0%
Transverse wake, V/pC/m	15.1	155	835	4420
Deflection over 1 μm, kV	0	1.5	8.0	67.4

The gradients quoted in Table 1 are room temperature maximum gradient estimates based on available experimental data. The numbers demonstrate that while the gradient increases with frequency, the strong increase in wakefields restricts operation at frequencies above C-band. The L-band SRF structure has superior efficiency, moderate gradients, and low short range wakes, however the extremely low Ohmic losses result in long-range wakes that are hard to manage. In addition, the bunch separation for a “MaRIE burst mode” [3] at L-band is too slow for good temporal resolution with a bunch proximity that will lead to strong multi-bunch wakes. Evaluation of the energy chirp of a beam for XFEL applications established another advantage for C-band. Beam transport through the RF accelerator introduces a chirp that needs to be removed for

---

* Work is supported by Los Alamos National Laboratory’s LDRD Program.
† smirnova@lanl.gov

ISBN: 978-3-95450-223-3 ISSN: 2673-7000 doi:10.18429/JACoW-NAPAC2019-WEPLE02

INTEGRATED ACCELERATOR SIMULATION WITH ELECTROMAGNETICS AND BEAM PHYSICS CODES*

L. Ge†, Z. Li, C.-K. Ng, L. Xiao, SLAC National Accelerator Laboratory, Menlo Park, CA, USA
D. A. Bizzozero, J. Qiang, J. -L. Vay, Lawrence Berkeley National Laboratory, Berkeley, CA, USA
D.P. Grote, Lawrence Livermore National Laboratory, Livermore, CA, USA

Abstract

This paper presents a high-performance computing (HPC) integrated simulation capability for accelerators including electromagnetic field and beam dynamics effects. The integrated codes include the parallel finite-element code suite ACE3P for electromagnetic field calculation of beamline components, the parallel particle-in-cell (PIC) code IMPACT for beamline particle tracking with space-charge effects, and the parallel self-consistent PIC code Warp for beam and plasma simulation. The integration between the application codes requires efficient data transfer, where the common data format, openPMD, has been adopted for field and particle I/O and transfer. One integration is to employ ACE3P for 3D realistic electromagnetic field calculations in accelerator cavities, which are then used for particle tracking in IMPACT for studying beam qualities such as emittance growth in accelerator beamlines. Another integration is to combine ACE3P electromagnetic field calculation and Warp plasma simulation for investigating plasma processing for operational performance of RF cavities. Realistic simulation requires the development of a mapping of CAD geometry used in ACE3P to Warp Cartesian grid representation. Furthermore, an efficient integrated simulation workflow has been implemented to enable the execution of integrated simulation using these codes on HPC systems. Examples for integrated simulation of the LCLS-II injector using ACEP-IMPACT and plasma ignition in SRF cavities using ACE3P-Warp will be presented.

KEYWORDS

High-performance computing, Electromagnetic field, Beam dynamics, Particle-In-Cell, Particle accelerators, openPMD

INTRODUCTION

Accelerator activities rely on advanced computer modelling which requires an integrated set of accelerator simulation software to speed up design and innovation in accelerator science and technologies. Through the support of DOE, advanced simulation codes which are used at many institutions have been developed and used worldwide for the modelling of particle beams and the design of particle accelerators. A progressive transition from the current state of the codes to an integrated solution that builds upon DOE's cumulative investment while maintaining continuity, thus minimizing disruptions to the users and the developers is ongoing. The main goal is to transform the existing collection of codes into a modular ecosystem of interoperable components that facilitate cooperation and reuse, while fostering creativity and constructive competition.

This paper presents two ecosystem code integrations works. The related codes are ACE3P, IMPACT and Warp.

CODE INTEGRATION

ACE3P (Advanced Computational Electromagnetic 3D Parallel) is a comprehensive set of conformal, higher-order, parallel finite element electromagnetics modelling suite developed for accelerator cavity and structure design including integrated multiphysics effects in electromagnetic, thermal, and mechanical characteristics with two unique features: 1). Based on higher order curved finite elements for high-fidelity modelling and improved solution accuracy; 2). Implemented on massively parallel computers for increased memory (problem size) and speed. The electromagnetic modules of the program are discretized in the frequency domain and time domain for the computational volume inside an accelerator cavity, while the thermal and mechanical solvers are formulated in the frequency domain for the computational volume of the cavity walls and their surroundings. Six simulation modules have been developed in ACE3P to address different physics aspects of accelerator applications [1-3].

IMPACT is a parallel particle-in-cell code suite for modelling high intensity, high brightness beams in RF proton linacs, electron linacs, and photoinjectors [4-6]. It consists of two parallel particle-in-cell tracking codes IMPACT-Z and IMPACT-T, an RF linac lattice design code, an envelope matching and analysis code, and a number of pre- and post-processing codes. The 3D Poisson equation is solved in the beam frame at each step of the calculation. The resulting electrostatic fields are Lorentz transformed back to the laboratory frame to obtain the electric and magnetic self-forces acting on the beam.

Warp[7-9] is a particle-in-cell (PIC) Python package designed to simulate high current particle beams and plasmas in a range of applications, incorporating a broad variety of integrated physics models and extensive diagnostics, most of which work in multiple dimensions to allow examination of modeling idealizations within a common framework. The Python interpreter user interface allows flexible problem descriptions in Python scripts, giving the advantage of the full versatility of Python and allowing inter-

---

* Work is supported by the US Department of Energy under contracts DEAC02-05CH1123, DE-AC02-76SF00515 and DE-AC52-07NA27344.

† lge@slac.stanford.edu

ISBN: 978-3-95450-223-3 ISSN: 2673-7000 doi:10.18429/JACoW-NAPAC2019-WEPLE04

RECENT DEVELOPMENTS AND APPLICATIONS OF PARALLEL MULTI-PHYSICS ACCELERATOR MODELING SUITE ACE3P*

Z. Li [#], L. Ge, C.-K. Ng, L. Xiao, SLAC, Menlo Park, CA, USA

Abstract

SLAC's ACE3P code suite is developed to harness the power of massively parallel computers to tackle large complex problems with increased memory and solve them at greater speed. ACE3P parallel multi-physics codes are based on higher-order finite elements for superior geometry fidelity and better solution accuracy. ACE3P consists of an integrated set of electromagnetic, thermal and mechanical solvers for accelerator modeling and virtual prototyping. The use of ACE3P has contributed to the design and optimization of existing and future accelerator projects around the world. Multi-physics analysis on high performance computing (HPC) platform enables thermal-mechanical simulations of largescale systems such as the LCLS-II cryomodule. Recently, new capabilities have been added to ACE3P including a nonlinear eigenvalue solver for calculating mode damping, a moving window for pulse propagation in the time domain to reduce computational cost, thin layer coating representation using a surface impedance model, and improved boundary conditions using perfectly matched layers (PML) to terminate wave propagation. These new developments are presented in this paper.

INTRODUCTION

High performance computing (HPC) for accelerator modeling and simulation has played an important role in the design and optimization of existing and future accelerators. Next generation x-ray free electron laser light source and ultra-fast electron diffraction/microscopy (UED/UEM) put stringent requirements for high electron beam quality. In order to design and to optimize accelerators to generate such high brightness beams, high-fidelity simulations that include both self-consistent charged particle interactions and RF fields of beamline components with realistic geometry details are needed.

ACE3P is a parallel finite element electromagnetics modeling suite developed for accelerator cavity and structure design including integrated multiphysics effects. While ACE3P is implemented on various parallel computing platforms, the unique advantage of ACE3P is its massively parallel capability running on supercomputers accessible to thousands of processors. With optimized scalability on high performance computing facilities, the multi-physics solvers of ACE3P are capable of handling large problem size with realistic details to achieve numerical prototyping analysis of RF, field emission, multipacting, and thermal/structural of the RF systems, leading to time and cost saving for accelerator development. The use of ACE3P has contributed to the design and optimization of existing and future accelerator projects around the world, such as the ILC, LHC, LCLS-I/II and high gradient accelerators. Reliable 3D accelerator structure models produced using the ACE3P solvers are being directly applied for engineering designs.

The code dissemination has been carried out via Code Workshops [1] and user support by the ACE3P development team. Over the years, new solvers and features have been added to existing capabilities to meet the demands of ever-growing comprehensive modeling needs. In addition, code integration of ACE3P with other high-performance beam dynamics and plasma codes are being carried out to provide a unique HPC capability on supercomputers to address critical accelerator design and operation issues including RF, beam breakup, beam quality and machine protection.

ACE3P CODE SUITE

Six simulation modules have been developed in ACE3P to address different physics aspects of accelerator applications [2-4]. The modeling capabilities of each ACE3P module are summarized as follows.

Omega3P: a complex eigensolver for finding normal modes in resonant structures with open ports, impedance boundaries or lossy materials;

S3P: a frequency domain solver for calculating scattering parameters of RF components;

T3P: a time-domain solver for simulating transient response of RF driven systems and for calculating wakefields due to charged beams;

Track3P: a particle tracking code for calculating dark current and analyzing multipacting in RF cavities and components;

Pic3P: a particle-in-cell code for self-consistent simulation of particle and RF field interactions in RF guns and klystrons;

TEM3P: an integrated multi-physics code including electromagnetic/thermal/mechanical effects for cavity design.

The 3D solid model and meshing is handled by the geometry and meshing tool CUBIT [5] developed at Sandia National Lab. Physics parameters of the solver data are analyzed using the postprocessing tool ACDTool and visualized using Paraview [6].

New solver and features have recently been added to the ACE3P capabilities that include the non-linear eigensolver, perfect boundary layer model, surface impedance model, and ongoing integration with beam dynamics codes IMPACT [7] and WARP [8]. These new implementations are described in the following sections.

---

*Work supported by the US Department of Energy under contract DE-AC02-76SF00515.

[#] lizh@slac.stanford.edu

ISBN: 978-3-95450-223-3 ISSN: 2673-7000 doi:10.18429/JACoW-NAPAC2019-WEPLE05

TRACKING WITH SPACE HARMONICS IN ELEGANT CODE*

Y. Sun†, C.-Y. Yao, ANL, Lemont, IL, USA

Abstract

The ELEGANT code has the capability of simulating particle motion in accelerating or deflecting RF cavities, with a simplified (or ideal) model of the electromagnetic fields. To improve the accuracy of RF cavity simulations, the ability to track with space harmonics has been added to the elegant code. The sum of all the space harmonics will mimic the real electromagnetic fields in the RF cavity. These space harmonics will be derived from electromagnetic fields simulation of the RF cavity. This method should be general, which can be applied to any traveling wave multi-cell RF cavity structure, including accelerating and deflecting cavities. In this paper this approach is illustrated with the deflecting cavity example.

INTRODUCTION

There are several ways to perform particle tracking simulations through an electromagnetic field which changes with time. The most complicated and possibly most accurate method is to directly tracking through a three dimensional field map with fine mesh size, and integrate the momentum/coordinates change due to the electromagnetic force $\vec{F} = q(\vec{E} + \vec{V} \times \vec{B})$.

The simplest method is to model the electromagnetic field as a thin element with zero length. The momentum change (or angular kick) is applied with an effective impulse of the dominant fields component which is usually integrated near-axis with some approximations. This method is efficient in simulation computing time, but may be less accurate.

An intermediate approach would be to expand the thin-lens single kick method to a combination of multiple components. These multiple components may be derived from measured or simulated three dimensional electromagnetic field map. One possibility is to use the space harmonics that are determined by the geometry of the structure, which provides boundary conditions of the electromagnetic field. This approach could provide a more accurate model, and at the same time are still efficient in simulation computing time. In the following sections the work is discussed on these three approaches.

THIN-LENS DEFLECTING CAVITY

The ELEGANT code [1] is capable of simulating particle's motion in the accelerating or deflecting RF cavities, with a simplified model of the electromagnetic fields. Take the horizontal deflecting cavity as an example, the Hamiltonian to describe the thin deflecting cavity is

$$H_0 = q\bar{V} \cdot \sin(kz + \phi_0) \cdot x, \tag{1}$$

where H denotes the Hamiltonian, q the particle charge, $\bar{V}$ the effective voltage, ϕ_0 the synchronous phase of the thin deflecting cavity rf wave, $k = \omega/c$ the wave number, ω the angular frequency of the fundamental deflecting mode, c the velocity of light, z the longitudinal coordinate relative to the bunch center, x the horizontal coordinate.

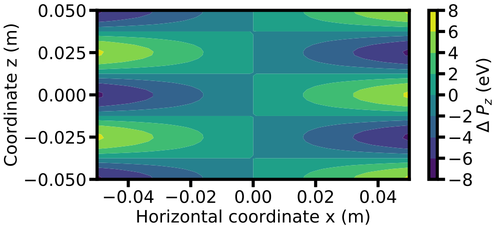

Figure 1: Longitudinal kick ΔP_z on x–z space. 6GHz deflecting cavity with $\bar{V} = 1$.

Using the Hamiltonian, it is possible to derive the deflection in the three dimensions from an ideal cavity, as listed in Eqs. (2)–(4). These are used for an ideal deflecting cavity in ELEGANT [1]:

$$\Delta P_x = -\frac{\partial H_0}{\partial x} = -q\bar{V} \cdot \sin(kz + \phi_0), \tag{2}$$

$$\Delta P_z = -\frac{\partial H_0}{\partial z} = -q\bar{V} \cdot k \cdot x \cdot \cos(kz + \phi_0), \tag{3}$$

$$\Delta P_y = 0, \tag{4}$$

where ΔP_x denotes the change of momentum in horizontal plane, ΔP_z denotes the change of momentum in longitudinal plane.

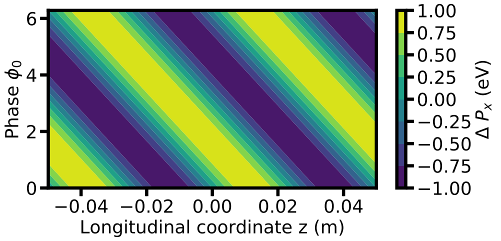

Figure 2: Horizontal kick ΔP_x on z–ϕ space. 6GHz deflecting cavity with $\bar{V} = 1$.

Figure 1 shows the longitudinal kick from a 6 GHz thin deflecting cavity with voltage of 1 volt. The horizontal kick on the z–ϕ space is shown in Fig. 2 for same deflecting cavity.

---

* Work supported by the U.S. Department of Energy, Office of Science, Office of Basic Energy Sciences, under Contract No. DE-AC02-06CH11357.

† yisun@aps.anl.gov

LINEAR AND SECOND ORDER MAP TRACKING WITH ARTIFICIAL NEURAL NETWORK*

Y. Sun†, ANL, Lemont, IL, USA

Abstract

In particle accelerators, the tracking simulation is usually performed with symplectic integration, or linear/nonlinear transfer maps. In this paper, it is shown that the linear/nonlinear transfer maps may be represented by an artificial neural network. To solve this multivariate regression problem, both random datasets and structured datasets are explored to train the neural networks. The achieved accuracy will be discussed.

INTRODUCTION

In particle accelerators, the numerical tracking simulation is usually performed with either symplectic integration [1], or linear/nonlinear transfer maps [1]. For large storage rings, the particle accelerator is composed of thousands (or tens of thousands) of components. Tracking simulation through these components for hundreds of turns may take a long computing time. In this paper, it is preliminarily explored on representing the linear/nonlinear transfer maps with an artificial neural network.

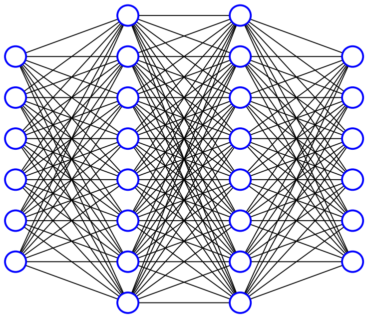

Figure 1: A fully connected feedforward network with two hidden layers and eight neurons on each hidden layer.

Using a basic neural network framework that has been developed in Python [2], it is possible to generate a fully connected feedforward neural network model. The details of this neural network framework are discussed in another paper of this proceedings [3]. Figure 1 shows a fully connected feedforward network with two hidden layers and eight neurons on each hidden layer, with input and output as particle's 3D coordinates. The default optimization algorithm *adam* and activations *Relu* are employed [3].

LINEAR MAP

With particle's 3D coordinates of $\mathbf{X} = (x, x', y, y', z, \delta)$, it is possible to perform tracking with a linear map. The linear map can be expressed in the form of a six by six matrix $\mathbf{R}$. The particle's final 3D coordinates $\mathbf{Y}$ are then calculated using the initial 3D coordinates of $\mathbf{X}$ and the transfer matrix of $\mathbf{R}$, $\mathbf{Y} = \mathbf{R} \cdot \mathbf{X}$. Here, two different linear transfer matrix are employed to evaluate the robustness of the neural network model, as shown in Fig. 2.

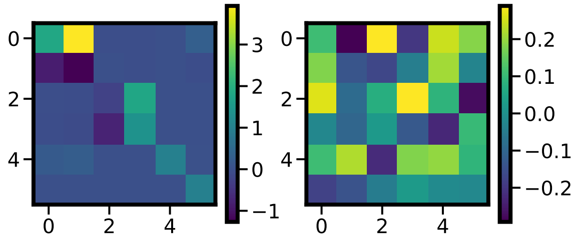

Figure 2: First order transfer matrix **R**. Left: from a FODO cell; right: generated using random numbers.

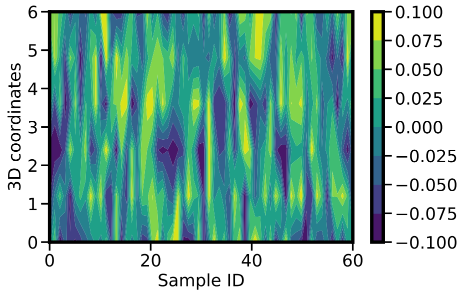

Figure 3: Input training data, size of 6 by 1000 (showing first 60).

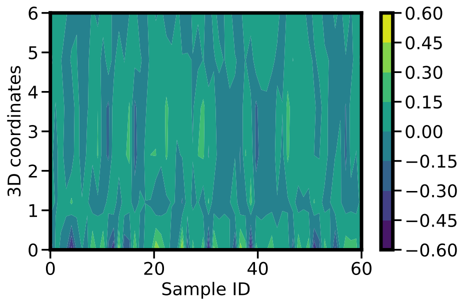

Figure 4: Output training data, size of 6 by 1000 (showing first 60).

The normalised input training data are generated randomly which comprises of 1000 different samples. The dimention

---

[*] Work supported by the U.S. Department of Energy, Office of Science, Office of Basic Energy Sciences, under Contract No. DE-AC02-06CH11357.

[†] yisun@anl.gov

TRANSFER MATRIX CLASSIFICATION WITH ARTIFICIAL NEURAL NETWORK*

Y. Sun†, ANL, Argonne, IL 60439, USA

Abstract

Standard neural network algorithms are developed for classification and regression applications. In this paper, some details of the neural network algorithms are presented on several optimization process. Artificial neural network is trained to classify multi-class transfer matrix of different types of particle accelerator components. It is shown that with a fully-connected feedforward neural network, it is possible to get high accuracy of 99% on training data, validation data and test data. Some hyperparameters are scanned for better performance. Different stochastic gradient descent algorithms are also benchmarked.

INTRODUCTION

Deep learning with artificial neural networks (ANN) has been successfully applied in many areas, such as image recognitions, natural language processing, internet advertising and automatic driving. An artificial neural network code has been developed in the programming language Python [1]. The modules/functions of this code include the following: initialization of parameters **W** and **b**; Forward and backward propagation with several popular activation functions; cost functions (such as mean square error, softmax, cross-entropy); optimization algorithms [2] (gradient descent and stochastic gradient descent algorithms, including *adam* [3]); variational autoencoders and so on.

In the following sections, the artificial neural network training are discussed and optimized, to classify multi-class transfer matrix of different types of particle accelerator components.

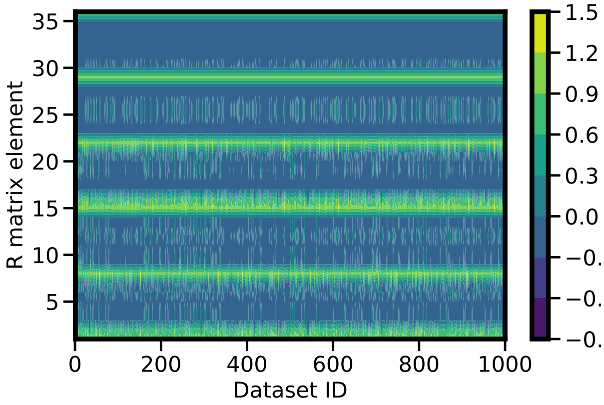

Figure 1: Input training data, size of 36 by 1000.

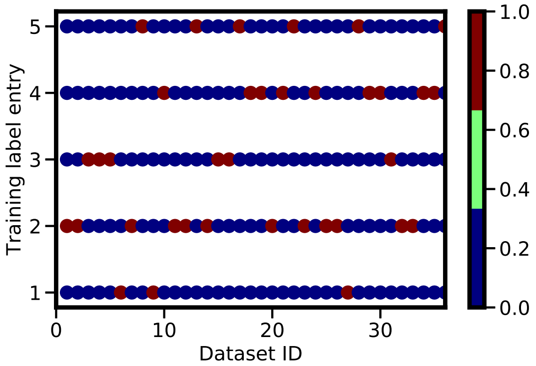

Figure 2: Output training data (label), size of 5 by 1000 (showing first 35).

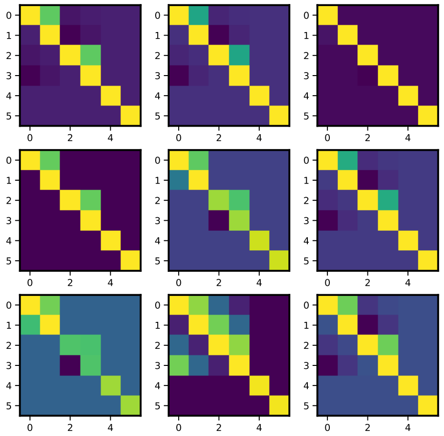

Figure 3: Selected samples of input training data, in the format of 6 by 6 matrix.

TRANSFER MATRIX CLASSIFICATION

In a particle accelerator, there are several common components which are listed below: quadrupole magnets, skew quadrupole magnets, transverse gradient dipoles, dipole fringe fields, and drift spaces. A neural network model is established to classify these 5 types of components. The linear transfer matrix of a quadrupole magnet is shown below [4].

$$R_Q = \begin{pmatrix} \cos kL & \frac{\sin kL}{k} & 0 & 0 & 0 & 0 \\ -k\sin kL & \cos kL & 0 & 0 & 0 & 0 \\ 0 & 0 & \cosh kL & \frac{\sinh kL}{k} & 0 & 0 \\ 0 & 0 & k\sinh kL & \cosh kL & 0 & 0 \\ 0 & 0 & 0 & 0 & 1 & 0 \\ 0 & 0 & 0 & 0 & 0 & 1 \end{pmatrix} \tag{1}$$

The transfer matrix of the other four types of components ($R_{skewquad}$, R_{dipole}, R_{fringe}, R_{drift}) are not shown here.

---

[*] Work supported by the U.S. Department of Energy, Office of Science, Office of Basic Energy Sciences, under Contract No. DE-AC02-06CH11357.

[†] yisun@anl.gov

PARALLEL TRACKING-BASED MODELING OF GAS SCATTERING AND LOSS DISTRIBUTIONS IN ELECTRON STORAGE RINGS*

M. Borland, ANL, Argonne, IL, USA

Abstract

Estimation of gas scattering lifetimes in storage rings is typically done using a simple approach that can readily be performed by hand. A more sophisticated approach uses linear mapping of the angular dynamic acceptance around the ring and allows including variation of gas pressure and composition [1]. However, neither approach is appropriate for highly nonlinear lattices, in which the angular acceptance does not map according to the linear optics. Further, these approaches provide no detailed information about the location of losses. To address these limitations, a tracking-based approach was implemented in the program `Pelegant` [2–4]. We describe the implementation and performance of this method, as well as application to the Advanced Photon Source Upgrade.

INTRODUCTION

In third-generation storage ring light sources, the lifetime is typically dominated by Touschek scattering, so an approximate knowledge of the gas-scattering lifetime is sufficient. Calculation of gas-scattering lifetime is thus often considered a closed subject needing little advancement beyond handbook-level formulae involving the minimum physical aperture and momentum acceptance (see, e.g., [5]). However, for fourth-generation storage ring light sources, the nonlinear dynamics is more challenging and gas scattering deserves a closer look. In [1], we described how to compute the gas scattering lifetime from the dynamic acceptance (DA) and local momentum acceptance (LMA) [6, 7], along with species-specific gas pressure distributions. The DA was mapped around the ring using the linear lattice functions to provide an s-dependent angular acceptance, which was then used with the s-dependent pressure data to compute the local out-scattering rate and hence the elastic-scattering lifetime. The LMA was used more directly with the s-dependent pressure data to compute the local out-scattering rate for inelastic scattering.

While this improves upon simpler approaches, mapping the DA using the linear lattice functions is not reliable in lattices with strong nonlinearities. In addition, this method provides no information on where out-scattered particles are lost. The present work addresses these issues through development of a tracking-based approach that reflects the full complexity of the nonlinear dynamics and s-dependent, multi-species gas pressure profiles.

The gas scattering lifetime is computed using [1]

$$\frac{1}{\tau} = \frac{c}{L} \sum_{g=1}^{G} \sum_{a=1}^{C_g} \int_0^L \sigma_{g,a}(s) S_{g,a} n_g(s) ds, \qquad (1)$$

where L is the length of a periodic section of the ring, G is the number of molecular gas constituents, C_g is the number of atomic components of gas g, $\sigma_{g,a}(s)$ is the out-scattering cross section for atomic component a of gas g at location s, $S_{g,a}$ is the number of atoms of type a in a molecule of gas g, and $n_g(s)$ is the number density of gas g at location s.

In order to evaluate this equation, we use tracking to determine the s-dependent out-scattering cross section,

$$\sigma_{g,a}(s) = \int_{q_1(s)}^{q_2(s)} \frac{d\sigma_{g,a}}{dq} dq, \qquad (2)$$

where q is the scattering coordinate, q_1 is the maximum surviving value of q, and q_2 is the physically-limiting value of q. For elastic scattering, q is the scattering angle θ, while for inelastic scattering, q is the change in fractional momentum deviation δ.

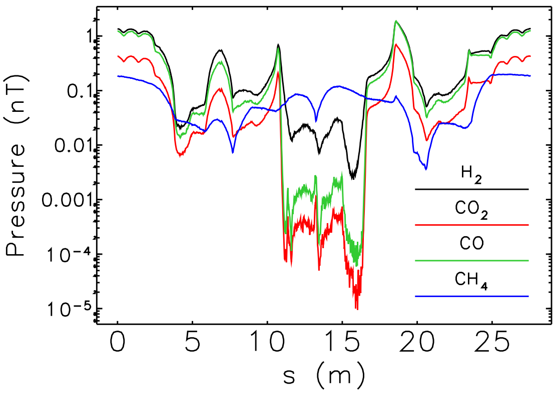

Figure 1: Simulated pressure profiles for one sector of APS-U. Data courtesy J. A. Carter (APS).

ELASTIC SCATTERING LIFETIME

Elastic scattering from atomic nuclei is described by the Rutherford cross section [8]

$$\frac{d\sigma_{g,a}}{d\Omega} = \frac{Z_{g,a}^2 r_e^2}{4\gamma^2} \frac{1}{\sin^4 \frac{\theta}{2}}, \qquad (3)$$

with θ the scattering angle, $Z_{g,a}$ the atomic number, r_e the classical electron radius, and γ is relativistic factor.

To compute the lifetime, we only need to know the DA boundary $\theta_a(\phi, s)$. However, to determine the loss distribution, we need to track particles that are scattered to angles

---

* Work supported by the U.S. Department of Energy, Office of Science, Office of Basic Energy Sciences, under Contract No. DE-AC02-06CH11357.

ISBN: 978-3-95450-223-3 ISSN: 2673-7000 doi:10.18429/JACoW-NAPAC2019-WEPLE09

MITIGATION OF NONLINEAR PHASE SPACE IN A SPACE-CHARGE-LIMITED INJECTOR DIODE

W. D. Stem*, Y.-J. Chen, J. Ellsworth
Lawrence Livermore National Laboratory, Livermore, CA, USA

Abstract

The performance of an accelerator is limited by the quality of the beam produced at the injector. For a Pierce-type diode structure, the cathode-shroud interface and the anode pipe entrance are sources for undesired, irreversible phase space nonlinearities that lead to emittance growth. In this contribution, we present ways to mitigate these nonlinearities by adjusting the cathode-shroud interface to meet the beam edge boundary conditions and by adjusting the solenoidal focusing magnet in the diode region such that the nonlinear focusing magnetic fringe fields compensate the nonlinear defocusing electrical fields of the anode pipe entrance.

INTRODUCTION

In a flash radiography linear induction accelerator (LIA), the spot size on target and therefore the radiographic image quality is limited by the emittance. The beam emittance is largely determined by the performance of the injector, since the high intensity beam is subject to larger space charge effects at lower energies, and thus is more difficult to control.

This contribution studies a 2 MV, 2 kA space-charge-limited injector diode with thermionic electron emission as a reference case. Pierce showed [1] that for such cases a shroud with angle of 67.5° with respect to the normal will allow the cathode to birth a beam with laminar flow in which particles are emitted perpendicularly from the cathode surface. Above the thermal threshold, the emitted current depends solely on the field stress, for which the required anode-cathode (AK) gap is approximately determined by the Child-Langmuir law (e.g. [2]) for planar diodes.

When designing an injector diode, these models are a good starting point, but they do not capture some of the more subtle physics. The limitation arises at the beam edge, where nonlinear electric fields cause the particle trajectories to cross. Once particles at a given radius have different velocities, the phase space is no longer single-valued. This leads to emittance growth and beam degradation that is nearly impossible to correct with external fields downstream, and this is what we refer to in this paper as the "phase space nonlinearity". Figure 2 shows how quickly the phase space degradation is exacerbated due to this nonlinearity. This contribution identifies two sources of nonlinear electric fields and offers simple, effective methods to mitigate the harmful effects using simulation results from the 2D particle tracking code Trak [3] and particle-in-cell (PIC) slice code Amber [4]. Due to the injection energy, the relativistic correction is included.

The first source of nonlinear fields is the interface between the cathode and the shroud, which can be mitigated by leaving a simple gap at thermal equilibrium. The second source is caused by the spherical aberration of the anode pipe aperture or anode hole. One way this can be mitigated is by positioning a focusing solenoid such that the spherical aberration of the fringe fields helps to cancel the spherical aberration from the anode hole. Trade-offs for the DARHT-II injector diode design were studied in [5,6]. A method to compensate for the anode hole with a spherical cathode on small length scales was studied in [7]. Mitigating the spherical aberration of the anode hole with a solenoid magnet was first demonstrated through simulations in [8].

CATHODE/SHROUD INTERFACE

To achieve uniform, laminar flow of electrons off of the cathode surface, the following boundary conditions must be satisfied [1,9]:

$$\left.\frac{\partial V}{\partial r}\right|_{r=R} = 0, \tag{1}$$

$$V \sim z^{4/3}, \tag{2}$$

for axisymmetric coordinate system (z, r), beam radius R, and space-charge-modified electrostatic potential V. With a traditional Pierce-type shroud structure, condition 1 is not automatically satisfied. The problem is caused by the corner of the cathode-shroud interface. At thermal equilibrium, the electrostatic model assumes that the cathode and shroud are in contact. The equipotential voltage lines follow the contour of the shroud, but the voltage lines are smooth by definition. At the edge of the cathode, the voltage lines do not intersect the beam perpendicularly and instead cause the particles there to over-focus.

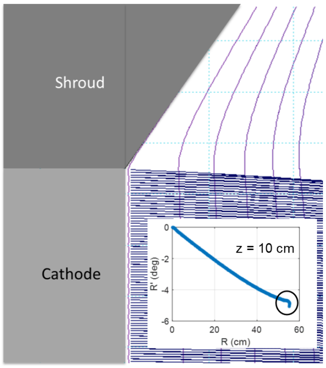

Figure 1: The phase space nonlinearity at the beam edge exists in the absence of an anode hole or magnetic fields, indicating that the cathode/shroud interface is a source.

---

[*] stem1@llnl.gov

ISBN: 978-3-95450-223-3 ISSN: 2673-7000 doi:10.18429/JACoW-NAPAC2019-WEPLE10

SIMULATING SPACE CHARGE DOMINATED BEAM DYNAMICS USING FMM[*]

S. A. Schmid[†], H. De Gersem, E. Gjonaj, TU Darmstadt, TEMF, Darmstadt, Germany
M. Dohlus, DESY, Hamburg, Germany

Abstract

In this contribution, we simulate the beam generation in the high brilliance photoinjector of the European XFEL developed at DESY-PITZ. The investigation addresses the influence of space charge on the emittance of bunches with up to 1.0 nC bunch charge. For the simulations, we implemented a mesh-less fast multipole method (FMM) in the 3D tracking code REPTIL. We present numerical convergence and performance studies as well as a validation with commonly used simulation tools ASTRA and KRACK3. Furthermore, we provide a machine parameter study to minimize the beam emittance in the injector.

INTRODUCTION

The photoinjector test facility at DESY-PITZ in Zeuthen (PITZ) develops the electron injector for the European XFEL. The photoinjector consists of a UV laser triggered Cs_2Te photocathode, a 1.6 cell L-band gun cavity, a focusing solenoid, and a 1.3 GHz booster module downstream of the gun [1]. Due to large charge density and saturation effects during photoemission, simulating the beam dynamics of the PITZ injector is a numerically cumbersome task. In order to resolve the space charge forces of bunches with a large number of macroparticles, we develop a simulation technique based on an adaptive FMM method. The FMM reduces the computational cost of the space charge calculation to linear scaling in the particle number N [2] and allows for high spatial resolution, in particular, in the region close to the photocathode. This method is implemented in the tracking code REPTIL. In the following, we present a numerical convergence and performance study of the code and validate the simulation results with ASTRA [3] and KRACK3 [4]. Furthermore, we provide a machine parameter optimization study with respect to the laser spot size on the photocathode.

THE FMM

For a detailed discussion of the FMM approach the reader may refer to [5]. We implemented an OpenMP parallelized FMM code which is optimized for particle tracking applications. The FMM solver uses an adaptive tree structure to classify the interaction between different subregions of the particle bunch. Figure 1 shows exemplary the tree structure for a relativistic particle bunch in the PITZ beam line. Three numerical parameters, n_0, l_0, and θ_0, control the trade-off between accuracy and speedup of the FMM approximation. The parameter n_0 controls the depth of the tree by defining the maximum number of particles in one leaf node. The admissibility parameter θ_0 categorizes the interaction between different subregions of the bunch into near- and far-field contributions. The smaller is θ_0 the larger is the proportion of near field contributions. For the far field approximation, we apply a spherical multipole expansion of maximum order l_0. The near-field contributions are computed as direct particle-to-particle interactions.

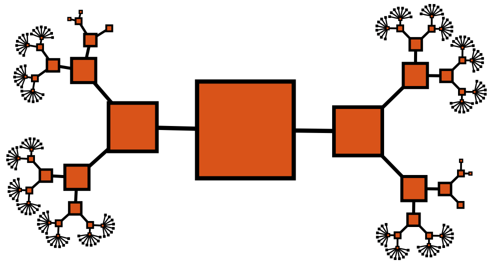

Figure 1: Tree structure of the FMM approach for a relativistic particle bunch in the PITZ beam line.

Figure 2 shows the trade-off between approximation error σ_{E_x} and speedup for the space charge field of a Gaussian bunch with 250 k macroparticles, 1 nC bunch charge, and 0.1 mm rms diameter. A direct particle-particle interaction approach provides the reference solution. The solid line shows the relative error as a function of θ_0 for $l_0 = 5$. In the region $\theta_0 > 0.3$, the truncation error of the multipole expansion dominates the total approximation error σ_{E_x}. For $\theta_0 < 0.2$, most of the interactions are computed by a near-field, particle-particle interaction approach rather than by the multipole expansion approximation. Therefore, the numerical efficiency of the method decreases significantly. In all cases, the error of the multipole approximation decreases exponentially with l_0 (dotted line).

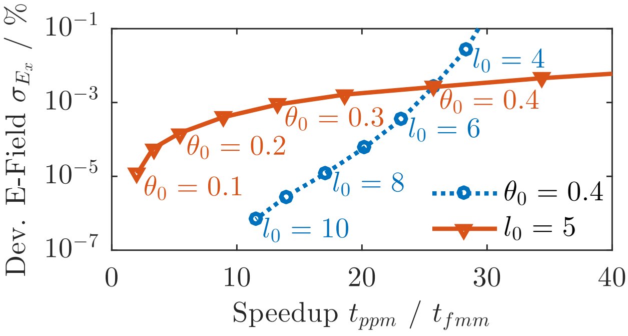

Figure 2: Approximation error and numerical speedup vs. admissibility parameter θ_0 and multipole order l_0.

---

[*] This work is supported by the DFG in the framework of GRK 2128.
[†] schmid@temf.tu-darmstadt.de

ANALYSIS OF BEAM POSITION MONITOR REQUIREMENTS WITH BAYESIAN GAUSSIAN REGRESSION

Y. Li*, W.X. Cheng[1], R.S. Rainer, Brookhaven National Lab, Upton, NY, USA
Y. Hao, Michigan State University, East Lansing, Michigan, USA
[1]now at Argonne National Lab, Lemont, Illinois, USA

Abstract

With a Bayesian Gaussian regression approach, a systematic method for analyzing a storage ring's beam position monitor (BPM) system requirements has been developed. The ultimate performance of a ring-based accelerator, based on brightness or luminosity, is determined not only by global parameters, but also by local beam properties at some particular points of interest (POI). BPMs used for monitoring the beam properties, however, cannot be located at these points. Therefore, the underlying and fundamental purpose of a BPM system is to predict whether the beam properties at POIs reach their desired values. The prediction process can be viewed as a regression problem with BPM readings as the training data, but containing random noise. A Bayesian Gaussian regression approach can determine the probability distribution of the predictive errors, which can be used to conversely analyze the BPM system requirements. This approach is demonstrated by using turn-by-turn data to reconstruct a linear optics model, and predict the brightness degradation for a ring-based light source. The quality of BPMs was found to be more important than their quantity in mitigating predictive errors.

INTRODUCTION

The ultimate performance of a ring-based accelerator is determined not only by certain critical global parameters, such as beam emittance, but also by local properties of the beam at particular points of interest (POI). The capability of diagnosing and controlling local beam parameters at POIs, such as beam size and divergence, is crucial for a machine to achieve its design performance. Examples of POIs in a dedicated synchrotron light source ring include the undulator locations, from where high brightness X-rays are generated. In a collider, POIs are reserved for detectors in which the beam-beam luminosity is observed. However, beam diagnostics elements, such as beam position monitors (BPM) are generally placed outside of the POIs as the POIs are already occupied.

Using observational data at BPMs to indirectly predict the beam properties at POIs can be viewed as a regression problem and can be treated as a supervised learning process: BPM readings at given locations are used as a training dataset. Then a ring optics model with a set of quadrupole excitations as its arguments is selected as the hypothesis. From the dataset, an optics model needs to be generalized first. Based on the model, the unknown beam properties at POIs can be predicted. However, there exists some systematic error and random uncertainty in the BPMs' readings, and the quantity of BPMs is limited. Therefore, the parameters in the reconstructed optics model have inherent uncertainties, as do the final beam property predictions at the POIs. The precision and accuracy of the predictions at the POIs depend on the quantity of BPMs, their physical distribution pattern around the ring, and their calibration, resolution, etc. When a BPM system is designed for a storage ring, however, it is more important to consider the inverse problem: i.e. How are the BPM system technical requirements determined in order to observe whether the ring achieves its desired performance? In ref. [1] and this paper, we developed an approach to address this question with Bayesian Gaussian regression.

In statistics, a Bayesian Gaussian regression [2, 3] is a Bayesian approach to multivariate regression, i.e. regression where the predicted outcome is a vector of correlated random variables rather than a single scalar random variable. Every finite collection of the data has a normal distribution. The distribution of generalized arguments of the hypothesis is the joint distribution of all those random variables. Based on the hypothesis, a prediction can be made for any unknown dataset within a continuous domain. In our case, multiple BPMs' readings are normally distributed around their real values. The standard deviations of the Gaussian distributions are BPM's resolutions. A vector composed of quadrupoles' mis-settings is the argument to be generalized. The prediction at the POIs is the function of this vector. The continuous domain is the longitudinal coordinate s along a storage ring.

BRIGHTNESS PERFORMANCE AND BEAM DIAGNOSTICS

Consider a dedicated light source ring. Its ultimate performance is measured by the brightness of the X-rays generated by undulators. The brightness is determined by the transverse size of both the electron and photon beam and their angular divergence at their source points [4–7]. Therefore, the undulator brightness performance $\mathcal{B}$ depends on the ring's global emittance and the local transverse optics parameters,

$$\begin{aligned}\mathcal{B} &\propto \frac{1}{\Sigma_x\Sigma_x'\Sigma_y\Sigma_y'} \\ \Sigma_{x,y} &= \sqrt{\epsilon_{x,y}\beta_{x,y}+\eta_{x,y}^2\sigma_\delta^2+\sigma_{ph}^2} \\ \Sigma_{x,y}' &= \sqrt{\epsilon_{x,y}\gamma_{x,y}+\eta_{x,y}'^2\sigma_\delta^2+\sigma_{ph}'^2}. \qquad (1)\end{aligned}$$

---

* yli@bnl.gov

North American Particle Acc. Conf. NAPAC2019, Lansing, MI, USA JACoW Publishing
ISBN: 978-3-95450-223-3 ISSN: 2673-7000 doi:10.18429/JACoW-NAPAC2019-THXBA3

ADAPTIVE MACHINE LEARNING AND FEEDBACK CONTROL FOR AUTOMATIC PARTICLE ACCELERATOR TUNING*

A. Scheinker†, Los Alamos National Laboratory, Los Alamos, NM, USA

Abstract

Free electron lasers (FEL) and plasma wakefield accelerators (PWA) are planning to create more and more complicated electron bunch configurations, including multi-color modes for FELs such as LCLS and LCLS-II and custom tailored bunch current profiles for PWAs such as FACET-II. These accelerators are also producing shorter and higher intensity bunches than before and require an ability to quickly switch between many different users with various phase space requirements, exotic setups require lengthy tuning. We present adaptive machine learning and model independent feedback techniques and their application in both the LCLS and European XFEL to control electron bunch longitudinal phase space (LPS) to create desired current profiles and energy spreads by tuning FEL components automatically, maximize the average pulse output energy of FELs by automatically tuning over 100 components simultaneously, and create non-invasive LPS diagnostics at PWAs.

AUTOMATIC ACCELERATOR TUNING

Precise control of bunch lengths, current profiles, and energy spreads of increasingly shorter electron beams at femtosecond resolution is extremely important for all advanced particle accelerators, including free electron lasers (FEL). FEL X-ray bursts with tunable wavelength are generated by tuning the energies of extremely short electron bunches (~fs). Two of the most advanced FELs are the Linac Coherent Light Source (LCLS) and the European XFEL (EuXFEL). The LCLS provides users with photon energies of 0.27 keV to 12 keV based on electron bunches with energies of 2.5 GeV to 17 GeV with electron bunch charges ranging from 20 pC to 300 pC and the bunch duration from 3 fs to 500 fs [1–3]. The EuXFEL, utilizes electron bunches with energies of up to 17.5 GeV, with charges ranging from 0.02 to 1 nC per bunch, and photon energies of 0.26 keV up to 25 keV [4]. Both the LCLS and the EuXFEL face challenges in quickly tuning between different beam types and achieving precise control for desired current and energy profiles and complex experiments such as two color mode and self seeding [5–8]

Extremum Seeking

The tuning algorithm that we utilized is based on a model-independent adaptive extremum seeking (ES) feedback approach developed for the stabilization of unknown, nonlinear, unstable dynamic systems. The main strengths of the method are that it works based on noisy measurements, can handle nonlinear, time-varying systems, and can tune many parameters simultaneously. Analytic proofs of convergence for a wide range of systems can be found in the literature [9–13].

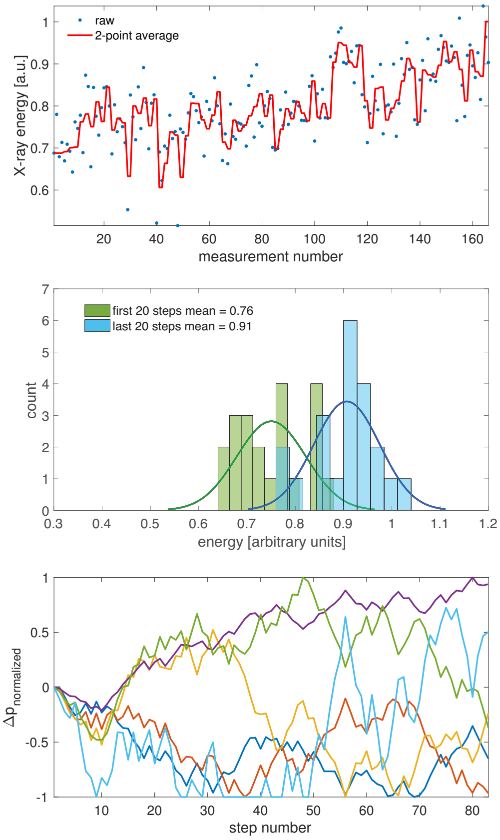

Figure 1: Maximization of nosiy pulse energy measurement at LCLS using only 2 point moving average.

For iterative accelerator tuning applications, we consider some analytically unknown cost function that we would like to minimize or maximize base only on noisy measurements, $C(\mathbf{p}, t)$. For this work, $C(\mathbf{p}, t)$ is the pulse energy of the light generated by an FEL and we would like to automatically maximize this cost function. This cost is a function of accelerator parameters $\mathbf{p} = (p_1, \ldots, p_m)$, such as magnet power supply settings which control magnetic field strengths or RF system phase and amplitude settings, which control the acceleration of the charged particle beams. Furthermore, all of these components, the beam itself, and the diagnostics drift with time due to external influences such as temperature variation, and therefore there is a time dependence. Also, we are usually only able to sample a noise-corrupted version of such a cost, of the form $\hat{C}(\mathbf{p}, t) = C(\mathbf{p}, t) + n(t)$. Although the interaction of charged particles with external sources of electromagnetic fields, including RF cavities, magnets, and other particles in the bunch, is analytically described via

---

* Work supported by Los Alamos National Laboratory
† ascheink@lanl.gov

ISBN: 978-3-95450-223-3 ISSN: 2673-7000 doi:10.18429/JACoW-NAPAC2019-THXBA4

UPDATE ON BPM SIGNAL PROCESSING CIRCUITRY DEVELOPMENT AT AWA*

W. Liu †, M. E. Conde, D. S. Doran, G. Ha, J. G. Power, J. H. Shao, C. Whiteford,
E. E. Wisniewski, Argonne National Laboratory, Argonne, IL USA
C. Jing, Euclid TechLabs LLC, Bolingbrook, IL USA

Abstract

Beam position monitor (BPM) is widely used in accelerator facilities worldwide. It is a device which is capable of providing, non-destructively, accurate beam centroid and charge information of a passing charged beam. A typical BPM system contains customized hardware and specialized processing electronics. The cost is often too high for small facilities to afford them. As a small facility, Argonne Wakefield Accelerator (AWA) decided to develop a solution with high cost-efficiency to fit in its budget. Some details about the development are presented in this paper.

INTRODUCTION

Beam position monitor is a device wide used on accelerator beamlines worldwide. It can provide information on beam centroid nondestructively. One can also obtain charge information from the signals with careful calibrations. For some applications, BPM might even provide the temporal distribution information of charged bunch. Researchers around the world have studied the properties of many different BPM configuration in details and published many review papers. For detail and quantitative expression on the BPM properties, one can find them in those review papers [1-6]. As presented in references, a typical BPM system is consisted of customized signal pick up device and a specialized processing electronics. The processing electrons are usually specialized to the BPM signals of the specific pickups chosen based on the specific beam parameters of the specific facilities and they are usually expensive.

AWA is a small accelerator research facility which has limited budget and resource. But since BPM is such a wonderful device, we would like to install as much as possible on our beamlines. In order to fulfill our need with the limited budget and resource, we decided to design our own BPM signal processing electronics.

As showing in Fig. 1, there are many places on our beamline that can use the help of BPMs. With the help from BPMs, we will be able to monitor the beam positions on the beamline without using YAG screens which will give us the opportunities to use feedback control to stabilize the beam and also provide us an objective for automatic beam tuning in the future.

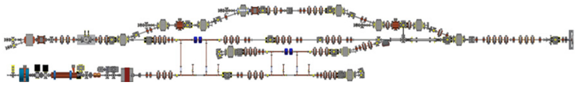

Figure 1: AWA major beamline layouts.

Currently at AWA, we have one stripline BPM pickup installed on our drive beam line right after the last linac. This stripline BPM pickup was specially designed to maximize the signal response at 1.3GHz, the L-band RF frequency of our RF system. The objective of this stripline BPM pickup is to enable us to be able to not only obtain the beam position information but also obtain the beam phase information from the same pickup. We have been working with Euclid TechLabs to develop such signal processing electronics, called Euclid BPPM funded by DoE 2009 SBIR Phase1 project under Contract # DE-SC0002513. The results are very impressive but the project was cut off due to lack of funding.

We also have two commercial inlange button-type BPM pickup purchased from MDC Vacuum Products®. One is installed on our ACT (Argonne Cathode Test Stand) beamline and one on our witness beamline. Some efforts were putted in to study and characterize the response of these button-type BPM to our beam structure. Some preliminary efforts were also putted in to design the signal processing circuitry [7].

Recently, some breakthroughs have been made on BPM signal processing circuitry design and prototype. We are now very close to complete and realize our low cost BPM signal processing electronics.

LOW COST BPM SIGNAL DETECTOR PROTOTYPING

AWA Beam Parameters and Typical Inflange Button BPM Response to AWA Electron Beam

At AWA, we typically operate our beamline at 2Hz repetition rate. The nominal bunch length of AWA beam is about 8ps. The charge of our electron bunches can be set from about 1 pC up to near μC. So the detector circuit need to be able to handle the input from mV up to kV.

As showing in Fig. 2, the typical response of the button BPM to AWA electron bunch is a short negative pulse followed by a positive pulse. The FWHM of the pulses is about 100ps. The magnitude varies with charge intensity and beam positions. The processing electronics for this kind of fast signal is going to be expensive. Our goal is to find a way to transform the short BPM response into a long

---

* Work supported by DOE Office of HEP and Office of BES

† wmliu@anl.gov

ISBN: 978-3-95450-223-3 ISSN: 2673-7000 doi:10.18429/JACoW-NAPAC2019-THYBA1

STATUS OF THE CBETA CORNELL-BNL ERL PROTOTYPE

K.E. Deitrick*, N. Banerjee, A.C. Bartnik, J.A. Crittenden, L. Cultrera, J. Dobbins, C.M. Gulliford,
G. H. Hoffstaetter, W. Lou, P. Quigley, D. Sagan, K.W. Smolenski, D. Widger,
CLASSE, Ithaca, NY, USA
J.S. Berg, S. J. Brooks, R.L. Hulsart, R.J. Michnoff, S. Peggs, D. Trbojevic,
Brookhaven National Laboratory, Upton, NY, USA

Abstract

CBETA, the Cornell-BNL ERL Test Accelerator, is an SRF multi-turn ERL which has been commissioned in the one-turn configuration from March to July 2019. During this time, the project has demonstrated an energy acceptance of 1.5 in the FFA arc, high-transmission energy recovery performance, and increased the CBETA energy-recovered maximum average current.

INTRODUCTION

CBETA, the Cornell-BNL Energy recovery linac Test Accelerator, is a superconducting radiofrequency (SRF) multi-turn ERL using a Fixed Field Alternating-gradient (FFA) arc, with the four-turn configuration seen in Fig. 1. CBETA consists of an injector, diagnostic line, main linac cyromodule (MLC), splitter section (SX), FFA arc (FA, TA, ZX, TB, FB), recombination section (RX), and beam stop (DU).

CBETA is designed to have a top energy of 42 to 150 MeV, dependent on the number of turns configured. The electron beam is injected at 6 MeV, before being accelerated up to 150 MeV in four passes; the top energies of the one, two, and three turn configurations are 42, 78, and 114 MeV, respectively.

The FFA arc is made of permanent Halbach magnets and can be divided into five sections. The FA and FB sections consist of repeating FFA cells, while the remaining sections are either transitions (TA and TB) or the straight (ZX). The FFA has a wide energy acceptance - all beams travel through a common pipe. In the SX and RX sections, beams of different energies pass through different lines; SX consists of S1, S2, S3, and S4 lines, with increasing number corresponding to higher beam energy (RX is similarly labeled). The chicanes which make up each SX and RX line have sliding joints between the two center dipoles, which allows for independent path length control at each beam energy [1].

Commissioning of the one-turn configuration, shown in Fig. 2 began in March 2019, with first beam sent through the FFA arc in May 2019. Since then, a significant amount of progress has been achieved, including an energy scan and demonstration of high transmission energy recovery. Figure 3 shows the accelerator enclosure before and after construction, while Fig. 4 shows a top-down view of the straight section of the FFA [2].

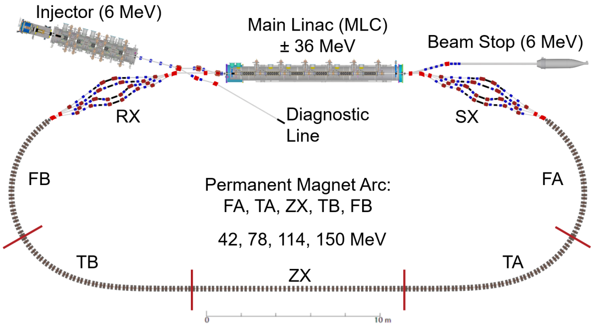

Figure 1: Layout of CBETA in the four-turn configuration; descriptions of the labels can be found in the text.

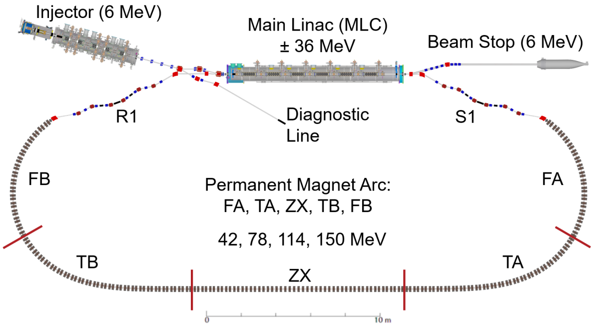

Figure 2: Layout of CBETA in the one-turn configuration; description of the labels can be found in the text.

MOTIVATION

An electron-ion collider (EIC) is one of the highest priorities for nuclear physics; by necessity, this spurs accelerator research and development. There are currently two potential EIC designs - eRHIC at Brookhaven National Laboratory (BNL) and Jefferson Lab EIC (JLEIC) at Thomas Jefferson National Accelerator Facility (TJNAF). In both designs, a high-power, high-average current ERL serves as an electron cooler for the ion beam, thus producing the desired high luminosity [3]. CBETA was originally intended to serve as a prototype demonstration for eRHIC; however, it has similarities to both cooler designs.

Additionally, the design parameters of CBETA push the bounds of state-of-the-art accelerator physics and technologies, particularly for ERLs. Some of the more challenging critical phenomena related to next-generation ERLs and the EIC effort include Beam-Breakup (BBU) instability, halo development and mitigation, and Coherent Synchrotron Radiation (CSR) microbunching and energy spread growth [1].

---

* kd324@cornell.edu

ISBN: 978-3-95450-223-3 ISSN: 2673-7000 doi:10.18429/JACoW-NAPAC2019-THYBA3

USE OF SOLID XENON AS A BEAM DUMP MATERIAL FOR 4TH-GENERATION STORAGE RINGS*

M. Borland, H. Cease, J. C. Dooling, ANL, Lemont, IL, USA

Abstract

Damage to tungsten, aluminum, and titanium beam dumps has been observed in the Advanced Photon Source (APS) due to the high charge (368 nC/store), high energy (7 GeV), and short loss time (~15μs). Owing to the higher charge (736 nC/store) and much lower emittance (42 pm vs 2.5 nm), this issue is expected to be much more severe in the APS Upgrade. This strongly suggests that carefully-designed dumps are necessary in 4th-generation electron storage rings to prevent catastrophic damage to vacuum systems when, for example, rf systems trip. However, it also implies that the dump will be damaged by each strike and will thus need to be "refreshed," perhaps by moving the dump surface vertically to expose undamaged material. Xenon, a gas that solidifies at 161K, is an intriguing possibility for a beam dump material. Calculations suggest that as the beam spirals in toward a dump in a high-dispersion area the tails of the electron beam would vaporize sufficient xenon to rapidly diffuse the beam and render it harmless. The dump surface could be periodically reformed without breaking vacuum. Issues with the concept include the need to protect the frozen xenon from wakefield heating.

INTRODUCTION

The electron beam in the existing APS storage ring has damaged copper, tungsten, aluminum, and titantium in various circumstances [1,2]. The electron beam in the APS-U storage ring [3] will have even higher energy density, so that removing the beam requires either taking steps to inflate the emittance or else accepting damage to the dump. In the case of swap-out, we have proposed the use of a pre-kicker to inflate the emittance of the target bunch through decoherence, which takes about 250 turns to fully develop [4]. This provides a ~100-fold decrease in particle density for a single bunch out of 48.

Using this method for whole-beam aborts is problematical, primarily because when the rf systems trip it takes only 50 turns before the beam strikes the dump. Since the whole beam has 48 times as much stored energy as a single bunch, we would need to inflate the emittance by a much larger factor compared to the swap-out case. For these reasons, we assume that the whole-beam dump will have a sacrificial surface that is damaged and refreshed after each abort.

An alternative method of decohering and even aborting the beam is using a gas jet. As we'll show, with a high-Z gas of sufficient density, the angular scattering can be large enough to significantly decrease the electron beam density. However, creating the jet in a conventional way is problematical, since it seems to require a very fast-opening valve and high-pressure, high-temperature gas storage, as well as a way to collect the gas after the fact. This inspired the idea of using a cryocooled beam dump made of solid xenon, which might yield a gas jet when the tails of the beam begin to vaporize the surface; it would also cryopump the xenon after the event. We start by modeling a hypothetical xenon gas column, then discuss the implications for a solid xenon dump. Xenon seems attractive because it is relatively inert and has a relatively high Z of 54. It solidifies at 161.4 K and vaporizes at 165.0 K. In the solid form, it has a relatively high density (3640 kg/m^3) and thus a relatively short radiation length of 2.3 cm.

EFFECTS OF A GAS COLUMN

For an initial exploration, we assumed a local pressure bump that covers the entire beam-pipe aperture, ignoring for now the process of creating the bump.

The `MATTER` element in `elegant` [5–7] allows modeling scattering from a material given the thickness, mass density, atomic number, and atomic mass. We inserted a single `MATTER` element in the APS-U lattice [3] at the location of the whole-beam dump in Sector 37. This location was chosen because of the high horizontal beta function (which accentuates the effect of angle scattering) and for other reasons described below.

Tracking was performed starting with with $\epsilon_x = \epsilon_y = 30$ pm, $\sigma_\delta = 0.13\%$, and $\sigma_t = 100$ ps, using 100k particles in each of 48 bunches. Both the beam-loaded main and harmonic rf cavities were included. The areal mass density d of the gas column was varied over 0.003 to 0.3 kg/m^2. For reference, note that a 1-mm-long column at STP corresponds to $d = 0.0059$ kg/m^2. As Fig. 1 shows, the emittances inflate by three orders of magnitude in a few turns, which is faster and more effective than decoherence from a kicker. This gives a three order of magnitude decrease in transverse particle density.

These simulations demonstrate the potential of a xenon gas column for diffusing an intense electron beam. Several options might be considered for creating such a gas column. A gas reservoir with a fast-opening valve is a possibility for creating a gas jet. One could also vaporize solid xenon with a laser. The concern with such schemes is that the valve or laser might fail to operate when needed, allowing the undiluted beam to hit the vacuum chamber. Alternatively, one could vaporize solid xenon with an intense electron beam, which just happens to be available and cannot fail to be present when needed.

---

* Work supported by the U.S. Department of Energy, Office of Science, Office of Basic Energy Sciences, under Contract No. DE-AC02-06CH11357.

ISBN: 978-3-95450-223-3 ISSN: 2673-7000 doi:10.18429/JACoW-NAPAC2019-THYBA4

STATUS OF THE MAGNETIZED THERMIONIC ELECTRON SOURCE AT JEFFERSON LAB

F.E. Hannon, D.B. Bullard, C. Hernandez-Garcia, M.A. Mamun, M. Poelker, M.S. Stefani[1],
R. Suleiman, Thomas Jefferson National Accelerator Facility, Newport News, VA, USA
J.V. Conway, B.M. Dunham, R.G. Eichhorn, C.M. Gulliford, V.O. Kostroun, C.E. Mayes,
K.W. Smolenski, N.W. Taylor, Xelera Research LLC., Ithaca, NY, USA
[1]also at Old Dominion University, Norfolk, VA, USA

Abstract

A 125kV DC gridded thermionic gun has been designed and constructed through a collaboration between Jefferson Lab and Xelera Research LLC. The gun has been recently installed at the Gun Test Stand diagnostic line at Jefferson Lab where transverse and longitudinal parameter space will be experimentally explored. The status and results characterizing the commissioning and trouble-shooting the thermionic gun are presented.

INTRODUCTION

The Jefferson Lab Electron Ion Collider Design includes a bunched beam cooling scheme to improve the luminosity of the ion beam [1]. The cooler injector requires an electron beam with beyond state-of-the-art properties, listed in Table 1. Furthermore, the beam must be magnetized by immersing the cathode inside a solenoid. The magnetization is removed from the beam as it enters the fringe of the cooling solenoid, where it co-propagates with the ion beam providing cooling. A magnetized beam has a correlated emittance component, and this is chosen specifically to be matched into cooling solenoid. The 36um correlated emittance is achieved through balancing the emitting area with the magnetic field in which it sits.

Table 1: JLEIC Cooler Injector Parameters

Parameter	
Bunch charge	3.2nC
Bunch repetition rate	43.3MHz
Injector Energy	5-7Mev
Uncorrelated transverse emittance	<10µm
Correlated (magnetized) emittance	36µm

The baseline design for the cooler injector invokes a multi-alkali photocathode inside an RF gun [2]. The combination of bunch charge and average current are demanding constraints for the typical photocathode. Thermionic cathodes are known for being robust, maintaining long lifetime and delivering high average current (several Amps). However, the technological know-how in the accelerator community has been somewhat lost since the advent of photocathodes which can provide well-tailored bunch shape and extremely low thermal emittance.

As a back-up to the RF photoinjector, DC photogun [3] and a thermionic DC gun are being investigated. On the research path towards a 500kV thermionic DC gun, Xelera Research LLC and Jefferson Lab are designing and testing a 125kV DC, thermionic gun. The JLEIC cooler design requires bunched beam, so the thermionic cathode must be modulated whilst simultaneously delivering a good quality beam with low transverse emittance and small energy spread.

THE ELECTRON GUN

The electron gun, shown in Fig. 1, is designed to deliver a maximum of 65mA beam at 125kV. The gun specifications can be found in Table 2. The electron emission is modulated at 500MHz, chosen to be compatible with JLab components, and can produce 130pC CW (higher could be achieved using pulsed mode operation).

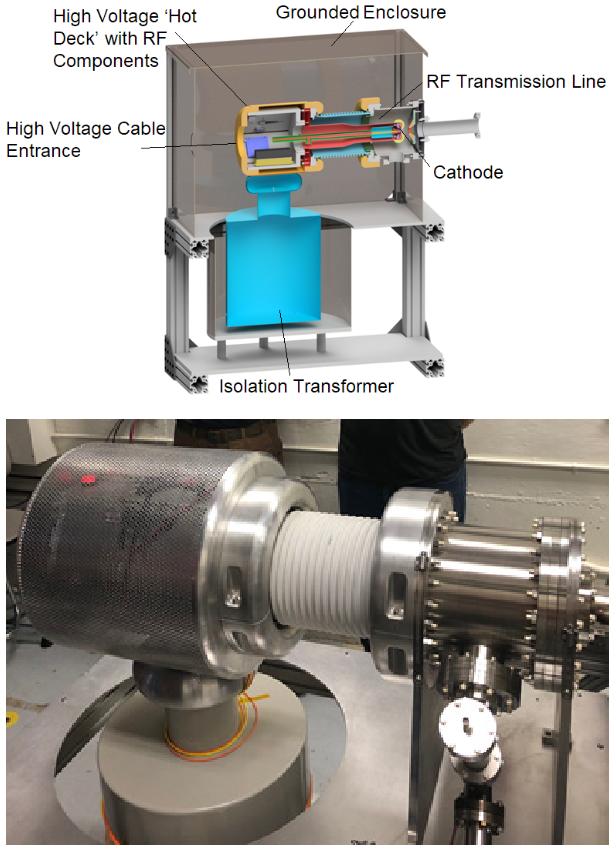

Figure 1: Thermionic gun (top) model, (bottom) as built.

The gun employs a commercial off-the-shelf thermionic cathode, which is gridded, as shown in Fig. 2. Applying a positive voltage to the grid with respect to the cathode, results in electron emission. In the geometry of this gun, the grid is connected to the potential of the cathode electrode

STUDY OF FLUCTUATIONS IN UNDULATOR RADIATION IN THE IOTA RING AT FERMILAB*

I. Lobach†, University of Chicago, Chicago, Illinois, USA
K. J. Kim[1], ANL, Argonne, Illinois, USA
T. Shaftan, BNL, Upton, New York, USA
V. Lebedev, S. Nagaitsev[1], A. Romanov, G. Stancari, A. Valishev, Fermilab, Batavia, Illinois, USA
A. Murokh, RadiaBeam, Los Angeles, California, USA
A. Halavanau, Z. Huang, V. Yakimenko, SLAC, Menlo Park, California, USA
[1]also at University of Chicago

Abstract

We study turn-by-turn fluctuations in the number of emitted photons in an undulator, installed in the IOTA electron storage ring at Fermilab, with an InGaAs PIN photodiode and an integrating circuit. In this paper, we present a theoretical model for the experimental data from previous similar experiments and in our present experiment, we attempt to verify the model in an independent and a more systematic way. Moreover, in our experiment we consider the regime of very small fluctuation when the contribution from the photon shot noise is significant, whereas we believe it was negligible in the previous experiments. Accordingly, we present certain critical improvements in the experimental setup that let us measure such a small fluctuation.

INTRODUCTION

Reference [1] reports on the results of experimental studies of statistical properties of wiggler and bending-magnet radiation in an electron storage ring at BNL. A silicon PIN photodiode combined with an amplifier and an integrator were used to obtain a signal (the number of photoelectrons $\mathcal{N}$) representing the number of detected synchrotron radiation photons per turn. Then, the average amplitude of this signal $\langle\mathcal{N}\rangle$ was varied by a set of neutral density (ND) filters, and the dependence of $\mathrm{var}(\mathcal{N})$ on $\langle\mathcal{N}\rangle$ was studied. Experimental data from this experiment are plotted in Fig. 1. In this plot, the noise of the apparatus (shown by the red line) was subtracted. The authors concluded that for the bending-magnet radiation $\mathrm{var}(\mathcal{N}) \propto \langle\mathcal{N}\rangle$, and for the wiggler radiation $\mathrm{var}(\mathcal{N}) \propto \langle\mathcal{N}\rangle^2$. Qualitative explanation of the results was provided in [1]. Here, we present a theoretical model for the effect, which can predict the fluctuations very precisely, and then we repeat the BNL experiment in IOTA [2] with several major improvements in the setup.

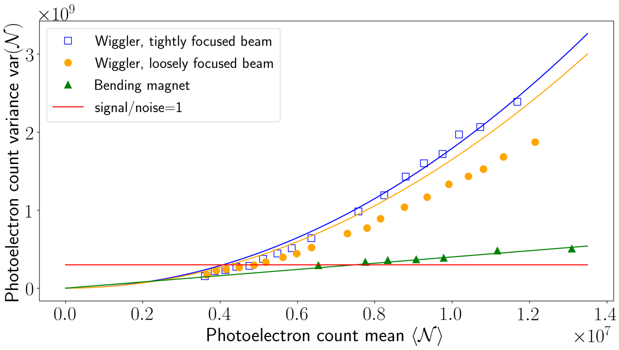

Figure 1: Experimental data from [1], predictions for wiggler radiation fluctuations made by our theoretical model, and a linear fit for the bending-magnet radiation.

THEORETICAL MODEL

It was shown in [3,4] that any classical current produces radiation with Poisson statistics. Since a bunch of electrons in a bending magnet, wiggler, or undulator constitute a classical current (negligible electron recoil), one may argue that the turn-by-turn statistics for photoelectron count for any of these kinds of radiation in a storage ring is Poisson, i.e., $\mathrm{var}(\mathcal{N}) = \langle\mathcal{N}\rangle$, where $\mathcal{N}$ is the number of detected photons (photoelectrons). However, it is not correct, because every turn relative positions of the electrons in the bunch change and hence, every turn, it is a new classical current. That is, the incoherent sum of electromagnetic fields produced by the electrons is slightly different from turn to turn, producing different amounts of emitted power. These effects result in the following equation for variance of the number of detected photons

$$\mathrm{var}(\mathcal{N}) = \langle\mathcal{N}\rangle + \frac{1}{M}\langle\mathcal{N}\rangle^2, \tag{1}$$

where M can be identified with the number of coherent modes [5], which depends on the kind of radiation (bending-magnet, wiggler, undulator, etc.), the bunch parameters, and the detection configuration. Although the Poisson contribution in Eq. (1) is related to the quantum nature of emitted light, the incoherence contribution (the second term) is purely classical [6]. The expression for $1/M$ takes the form

---

[*] This manuscript has been authored by Fermi Research Alliance, LLC under Contract No. DE-AC02-07CH11359 with the U.S. Department of Energy, Office of Science, Office of High Energy Physics.

[†] ilobach@uchicago.edu

North American Particle Acc. Conf. NAPAC2019, Lansing, MI, USA JACoW Publishing
ISBN: 978-3-95450-223-3 ISSN: 2673-7000 doi:10.18429/JACoW-NAPAC2019-THYBA6

ACTIVE POINTING STABILIZATION TECHNIQUES APPLIED TO THE LOW ENERGY RHIC ELECTRON COOLING LASER TRANSPORT AT BNL*

L.K. Nguyen[†], A.J. Curcio, W.J. Eisele, A.V. Fedotov, A. Fernando, W. Fischer, P. Inacker, J.P. Jamilkowski, D. Kayran, K. Kulmatycski, D. Lehn, T.A. Miller, M.G. Minty, A. Sukhanov,
Brookhaven National Laboratory, Upton, NY, USA

Abstract

The electron beam for the Low Energy RHIC electron Cooler (LEReC) at Brookhaven National Laboratory (BNL) is generated by a high-power fiber laser illuminating a photocathode. The pointing stability of the electron beam, which is crucial given its long transport, is highly dependent on the center-of-mass (CoM) stability of the laser spot on the photocathode. For reasons of accessibility during operations, the laser is located outside the accelerator tunnel, and the laser beam is propagated over a total distance of 34 m via three laser tables to the photocathode. The challenges to achieving the required CoM stability of 10 μm RMS on the photocathode include mitigation of the effects of vibrations along the transport and of weather- and season-related environmental effects, while preserving accessibility and diagnostic capabilities. Due to the insufficiency of infrastructure alone in overcoming these challenges, two active laser transport stabilization systems aimed at addressing specific types of position instability were installed during the 2018 Shutdown. After successful commissioning of the full transport in 2018/19, we report on our solutions to these design challenges.

INTRODUCTION

The Low Energy RHIC electron Cooler (LEReC) is the first electron cooler using RF-accelerated bunched electron beams. It was successfully commissioned in 2018 [1] and subsequently demonstrated Au ion cooling in the Relativistic Heavy Ion Collider (RHIC) at Brookhaven National Laboratory (BNL) in 2019 [2]. In the process, the LEReC project needed to overcome many engineering challenges, including the necessary transverse stability of the electron beam along the full 100 m of beam transport.

Although many factors contribute to the transverse stability of the electron beam, it was understood during the design phase that the laser beam illuminating the photocathode also needed to be adequately stable transversely in order for the resultant electron beam to behave efficaciously. As such, a limit of 10 μm rms position variation was placed on the center-of-mass (CoM) of the laser beam spot on the photocathode. For LEReC, the laser beam is generated by a high-power fiber laser located outside the accelerator tunnel for reasons of accessibility during operations [3,4]. The shaped laser beam is then steered over a total distance of 34 m down to the photocathode, and this optical path involves three independent laser tables. Initial laser and transport design focused on the passive stabilization of the transverse movement of the beam, known as its pointing stability, via structural methods [4]. However, the LEReC commissioning process demonstrated the need for active stabilization, as the cited passive stabilization methods proved to be insufficient for achieving the required pointing stability of 10 μm rms.

DESIGN MOTIVATIONS

Data logged as part of the diagnostics system that monitors the LEReC laser transport tracks the beam's center-of-mass as it would appear on the photocathode [4]. In the absence of any active stabilization, the data from the 2018 Run consistently showed the presence of two types of unwanted CoM movement. The first type, herein referred to as "fast fluctuations", consists of shot-to-shot variations superimposed on a second type, herein referred to as "slow drifting", occurring over the course of hours. Investigations into the nature of these position variations determined that the fast fluctuations originate in the drive laser components and are compounded by the presence of air currents prior to the beam's injection into the transport, whereas the slow drifting arises from the weather- and season-related relative movement of the three laser tables composing the transport [4]. Figure 1 shows data collected towards the end of the 2018 Run as an example. Fast and slow mechanisms of pointing instability are clearly visible in the plot, as are two instances of user corrections. Such user corrections can cause excursions in the electron beam orbit that trip the machine protection system in high-current conditions, underlining the need for a continuous feedback mechanism in lieu of periodic user corrections.

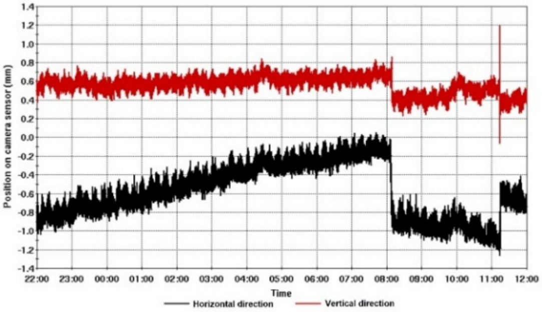

Figure 1: Example data of CoM laser position (horizontal position in black, vertical position in red) during operations without active pointing stabilization, showing fast fluctuations, slow drifting, and user corrections.

---

* Work supported by Brookhaven Science Associates, LLC under Contract No. DE-AC02-98CH10886 with the U.S. Department of Energy.

† lnguyen@bnl.gov

COMPACT 1 MeV ELECTRON ACCELERATOR

S.P. Antipov, P. Avrakhov, S.V. Kuzikov, Euclid Techlabs LLC, Solon, OH, USA

Abstract

The cost of accelerating structures in modern medical accelerators and industrial linacs is substantial. This comes as no surprise, as the accelerating waveguide is comprised of a set of diamond-turned copper resonators brazed together. Such a multistep manufacturing process is not only expensive, but also prone to manufacturing errors, which decrease the production yield. In the big picture, the cost of the accelerating waveguide precludes the use of accelerators as a replacement option for radioactive sources. Here we present a new low-cost brazeless electron accelerating structure assembled from two copper plates fastened to each face of an additional stainless-steel plate. This additional plate, possessing a machined knife-edge on each face, is designed to bite into the copper plates, thus providing vacuum inside the entire system. The designed X-band 1 MeV structure consists of eight different length cells and accelerates field-emitted electrons from a copper cathode. The structure is fed by a 9 GHz magnetron which produces 240 kW, 1 μs pulses. The average gradient is as high as 10.6 MV/m and maximum surface fields do not exceed 23 MV/m.

INTRODUCTION

Brazeless accelerator design considered here assumes replacement of brazed joints with stainless-steel – copper RF and vacuum joints. Typically brazeless assembly relies on a stainless-steel part with knife edge biting into a copper part, i.e. stainless-steel is inevitably a part of the microwave structure. To alleviate microwave losses associated with stainless-steel, it was originally proposed to plate the stainless-steel part with copper. While this approach had been proven effective at low gradients, the long-term stability of the plating, especially at ultra-high microwave power has yet to be verified. This brazeless split block design eliminates this concern completely. In this assembly, the stainless-steel knife-edge connection occurs outside of the microwave volume.

ACCELERATING STRUCTURE DESIGN

The choice of acceleration structure design is a multiparametric task. It is, as usual, a trade-off between price and complexity of fabrication and tuning. In our case, deciding factors were the split block dimensions and available RF power source. These limitations lead us to develop a standing wave (SW) disk loaded accelerating structure in X-band frequency range (powered by radar pulsed magnetron).

The 8-cell 9.4 GHz accelerating cavity (see Fig. 1) provides a 1 MeV energy gain for a low-energy 20 keV electron beam, utilizing around 200 kW RF power. The main accelerator parameters are presented in Table 1. Due to variable beam velocity, each cell is of different length and radius, but maintains a fixed aperture of 10 mm. The input iris (3 mm radius) collimates the low-energy beam. Waveguide dump, located in the last cell of the coupler, symmetrizes accelerating field and reduces transverse components kick.

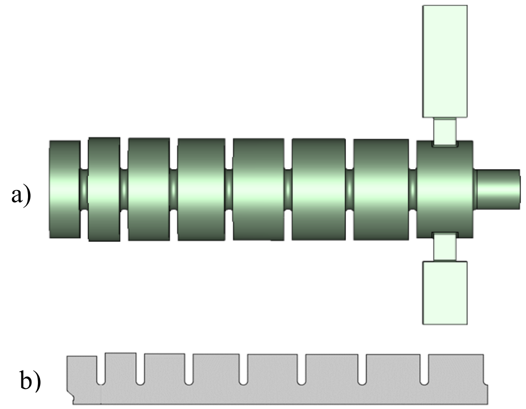

Figure 1: 8 cell SW accelerating cavity design with input waveguide coupler and waveguide dump: a) 3D model; b) accelerating cell's shape.

Electric field map in 3D (CST Studio 2018 [1]) simulation and energy gain vs input accelerating field phase are shown in Fig. 2 and Fig. 3, respectively.

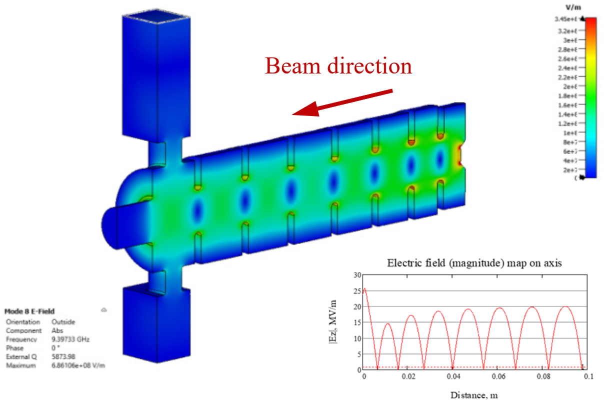

Figure 2: The π mode electric field map in the 8-cell 9.4 GHz accelerating cavity.

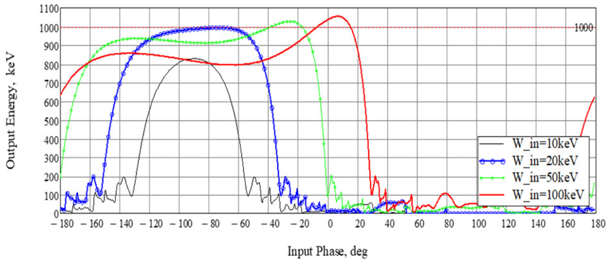

Figure 3: Energy gain vs initial accelerating field phase and input beam energy.

THE MYRRHA PROJECT*

H. Podlech†, K. Kümpel, S. Lamprecht, N. F. Petry, P. P. Schneider,
Goethe University, Frankfurt, Germany
T. Junquera, ACS, Orsay, France
H. Höltermann, U. Ratzinger, Bevatech GmbH, Frankfurt, Germany
F. Senee, D. Uriot, CEA Saclay, Saclay, France
A. Apollonio, J. A. Uythoven, CERN, Geneva, Switzerland
R. Modic, Cosylab, Ljubljana, Slovenia
A. E. Pitigoi, P. Fernandez Ramos, Empresarios Agrupados, Madrid, Spain
F. Bouly, Univ. Grenoble Alpes, Grenoble, France
C. Zhang, GSI Helmholtzzentrum für Schwerionenforschung GmbH, Darmstadt, Germany
M. Abs, J. Brison, IBA, Louvain-la-Neuve, Belgium
J.-L. Biarrotte, C. Joly, D. Longuevergne, IPNO, CNRS, Orsay, France
A. Bechtold, NTG GmbH, Gelnhausen, Germany
C. Angulo, J. Belmans, F. Doucet, A. Gatera, F. Pompon, A. Ponton, D. Vandeplassche,
SCK•CEN, Mol, Belgium

Abstract

The main objective of MYRRHA (Multi-purpose hybrid Research Reactor for High-tech Applications) at SCK•CEN, the Belgian Nuclear Research Centre, is to demonstrate the large scale feasibility of nuclear waste transmutation using an Accelerator Driven System (ADS). It is based on a high power cw operated 600 MeV proton Linac with an average beam power of 2.4 MW. Due to the coupling of the accelerator with a fast reactor, a major concern is reliability and availability of the accelerator. Only 10 beam trips longer than 3 s are allowed per 3-month operation cycle, resulting in an overall required Mean Time Between Failure (MTBF) of at least 250 hours. The MYRRHA Linac consists of a room temperature 17 MeV Injector based on CH-cavities and the superconducting main Linac using different RF structures as Single Spokes, Double-Spokes and elliptical cavities. In 2017 it has been decided to stage the project and to start with the construction of a 100 MeV Linac (Injector and Single Spoke section) including a 400 kW proton target station. This facility will be operational in 2026 aiming to evaluate the reliability potential of the 600 MeV Linac. The Front-End consisting of an ECR source, LEBT and 1.5 MeV RFQ is already operational while the first 7 CH-cavities are under construction. The presentation gives an overview about the MYRRHA Project, its challenges and the status of construction and testing.

INTRODUCTION

The Belgian nuclear research centre SCK•CEN has been working for several years on the development of an accelerator-driven multi-purpose neutron source to replace the ageing BR2 reactor. This project, known as MYRRHA, couples a high power proton accelerator with a fast 50-100 MW_{th} reactor [1]. The 600 MeV beam delivered by the accelerator hits a liquid metal spallation target (Pb-Bi). A focus of MYRRHA is the demonstration of the large-scale feasibility of nuclear waste transmutation. In addition, far-reaching possibilities open up in materials research, component testing and the production of radioisotopes. Furthermore, it is planned to make part of the beam available for an ISOL-target. The MYRRHA accelerator must be able to deliver the 600 MeV beam with a beam current of up to 4 mA in cw operation with a beam power of up to 2.4 MW. Particular attention was paid to the reliability of the accelerator. The MTBF shall be at least 250 hours. This was also taken into account in the design of the accelerator. The design philosophy was that the accelerator should be as conservative as necessary and as efficient as possible. This applies to both the hardware components and the beam dynamics. The latter is particularly important with regard to methods for increasing reliability (Dynamic Fault Compensation Scheme) [2]. In a first step the construction of the MYRRHA Linac up to an energy of 100 MeV has started. In parallel, a proton target facility (PTF) will be built to use the beam for first experiments from 2026 [3]. This first stage of MYRRRHA is named MINERVA. Table 1 summarizes the top level requirements for MYRRHA and MINERVA. The development of the MYRRHA project has been supported in recent years by various funding programmes from the European Union between 2001 and 2019 (PDS XT-ADS, Eurotrans, MAX, MYRTE). In 2016 the decision was taken to divide the MYRRHA project into different phases. Phase 1 (2019-2026) includes the design and commissioning of MINERVA and further R&D on the 600 MeV Linac. Phase 2 includes the construction of the Linac up to 600 MeV and phase 3 the reactor. At a later stage it will be decided whether phase 2 and phase 3 will be executed sequentially or in parallel [3]. The reasons for this

---

* Work supported by the European Commission Framework Programme H2020, MYRTE project No. 662186

† h.podlech@iap.uni-frankfurt.de

ISBN: 978-3-95450-223-3 ISSN: 2673-7000 doi:10.18429/JACoW-NAPAC2019-THZBA3

STATUS OF BEAM COMMISSIONING IN FRIB DRIVER LINAC*

T. Maruta†, S. Cogan, K. Fukushima, M. Ikegami, S.H. Kim, S.M. Lidia, G. Machicoane, F. Marti, D. Morris, P. Ostroumov, A. Plastun, J.T. Popielarski, J. Wei, T. Xu, T. Yoshimoto, T. Zhang, Q. Zhao, S. Zhao
Facility for Rare Isotope Beams, Michigan State University, East Lansing, MI, USA

Abstract

The staged beam commissioning is underway in the Facility for Rare Isotope Beams (FRIB) being constructed at Michigan State University (MSU). The beam commissioning of the first linac segment (LS1) and a section of the first folding segment (FS1) took place in March 2019. Four different ion species were accelerated up to 20.3 MeV/u and transported to the beam dumps in FS1 with 100% transmission. This paper reports the beam measurement results performed during the commissioning of the LS1 and FS1.

INTRODUCTION

The FRIB is based on a continuous wave (CW) superconducting (SC) linear accelerator which is designed to deliver 400 kW heavy ion beams to the fragmentation target. The multi-stage beam commissioning activities started in the summer 2017 with expected completion in 2021 [1]. The direct current (DC) beam extracted from the electron cyclotron resonance ion source (ECRIS) is transported to the Radio Frequency Quadrupole (RFQ) located in the tunnel. Beam is bunched longitudinally by a multi-harmonic buncher (MHB) and then accelerated to 0.5 MeV/u in the RFQ followed by three SC linac segments (LS1 to LS3) to deliver beams to the fragmentation target. Two folding segments (FS1 and FS2) are connecting the linac segments and the beam will be transported to the production target by the beam delivery system (BDS). To reach the design beam energies of 200 MeV/u, the linac requires a charge stripper which is located at the end of LS1.

The beam commissioning of the LS1, shown in Fig.1, took place in the spring 2019 [2, 3]. Four ion species of ^{20}Ne, ^{40}Ar, ^{86}Kr and ^{129}Xe were accelerated to 20.3 MeV/u. The charge state distribution of each ion specie was measured after the 45° bending magnet.

The LS1 includes three CA type cryomodules housing four $\beta_{\mathrm{OPT}} = 0.041$ SC quarter wave resonators (QWRs) and two 25-cm-long SC solenoids, and eleven CB type cryomodules containing eight $\beta_{\mathrm{OPT}} = 0.085$ SC QWRs and three 50-cm-long SC solenoids, respectively. Their operating frequency is 80.5 MHz and design accelerating voltages are 0.81 and 1.78 MV. While a liquid lithium stripper is a main option for the high power operation, a carbon foil stripper was used for our measurements. The carbon foils of thicknesses of 0.4, 0.6 and 0.8 mg/cm^2, were mounted on a stripper wheel. A charge selection slits are located after the 45° bending magnet of the FS1 to intercept unwanted charge states of the beam. The location of two beam dumps, FS1a and FS1b is shown in Fig.1. In addition to these dumps, a movable niobium plate after the third cryomodule was also used as a beam dump for beam studies in the upstream section, because the transportation of low energy beam to the beam dump FS1a requires too much tuning time.

A large variety of beam diagnostics devices was available during the beam commissioning in LS1 and FS1 including AC-coupled Beam Current Monitors (BCMs), Beam Position and Phase Monitors (BPMs), Halo Monitor Rings (HMRs), Profile Monitors (PMs), scintillator-based neutron monitors and parallel plate ion chambers.

An electrostatic chopper located in the LEBT was used to produce a pulsed beam structure necessary for BCM beam current measurements and control the average beam power.

BEAM COMMISSIONING

The stage three of the FRIB beam commissioning took place in the spring 2019 over the 3-week period. Only major beam commissioning procedures and beam parameters' measurements are discussed in this paper. More extended discussion of the beam commissioning results was presented in recent publication [3]. Both transverse and longitudinal tuning of the linac were performed with ^{40}Ar^{9+} beam. Then, all electromagnetic fields were scaled for other ion species according to the charge-to-mass ratio.

Longitudinal Tuning

At the beginning of the beam commissioning, the phases and amplitudes of each resonator were tuned by 360° phase scan and time-of-flight measurements using BPMs. The latter was applied to tune each MEBT buncher and each SC cavity. This procedure was applied at ~1 MV/m accelerating gradient to avoid transverse steering of the beam which strongly depends on the RF field phase. The cavity accelerating phase was set to the design value, which is typically equal to -30° from the maximum acceleration phase. The cavity accelerating gradient was calibrated by measuring the absolute beam energy. For robust TOF measurements by three BPM pairs were utilized. The BPM signal amplifiers have very high sensitivity, therefore stable measured data can be obtained for ~40 nA beam current. The accuracy of the absolute beam energy measurements is high, typically ~20 keV/u at 20.3 MeV/u. In this manner, the beam energy is known with high accuracy upstream of the SC cavity which is being set. In addition, the beam energy

---

* Work supported by the U.S. Department of Energy Office of Science under Cooperative Agreement DE-SC0000661, the State of Michigan and Michigan State University

† maruta@frib.msu.edu

ISBN: 978-3-95450-223-3 ISSN: 2673-7000 doi:10.18429/JACoW-NAPAC2019-THZBA4

CHARACTERIZATION AND MODELING OF HIGH-INTENSITY EVOLUTION IN THE SNS BEAM TEST FACILITY*[†]

K. J. Ruisard[‡], A. Aleksandrov, S. Cousineau, Z. Zhang
Oak Ridge National Laboratory, Oak Ridge, TN, USA

Abstract

Modern high-power accelerators are charged with delivering reliable beam with low losses. Resolving the complex dynamics arising from space charge and nonlinear forces requires detailed models of the accelerator and particle-in-cell simulation. There has historically been discrepancy between simulated and measured beam distributions, particularly at the low-density halo level. The Beam Test Facility (BTF) at the Spallation Neutron Source is outfitted to study beam evolution in a high-power linear accelerator MEBT. This includes capability for high-dimensional measurements of the post-RFQ beam distribution, including interplane correlations that may be the key to accurate simulation. Beam is transported through a 4.6 m FODO channel (9.5 cells) to a second distribution measurement stage. Plans for validating simulations against BTF measurements of beam evolution in the FODO channel are discussed.

INTRODUCTION

Modern high-power accelerators are charged with delivering reliable beam with low losses. For future facilities, which aim for order-of-magnitude power increase above existing state-of-the-art, tighter control over beam loss is required. In the >10 MW class, losses should be controlled to within one part-per-million to maintain a safe accelerator environment [1].

A pervasive source of uncontrolled loss is beam halo. Halo is the low-density particle population composing a “heavy-tailed” (above-Gaussian) feature in the beam distribution. Due to the large extent, this small fraction of beam contributes disproportionately to scraping losses. This paper adheres to the definition outlined in [2,3]: halo is phase space feature emerging at densities below 10^{-4} of peak.

The SNS beam test facility (BTF, see Fig. 1) is a replica of the SNS front-end system. It is comprised of an H^- ion source, 2.5 MeV/402.5 MHz RFQ and alternating-gradient MEBT. The BTF is a multi-use test facility. In addition to being used for commissioning new diagnostics and accelerator components, it supports beam physics studies. In particular, the BTF is equipped with both high-dimensional and high-dynamic range capabilities for diagnosis of beam distribution. The focus of the ongoing BTF beam physics program is the halo-inclusive benchmarking of front-end beam evolution.

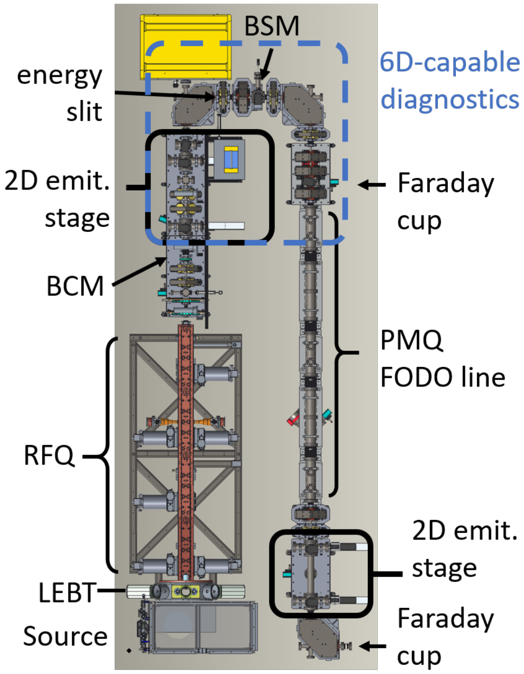

Figure 1: Diagram of major BTF components and relevant diagnostics.

PRIOR WORK AND STATE OF THE ART

Many preceding studies have similarly focused on characterizing halo. The landmark study at the Low Energy Demonstration Accelerator (LEDA) at LANL was accompanied with a detailed simulation study [4,5]. In this study, PIC simulations were unable to consistently reproduce the RMS beam profiles, much less accurately predict the low-level features (down to 10^{-4} of peak). The source of errors was judged to be incomplete understanding of the initial beam distribution.

Since then, it has been demonstrated that agreement at the core/RMS level is possible with PIC codes. In particular, the benchmarking effort at the GSI UNILAC tested a selection of codes and showed agreement over a range of optics configurations for heavy ions [6]. However, extending predictions to the required 1 ppm halo level is still a major hurdle.

---

* This manuscript has been authored by UT-Battelle, LLC, under Contract No. DE-AC05-00OR22725 with the U.S. Department of Energy. The United States Government retains, and the publisher, by accepting the article for publication, acknowledges that the United States Government retains a non-exclusive, paid-up, irrevocable, world-wide license to publish or reproduce the published form of this manuscript, or allow others to do so, for United States Government purposes. The Department of Energy will provide public access to these results of federally sponsored research in accordance with the DOE Public Access Plan (`http://energy.gov/downloads/doe-public-access-plan`).

[†] This work has been partially supported by NSF Accelerator Science grant 1535312.

[‡] ruisardkj@ornl.gov

ISBN: 978-3-95450-223-3 ISSN: 2673-7000 doi:10.18429/JACoW-NAPAC2019-THZBA5

FIRST ELECTRON COOLING OF HADRON BEAMS USING A BUNCHED ELECTRON BEAM*

A.V. Fedotov[#], Z. Altinbas, M. Blaskiewicz, M. Brennan, D. Bruno, C. Brutus, M. Costanzo, A. Drees, W. Fischer, J. Fite, M. Gaowei, D. Gassner, X. Gu, J. Halinski, K. Hamdi, L. Hammons, T. Hayes, R. Hulsart, P. Inacker, J. Jamilkowski, Y. Jing, P. Kankiya, D. Kayran, J. Kewisch, R. Lehn, C.J. Liaw, C. Liu, J. Ma, G. Mahler, M. Mapes, A. Marusic, K. Mernick, C. Mi, R. Michnoff, T. Miller, M. Minty, S. Nayak, L. Nguyen, M. Paniccia, I. Pinayev, S. Polizzo, V. Ptitsyn, T. Rao, G. Robert-Demolaize, T. Roser, J. Sandberg, V. Schoefer, S. Seletskiy, F. Severino, T. Shrey, L. Smart, K. Smith, H. Song, A. Sukhanov, R. Than, P. Thieberger, S. Trabocchi, J. Tuozzolo, P. Wanderer, E. Wang, G. Wang, D. Weiss, B. Xiao, T. Xin, W. Xu, A. Zaltsman, H. Zhao, Z. Zhao
Brookhaven National Laboratory, Upton, NY, USA

Abstract

The Low Energy RHIC electron Cooler (LEReC) was recently commissioned at BNL. LEReC is the first electron cooler based on RF acceleration of electron bunches (previous electron coolers all used DC beams). Bunched electron beams are necessary for cooling hadron beams at high energies. The challenges of such an approach include generation of electron beams suitable for cooling, delivery of electron beams of the required quality to the cooling sections without degradation of beam emittances and energy spread, achieving the required small angles between electrons and ions in the cooling sections, precise velocity matching between the two beams, high-current operation of the electron accelerator, as well as several physics effects related to bunched beam cooling. Following successful commissioning of the electron accelerator in 2018, the focus of the LEReC project in 2019 was on establishing electron-ion interactions and demonstration of the cooling process. Here we report on the first demonstration of Au ion cooling in RHIC using this new approach.

INTRODUCTION

Electron cooling is a well-established technique for obtaining high-quality ion beams [1]. In this method, the phase-space density of an ion beam is increased by means of dissipative forces – the dynamic friction on individual ions undergoing Coulomb collisions with a lower temperature electron distribution.

Until now, all electron cooling systems used DC electron beams. LEReC is first electron cooler which employs RF acceleration of electron bunches [2]. Such a scheme of cooling with a bunched electron beam is a natural approach for high-energy electron cooling which requires RF acceleration. As such, LEReC is also a prototype for future high-energy electron coolers, both in physics and technology. With acceleration of electron bunches starting inside the gun, beam dynamics and resulting electron beam temperatures are very different from those typically obtained with electrostatic acceleration of DC beams, which is crucial for the electron cooling process. In addition, LEReC is the first electron cooler to cool hadron beams in collisions.

The high-current high-brightness electron accelerator was successfully commissioned in 2018 with all required electron beam parameters demonstrated [3]. During the 2019 RHIC run with Au ions, electron cooling was successfully commissioned for 3.85 GeV ion beam using 1.6 MeV electrons and then for 4.6 GeV ions using 2 MeV electrons.

THE LEReC ACCELERATOR

LEReC is based on state-of-the-art accelerator physics and technology: photocathodes with sophisticated delivery system; a high-power laser beam with laser shaping and stabilization; a high-voltage high-current DC gun; RF gymnastics using several RF cavities; instrumentation, controls and a machine protection system [4-14].

Electron bunches are generated by illuminating a multi-alkali photocathode, inserted into a DC gun with an operating voltage around 400 kV. The 704 MHz fiber laser produces bunch trains with individual electron bunches of about 40 ps full length at ~9 MHz bunch train frequency, which is the same as the repetition rate of ion bunches in RHIC, as illustrated in Fig. 1.

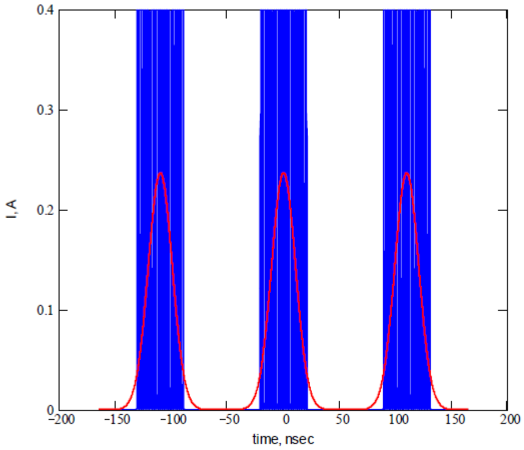

Figure 1: The LEReC beam structure. Thirty electron bunches (blue) spaced by 1.4ns placed on a single ion bunch (red), with ion bunch repetition frequency of 9 MHz.

---

* Work supported by the US Department of Energy under contract No. DE-AC02-98CH10886.

#fedotov@bnl.gov

NOVEL EMITTANCE MEASUREMENT COMBINING FOIL FOCUSING AND PEPPER-POT TECHNIQUES*

K.A. Schultz†, G.T. Ortiz, M.E. Schulze, Los Alamos National Laboratory, Los Alamos, NM, USA
C. Carlson, D. Guerrero, National Security Technologies, Los Alamos, NM, USA

Abstract

In this paper, we describe a direct measurement of foil focusing of an intense, relativistic electron beam combined with the pepper-pot technique to perform emittance measurements. Foil focusing occurs when a thin, grounded, conducting foil shorts out the radial electric field of a transiting electron beam, causing its self-magnetic field to focus the beam. A 40-ns pulse was extracted from the main pulse of the 16-MeV, 1.65 kA beam from Axis-II of the Dual Axis Radiographic Hydrodynamic Test Facility to perform the measurements. We show that not accounting for foil focusing significantly reduces the measured emittance.

INTRODUCTION

The use of thin foils or semi-transparent meshes to focus and transport intense relativistic electron beams (IREB) is well established [1-3]. In this article, we present a new method of inferring beam emittance by using a combination of foil-focusing and the pepper-pot method [4,5].

Currently, emittance measurements on the Dual-Axis Radiographic Hydrodynamic Test (DARHT) Facility are done via solenoid scan. The issues of using a solenoid scan on beams with intense space charge have long been investigated [4], [6-8] due to the radial-dependence of space-charge forces. Dynamic changes in the spot size occur for very small spots which can significantly skew the results. Solenoid scans at DARHT also require a series of tens of shots, which can take several days to complete. We introduce here a new method of emittance measurement that needs only one shot and is relatively independent of space-charge effects.

A thin foil (~250-µm) scatters electrons in the foil while also providing a focusing 'kick' to the beam due to foil focusing effects in IREBs. This avoids the conventional pepper-pot requirement of stopping the electrons in the masking foil and removes the associated vignetting issues. This paper is an introduction to the new method for circular, uniform, axisymmetric beams. Future work will be expanded for off-center and elliptical beams.

THEORY

In addition to multiple Coulomb scattering, a relativistic, cold ($p_z \gg p_r$) beam passing through a thin, conducting foil experiences a radial deflection $\delta p_r/p_z$ where δp_r is the change in transverse momentum and p_z is the longitudinal momentum. This momentum 'kick' is due to the boundary conditions imposed by the foil, shorting the transverse electric field (space charge) of the beam. This causes the beam's self-magnetic field to pinch the beam.

The momentum change experienced by a uniform, and axisymmetric beam, given by Adler [1], is

$$\frac{\delta p_r}{p_z} = \delta\theta = -16\frac{I_b}{I_A}\frac{b}{r_{beam}}\sum_{n=1}^{\infty}\frac{J_1\left(\frac{\chi_{0n}r_{beam}}{b}\right)J_1\left(\frac{\chi_{0n}r}{b}\right)}{\chi_{0n}^3 J_1(\chi_{0n})^2} \quad (1)$$

where I_b is the beam current, $I_a = 17.05\beta\gamma$ is the Alfven current in kA, r_{beam} is the beam radius, b is the beam pipe radius, and χ_{0n} is the nth root of the zero-order Bessel function $J_0(x)$. For the beam parameters in the article, $\delta\theta$ is roughly -8 mrad at the edge of the beam. To first order, this produces a radially linear kick as long as the beam radius is small compared to the pipe radius [9]. This would be a good approximation for the central beamlets, but tends to overestimate the kick for the outer beamlets and give a slightly too-large (a few percent) emittance.

The beamlets passing through the holes in a thin pepper-pot also experience the same radial kick as long as the hole radius is smaller than the Debye length. Unlike the rest of the beam that directly interacts with the foil, these beamlets, are effected only by foil focusing, not multiple Coulomb scattering. The foil thickness is chosen so that the electrons that pass through the foil are sufficiently dispersed and only contribute a small background subtraction.

EXPERIMENTAL DETAILS

The experiments were carried out on the DARHT Axis-II downstream transport. DARHT Axis II produces a 16-MeV, 1.65-kA electron beam with a 1.6-µs flattop; downstream of the accelerator, multiple pulses can be 'kicked' from the beam[10]. For these experiments, we used a single, 40-ns pulse. The setup consisted of a focusing foil, imaging screen, and camera (Fig. 1a). A 250-µm thick Mo foil with a regular grid of 1.5-mm diameter holes with 5-mm center-to-center spacing served as the pepper-pot mask and focusing foil (Fig. 1b). This was centered within a grounded, 7.24-cm radius tube. A central cutout was included on the mask and provided a fiducial to determine beam position within the vacuum pipe. The grid was oriented such that the rows were parallel to the floor. Current densities of less than 200 A/cm^2 were incident on the foil. After a drift of 155 cm with no intervening magnets, the masked beam was imaged by viewing optical transition radiation (OTR) in the near-field limit. A PI-MAX4 camera captured images of the stainless steel OTR target, situated at 45° to the beamline.

Pepper-pot masks are typically designed to be range thick to reduce background at the imaging plane. The thin foil relies on the multiple coulomb scattering of electrons

---

* Work supported by the US National Nuclear Security Agency and the US Department of Energy under contract DE-AC52-06NA25396.
† kimberlys@lanl.gov

BEAM LOSS IN THE FIRST SEGMENT OF THE FRIB LINAC*

R. Shane†, S. Cogan, S. M. Lidia, T. Maruta,
Facility for Rare Isotope Beams, Michigan State University, East Lansing, MI, USA

Abstract

Beam loss in accelerators is an unavoidable and often unwanted reality, but it is not without its use. Information from beam loss can be leveraged to optimize the tune and improve beam quality, in addition to monitoring for machine fault and failure conditions. The folded geometry at the Facility for Rare Isotope Beams (FRIB) presents a unique challenge in the detection of radiative losses, resulting in the introduction of non-traditional measurement schemes. In addition to neutron detectors and pressurized ionization chambers, FRIB will utilize halo ring monitors, fast thermometry within the cryomodules, and differential beam-current measurements. This paper will present an analysis of beam-loss measurements from commissioning the first segment of the FRIB accelerator, and a discussion of ways to evaluate and monitor the health of the beam loss monitoring system.

INTRODUCTION

Beam loss is an expected and unavoidable consequence of accelerating ions in any accelerator facility. Such losses occur throughout the linear accelerator (linac) as an unwanted consequence to beam transport, as well as intentionally at fixed locations where beam scraping and filtering occurs to improve beam quality, e.g. size, energy spread, or isotopic composition. Both of these types of loss create a background to normal beam operation. Small losses play a crucial role during linac commissioning stages. In addition, failure of accelerator components (magnets, etc.) will cause unexpected, and often large, losses.

Slow Versus Fast Losses

Machine background losses typically change very gradually. In contrast, losses from part failure arise quickly and are often large – enough so to cause significant machine damage. The techniques for monitoring or detecting these losses are different due to their time-scale and magnitude.

With small losses, the risk of immediate damage is absent, so we have the benefit of time with which to detect the loss and correct the issue, provided we have sufficient sensitivity. With large losses, the risk of immediate damage is great, but the magnitude of the loss makes it easier and faster to identify.

Machine Protection

Machine protection is a primary motivation for beam-loss monitoring. It's true that radiation damage is unavoidable, due to ever-present background. However, monitoring losses will allow operators to correct beam tunes to minimize such background radiation and maximize the lifetime of the machine. In addition, misdirected beam, e.g. due to magnet failure, requires fast identification of large losses to prevent immediate damage.

Beam losses deposit energy (heat) into the surrounding material. The resulting increase in temperature can be disastrous in the cryogenic areas of the accelerator, and can lead to dangerous quenching of the superconducting magnets.

FRIB is somewhat unusual in that the loss limits, shown in Table 1, are set primarily by the allowable heat load and machine degradation, rather than activation of machine parts.

Table 1: Loss Limits for the FRIB Linac

Beam Loss (W/m)	Stop beam?	Response Time
$P < 1$	No	≥ 1 sec
$1 \leq P < 10$	Yes	1 sec (slow)
$P \geq 10$	Yes	< 15 μs (fast)

CHALLENGES FOR FRIB

FRIB faces several challenges in the detection of beam losses in the linear accelerator (linac). FRIB linac is designed for a beam power of up to 400 kW. Such a high beam intensity means significant damage is possible quickly, making prompt detection of beam losses crucial. Magnet quenching can occur due to heating of irradiated superconducting components.

Due to the folded "paper clip" shape of the FRIB linac, we expect that background radiation from the high-energy linac segment (LS3) will swamp the detectors at the adjacent lowest-energy segment (LS1). Shielding of the beamline and superconducting cavities will help reduce this so-called radiation cross-talk, however it will still limit the effectiveness of radiation measurements in monitoring beam losses in LS1. Calculations indicate that only 1.5% of dose detected at LS1 is from LS1 losses, and cross talk from LS3 dominates low-energy half of LS2 [1].

DEVICES AND DISTRIBUTION

The most effective detection methods will differ for each section of the accelerator, as well as for fast and slow beam losses. The choice of detector is guided by the energy of the beam, the radiation type and magnitude, and the expected background. Table 2 shows the primary, secondary, and tertiary detection methods for fast and slow losses in each area.

Radiation

Radiation cross-talk limits the usefulness of standard radiation detectors. However there are several locations where these play an important role. Ionization chambers (IC) will be used primarily in the folding segments, near

---

* Work supported by the U.S. Department of Energy Office of Science under Cooperative Agreement DE-SC0000661.

† shane@frib.msu.edu

North American Particle Acc. Conf. NAPAC2019, Lansing, MI, USA JACoW Publishing
ISBN: 978-3-95450-223-3 ISSN: 2673-7000 doi:10.18429/JACoW-NAPAC2019-THZBB5

PRESENT STATUS AND UPGRADES OF THE SNS ION BEAM BUNCH SHAPE MONITORS*

V. Tzoganis[†], A.V. Aleksandrov, R. Dickson, Oak Ridge National Laboratory, Oak Ridge, USA

Abstract

Six interceptive Feschenko-style longitudinal bunch profile monitors have been deployed in the normal conducting part of the SNS linac and HEBT. They have been operational for more than 10 years and although their performance has been satisfactory, reliability and parts obsolescence must be addressed. The upgrade plan focuses in mainly two areas, electronics architecture modernization and improvement of measurement resolution. In the first phase that is presented here the objective is to improve the control and readout electronics taking advantage of more recent technology. This will primarily address the obsolescence issues with older components, the frequent RF power failures, the non-trivial maintenance and troubleshooting and will lead to a simpler and more reliable system. This contribution describes in detail the implemented upgrades and presents the first experimental data.

INTRODUCTION

The beam Bunch Shape Monitor (BSM) or Feschenko-style monitor has been developed at INR [1] based on a detector built by R Witkover for the BNL Linac BSM's [2] are used in several proton machines [3], [4] for measuring longitudinal profiles of short bunches where faraday cups cannot be used. The operating principle of the BSM is shown in Fig. 1. Beam bunches hit a wire biased at high voltage (10 kV) which results in emission of low energy secondary electrons. These electrons maintain the temporal distribution of the impinging beam. As the wire is biased at high negative potential, it accelerates the electrons radially away from itself. A small fraction of them passes through an aperture and enters a region where superimposed electrostatic an RF fields focus, steer and deflect the electrons. Depending on the phase of the RF field with respect to the beam RF the electrons are scanned by the RF field and their positions depend on the RF phase. This way, the longitudinal structure of the electron bunch is transformed into a spatial distribution due to the RF deflecting field. For a complete profile the entire bunch must be scanned by the second aperture. The typical Feschenko monitors use a secondary electron multiplier for electron detection. There are 4 BSMs at the SNS, 4 at the CCL and 2 at the HEBT. Additionally, the Beam Test Facility which is a replica of the SNS accelerator front end with some additional elements for specific beam studies is equipped with a BSM too. The BTF BSM was chosen for this development as it is more readily available compared to the main accelerator. The BTF BSM system is slightly different that the others, it is equipped with a multi-channel plate detector (MCP) and a phosphor screen. In this configuration the last aperture is eliminated so a complete bunch profile measurement doesn't require scanning and it is taken in one shot. One shot in this context implies imaging several bunches under the assumption that they are identical.

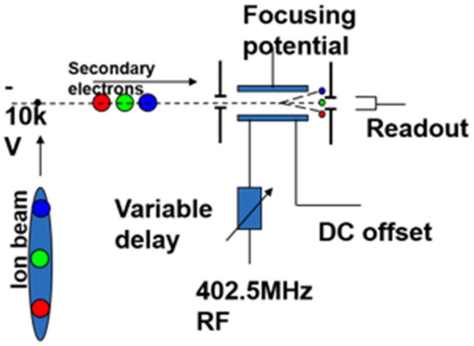

Figure 1: BSM working principle.

The original BSM systems as delivered by the Institute of Nuclear Research have been operational for several years but there are certain shortcomings that needed to be addressed. This R&D effort presented here was motivated by several reasons that had to do with the systems reliability, ease of maintenance, easy of configuration and component availability. The existing BSM suffers from frequent RF amplifier failures due to overheating as it operates in continuous mode. Replacing components is not a trivial task as many of them have become obsolete. Moreover, the system is not modular and thus subsystems cannot be swapped out easily. The focus of this effort is to simplify the high voltage power supply configuration, have the RF amplification chain operating in pulsed mode, use modular off the shelf components where possible and resort to custom hardware only when necessary. This will simplify the entire system making maintenance easier and faster

HARDWARE DESCRIPTION

Figure 2 shows the BSM electronics chassis, all components are contained in a single assembly. The main discrete sections are RF, high voltage power supplies, AC-DC, Timing and triggers and constant current power supplies.

---

* This manuscript has been authored by UT-Battelle, LLC, under Contract No. DE-AC05-00OR22725 with the U.S. Department of Energy. The United States Government retains, and the publisher, by accepting the article for publication, acknowledges that the United States Government retains a non-exclusive, paid-up, irrevocable, world-wide license to publish or reproduce the published form of this manuscript, or allow others to do so, for United States Government purposes. The Department of Energy will provide public access to these results of federally sponsored research in accordance with the DOE Public Access Plan (http://energy.gov/downloads/doe-public-access-plan).

[†] tzoganisv@ornl.gov.

ERROR MINIMIZATION IN TRANSVERSE PHASE-SPACE MEASUREMENTS USING QUADRUPOLE AND SOLENOID SCANS*

C.Y. Wong[†], National Superconducting Cyclotron Laboratory, East Lansing, MI, USA
S.M. Lund, Facility for Rare Isotope Beams, East Lansing, MI, USA

Abstract

Quadrupole and solenoid scans are common techniques where a series of beam profile measurements are taken under varying excitation of the linear focusing elements to unfold second-order phase-space moments of the beam at an upstream location. Accurate knowledge of the moments is crucial to machine tuning and understanding the underlying beam dynamics. The scans have many sources of errors including measurement errors, field errors and misalignments. The impact of these uncertainties on the moment measurement is often not analyzed. This study proposes a scheme motivated by linear algebra error bounds that can efficiently select a set of scan parameters to minimize the errors in measured initial moments. The results are verified via a statistical error analysis. These techniques are being applied at the Facility for Rare Isotope Beams (FRIB). We find that errors in initial moments can be large under conventional scans but are greatly reduced using the procedures described.

INTRODUCTION

Quadrupole and solenoid scans (Q-scans and S-scans) are standard techniques for measuring a beam's transverse phase-space moments. The moments at an initial location are obtained by varying the strengths of focusing elements and making multiple spatial profile measurements at a downstream location, typically with wire scanners. With the assumption of linear single-particle dynamics, which is often a good approximation over a short transport length, transverse phase-space moments can be solved via a system of linear equations: $A\mathbf{x} = \mathbf{b}$ where $\mathbf{b}$ consists of measurement results, $\mathbf{x}$ are the unknown initial beam moments, and A is the coefficient matrix derived from the linear transfer map between the measurement and reconstruction points.

Transverse phase-space moments obtained by Q-scans and S-scans are subject to many sources of errors. Errors in profile measurements correspond to errors in $\mathbf{b}$, whereas errors in the matrix A arise come from errors in the linear transfer map which have many potential causes including mechanical misalignments and field errors. This study first introduces how the errors in transverse phase-space moments can be quantified. Next, we discuss how such errors can be minimized via a suitable set of scanning parameters and present an efficient method for their selection. The method is illustrated by Q-scans performed at the FRIB [1] front end. Lastly, we conclude with an outlook for further work.

ERROR QUANTIFICATION

The errors of Q-scans and S-scans can be quantified in two ways: 1) *Statistical Analysis*; and 2) *Sensitivity Analysis*. These two approaches provide complementary information.

Statistical Analysis

To perform statistical error analysis, one repeatedly solves the equation:

$$(A + \delta A)\,(\mathbf{x} + \delta\mathbf{x}) = (\mathbf{b} + \delta\mathbf{b}) \tag{1}$$

where $\mathbf{x}$ is the unperturbed solution to $A\mathbf{x} = \mathbf{b}$, $\delta\mathbf{x}$ is the change to the unperturbed solution, and $\delta\mathbf{b}$ and δA are random perturbations to measurement results $\mathbf{b}$ and the coefficient matrix A respectively. The magnitudes of $\delta\mathbf{b}$ and δA are determined by estimates from all sources of errors. The resulting set of perturbed solutions $(\mathbf{x} + \delta\mathbf{x})$ can be plotted in histograms whose corresponding distributions can be interpreted as the probability distributions of the unknowns. As opposed to the sensitivity analysis discussed below, this treatment allows one to obtain detailed information on the error distribution.

Sensitivity Analysis

Instead of calculating the error bars on the solutions explicitly, one can employ techniques from linear algebra to analyze how sensitive the linear system of equations $A\mathbf{x} = \mathbf{b}$ is to perturbation terms δA and $\delta\mathbf{b}$. The key parameter that measures sensitivity is the condition number of A denoted by $\kappa(A)$ where:

$$\kappa(A) = \frac{\sigma_{\max}(A)}{\sigma_{\min(A)}} \tag{2}$$

with $\sigma_{\max}(A)$ and $\sigma_{\min}(A)$ being the largest and smallest non-zero singular value A respectively. We refer the reader to Ref. [2, 3] for details. Upon linearizing Eq. (1) in δ, an expression can be derived to bound the relative error of the the solution given the relative error in A and $\mathbf{b}$:

$$\begin{aligned}\frac{\|\delta\mathbf{x}\|_2}{\|\mathbf{x}\|_2} \leq & \kappa(A)^2 \frac{\|\mathbf{r}\|_2}{\|A\mathbf{x}\|_2}\frac{\|\delta A\|_2}{\|A\|_2} \\ & + \kappa(A)\left(\frac{\|\mathbf{b}\|_2}{\|A\mathbf{x}\|_2}\frac{\|\delta\mathbf{b}\|_2}{\|\mathbf{b}\|_2} + \frac{\|\delta A\|_2}{\|A\|_2}\right)\end{aligned} \tag{3}$$

where $\mathbf{r} \equiv A\mathbf{x} - \mathbf{b}$ is the residual vector, and $\|.\|_2$ denotes the Euclidean norm (i.e. L_2 norm) and the associated induced norm for vectors and matrices respectively.

Given the dependence of relative errors in $\mathbf{x}$ on $\kappa(A)$ in Eq. (3), one can use $\kappa(A)$ to compare which system's solutions will have a sharper probability distribution. This

---

* Work supported by the U.S. DOE Office of Science under Cooperative Agreement DE-SC0000661 and the NSF under Grant No. PHY-1565546.

[†] wong@nscl.msu.edu

THE FUTURE CIRCULAR COLLIDER AND PHYSICAL REVIEW ACCELERATORS & BEAMS

F. Zimmermann[*], CERN, Geneva, Switzerland

Abstract

The proposed integrated program of the Future Circular Collider (FCC) goes a huge step beyond LEP and LHC. The FCC consists, in a first stage, of an energy- and luminosity-frontier electron-positron collider, which will operate at centre-of-mass (c.m.) energies from about 90 to 365 GeV, and serve as electroweak factory. The second stage of the FCC will be a 100 TeV proton collider based on novel high-field magnets. A similar project is being proposed in China.

In parallel to the development of future colliders, also the field of publications is undergoing profound changes. Physical Review Accelerators and Beams (PRAB) was founded in 1997 as a pioneering all-electronic diamond open-access journal, far ahead of its time. For many years PRAB was the fastest growing journal in the Physical Review family. Authors, editors and referees are highly internationalized.

In this paper, on the occasion of the acceptance of the 2019 USPAS Prize for Achievement in Accelerator Science and Technology, I sketch the history, status, and challenges of FCC and PRAB.

FCC: FUTURE CIRCULAR COLLIDERS

Hadron colliders with collision energies far exceeding those of the Large Hadron Collider (LHC) have been considered since decades, e.g. [1–6]. A European workshop in 2010 again highlighted the cost advantages of a tunnel larger than the LHC's [7]. With first hints of a Higgs boson of mass around 125 GeV, in 2011 a circular Higgs factory e^+e^- collider was proposed [8], whose performance would equally profit from a larger ring circumference.

In 2014, the Future Circular Collider study (FCC) was launched in response to the 2013 Update of the European Strategy for Particle Physics (ESPP). The emerging global FCC collaboration has been developing a ~100 km tunnel infrastructure in the Geneva area, linked to CERN, comprising a highest-energy highest-luminosity circular e^+e^- collider (FCC-ee) as a potential first step, and a pp-collider (FCC-hh) as the long-term goal, the latter defining the infrastructure requirements. Reaching the pp target energy of 100 TeV in a ring of 100 km circumference requires dipole magnets with a field of about 16 T, which is achievable with Nb_3Sn as superconductor. The FCC study also includes a High-Energy LHC (HE-LHC) based on FCC-hh magnet technology, the corresponding ion colliders plus a number of lepton-hadron collision options.

In late 2018 the FCC Conceptual Design report was released, in time for the next ESPP Update. It covers the physics opportunities [9], the lepton collider FCC-ee [10], the hadron collider FCC-hh [11], and the HE-LHC [12]. The FCC CDR results have led to an integrated program plan [13], where first the FCC-ee will operate for about 15 years, later followed by 25 years of FCC-hh operation. The entire FCC schedule extends almost through the end of the 21st century. This cost-effective staged long-term strategy of FCC-ee/FCC-hh, or CEPC/SPPC, is highly reminiscent of the successful earlier LEP-LHC sequence at CERN: The LEP design started in the 1970s and LHC operation is expected to end in the late 2030s, spanning more than 65 years. It is noteworthy that IHEP Beijing is proposing a similar set of consecutive lepton and hadron colliders for China, also in a ~100 km tunnel, named CEPC and SPPC, respectively, albeit both with somewhat lower luminosity and lower energy reach than their FCC counterparts (e.g., CEPC without $t\bar{t}$ operation, SPPC with an initial c.m. energy of 75 TeV) [14].

Figure 1 illustrates the FCC-ee and FCC-hh layouts: The two colliders follow a common footprint over most of the 97.8 km circumference. Only around the two primary interaction points (IPs) they are separated, by up to about 10 m. This is due to the 30 mrad crossing angle of the lepton collider and its asymmetric final-focus layout with smaller bending fields on the incoming side, introduced to minimize synchrotron radiation shining towards the detector, and stronger dipole fields after the IP [15]. The full-energy lepton injector (needed for top-up injection) follows the path of the hadron collider. The separation of the footprints at the IP conveniently allows the booster to bypass the experimental detectors of the lepton collider. The total duration of FCC tunnel construction is estimated at about 7 years. The first sectors could be ready for installation of technical equipment about 4.5 years after the start of civil construction.

FCC-ee plans to operate at four different beam energies — 45.6, 80, 142 and 182.5 GeV — corresponding to the production of Z, W and H boson, and the top quark, respectively. Figure 2 sketches how FCC-ee reaches highest luminosities and energies by combining ingredients and well-proven concepts of several recent colliders: The B-factories KEKB & PEP-II demonstrated the possibility of double-ring lepton colliders, high beam currents, positron sources with the required production rates, and top-up injection. At DAΦNE, another double-ring collider, still in operation, a novel collision scheme called crab waist was implemented in 2008. The crab waist tripled the DAΦNE luminosity [16]. All future circular colliders foresee the use of the crab-waist scheme. SuperKEKB, presently under commissioning, aims at operating with an extremely low β_y^* of 0.3 mm. It has already reached β_y^* of 2 mm, about equal or close to the design values of FCC-ee. LEP has operated at the highest lepton beam energy so far; it required a significant RF voltage and experienced the effects of synchrotron-radiation photons with MeV energies. VEPP-4M and LEP pioneered the precision

---

[*] frank.zimmermann@cern.ch

ISBN: 978-3-95450-223-3 ISSN: 2673-7000 doi:10.18429/JACoW-NAPAC2019-FRXBA3

APPLICATIONS AND OPPORTUNITIES FOR THE EMITTANCE EXCHANGE BEAMLINE

G. Ha†, M.E. Conde, J.G. Power, Argonne National Laboratory, Lemont, USA
M. Chung, J. Seok, UNIST, Ulsan, Korea

Abstract

Emittance exchange (EEX) provides a powerful method for controlling the longitudinal phase space distribution using the relatively simpler methods of transverse control. An EEX beamline was installed at the Argonne Wakefield Accelerator (AWA) facility in 2015. Several experiments important to wakefield acceleration, such as a high transformer ratio from shaped bunches, have already been demonstrated. A on-going program to seek new opportunities for the EEX beamline including beam's temporal profile shaping, THz radiation generation, time-energy correlation control, diagnostics uses of EEX, etc is underway. In this paper, we present the status of this program and discuss potential applications.

EMITTANCE EXCHANGE

Emittance exchange (EEX) is a unique beam manipulation method for exchanging the transverse and longitudinal phase spaces. The concept was first introduced in 2002 by M. Cornachia and P. Emma [1] with an incomplete exchange, and was subsequently modified to give a complete exchange in 2006 by K.-J Kim et al. [2]. A thorough and intuitive description of how EEX works is given in appendix A of Ref. [3]. The A0 photoinjector at Fermialb was the first facility to demonstrate the exchange of emittance [4], as well as the first to generate a bunch train [5]. These achievements provided new opportunities for phase space manipulation and inspired various new applications.

Early applications of EEX seeked to generate small transverse emittances. The idea was to make one of the transverse emittance extremely small (e.g. $\varepsilon_y \gg \varepsilon_x$) by a flat beam transform (FBT) [6] and then exchange the large emittance (ε_y) with the small longitudinal emittance ($\varepsilon_y \gg \varepsilon_z$) by using the EEX beamline. This emittance repartition would be a feasible application for a linear collider without damping rings. At the same time, it can ease the stringent transverse emittance requirements for linac based light sources such as XFEL and XFELO [2].

In addition to repartitioning, EEX provided a new way to control the longitudinal beam properties. Researchers started to work on utilizing this new opportunity and published many theory and simulation papers beginning in 2010. For example, a multi-slit was applied to the beam to generate multiple transverse beamlets, and EEX successfully converted it to a longitudinal bunch train [5]. Similarly, there were other concepts to extend this capability to X-ray generation such as Ref. [7-9]. At that time, a similar concept for triangular bunch generation arose [10]. Here, a transverse mask was applied to the beam to shape the electron beam's transverse distribution so that EEX converts it to a triangular longitudinal profile. Follow-up work continued to improve the quality of the method [3, 11]. It was finally demonstrated in 2016 at Argonne Wakefield Accelerator (AWA) facility [12].

AWA's EEX R&D program has two purposes: to experimentally demonstrate and improve EEX methods at the AWA facility and to explore new applications for EEX. This paper describes the most recent research taking place at the AWA facility and shows the potential benefits that EEX can provide to the Accelerator community.

ARGONNE WAKEFIELD ACCELERATOR FACILITY

The AWA facility installed and commissioned an EEX beamline in 2015 [13]. After the shutdown of the A0 photoinjector facility, the AWA facility currently has the only operating EEX beamline in the world. More recently, the AWA facility upgraded this beamline to a double EEX beamline, that is well equipped with diagnostics, to extend our EEX capability and research scope.

The upgraded EEX beamline is shown in Fig. 1 and its detailed parameters are listed in Table 1. This beamline consists of four sections: matching, 1st EEX, middle matching, and 2nd EEX. At the end of each EEX beamline, we have diagnostics for measurement of both the transverse and longitudinal phase spaces.

In addition to the EEX beamline, the AWA facility also has other complimentary capabilities enabling various proof-of-principle experiments vital to beam control [14]. These capabilities have been demonstrated through many collaborations with the AWA group and strongly support EEX R&D at AWA facility.

Table 1: The AWA Facility Operational Parameters and the EEX Beamline Design Parameters

AWA facility parameters	**Value**	**Unit**
Operational charge	0.01-100	nC
Laser spot radius	0.1-12	mm
Laser pulse length (FWHM)	0.3-10	ps
Maximum beam energy	62	MeV
EEX beamline parameters	**Value**	**Unit**
Bending angle	20	degree
Dipole-to-dipole	1.5	m
Dispersion of dogleg	0.7	m
R56 of dogleg	0.3	m

---

† gha@anl.gov

MAXIMIZING 2-D BEAM BRIGHTNESS USING THE ROUND TO FLAT BEAM TRANSFORMATION IN THE ULTRALOW CHARGE REGIME*

F. Cropp†, N. Burger, P. Denham, J. Giner Navarro, E. Liu, P. Musumeci, L. Phillips
Department of Physics and Astronomy, University of California, Los Angeles, CA, USA
A. Edelen, C. Emma, SLAC National Accelerator Laboratory, Menlo Park, CA, USA

Abstract

A method for maximizing 2-D beam brightness in an RF photoinjector in an ultralow charge regime (<1 pC) is presented. Theory and particle tracking simulations suggest that by utilizing the flat beam transform technique, normalized projected emittances smaller than 5 nm in one spatial dimension can be obtained at the UCLA Pegasus facility with up to 100 fC beam charge. This is achieved by starting the beam at the photocathode in a tunable magnetic field in order to introduce canonical angular momentum into the beam. A skew quadrupole triplet is then used to block-diagonalize the beam matrix and recover the vastly different eigenemittances as the projected emittances. Advanced emittance measurement techniques, including 4-D grid-based and two-quadrupole scan routines, are used for the reconstruction of the 4-D beam matrix. Preliminary measurements indicate a small emittance smaller than the thermal emittance of an equivalent round beam.

INTRODUCTION

A common metric for overall beam quality is the beam brightness, defined as

$$B_{4D} = \frac{Q}{\epsilon_{4D}}, \tag{1}$$

where Q is the beam charge and ϵ_{4D} is the 4-D emittance. The 4-D beam brightness is effectively the number of electrons in the 4-D phase space volume of the beam associated with the two transverse spatial dimensions. One can define a similar metric for one spatial dimension:

$$B_{2D} = \frac{Q}{\epsilon_{2D}}, \tag{2}$$

where ϵ_{2D} is the 2-D projected emittance in the desired spatial dimension. Maximizing 2-D beam brightness has broad applications to scenarios where a high-quality beam is only required in one spatial dimension, but there are less stringent requirements on the beam quality in the other. These applications include slab-geometry dielectric laser acceleration, where the phase space acceptance is extremely small in the small gap, but orders of magnitude larger in the other dimension. Another example of such an application is electron imaging of certain sample geometries where high resolution imaging is only desired in one spatial dimension.

There is also a fundamental reason to minimize the 2-D emittance that is related to the non-squeezing theorem from Gromov [1]. The theorem states that it is impossible to find a symplectic transformation that reshapes a finite 4-D spherical volume into an infinitely large cylindrical volume of smaller (phase-space) radius than the initial sphere. In the language of accelerator and beam physics, this means that there are strong limits on the freedom to reshape the phase space occupied by the beam in a transport system for a given target application. More quantitatively, not only is the phase space volume preserved, as the often cited Liouville theorem implies, but also Hamiltonian transport keeps invariant another set of quantities associated with the beam phase space distribution: the so-called eigenemittances [2]. The lowest of these invariants sets the limit on the smallest projected emittance achievable [3].

The Round to Flat Beam Transformation (FBT) makes use of emittance exchange to shrink the 2-D projected emittance in one spatial dimension at the expense of the other (while maintaining constant the 4-D phase space volume of the beam). The scheme is based on generating the beam in a region with non-zero magnetic field, which imparts canonical angular momentum on the beam and makes one eigenemittance much smaller than the other. The FBT transformation simply retrieves the eigenemittance as the projected emittance. The beam matrix of a round magnetized beam can be written as follows:

$$\sigma^{4D} = \begin{pmatrix} \sigma_c & 0 & 0 & \mathcal{L} \\ 0 & \sigma_{x'x'} & -\mathcal{L} & 0 \\ 0 & -\mathcal{L} & \sigma_c & 0 \\ \mathcal{L} & 0 & 0 & \sigma_{y'y'} \end{pmatrix}, \tag{3}$$

where σ_c is the beam size on the cathode, $\sigma_{x'x'} = \sigma_{y'y'}$ represent the initial angles in the beam and

$$\mathcal{L} = \frac{eB_c}{2\gamma\beta mc}\sigma_c^2 = \frac{L}{\gamma\beta} \tag{4}$$

is proportional to the angular momentum in the beam, where B_c is the magnetic field on the cathode, and γ and β are the relativistic factors. The beam eigenemittances can be found by [4]

$$\epsilon_1 = \frac{1}{2}\sqrt{-\mathrm{Tr}[(\sigma^{4D}J)^2] + \sqrt{\mathrm{Tr}[(\sigma^{4D}J)^2] - 16\det(\sigma^{4D})}}, \tag{5}$$

$$\epsilon_2 = \frac{1}{2}\sqrt{-\mathrm{Tr}[(\sigma^{4D}J)^2] - \sqrt{\mathrm{Tr}[(\sigma^{4D}J)^2] - 16\det(\sigma^{4D})}}, \tag{6}$$

where J is the symplectic matrix.

Calculating these quantities for the magnetized beam matrix in Eq. (3) it can be shown [5] that given a large enough

---

[*] NSF Grant No. PHY-1549132
[†] ericcropp@physics.ucla.edu

ISBN: 978-3-95450-223-3 ISSN: 2673-7000 doi:10.18429/JACoW-NAPAC2019-FRXBA5

THE ROLE OF LASER SHAPING IN MICROBUNCHING INSTABILITY SUPPRESSION AND SEEDED X-RAY FREE ELECTRON EMISSION

J. Tang, S. Carbajo*, F.-J. Decker, Z. Huang, J. Krzywinski, R. Lemons, W. Liu,
A. A. Lutman, G. Marcus, T. J. Maxwell, S. Moeller, D. Ratner, S. Vetter
SLAC National Accelerator Laboratory, Menlo Park, CA, USA

Abstract

Microbunching instability (MBI) driven by collective effects in an accelerator is known to be detrimental for the performance of X-ray free electron lasers. At the Linac Coherent Light Source (LCLS), laser heater (LH) system was installed to suppress the microbunching instability by inducing a small amount of slice energy spread to the electron beam. The distribution of the induced energy spread greatly effects MBI suppression and can be controlled by shaping the transverse profile of the heater laser. In this paper, we present theoretical and experimental results on utilizing a Laguerre-Gaussian 01 Mode (LG01) laser at LCLS to obtain better suppression of the instability. We demonstrate experimentally that Gaussian-shaped energy distribution is induced by LG01 mode LH and final microbunching gain is better suppressed. We finally discuss the role of LH spatial shaping in soft X-ray self-seeded (SXRSS) FEL emission and demonstrate that this LH configuration is capable of generating high spectral brightness FEL pulses.

INTRODUCTION

Control and reduction of microbunching instability (MBI) is central to accelerator physics and accelerator-based light sources, particularly free electron lasers (FEL) [1]. In a linear accelerator, MBI arises primarily from the interplay between longitudinal space charge of an electron beam (e-beam) and energy-dispersion correlations in e-beam optics. MBI is known to degrade emission performance of X-ray FELs and can be well suppressed from stochastic heating using a laser, namely a laser heater (LH). At the Linac Coherent Light Source (LCLS), the LH consists essentially of an electron beam undulator and a co-propagating infrared (IR) laser that modulates and increases the energy spread of the e-beam by about one order of magnitude and without exceeding FEL tolerances [2]. The shape and magnitude of this modified e-beam energy distribution depends highly on the transverse intensity distribution of the IR laser. The current laser at the LCLS LH employs a Gaussian transverse beam distribution, which has shown to partially suppress MBI and result in a greater FEL intensity by an order of magnitude [3].

Recent theoretical studies have investigated cylindrically symmetric and other non-conventional laser beam shapes to provide better suppression of microbunching [4–6]. For instance, a transverse Laguerre-Gaussian 01 (LG01) mode provides a mathematically ideal solution to suppressing MBI. This beam mode has been proposed because under ideal laser and electron beam conditions the suppression of microbunching is at best more than 23 times better than that of an equivalent transversely Gaussian laser.

Here, we present the first experimental demonstration of effective MBI suppression using a LG01 transverse mode laser at the LCLS LH, and we compare the improved results with respect to MBI suppression using the Gaussian-shaped laser. The effects on MBI suppression are characterized by multiple downstream measurements, including analysis of the e-beam's longitudinal phase space and coherent radiation spectroscopy. We also experimentally investigate its impact on soft X-ray self-seeded (SXRSS) FEL emission, one of the most advanced operation modes of a FEL for which controlled suppression of MBI is critical [7].

METHODS AND RESULTS

The LH transverse profile, originally Gaussian at LCLS, was converted to a LG01 distribution using a 1-inch diameter spiral phase plate (SPP), as in Fig. 1. The SPP is a diffractive optic with 16 steps, each of increasing thickness, circumferentially around the plate resembling a spiral stair case. This spiral stair case writes an increasing spiral phase onto the beam for a total phase change of 2π. The polarization of the laser is unaffected by this type of diffractive optic since the SPP only effects the phase structure of the beam. A short distance after interaction with the plate, a null in the field amplitude at the center of the laser due the phase singularity is generated and is maintained as the laser propagates. For best diffractive efficiency, two Galilean telescopes were placed before and after the SPP to fill the full clear aperture and then to restore the laser to proper size for propagation to the undulator respectively.

The first diagnostic, directly downstream of the LH where the e-beam's energy is 135 MeV, is a longitudinal phase-space spectrometer. The slice energy distribution is extracted from the central time slice of the streaked e-beam. For either transverse shape, the width of the energy distribution can be tuned by varying the IR laser energy. However, the Gaussian laser distribution is known and measured to provide a double-horn structure instead of an ideal Gaussian-like e-beam energy distribution for best energy suppression. We prove, according to our simulation, that we can achieve Gaussian-like e-beam heating with varying width by simply tuning the LG01 mode energy. Figure 2 shows that we can heat the e-beam up to 68 eV energy spread (Fig. 2(a)) while preserving a Gaussian energy distribution (Fig. 2(b-e)). We would like to note that when the e-beam is heated to 20-

---

* scarbajo@slac.stanford.edu

RARE ISOTOPE BEAMS AND HIGH-POWER ACCELERATORS*

J. Wei†, Facility for Rare Isotope Beams, Michigan State University, East Lansing, MI, USA

Abstract

Facilities for rare isotope beams provide tools for nuclear science research and tools for applications ranging from fundamental nuclear structure and dynamics to societal benefits in medicine, energy, material sciences and national security. State-of-the-art rare isotope facilities can be based on an isotope separation on-line (ISOL) approach using mostly high-power proton beams striking a thick target where the isotopes are produced in the target, or an in-flight fragment separation (IF) approach using high-power heavy ion beams striking upon a thinner target where the isotopes continue out of the target followed by fragment separation. This tutorial class introduces high power hadron accelerators as driver machines for rare isotope production, summarizing the key design philosophy, physical and technical challenges, and current world-wide development status. As an example, the Facility for Rare Isotope Beams (FRIB) project is used to illustrate the process of establishing such facilities.

MOTIVATION

The primary goals of studies using rare isotope beams are to (1) understand the origin of elements and model extreme astrophysics environments (nuclear astrophysics); (2) develop a comprehensive model of atomic nuclei (nuclear structure); (3) use atomic nuclei to test fundamental symmetries and search for hints of new particles (fundamental physics); and (4) explore new applications of isotopes and solutions to societal problems including medicine, energy, material sciences and national security (applications). Such studies may answer basic questions such as: (1) How does subatomic matter organize itself and what phenomena emerge? (2) How did visible matter come into being and how does it evolve? (3) Are the fundamental interactions that are basic to the structure of matter fully understood? (4) How can the knowledge and technological progress provided by nuclear physics best be used to benefit society? Current research has demonstrated that to answer such challenging questions, studies at the extremes of neutron and proton number are necessary [1].

A chemical element is a species of atom having the same number of protons in their atomic nuclei. Isotopes are variants of a particular chemical element which differ in neutron number and, consequently, in nucleon number. There exist nearly 300 stable nuclei in natural environment. As shown in Fig. 1, more than 3000 nuclei have been discovered in laboratories – the so called rare isotopes [2]. There are an unknown number (predicted 5000 ~ 12,000) of nuclei in the unexplored territory to be discovered. For exploration on the broad frontiers of nuclear studies discussed above, we must deal with a diverse selection of isotopes both near and far from the more common, stable isotopes found in nature.

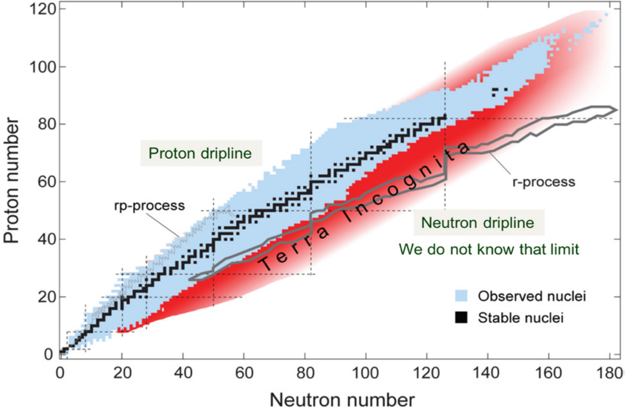

Figure 1: Chart of elements and isotopes showing about 300 stable nuclei found in natural environment (black), more than 3000 nuclei discovered in the laboratories (blue), and unknown number in the unexplored territory (red).

APPROACHES

Although human beings have mined and crafted elements like copper as early as 7,000 B.C., rise of modern chemistry and the discovery of many more elements occurred as late as 1700's and further accelerated with the discovery of Dalton's atomic theory (1804) and Mendeleev's periodic table (1869). In 1910, F. Soddy discovered isotopes and a new dimension of atomic nuclei was revealed. In 1934, F. Joliot and I. Curie made the first "artificial" isotopes by bombarding B, Mg, and Al with alpha particles from Po. The rate of new isotope discovery peaks upon introduction of new experimental methods: mass spectroscopy, accelerators, and reactor, as shown in Fig. 2 [2].

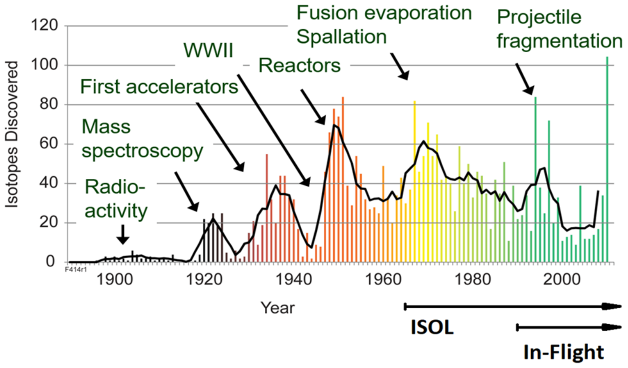

Figure 2: Annual discovery of new isotopes by various kinds of experimental methods [2].

During the recent decades, discoveries of new isotope have primarily relied on two accelerator-based methods: the isotope separation on line (ISOL) used since around

---

*Work supported by the U.S. Department of Energy Office of Science under Cooperative Agreement DE-SC0000661 and the National Science Foundation under Cooperative Agreement PHY-1102511.

† wei@frib.msu.edu

ISBN: 978-3-95450-223-3 ISSN: 2673-7000 doi:10.18429/JACoW-NAPAC2019-FRCHC2

POSSIBILITIES FOR FUTURE SYNCHROTRON RADIATION SOURCES

M. E. Couprie*, Synchrotron SOLEIL, Gif-sur-Yvette, France

Abstract

The landscape of present accelerator based light sources is drawn. The photon beam brightness increases opens new areas of user applications, both with the arrival of low emittance rings getting closer to diffraction limit and the advent of X-ray Free Electron Lasers, providing agility in terms of performance (two colors, attosecond pulse....). Finally, the path towards light sources using alternate accelerator schemes, such as plasma acceleration is discussed.

INTRODUCTION

The 20th century saw the rapid development of vacuum tubes, in particular the klystron [1] where bunching is a key process for wave amplification. Accelerator based light sources rely on the emission of synchrotron radiation, first observed in 1947 [2], by accelerated relativistic particles of Lorentz factor γ subjected to a magnetic field, generated for example in bending magnets in circular accelerators. The radiation is collimated in a thin cone of typically $1/\gamma$ angle thanks to the relativistic projection of angles. It covers a wide spectral range from the infra-red to the X-rays. It is pulsed, with a repetition rate and bunch duration depending on the accelerator type. Synchrotron radiation from Insertion Devices (ID) (undulators and wigglers) which create a periodic permanent magnetic field (amplitude B_u, period λ_u) with alternated poles was considered in the mid 20th century [3]. For a planar undulator creating a vertical sinusoidal field, the radiation from the different periods N_u can constructively interfere and emit on-axis at the resonant wavelength λ_r and n^{th} order odd harmonics: $\lambda_r = \lambda_u(1 + K_u^2/2 + \gamma^2\theta^2)/2n\gamma^2$, with K_u the undulator deflexion parameter $K_u = 0.94\lambda_u(cm)B_u(T)$ and θ the observation angle. Variable polarisation can be provided, depending on the undulator helicity. The wavelength can be tuned by the electron energy or by the undulator magnetic field. It is well collimated ($\sigma'_p = \sqrt{\lambda/4L_u}$), has a small source size ($\sigma_p = \sqrt{\lambda_r L_u}/2\pi$), resulting photon emittance ($\epsilon_p = \sigma_p\sigma'_p = \lambda_r/4\pi$), and an associated Rayleigh length $Z_p = \sigma_p/\sigma'_p = L_u/\pi$ [4, 5]. The homogeneous linewidth $\Delta\lambda/\lambda = 1/nN_u$ can be broadened with multi-electron emission (emittance and energy spread terms).

Stimulated emission, in black-body studies [6], was first analysed as addition of photons to already existing ones, and not as the amplification of a monochromatic wave with phase conservation. In «quantum» microwave sources (masers (microwave amplification by stimulated emission of radiation)), the klystron electron beam amplification is replaced by stimulated emission of excited molecules introduced in a microwave cavity resonant for the frequency of the molecule transition [7]. The use of an optical resonator [8] was proposed to extend the radiation to the optical spectral range, and the first Ruby laser was achieved [9]. The vacuum tubes came back into play with the invention of the Free Electron Laser (FEL) [10] with free electrons in an undulator field to replace the molecule in optical cavity for short wavelength operation. A light wave of wavelength λ interacts with the electron bunch in the undulator, inducing an energy modulation of the electrons; which is gradually transformed into density modulation at λ, the phased electrons then emit coherently emission at λ and its harmonics. This wave-electron interaction can lead to a light amplification to the detriment of the electron kinetic energy. The small signal gain is proportional to the electronic density, varies as γ^{-3}, and grows with the undulator length. FELs can be implemented on various accelerators : storage rings with rather long electron bunches (10-30 ps), linacs with 10 fs -10 ps bunch, energy recovery linac with short pulses, few turn recirculation and low power consumption... FELs are tuneable by merely modifying the magnetic field of the undulator in a given spectral range set by the electron beam energy. On linacs, FEL radiation can be emitted in ultra short pulses. The polarization depends on the undulator configuration. It can easily be changed form linear to circular, using suitable undulators.

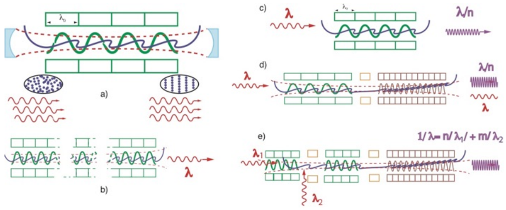

Figure 1: Free Electron Laser configurations : a) oscillator, b) SASE, c) seeding d) HGHG e) EEHG.

Different configurations are used (see Fig. 1). In the historical oscillator mode (a), the synchrotron radiation spontaneous emission stored in an optical cavity enables interaction on many passes. FEL oscillators cover a spectral range from THz to VUV, where mirrors are available. FEL was first achieved in 1977 on a superconducting linac (Stanford, USA) in the infra-red [11]. and then in 1983 on the ACO storage ring (Orsay, France) [12] in the visible and coherent harmonic generation was measured. FEL oscillators cover a spectral range from the THz to the VUV [13]. In the Self Amplified Spontaneous Emission (SASE) (b) setup [14–16], the spontaneous emission is exponentially amplified thanks to a collective instability in a single pass. Once the saturation is reached, the amplification process is replaced by a cyclic energy exchange between the electrons and the radiated field. The emission usually presents poor longitudinal coherence properties, with temporal and spectral spiky emission [17], resulting from non correlated trains of pulses. SASE suits for short wavelength FELs because of the limited perfor-

---

[*] couprie@synchrotron-soleil.fr